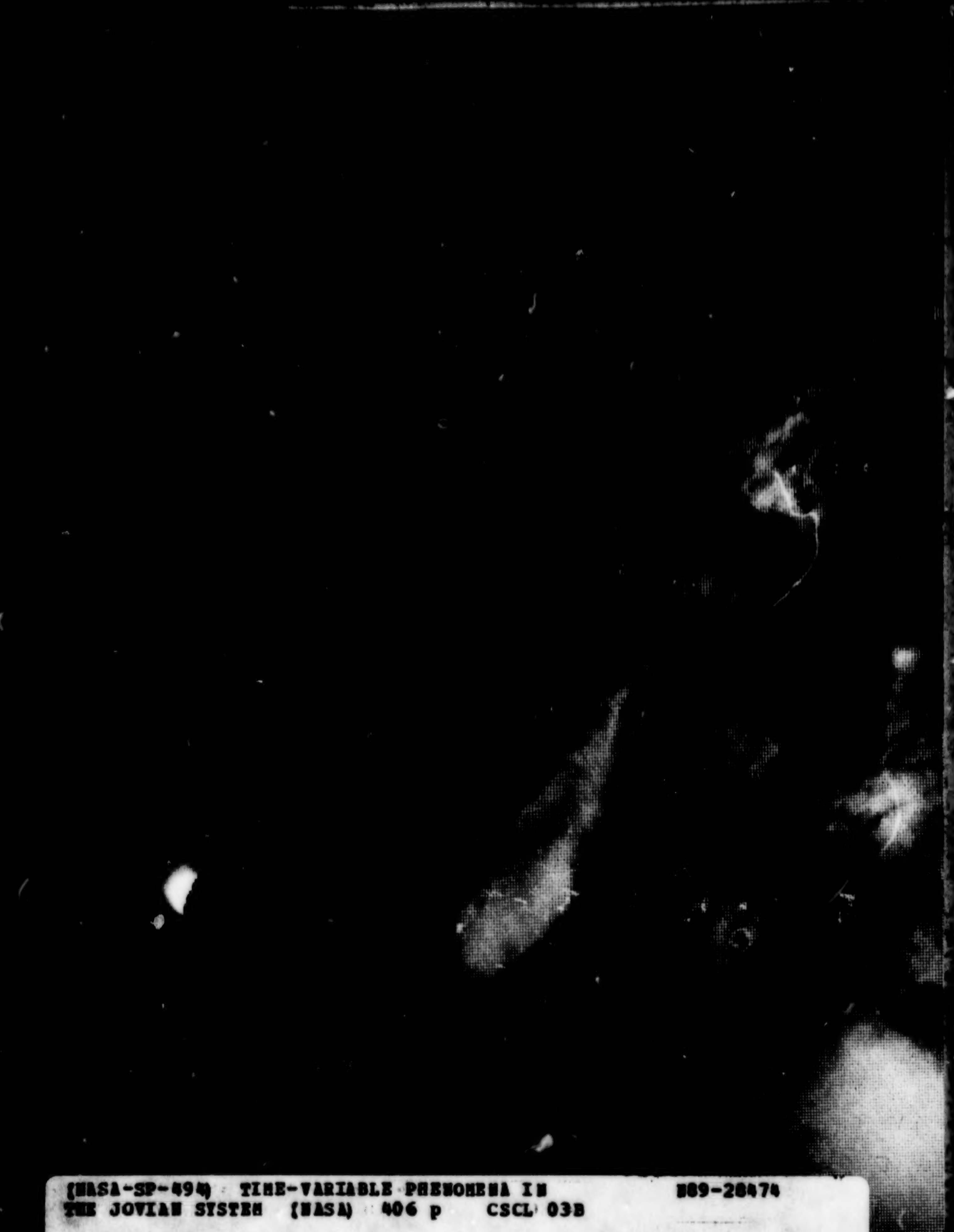

(NASA-SP-494) TIME-VARIABLE PHENOMENA IN THE JOVIAN SYSTEM (NASA) 406 p CSCL 03B

N89-26474

Unclas

H1/91 0157237

TIME-VARIABLE PHENOMENA in the JOVIAN SYSTEM

ORIGINAL CONTAINS
COLOR ILLUSTRATIONS

NASA SP-494

TIME-VARIABLE PHENOMENA in the JOVIAN SYSTEM

Proceedings of the Workshop on Time-Variable Phenomena in the Jovian System

Lowell Observatory, Flagstaff, Arizona
25–27 August 1987

Edited by

MICHAEL J. S. BELTON
NATIONAL OPTICAL ASTRONOMY OBSERVATORIES, TUCSON

ROBERT A. WEST
JET PROPULSION LABORATORY, PASADENA

JÜRGEN RAHE
NATIONAL AERONAUTICS AND SPACE ADMINISTRATION, WASHINGTON

With the assistance of

MARGARITA PEREYDA

NASA
National Aeronautics and Space Administration
Office of Management
Scientific and Technical Information Division
Washington, DC 1989

The cover: Voyager 1 image showing active volcanic plumes on Jupiter's moon Io.

Library of Congress Cataloging-in-Publication Data

Time-variable phenomena in the Jovian system.

"NASA SP-494."
"Proceedings of the Workshop on Time-variable Phenomena in the Jovian System, Lowell Observatory, Flagstaff, Arizona, 25-27 August, 1987."—P.
Includes index.
1. Jupiter (Planet)—Congresses. I. Belton, M. J. S. II. West, Robert A. III. Rahe, Jürgen. IV. Workshop on Time-variable Phenomena in the Jovian System (1987 : Lowell Observatory)
QB661.T55 1989 559.9'25 88-25450

Contents

Preface ix

1. Introduction 1

Part I SATELLITE PHENOMENA and RINGS 9

2. Dynamic Geophysics of Io 11
Alfred S. McEwen, Jonathan I. Lunine, and Michael H. Carr

3. Io and Europa: The Observational Evidence for Variability 47
Robert R. Howell and William M. Sinton

4. Sulfur Lakes and Silicate Flows: Thermal Emission from Io's Hot Spots 63
Jonathan I. Lunine (Contributed Paper)

5. Search for Temperature Effects in the Photometry of the Ionian Dayside 71
Damon P. Simonelli and Joseph Veverka (Contributed Paper)

6. Io's Atmosphere and Neutral Clouds 75
Nicholas M. Schneider, William H. Smyth, and Melissa A. McGrath

7. Time-varying Orbits and Tidal Heating of the Galilean Satellites 100
Richard Greenberg

8. Anticipated Time Variations in (Our Understanding of) Jupiter's Ring System 116
Mark R. Showalter

Part II MAGNETOSPHERIC PHENOMENA, IO'S TORUS, AND AURORAE 127

9. Possible Time Variations of Jupiter's Magnetic Field 129
E. H. Levy

10. Time Variability in Jupiter's Synchrotron Radiation 139
Imke de Pater and Michael J. Klein

11. Systematic Observations and Correlation Studies of Variations in the Synchrotron Radio Emission from Jupiter 151
M. J. Klein, T. J. Thompson, and S. Bolton (Contributed Paper)

12. Jupiter Decametric Radiation 156
Françoise Genova, Philippe Zarka, and A. Lecacheux

13. Solar Wind Effect on Jovian Low-Frequency Magnetospheric Radio Emissions from Ground-based and Spacecraft Observations 175
Philippe Zarka and Françoise Genova (Contributed Paper)

14. New Longitude System for the Jovian Magnetosphere 179
B. R. Sandel and A. J. Dessler (Contributed Paper)

15. Energetics, Luminosity, and Spectroscopy of Io's Torus 183
Darrell F. Strobel

16. Torus-Magnetosphere Coupling 196
Fran Bagenal

17. The Aurora and Airglow of Jupiter 211
John Clarke, John Caldwell, Tom Skinner, and Roger Yelle

18. Spectral Analysis of Jovian Auroral Emissions 221
G. R. Gladstone and T. E. Skinner (Contributed Paper)

19. Jupiter's Aurora: Detection of Quadrupole H_2 Emission 229
L. Trafton, J. Carr, D. Lester, and P. Harvey (Contributed Paper)

20. Is Ethane Varying in the Jovian North Polar "Hot Spot"? 234
Theodor Kostiuk, Fred Espenak, and Michael J. Mumma (Contributed Paper)

Part III PHENOMENA IN THE JOVIAN ATMOSPHERE 243

21. Time-Variable Nature of the Jovian Cloud Properties and Thermal Structure: An Observational Perspective 245
R. F. Beebe, G. S. Orton and R. A. West

22. Spatial and Temporal Variations in the Atmosphere of Jupiter: Polarimetric and Photometric Constraints 289
Barbara E. Carlson and Barry L. Lutz (Contributed Paper)

23. Photometric Properties and Classification of Small Jovian Cloud Features 297
W. Reid Thompson and Carl Sagan (Contributed Paper)

24. Great Scale Changes in the Belts and Zones of Jupiter: The Outbursts of Activity and Disturbances in the SEB and NTrZ-NTBs Regions 306
Agustin Sanchez-LaVega (Contributed Paper)

25. Jupiter: Short-Term Variations of the Mean Zonal Flow at the Cloud Level 311
Sanjay S. Limaye (Contributed Paper)

26. Temporal Behavior of Jupiter's Meteorology 324
F. M. Flasar

27. Variations in the Jovian Atmospheric Composition and Chemistry 344
Pierre Drossart, Régis Courtin, Sushil Atreya, and Alan Tokunaga

28. Spatial and Temporal Variations of NH_3 Abundance and Cloud Structure in the Jovian Troposphere Derived from CCD/Coude Observations 363
Kevin Baines, William Hayden Smith, and Claudia Alexander (Contributed Paper)

29. A New Analysis of the Jovian 5 μm IRIS Spectra 371
E. Lellouch, P. Drossart, T. Encrenaz, G. Guelachvili, N. Lacome, and G. Tarrago (Contributed Paper)

30. Jovian Lightning 374
L. J. Lanzerotti, K. Rinnert, E. P. Krider, and M. A. Uman

31. Jupiter Lightning Locations 384
Laurance R. Doyle and William J. Borucki (Contributed Paper)

Index 391

Preface

The next element in the National Aeronautics and Space Administration's program of exploration of the outer solar system is the Galileo mission, a joint enterprise of the United States and the Federal Republic of Germany. Scheduled for launch in late 1989, it consists of an orbiter spacecraft and atmospheric probe that should arrive at Jupiter during December, 1995, approximately 22 years after an initial reconnaissance of the planet by the Pioneer 10 spacecraft and almost 17 years after the highly productive exploratory surveys of the entire system by Voyagers 1 and 2.

Unlike its predecessors, Galileo will be able to directly sample the composition and physical environment in Jupiter's atmosphere, and then, as engineers at the Jet Propulsion Laboratory navigate the orbiter spacecraft from one galilean satellite to another, it will spend roughly 20 months in orbit characterizing the morphology, chemistry, and active processes on satellite surfaces; directly probing and mapping the extensive and energetic magnetosphere; following magnetospheric interactions with Io, Europa, and Jupiter's upper atmosphere; investigating the evolution of possible structures in the planet's ring system; and diagnosing the forces that presumably cause the ever-changing dynamic structures—traced out by clouds—that dominate the face of the planet itself. If all goes well we can expect the prime mission to extend well beyond the nominal end-of-mission in October 1997, and the Galileo characterization of Jupiter phenomena may easily continue productively into the next millennium. Unlike the four earlier flyby encounters, each of which was completed in a period of a few days, we can expect the Galileo mission to fully open up the dimension of *time* in the study of jovian phenomena.

When such exciting prospects are incorporated with the rich history and future capabilities of Jupiter studies utilizing astronomical techniques from the ground and from earth-orbit, it is not surprising to find growing research interest in a concerted *international* effort to coordinate an observational program that will provide a solid factual basis for the future study of time-variable phenomena in the Jupiter system. Called the International Jupiter Watch (IJW), this "grass-roots" organization seeks to build on the rich legacy of *Voyager* and *Pioneer*, and the more than two decades of ground-based and Earth-orbital planetary astronomy, to ensure that, by the time Galileo is injected into orbit, planetary science will be in the best possible position to advance our knowledge of the jovian system. As this effort began it became clear to the organizers of the IJW that 1987, standing almost midway between the epochs of Voyager and Galileo, was an auspicious time for a detailed appraisal of the status of our knowledge and an attempt to identify the critical scientific and observational issues that need to be addressed in the time between then and the beginning of the Galileo mission at Jupiter in 1995. It was for this reason that the workshop on "Time-Variable Phenomena in the Jovian System," at which most of the material in this book was presented and discussed, was held at the Lowell Observatory in August 1987.

PRECEDING PAGE BLANK NOT FILMED

The material in this volume emphasizes time-variable, dynamic phenomena that need continuing and systematic observations for their elucidation. It does not attempt to give a comprehensive review of the full range of our knowledge of the Jovian system; rather we view it as a companion to the several excellent books that have already appeared. These include the large compendium of results that appeared after the Pioneer missions (Jupiter, Gehrels, 1976), and the post-Voyager books devoted to the satellites (Morrison, 1982), the jovian magnetosphere (Dessler, 1983), and Jupiter's atmosphere (Allison and Travis, 1986).

It is a great pleasure to thank the following colleagues who helped organize the workshop, participated in its development, and helped review and prepare the articles published here: M. Allison, S. Atreya, W. A. Baum, R. Beebe, A. Boishot, R. A. Brown, G. Bjoraker, J. Caldwell, M. Carr, W. Cochran, I. de Pater, A. Dessler, Th. Encrenaz, A. Eviatar, U. Fink, F. Fanale, P. Feldman, L. Frank, S. Gulkis, B. Hapke, J. Head III, G. E. Hunt, D. M. Hunten, T. V. Johnson, A. Ingersoll, M. J. Klein, M. Kivelson, A. Lacis, S. Limaye, G. W. Lockwood, B. L. Lutz, A. V. Morozhenko, H. Masursky, R. L. Millis, W. Moos, P. Morgan, G. Neukum, P. Nicholson, C. Russell, B. Sandel, N. Sharp, D. Shemansky, K. Simon, W. Sinton, L. Soderblom, C. Stoker, L. Trafton, V. G. Teifel, and J. Warwick. We would also like to thank the directors of Lowell Observatory and of the National Optical Astronomy Observatories for institutional support without which it would not have been possible to complete either the workshop or this book. Margarita Pereyda acknowledges support under the National Science Foundation Minority Research Program at the National Observatories. Michael Belton acknowledges support from NASA grant PR #10-40077. Robert West acknowledges support from the NASA Planetary Atmospheres Program. The National Optical Astronomy Observatories are operated by AURA Inc. under contract to the National Science Foundation.

Michael J. S. Belton
Robert A. West
Jürgen Rahe

References

Allison, M., and L. D. Travis (Eds.) (1986). *The Jovian Atmospheres*. NASA Conf. Pub. 2441, NASA, Washington, D.C.

Dessler, A. J. (Ed.) (1983). *Physics of the Jovian Magnetosphere*. Cambridge Univ. Press, Cambridge.

Gehrels, T. (Ed.) (1976). *Jupiter*. Univ. of Arizona Press, Tucson.

Morrison, D. (Ed.) (1982). *Satellites of Jupiter*. Univ. of Arizona Press, Tucson.

1

Introduction

An introduction is perhaps unusual in a book dealing with the proceedings of a scientific workshop. However, the contents of this book cover such a wide range of scientific interests and observational techniques that there seems obvious value in providing a short overview of its contents in order to unify their presentation. The book is intended to be a contemporary assessment of the state of our knowledge of dynamic processes in the jovian system that should help to stimulate new research initiatives to answer some key questions about the intriguing and complex processes responsible for much that is observed. It is also intended to serve as a reference point and therefore provides summaries of both the theoretical and observational foundations upon which future studies will be based.

The book is organized into three sections: satellite phenomena and rings: magnetospheric phenomena, Io's torus, and aurorae; and a final section on atmospheric phenomena on Jupiter itself. Each of the chapters discusses the dynamic or stationary nature of a particular part of the jovian system. Some chapters provide the theoretical framework for understanding various phenomena and interpreting the observations; others describe the evidence and nature of observed change or the lack of it. A few chapters give an historical perspective and attempt a comprehensive synthesis of the current state of knowledge. The contributed chapters focus on new results or approaches to specific problems. The remainder of this introduction gives an overview of the main themes of the review chapters and draws attention to a few of the key scientific issues that are addressed.

SATELLITE PHENOMENA AND RINGS

Io is, of course, the central player in the satellite-torus-magnetosphere ménage à trois. It is the most active geologic structure in the solar system, characterized by interior processes that are driven by tidal stresses arising from a large orbital eccentricity forced by orbital resonance with Europa and Ganymede. It is appropriate, therefore, that the discussion of Io dominates this section of the book.

McEwen et al. give a comprehensive review of the geophysics and geochemistry of Io starting with ideas about tidal heat dissipation in the interior, its transport by convection, and the possibility of rising magma parcels in the crust, which is thought to be at least 30 km thick in the region where high mountains are located. Bulk composition is primarily silicate, based on Io's density and the presence of considerable (up to 10 km) topographic relief, but the surface is coated with sulfur compounds. The abundance of sulfur and silicates in the upper crust is controversial, as is the question of the composition of some of the lava flows. Sulfur is present in large amounts, but the hottest flows may be silicate. Early identifications of quenched sulfur allotropes based on color have been hotly contested because of the instability of the quenched state and the details of the spectrophotometry.

The thermodynamics and physical processes involved in the volcanic eruptions discovered on Io are quite unlike those found on Earth because the physical chemistry of the volatiles driving eruptions is very different in the two cases. In addition, the plumes on Io erupt into a near-vacuum, low-gravity environment that allows them to extend to great heights and spread over very large areas. Two classes of plumes are present, and differences between them (plume altitude, lifetime, temperature, latitude distribution, surface deposits) may reflect differences in the composition of magma and volatile reservoirs (Prometheus type driven by SO_2, and Pele type by S_2). One large active feature, Loki, that has been observed with ground-based instruments for the past eight years, is especially complex and has both components.

Several different observational methods are employed to detect possible changes in the surface properties of Io owing to eruption of hot fluid, resurfacing by particulates and frosts, or changes in the reflectivity due to warming or cooling. Howell and Sinton review the methods, and chapters by Lunine and by Simonelli and Veverka report on particular efforts to understand the thermal infrared and reflected sunlight signatures, respectively.

Howell and Sinton summarize the ground-based observations, dating back to 1964, that suggest temporal variations and that, in recent years, have been powerful enough to reveal the locations, sizes, and temperatures of individual lava lakes. There is also evidence that Europa may be geologically active; however, the validity of the evidence for this is controversial.

A variety of ground-based infrared techniques that have come into use during the past several years provide detailed information on the location, size, and temperature of individual lava lakes. Speckle interferometry can be used any time Io is visible and therefore is a particularly valuable tool to measure time dependencies. Infrared polarimetry gives location and flux, provided the spot is observed during at least a quarter of Io's orbit, but suffers from a confusion limit when several sources are present. The most precise information on the location and size of small hot regions comes from mutual satellite occultation events that occur only a few times every six years. Eclipse photometry has been in use for some time but gives less specific information regarding spot location and probes only a limited range of longitudes. These techniques have proved useful for monitoring lava lake activity in the post-Voyager era even though their full potential, which requires coordinated observations at several wavelengths, has not yet been realized.

The total heat flow from the interior of Io is a quantity of fundamental importance and seems to be concentrated in the vicinity of one or two active regions. If lifetimes of active regions are roughly several decades or less, we may be seeing a larger than average heat flow at the current epoch. Loki, a large feature observed by Voyager instruments, is still active but its thermal emission is declining. The plume from Pele was prominent during the Voyager 1 encounter but absent four months later when Voyager 2 flew by. Later, a lava lake that was not present during the Voyager encounters appeared and disappeared. The ground-based data confirm the intepretation of Voyager observations that holds that two types of eruptions are common: long-lived small plumes like Prometheus, and a larger, hotter, and much shorter-lived type like Pele.

Disk-integrated photometry has been carried out for over two decades and provides the longest baseline for monitoring the Io surface, but gives information only on the hemispheric average that is insensitive to the comings and goings of individual eruptions. Early reports of posteclipse brightening suggested the presence of a condensing atmosphere, but measurements during the past decade failed to reproduce the earlier results. Local diurnal SO_2 frost deposits near the terminator may be seen in the Voyager images as discussed by Simonelli and Veverka.

The available knowledge and expectations for the state and stability of Io's atmosphere are addressed in the chapter by Schneider et al. Competing models differ by four orders of magnitude in terms of the surface column density. One model calls for subsurface cold-trapping and an atmosphere so tenuous that impinging plasma particles impact the surface and sputter atoms and molecules directly to a gravitationally bound corona or to near-Io orbit around Jupiter where neutrals reside in an irregularly shaped cloud. A second scheme has a thicker, more dynamic atmosphere supplied by subliming SO_2 frost on the dayside, with near-supersonic flows leading to condensation on the nightside. This subliming atmosphere can be collisionally thick, in which case dayside sputtering takes place above the exobase. The size of the atmosphere and the radial extent of the exobase may vary with the supply of gas from plumes. A third model envisions the process of sublimation of surface frosts to be of minor importance compared to the direct supply of gas from active volcanic vents.

Whether or not plume activity directly influences phenomena in the torus depends on the actual nature of the Io atmosphere and its interaction with the magnetosphere. As Schneider et al. discuss, it is possible but by no means certain that changes in plume activity lead to changes in the torus. If the main process for supplying the torus is sputtering from the surface or from an extended exobase, volcanic activity may provide only very weak modulation.

Schneider et al. also cover the work that has been done on neutral sodium, which although it constitutes only about 1 percent of the composition of the atmosphere and torus, is relatively easy to observe owing to the large resonant cross section at the D-lines. Over the long term, sodium densities have been roughly constant to within a factor of two, in contrast to larger variations in ion and electron densities. Other puzzling phenomena occur, such as the occasionally observed high-speed neutral jets, spawned by charge exchange, sometimes at peculiar directions with respect to the orbit plane. We now have many more questions than answers about most of the Io atmosphere-torus-magnetosphere interaction. Continued observation, using better equipment in a more coordinated fashion than in the past, together with more complete modeling and laboratory data, are the only means to address many of the outstanding issues.

In his review of the orbital evolution of the Galilean satellites, Greenberg explains why it is important that we get a much better understanding of the temporal characteristics of the heat flow. The energy that produces the active volcanoes and large heat flux comes from Io's orbital energy through the medium of tides raised on Jupiter and by orbital interaction with Europa and Ganymede. Physical models of tidal dissipation in Jupiter's interior lead us to believe that jovian tidal torques cannot contribute much to modify Io's orbit. Work by Lieske (1987) and by Greenberg on the rate of change of Io's mean motion determined from timing satellite eclipses during the last 300 years, show it to be much smaller than expected for Io's current heat flux. The implication is that Io's present energy release is anomalously high, because energy generation, storage, and/or release is episodic. As Greenberg comments, "The indication from study of past orbital motion is that Io was less active when airplanes and telephones were being invented." Clearly, the Io heat flux is something we want to keep track of in the next decades.

The same forces that lead to the liberation of heat in Io's interior also work at Europa, and there are suspicions that heating in its interior may be large enough to produce geysers or other temporally variable phenomena that might be observed in the future. At present there are only two observations that suggest contemporary activity on Europa, and both are controversial. Howell and Sinton review the evidence, which consists of a bright region near the limb in one of the Voyager images, and an anomalously high flux during the first ground-based observation of Europa at 4.8 μm. None of the other satellites is seen to be or is expected to be presently active, although surface morphology of Ganymede shows it to have been active in the past, possibly in connection with an orbital resonance.

An examination of time-variability in the jovian system could not be complete without an assessment of the jovian ring system, and the chapter by Showalter summarizes current knowledge. The smaller, but most visible, ring particles can be strongly influenced by Lorentz and plasma drag forces and by sputtering. Typical lifetimes of micron-size particles are estimated to be in the range of 10 to 1000 years. It is not possible with the limited data we now have (a few Voyager images and detections from ground-based instruments) to perceive any temporal variations, but one should not be surprised to find differences among Galileo camera images during the two-year nominal mission in the next decade.

MAGNETOSPHERIC PHENOMENA, IO's TORUS, AND AURORAE

In one way or another the magnetosphere is related to almost every other aspect of the jovian system. The ultimate source of magnetospheric energy is of course the electrically conducting convective interior of Jupiter, and what we may learn about the time-variable nature of the magnetic field may help tell us about the time scales, spatial scales, and organization of the convective motion of the deep interior.

In a chapter on planetary dynamos, Levy guides us through the basic concepts of planetary magnetic field generation. The ideas are motivated primarily by observations of the fields of the Earth and Sun. These are the only solar system bodies for which the time-variability of their magnetic fields has been measured, and the observable aspects of the two dynamos could hardly be more dissimilar. The dipole component of the geomagnetic field is quasi-stationary with aperiodic polarity reversals; the dipole part of the solar field oscillates with a period of 22 years. One of the key questions is whether the jovian dynamo resembles either the terrestrial or solar cases. Even if its character is similar to that of the terrestrial field, convective motions must be more vigorous by a factor of 1000, so we might expect to see major changes on time scales of decades.

High-order multipole fields are present at the surfaces of both the Earth and Sun and display a variety of temporal behavior. The geomagnetic high-order fields drift with respect to the solid body and continuously reform on time scales of about 1000 years. We expect that high-order fields near Jupiter's surface are time-variable for some of the same reasons as for the Earth's field, and measurement of their amplitudes and directions may tell us something about the nature of convection in the interior. Unfortunately, the Galileo orbiter will not penetrate deep enough into the field to measure many high-order terms, and we are dependent on remote sensing methods, such as mapping of synchrotron emission, to probe changes in the inner field. It remains to be seen if these kinds of observations can be unambiguously interpreted to yield information on the field components.

What we do know from synchrotron radiation is reviewed by de Pater and Klein. The generation of synchrotron radiation is a well-understood process and is the dominant contributor at decimeter wavelengths. Two periodicities must be fully accounted for before searches for aperiodic or long-term variations can be made. The signal varies as Jupiter rotates (period near 10 hours), as as the jovicentric declination of the Earth varies during one jovian year. Most of the signal variations that are observed can be explained by such beaming effects, but a few may imply variations of one or more characteristics of the magnetic field or energetic particle population.

Between 1967 and 1972 the peak flux density dropped by about 30 percent, the "standoff distance" (distance from the center of the planet to the brightest part of the emission) also decreased, and the System III longitude of the decimeter "hot spot" shifted by 60 degrees. The flux density recovered to its 1967 level by 1977. Changes in the flux density and standoff distance can be explained by a combination of a decrease in radial diffusion with an increase in electron density. The migration in the longitude of the hot spot may be evidence for a change in the high-order multipole field.

Many questions about the stability of the field and particle parameters remain to be investigated. Changes may be occurring on time scales of a few weeks or months, and they may be influenced by a variety of events such as volcanic eruption on Io. The Chapter by Klein et al. discusses the results of a long-term monitoring program and suggests a correlation between synchrotron emission and the ion number density in the solar wind.

A connection between the solar wind and jovian hectometric and decametric emissions has been established by analyses of data from the Voyager planetary radio astronomy experiment, and ground-based radio arrays. Genova et al. review the complex nature of radio emission in the wavelength range from about 10 m to 30 km. Emissions in this spectral band are best characterized by their structure in a plot of frequency versus time, and several different types are apparent. One class of emissions may be associated with the auroral activity. They are not modulated by Io, and they are correlated with solar wind parameters (see the chapter by Zarka and Genova). In the future, we may better understand the possible auroral connection by correlating auroras seen at ultraviolet and infrared wavelengths with the hectometric (which can only be observed by spacecraft) and decametric emissions, and by getting better estimates of the location of the source region from instruments on the Ulysses, Galileo, and possibly the Cassini spacecraft.

The Io-independent emissions are only one class of a wide variety of emission phenomena that vary over a wide range of time scales. Another example is the narrow-band kilometric emission (nKOM). Sandel and Dessler have found that the nKOM emissions can be organized in a rotating frame whose phase slips by 25.486 degrees per day with respect to System III. They propose a System IV rotation frame that organizes the nKOM and ionized sulfur emissions in the torus observed by the Voyager ultraviolet spectrometer (UVS) experiment and by ground-based spectra. The physical basis for this new system is not yet understood, but possibilities include slippage of the torus plasma with respect to the local magnetic field (a consequence of ion mass-loading), and/or a component of the magnetic field that drifts with respect to System III (Dessler, 1985).

To understand how the properties of the jovian magnetosphere vary on medium to long time scales, one must first disentangle periodicities introduced by Jupiter's rotation, the modulating properties of Io (for some emissions), and, for Earth-based observations, diurnal effects. It may not be easy to determine the location of source regions for a variety of reasons that include strong beaming effects and substantial refractivity gradients in the jovian magnetosphere. It seems clear, however, that the Io-modulated emissions are generated along field lines that pass through Io's orbit, or at least the torus. A number of suggestions has been advanced to account for the characteristics of the Io-related emissions. The two classes of candidates are indirect (beam driven) mechanisms and direct (loss-cone driven) mechanisms. These are discussed in a number of papers cited by Genova et al.

The subject of magnetosphere-satellite interactions is a complex one that commands increasing attention. Although all the inner satellites interact with the magnetosphere, Io is the source of its major ions and is responsible for a variety of unique and fascinating phenomena that have come under intense scrutiny during the past decade.

Conditions in the middle and inner magnetosphere and the Io torus are thought to be primarily influenced by the availability of material from Io. Io plume activity may impact the torus composition, number density, and energy density, and we have strong evidence that the torus electron density changed by as much as a factor of 25 between the Pioneer and Voyager encounters. Two chapters by Bagenal and by Strobel examine the interactions between Io's torus and the magnetosphere. Bagenal focuses special attention on the results from the Voyager plasma science (PLS) investigation and on available models of the energetics and magnetospheric current distributions. Strobel's emphasis is more on the interpretation of spectroscopic data and a review of the time constants that are associated with the physical processes thought to be most important in determining the stability of the torus.

The interpretation is aided by additional constraints from the Voyager UVS, the International Ultraviolet Explorer (IUE), and ground-based spectra that give information on some sulfur and oxygen ions. However, even those investigations experienced difficulties from lack of laboratory data, and analyses for some ions have been slow to converge. Nevertheless, it now seems that agreement among investigators has been achieved on the composition of the plasma.

Ideas about the mechanisms that energize the torus have evolved in several stages. Until recently, pickup by Jupiter's magnetic field of S and O ions originating near Io was thought to provide sufficient energy (neutral cloud theories). New and detailed calculations by Shemansky (1988) that fully account for radiative energy loss by SII ions, indicated that ion pickup is an inadequate energy source. An additional process that can provide the missing energy is the acceleration of S and O ions in the outer magnetosphere with subsequent diffusion into and thermalization within the torus. The S and O ions start out in the Io torus where they undergo charge exchange and shoot out to the outer magnetosphere as fast neutrals, then reionize by electron impact. The same population of high-energy ions thus created can supply much of the auroral energy. Charge exchange and reionization processes may also help account for the inferred source of ions (see Bagenal) in the region around 9 R_J, although material from Europa is also a possibility.

The temporal and spatial variability of the torus is evident on several scales, and evidently there is still considerable confusion about its nature. Observations of SII and SIII emissions have been interpreted in terms of System III structures but are also used as evidence for a System IV organization (see above). Clearly, additional observations are needed to clarify the issues. Longer-term (months to years) variations are evident in comparison of the two Voyager and two Pioneer data sets, and in ground-based and IUE spectra. These variations are indicative of global changes in the plasma composition, temperature, and mass. A number of intriguing questions need to be answered. For example, does the much lower electron density inferred by Pioneer instruments indicate Io volcanism was either anomalously active prior to the Voyager encounters or remarkably passive prior to Pioneer encounters? Hopefully, consistent monitoring of future volcanic activity will show how changes in the level of volcanism correlates with changes in torus and magnetospheric properties.

The variety and intensity of jovian upper atmospheric phenomena are remarkable. In addition to auroras and airglow, which resemble terrestrial processes, a new phenomenon called electroglow is thought to have been discovered in the Voyager UVS experiment data for Jupiter, Saturn, and Uranus. The chapters by Clarke et al., by Gladstone and Skinner, by Trafton et al., and by Kostiuk et al. review the relevant observations and describe current theoretical ideas.

Auroras are apparent in widely separated spectral regions from the X-ray to the infrared. They are much more energetic, by three orders of magnitude, than their terrestrial counterparts. In some localities near the poles some of the energy is deposited below the homopause and produces elevated temperatures that are seen in images of the planet in the 7.8-micron methane band. Molecular hydrogen emissions near 2.1 μm have also been recently observed. The most efficient process to produce the localized X-rays observed by the High Energy Astronomical Observatory from earth-orbit is K-shell emission from impacting S and O ions, which are presumed to come from the Io torus or possibly more distant magnetospheric regions. Inability to detect ion emission in the far ultraviolet (FUV) suggests that ions penetrate below the homopause, whereas precipitating electrons near or above the homopause are mainly responsible for the emissions that are observed in the FUV. Details can be found in the Chapter by Gladstone and Skinner.

Ideas about airglow and electroglow are rapidly evolving. One of the most fundamental and hotly contested questions is how much of the observed emission is caused by resonance fluorescence and how much by photoelectron excitation and other indirect processes called electroglow. The latter is believed to occur on Jupiter, Saturn, and Uranus; and the number of photons required to produce the observed emission is calculated to exceed that supplied by sunlight by about a factor of 5 at Jupiter, and by a factor of 10 to 100 at Uranus. A mechanism proposed by Clarke et al. (1988) accounts for excess emission by electrons and ions accelerated by the action of an ionospheric dynamo, a mechanism that operates in the terrestrial atmosphere.

PHENOMENA IN THE JOVIAN ATMOSPHERE

This final section is devoted to discussions of the variable nature of jovian meteorology, chemistry, cloud properties, thermal structure, and lightning. The Chapters by Beebe et al., Carlson and Lutz, Thompson and

Sagan, La Vega, and Limaye describe what is known from the observational point of view about the meteorology on the planet, whereas Flasar provides a theoretical context for the interpretation of the observed phenomena. Chapters by Drossart et al., Baines et al., and Lellouch et al. complement the discussions of atmospheric structure by emphasizing details of the chemical composition in the atmosphere and the relationship of trace constituents to small scale dynamic atmospheric processes.

The processes that give rise to and maintain the zonal jets remain controversial. Presumably, the apparent stability of the zonal jets is an indication that the mean zonal motion is deeply rooted. But just how stable are the jets? Some studies indicate that the eddies are energetic enough to produce the jets in less than a year from some random initial condition. Should we be looking for variations in the jet patterns? Prior to the workshop there was little evidence that the jets vary with time. However, the Chapter by Limaye presents new evidence that a change occurred in at least one narrow latitude band between the Voyager 1 and Voyager 2 encounters.

Embedded in the relatively stable jet pattern is a rich variety of cloud features that often display rapidly changing structure with strong hints of periodicity and organization on global scales. These clouds display a wide range of stability. The smallest clouds have short lifetimes (as short as a few hours), whereas the largest features, such as the Great Red Spot, remain intact at least a century—even though their velocities, color, albedo, and sizes may vary on time scales of months to decades.

The poorly understood nature of cloud albedo and other cloud properties challenges many of our long-held beliefs about the jovian atmosphere. The traditional picture has ammonia and other condensible constituents forming thick white clouds in upwelling anticyclonic zones, whereas dry descending currents in cyclonic belts remove cloud material and allow us to see to deeper levels. Why then, do some large-scale regions change from relatively bright areas to relatively dark areas, although jet vorticity remains constant? The simple traditional picture seems inadequate. There is a multitude of evidence that shows that the locations, colors, and optical depths of clouds do not follow a simple pattern. It has become clear that attention must be paid to the correlation of a wide variety of observations from the near ultraviolet to the thermal infrared to understand how clouds at several levels form and change.

Tracing the motion and evolution of cloud structures is but one measure of meteorological conditions. Observations of temperature and trace chemical species may tell us something about vertical transports of material and heat. In the troposphere there are belt-zone variations in local ammonia humidity and water abundance. There may also be variations in C_2H_2 and C_2H_6 in the stratosphere, although it is difficult to disentangle temperature variations from abundance variations (see the review chapter by Drossart et al., and the Chapter by Kostiuk et al.). Stratospheric temperatures as inferred from images at 7.8 μm wavelength shows temporal variations on belt-zone scales whose morphology seems to be unrelated to the cloud albedo patterns in the underlying atmosphere. Sporadic evidence for planetary-scale waves is also seen in some 7.8 μm images (Chapter by Beebe et al.). Although we are clearly beginning to confront the issue of circulation and chemistry in the jovian stratosphere, more detailed and more thorough observations of temperature and possible photochemical tracers are required to provide a basis for a substantial advance in our knowledge in the future.

A novel observation made by Voyager 1 was the detection of lightning both by the Plasma Wave experiment and by the Imaging experiment. Doyle and Borucki refine the interpretation and details of the imaging data whereas the Chapter by Lanzerotti et al. examines lightning processes in more detail and tells how the lightning detection experiment on the Galileo probe should expand our knowledge. The occurrence of lightning has implications for local dynamic regimes and cloud microphysics. It conjures up images of violent storms selectively transporting charged particulates high into the upper troposphere through vigorous convective activity fed by latent heat release. Water vapor, with its large latent heat of vaporization, is naturally the medium of choice and some investigators have even suggested that the enormous "plume" features that circle the planet at the northern edge of the equatorial belt might morphologically resemble (the much smaller) terrestrial anvil clouds. These ideas face a severe problem however if, as Bjoraker et al. (1986) argue, the H_2O abundance is about a factor of 30 less than solar abundance. Other important questions for lightning concern the vertical and latitudinal location of the flashes, the total discharge energy, and its efficiency for creating nonequilibrium species.

CONCLUSION

The motivation for a workshop and book on *Time-Variable Phenomena in the Jovian System* stems from a desire both to prepare for and to make the best use of the Galileo mission in understanding the workings of the Jupiter system. It also derives from failures (and some cases are discussed in this book) of otherwise well-based scientific ideas to account for many of our observations of the Jupiter system. It is perhaps not surprising that questions about the dynamic behavior of a system, because of its complexity, are usually addressed only after questions about the general state have become reasonably well understood. However, we believe that the material presented in this book demonstrates that our knowledge has reached the level of maturity where it becomes particularly productive to increasingly focus research interest on the behavior of phenomena in the jovian system with time.

Our attempts to understand the jovian system, a miniature solar system, should serve us well as we strive for an understanding of other planetary bodies, as well as some astrophysical environments, because of the rich and varied nature of the jovian phenomena. Where else can we examine in such detail the meteorology of a deep fluid atmosphere; the complex interactions of hot and cold plasma tori embedded within an energetic magnetosphere; with a tenuous satellite atmosphere that is fed by ephemeral volcanic fountains; auroras energetic enough to noticeably heat the planet's atmosphere; and a magnetosphere that displays a host of complex, varied, and energetic phenomena on a grand scale?

References

Bjoraker, G. L., H. P. Larson, and V. G. Kunde (1986). The abundance and distribution of water vapor in Jupiter's atmosphere. *Astrophys. J.* 311:1058–1072.

Clarke, J. T., M. K. Hudson, and Y. L. Yung (1988). The excitation of the far ultraviolet electroglow emissions on Uranus, Saturn, and Jupiter. *J. Geophys. Res.* 92:15139–15147.

Dessler, A. J. (1985). Differential rotation of the magnetic fields of gaseous planets. *Geophys. Res. Lett.* 12:299–302.

Lieske, J. H. (1987). Galilean satellite evolution: Observational evidence for secular changes in mean motions. *Astron. Astrophys.* 176:146–158.

Shemansky, D. E. (1988). Energy branching in the Io plasma torus: The failure of neutral cloud theory. *J. Geophys. Res.*, in press.

PART I

SATELLITE PHENOMENA AND RINGS

PRECEDING PAGE BLANK NOT FILMED

2

Dynamic Geophysics of Io

Alfred S. McEwen
U.S. Geological Survey, Flagstaff

Jonathan I. Lunine
Lunar and Planetary Laboratory, Tucson

Michael H. Carr
U.S. Geological Survey, Menlo Park

Abstract

Numerous volcanic eruptions and hot spots show that Io is the most geologically active solid body known in the solar system. The resurfacing rate is remarkably high; as much as 10 cm yr^{-1} is the global average. Surface landforms include calderas, mountains, shield volcanoes, plateaus, flows, grabens, and eroded scarps. The bulk density and topographic relief suggest a dominantly silicate composition, but spectral observations indicate that the surface is covered by SO_2 and other sulfurous materials. The lithosphere is probably more than 30 km thick under regions showing substantial relief. Io's volcanism is most likely powered by tidal heating mechanisms that also differentiated the satellite and drove volatiles to the surface. All recent models place the tidal heating below the lithosphere; disagreement exists, however, as to whether the heating is episodic over geologic time. Active volcanic plumes are of two types. The Prometheus type, concentrated within 30 degrees of the equator, is relatively small (~100 km high) and of long duration (months to years), producing bright halo deposits 200–600 km in diameter. The Pele type, concentrated in the region from longitude 240° to 360°, is large (~300 km high) and of short duration (days to months), depositing relatively dark and reddish materials over areas of 1000–1500 km diameter. The Prometheus-type plumes are probably driven by SO_2 vapor from reservoirs near 400 K, whereas the Pele-type plumes may be driven by sulfur vapor from reservoirs near 1000 K. The hot spots on Io correspond to low-albedo areas, usually on the floors of calderas. Hot-spot temperatures generally range from 200 to 400 K, and the radiation may be due to convecting sulfur lakes with rapid evaporative outflow or to cooling silicate lavas. The global energy flow from the hot spots, by

PRECEDING PAGE BL NOT FILMED

conduction through the lithosphere, and by the kinetic energy of the plumes is from 1 to 3 W m^{-2}. A global asymmetry in the structure or composition of Io is suggested by the longitudinal variation of the orbital lightcurve, SO_2 abundance, Pele-type plumes, steady-state heat flow, short-lived enhancements at 5 μm, and topographic relief.

INTRODUCTION

Volcanically active Io has been described as "a wonderland of physics and chemistry" (Nash et al., 1986). Among the observations made by the Voyager spacecraft in 1979 were active volcanic plumes up to 300 km high, hot spots more energetic than thousands of Yellowstones, and color and albedo changes over areas the size of Alaska. Changes in plume activity, surface features, and thermal emission have been observed on time scales ranging from hours to years. However, in spite of the tremendous activity, certain observations, such as the disk-integrated lightcurve and the longitudinal variation in heat flow, have remained remarkably constant for years to decades.

This chapter reviews the dynamic geophysical phenomena in the interior and on the surface of Io, including tidal heating mechanisms, heat transfer to the surface, and dynamics of the volcanic plumes and hot spots. The chapter concludes with a discussion of some of the outstanding problems that future research could address. Excellent reviews on Io have been published by Johnson and Soderblom (1983) and by Nash et al. (1986), but research on Io is vigorous, and many significant studies have been completed since these reviews were written.

Physical Properties

Io is the innermost of the galilean moons of Jupiter, with an orbital radius (semimajor axis) of 4.2×10^5 km. Io's radius (1815 km) and bulk density (3.57 g cm^{-3}, Burns, 1986) are comparable to those of the Moon. However, whereas the Moon has a global heat flow of about 0.02 W m^{-2} (Langseth et al., 1976), Io's heat flow is at least 1 W m^{-2} (Johnson et al., 1984) and may be as high as 3 W m^{-2}. This enormous heat flow is thought to result from tidal dissipation of orbital energy resulting from Io's forced eccentricity coupled with the enormous tides induced by Jupiter (Peale et al., 1979). The Laplace resonance with Europa and Ganymede continuously forces the eccentricity of Io's orbit (cf. Yoder, 1979; Greenberg, 1982).

The surface environment of Io is unlike that of any other planetary body. Surface temperatures, away from thermal anomalies, range from ~130 K near the subsolar point to ~90 K on the nightside or during eclipse (Pearl et al., 1979; Morrison and Telesco, 1980). Io has a tenuous SO_2 atmosphere, with subsolar pressures of no more than 10^{-7} bar (see review by Nash et al., 1986). The surface is probably bombarded by low-energy ions and electrons from the plasma torus, high-energy protons and electrons trapped in Jupiter's magnetosphere, and energetic solar ultraviolet (UV) radiation, resulting in sputtering erosion (and subsequent redeposition) and chemical modifications (see review by Cheng et al., 1986).

Composition

The bulk density of Io (3.57 g cm^{-3}) and the presence of large-scale topographic features with steep slopes (Carr et al., 1979; Clow and Carr, 1980; Schaber, 1980) suggest that the bulk composition of the crust and mantle is silicate. A bulk silicate composition is also suggested by models of satellite origin. No spectral features diagnostic of silicates have been detected, but the silicates may be masked by thin coatings of sulfurous compounds or other materials.

Although Io's bulk composition is probably silicate, the surface composition has been profoundly altered by volcanic resurfacing and outgassing (Johnson et al., 1979). SO_2 has been positively identified both as a gas (Pearl et al., 1979) and as a surface frost (Fanale et al., 1979; Smythe et al., 1979). SO_2 frost may cover 30 percent or more of Io's surface (Howell et al., 1984; McEwen et al., 1988). Elemental sulfur is considered a likely surface component on the basis of (1) the similarity of Io's UV through near-infrared (IR) spectral reflectance to laboratory reflectance spectra of powdered sulfur (Fanale et al., 1974; Wamsteker et al., 1974) and (2) the detection of sulfur ions in Io's plasma torus (Kupo et al., 1976). Colorful "quenched" sulfur allotropes became popular candidates for Io's surface after the Voyager encounters (Sagan, 1979; Smith et al., 1979a, b, c; Soderblom et al., 1980), but this interpretation has become controversial (Young, 1984). The detection of clouds of Na (Brown, 1974) and K (Trafton, 1975) around Io has led to proposals that Na and K sulfides may be present on the surface (Fanale et al., 1979; Nash and Nelson, 1979).

The dominant volatiles driving explosive volcanism on Earth, H_2O and CO_2, seem to be highly depleted on Io. Discernible H_2O or carbonate absorption bands are absent (Cruikshank et al., 1978; Pollack et al., 1978; Fanale et al., 1979; Pearl et al., 1979), and C has not been detected in the magnetosphere near Io (Pilcher and Strobel, 1982). These absences argue strongly against the presence of significant H_2O, carbonates, or hydrated minerals on the surface and of H_2O or CO_2 gases in the atmosphere or volcanic plumes. Therefore, other volatiles such as SO_2 or sulfur must be driving the explosive volcanism (Smith et al., 1979a; Kieffer, 1982).

Detailed reviews of the surface composition of Io are found in Fanale et al. (1982), Sill and Clark (1982), Clark et al., (1986), and Nash et al. (1986).

Origin and Cosmochemistry

Io's bulk density is consistent with a rocky body, perhaps containing an iron core, but devoid of the water ice that is a major constituent of most satellites of the outer solar system. The formation of Io and the other galilean satellites apparently occurred during the earliest evolutionary stage of the jovian system (Pollack and Fanale, 1982). The coplanar, circular orbits of Jupiter's major satellites strongly suggest formation in a disk of material spun out of the planet during its collapse. Whether such a disk retained a solar ratio of rock-forming to ice-forming elements is difficult to quantify (Bodenheimer and Pollack, 1986), but this knowledge is essential if we are to tie the present rock-to-ice ratio and composition of the satellites to accretion models (Stevenson et al., 1986; Stevenson and Lunine, 1987). The outward radial trend in density and composition from rock to rock-ice among the galilean satellites strongly suggests that a protosatellite nebular gas had a temperature gradient that permitted ice to condense beyond the orbit of Europa (Prinn and Fegley, 1981; Lunine and Stevenson, 1982). However, different processes are possible; for example, differing postaccretional impact rates may have devolatilized the inner satellites more than the outer satellites (Stevenson et al., 1986). Some models for the accretional heating of the galilean satellites permit sufficiently high temperatures to dehydrate silicates in Io and perhaps in Europa (Lunine and Stevenson, 1982).

The origin of Io's sulfur has received much attention. Consolmagno (1979) proposed near-surfacing melting of a metal-bearing rock (C3 chondrite) as the source of sulfur. Hapke (1979) suggested the origin of sulfur and SO_2 to lie in decomposition of hot FeS. Both of these models run into serious thermodynamic problems, as explained by Lewis (1982), who argued that metal-free C3V or C2M chondrites would evolve into buoyant, sulfur-rich liquids and SO_2 upon heating at depth in Io. Whether these particular chondrites are reasonable starting materials for Io cannot be addressed with the information at hand. Moreover, because the total abundance of sulfurous materials at Io's surface is not known, constraints are weak on the required yield of sulfur from various schemes. Such uncertainties also plague an early (but still plausible) model for driving sulfur to Io's surface: leaching of sulfur during dehydration of silicates (Fanale et al., 1974). A more extensive review of models for the origin of sulfur is given by Lewis and Prinn (1984). Further progress in these areas requires more detailed mineralogical analyses of the galilean satellites from the Galileo Near-Infrared Mapping Spectrometer (NIMS) and constraints from cosmochemical investigations of primitive solar system bodies, such as the proposed Comet Rendezvous Asteroid Flyby (CRAF) mission.

TIDAL HEATING MECHANISMS AND INTERNAL STRUCTURE

The importance of tidal heating in controlling the enhanced heat flow and active volcanism of Io, first proposed by Peale et al. (1979), is now widely accepted. This section relies largely on the excellent reviews of Nash et al. (1986) and Schubert et al. (1986).

Background

All commonly occurring, nontidal heat sources fall short of explaining the power output of Io (at least 4×10^{13} W) by about two orders of magnitude. Accretional heating can supply, at a maximum, half the gravitational potential energy of Io; if released over the age of the solar system, the power output is 5×10^{11} W. However, accretional heat is removed by conduction or convection on a much shorter time scale. Core formation can supply only a fraction of the maximum accretional energy, and it is short-lived. Radiogenic heating is a continuous process and is estimated to supply 5×10^{11} W (Schubert et al., 1986). Heating of the surface by an electrical current running between Io and Jupiter's ionosphere (Goldreich and Lynden-Bell, 1969) provides a maximum power of 2×10^{11} W, but an ionosphere is likely to divert most of the current around Io (Colburn, 1980).

Peale et al. (1979) first recognized the importance of tidal interactions in heating the interior of Io. Since that time, a number of models for steady-state and variable tidal heating, in thin shells and through the bulk of the interior, have been advanced. Detailed expositions of the physics of tidal heating mechanisms are given by Peale (1986), Schubert et al. (1986), and Nash et al. (1986). This section outlines the various tidal heating models, including their predicted power output, and briefly indicates their implications for the internal structure of Io.

The basic tidal heating mechanism involves Jupiter's gravitational field deforming Io into a prolate spheroid. Because Io's orbit is eccentric, the satellite undergoes a periodic forcing and deformation, which generates internal heat. The dissipation also decreases the orbital eccentricity of Io, which is forced to remain nonzero by orbital resonances among Io, Europa, and Ganymede (e.g., Peale et al., 1979; Yoder, 1979; Greenberg, 1982; Peale, 1986). The total rate of tidal dissipation within Io depends inversely upon its rigidity and "quality" factor, Q_J, which are functions of the internal structure and material properties of the satellite. However, the transfer of orbital energy from Jupiter to Io is a consequence of the bulge raised on Jupiter by Io, and the rate of such transfer depends inversely on Jupiter's rigidity and quality factor, Q_J. An upper bound to the rate of transfer can be obtained by assuming Io is in an equilibrium resonant orbit with Europa and Ganymede (for which the material properties of Io cancel out; Peale, 1986) and by assuming a lower value of Q_J, which brings Io out from Jupiter's center to its present orbit over the age of the solar system. These assumptions yield $Q_J = 2.5 \times 10^4$ and an upper limit to the energy dissipation rate of 9×10^{13} W (2.1 W m^{-2}). Such a value of Q_J is, however, much lower than other estimates derived from the properties of Jupiter itself (Greenberg, 1982; Ojakangas and Stevenson, 1986). Furthermore, recent calculations of Io's acceleration suggest that the tidal dissipation rate in Io over the past 300 years is an order of magnitude lower than the present rate of heat flow (Greenberg, this volume).

Lithospheric Thickness

The mechanism of heat dissipation in Io is intimately tied to its internal structure. Peale et al. (1979) suggested that Io's interior is entirely molten and that the tidal energy is dissipated within a thin elastic lithosphere, but this model now seems unlikely. Dissipation of all the tidal energy within the lithosphere requires that it be 8–18 km thick (Nash et al., 1986), and such a thin lithosphere appears inconsistent with the presence of 10-km-high mountains (O'Reilly and Davies, 1981; Carr, 1986; Webb and Stevenson, 1987). The Peale et al. model may be modified by invoking a thicker lithosphere and advective heat transfer (Kawakami and Mizutani, 1987), but Schubert et al. (1981) argued that runaway melting might never occur because subsolidus convection would remove the heat. Moreover, efficient liquid-state convection would solidify most of the satellite in 10^8 to 10^9 years, leaving a differentiated satellite with an iron-rich core, a solid mantle, and a partially molten asthenosphere (Schubert et al., 1986). Nash et al. (1986) suggest that, to support the 10-km-high mountains, the lithosphere must be at least 30 km thick. This estimate was based on the assumption that Io is an isostatic equilibrium and the difference in density between the mountains and plains is no more than 0.5 g cm^{-3}. Therefore, most of the tidal energy is probably dissipated below the lithosphere by viscous or viscoelastic deformation (Schubert et al., 1981; Ross and Schubert, 1985, 1986; Carr, 1986).

If most of the tidal energy is dissipated below the lithosphere, as appears probable, then only a small fraction of the tidal energy is lost by conduction through the lithosphere (or it would thin). Most of the heat is transported toward the surface as silicate magma. Carr (1986) showed that for plausible lithosphere thicknesses (>30 km), silicate magma must be carried toward the surface in amounts sufficient to cover the surface at a rate of a few millimeters per year. This resurfacing could occur directly through silicate volcanism or by mobilization of sulfurous materials.

Steady-State Tidal Heating

Those tidal heating models that are consistent with the constraints on lithospheric thickness and mantle convection are described in the following paragraphs.

A variety of viscous and viscoelastic steady-state models have been developed in recent years. Ross and Schubert (1985) considered both the tidal flexing of the elastic shell and dissipation in the fluid asthenosphere beneath; such a model produces 1.8 W m^{-2} for $Q_J = 100$, a lithospheric shell roughly 900 km thick, and an asthenospheric viscosity corresponding to a silicate magma containing approximately 50 percent crystals. Results are similar for asthenospheres extending all the way to the center of Io, as well as "thin asthenosphere" models. A viscoelastic Io is also possible in which the interior is solid but of low viscosity, with tidal heating concentrated toward the center of the planet (Ross and Schubert, 1986).

Segatz et al. (1988) examined two models of Io's interior and determined how the tidal energy would be dissipated in each. Both models assumed a 980-km-diameter core, consistent with the range of 700–1000 km suggested by others (Consolmagno, 1981a; Dermott, 1984; Nash et al., 1986). The 980-km diameter was derived on the basis of mantle and core densities of 3.45 g cm^{-3} and 5.4 g cm^{-3} respectively—these being the densities of the Earth's mantle and a eutectic Fe–FeS melt. The two models of Segatz et al. differ in the presence or absence of an asthenosphere. If Io lacks an asthenosphere, then dissipation in a mantle with a viscosity less than or equal to 6×10^{16} Pa · s is sufficient to balance the observed heat flow. This is about the minimum solid-state value for the viscosity of solid rock. If an asthenosphere is present, then most of the tidal energy will be dissipated within this zone. Segatz et al. show that a 50-km-thick asthenosphere requires an asthenospheric viscosity of 10^8 Pa · s, whereas a 100-km-thick asthenosphere requires a viscosity of 10^9 Pa · s. The pattern of dissipation is different for each model: With deep mantle dissipation, the polar heat flux should be larger than the equatorial heat flux; with asthenosphere dissipation the reverse is true. Thus, observations of heat fluxes may allow us to choose the best model. However, the observed distributions of hot spots and active plumes are more complex than either of the model predictions.

Time-Variable Tidal Heating

The steady-state models, although accounting for the estimated heat flux and lithospheric thickness, do not solve the problem of Q_J: Most estimates of this quantity that are not tied to Io's thermal output yield values higher than 10^5 (Schubert et al., 1986), thereby lowering the maximum steady-state tidal heating to well below the observed value. Time-variable tidal heating models avoid this difficulty but introduce the added complication of time-variable behavior. Greenberg (1982) proposed that Io, Europa, and Ganymede were once deeper in the Laplace resonance and are decaying out of the resonance to a state of lower eccentricity and tidal heating. This relaxes the constraint of a small Q_J. Ojakangas and Stevenson (1986) developed a model in which Io undergoes short episodes of large tidal heating rates. The satellite experiences a cycle in which low internal temperatures place the satellite's eccentricity below the equilibrium resonance value, causing it to increase and producing high rates of tidal heating with accompanying volcanism and large internal temperatures. The high temperatures, in turn, drop the equilibrium-forced eccentricity, causing the actual eccentricity and tidal heating to decrease, shutting off the volcanism and cooling the satellite. Ojakangas and Stevenson showed that periodic solutions are possible, with volcanic episodes of 20–30 million years followed by quiescent epochs of 10^8 years, for values of $Q_J > 10^5$. The model assumes a convecting, uniform interior, although heterogeneous internal flows (corresponding to areal surficial variations) are possible.

Both steady-state and time-variable models of tidal heating appear capable of accounting for Io's hot-spot heat flux. Although specific internal rheologies and structures for Io can be constructed that predict different surface heat-flux distributions, none seem to match the observed hot-spot distribution. A more thorough understanding of hot-spot processes and distribution, crustal structure, conductive heat loss, and time-variability of the heat flow are required before we can choose the best heating model.

GEOMORPHOLOGY AND TECTONICS

The morphology and surface markings on Io are almost entirely the result of volcanic processes. Impact craters, the dominant landform on almost every solid planetary body other than the Earth and Venus, are completely absent on Io, in spite of the comet flux concentration by Jupiter's gravity (Shoemaker and Wolfe, 1982). The absence of impact craters indicates that the surface is very young, which is consistent with estimates of resurfacing by volcanic activity and from the heat flow (Johnson et al., 1979).

Surface Features

The intense volcanic activity has resulted in a variety of surface features that can be crudely classified into three categories: calderas, plains, and mountains (Smith et al., 1979b; Carr et al., 1979; Schaber, 1982; see fig. 1).

Io is spotted by local dark markings; where picture resolution and illumination conditions permit discrimination of surface relief, most of these features are seen to lie within depressions that resemble terrestrial calderas (e.g., fig. 2). Calderas are depressions with steep scalloped walls, flat floors, and smooth rims, which form by collapse over shallow magma chambers following eruption of volcanic materials onto the surface. Where relief cannot be seen, local dark markings are presumed, by analogy, to also be associated with calderas. Several of the dark markings are demonstrably at the site of volcanic vents since they are the source of volcanic plumes. Caldera depths generally have not

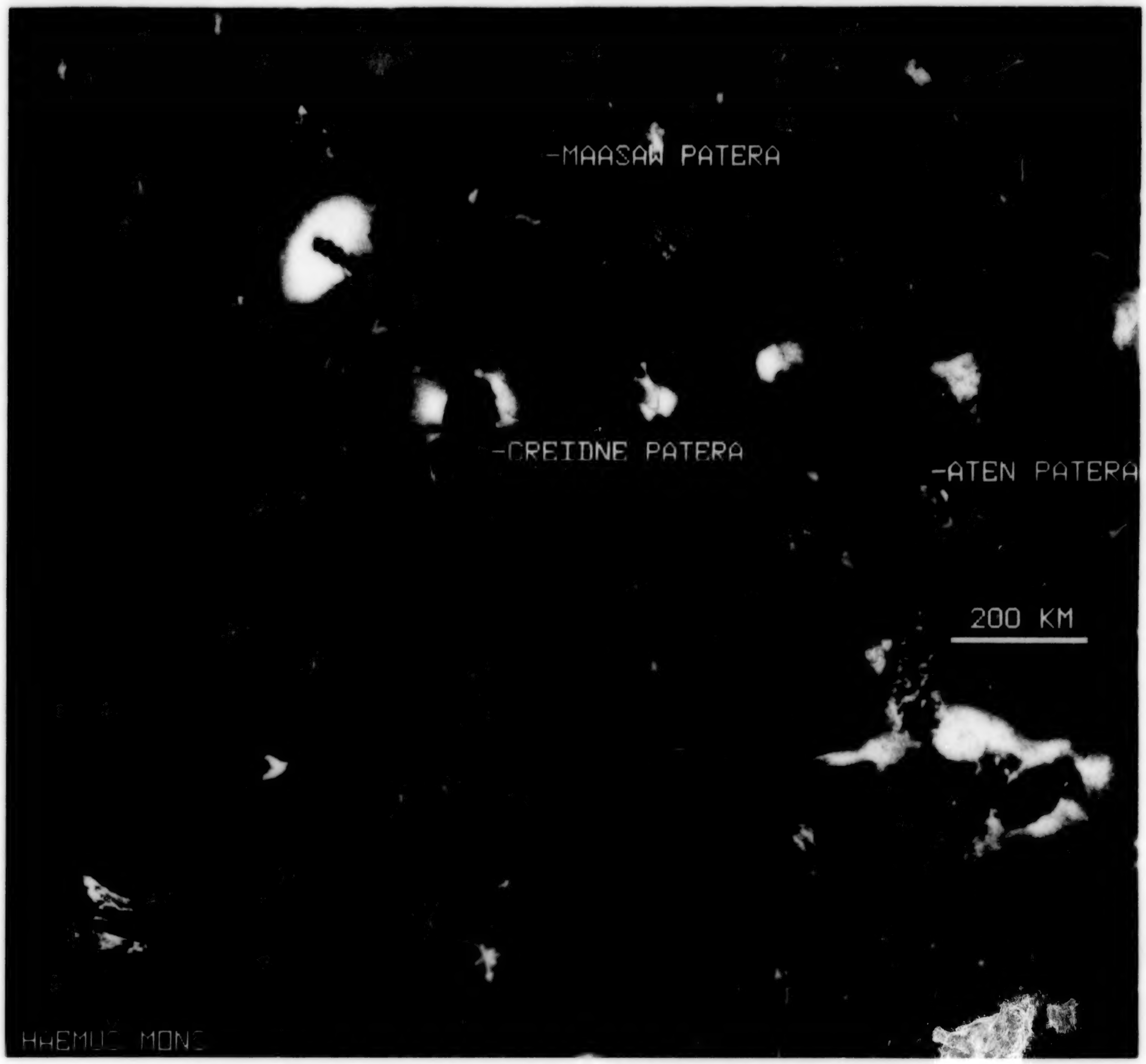

Figure 1. South polar region of Io, from latitude −85° to −30°, longitude 270° to 0°. Model limb-darkening has been normalized. Features discussed in text are labeled. Wide-angle camera images FDS 16392.39 (blue filter), 16392.41 (violet), and 16392.43 (orange).

ORIGINAL PAGE
COLOR PHOTOGRAPH

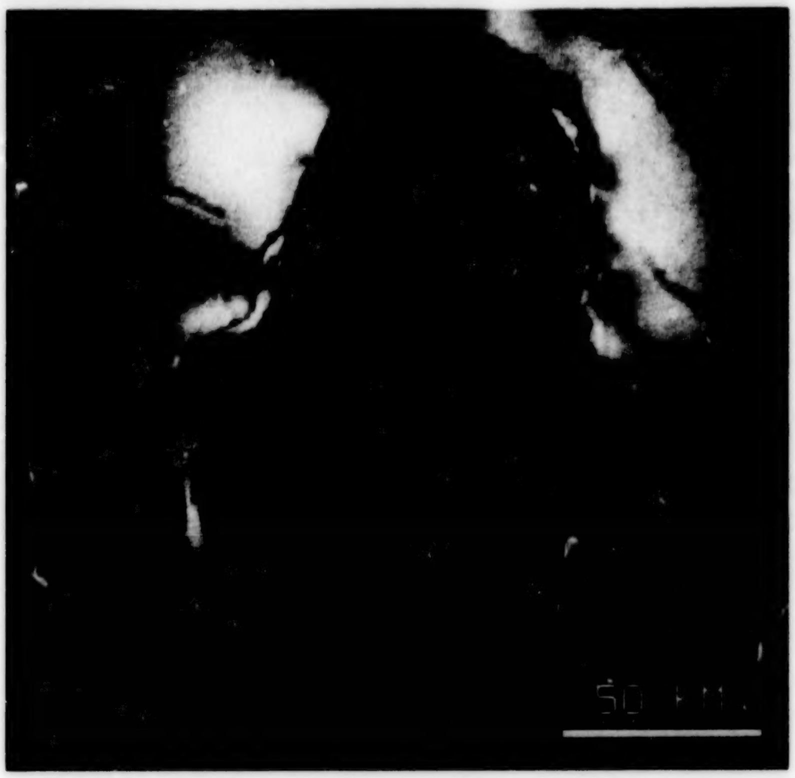

Figure 2. Creidne Patera (latitude −53°, longitude 345°) is a caldera measuring about 100 km by 180 km in diameter and was a hot spot (230 K) during the Voyager 1 encounter. Voyager frame FDS 16391.48, clear filter.

been determined, but the deepest part of the floor of Maasaw Patera (fig. 3) lies 2.1 km below the rim (Schaber, 1982). The calderas range in size from about 20 to 200 km in diameter. They and inferred calderas are fairly evenly distributed across the surface, although they are only about half as abundant and have a slightly larger average size in the polar regions (Schaber, 1982). Dark markings may cover all or part of a caldera floor (fig. 2) and have been interpreted as sulfur lava lakes or recent basaltic lava flows. Diffuse bright markings in and around calderas are common and may be the result of SO_2 fumarolic activity. Most of the calderas are not associated with any obvious edifice. Exceptions are two low circular shields at latitude −17°, longitude 350° and a 2.5-km-high shield at latitude −30°, longitude 246° (Moore et al., 1986). Even where no edifice is visible, radial flows sometimes indicate that the caldera is at the summit of a small rise (fig. 3). Several calderas have anomalously high surface temperatures (Pearl and Sinton, 1982).

Calderas cover less than 5 percent of the surface, and, except for an occasional high mountain, the rest of the surface is covered by "plains" or areas with little apparent relief (see fig. 1). The plains have complex albedo and color patterns, and where relief is discernible, as in the southern hemisphere from longitude 40° to 240°, they are complexly layered (fig. 4). The plains and their surface patterns have formed from a variety of processes: (1) The active plumes are surrounded by diffuse halos that apparently result from deposition of pyroclastics and condensed volatiles. (2) Local diffuse bright markings occur around individual mountains and calderas, along escarpments, around dark flows or other dark markings, or as isolated markings (see figs. 2 and 4). These diffuse bright markings have been interpreted as the result of condensation of volatiles, possibly SO_2, driven from the ground by surface or subsurface heating (e.g., McCauley et al., 1979; Baloga et al., 1983). (3) Many surface markings are not diffuse but crisply outlined. Most are dark, but some are bright and many appear to emanate from vents. These are probably flows, perhaps of sulfur and/or silicate lava (Carr et al., 1979; Sagan, 1979). Dark, long, linear features, with lobate margins, that radiate from local calderas or dark spots (fig. 5) are clearly flows.

In several areas, particularly in the high southern latitudes, the plains are clearly layered (fig. 4). The layering may be present in other regions, but it is visi-

ORIGINAL PAGE
BLACK AND WHITE PHOTOGRAPH

Figure 3. Maasaw Patera (latitude −40°, longitude 340°), a caldera measuring about 25 km by 35 km in diameter, surrounded by radial flows. Voyager image FDS 16392.40, clear filter.

ble only where images with low illumination are available. The layers form tabular, smooth-topped plateaus, commonly outlined by escarpments 150 to 1700 m high (Schaber, 1982). Some of the escarpments are smoothly arcuate, as though formed by faulting; others are jagged as though eroded. The origin of the plateaus is unclear. Some appear to surround calderas such as Creidne Patera (figs. 1 and 2) and may be ignimbrites (ash-flow tuffs), but it is not known whether significant ash flows could form in the absence of an appreciable atmosphere (Wilson and Head, 1983). Moreover, isolated plateaus, seemingly unrelated to vents, are also present, such as Echo Mensa (fig. 4). Many of the plateau units are adjacent to rugged mountains, so they may be sediment gravity flows. Diffuse bright markings occur along some of the escarpments, and McCauley et al. (1979) suggested that the plateau units act as aquifers for SO_2, which escapes along the escarpments, thus forming the bright deposits. They suggested that this sapping undermined the escarpment, thereby accounting for the erosion. However, to produce the observed erosional patterns, the plateau materials themselves must also be volatilized or removed in some other way (perhaps they are blown away by escaping gases). Both the origin of the layers and the cause of their subsequent modification thus remain unsolved problems.

The third major class of surface feature is the mountains. These typically have irregular outlines and rugged surfaces that appear tectonically disrupted. They range in size up to 600 km in base diameter and 10 km in height. Smith et al. (1979a, b) interpreted the mountains as exposures of a silicate lithosphere that is almost everywhere else covered with sulfur-rich materials. Several mountains have characteristics that suggest volcanic origins (e.g., Schaber, 1982; Whitford-Stark, 1982): Haemus Mons (fig. 6) is surrounded by a

ORIGINAL PAGE
BLACK AND WHITE PHOTOGRAPH

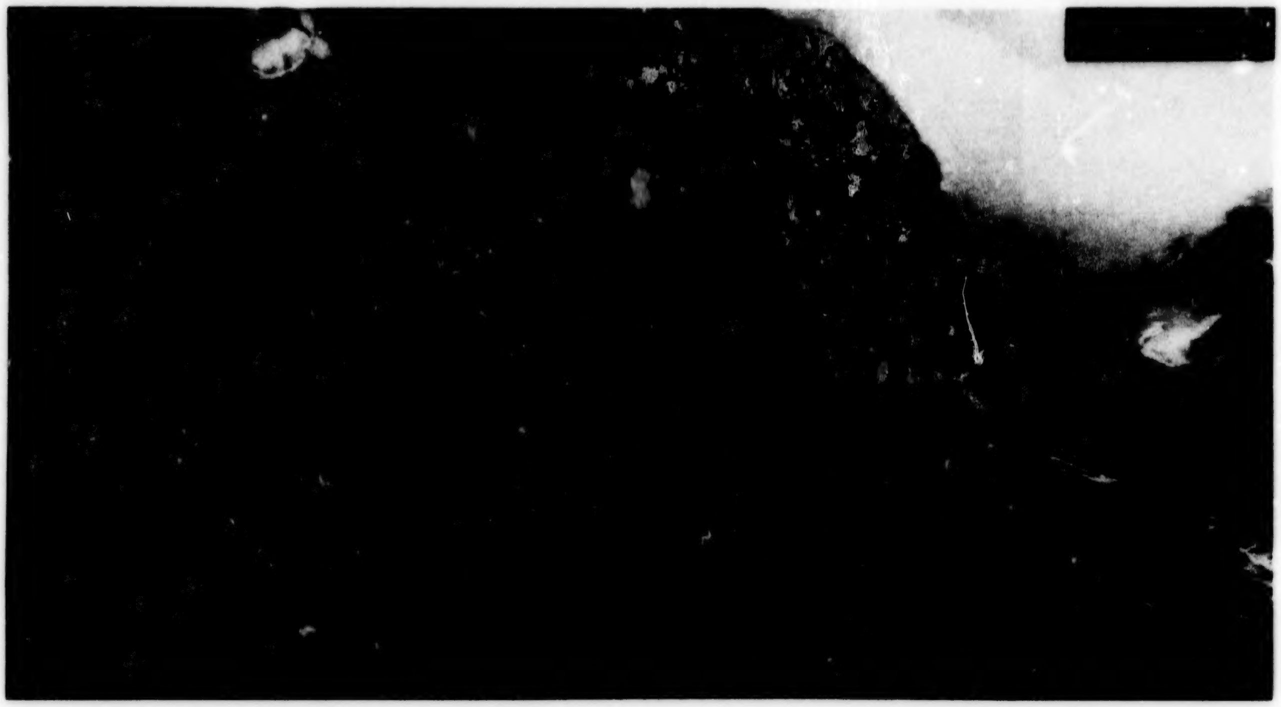

Figure 4. Layered terrain, eroded layered terrain, and long arcuate scarps in south polar region of Io (latitude −90° to −60°, longitude 240° to 30°). Voyager images FDS 16391.44, .50, clear filter.

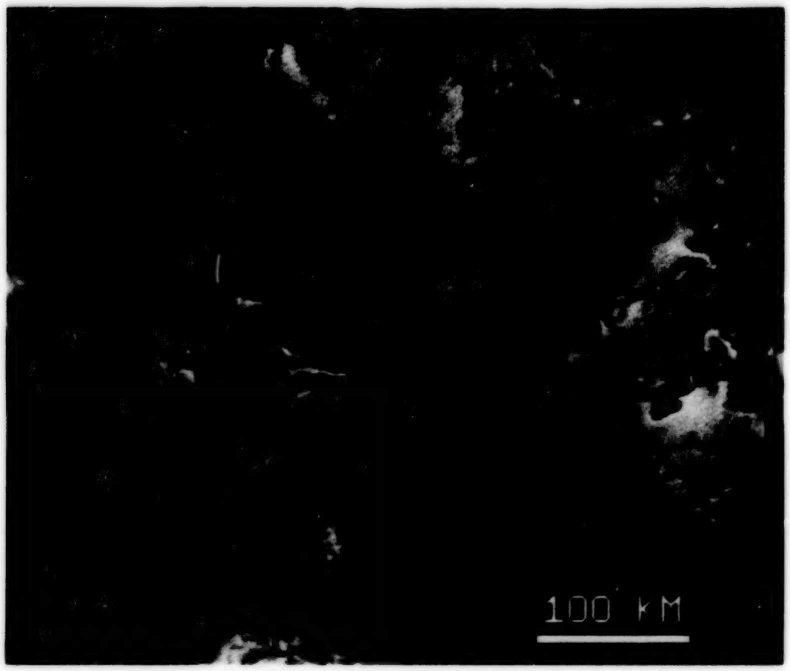

Figure 5. Ra Patera (latitude −8°, longitude 325°) and surrounding flows. Voyager frame FDS 16390.06, blue filter.

ORIGINAL PAGE
BLACK AND WHITE PHOTOGRAPH

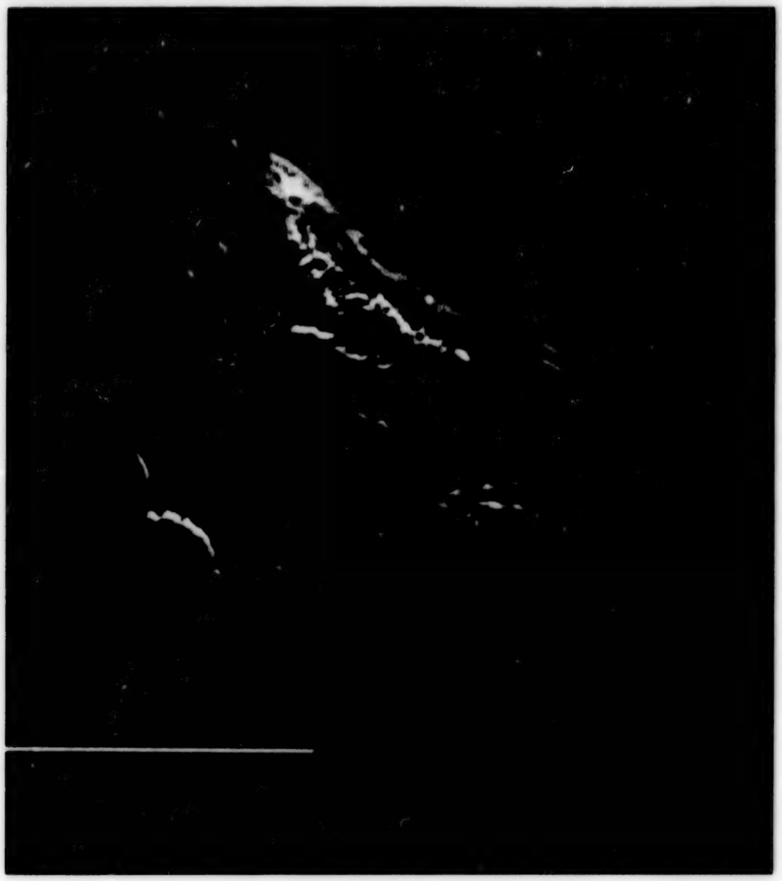

Figure 6. Haemus Mons (latitude −68°, longitude 46°), a mountain ~ 10 km high. FDS 16392.00, clear filter.

bright aureole and the Boösaule Montes (fig. 7) form a partial ring. There is general agreement that the mountains must be dominantly silicate rather than sulfur, because sulfur does not have sufficient strength to support the observed relief (Clow and Carr, 1980). Although superposition relationships are unclear, the mountains are generally considered to be the oldest materials exposed on Io's surface (Schaber, 1980, 1982); higher resolution images are required to confirm this hypothesis. The mountains appear to be preferentially located in a 120-degree-wide longitudinal band centered on longitude 300°, although there is clearly an observational bias to the Voyager images (McEwen and Soderblom, 1983) This topographic asymmetry if real, may relate to the global asymmetry apparent from other observations.

Sulfur Versus Silicates

The abundance of sulfur and silicates in the upper crust of Io is controversial. Abundant evidence of sulfur and sulfur compounds in the vicinity of Io led Smith et al. (1979a) and Sagan (1979) to suggest that the upper crust of Io consists largely of elemental sulfur and SO_2, and that this crust overlies a layer of molten sulfur that may be kilometers thick. In contrast, Carr et al. (1979), although acknowledging that sulfur compounds may be abundant at the surface, suggested that the near surface consists of silicates interbedded with sulfur-rich materials. Clow and Carr (1980) concluded that sulfur does not have sufficient strength to support the steep caldera walls of Maasaw Patera (fig. 3), so the nearby crust may be dominantly silicate. Furthermore, the caldera walls of Pele (fig. 7) are adjacent to a 650 K hot spot, far above the melting point of sulfur (393 K), so the walls cannot be made of sulfur (Pearl and Sinton, 1982). In contrast, the erosional patterns in the layered terrain (fig. 4) suggest a dominantly volatile composition (Schaber, 1982).

The respective roles of sulfur and silicates in creating the observed landforms on Io are also controversial. Sulfur and silicate lava flows might be distinguishable on the basis of morphology (Fink et al., 1983; Greeley

ORIGINAL PAGE
BLACK AND WHITE PHOTOGRAPH

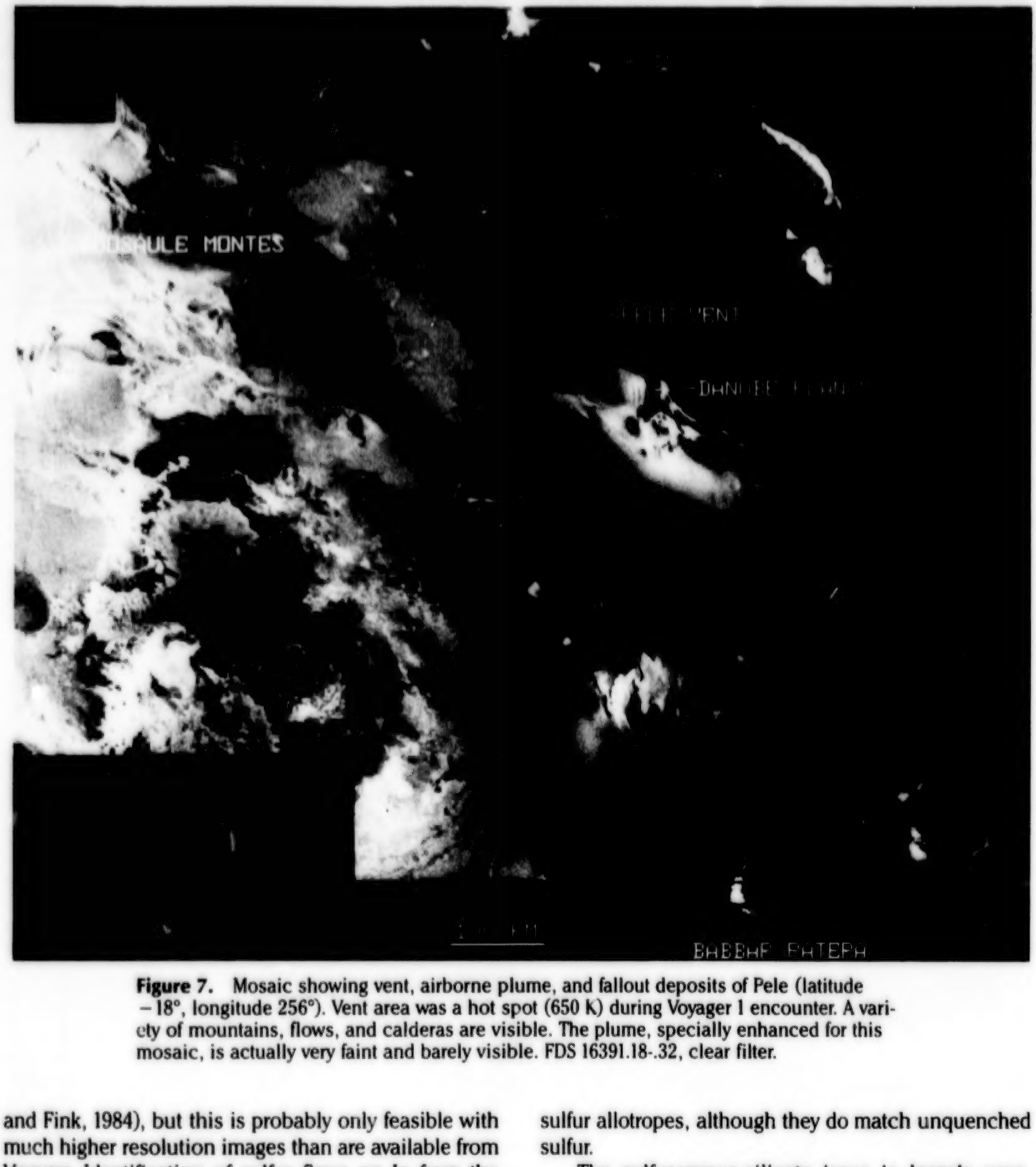

Figure 7. Mosaic showing vent, airborne plume, and fallout deposits of Pele (latitude −18°, longitude 256°). Vent area was a hot spot (650 K) during Voyager 1 encounter. A variety of mountains, flows, and calderas are visible. The plume, specially enhanced for this mosaic, is actually very faint and barely visible. FDS 16391.18-.32, clear filter.

and Fink, 1984), but this is probably only feasible with much higher resolution images than are available from Voyager. Identification of sulfur flows on Io from the color variations in quenched sulfur (Sagan, 1979) has been contested by Young (1984). According to Pieri et al. (1984), the flows at Ra Patera (fig. 5) change color radially outward from dark brown at the vent to orange near the margins, as expected from cooling with distance from the vent and quenching of sulfur allotropes. However, according to McEwen (1988), the spectral reflectivities of the Ra flows do not match the quenched sulfur allotropes, although they do match unquenched sulfur.

The sulfur-versus-silicate issue is largely unresolved, although hybrid models in which both silicates and sulfur participate in the volcanism have gained favor (Schaber, 1982; McEwen and Soderblom, 1983; Greeley et al., 1984; Lunine and Stevenson, 1985; McEwen et al., 1985; Carr, 1986). Most current workers accept (1) that transport of silicate magma upward through a silicate crust is the main mechanism for transporting tidal energy dissipated below the

ORIGINAL PAGE
BLACK AND WHITE PHOTOGRAPH

lithosphere and (2) that these magmas may mobilize more volatile species near the surface, thereby causing plumes, lakes, or eruptions of low-temperature melts, such as sulfur, onto the surface. More controversial is the extent to which silicate magmas are erupted onto the surface. The landforms, color variations, and thermal anomalies can be interpreted as the result of silicate eruptions (with fumarolic activity), sulfur eruptions, or a combination of the two. Resolutions of this question must await more definitive information on the composition, thermal properties, and morphology of the surface.

Tectonics

There is little evidence for a global tectonic pattern on Io in the form of regional faults or alignments of moun-

Table 1. Best Observations of Active Plumes

Plume Number	Site Name	Coordinates[a] (latitude, longitude)	FDS	Time (1979) (day:hour:minute)	Filter[b]	Height[c]
1	Pele	−19, 256	16368.28	63:19:20	Cl	287 ± 24
			16368.50	63:19:37	Uv	305 ± 22
2	Loki	19, 305	16375.34	64:01:01	Cl	166 ± 11
			16375.44	64:01:09	Uv	213 ± 18
			16377.52	64:02:51	Cl	210 ± 26
			20513.48	186:01:57	Uv	393 ± 76
			20513.51	186:01:59	Cl	351 ± 76
			20592.13	188:16:41	Cl	189 ± 51
			20592.23	188:16:49	Uv	224 ± 50
			20621.30	189:16:06	Uv	212 ± 18
			20621.33	189:16:09	Cl	149 ± 18
3	Prometheus	− 2, 152	16377.48	64:02:48	Cl	76 ± 9
4	Volund	23, 177	16382.17	64:06:23	Vi	83 ± 10
			16382.23	64:06:28	Uv	73 ± 16
5	Amirani	28, 114	16372.36	63:22:38	Cl	93 ± 21
			16372.50	63:22:49	Uv	112 ± 24
			16375.28	64:00:56	Cl	77 ± 25
			20621.30	189:16:06	Uv	88 ± 23
			20621.33	189:16:09	Cl	71 ± 23
			20666.12	191:03:52	Cl	98 ± 19
			20667.00	191:04:30	Cl	82 ± 18
6	Maui	19, 122	16375.28	64:00:56	Cl	61 ± 9
			16372.50	63:22:49	Uv	159 ± 28
			16372.36	63:22:38	Cl	161[d] ± 27
			20621.30	189:16:06	Uv	56[d] ± 19
			20621.33	189:16:09	Cl	77 ± 19
			20666.12	191:03:52	Cl	83 ± 24
			20667.00	191:04:30	Cl	105 ± 23
7	Marduk	−27, 210	16389.21	64:12:02	Bl	85 ± 18
			20608.01	189:05:19	Uv	56 ± 29
			20608.05	189:05:22	Cl	64 ± 29
8	Masubi	− 44, 54	16390.28	64:12:56	Cl	64 ± 6
			20641.52	190:08:24	Cl	61 ± 22
9	Loki	17, 301	16375.34	64:01:01	Cl	20 ± 9
			16375.44	64:01:09	Uv	26 ± 10
			20621.33	189:16:09	Cl	33 ± 15
10	Surt	45, 338	Plume not observed			
11	Aten	−48, 311	Plume not observed			

[a] Coordinates of plume source vents, from U.S. Geological Survey (1987); planimetric control from Davies and Katayama (1981). [b] Filters: Cl = clear, Uv = ultraviolet, Vi = violet, Bl = blue. [c] Heights computed from measured heights in Strom et al. (1981, table 1) and corrected for position of source with respect to limb. These values differ slightly from corrected heights given by Strom et al. because these source vent coordinates are based on newer, more accurate geodetic control. Errors computed from errors in measured height given by Strom et al. and errors resulting from 1-degree uncertainty in the surface coordinates of highest or measured portion of each plume (assumed to lie directly over vent). [d] This part of plume 6 may be low-angle ejection arm (Strom et al., 1981), so it may not overlie vent and listed height may be incorrect.

tains or other features. Instead, only local faults and scarps occur, often associated with local volcanic centers (Masursky et al., 1979; Schaber, 1980, 1982). The grabens and other lineaments show dominant northwest and northeast trends and may result from tidal flexing (Schaber, 1980, 1982). Nearly all of the faulting appears to be normal rather than lateral or thrust faulting. The largest continuous faults and scarps occur in the south polar region (fig. 4), and these are approximately concentric to the south polar ring, a low-albedo feature with a diameter of ~1000 km centered at latitude −75°, longitude 140° (McEwen et al., 1985).

Extensional tectonics and low-angle detachment faulting may occur on Io in association with the hot spots (McEwen, 1985). Like the late Cenozoic crustal extension of the Basin and Range Province, the basic model consists of high-heat flow and associated magmatism, topographic uplift, and thin-skinned tectonics involving listric normal faults and low-angle detachment faults. Liquid SO_2 at depth may provide high pore pressures to facilitate low-angle fault movements as does water on Earth. The best example on Io is the rifted plateau just south of the vent and hot spot of Pele (Danube Planum, fig. 7). The plateau is broken into segments that apparently have rotated and moved rapidly outward. These segments fit together ina jigsawlike fashion but have separated by ~30 km. This plateau caps a large, broad topographic uplift, according to the work of Gaskell and Synnott (1987).

VOLCANIC PLUMES

The most dramatic time-variable phenomenon on the surface of Io is the active volcanism (Morabito et al., 1979; Smith et al., 1979b). The active volcanic plumes are of fundamental importance to the science of volcanology, to the geology and geophysics of Io, and to the behavior and composition of the surface, atmosphere, and plasma torus. The plumes erupt under conditions of pressure, temperature, and gravity very different from those on Earth, and they are probably driven by SO_2 and/or sulfur in which multiple phase changes can occur, so the plume dynamics and thermodynamics are unlike terrestrial eruptions (Smith et al., 1979a; Kieffer, 1982; Wilson and Head, 1983). The low gravity and especially the very low atmospheric pressure on Io result in eruption plumes up to 10^4 times larger on Io than would be produced by comparable eruptions on Earth. A nonvolcanic interpretation of the plumes (Gold, 1979) has been countered by Cook et al., (1981). This section describes the observed characteristics of the plumes, models of the plume and Io's volatile inventory, and spatial and temporal effects on the surface, atmosphere, and torus.

Plume Characteristics

Nine eruption plumes were observed during the Voyager 1 encounter, and eight of these plumes were reobserved by Voyager 2 four months later (Smith et al., 1979c; Strom et al., 1979, 1981; Strom and Schneider, 1982). Plume locations and the best height observations are listed in table 1. Many of the plumes, such as that of Prometheus (fig. 8), were 50–100 km high. The plume of Pele (fig. 7), active during the first encounter and having the greatest height (~300 km), had ceased activity sometime before the second encounter. In addition, surface markings visible in Voyager 2 images, which were not present during the first encounter, revealed that two additional eruptions similar to Pele had occurred, erupting from calderas named Aten and Surt (figs. 9 and 10; McEwen and Soderblom, 1983). Loki showed convincing evidence for a major fluctuation in eruptive activity during the Voyager 2 encounter; Maui may also have had some fluctuations in eruptive height (see table 1).

The plume eruptions can be grouped into two major classes (McEwen and Soderblom, 1983; table 2): (1) Prometheus-type eruptions are smaller (50–120 km high, 200–600 km diameter surface deposits), long lived (months to years), contain optically thick, dark jets, deposit bright white materials, erupt at velocities of ~0.5 km s^{-1}, and are concentrated at low latitudes in an equatorial band around the satellite (fig. 11). (2) Pele-type plumes are very large (~3004 km high, 1000–1500 km diameter surface deposits), are optically thin, deposit relatively dark red material, erupt at ~1.0 km s^{-1}, and occur in the region from longitude 240° to 360°. Surface patterns indicating previous Prometheus- and Pele-type eruptions occur with the same global distributions as the active plumes. The distribution of Pele-type deposits seems the logical explanation for the pronounced longitudinal variation of the disk-integrated lightcurve (Morrison et al., 1974). The Pele-type eruptions are associated with hot-spot temperatures near 600 K, whereas the Prometheus-type plumes are associated with temperatures <450 K or with no thermal anomaly sufficiently energetic for detection by infrared interferometric spectrometer (IRIS) (Pearl and Sinton, 1982). All of the observed hot spots associated with active plumes are comparable in size to calderas

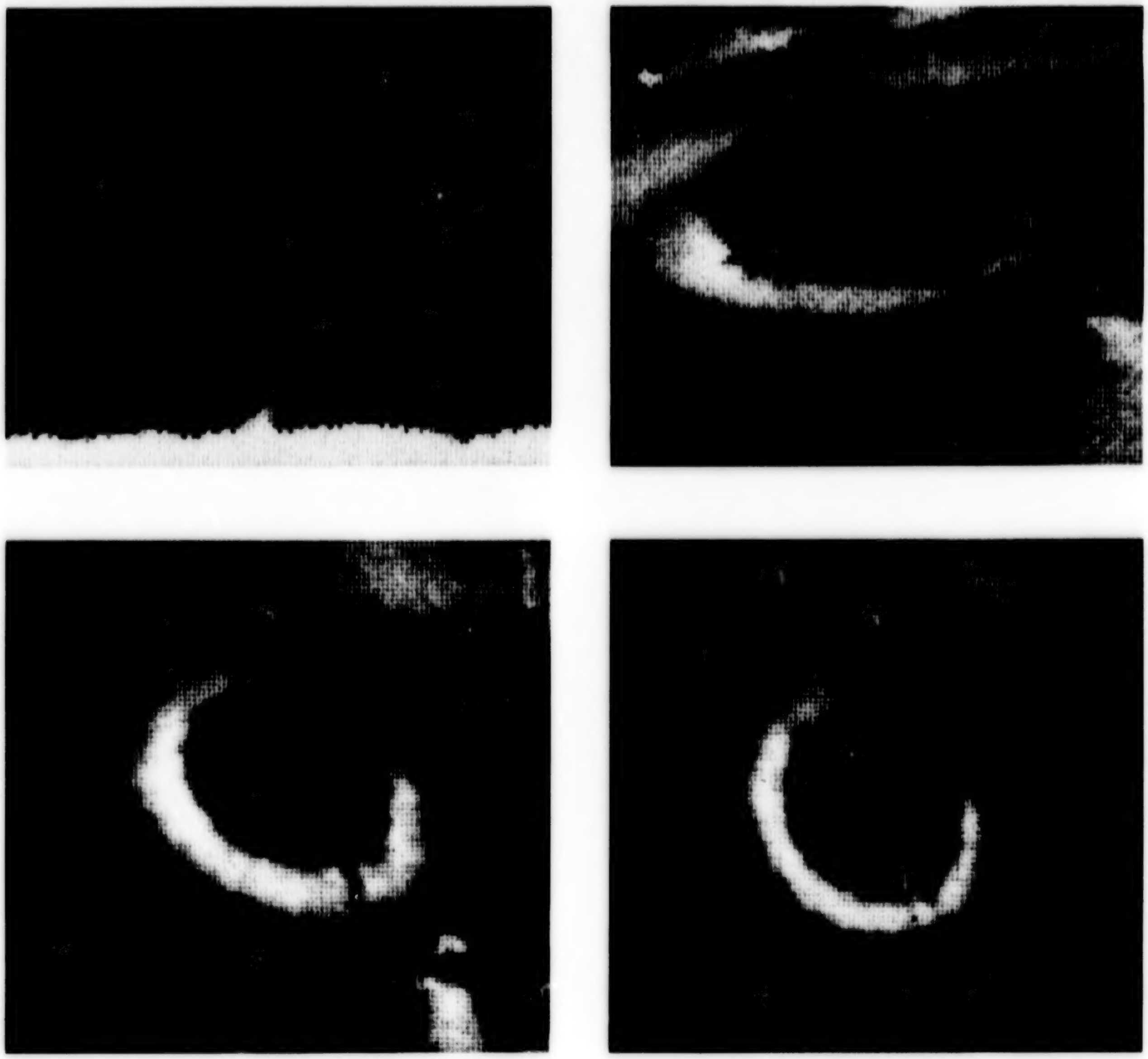

Figure 8. Four views of the active plume Prometheus (latitude −2°, longitude 152°), from different viewing angles. Dark jets have the same albedo when seen against bright surface or against space, so material is optically thick. Plume's height is 75 km and bright ring has a diameter of about 300 km. From left to right, FDS 16368.26, 16372.36, 16375.28, and 16377.50, clear filter.

(20–200 km in diameter) and are much smaller in area than the plumes, so the actual plumes do not seem to be pronounced thermal anomalies.

The Loki plumes may represent a hybrid between the two classes. Two plumes were observed, emanating from each end of a linear marking or fissure on the northeast margin of Loki Patera (fig. 12). Plume deposits from Loki are intermediate, with respect to the two plume types, in terms of diameter and spectral properties. According to Strom et al. (1981), images acquired a few days prior to the Voyager 2 closest approach show that one or both of the Loki plumes reached a height of ~350 ± 75 km, but by the time of closest approach the height had dropped to about that seen in Voyager 1 images (~165 km; see table 1). Therefore, Loki may behave like a Pele-type eruption for short periods of time.

Perhaps the most remarkable characteristic of the two plume classes is the markedly bimodal durations of the eruptions. During both encounters, separated by

ORIGINAL PAGE
BLACK AND WHITE PHOTOGRAPH

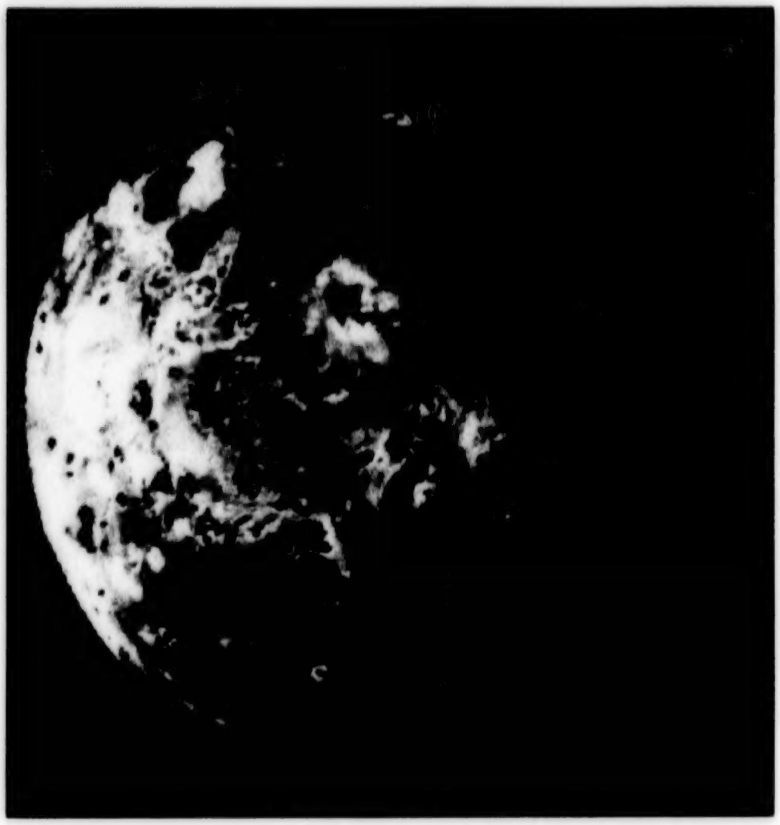

Figure 9. Voyager 2 image showing surface changes caused by eruptions of Surt and Aten. Each eruption filled 50-km diameter calderas with dark material, and plumes cover areas of about 1400 km diameter. FDS 20641.58, blue filter.

4 months, all six Prometheus-type plumes were continuously active at about the same level and the two Loki plumes were continuously active at fluctuating levels. It is highly probable that all eight were continuously active during the period between encounters. If they were sporadically turning on and off between encounters, the probability of their all being active during all observations is 1 in 2^n where n is the number of observations (>20, see table 1), so the probability of their being short-lived compared to 4 months is less than 1 in 10^6. For all eight to remain active for both encounters, their probable mean lifetime must be greater than 32 months.

The Pele-type eruptions (Pele, Surt, and Aten) erupt for much shorter periods, probably from days to a few months. Pele was active during the first encounter but ceased activity sometimes before the first Voyager 2 images were acquired. Surt was not active during the first encounter and was probably not active during the second (unless it was less than 100 km high, but the size of the ejecta blanket suggests that Surt reached a height of ~300 km). The rapid decay of an outburst of 5-μm radiation located at the longitude of Surt (Sinton, 1980a) suggests that the eruption (or an event associated with it) lasted less than a day or two. Aten showed no plume activity during either encounter, so the eruption must have lasted less than 4 months.

Thermodynamics

A thorough treatment of the thermodynamics of volcanic plumes on Io was provided by Kieffer (1982). She considered both SO_2 and sulfur (S_2) as working fluids for driving plume volcanism. Distinct styles of volcanism are possible for either fluid depending on the temperature and depth (hence pressure) of the magma chamber; these styles are characterized by the phase (gas or liquid) of the fluid in the reservoir, velocity of plumes exiting the volcanic crater, presence of solid and/or liquid in the outgoing plume, and symmetry of the plume. Two energetically distinct eruptive processes, with ejection velocities up to 1 km s^{-1}, are possible. Low-entropy volcanism could occur from SO_2 in

ORIGINAL PAGE
BLACK AND WHITE PHOTOGRAPH

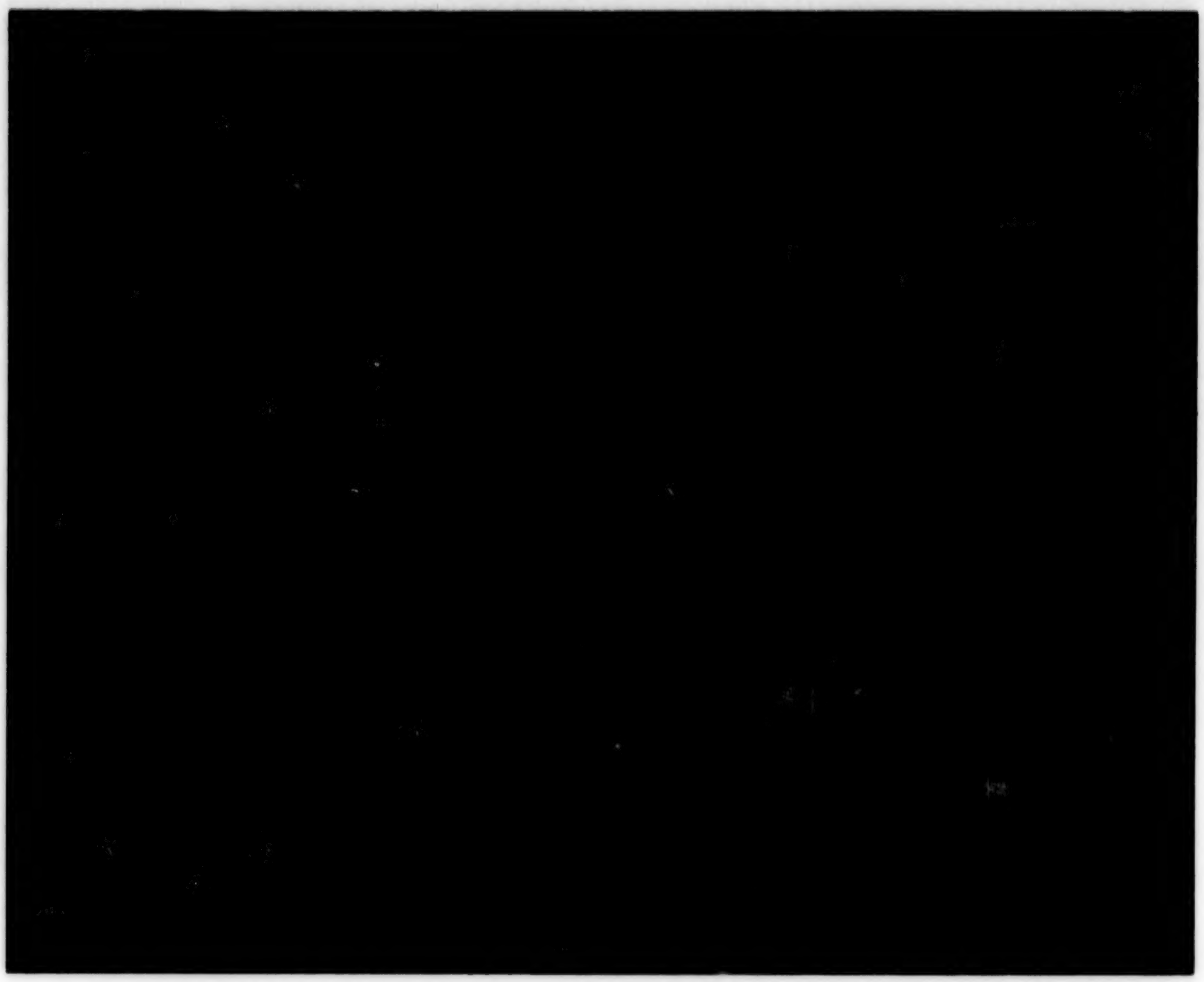

Figure 10. Voyager 1 and 2 global mosaics in simple cylindrical projections, from McEwen (1988). Color consists of narrow-angle camera orange-, blue-, and violet-filter mosaics, each linearly stretched to maximize contrast. Limb-darkening and phase variations have been corrected to normal albedo. Major changes between Voyager encounters occurred in region from longitude 240° to 360°.

shallow reservoirs ($P < 40$ bars) and at modest temperatures ($T < 393$ K, the melting point of sulfur). This type of eruption may explain the diffuse white deposits near the bases of scarps on Io (McCauley et al., 1979). High-entropy volcanism could occur with either SO_2 or sulfur in reservoirs ~1.5 km deep ($P = 40$ bars) and at temperatures greater than 393 K. Plumes do not form under the entire range of conditions, however. Sulfur dioxide plumes can originate in reservoirs with temperatures either below or above 393 K; hence, such plumes could be powered by subsurface reservoirs of near-liqudus sulfur. Sulfur plumes, on the other hand, require temperatures in subsurface magma chambers in excess of 600 K; cooler conditions produce vesicular flows. Such high temperatures suggest contact of a sulfur magma chamber with hot or even molten silicates. An ejection velocity of 1 km s^{-1} can be produced by either SO_2 or S_2 heated to ~1000 K.

The most striking success of Kieffer's treatment lies in its application to the two classes of volcanic plumes (table 2). The Prometheus-type plumes are entirely consistent with SO_2 as the working fluid, powered by near-liquidus subsurface sulfur. The large Pele-type plume eruptions are consistent with sulfur as the working fluid driven by near-liquidus silicates ($T \sim 1000$ K). Associated hot spots (representative of minimum reservoir temperatures) and plume ejection velocities match Kieffer's models, and spectral properties of the plume

ORIGINAL PAGE
COLOR PHOTOGRAPH

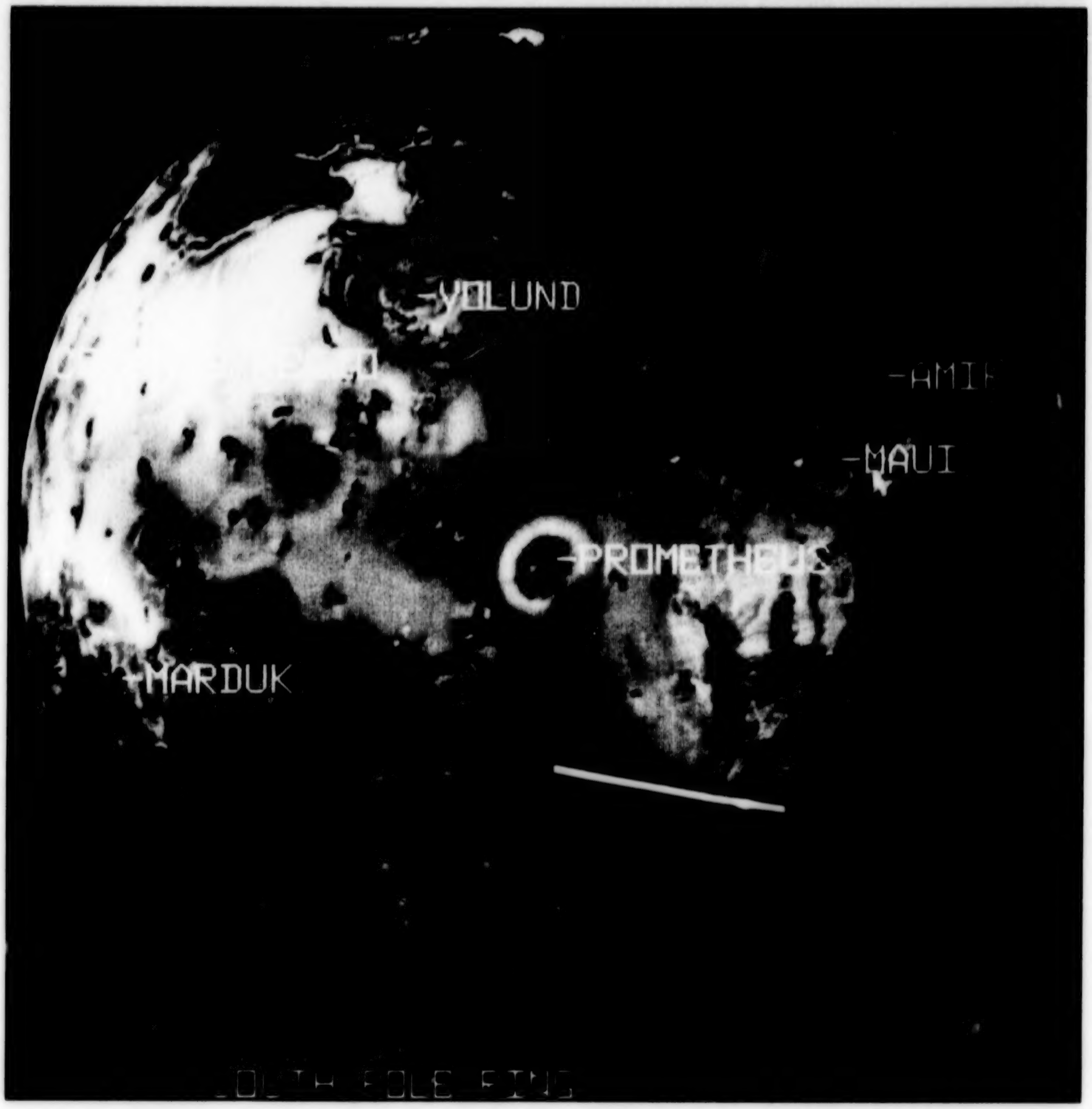

Figure 11. Full-disk image centered on Prometheus (latitude −2°, longitude 153°), showing bright white equatorial band and 1000-km-diameter south pole ring (*extreme bottom of picture*). Five active Prometheus-type plumes shown here: Volund, Amirani, Maui, Marduk, and Prometheus. FDS 16368.38, blue filter.

deposits are consistent with SO_2 for the Prometheus-type deposits and sulfur for the Pele-type deposits.

If the Prometheus- and Pele-type plumes are driven by SO_2 and sulfur, respectively, then this may explain the bimodal eruption durations (McEwen and Soderblom, 1983). Liquid SO_2 has a very low viscosity (~0.005 poise, about half that of water) so it can move freely through the subsurface to supply the long-lived Prometheus-type eruptions. Liquid sulfur has a much higher viscosity (0.1 to 600 poise, depending on temperature) and would move much more slowly through the subsurface, so a Pele-type eruption could deplete

ORIGINAL PAGE
BLACK AND WHITE PHOTOGRAPH

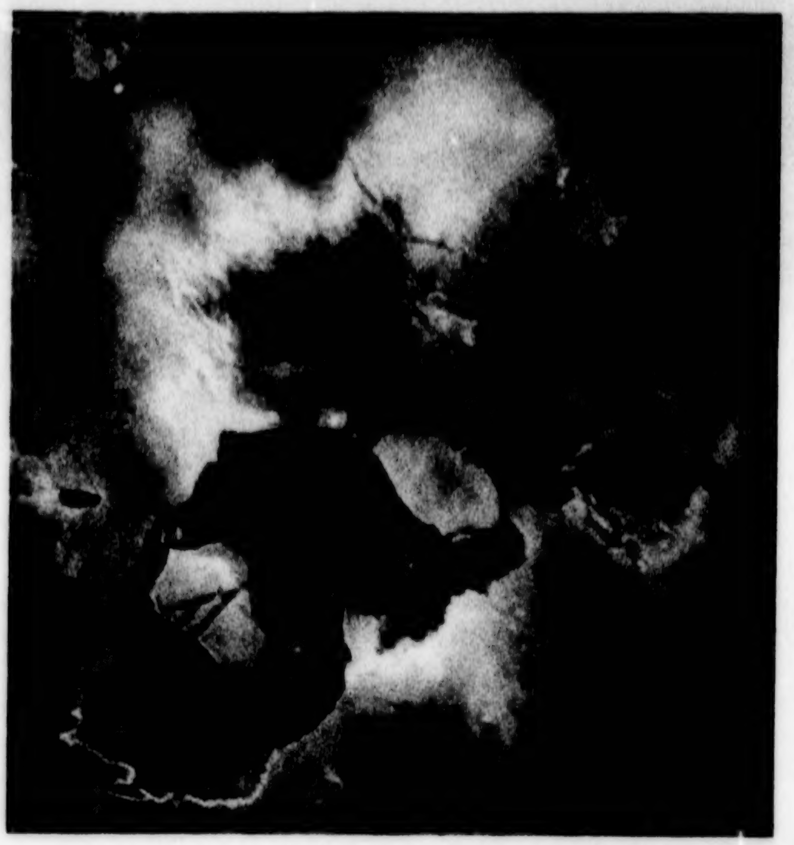

Figure 12. Loki Patera (latitude +12°, longitude 309°) and plumes. Several workers have commented that Loki Patera looks like a lake covered by crusts of various ages, indicating a complex history of overturn and reannealing. FDS 16389.42, clear filter.

the reservoir region of sulfur, thereby ending the eruption. The plume ejection velocities of 0.5–1.0 km/s^{-1} indicate large proportions (up to 50 percent by weight) of volatiles (Wilson and Head, 1983), so the long-lived nature of Prometheus-type eruptions indicates that substantial SO_2 reservoirs must be present in the equatorial regions of Io.

Plume Geometry and Dynamics

Two types of plume geometry on Io have been postulated by Kieffer (1982, 1984). "Balanced" or umbrella-shaped plumes such as those of Pele and Prometheus may form when the erupting fluid traverses a crater deeper than about 1 km, so that the initial plume pres-

Table 2. Characteristics of Io's Two Plume Classes

	Pele Type	**Prometheus Type**
Eruptive height	250–300 km	50–120 km
Diameter of plume deposits	1000–1500 km	200–600 km
Eruptive velocity	1 km s^{-1}	0.5 km s^{-1}
Eruptive duration	Days–months	Months–years
Frequency of new eruptions	10 yr^{-1}	<3 yr^{-1}
Associated surface temperatures	600–650 K	<450 K
Plume optical densities	Optically thin	Portions optically thick
Spectra of plume deposits	Relatively dark red	Bright white
Compositional association	S-rich, SO_2-poor	SO_2-rich
Global distribution	Longitude 240–360°; possibly longitude 0–100°	Latitude +30° to −30°
Geologic interpretations	S vaporized by molten silicates; dominantly silicate crust	SO_2 vaporized at low T (~400 K), perhaps by molten S; abundant SO_2 in crust

ORIGINAL PAGE
BLACK AND WHITE PHOTOGRAPH

sure is close to ambient and the particles and vapor will follow ballistic trajectories. "Overpressured" or diffuse plumes may form when the fluid erupts from a fissure or shallow crater. Kieffer suggested that plume 2 (western Loki plume) may be an example of a diffuse plume, although the plume had an inner dark curtain with a looping path suggestive of a ballistic trajectory (fig. 12). Other workers (Cook et al., 1979; Strom et al., 1981; Wilson and Head, 1981) have analyzed plume dynamics in terms of ballistic versus shock-front or aerodynamic models. In the ballistic model, particles become detached from the gas flow and follow parabolic trajectories determined by initial velocities and ejection angles at the vent. Based on computer simulations, Strom et al. (1981) and Wilson and Head (1981) concluded that the shape, brightness distribution, and pattern of surface deposits of Prometheus can be simulated by a ballistic model with an ejection velocity of 0.5 km s^{-1} and ejection angles varying from 0° (vertical) to 55°. In the shock-front model, particles are entrained and transported upward by the gas, and a dome-shaped shock front forms by collision between rising and falling parcels of gas (Cook et al., 1979; Strom et al., 1981). Strom et al. (1981) concluded that the brightness distribution of Pele, which has a bright outer margin, is best explained by a shock front near the top of the plume. Pele was the only observed plume with a bright outer margin; all other plumes continuously decrease in brightness with distance from the vent. However, Wilson and Head (1981) showed that the bright outer margin of Pele could be reproduced by a ballistic model. Additional evidence for aerodynamic behavior in Pele's plume is the complex filamentary structures and swirls seen in the plume (fig. 7), which indicate that the visible particles are interacting with the gas.

Particle sizes in the plumes should have a major effect on the plume dynamics (Wilson and Head, 1981, 1983): Only very small particles (<10 μm) will stay locked to the motion of the gas, whereas larger particles (>100 μm) will decouple from the gas flow near the vent and follow isolated ballistic trajectories. Particle sizes may be estimated from photometric and dynamic models. Two photometric observations suggest that some of the plumes contain particles of the order of 1 μm in diameter or smaller (Smith et al., 1979c): (1) the plumes are generally brightest at shorter wavelengths (violet and ultraviolet filters, 0.32–0.44 μm); and (2) plumes 5 and 6 (Amirani and Maui) appear to scatter light more strongly in the forward than the backward direction. Plume 2 (Loki) probably has two particle populations (Collins, 1981): an outer zone with particles 0.002–0.02 μm in diameter (from a Rayleigh-like scattering model), and an inner zone with particles greater than 2 μm in diameter (based on the reddish color of the material and the size and structure of the jet). Kieffer (1982) predicted that SO_2-driven plumes should contain SO_2 snowflakes no larger than 0.1 μm in diameter, consistent with Collins's model for the outer region of Loki, and infrared spectra during eclipse show possible evidence for SO_2 snow above Loki (Cruikshank et al., 1985). The ballistic models of Strom et al. (1981) and Wilson and Head (1981) for Prometheus suggest that the particles must be at least 10 μm in diameter. No multispectral or high-phase observations of Prometheus were acquired, so there is no direct photometric constraint on particle sizes for this plume. However, the morphology, albedo, and surface deposits of Prometheus are similar to the other Prometheus-type plumes, such as Amirani and Maui, for which scattering properties indicate small particles. Perhaps the scattering and dynamic constraints on particle sizes may be reconciled by the balanced plume model of Kieffer (1982, 1984), in which both the gas and small particles coupled to the gas follow ballistic paths.

The idea that the plumes may be affected by an electrical current running between Io and Jupiter's ionosphere, initially suggested by Gold (1979) and rebutted by Cook et al. (1981), has been revived by Peratt and Dessler (1987). They suggest that the eruptions are initiated by volcanic processes but that the plume dynamics can be influenced by the plasma arcs, and that the shape and "filamentation" (dark jets) of Prometheus (fig. 8) are consistent with this mechanism. However, the shape and brightness distribution of Prometheus can be explained by simple ballistic models (see above), and the dark jets may be due to irregularities in the shape of the vent. Furthermore, the plasma-arc model is based on the idea that Io has a highly conducting molten interior, but this model is now considered unlikely. Therefore, most of the current is likely to pass through Io's ionosphere rather than through the satellite's interior (Colburn, 1980). Nevertheless, the observation of nighttime auroras in the vicinity of active plumes (Cook et al., 1981) does suggest some sort of electrical interaction with the plumes.

Resurfacing Rates

A variety of ways of estimating the total resurfacing rate yield a range of 10^{-3} to 10 cm yr^{-1} (Johnson et al., 1979; Johnson and Soderblom, 1982). The absence of impact craters on the visible surface of Io requires a rate >0.1 cm yr^{-1}. The energy required to bring internal material to the surface at this rate is less than 10 percent of the global average heat loss. If the hot spots are equivalent to resurfacing by surface flows (Reynolds et al., 1980), then the resurfacing rate is from 1 cm yr^{-1} (by silicates) to 10 cm yr^{-1} (by sulfur). The plumes might constitute an insignificant fraction or a significant bulk of the resurfacing material, depending on the plume particle sizes (see discussion above). If ~1 μm particles are assumed, the plume resurfacing rate may be as low as 3.5×10^{-4} cm yr^{-1} (Johnson et al., 1979). However, the mass flux from the plumes may be several orders of magnitude larger than this lower limit if either smaller or larger particles are present. Collins' (1981) estimate of 0.02–0.002 μm particle sizes in the outer Loki plume (see above) implies a resurfacing rate from this plume alone of up to 1 cm yr^{-1}. The 100 μm particle-size model of Wilson and Head (1981) for Prometheus also leads to much larger mass fluxes; if this model is applied to all of the Prometheus-type plumes and the inner portion of plume 2 (western Loki), then the resurfacing rate is again about 1 cm yr^{-1}. Therefore, the total resurfacing rate from the plumes could be as high as 2 cm yr^{-1}. Resurfacing by flows must be at least as significant as resurfacing by plumes, or else the flows would be buried and we wouldn't see them in the images. If the sulfur-lake model of Lunine and Stevenson (1985) applies, this could also be a significant resurfacing mechanism.

Spatial and Temporal Effects on Color and Albedo

The color and albedo variability of Io's surface during three different time spans has been described by McEwen (1988): (1) that of years to decades, (2) that of the four months between Voyager encounters, and (3) that of the hours of the Voyager 1 encounter.

Variability over years to decades can be judged only on the basis of Io's disk-integrated lightcurve. Although relatively minor changes have been reported by Lockwood et al. (1980), major changes have not been apparent during the past 50 years (Morrison et al., 1979). The global mosaics (fig. 10) were convolved into simulated disk-integrated lightcurves at a phase angle

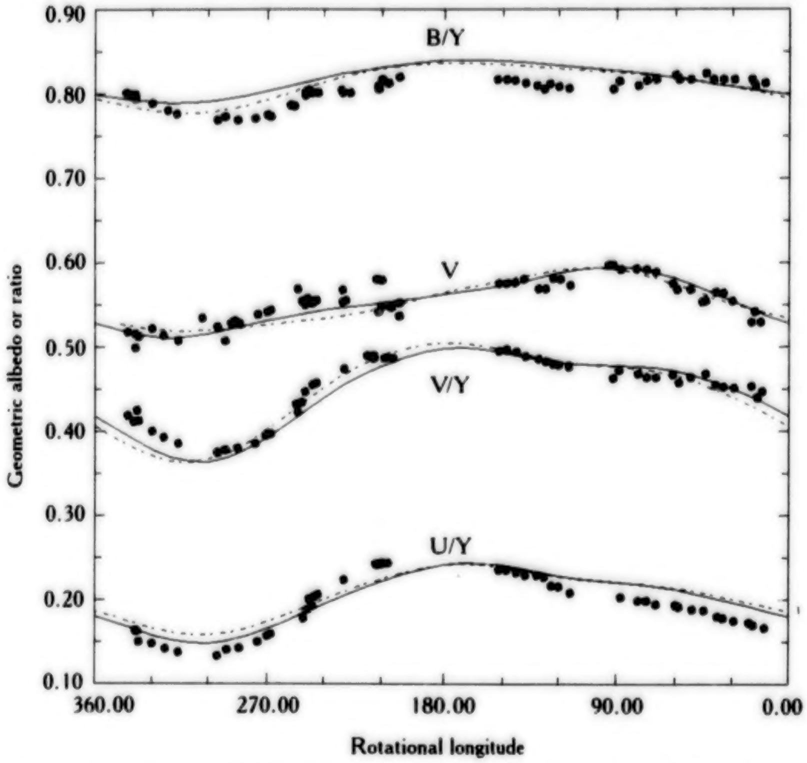

Figure 13. Disk-integrated lightcurves of Io, showing observations of Morrison et al. (1974) (*circles*) and model values derived from global mosaics (*solid line*, Voyager 1; *dashed line*, Voyager 2). All values normalized to 6-degree phase angle. Ratios B/Y, V/Y, and U/Y from uvby system; geometric albedo in visual filter (V) from UVB system. From McEwen (1988).

of 6° (fig. 13) for comparison with the telescopic observations of Morrison et al. (1974). Both the Voyager 1 and Voyager 2 global mosaics agree surprisingly well with the Earth-based observations from 1973, considering the volcanic activity. Given Io's resurfacing rate, the optically active surface must be only a few years old, on average. To explain the constancy of the lightcurve, Morrison et al. (1979) suggested that there must be a deep-seated asymmetry in the volcanic sources that outlives individual eruptions, such that the relatively dark red material has been deposited over the same hemisphere during at least the past 60 years. McEwen and Soderblom (1983) expanded on this idea by demonstrating that the hemispheric-scale color and albedo variations are dominated by the distribution of Pele-type eruptions.

Color and albedo changes that occurred during the four months between Voyager encounters have been described by various workers (e.g., Smith et al., 1979c; Strom et al., 1981; McEwen, 1988; see fig. 10). The pronounced and large-scale changes all occurred in the "active" hemisphere of Io, from longitude 240° to 360°. New surface deposits ~1400 km in diameter formed around the calderas Aten and Surt, and the "cleft" was filled in the southern portion of Pele's deposits. The floors of Aten and Surt darkened, and apparently these 50-km-diameter depressions were resurfaced by lava flows and/or foundering of lava lakes. Two calderas with low albedos became much brighter, apparently covered by deposits from the Aten and Surt eruptions. Substantial changes occurred in Loki Patera: The northern two-thirds brightened whereas the lower third became darker, and there were new deposits from the two Loki plumes. Other, smaller or less pronounced differences between the Voyager 1 and 2 mosaics are described by McEwen (1988).

Short-lived color and albedo changes occurred around Pele, especially southeast of the plume fallout, during a period of just hours during the Voyager 1 encounter (fig. 14). The area southeast of the plume fallout became brighter and bluer, and changes occurred in the pattern of streaks radial to Pele. These patterns were not present during acquisition of image FDS 16375; they appeared sometime before the acquisition of FDS 16382 five hours later; and they disappeared before FDS 16390 was acquired after another six hours. The transient patterns are also absent in Voyager 2 images. The changes could have been due to the condensation and later sublimation of SO_2 frost on the surface or in the atmosphere, or alternatively, by scattering from fine particles of dust above the surface. Lee and Thomas (1980) demonstrated that small particles (<10

Figure 14. Transient changes near Pele during Voyager 1 encounter. *Left:* FDS 16375.36; *right:* FDS 16382.17, acquired 5 hours after 16375. Both are violet-filter images, simple cylindrical projections.

ORIGINAL PAGE
BLACK AND WHITE PHOTOGRAPH

μm) could be transported by a flow of gas with at least 10^{-9} bar pressure, provided that the particles are first injected into the flow (by volcanic venting) rather than being entrained from the surface. The radial patterns may be due to the active horizontal transport of fine particles away from Pele. "Rays" can be seen extending up to 1500 km from the vent of Pele, or up to 800 km from the outer margin of direct plume fallout (fig. 15). The ray particles may be transported by gas expansion from the vent, as modeled by Moreno et al. (1988), or by ballistic mechanisms such as those proposed for impact-crater rays (Oberbeck, 1975). At least one of the rays may have been active during the Voyager 1 encounter; it can be seen on the bright limb as a lateral extension, about 50 km high, extending to the north of the main plume (see fig. 2 of Strom et al., 1981). Numerical modeling of this event may provide useful constraints on the plume and atmospheric properties and dynamics. Transient changes such as those near Pele should be detectable from Earth orbit with the Space Telescope.

Short-term albedo and color changes may have also occurred during the first encounter over the area north and west of plume 4, Volund (Strom et al., 1981).

Figure 15. "Rays" radial to Pele extending up to 800 km farther from the vent than heart-shaped plume fallout. Ratio of images FDS 16375.36 (violet)/FDS 16375.40 (orange).

ORIGINAL PAGE
BLACK AND WHITE PHOTOGRAPH

However, the differences between the images of this area are very subtle, and may be due to differences in photometric conditions and resolution.

Effects on Atmosphere, Torus, and Sodium Cloud

The volcanic plumes must significantly affect the composition and dynamics of Io's atmosphere, plasma torus, and sodium cloud. The effects could be direct, from injection of materials, or indirect, by affecting the surface composition. Understanding the precise interactions between plume, atmosphere, and magnetosphere is important in order to relate atmospheric and magnetospheric observations to variations in volcanic activity (Johnson et al., 1979; Johnson and Soderblom, 1982; Nash et al., 1986; Schneider et al., this volume).

There are three plausible SO_2 atmospheric models: (1) abundant solid SO_2 on the surface, buffering a "thick" equilibrium atmosphere with a subsolar pressure of $\sim 10^{-7}$ bar (e.g., Kumar and Hunten, 1982); (2) the model of Fanale et al. (1982), with atmospheric pressures below about 10^{-8} bar, which emphasizes the importance of local coldtrapping over bright patches of SO_2, frost; and (3) a time-variable atmosphere with pressures ranging from less than 10^{-12} bar (buffered by subsurface coldtrapping) up to 10^{-7} bar, depending on the level of active volcanic venting of SO_2 (Matson and Nash, 1983).

The densities and distributions of materials in the torus (mostly ionized S and O) and sodium cloud leave little doubt that the material has escaped from Io. However, the loss rates are insignificant relative to resurfacing rates, so virtually all of the volcanically erupted material must remain on the surface (Johnson and Soderblom, 1982). Sputtering from the surface, atmosphere, or plume canopies may supply sulfur and sodium, and thermal escape may supply oxygen (see reviews by Nash et al., 1986; Cheng et al., 1986).

Recently, models have been proposed in which the volcanic plume activity is the major control over the atmospheric and torus densities (Eviatar, 1987), but these models may be controversial.

HOT SPOTS

Evidence for hot spots or thermal anomalies on Io existed years before the Voyager encounters, but the evidence was not understood (see Johnson and Soderblom, 1983). Thermal IR observations revealed two curious relations. First, when Io is eclipsed by Jupiter its temperature falls as expected for a surface with low thermal inertia, but the minimum temperature is too high. Second, the infrared brightness temperature of Io is significantly higher at shorter wavelengths. After the Voyager 1 encounter and the discovery of active volcanism, these observations were understood as due to hot spots with temperatures ranging up to ~600 K covering 1 to 2 percent of Io's surface, whereas the "passively" heated surface (heated only by insolation) reaches temperatures no higher than ~140 K (Morrison and Telesco, 1980; Matson et al., 1981; Sinton, 1981). The global heat flow of Io indicated by the infrared observations is about 20 times greater than Earth's heat flow (0.08 W m^{-2}, Sclater et al., 1980).

Individual Features

The IRIS carried by the Voyager 1 spacecraft observed individual thermal anomalies on Io from about 4- to 55-μm wavelength (Hanel et al., 1979). The circular fields of view range from 50 to 700 km in diameter at Io. Nine major hot spots were identified from IRIS by Pearl and Sinton (1982), and a tenth hot spot was recently identified by Pearl (1987) (see table 3).

All of the IRIS hot spots correspond to low-albedo surface features (Pearl and Sinton, 1982); all of the largest and most prominent low-albedo features in the areas observed by IRIS were identified as hot spots (McEwen et al., 1985). Most of the features correspond to calderalike structures (e.g., figs. 2, 7, and 11). The dark features in Creidne Patera (fig. 2), Nemea Planum (fig. 4), and northwest Colchis Regio (fig. 11) appear to be lava flows. Three of the IRIS hot spots were associated with active volcanic plumes: Loki, Pele, and Amirani/Maui.

Four lines of evidence suggest a 1:1 correspondence between hot spots and low-albedo features (orange-filter albedo < 0.3; McEwen et al., 1985): (1) the 1:1 correspondence between dark features and IRIS hot spots; (2) a match between the longitudinal distributions of dark material and of the 8.7- and 10-μm emission from Io (from Johnson et al., 1984, 1985); (3) an association between dark features and the source regions for recent or active volcanism; and (4) the correlation of dark areas with calderas, which form by collapse over shallow magma chambers and are characterized by elevated heat flows (e.g., Williams and McBirney, 1979). McEwen et al. (1985) used this correlation to identify additional potential hot spots in regions not observed by IRIS; a catalog of 88 features was produced. The largest additional feature is a gigantic (~1000-km-diameter) ringlike structure near the south pole ("south pole ring," see table 3 and fig. 11). If this south polar hot spot hypothesis is correct, then the global heat flow is significantly increased, and the polar location has important implications for tidal heating mechanisms (Segatz et al., 1988). However, recent observations (Goguen et al., 1988; Howell and Sinton, this volume) show no evidence for the south pole ring, so it is either not a hot spot or has a significantly lower temperature than that modeled by McEwen et al. (1985) (i.e., $T < 280$ K).

Temporal Variability

The most spectacular time-variable thermal anomalies observed on Io are the 5-μm outbursts, consisting of short-lived (hours to days) enhancements of 5 μm, consistent with relatively high-temperature (~600 K) hot spots. There are only three simultaneous observations at multiple wavelengths from which reliable temperature area models can be derived (Witteborn et al., 1979; Johnson et al., 1986; Goguen et al., 1988); the resulting temperatures are 550 to 600 K. The Voyager 1 Pele observation (650 K; Pearl and Sinton, 1982) may be another example, thought to be short-lived due to the short-lived nature of the associated plume. The best time-resolved measurement (Sinton, 1980a) was probably an observation of Surt. Other 5-μm outbursts have been reported by Fink et al. (1978), Sinton et al. (1983), and Goguen and Sinton (1985; see also Howell and McGinn, 1985). A single feature at 3.8 μm observed during occultation (Goguen et al., 1988) may correspond to a small area (~20 km²) with a temperature of at least 1000 K, thereby suggesting active silicate volcanism.

The 5-μm outbursts may correspond to Pele-type plume eruptions (Sinton, 1980b; McEwen and Soderblom, 1983). The Pele-type eruptions seem to be

Table 3. Hot Spots and Temperature/Area Models[a]

Feature Name	Latitude, Longitude (degrees)	Area (km²)	Temperature (K)	Power (10^{12} W)	Percent Total Heat Flow[b]	
					Model 1	Model 2
South pole ring	−67, 100–180	86,680	280	30	39.5	—
Loki Patera	12, 309	1,385 45,996	450 245	12.6	16.6	21.0
Babbar Patera	−40, 272	88 16,286	322 175	0.9		
Ülgen Patera	−40, 289	616 19,113	355 191	2.0	4.3	5.5[c]
Svarog Patera	−48, 268	2,827	221	0.4		
Pele	−18, 256	113 20,106	654 175	2.2	2.9	3.7
Amaterasu Patera	38, 307	5,000	283	1.8	2.4	3.0
Amirani/ Maui	22, 120	531 7,543	395 200	1.4	1.8	2.3
Near NW Colchis	31, 208	254 9,503	385 165	0.4	0.5	0.7
Creidne Patera	−53, 344	1,257	231	0.2	0.3	0.3
Near Nemea Planum	−81, 330	908	225	0.1	0.1	0.2

[a] All temperature-area models from Pearl and Sinton (1982), except for Amaterasu Patera (from Pearl, 1987) and south pole ring (from McEwen et al., 1985). [b] Model 1 assumes south pole ring is major hot spot (from McEwen et al., 1985), resulting in total power of 7.6×10^{13} W, whereas Model 2 neglects south pole ring and total power is 6×10^{13} W (from Johnson et al., 1984, 1985). [c] Most likely, only part of thermal anomaly of Babbar Patera was observed in IRIS footprint labeled Babbar, and much of Ülgen and Svarog Paterae footprints included parts of Babbar Patera (see Pearl and Sinton, 1982, figs. 19.9, 19.10, and 19.13; McEwen et al., 1985). Therefore, we have combined these three observations here.

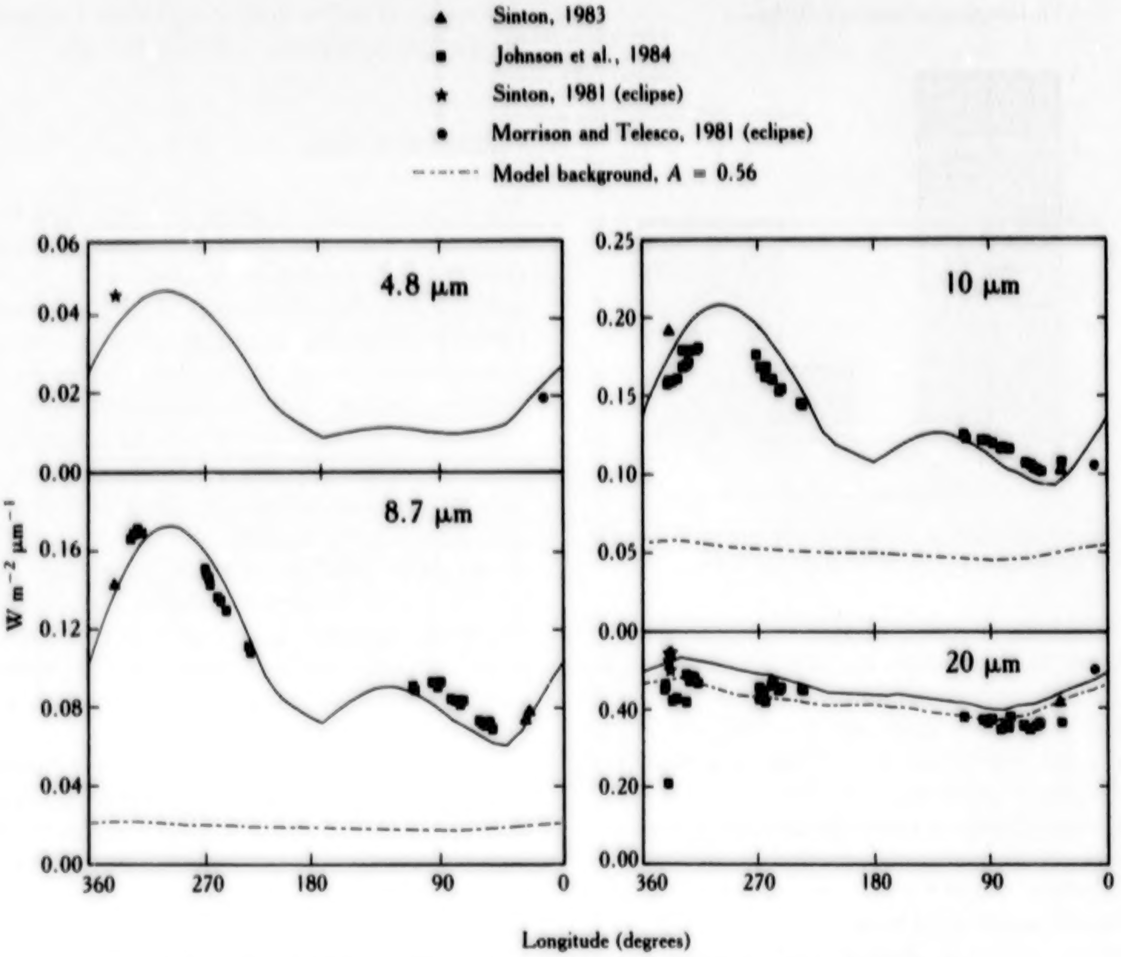

Figure 17. Infrared observations at four wavelengths, primarily from Johnson et al. (1984), compared to model flux curves of McEwen et al. (1985) based on distribution of low-albedo features.

hemisphere-scale regions where hot spots are radiating significant power (McEwen et al., 1985). Tidal heating models predict relatively uniform heat production over the satellite, or patterns that are symmetric about the axes of the triaxial ellipsoid (Segatz et al., 1988), but the hot-spot heat flow does not match any of these patterns. Therefore, perhaps some of the regions where hot spots and mountains are absent are characterized by a greater conductive heat flux and a thinner lithosphere.

Enhanced conductive heat fluxes may also occur in association with hot spots. For example, conducted heat loss from the Hawaiian hot spot on Earth is about 10 times greater than the volcanic heat loss (Detrick et al., 1981; Morgan and Phillips, 1983). The distribution of large topographic features on Io (U.S. Geological Survey, 1987) shows a zone around Loki where no appreciable topographic relief is apparent; perhaps this is due to enhanced conductive heat loss and a thin lithosphere in this region. However, the topographic measurements of Gaskell and Synnott (1987) indicate that the Loki region is a large topographic low, rather than a topographic swell as expected due to the buoyant effect of heating silicate rock.

The active volcanic plumes release energy from Io's interior in the form of kinetic energy (Johnson and Soderblom, 1982). Whether this is a significant energy-loss mechanism relative to hot-spot heat loss depends on the mass eruption rate estimates, which in turn depend on particle-size estimates. If the mass eruption rate is near the minimum value of $\sim 10^8$ g s^{-1}, then the energy flow is less than one-tenth of 1 percent of the hot-spot output. If the mass eruption rate is near the highest estimates ($\sim 2 \times 10^{11}$ g s^{-1}), then the energy flow is near 0.5 W m^{-2}.

The total energy loss from Io may be estimated as follows: About 1.5 W m^{-2} is released from the hot spots, with uncertainties of about ±0.5 W m^{-2} due to uncertainties in the background emission and latitudinal distribution of hot spots. The conducted heat flow is poorly constrained over much of Io, but probably doesn't exceed 0.5 W m^{-2} as a global average. Kinetic energy from the plumes may be as high as 0.5 W m^{-2}. Therefore, the total energy loss from Io may range from 1.0 to 3.0 W m^{-2}. This is a considerably greater range of uncertainty than most workers have acknowledged. Note that the maximum steady-state energy flow theoretically possible from tidal heating is ~2 W m^{-2}, so if Io's energy flow exceeds this value, then either episodic tidal heating (Greenberg, 1982, 1987; Ojakangas and Stevenson, 1986) or intermittent heat loss (Consolmagno, 1981b; Sinton, 1982) must be invoked. Furthermore, if the analysis of Greenberg (this volume) is correct, then Io's energy flow exceeds the average dissipation rate (over the past 300 years) by about a factor of 10.

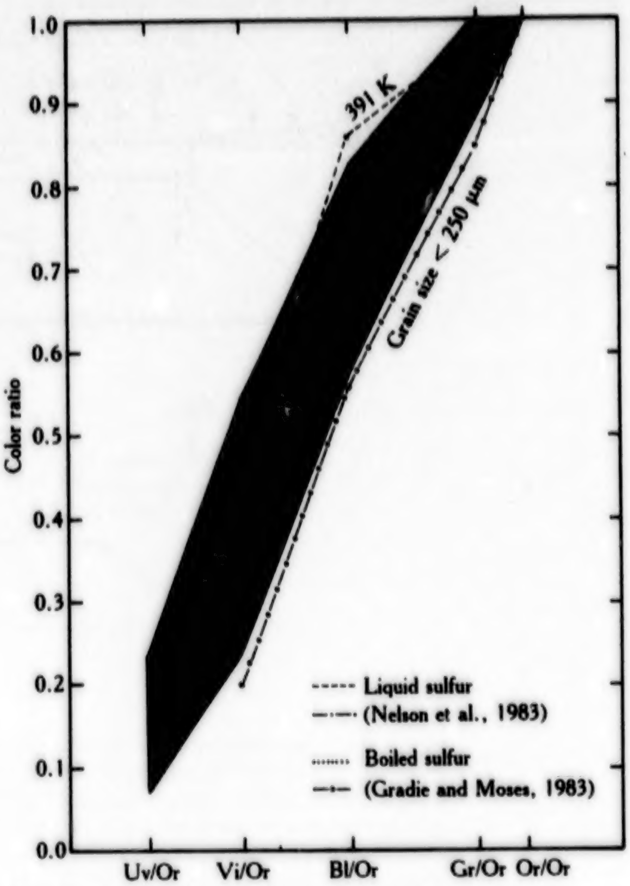

Figure 18. Spectral reflectance of low-albedo features (*area inside solid outline*) compared to laboratory spectra for liquid sulfur and boiled sulfur. Figure from McEwen et al. (1985).

Models: Sulfur Lakes or Silicate Flows?

What are the actual hot materials radiating as hot spots? Two models have been developed: sulfur (Lunine and Stevenson, 1985) and silicates (Carr, 1986). We review the evidence for each model below; for further discussion, see Lunine (this volume).

Sulfur Lakes Several lines of evidence suggest the importance of elemental sulfur to the volcanism on Io: (1) evidence for sulfur on the surface and in the plasma torus (e.g., Nash et al., 1986); (2) demonstration that elemental sulfur is a thermodynamically plausible working fluid for the large volcanic plumes (Reynolds et al., 1980; Kieffer, 1982; McEwen and Soderblom, 1983); (3) consistency of spectral properties of dark, hot regions on Io with liquid sulfur and thermally altered solid sulfur (McEwen et al., 1985; see fig. 18); (4) the presence of hot spots (e.g., Loki, Amirani/Maui) with temperatures above or near the elemental sulfur melting point (Pearl and Sinton, 1982); and (5) morphologies of some hot-spot areas suggestive of molten lakes (Smith et al., 1979a; Johnson and Soderblom, 1983; McEwen et al., 1985; see fig. 12).

Lunine and Stevenson (1985) considered the physical and chemical processes that would operate in a molten sulfur lake exposed to near-vacuum conditions at Io's surface and applied the model to several hot spots, primarily Loki Patera. Figure 19 schematically illustrates the important processes. The lake is heated from below by near-liquidus silicates and is confined perhaps by a silicate caldera. The primary mechanism of heat transport within the lake is convection, powered by the hot silicates beneath; at the surface, heat is removed by radiation at a specified surface temperature above the sulfur melting point and by evaporation. The evaporated sulfur expands outward, cooling and condensing in regions adjacent to the lake. The infrared radiation coming from the region is then composed of the direct radiation off the lake, radiation from sulfur condensing in regions adjacent to the lake, and a background temperature. The second source is nonisothermal and has a temperature profile determined by the density profile of vapor transported away from the lake.

Pearl and Sinton (1982) analyzed Voyager IRIS spectra of hot-spot regions. They found a significantly better fit to spectra of Loki when two distinct temperature components (plus the background) were used in place of one. The high-temperature component, with an equivalent radius of 20 km, is above the sulfur melting point and can be identified with the lake. The moderate temperature component, occupying an equivalent radius of 120 km, is subsolidus and can be considered the isothermal equivalent of the decreasing tempera-

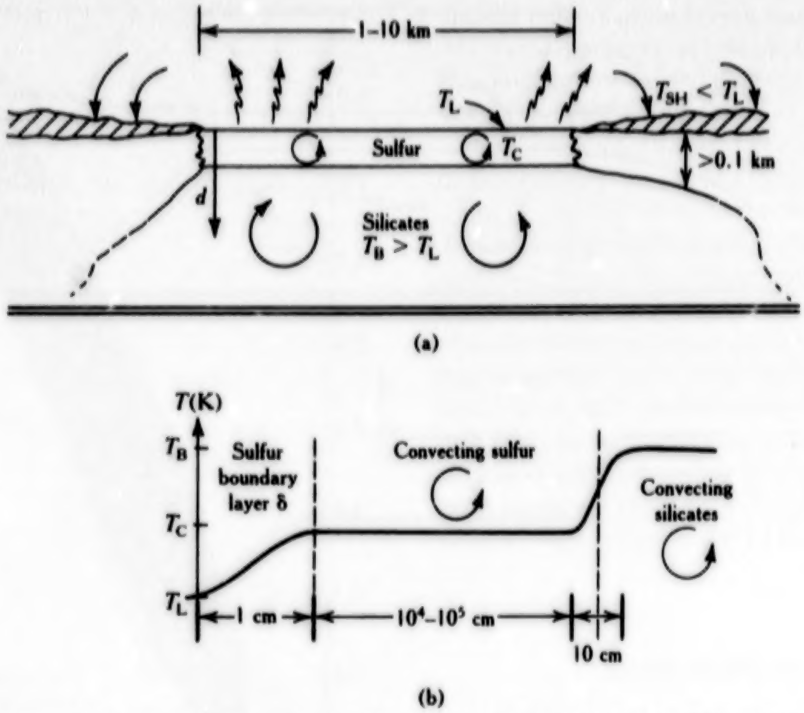

Figure 19. **(a)** Schematic model of a sulfur lake on Io, from Lunine and Stevenson (1985). T_L is surface temperature of lake; T_C is convective "operating" temperature; T_B is temperature of the molten silicate magma chamber; T_{SH} is lake shore temperature, a function of radial distance from the lake; and d is depth from the surface. *Arrows* suggest convecting regions and transport of vapor from lake to shore. **(b)** Illustrates schematic temperature profile versus depth within lake. Sizes of sulfur and silicate boundaries not drawn to scale.

ture profile due to vapor condensation with increasing distance from the lake. Figure 20 shows a fit of the sulfur lake radiation pattern to summed IRIS spectra. Also shown is an attempted fit using a sodium polysulfide lake. The higher melting point and reduced vapor pressure of the polysulfide system produce a poorer fit (this would be a general problem for any chemical system with a significantly different volatility than sulfur). Several other hot-spot IRIS signatures were fit with the sulfur-lake model by Lunine and Stevenson (1985); the fit was acceptable for Amirani/Maui but not for Ülgen or Babbar Paterae. Lunine and Stevenson did not attempt to fit hot spots that were clearly dominated by high-temperature plume volcanism, such as Pele.

The sulfur-lake model of Lunine and Stevenson (1985) has a number of interesting implications: (1) The exponential dependence of vapor pressure on temperature sets a strong energy constraint on the lake temperature. This explains the existence of hot-spot features with a high-temperature component between 350 and 450 K, as well as an accompanying, lower-temperature component. (2) The total heat flux from Loki Patera, the most energetic hot spot examined by Voyager, is close to the maximum that can be extracted by convection from molten silicates. This is indirect evidence that the Loki region is powered by molten silicate activity, with the overlying molten sulfur lake acting as an energy-transfer medium that converts energy of tidally heated silicates into infrared radiation (directly and through evaporation and recondensation). In effect, a Loki sulfur lake (or lakes) is the boiling pot of water on the stove. (3) The lifetime of an evaporating sulfur lake, for depths constrained by other models of the sulfur crust, is between 1 and 100 years. Variability may be seen within this time scale as individual lake regions are depleted, chemically altered by silicates, or undergo shifts in lake convective temperatures dictated by the peculiar dependence of sulfur viscosity on temperature.

Several uncertainties remain with the sulfur-lake model. The visual appearance of the Loki Patrea region is complex, and it is hard to identify an area that is clearly molten sulfur. McEwen et al. (1985) pointed out that an area of 650 km^2 on the southwest margin of Loki Patera had spectral properties (during the Voyager 1 encounter) consistent with liquid sulfur and is sur-

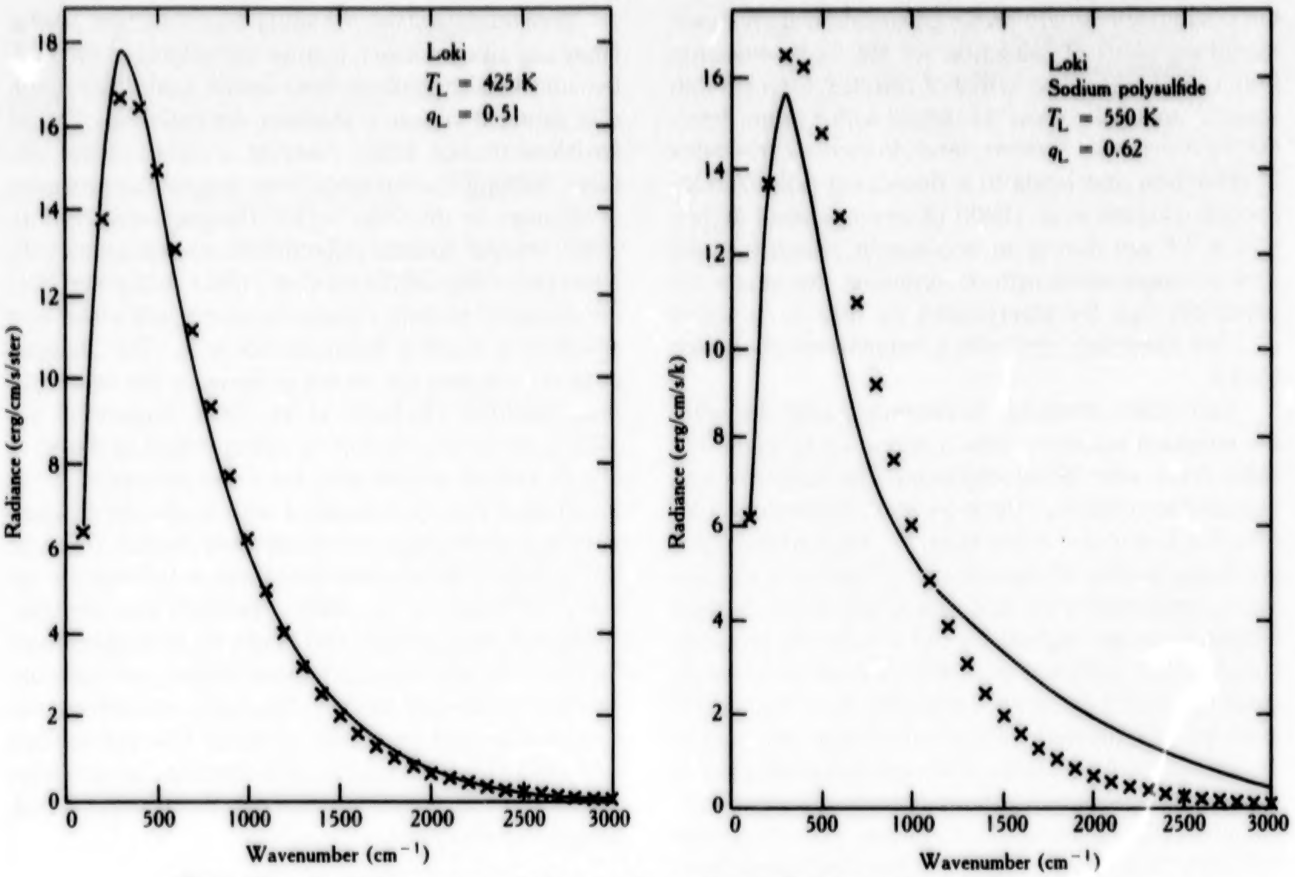

Figure 20. (*Left*) Comparison of infrared radiance from sulfur-lake model (*solid line*) to an IRIS spectrum of Loki Patera region (*crosses*). Lake temperature is 425 K; temperatures along lake shore decrease in accordance with a model for transport of vapor away from lake. (*Right*) Same for a molten sodium polysulfide lake. Figures from Lunine and Stevenson (1985).

rounded by a halo that has a spectral reflectivity consistent with condensed sulfur. (Most of the dark horseshoe-shaped area has a normal albedo at 0.59 μm of ~0.4, much too high for liquid sulfur, but the entire area appears black in saturated photographic prints, a source of continuing confusion.) However, recent infrared observations place the Loki high-temperature region further to the northeast, near the Loki fissure and active plumes (Goguen and Sinton, 1985; Howell and McGinn, 1985; Goguen et al., 1988). Considering the substantial changes in the albedo patterns of Loki Patera during the four months between Voyager encounters (figs. 10, 11, and 12), many additional changes may have occurred since 1979. The Loki plumes, if similar to the equatorial sulfur dioxide plumes, probably do not emit much thermal energy, although calculation of the energy released during condensation of plume particles depends sensitively on the particle size and radiating properties of the particles. However, the presence of the plumes does indicate hot magma at depth, which may erupt onto the surface effusively as well as explosively.

Silicate Flows The hot-spot temperatures may be the result of silicate eruptions, with mobilization of lower-temperature melts such as sulfur being only a minor factor. The low temperatures of the hot spots (Pearl and Sinton, 1982) are inconsistent with active silicate lava lakes, even with the rapid growth of a crust. If the hot spots are due to silicate eruptions, then they are most probably due to eruption of flows. Flow morphologies and discrete albedo units are discernible in the hot spots and on the floors of many calderas (e.g., figs. 2 and 4). Carr (1986) suggested that these could result from the progressive filling of the calderas by basaltic flows, as commonly occurs within terrestrial calderas.

Two observations provide tantalizing but inconclusive evidence for active silicate volcanism on Io. First, the Goguen and Sinton (1985) polarization study determined an index of refraction for the 5-μm emission from Loki that is close to that of silicates, for a smooth surface, and well below the liquid sulfur value. Introducing roughness, however, tends to increase the index of refraction and leads to a decreased polarization. Second, Goguen et al. (1988) observed a small deflection at 3.8 μm during an occultation, which was not seen in longer-wavelength observations; this single observation can be interpreted as due to a small (2–3 km diameter) spot with a temperature of at least 1000 K.

Carr (1986) attempted to determine what the infrared emission would be from a region on Io where basaltic flows were being emplaced. The emission was assumed to come from three sources: (1) channels carrying the lava to the active front, (2) areas where flows are being actively emplaced, and (3) areas of inactive but recently emplaced (and still warm) flows. Surface temperatures are highest for the lava in the channel. However, the emission from the channel is relatively small because it occupies a relatively small area and is assumed to crust over. Temperatures were assigned to the channels by analogy with terrestrial eruptions, since at the relatively high temperatures of the channel, radiative heat losses would dominate, both on Io and the Earth. Temperatures on the active flows range from several hundred degrees kelvin up to the melting temperature (at least 1000 K). The areas at each temperature were calculated for a variety of assumed conditions such as the eruption rate, the rate at which the crust forms on the lava, how quickly the lava surface overturns, how thick the flow is, and what the temperature of the lava is when it ceases to flow. Similarly, temperatures were estimated for recently emplaced flows. Finally, the radiation from the three components were summed to give the total emitted radiation.

Comparisons between the model spectral emissions from silicate flows and those measured by IRIS at Loki and Pele show that the observed emissions were roughly simulated by high-volume eruptions sustained for several months in the case of Pele to several years in the case of Loki. In neither case was the emission spectrum exactly duplicated, but exact duplication should not be expected because a wide range of eruption characteristics, such as superposition of flows, changes in flow thickness, and outgassing of volatiles, were not modeled. However, the general conclusion of the simulations is that, although the temperatures of the Io's hot spots are low compared to temperatures of silicate melts, they still could be the result of silicate volcanism.

Both models of the hot spots described here, sulfur lakes and silicate flows, involve some form of the molten silicates. The silicate-flow model postulates extrusive, exposed silicate volcanism; the sulfur-lake model envisions molten sulfur covering a region of hot silicates. Although polarization data suggest the presence of silicates in the Loki region (Goguen and Sinton, 1985), Voyager spectral reflectivities are consistent with elemental sulfur (McEwen et al., 1985). Additional data are available to help choose between sulfur-lake and silicate-flow models for major hot spots. The observations of Io during the recent eclipses by the other galilean satellites (McEwen et al., 1986; Goguen et al., 1988) provide information on power output and area at one of several wavelengths for a few hot spots. Such information can be compared with synthesized signatures from sulfur-lake and silicate-flow models (Lunine, this volume). Better determination of bolometric albedos (McEwen et al., 1988; Simonelli and Veverka, 1988) may provide improved background temperatures for use with IRIS data, to provide tighter spectral constraints for hot-spot models. Ultimately, identifying the composition and processes of major hot-spot regions such as Loki is crucial to determining the physical mechanisms by which Io transports its prodigious heat budget to the surface.

DISCUSSION

Global Variations and Geophysical Implications

Many observations of IO have revealed pronounced longitudinal asymmetries. Hemispheric variations in color and albedo have long been recognized from the orbital lightcurve (e.g., Morrison et al., 1974, 1979; see fig. 13). The lightcurve shows a deep brightness minimum, most pronounced at shorter wavelengths (i.e., increased redness), centered on longitude 300°; and the maximum albedo occurs from longitude 200° (in the UV) to 120° (in the visible). Many other observations show this same general longitudinal distribution, with a sharp maximum or minimum near longitude 300° and a broad maximum or minimum in the leading/anti-Jove hemisphere:

1. The longitudinal distribution of SO_2 frost on Io, both from UV (Nelson et al., 1980) and infrared (Howell et al., 1984) observations, follows this same pattern, with a clear minimum near longitude 300° and a broad maximum from longitude 90° to 180° (see also McEwen et al., 1988).

2. All four of the observed Pele-type plumes (including Loki or brief periods) erupted from vents within longitude 240° to 360°, as discussed previously. The occurrence of these plumes, covering the SO_2-rich areas, seems to be responsible for the longitudinal pattern in the orbital lightcurve and the SO_2 abundance.

3. The steady-state (over the past decade) hot-spot heat flow from Io, as seen from the 8.7- and 10-μm observations, shows a sharp maximum near longitude 310° and a broad minimum from longitude 60° to 180° (Johnson et al., 1984, 1985; see fig. 17). Johnson et al. (1984) accounted for the peak at longitude 310° as primarily due to Loki Patera, but there are other significant hot spots in this region (see table 3).

4. The observations of 5-μm outbursts, short-lived hot spots near 600 K, have been most frequent when Io's central meridian is from 240° to 360° and moderately frequent from 0° to 120° (see fig. 16). There is clearly an observational bias here, as Io is difficult to observe when it is near to Jupiter (rotational longitudes 180° or 360°). There have been many outbursts observed with Io's orbital longitude near 360°, but this may be biased by eclipse observations. Therefore, the gap in outburst observations near longitude 180° may be partly or largely an observational effect. Nevertheless, the occurrence of more outbursts on the trailing hemisphere than on the leading side seems to be real (Sinton et al., 1983). At least some of the outbursts are probably associated with Pele-type plume eruptions.

5. There may be a longitudinal asymmetry in the distribution of large mountains on Io. The clearly observed mountains occur from longitude 230° to 360°, and from longitude 0° to 60° near the south pole. This is about the same region covered by high-resolution images from the Voyager 1 spacecraft (Smith et al., 1979b). However, in low-resolution images (~10 km/pixel) the mountains can still be seen near the terminator (from their shadows) from longitude 230° to 360° and near the south pole, and some relief can be seen near longitude 120°, but large mountains are not apparent elsewhere. Furthermore, observations of the bright limb near longitude 182° (from FDS 16382.09–16382.23) at a resolution of 3.5 km/pixel show a very systematic brightness pattern consistent with a perfectly smooth, circular limb; this indicates that the topographic relief is less than 4 km.

All of the above observations can be explained as due to a global asymmetry in the lithospheric structure and/or composition of Io. This asymmetry would somehow control the style of heat transfer, such that the "active" region (longitude 240° to 360° and the south pole) is characterized by advective heat transfer whereas the leading/anti-Jove hemisphere is characterized by conductive heat transfer. Advective heat transfer through the lithosphere may occur in the form of silicate magma up to the near surface, and the hot or molten silicates volatilize sulfur to drive the Pele-type plumes. The Pele-type eruptions cause the 5-μm outbursts and deposit relatively dark red material, covering the surface SO_2. The occurrence of molten silicates near the surface causes the greater hot-spot heat flow. The hot-spot distribution may in turn affect the asymmetry in Io's hot plasma torus (Linker et al., 1985). On the leading/anti-Jove hemisphere, a thinner lithosphere and higher conductive heat flux would not support large mountains or lead to as much hot-spot activity.

Perhaps the evidence for a global dichotomy is simply due to the absence of sufficiently long term observations. In other words, the Pele-type plumes and hot spots may shift to the leading/anti-Jove hemisphere in future years, decades, centuries, or millennia, consistent with the intermittent volcanism model of Consolmagno (1981b). However, major terrestrial hot spots such as Hawaii tend to be very long-lived, persisting for millions of years. Shaw (1969) showed how a frictional-heating mechanism (first described by Gruntfest, 1963) could serve to concentrate heat in discrete zones and produce long-lived hot spots. If shearing is initially distributed over a large area, those rocks in the center of the zone will lose less heat by conduction. Because viscosity varies inversely and nonlinearly with temperature in silicate rocks, the central location will be less viscous and preferentially sheared, thus leading to progressively greater heat production and lower viscosity or "thermal feedback." When a liquid is produced, the less-dense magma will rise and erupt or intrude at shallower depths, and the enhanced viscous heating will continue, perhaps periodically, in warm wall rocks. Thus, the tidal heating of Io may have led to formation of long-lived thermal pipes, which intersect the surface at the hot spots.

The global asymmetry could easily provide the small-mass asymmetry needed to overcome the tidal torque and lock Io in synchronous rotation (cf. Greenberg and Weidenschilling, 1984). However, if the asymmetry is dynamically supported, then Io may reorient intermittently, between intervals of synchronous rotation. Schaber (1986) suggested that nonsynchronous rotation might help explain the distribution of shield volcanoes, active plumes, and hot spots on Io. However, the distributions on Io are complex, and no systematic patterns are obvious except (1) the basic global dichotomy and (2) the equatorial concentration of Prometheus-type plumes.

OUTSTANDING PROBLEMS AND FUTURE RESEARCH NEEDS

A fundamental understanding of the structure and composition of the outer portion of Io, where volcanic activity is generated, still eludes us. It is likely that tidally heated silicates drive a range of explosive, effusive, and intrusive phenomena involving molten silicates, molten and gaseous elemental sulfur, and gaseous SO_2. Other sulfur compounds may also be involved. Many interesting questions remain for future research.

Composition

What are the relative abundances of sulfur, SO_2, and silicates in the upper crust? Can the presence of molten sulfur or silicates be established from infrared observations? How and when did Io lose volatiles such as H_2O and CO_2? Are these volatiles really completely depleted from Io's interior? Are SO_2 and S_2 the only important gaseous species? What other materials are present? How did sulfur evolve on the surface? Does Io have an Fe-rich core? How differentiated are the silicates? What is the composition of the low-albedo features?

Geomorphology and Tectonics

Can sulfur or silicate lava flows be distinguished on the basis of morphology or spectral properties? If there are silicate constructs, is the lava basic or silicic? How old are the surface features? Do all of the calderas overlie potentially active magma chambers? Are caldera diameters or depths controlled by the sizes or depths of the magma chambers or by crustal strengths or thicknesses? Why are most of the calderas on level plains rather than on volcanic constructs? Why is there no apparent caldera resurgence? Do the layered plains occur everywhere or just in the south polar region? What are the layered plains? How do they form and erode? Are the mountains formed by volcanic or tectonic processes? What are the plateau units associated with the mountains? How do faults and lineaments relate to volcanic or tidal stresses? Does low-angle detachment faulting occur? Does SO_2 facilitate fault movements? How frequent and intense are seisms and how do they affect the geomorphology?

Explosive Volcanism

What are the plume particle sizes and dynamics? What is the mass flux and kinetic energy transfer from the plumes? Is the resurfacing dominated by plume activity, flows, or other mechanisms? How short lived are the Pele-type plumes and how long lived are the Prometheus-type plumes? Are there other types of plume eruption? Are SO_2 and sulfur the only driving volatiles? What are the Prometheus-type plumes concentrated within 30 degrees of the equator? Do Pele-type plumes occur outside the region from longitude 240° to 360°? How are atmospheric and magnetospheric variability related to volcanic activity? What caused the transient changes near Pele? Do pyroclastic flows or surges occur on Io?

Hot Spots

Is the south polar ring a major hot spot? Are there other unidentified hot spots near the poles? What accounts for the 8.7- and 10-μm flux from the leading/anti-Jove regions of Io? Are there many relatively small, unidentified hot spots? Are there large-scale but low-temperature hot spots that have not been identified? How long do hot spots persist? How frequently do new hot spots appear? How do individual hot spots such as Loki change with time? Are fluctuations in thermal flux related to changes in eruptive behavior? Do the sulfur-lake and silicate-flow models apply? What causes the 5-μm outbursts? How often do hot spots near the silicate liquidus temperature (at least 1000 K) occur? Is the hot-spot activity episodic? Does thermal feedback occur to create and maintain the hot spots?

Tidal Heating and Internal Structure

Which tidal heating mechanisms are most important? What is Jupiter's rigidity and quality factor (Q_J)? Is the tidal heating episodic? What is Io's total present-day energy flow? Does the energy flow correspond to energy production? Is this energy flow steady-state? If not, does the energy flow vary in a cyclical or a stochastic manner? Does Io have an asthenosphere or partially molten to molten layers? What is the conductive heat flow and the consequent lithospheric thickness? Are variations in topographic relief due to variations in conductive heat flow? What is the global distribution of mountains and other topographic features? What is the shape of the geoid? Why is Loki in a large topographic low? What causes the global dichotomy? Is the global dichotomy due to a fundamental asymmetry in the structure or composition of Io, or is it a relatively short-lived pattern?

Such questions only emphasize the remarkable progress that has been made in elucidating Io's geophysical nature from Voyager and ground-based observations. The Voyager discoveries stand as an outstanding achievement of exploration of the solar system by spacecraft. It is a sobering but instructive exercise to ask what our 1988 understanding of Io would be in the absence of Voyager. The presence and styles of active volcanism, the absence of impact craters, the sulfur dioxide associated with plumes, the presence and morphology of hot spots and mountainous topography, and the rapid temporal changes in surface features would have been unknown. Although ground-based and Earth-orbital studies will continue to make important contributions, particularly in monitoring for temporal variations, they are not a substitute for close-up observations.

The Galileo spacecraft will complete mapping of Io in the hemisphere poorly observed by Voyager, and it will provide information on geologic processes, crater abundance, and surface morphology on spatial scales smaller than the Voyager observations. The NIMS instrument will obtain spatially resolved near-infrared spectra and hence compositional information, and it will monitor the short-wavelength thermal output of Io. The gap of over a decade between the two missions will provide information on temporal processes over small spatial scales.

Ground-based studies with improved instrumentation can continue to provide information on temporal variations in global heat flux, and compositional issues such as the large-scale distribution of spectroscopically active sulfur compounds. Time scales for variations in the behavior of plumes and hot spots may range from hours to centuries. The next set of mutual occultations of the galilean satellites in 1991–1992 will provide an additional opportunity to identify new hot spots and to determine hot-spot locations, temperatures, and areas. Earth-orbital facilities provide additional capability: The Hubble Space Telescope will be able to image Io on quarter-hemisphere scales, thereby monitoring changes in the global appearance and surface composition of the satellite. A large infrared Earth-orbiting telescope such as Space Infrared Telescope Facility (SIRTF) could look for sulfur, SO_2, and other emission features in the mid-infrared and observe the full infrared spectrum due to hot-spot emission. Laboratory studies of the chemical and physical properties of sulfur-bearing and silicate materials are essential complements to observing programs. Continuing work with the Voyager data is also worthwhile, especially analysis of the IRIS spectra; measurements of the topography and triaxial figure (e.g., Davies, 1983; Gaskell and Synott, 1987; Wu et al., 1987); spectrophotometric analyses; and comparison and correlation with new telescopic and spacecraft data. Finally, theoretical work will continue to provide physical constraints and interesting models that attempt to explain the observations.

ACKNOWLEDGMENTS

We thank S. W. Kieffer and P. D. Spudis for reviews and T. V. Johnson and D. L. Matson for useful discussions. This work supported by NASA contract W-15,814 and grant NAGW-1039.

References

Baloga, S. M., D. L. Matson, and D. C. Pieri (1983). Auras and Io regolith outgassing by sulphur flows. *Lunar and Planetary Science* 14:15–16.

Bodenheimer, P., and J. B. Pollack (1986). Calculations of the accretion and evolution of giant planets: The effects of solid cores. *Icarus* 67:391–408.

Brown, R. A. (1974) Optical line emission from Io. In *Exploration of the planetary system* (A. Woszczyk and C. I. Waniszewska, eds.), pp. 527–531. D. Reidel, Dordrecht, Holland.

Burns, J. A. (1986). Some background about satellites. In *Satellites* (J. A. Burns and M. S. Matthews, eds). pp. 1–38. Univ. of Arizona Press, Tucson.

Carr, M. H. (1986) Silicate volcanism on Io. *J. Geophys. Res.* 91:3521–3532.

Carr, M. H., H. Masursky, R. G. Strom, and R. J. Terrile (1979). Volcanic features of Io. *Nature* 280:729–733.

Cheng, A. F., P. K. Haff, R. E. Johnson, and L. J. Lanzerotti (1986). Interactions of planetary magnetospheres with icy satellite surfaces. In *Satellites* (J. A. Burns and M. S. Matthews, eds.), pp. 403–436. Univ. of Arizona Press, Tucson.

Clark, R. N., F. P. Fanale, and M. J. Gaffey (1986). Surface composition of natural satellites. In *Satellites* (J. A. Burns and M. S. Matthews, eds.), pp. 437–491. Univ. of Arizona Press, Tucson.

Clow, G. D., and M. H. Carr (1980). Stability of sulfur slopes on Io. *Icarus* 44:268–279.

Colburn, D. S. (1980). Electromagnetic heating of Io. *J. Geophys. Res.* 85:7257–7261.

Collins, S. A. (1981). Spatial color variations in the volcanic plume at Loki, on Io. *J. Geophys. Res.* 86:8621–8626.

Consolmagno, G. J. (1979). Sulfur volcanoes on Io. *Science* 205:397–398.

Consolmagno, G. J. (1981a). Io: Thermal models and chemical evolution. *Icarus* 47:36–45.

Consolmagno, G. J. (1981b). An Io model with intermittent volcanism. *Proc. Lunar Planet. Sci. Conf.* 12:1533–1542.

Cook, A. F., E. M. Shoemaker, and B. A. Smith (1979). Dynamics of volcanic plumes on Io. *Nature* 280:743–746.

Cook, A. F., E. M. Shoemaker, B. A. Smith, G. E. Danielson, T. V. Johnson, and S. P. Synnott (1981). Volcanic origin of the eruptive plumes on Io. *Science* 211:1419–1422.

Cruikshank, D. P., R. R. Howell, T. R. Geballe, and F. P. Fanale (1985). Sulfur dioxide on Io. In *Proc. NATO Workshop Ices in the Solar System* (J. Klinger, D. Benest, A. Dollfus, and R. Smoluchowski, eds.), pp. 805–815. D. Reidel, Dordrecht, Holland.

Cruikshank, D. P., T. J. Jones, and C. B. Pilcher (1978). Absorption bands in the spectrum of Io. *Astrophys. J.* 225:L89–L92.

Davies, M. E. (1983). The shape of Io. I.A.U. *Colloquium 77, Natural Satellites*, 14.

Davies, M. E., and F. Y. Katayama (1981). Coordinate features on the Galilean satellites. *J. Geophys. Res.* 86:8635–8657.

Dermott, S. F. (1934). Rotation and the internal structures of the major planets and their inner satellites. *Phil. Trans. Roy. Soc. London* A313:123–138.

Detrick, R. S., R. P. von Herzen, S. T. Crough, D. Epp, and U. Fehn (1981). Heat flow on the Hawaiian swell and lithospheric reheating. *Nature* 292:141–142.

Eviatar, A. (1987). Volcanic control of the Io atmosphere and plasma torus. *J. Geophys. Res.* 92:8800–8804.

Fanale, F. P., W. B. Banerdt, L. S. Elson, T. V. Johnson, and R. W. Zurek (1982). Io's surface: Its phase composition and influence on Io's atmosphere and Jupiter's magnetosphere. In *Satellites of Jupiter* (D. Morrison, ed.), pp. 756–781. Univ. of Arizona Press, Tucson.

Fanale, F. P., R. H. Brown, D. P. Cruikshank, and R. N. Clark (1979). Significance of absorption features in Io's IR reflectance spectrum. *Nature* 280:761–763.

Fanale, F. P., T. V. Johnson, and D. L. Matson (1974). Io: A surface evaporite deposit? *Science* 186:922–925.

Fink, J. H., S. O. Park, and R. Greeley (1983). Cooling and deformation of sulfur flows. *Icarus* 56:38–50.

Fink, U., H. P. Larsen, L. A. Lebofsky, M. Feierberg, and H. Smith (1978). The 2–4 μm spectrum of Io. *Bull. Amer. Astron. Soc.* 10:580.

Gaskell, R. W., and S. P. Synnott (1978). Large scale topography of Io. *NASA Tech. Memo.* 89810:522–523.

Goguen, J. D., W. M. Sinton, D. L. Matson, R. R. Howell, H. M. Dyck, T. V. Johnson, R. H. Brown, G. J. Veeder, A. L. Lane, R. M. Nelson, and R. A. McLaren (1988). Multicolor IR photometry of occultations of Io by Ganymede and Callisto during 1985. *Icarus*, in press.

Goguen, J. D., and W. M. Sinton (1985). Characterization of Io's volcanic activity by ground-based IR polarimetry. *Science* 230:65–69.

Gold, T. (1979). Electrical origin of the outbursts on Io. *Science* 206:1071–1073.

Goldreich, P., and D. Lynden-Bell (1969). Io: A jovian unipolar inductor. *Astrophys. J.* 156:59–78.

Gradie, J., and J. Moses (1983). Spectral reflectance of unquenched sulfur. *Lunar and Planetary Science* 14:255–256.

Greeley, R., and J. H. Fink (1984). Sulfur volcanoes on Io? *Astron. Express* 1:25–31.

Greeley, R., E. Theilig, and P. R. Christensen (1984). The Mauna Loa sulfur flows as an analog to secondary sulfur flows ? on Io. *Icarus* 60:189–199.

Greenberg, R. (1982). Orbital evolution of the Galilean satellites. In *Satellites of Jupiter* (D. Morrison, ed.), pp. 65–92. Univ. of Arizona Press, Tucson.

Greenberg, R. (1987). Galilean satellites: Evolutionary paths in deep resonance. *Icarus* 70:334–347.

Greenberg, R. (1989). Time-varying orbits and tidal heating of the galilean satellites. This volume.

Greenberg, R., and S. J. Weidenschilling (1984). How fast do Galilean satellites spin? *Icarus* 58:186–196.

Gruntfest, I. J. (1963). Thermal feedback in liquid flow; plane shear at constant stress. *Trans. Soc. Rheol.* 7:195–207.

Hanel, R., and the Voyager IRIS Team (1979). Infrared observations of the jovian system from Voyager 1. *Science* 204:972–976.

Hapke, B. W. (1979). Io's surface and environs: A magmatic-volatile model. *Geophys. Res. Lett.* 6:799–802.

Howell, R. R., D. P. Cruikshank, and F. P. Fanale (1984). Sulfur dioxide on Io: Spatial distribution and physical state. *Icarus* 57:83–92.

Howell, R. R., and M. T. McGinn (1985). Infrared speckle observation of Io: An eruption in the Loki region. *Science* 230:63–65.

Howell, R. R., and W. M. Sinton (1987). Io and Europa: The observational evidence for variability. This volume.

Johnson, T. V., A. F. Cook, C. Sagan, and L. A. Soderblom (1979). Volcanic resurfacing rates and implications for volatiles on Io. *Nature* 280:746–750.

Johnson, T. V., and L. A. Soderblom (1982). Volcanic eruptions on Io: Implications for surface evolution and mass loss. In *Satellites of Jupiter* (D. Morrison, ed.), pp. 634–646. Univ. of Arizona Press, Tucson.

Johnson, T. V., and L. A. Soderblom (1983). Io. *Scientific American* 249(6):56–67.

Johnson, T. V., D. Morrison, D. L. Matson, G. J. Veeder, R. H. Brown, and R. M. Nelson (1984). Io volcanic hot spots: Stability and longitudinal distribution. *Science* 226:134–137.

Johnson, T. V., D. L. Matson, G. J. Veeder, R. H. Brown, R. M. Nelson, and D. Morrison (1985). Io's hotspots: Limits on spatial and temporal variability. *Bull. Am. Astron. Soc.* 17:690.

Johnson, T. V., D. L. Matson, R. H. Brown, and G. J. Veeder (1986). Infrared emission from Io's volcanoes: Evidence for change in a Pele-class source in 1985. *Bull. Am. Astron. Soc.* 18:774.

Kawakami, S.-I., and H. Mizutani (1987). Thermal history of the Jovian satellite Io. *Icarus* 70:78–98.

Kieffer, S. W. (1982). Dynamics and thermodynamics of volcanic eruptions: Implications for the plumes on Io. In *Satellites of Jupiter* (D. Morrison, ed.), pp. 647–723. Univ. of Arizona Press, Tucson.

Kieffer, S.W., (1984). Factors governing the structure of volcanic jets. In *Explosive volcanism: Inception, evolution, and hazards*, pp. 143–157. National Academy Press, Washington.

Kumar, S., and D. M. Hunten (1982). The atmospheres of Io and other satellites. In *Satellites of Jupiter* (D. Morrison, ed.), pp. 782–806. Univ. of Arizona Press, Tucson.

Kupo, I., Yu. Mekler, and A. Eviatar (1976). Detection of ionized sulfur in the Jovian magnetosphere. *Astrophys. J.* 205:L51–L53.

Langseth, M., S. J. Keihm, and K. Peters (1976). The revised lunar heat flow values. *Lunar Science* 7:474–475.

Lee, S. W., and P. C. Thomas (1980). Near-surface flow of volcanic gases on Io. *Icarus* 44:280–290.

Lewis, J. S. (1982). Io: Geochemistry of sulfur. *Icarus* 50:103–114.

Lewis, J. S., and R. G. Prinn (1984). *Planets and their atmospheres.* Academic Press, Orlando.

Linker, J. A., M. G. Kivelson, M. A. Moreno, and R. J. Walker (1985). Explanation of the inward displacement of Io's hot plasma torus and consequences for sputtering sources. *Nature* 315:373–378.

Lockwood, G. W., K. Lumme, and D. T. Thompson (1980). The recent photometric variability of Io. *Icarus* 44:240–248.

Lunine, J. I. (1989). Sulfur lakes and silicate flows: Thermal emission from Io's hot spots. This volume.

Lunine, J. I., and D. J. Stevenson (1982). Formation of the galilean satellites in a gaseous nebula. *Icarus* 52:14–39.

Lunine, J. I., and D. J. Stevenson (1985). Physics and chemistry of sulfur lakes on Io. *Icarus* 64:345–367.

Masursky, H., G. G. Schaber, L. A. Soderblom, and R. G. Strom (1979). Preliminary geologic mapping of Io. *Nature* 280:725–729.

Matson, D. L., G. A. Ransford, and T. V. Johnson (1981). Heat flow from Io (J1). *J. Geophys. Res.* 86:1664–1672.

Matson, D. L., and D. B. Nash (1983). Io's atmosphere: Pressure control by regolith coldtrapping and surface venting. *J. Geophys. Res.* 88:4771–4783.

McCauley, J. F., B. A. Smith, and L. A. Soderblom (1979). Erosional scarps on Io. *Nature* 280:736–738.

McEwen, A. S. (1985). Hot-spot tectonics on Io. In *Conf. on Heat & Detachment in Crustal Extension on Continents and Planets, LPI Contr.* 575:76–80.

McEwen, A. S. (1988). Global color and albedo variations on Io. *Icarus*, in press.

McEwen, A. S., and L. A. Soderblom (1983). Two classes of volcanic plumes on Io. *Icarus* 55:191–217.

McEwen, A. S., T. V. Johnson, D. L. Matson, and L. A. Soderblom (1988). The global distribution, abundance, and stability of SO_2 on Io. *Icarus*, in press.

McEwen, A. S., D. L. Matson, T. V. Johnson, and L. A. Soderblom (1985). Volcanic hot spots on Io: Correlation with low-albedo calderas, *J. Geophys. Res.* 90:12345–12379.

McEwen, A. S., L. A. Soderblom, D. L. Matson, T. V. Johnson and J. I. Lunine (1986). Calculated occultation profiles of Io and the hot spots. *Geophys. Res. Lett.* 13:201–204.

Moore, J. M., A. S. McEwen, E. F. Albin, and R. Greeley (1986). Topographic evidence for shield volcanism on Io. *Icarus* 67:181–183.

Morabito, L. A., S. P. Synnott, P. K. Kupferman, and S. A. Collins (1979). Discovery of currently active extraterrestrial volcanism. *Science* 204:972.

Morgan, P., and R. J. Phillips (1983). Hot spot heat transfer: Its application to Venus and implications to Venus and Earth. *J. Geophys. Res.* 88:8305–8317.

Morrison, D., N. D. Morrison, and A. Lazarewicz (1974). Four-color photometry of the galilean satellites. *Icarus* 23:399–416.

Morrison, D., D. Pieri, J. Veverka, and T. V. Johnson (1979). Photometric evidence on long-term stability of albedo and colour markings on Io. *Nature* 280:753–755.

Morrison, D., and C. M. Telesco (1980). Io: Observational constraints on internal energy and thermophysics of the surface. *Icarus* 44:226–233.

Nash, D. B., M. H. Carr, J. Gradie, D. M. Hunten, and C. F. Yoder (1986). Io. In *Satellites* (J. A. Burns and M. S. Matthews, eds.), pp. 629–688. Univ. of Arizona Press, Tucson.

Nash, D. B., and R. M. Nelson (1979). Spectral evidence for sublimates and adsorbates on Io. *Nature* 280:763–766.

Nelson, R. M., A. L. Lane, D. L. Matson, F. P. Fanale, D. B. Nash, and T. V. Johnson (1980). Io: Longitudinal distribution of sulfur dioxide frost. *Science* 210:784–786.

Nelson, R. M., D. C. Pieri, S. M. Baloga, D. B. Nash, and C. Sagan (1983). The reflection spectrum of liquid sulfur: Implications for Io. *Icarus* 56:409–413.

Oberbeck, V. R. (1975). The role of ballistic erosion and sedimentation in Lunar stratigraphy. *Rev. Geophys. Space Phys.* 13:337–362.

Ojakangas, G. W., and D. J. Stevenson (1986). Episodic volcanism of tidally heated satellites with application to Io. *Icarus* 66:341–358.

O'Reilly, T. C., and G. F. Davies (1981). Magma transport of heat on Io: A mechanism allowing a thick lithosphere. *Geophys. Res. Lett.* 8:313–316.

Peale, S. J. (1986). Orbital resonances, unusual configuration and exotic rotation states among planetary satellites. In *Satellites* (J. A. Burns and M. S. Matthews, eds.), pp. 159–223. Univ. of Arizona Press, Tucson.

Peale, S. J., P. Cassen, and R. T. Reynolds (1979). Melting of Io by tidal dissipation. *Science* 203:892–894.

Pearl, J. C. (1987). Io: Amaterasu Patera is hot. Submitted to *J. Geophys. Res.*

Pearl, J. C., R. Hanel, V. Kunde, W. Maguire, D. Fox, S. Gupta, C. Ponnaperuma, and F. Raulin (1979). Identification of gaseous SO_2 and new upper limits for other gases on Io. *Nature* 280:755–758.

Pearl, J. C., and W. M. Sinton (1982). Hot spots of Io. In *Satellites of Jupiter* (D. Morrison, ed.), pp. 724–755. Univ. of Arizona Press, Tucson.

Peratt, A. L., and A. J. Dessler (1987). Filamentation of volcanic plumes on the jovian satellite Io. *Astronomy and Space Sci.*, in press.

Pieri, D. C., S. M. Baloga, R. M. Nelson, and C. Sagan (1984). Sulfur flows of Ra Patera, Io. *Icarus* 60:685–700.

Pilcher, C. B., and D. F. Strobel (1982). Emissions from neutrals and ions in the jovian magnetosphere. In *Satellites of Jupiter* (D. Morrison, ed.), pp. 807–845. Univ. of Arizona Press, Tucson.

Pollack, J. B., and F. P. Fanale (1982). Origin and evolution of the Jupiter satellite system. In *Satellites of Jupiter* (D. Morrison, ed.), pp. 872–910. Univ. of Arizona Press, Tucson.

Pollack, J. B., F. C. Witteborn, E. F. Erickson, D. W. Strecker, B. J. Baldwin, and T. E. Bunch (1978). Near-infrared spectra of the galilean satellites: Observations and compositional implications. *Icarus* 36:271–303.

Prinn, R. G., and M. B. Fegley, Jr. (1981). Kinetic inhibition of CO and N_2 reduction in circumplanetary nebulae: Implications for satellite composition. *Astrophys. J.* 249:308–317.

Reynolds, R. T., S. J. Peale, and P. Cassen (1980). Io: Energy constraints and plume volcanism. *Icarus* 44:234–239.

Ross, M. N., and G. Schubert (1985). Tidally forced viscous heating in a partially molten Io. *Icarus* 64:391–400.

Ross, M. N., and G. Schubert (1986). Tidal dissipation in a viscoelastic planet. *J. Geophys. Res.* 91:D447–D452.

Sagan, C. (1979). Sulfur flows on Io. *Nature* 280:750–753.

Schaber, G. G. (1980). The surface of Io: Geologic units, morphology, and tectonics. *Icarus* 43:302–333.

Schaber, G. G. (1982). The geology of Io. In *Satellites of Jupiter* (D. Morrison, ed.), pp. 556–597. Univ. of Arizona Press, Tucson.

Schaber, G. G. (1986). Io: Shield volcanism, tidally forced viscous heating, and the shift of active volcanism from the sub-Jupiter and anti-Jupiter points. *Lunar and Planetary Science* 17:758–759.

Schneider, N. M., W. H. Smyth, and M. A. McGrath (1989). Io's atmosphere and neutral clouds. This volume.

Schubert, G., T. Spohn, and R. T. Reynolds (1986). Thermal histories, compositions, and internal structure of the moons of the solar system. In *Satellites* (J. A. Burns and M. S. Matthews, eds.), pp. 224–292. Univ. of Arizona Press, Tucson.

Schubert, G., D. J. Stevenson, and K. Ellsworth (1981). Internal structures of the Galilean satellites. *Icarus* 47:46–59.

Sclater, J. G., C. Jaupart, and D. Galson (1980). The heat flow through oceanic and continental crust and the heat loss of the Earth. *Reviews Geophys. Space Phys.* 18:269–311.

Segatz, M., T. Spohn, M. N. Ross, and G. Schubert (1988). Tidal dissipation, surface heat flow, and figure of viscoelastic models of Io. Submitted to *Icarus.*

Shaw, H. R. (1969). Rheology of basalt in the melting range. *J. Petrology* 10:510–535.

Shoemaker, E. M., and R. F. Wolfe (1982). Cratering time scales for the galilean satellites. In *Satellites of Jupiter* (D. Morrison, ed.), pp. 277–339. Univ. of Arizona Press, Tucson.

Sill, G. T., and R. N. Clark (1982). Composition of the surface of the galilean satellites. In *Satellites of Jupiter* (D. Morrison, ed.), pp. 174–212. Univ. of Arizona Press, Tucson.

Simonelli, D. P., and J. Veverka (1988). Bolometric albedos and diurnal temperatures of the brightest regions on Io. *Icarus* 74:240–261.

Sinton, W. M. (1980a). Io's 5-μm variability. *Astrophys. J.* 235:L49–L51.

Sinton, W. M. (1980b). Io: Are vapor explosions responsible for the 5-μm outbursts? *Icarus* 43:56–64.

Sinton, W. M. (1981). The thermal emission spectrum of Io and a determination of the heat flux from its hot spots. *J. Geophys. Res.* 86:3122–3128.

Sinton, W. M. (1982). Io: A volcanic flow model for the hot spot emission spectrum and a thermostatic mechanism. *Icarus* 51:563–573.

Sinton, W. M., D. Lindwall, F. Cheigh, and W. C. Tittemore (1983). Io: The near-infrared monitoring program, 1979–1981. *Icarus* 54:133–157.

Smith, B. A., E. M. Shoemaker, S. W. Keiffer, and A. F. Cook (1979a). The role of SO_2 in volcanism on Io. *Nature* 280:738–743.

Smith, B. A., and the Voyager Imaging Team (1979b). The Jupiter system through the eyes of Voyager 1. *Science* 204:951–972.

Smith, B. A., and the Voyager Imaging Team (1979c). The galilean satellites and Jupiter: Voyager 2 imaging science results. *Science* 206:927–950.

Smythe, W. D., R. M. Nelson, and D. B. Nash (1979). Spectral evidence for SO_2 frost or adsorbate on Io's surface. *Nature* 280:766–767.

Soderblom, L. A., T. V. Johnson, D. Morrison, E. Danielson, B. Smith, J. Veverka, A. Cook, C. Sagan, D. Kupferman, D. Pieri, J. Mosher, C. Avis, J. Gradie, and T. Clancy (1980). Spectrophotometry of Io: Preliminary Voyager results. *Geophys. Res. Lett.* 7:963–966.

Stevenson, D. J., A. W. Harris, and J. I. Lunine (1986). Origins of satellites. In *Satellites* (J. A. Burns and M. S. Matthews, eds.), pp. 39–88. Univ. of Arizona Press, Tucson.

Stevenson, D. J., and J. I. Lunine (1987). Rapid formation of Jupiter by diffusive redistribution of water vapor in the solar nebula. *Icarus,* submitted.

Strom, R. G., R. J. Terrile, H. Masursky, and C. Hansen (1979). Volcanic eruption plumes on Io. *Nature* 280:733–736.

Strom, R. G., N. M. Schneider, R. J. Terrile, A. F. Cook, and C. Hansen (1981). Volcanic eruptions on Io. *J. Geophys. Res.* 86:8593–8620.

Strom, R. G., and N. M. Schneider (1982). Volcanic eruption plumes on Io. In *Satellites of Jupiter* (D. Morrison, ed.), pp. 598–633. Univ. of Arizona Press, Tucson.

Trafton, L. (1975). Detection of a potassium cloud near Io. *Nature* 258:690–692.

U. S. Geological Survey (1987). Shaded relief and surface markings map, shaded relief map, and controlled photomosaic of Io. USGS Misc. Inv. Map I-1713, scale 1:15M.

Wamsteker, W., R. L. Kroes, and J. A. Fountain (1974). On the surface composition of Io. *Icarus* 10:1–7.

Webb, E. K., and D. J. Stevenson (1987). Subsidence of topography on Io. *Icarus* 70:348–353.

Whitford-Stark, J. L. (1982). The mountains of Io. *Lunar and Planetary Science* 13:859–860.

Williams, H., and A. R. McBirney (1979). *Volcanology.* Freeman, Cooper and Co., San Francisco, 397 pp.

Wilson, L., and J. W. Head (1981). Io volcanic eruptions: Mass eruption rate estimates. *Lunar and Planetary Science* 12:1191–1193.

Wilson, L., and J. W. Head (1983). A comparison of volcanic eruption processes on Earth, Moon, Mars, Io and Venus. *Nature* 302:663–669.

Witteborn, F. C., J. D. Bregman, and J. B. Pollack (1979). Io: An intense brightening near 5 micrometers. *Science* 203:643–646.

Wu, S. S. C., F. J. Schafer, R. Jordan, and A. Howington (1987). Aspects of Voyager photogrammetry. *NASA Tech. Memo.* 89810:528–529.

Yoder, C. F. (1979). How tidal heating in Io drives the galilean orbital resonance locks. *Nature* 279:767–800.

Young, A. T. (1984). No sulfur flows on Io. *Icarus* 197–226.

3

Io and Europa: The Observational Evidence for Variability

Robert R. Howell
University of Wyoming, Laramie
William M. Sinton
University of Hawaii, Honolulu

Abstract

Observations of Io show variability over a wide range of wavelengths and time scales. The early reports of posteclipse brightening were largely responsible for focusing attention on this satellite. Although no such brightenings have been seen for the past decade, the original reports may have been accurate, and if so they indicate long-term changes in Io's atmosphere and volcanic activity. The observation of infrared outbursts from Io were direct detections of volcanic activity, although they were not recognized as such until after the Voyager mission. Studies of the infrared flux from Io let us monitor the volcanic activity, and recently developed "high-resolution" techniques let us study individual active regions and eruptions. These techniques show that Loki is still active seven years after the Voyager encounter. However, a recent analysis of eclipse data over that time suggests that its thermal output is declining. Observations have also shown high-temperature, short-lived eruptions taking place in regions that showed no activity during the Voyager encounters. Finally, the discovery that most of the heat flow comes from just one or two active regions on Io suggests that we should expect fluctuations in total output by roughly a factor of two as these active regions die out and new ones are born. The long-term average heat flow may in fact be consistent with the predictions of equilibrium tidal dissipation theories. Europa clearly does not show the level of activity that is present on Io, but some unconfirmed evidence of activity has been reported, and is discussed in this review.

INTRODUCTION

Io is one of the few solid bodies in the solar system that clearly varies on time scales that humans can observe. The evidence of such variability has been accumulating for some time, but it was the Voyager observations of volcanism that provided the context within which that variability can be understood. The goal of understanding the fundamental causes and detailed mechanisms of that volcanism now provides the primary reason for studying Io's variability. The existence of tidally driven volcanism on Io suggests the possibility of less intense activity on Europa, and some claims of observed activity on this satellite have in fact been made.

The evidence for variability on Io ranges from still puzzling early reports of posteclipse brightening to the more recent unmistakable evidence of infrared outbursts. Both of these were "whole disk" measurements. In the last few years a variety of techniques have enabled us to study the thermal emission from individual active regions. These measurements are just now beginning to reveal a picture in which different types of volcanism show different degrees of variability, confirming suggestions made based on the more limited Voyager data.

Studies of the variability of Io are important for several reasons. Among these are

- The time-averaged global heat flow is uncertain. Discrepancies between the current heat flow and the predictions of some tidal dissipation models might be explained by short-term, statistically reasonable variations in output.
- The characteristics of actual eruptions are unknown. Studies of the lifetimes of individual active regions would lead to an understanding of the eruption mechanisms. For example, the temperatures and cooling times for "lava" lakes, "lava" flows, and pyroclastic eruptions would be very different.
- The Galileo spacecraft will have only one close encounter with Io, as it first enters Jupiter orbit. Since the imaging sequences must be planned well in advance, it is important to know which regions will be active at the time of the encounter. There is currently no guarantee that the surface that will eventually be seen by Galileo will at all resemble that seen by the Voyager spacecraft 15 years earlier.

The variability of Europa remains open to question. A single Voyager image shows possible evidence of activity, and some anomalous infrared measurements also suggest such an effect.

IO

Io is the only body in the solar system except for Earth on which active volcanism has been directly observed. Viewing this satellite allows us to see those volcanic processes under a different set of circumstances, involving different materials and a different fundamental heat source than on Earth. Io has long been considered an interesting target for planetary astronomy, because of the unusual, and until recently, unexplained measurements that were obtained by a multitude of observers.

Pre-Voyager Observations from Earth

Posteclipse Brightening The finding of Binder and Cruikshank (1964) that Io had an enhanced brightness for the first 10–15 minutes following its emergence from eclipse by Jupiter and then settled to its normal brigntness was one of the very first observations that called attention to the unusual nature of this satellite. Subsequent observations by many different observers have both confirmed and denied the existence of this effect. Fanale et al. (1981) (fig. 21) give a list of references to most of these observations. The observations are difficult, especially with the small-size telescopes with which the early observations were made. The reason the observation of the effect is difficult is that, when seen, the brightening is only ~10 percent and correction for scattered light from Jupiter requires special precautions to eliminate the contribution from this source as Io, in emerging from Jupiter's shadow, moves away from the planet.

Even today, one cannot say unequivocally whether the effect exists, does not exist, or is sporadic, thus producing both the positive and the negative results. Fanale et al. conclude that the effect is probably sporadic. In view of the sporadic nature of volcanism on Io and the variation that might be expected of sulfur dioxide in Io's atmosphere, there may well be a condensation of additional sulfur dioxide frost on the surface during the cooling in an eclipse. It is the sublimation of this frost that leads to the 10 percent drop in light 10 minutes after emergence from eclipse. The reason that Binder and Cruikshank initially sought the effect was to test whether Io had an atmosphere having components that might condense on the surface during an eclipse.

A careful search was made for the effect with the Voyager cameras. These offered the advantages of eliminating the scattered Jupiter light problem and moreover allowed testing the surface of Io area-by-area and not just in disk-integrated light (Vereka et al. 1981). No

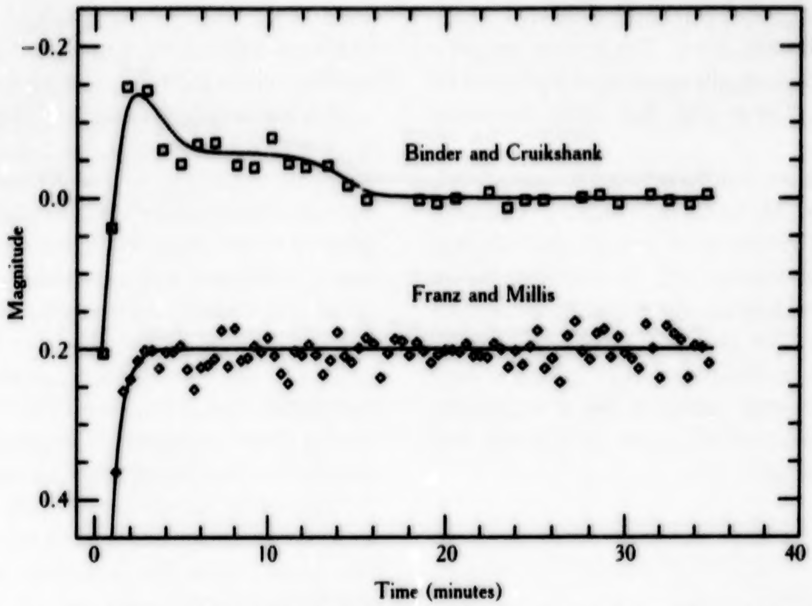

Figure 21. The top curve is a typical posteclipse brightening of Io, as observed on 15 October 1962 by Binder and Cruikshank (1964). The lower curve is a posteclipse observation obtained on 18 September 1973 by Franz and Millis (1974). Although the latter authors attribute all reported "brightenings" to systematic observational error, the former authors did attempt to test for any such errors, by a variety of methods such as observing eclipse disappearances.

posteclipse brightening that conformed to the classical description of the effect was found, although some isolated areas behaved abnormally (some brightened slightly; others darkened for the first few minutes after emergence into sunlight). Vereka et al. concluded that they could not eliminate flexible hypotheses such as the proposal of sporadic activity mentioned above. It would seem, on the basis of ground-based observations reported herein, that the volcanic activity has declined since the Voyager encounters. Presumably, if our measurements of activity over the last seven years are typical, the Voyager data were taken at a high state of activity.

Compounded with the negative Voyager result is that techniques for eliminating the scattered contribution from Jupiter have improved over the years (see, for example, Hammel et al. 1985). These reviewers are not aware of any published positive result for the classically described effect for the last ten years. Yet we do not believe that we should conclude that the positive observations were spurious until a longer period of nondetection has been recorded.

5 μ Outbursts Witteborn et al. (1979) reported a greatly enhanced flux (five-fold at 5 μm) over that observed five hours earlier in spectra taken of Io in 1978. Their observation was not, however, the first such observation as their colleagues (L. Lebofsky, U. Fink, and H. Larson) had observed a similar enhancement a month earlier and also again earlier on the same night, which is the reason that they returned to Io after the five-hour interval. There is, thus, no doubt about the reality of this observation. Witteborn et al. fitted a blackbody spectrum to the excess flux that they found in the 2–5 μm region and derived a color temperature ~600 K. One of the possible explanations that they listed for the observed phenomenon was that of a volcanic eruption. Since Voyager, we now know that this was the correct explanation. Sinton (1980) also observed a five-fold brightening at 5 μm between the two Voyager encounters in 1979. This observation will be discussed in more detail below. However, we cite it here to emphasize that there is no doubt about the existence of such major increases in Io's 5 μm flux. Except for minor increases, less than two-fold, only one major outburst (Johnson et al. 1987) has been seen since 1979 despite the order of magnitude increase in the frequency of observing Io in the near infrared.

Voyager Observations of Variability

Although it is the Voyager observations that provide the context for interpreting variability, the Voyager observations themselves provide only limited information concerning variability, since they represent only two "snapshots" taken a few months apart. The surface seen by Voyager 2 in July 1979 generally resembles that seen by Voyager 1 in March of that year, but there are some significant differences.

Of the eight plumes that were seen by Voyager 1, seven could have been observed by Voyager 2. Of these, six were still active. The largest plume (#1, at Pele) had stopped. The second largest (#2, at Loki) was even larger than before, and had developed a more complex structure. In addition, the presence of new plume deposits indicates that at least two more plumes were active during the interval between the encounters. McEwen and Soderblom (1983) have concluded that two types of plumes exist:

1. Low-temperature SO_2 driven plumes such as Prometheus, which are long lived (compared to the time between encounters).
2. High-temperature sulfur driven plumes such as Pele and Surt, which are short lived.

There is one possible inconsistency in this argument. One of the unseen plumes is identified with the Surt deposit, and this eruption was believed to be associated with the 5 μm brightening seen by Sinton. The Voyager results indicate that such eruptions should be fairly common. However, as we point out, only one such brightening (Johnson et al. 1987) has been seen during the past seven years. Furthermore, the infrared flux from the active Pele (Pearl and Sinton, 1982) was considerably less than that seen from Earth during outbursts. The size of the Surt caldera was somewhat larger than the source region for Pele, so there may be a range of fluxes expected from this type of eruption. The problem could also be resolved if Sinton's outburst was not in fact associated with Surt, but rather with some other eruption, or if there has been a drastic reduction in such activity since the time of the Voyager encounters.

In addition to the changes in plumes and plume related deposits, other differences were seen between Voyager 1 and 2. In particular, the albedo of the northern part of the Loki "lava lake" increased significantly.

Voyager observations also shed some light on long-term variability. Johnson and Soderblom (1982) derived resurfacing rates of 10^{-3} to 10 cm yr^{-1}, based on the absence of impact craters and estimates of plume deposition. These suggest that the surface should change dramatically in a few years' time. However, there seem to be processes operating that maintain the overall appearance of Io, despite such active resurfacing. Morrison et al. (1979) have pointed out that the visible rotational lightcurves of the satellites have not changed significantly in the many decades that photometric observations have been obtained. [Lockwood et al. (1980) have seen variations of a few percent.] In the past, the wavelengths used in visible photometry programs were not optimized to show variations on Io. These would be greatest in the near-ultraviolet, where the contrast between sulfur and sulfur-dioxide is greatest. Future observations at these wavelengths should be able to detect the effect of deposition from a single large plume such as Pele. Nevertheless, neither the visible lightcurves nor (as discussed below) the infrared lightcurves have changed dramatically. Apparently, although the resurfacing rates are high and the details of the lightcurve may change slightly, some process operates that maintains the overall appearance of the satellite, in particular, the dichotomy between the leading and trailing hemispheres.

Post-Voyager Infrared Observations

During the 8 years since the Voyager encounters, several groups have maintained active programs monitoring Io. The techniques used have included rotational lightcurve photometry (Johnson et al., 1984) eclipse photometry (Sinton and Kaminski, 1988), infrared polarimetry (Goguen and Sinton, 1985), speckle interferometry (Howell and McGinn, 1985), and mutual event occultation photometry (Goguen et al., 1987). Each technique has its own advantages and disadvantages:

Light curve photometry The raw data can be obtained with standard instruments and techniques, at a wide range of wavelengths, and data covering more than the past decade are available. However, since only the total flux is measured, modeling or comparison with past data is necessary to determine the hot-spot component. No information on the latitude of hot spots can be obtained.

Eclipse photometry Again, the raw data can be obtained with standard instruments, at a wide range of wavelengths. At short wavelengths, where reflected light is negligible, the technique gives a direct measurement of the hot-spot component. At the longer wavelengths, the contribution from the cooling background surface confuses matters, but this can be modeled with reasonable accuracy. However, only a limited number of eclipses can be observed per year and they occur only over a limited range of longitudes. This can bias estimates of the global heat flow.

Polarimetry By sensing the changes in polarization as the satellite rotates and the hot spots move across the disk, this technique directly determines the hot-spot location. The hot-spot flux is also determined directly, except for a factor related to the depolarization caused by surface roughness. However, the observations require measurements over a good fraction of the satellite's rotation. A confusion limit will be reached when several sources are present.

Speckle interferometry The technique allows one to obtain diffraction-limited "images" of Io. It directly measures the flux and position from hot spots, and can therefore be used to determine locations of short-lived events. With isolated hot spots one can obtain positions good to a few hundred kilometers. However, with current telescopes, the diffraction limit corresponds to only a few pixels in each direction across the satellite, and hot spots closer than this cannot be separated. Systematic errors currently limit the hot spots that can be detected to those whose flux is at least 10 percent of that from the whole disk. However, instrumental improvements should soon allow weaker ones to be seen.

Occultation photometry Since this is again a photometric technique, the data are relatively easy to obtain. It readily separates the discrete hot spots from the overall background, and can provide hot-spot positions accurate to tens of kilometers. However, a series of mutual events can occur only every 6 years, when the Earth passes through the equatorial plane of Jupiter. Most events take place so rapidly (in a few minutes) that good signal-to-noise ratios can only be obtained at wavelengths of 5 μm and shorter. Lunar occultation observations are also possible, but because these take place at such high speed, only relatively low signal-to-noise ratios are obtained.

Overall Stability The initial results of the rotational and eclipse photometry programs seemed to suggest an object that was occasionally subject to dramatic outbursts at wavelengths of 5 μm and less (Sinton et al., 1983), but whose average emission was relatively constant with *time*. In particular, little change was detected at wavelengths longer than 8 μm, where the bulk of the energy is emitted. Modeling of the clear variation in hot-spot flux with *rotation* implied that at most a few sources dominated (Johnson et al., 1984), and that the most prominent of these was located near the longitude of Loki, the strongest infrared sources seen by Voyager. Sinton reported smaller temporal variations, which had a possible correlation with Io's position in the magnetosphere, and detected short period "flickering" with a time scale of a few minutes.

Continued analysis of the Voyager images, combined with Earth-based observations, led to two conclusions that have implications for long-term variability. The first was the result discussed above, stating that the bulk of the emission came from the Loki hemisphere. Because this is the hemisphere that is always viewed when Io is in eclipse, its unusual activity results in an overestimate of the global heat flow. The revised heat-flow estimates were perhaps low enough to be consistent with the equilibrium predictions of standard tidal theory, without invoking episodic volcanism. However, shortly after this McEwen et al. (1985) discovered a correlation between temperature and visible albedo, and used this to predict the existence of a large south polar ring hot spot, in a region unobserved by Voyager's infrared interferometric spectrometer (IRIS) experiment, and at high enough latitude that it could only be seen obliquely from Earth. This hot spot, if real, would be emitting flux comparable to Loki, and would again clearly introduce the problem of too high a heat flow to be continuously sustained by the standard tidal dissipation models. But perhaps more important than the actual heat-flow measurements, both techniques showed that most of the flux came from just one or two active areas.

In the past few years, the more detailed measurements and analysis of Io show that significant variations do occur. Although the bulk of this variation is at 5 μm, some changes in longer wavelengths emission have also been seen. The Loki hot spot is still active, eight years after Voyager discovered it, but its flux has changed with time. It has undergone temporary increases in brightness, but may be declining over the long term. New hot spots have been detected at locations where nothing was present during the Voyager encounters. Finally, recent speckle measurements at 8.7 μm failed to detect emission from the south polar ring.

Variations at Loki The first high-resolution measurements were obtained in the summer of 1984. At that time photometry showed a moderate increase in the 5-μm flux from the trailing hemisphere, as can be seen in figure 22. On July 3 speckle measurements at 4.8 μm showed that 30 to 40 percent of the light from the trailing hemisphere was coming from an unresolved hot spot in the Loki region (Howell and McGinn, 1985). One

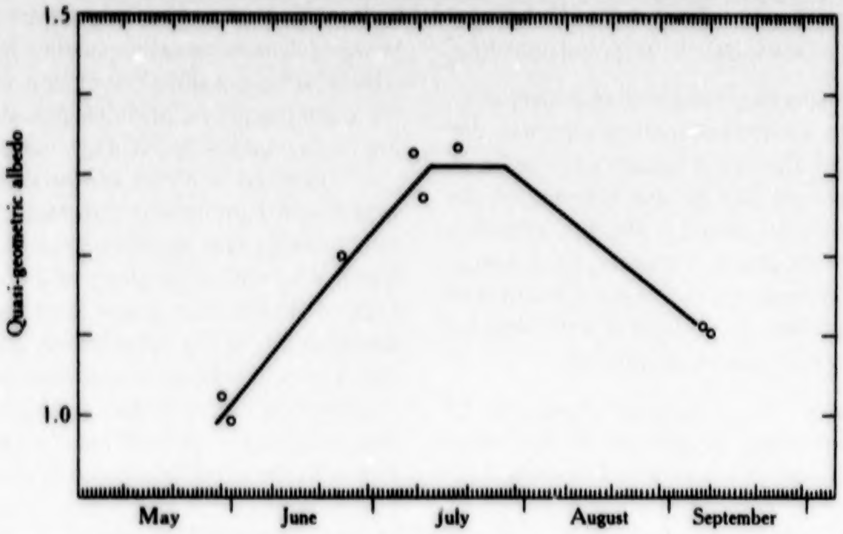

Figure 22. The brightness of Io, as measured at 4.8 μm, during an enhancement in the activity at Loki.

week later this result was confirmed by infrared polarimetry (Goguen and Sinton, 1985). The polarimetry technique also detected a new hot spot in the leading hemisphere where none had been present during the Voyager encounters. A third spot (in addition to Loki) may have been detected in the trailing hemisphere.

Since 1984 additional speckle and polarization measurements have shown that the enhanced eruption in the Loki region has subsided. Figure 23 compares the visibility curve obtained on 3 July 1984 with a more recent one. The point source contribution is considerably less in the more recent data. Polarization measure-

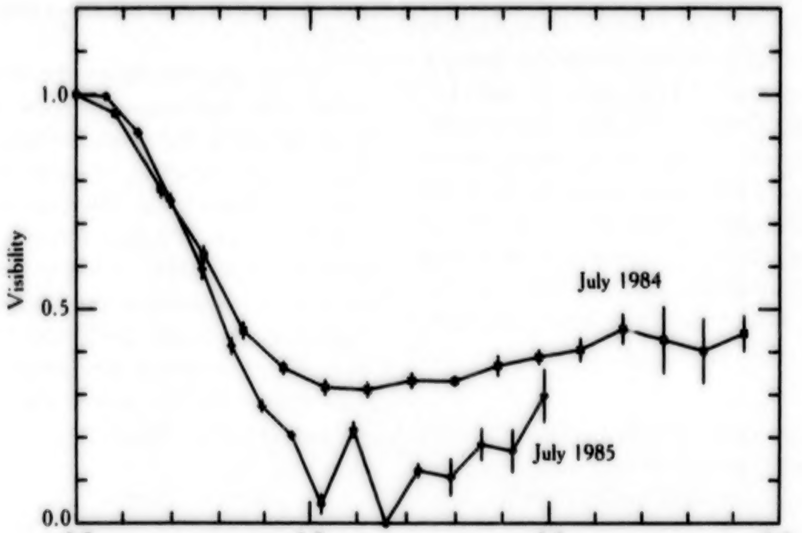

Figure 23. The 4.8-μm visibility curves for data on Loki hemisphere obtained in July 1984 and July 1985. The 1984 data were obtained during a time when Loki was unusually active at short wavelengths. Roughly 40 percent of the total flux from Io was coming from a point source in the Loki region. This is shown by the level of the flat, high-frequency section of the curve. By one year later the point source flux had dropped significantly, as shown by the lower visibility at these spatial frequencies.

ments confirm this result. In 1984 the 4.8-μm polarization was as large as 1.6 percent. Recent measurements indicate 3σ upper limits of 0.4 percent at 4.8 μm and 0.19 percent at 3.8 μm. In fact, these results suggest that the hot-spot emission is even less than in years before 1984. However, there are no speckle or polarization observations from that time with which to make a direct comparison.

On 25 December 1985, Io was occulted by Callisto, and the 3.8-μm lightcurve shown in figure 24 was obtained. The disappearance and reappearance of Loki are clearly visible. The diameter of the emitting area was found to be 200 km, and its location was 308° W, 20° N. The flux is in general agreement with that expected for this wavelength. However, because no previous 3.8-μm data of Loki itself are available, it is impossible to determine variability to within factors of roughly two.

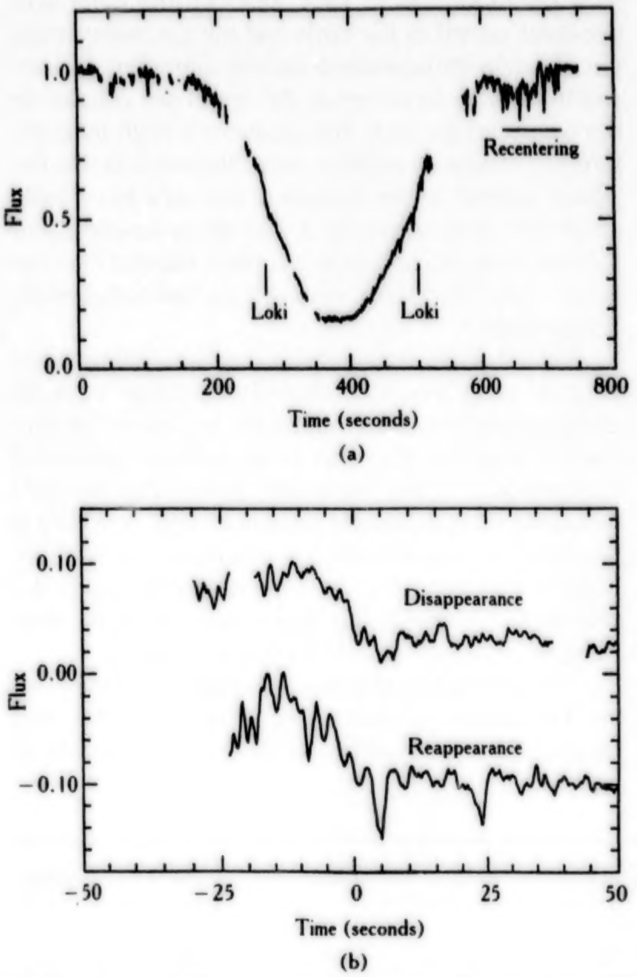

Figure 24. **(a)** Shows the lightcurve at 3.8 μm as Io was occulted by Callisto on 25 December 1985. The mission sections of data resulted from DC saturation of the detector when very thin fog occasionally passed by above the dome. It has negligible effect on the photometry (measured as a chopped AC signal) between dropouts. The sharp drop, which occurs at roughly 270 seconds, is the disappearance of Loki. It reappears at 500 seconds. These sections of the curve are shown in more detail in **(b)**, where the baseline slope has been subtracted, and the reappearance has been plotted from right to left.

The lack of consistent sampling at any given wavelength is a general problem with the high-resolution data set. That data set now spans three years, but for the most part data from different years are all at different wavelengths. This largely results from the difficulties attendant to occultation observations, and the still developing character of the speckle and polarization techniques. For example, only 3.8-μm data were obtained from the 25 December occultation. All of the major telescopes on Mauna Kea were used for that event, each at a different wavelength, but poor weather and high winds affected either the data themselves or the telescope operation at all the other telescopes and wavelengths.

A proper characterization of the individual hot spots will require nearly simultaneous observations at a range of wavelengths. Good measurements of variability will require data at the same wavelength covering at least several years. In particular, measurements in the 10-μm region are necessary to monitor the total heat flow, which comes predominately at these wavelengths. The programs now underway are beginning to acquire such a data set.

In the meantime, it may be possible to determine variations in Loki's heat flow from detailed modeling of the existing eclipse data. Historically, some of the first observations that indicated an unusual nature to the surface of Io were the infrared eclipse observations of eclipses made in 1971 and 1972 by Hansen (1973) at 10 μm and by Morrison and Cruikshank (1973) at 20 μm. These investigators found that thermophysical models for eclipse cooling and subsequent reheating that were based on 10-μm data were incompatible with those based on 20-μm data. What was missing from the modeling was the thermal emission from the volcanoes. It is important to note, as these investigators did, that no model could fit both the eclipse cooling curve (observations made at eclipse disappearances) and the eclipse heating curve (observations made at reappearances) simultaneously at either wavelength. The preeclipse flux was always much greater than the asymptotically approached posteclipse flux. Even after the discovery of the thermal emission from the volcanoes and their influence on the eclipse observations, it was not recognized for several years that the main reason for the apparent slope between the preeclipse and posteclipse flux was the dominant emission of the Loki volcano. The volcano was closer to the center of the disk at the sub-Earth longitude of a disappearance observation than at a reappearance observation where it was near to a limb. Thus it can be said that Loki was most likely active in 1971 and 1972, and in fact, a reanalysis of the old data, which has not been done, should allow an assessment of the heat flux from Loki in these pre-Voyager observations.

The interpretation of eclipse observations made between 1980 and 1984 has recently been accomplished by Sinton and Kaminski (1988). They have developed a detailed thermophysical model involving horizontal as well as vertical inhomogeneities in order to obtain the best possible fitting of the eclipse cooling and heating curves. The difference between observations and the model predictions, at each wavelength, is the flux of volcanic heat. The volcanic component is assumed to arise from both a high-temperature source and a low-temperature source, each with a different area in order to fit the eclipse data that consist of observations at seven wavelengths between 3.5 and 30 μm. The observations for each year consist of disappearances, observed about two months before opposition, and reappearances, observed a similar time after opposition. Sinton and Kaminski assume that the volcanic flux is constant over the intervening four months and that the difference seen is the result of the different amount of foreshortening. From the decrease, as mentioned above, between the flux at disappearances and reappearances it is possible to determine an effective longitude if a single hot spot is assumed.

In all years where both disappearances and reappearances were observed, the effective longitude of both the high- and low-temperature hot spots was within a few degrees of that of Loki. By adding the contributions from the various volcanos in the vicinity of Loki to that of Loki as recorded in Voyager data, they find that if eclipse observations were made then, they would have produced a longitude of 306° west and a flux that would have been mostly due to Loki. Since they found large variations in both the high-temperature and low-temperature hot-spot fluxes in the 1980–1984 data, it is apparent that Loki has varied considerably and in general has decreased substantially since 1980. Some results of their analysis are given in table 4. The data from 1986 is unpublished but has been added to their results for 1980 to 1984. Although the color temperatures quoted in the table and the necessary areas (as shown by the equivalent circular diameter) are subject to relatively large errors, the errors are coupled in the sense that an error that produces a high temperature will produce a smaller area. The result is that the power radiated by the equivalent hot spot has a fairly small error associated with it. Also the error associated with the total radiated power is often smaller than the errors associated with the high- or low-temperature components.

Table 4 shows a remarkable decline in the amount of power radiated by Loki. Most of the decline is a result of changes in the low-temperature or "warm" source. Notice, however, that the most extreme fractional changes occur in the hot source. With either the high- or low-temperature source there is a strong correlation of power output and equivalent diameter. Thus it would seem that the main cause of the variability lies in the change in the area of the region rather than the temperature of the flow or caldera that is radiating.

The assumption that the hot spots are stable over the four months between eclipse disappearance and reappearance observations needs some comments in

Table 4. Volcanic Fluxes—Loki and Environs, 1980–1986

Year		**1980**	**1981**	**1982**	**1983**	**1984**	**1986**
Hot source							
Size	(km)	30	10	28	34	17	16
Temperature	(degrees K)	564	522	[600]	541	[600]	475
Longitude	(degrees W)	305	[310]	293	304	[310]	339
Warm source							
Size	(km)	382	150	202	197	150	116
Temperature	(degrees K)	250	368	297	292	360	336
Longitude	(degrees W)	[310]	[310]	312	316	[310]	328
Power (hot source)	(terawatts)	4.0	0.4	3.0	4.4	1.6	0.5
Power (warm source)	(terawatts)	25.5	18.3	14.2	12.6	16.9	7.6
Total power	(terawatts)	29.5	18.6	18.7	17.0	18.5	8.1
(Standard error)	(terawatts)	2.7	0.6	0.8	0.6	1.0	0.4

Bracketed quantities were assumed, the remainder were solved for.

view of the variation that is evident in table 4. The justification for the assumption of stability lies in the fact that the derived longitudes of the hot spots appear to be fairly stable. The observations for 1984, however, need further discussion in view of the fact that there was an eruption in Loki in the summer of 1984 as documented by speckle and polarization observations mentioned above. Sinton and Goguen (1985) in their efforts to measure polarization, made 4.8-μm observations in April, May, and June and, although these did not have enough sensitivity to measure the polarization, they did adequately measure the quasi-geometric albedo. These observations plus other unpublished photometry by Sinton and Tittemore (1987) in July, August, and September show that at the central meridian longitude of 300° (near Loki) the quasi-geometric albedo (p') increased steadily from April ($p' = 0.9$) to July (where p' peaked at ~1.3) and declined in August and September ($p' \sim 1.1$). The eclipse data used for the values in table 4 consisted of one eclipse observed in September. The latitude of Loki was assumed in the reduction. The eruption of Loki was documented only in the short wavelength region, and thus we cannot make any assertions about changes in the low-temperature, large-area component of the hot spot. Thus the 1984 high-temperature source, as shown in the table, is expected to yield a lower radiated power than the speckle and polarization data yield.

Other Changes Since the Voyager Encounters The polarimetry observations mentioned above gave the first indication of active regions that had appeared since the time of Voyager, and additional ones were discovered during the mutual occultations.

A new volcano that was not seen either in Voyager photography or by the Voyager IRIS instrument was discovered during observations of occultations of Io by Ganymede or Callisto in 1985. The signature of the volcano was detected at the occultation of Io by Callisto on 10 July simultaneously at two telescopes on Mauna Kea (Goguen et al., 1987). Both the ingress and egress behind Callisto were observed at both telescopes. Howell, at the UKIRT telescope, detected the signature at 4.8 μm, and Sinton, at the University of Hawaii 2.2-m telescope, similarly detected the events, and each within a second of time of the UKIRT times. The durations of the drop in flux at ingress and the rise in flux at egress are both less than one second. Since the relative speed of the limb of Callisto across Io is ~20 km s^{-1} the hot spot is less than 20 km in diameter. Corrections to the relative positions of Io and Callisto given by the DE 118 ephemeris (Newhall et al., 1983) were determined from fitting a photometric model that included limb darkening on Io to the observed lightcurves. The magnitudes of these corrections and those of corrections to similarly excellent ephemerides indicate that an upper limit to the errors in the position are ~200 km or about 6 degrees of latitude or longitude on Io. The position for the new volcano is 79° W and 23° S. It lies in Tarsus Regio, a region that was not well observed in Voyager images.

Since the volcano was observed at two different wavelengths, a color temperature may be determined for it. The resulting temperature was 546 K. This value, when combined with the observed flux at either wavelength, leads to an area that is equivalent to a hot spot of 19 km diameter, which is in good agreement with the upper limit mentioned above.

The new hot spot might have been observed at several other mutual occultations. The region was certainly occulted by Callisto again, a mere 16 days later at the extraordinary two-hour long occultation that was observed by Sinton from the Anglo-Australian Telescope on 26 July 1985. Emission from the volcano would have been observed at both 4.8 μm (observed in the ingress phase) and 3.8 μm (observed in the egress phase). Yet, it was not detected in observations at high signal-to-noise ratio especially at 3.8 μm. At 4.8 μm, it possibly fell in a region of the lightcurve where observation was suspended momentarily. If one assumes the 19-km diameter found on 10 July, then an upper limit to its temperature on 26 July is 450 K. The region was also occulted on 24 December and successful observations were made at 3.8 μm on the 2.2-m Hawaii telescope. These were also negative for measurable emission by the hot spot, and a similar upper limit is derived.

It may be concluded on the basis of the high temperature and the apparently short duration of the eruption that this volcano should be classified as a Pele type (McEwen and Soderblom, 1983). The other distinguishing features of this class of eruption are a very large diameter plume deposit and the extreme height to which the plume rises. It will be of great interest when Galileo arrives at Io to see whether this prediction of a large deposit is fulfilled. Unfortunately, the visible record of pyroclastic deposits may have been obliterated by subsequent resurfacing. Goguen et al. (1987) suggest that this volcano be named Poliahu. The suggestion will probably not be acted upon until there is a feature visible in images to which the name may be applied.

No clear signatures of hot spots other than the new spot and Loki were found in observations of seven mutual events.

Johnson et al. (1986) reported that they observed a change in the 4.8-μm rotational lightcurve between June and July of 1985. The data indicate that a small (~10 km radius) hot (~600 K) source that was located near 260° W longitude turned off during this time.

The failure of 8.7-μm speckle interferometry to detect the south polar ring also may represent a significant change on Io. Figure 25 presents the first good long-wavelength speckle data obtained on Io. The visibility curve of the Loki hemisphere shows considerable point source emission, indicating the continued heat flow from this source (although perhaps at a lower level than in previous years). However, the visibility curve for the south polar ring hemisphere shows very little point source contribution, despite the fact that the ring should be a major source at this wavelength. It is also possible to examine the individual scans across Io that were processed to obtain the visibility curve. They show no indication of enhanced emission in the south polar region. The occultation observations, although primarily at shorter wavelengths, also fail to show any sign of the ring.

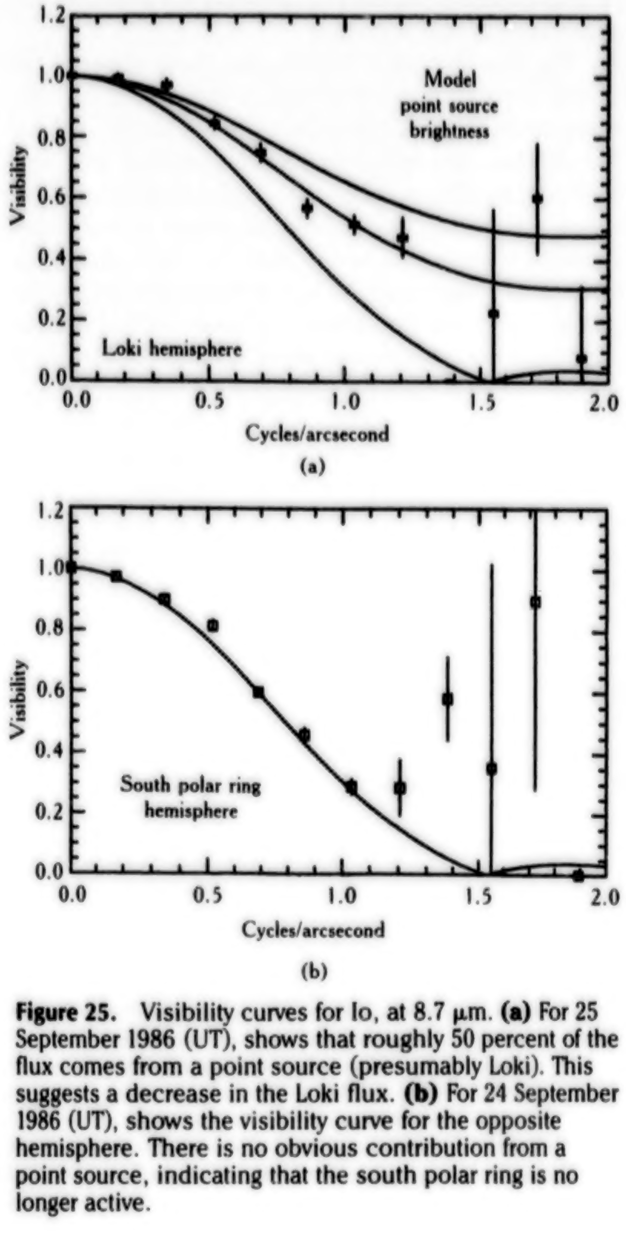

(a)

(b)

Figure 25. Visibility curves for Io, at 8.7 μm. **(a)** For 25 September 1986 (UT), shows that roughly 50 percent of the flux comes from a point source (presumably Loki). This suggests a decrease in the Loki flux. **(b)** For 24 September 1986 (UT), shows the visibility curve for the opposite hemisphere. There is no obvious contribution from a point source, indicating that the south polar ring is no longer active.

Voyager never directly saw infrared emission from the ring; it was only predicted on the basis of the temperature-albedo correlation. However, that correlation seems very well established, and led correctly to the prediction that Amaterasu Patera is hot (Pearl, 1985). Since the predicted heat flow from the ring is so large (roughly the same as Loki) its disappearance would constitute a significant change in the total heat flow from the satellite.

In summary, the observed variability seems consistent with the proposal of McEwen et al. (1983) that the small hot sources such as that found with Pele are short lived, but that the larger sources such as Loki have lifetimes of many years.

However, there is now evidence for change in the flux from Loki and the presumed flux from the south polar ring, and this has important implications for the total heat flow. Because these two sources contribute much of the total heat flow from Io, it is very dangerous to draw conclusions about the correct time averaged flow from Io from the relatively limited data available. If the heat flow came from many sources, then it would be unlikely that, by chance, we were observing Io during a time when the heat flow was twice normal. But if most of the flux comes from just one or two sources that have lifetimes of roughly a decade, then it is perfectly reasonable that the heat flow measured over a few years could be twice the long-term average. The time-averaged heat flow may well be within the limits set by equilibrium tidal dissipation theory.

Spectroscopic Variations

Although most of the study of variability has been aimed at locating hot spots, some spectroscopy and multi-color photometry has been obtained, in order to determine the composition of the surface, and variations in it.

One such program was the multi-color eclipse photometry of Hammel et al. (1985). As the surface of Io warms up after emersion from eclipse, there should be a shift in the edge of the absorption band in any "yellow" sulfur (S_8) on the surface. Their observations failed to show any such variation, which led them to conclude that at most 50 percent of the surface could be covered with such sulfur. Since that time, Nash (1987) has discovered that when sulfur is mildly heated in a vacuum much of the material sublimates, and the fraction left behind does not show the temperature dependent color shift.

Observations that Witteborn et al. obtained during outbursts (reported in Witteborn et al., 1979 and in Pearl and Sinton, 1982) may show infrared absorption features. However, the apparent bands in the February 1978 spectra do not agree with those in the December 1979 spectra, and their interpretation remains unclear. They do not match that expected for any obvious materials.

Howell et al. (1984) obtained infrared spectroscopy of Io in order to determine the surface composition, and to search for temporal changes. Sulfur dioxide has a prominent band in the 4-µm region, and the depth of that band, seen on Io, varies significantly with rotation. Any redistribution of the sulfur dioxide on the surface should be evident at this wavelength. So far, no detectable changes have been seen. Several spectra that appear anomalous in the region just short of the band were obtained. This is a region where an SO_2 gas band is present, but the anomalies do not seem to match the absorption or emission expected for the gas. They could perhaps be instrumental effects, but in light of the many peculiarities of Io, such observations should be continued.

Howell, Cruikshank, and Geballe also obtained spectra of Io in eclipse. A spectra obtained in August 1983 appeared to show a narrow absorption feature at the 4.07-µm wavelength of the SO_2 frost band (fig. 26). Since the light observed in eclipse comes from the thermal hot spots, the SO_2 frost causing the apparent band cannot be on the surface. Frost would instantly sublimate on any surface hot enough to emit significantly at this wavelength. They proposed that the absorption was due to frost suspended in a plume above a hot spot. The amount of frost required was similar to that seen by Voyager in the Loki plume.

The following opposition they obtained spectra during four eclipses, and those data show no sign of the band. The spectra are of higher signal-to-noise ratio, and show only a flat continuum during eclipse. The August 1983 spectrum was obtained on one of the first observing runs with a new instrument, and the band is apparent only in a single detector channel. In light of that and the later spectra, the result must be viewed with some skepticism. However, if the feature was due

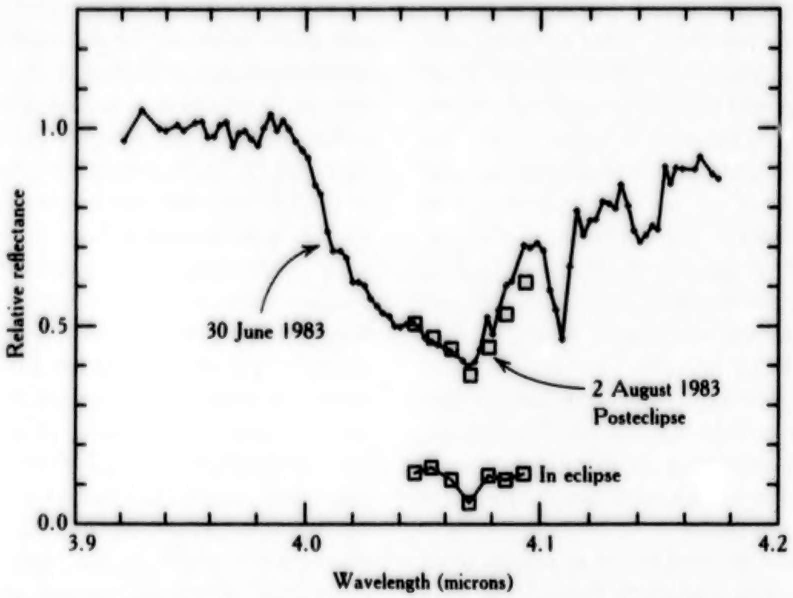

Figure 26. The *solid curve* is a typical out-of-eclipse spectrum of Io, showing the prominent broad saturated sulfur dioxide frost absorption band, whereas the *open boxes* are spectra obtained during and immediately after eclipse. The in-eclipse spectrum appears to show a narrow absorption feature due to frost. If real, this must be from plume material located above a hot spot. However, spectra obtained the following year show no evidence of the feature.

to frost in a plume, then variations should well be expected. The Voyager data, which show two plumes near the Loki hot spot, suggest that the band *should* be present in eclipse spectra. Monitoring should continue. If the nearby gas absorption band can be measured in addition to the frost band, then one would have a direct measure of the SO_2 gas-to-solid ratio in the plume, and this would give important information concerning the driving gas (SO_2 versus sulfur) and the temperature of the source (Kieffer, 1982).

EUROPA

Because Europa is also subject to tidal heating, it may also show some activity. Some has been reported, but none that could be confirmed by independent observations. To an extent, this is the result of the less intense monitoring of Europa, but it also is clearly due to the fact that Europa, if active at all, is much less so than Io.

Evidence for Variability and/or Thermal Activity

Voyager Observations On the final frame (FDS 20767.37) taken of Europa by Voyager 2, on the southern part of a thin crescent there is a bright spot of contrast much greater than on any other Europa images. There is also a brightening of the sky above this spot and exterior to the crescent. It is not accompanied by a similar brightening interior to the terminator. Cook et al. (1983) have proposed that this image records the eruption of a material, perhaps water vapor or ice, and the light above the crescent may be produced by scattering from some kind of plume, perhaps similar to those above Io's volcanoes. The location of the presumed activity is 333° W and 31° S. Earlier frames of this region, taken by both Voyagers, were searched and no comparable brightening was found. Also, no other similar features were found on other Voyager frames of Europa. Thus, this single image represents the possible detection of geyserlike activity that has previously been suggested as possibly occurring on Europa as the result of tidal heating in the same way as the volcanism of Io is almost certainly produced.

The interpretation of the final frame as representing an eruption has been criticized by McEwen (1986). He finds that the increase in contrast is just what should be expected for an observation at such a large phase angle (143°), and that there is nothing unusual in this observation. It is the phase behavior expected from multiple scattering in a bright surface material. He further points out that there is an increase in dark current and noise in the corners of Voyager images and the "plume detection" may be due to the increase noise.

Uniformity of Photometric Properties Of importance to the interpretation of the Cook et al. (1983) observation, and to the whole question of whether there is active volcanism on the surface of Europa, is the photometric uniformity of the surface and interpretations that may be given to this in terms of the existence of exogenic and endogenic processes and the time scales appropriate to these. Photometry of Voyager images has been carried out by Buratti and Veverka (1983), Buratti (1983, 1985), and by McEwen (1986). Outside of the albedo variations imposed on the surface by the numerous lineaments and dark spots there is a remarkable uniformity of the photometric response of the surface that is dominated by a function dependent upon the cosine of the angle from the apex of its orbital motion (i.e., it is bright on the leading hemisphere and dark on the trailing hemisphere). The exogenic processes that have been considered include impact gardening and magnetospheric interactions such as sulfur ion implantation and sputtering. Endogenic processes may include geyserlike volcanic activity and ensuing frost condensation.

According to McEwen (1986), the impact gardening may bring about a cosine-like photometric response in several ways; for example, it may influence the particle size distributions and it will undoubtedly produce contamination and darkening of the surface. The contamination is expected to darken the leading side relative to the trailing side. Whether the particle size distribution effect darkens or brightens the leading side relative to the trailing side depends on the size distribution in the incoming cometary flux. The magnetospheric interaction may also produce differing effects. Slow ions (sulfur ions) that are corotating with the magnetosphere will preferentially impact and darken the trailing hemisphere. Fast ions, on the other hand, will preferentially impact the poles and produce a dependence on the square of the cosine of the latitude. It is known that implantation of sulfur ions from the corotating torus does occur (see below). The fact that the cosine-like response is not saturated at either the apex or antapex of the orbital motion suggests that there are two competing processes and that an equilibrium of darkening and lightening is maintained. (If a single process alone were responsible, then saturation should have been reached and a "flat" dependence found at either the apex or antapex.) McEwen found a dependence that included both first-order and second-order terms in the cosine, but not third order. He cites this as further evidence of the competition of two exogenic effects. However, we are not convinced by this argument. It appears to us that this might also result from partial saturation of a single process possibly in competition with an uniform endogenic process.

It is against this careful background of photometry that the criticism of the Cook et al. (1983) observation must be viewed. It does seem to us, however, that in regard to the observation itself neither side has made their case sufficiently quantitative for an outside reviewer to make a judgment. How much was the contrast increase? Is such an increase within expectation of multiple scattering theory? What was the intensity of the "plume" and is this beyond what may be expected from noise in the image frame? Surely these questions can be answered. The question of activity on Europa is important enough in reference to models of internal structure and theories of orbital evolution to warrant the quantitative evaluation that is required.

Observation of a Possible IR Outburst Infrared (IR) photometry (2.2, 3.8, and 4.8 μm) of the galilean satellites have recently been compiled (Tittemore and Sinton, 1987). The number of Europa observations is rather meager (eight only at 4.8 μm) owing to the amount of time required to make satisfactory observations of this satellite. Observation of Europa is much more difficult than observation of Io because of the strength of the water-ice band in the 3- to 5-μm region. The magnitude of Europa at 4.8 μm is normally between seven and eight and most of the observations have been made at the IRTF. It was discovered in making this compilation that one very early observation (23 April 1981) was unusual because of its strong 4.8-μm flux. The unusual circumstance was not recognized at the time because this was among the first Europa observations made.

Efforts to find that the unusual observation is spurious have been made but this does not seem tenable. The observation was made at the IRTF. The telescope position recorded by the data acquisition system agrees with the position of Europa. Observations made at longer wavelengths, immediately afterward, are consistent with the background thermal emission expected from Europa. This was the only observation that has been made with a bolometer detector; the others were with an InSb photoconductor. It was considered that a long wavelength filter leak might have produced a spurious flux from a very cold object, but careful investigation of this possibility by the IRTF staff has eliminated this as a possible cause. The observation consisted of three groups of data extending over ~20 minutes, which were separated by centering checks in between. Each group had a signal-to-noise ratio ~10.

Although the ~6 times increase over normal flux seems to be exceptionally well documented, the existence of outbursts from Europa must be considered tentative because (1) it was not recognized at the time and checks were not made and (2) no other outbursts have been seen. Figure 27 shows the derived phase variation of Europa at 4.8 μm and the outstanding point. The two points near 2 degrees phase angle were made in September 1986 with the University of Hawaii 2.2-m telescope to enable the determination of the phase coefficient. These two points required ~20 and ~40 minutes of integration. The reduction in error-bars is due mostly to photometer sensitivity improvements. The other observations were made with the IRTF.

Hemispherical Asymmetry and the Time Scales Implied

The question of volcanic activity of Europa can be approached from the standpoint of the age of the surface and whether endogenic processes are required for renewing it. The fact that only a few impact craters appear to be visible in Voyager images does not necessarily imply that the surface is young and due to endogenic processes. The conclusion reached by several investigators is that either the surface is older than 10^9 years or is younger than 10^8 years (Shoemaker and Wolfe, 1982; Lucchitta and Soderblom, 1982). Given estimates of the thickness of the ice crust and the proba-

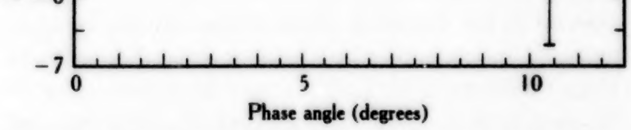

Figure 27. Photometry of Europa at 4.8 μm. A nearly linear dependence of the magnitude of Europa on the solar phase angle is expected. However, the observed magnitude on one night (23 April 1981, *arrow*) is six times brighter than the expected linear relation and suggests that an outburst occurred at that time.

ble temperature gradient, craters larger than 20 km would disappear over times greater than 10^9 years by creep in the viscous ice, whereas craters smaller than 10 km would remain but not be visible in Voyager images. The system of lineaments could not have persisted through the period of heavy bombardment 4 Gy ago, so the surface is younger than that age. If the age is less than 0.1 Gy, then one can assume that the process that renewed it is still occurring today.

The homogeneous photometric response mentioned above has been cited as evidence of active resurfacing by formation of frost from geyser activity (Squyres et al., 1983). They argue that the homogeneous scattering requires much more tenuous microstructure of the ice than is produced by impact produced ejecta deposits such as on Ganymede and Callisto. They point out that such a tenuous deposit would be produced by water boiling as it reached the surface and depositing ice crystals over a wide area. They cite Buratti and Veverka (1983) to support their argument of a tenuous structure. This argument was not given in the version published by Buratti and Veverka, and McEwen (1986) states that actually the homogeneous nature of the scattering requires a more compact rather than more tenuous surface than is required for Ganymede and Callisto.

Another argument given by Squyres et al. (1983) for active resurfacing by ice deposition concerns the intensity of the ultraviolet sulfur-dioxide-like band that was discovered in International Ultraviolet Explorer (IUE) spectra (Lane et al., 1981; Ocert et al., 1987). The band is found to be concentrated on the trailing hemisphere of Europa and, on the leading hemisphere, is much weaker and not detectable. It closely resembles laboratory spectra of SO_2 frost but is assumed to be produced by implantation of sulfur ions into the ice matrix primarily from the corotating sulfur plasma that extends outward from Io's distance to encompass Europa. Lane et al. find that the required column density of sulfur atoms on the trailing hemisphere is 2×10^{16} cm^{-2}. The comparison of this column density with the flux rate of sulfur ions to derive a time to reach the observed density is complicated by a number of processes considered in the modeling (such as the removal by sputtering of ice and sulfur by energetic ions). The estimate given by Eviatar et al. (1981) is used by Squyres et al. to derive a time of seven years to reach the observed column density. They conclude that there must be a competing endogenic process of ice deposition to produce the observed column density, which is then an equilibrium value achieved by dilution of the sulfur implantation. McEwen (1986), in arguing against this time scale and the assumption of an endogenic process, cites the many uncertainties that are involved. He finds, as mentioned above, that there are at least two exogenic processes that are competing and that the observed sulfur column density says nothing about the presence of an active endogenic process.

Future Work

The question of whether there is sufficient tidal dissipation in Europa to require convective transport and hence an active volcanism is an important one. There is the strong suggestion in the one infrared observation that Europa is active. The hypothesis should be followed up with further infrared observations. Although Europa does require some amount of time to observe at 4.8 μm with modest-sized telescopes, improvement in detectors, and particularly the reduction of background flux arising within the telescope, will improve the situation. Observations that should be made with Galileo include imaging to see whether the observations of the bright spot and the plume were real and infrared observations to test for hot spots.

CONCLUSIONS

Io is clearly variable, and monitoring that variability is important both in understanding the nature of that satellite and in planning the Galileo encounter.

- Infrared observations can now study the emission of individual active volcanic regions. Detailed study of their temperatures, locations, and lifetimes would give much insight into the nature of the volcanic processes operating on Io.
- Loki is still active 7 years after its discovery by Voyager. Eclipse observations from the early 1970s suggest that it was active even then. However, recent eclipse observations suggest that its thermal output is declining.
- Observations have clearly shown the existence of relatively short lived high-temperature eruptions, at places that were not the site of volcanic activity during the Voyager encounters.
- The fact that most of the heat flow comes from just one or two active regions, combined with recent results suggesting that the lifetimes of those active regions may be roughly a decade, suggests that fluctuations in output by a factor of two should be expected as active regions die and are born. The problem of

excess heat flow (compared to standard equilibrium tidal heating theories) could be due to statistically reasonable fluctuations in output.

- The overall visible rotational lightcurve has been stable for many decades, but recent visible photometry shows variations of a few percent. These are probably due to resurfacing of significant parts of the satellite. Careful observations at the infrared and ultraviolet wavelengths where the contrast between SO_2 and sulfur is large might enable us to map changes on the surface. However, the stability of the general lightcurve suggests that some process preserves the general dichotomy between the hemispheres.
- Interesting, but unconfirmed, observations of variable absorption bands on Io suggest the possibility of measuring the composition of erupting material and determining the physics of the eruption.
- Interesting, but unconfirmed, observations suggest that some activity may be taking place on Europa.

Future observations will refine and extend the above conclusions. In the infrared a special effort should be made to obtain good wavelength coverage. This will enable us to determine the characteristics of the new eruptions that are seen and confirm changes in the ongoing activity at Loki. The series of mutual events in 1991 will be especially important. Observations that can detect changes on the "inactive" low-temperature surface are also important; using these we should be able to estimate overall resurfacing rates.

The Hubble Space Telescope will allow us to obtain "moderate" resolution images of Io. Although these will not be able to show the individual active regions, they could detect widespread changes such as those due to major plumes. In fact, they should be able to see plumes above the limb.

Finally, it will be important to coordinate observations of Io itself with those of the surrounding region that Io affects. As reported in other chapters in this volume, changes in the torus and magnetosphere have been seen, and may be related to changes in activity on Io. Comparing the variations on Io to those of the magnetosphere will lead to a better understanding of both.

References

Binder, A. B., and D. P. Cruikshank (1964). Evidence for an atmosphere on Io. *Icarus* 3:299–305.

Buratti, B. J. (1983). Photometric properties of Europa and the icy satellites of Saturn. Ph.D. Thesis, Cornell Univ., Ithaca, N.Y.

Buratti, B. J. (1985). Application of a radiative transfer model to bright icy satellites. *Icarus* 61:208–217.

Buratti, B. J., and J. Veverka (1983). Voyager photometry of Europa. *Icarus* 55:92–110.

Cook, A. F., E. M. Shoemaker, L. A. Soderblom, K. F. Mullins, and R. Fiedler (1983). Volcanism in ice on Europa. *Reports of the Planetary Geology Program–1982 NASA Tech. Memo.* TM-85127:415–416.

Eviatar, A., G. Siscoe, T. V. Johnson, and D. L. Matson (1981). Effects of Io ejecta on Europa. *Icarus* 47:75–84.

Fanale, F. P., W. B. Banerdt, and D. P. Cruikshank (1981). Io: Could SO_2 condensation/sublimation cause the sometimes-reported post-eclipse brightening? *Geophys. Res. Lett.* 8:625–628.

Franz, O. G., and R. L. Millis (1984). A search for posteclipse brightening of Io in 1973 II. *Icarus* 23:431–436.

Goguen, J., and W. Sinton (1985). Characterization of Io's volcanic activity by infrared polarimetry. *Science* 230:65–69.

Goguen, J. D., W. M. Sinton, D. L. Matson, R. R. Howell, H. M. Dyck, T. V. Johnson, R. H. Brown, G. J. Veeder, A. L. Lane, R. M. Nelson, and R. A. McLaren (1987). Multi-color IR photometry of occultations of Io by Ganymede and Callisto during 1985: Temperatures, areas and locations of major hot spots and relative satellite astrometry. Submitted to *Icarus*.

Hammel, H. B., J. D. Goguen, W. M. Sinton, and D. P. Cruikshank (1985). Observational tests for sulfur allotropes on Io. *Icarus* 64:125–132.

Hansen, O. L. (1973). Ten-micron eclipse observations of Io, Europa, and Ganymede. *Icarus* 18:237–246.

Howell, R. R., D. P. Cruikshank, and F. P. Fanale (1984). Sulfur dioxide on Io: Spatial distribution and physical state. *Icarus* 57:83–92.

Howell, R. R., and M. T. McGinn (1985). Infrared speckle observations of Io: An eruption in the Loki region. *Science* 230:63–65.

Johnson, T. V., D. L. Matson, R. H. Brown, and G. J. Veeder (1986). Infrared emission from Io's volcanoes: Evidence for change in a Pele-class source in 1985. *Bull. Amer. Astr. Soc.* 18:774.

Johnson, T. V., D. L. Matson, R. H. Brown, G. J. Veeder, R. M. Nelson, and D. Morrison (1987). Volcanism on Io's leading hemisphere in 1986. *Bull. Amer. Astr. Soc.* 19:1148.

Johnson, T. V., D. Morrison, D. L. Matson, G. J. Veeder, R. H. Brown, and R. M. Nelson (1984). Volcanic hotspots on Io: Stability and longitudinal distribution. *Science* 226:134–137.

Johnson, T. V., and L. A. Soderblom (1982). Volcanic eruptions on Io: Implications for surface evolution and mass loss. In *Satellites of Jupiter* (David Morrison, ed.), pp. 634–646. Univ. of Arizona Press, Tucson.

Kieffer, S. W. (1982). Dynamics and thermodynamics of volcanic eruptions: Implications for the plumes of Io. In *Satellites of Jupiter* (D. Morrison, ed.), pp. 647–723. Univ. of Arizona Press, Tucson.

Lane, A. L., R. M. Nelson, and D. L. Matson (1981). Evidence for sulphur implantation in Europa's UV absorption band. *Nature* 292:38–39.

Lockwood, G. W., K. Lumme, and D. T. Thompson (1980). The recent photometric variability of Io. *Icarus* 44:240–248.

Lucchitta, B. K., and L. A. Soderblom (1982). The geology of Europa. In *Satellites of Jupiter* (D. Morrison, ed.), pp. 521–555. Univ. of Arizona Press, Tucson.

McEwen, A. S. (1986). Exogenic and endogenic albedo and color patterns on Europa. *Jour. Geophys. Res.* 91:8077–8097.

McEwen, A. S., D. L. Matson, T. V. Johnson, and L. A. Soderblom (1985). Volcanic hot spots on Io: Correlation with low-albedo calderas. *Jour. Geophys. Res.* 90B:12345–12379.

McEwen A. S., and L. A. Soderblom (1983). Two classes of volcanic plumes on Io. *Icarus* 55:191–217.

Morrison, D., and D. P. Cruikshank (1973). Thermal properties of the galilean satellites. *Icarus* 18:224–236.

Morrison, D., D. Pieri, J. Veverka, and T. V. Johnson (1979). Photometric evidence on long-term stability of albedo and colour markings on Io. *Nature* 280:753–755.

Newhall, X., E. M. Standish, Jr., and J. G. Williams (1983). DE 102: A numerically integrated ephemeris of the Moon and planets spanning forty-four centuries. *Astron. Astrophys.* 125:150–167.

Nash, D. B. (1987). Sulfur in vacuum: Sublimation effects on frozen melts, and applications to Io's surface and torus. *Icarus* 72:1–34.

Ockert, M. E., R. M. Nelson, A. L. Lane, and D. L. Matson (1987). Europa's ultraviolet absorption band (260 to 320 nm): Temporal and spatial evidence from IUE. *Icarus* 70:499–505.

Pearl, J. C. (1987). Io: Amaterasu Patera is hot. *Bull. Amer. Astr. Soc.* 17:691.

Pearl, J. C., and W. M. Sinton (1982). Hot spots of Io. In *Satellites of Jupiter* (David Morrison, ed.), pp. 724–755. Univ. of Arizona Press, Tucson.

Shoemaker, E. M., and R. F. Wolfe (1982). Cratering time scales for the galilean satellites. In *Satellites of Jupiter* (D. Morrison, ed.), pp. 277–339. Univ. of Arizona Press, Tucson.

Sinton, W. M. (1980). Io's 5-μm variability. *Astrophys. J.* 235:L49–L51.

Sinton, W. M., and C. Kaminski (1988). Infrared observations of eclipses of Io, its thermophysical parameters, and the thermal radiation of the Loki volcano and environs. *Icarus* in press.

Sinton, W. M., D. Lindwall, F. Cheigh, and W. C. Tittemore (1983). Io: The near-infrared monitoring program, 1979–1981. *Icarus* 54:133–157.

Smith, B. A., L. A. Soderblom, R. Beebe, J. Boyce, G. Briggs, M. Carr, S. A. Collins, A. F. Cook II, G. E. Danielson, M. E. Davies, G. E. Hunt, A. Ingersoll, T. V. Johnson, H. Masursky, J. McCauley, D. Morrison, T. Owen, C. Sagan, E. M. Shoemaker, R. Strom, V. E. Suomi, and J. Veverka (1979). The galilean satellites and Jupiter. Voyager 2 imaging science results. *Science* 206:927–950.

Squyres, S. W., R. T. Reynolds, P. M. Cassen, and S. J. Peale (1983). Liquid water and active resurfacing on Europa. *Nature* 301:225–226.

Tittemore, W. C., and W. M. Sinton (1987). Near-infrared photometry of the galilean satellites. *Icarus.*

Veverka, J., D. Simonelli, P. Thomas, D. Morrison, and T. V. Johnson (1981). Voyager search for posteclipse brightening on Io. *Icarus* 47:60–74.

Witteborn, F. C., J. D. Bregman, and J. B. Pollack (1979). Io: An intense brightening near 5 micrometers. *Science* 203:643–646.

4

Sulfur Lakes and Silicate Flows: Thermal Emission from Io's Hot Spots

Jonathan I. Lunine
Lunar and Planetary Laboratory, Tucson

Abstract

A series of models are constructed to simulate the brightness temperature and size of the Loki hot spots, at several infrared wavelengths, using kinetic temperature distributions for molten sulfur lakes and silicate flows. The physical models for the sulfur and silicate systems have been published; however, the simulations described in this chapter are new. We show that ground-based observations capable of resolving area and brightness temperature at two wavelengths are diagnostic of the physical mechanisms and materials radiating energy away from the Loki region. The mutual events data obtained in 1985 yield a brightness temperature and area for the Loki hot spot at 3.8 μm (Goguen et al., 1987). For the derived hot-spot area, the brightness temperature agrees with Carr's (1986) silicate-flow model or a sulfur-lake model with lake temperature elevated by 20 K since the Voyager flybys. However, the spot area itself is somewhat larger than either simulation would predict, and is smaller than that predicted by the simple three-temperature fit to the Voyager infrared interferometric spectrometer (IRIS) data of Pearl and Sinton (1982). The effect on the infrared spectrum of changes in thermal output of Loki is explored for the case of the sulfur-lake model.

INTRODUCTION

The crustal and surface mechanisms by which Io removes its large heat budget, and the importance of elemental sulfur, sulfur dioxide, and silicates on the surface remain outstanding issues raised by the Voyager encounters. These questions converge in our attempts to understand the largest hot-spot regions, particularly Loki Patera and the Loki plumes. One means of attacking these issues lies in constructing models of physical mechanisms by which silicates, sulfur, and sulfur dioxide could transfer heat from the interior to space, and simulations of the spectral and spatial distribution of the resulting infrared radiation that can be observed from earth or by spacecraft. Lunine and Stevenson (1985) presented a model of a convecting lake of elemental sulfur, heated from below by silicates, that transferred thermal energy by direct radiation and evaporation and subsequent recondensation of sulfur vapor. They synthesized spectra of such a lake, which for reasonable physical parameters could be successfully fitted to Voyager IRIS data of Loki and several other hot spots reduced by Pearl and Sinton (1982). Carr (1986) explored a model in which a silicate lava channel, active and inactive flows all contribute to the infrared signature of Loki. The emitted radiation for eruption rates between 3000 and 4000 $m^3 s^{-1}$ were compared to Voyager IRIS spectra.

Because the unresolved field-of-view of the IRIS instrument was larger than the size of the Loki region (Pearl and Sinton, 1982), independent information on the size of the hot-spot region was not available. Thus an additional constraint can be applied to the competing models if the area of the emitting region could be constrained. The mutual eclipse of the galilean satellites provided such an opportunity in 1985 (McEwen et al., 1986). The data collected included a 3.8 micron brightness temperature and area of excess emission for the Loki region (Goguen et al., 1987). The sulfur-lake and silicate-flow models each predict values for the Loki brightness temperature and area because they have specified areal distributions of kinetic temperatures.

This contribution describes the synthesis of brightness temperature-area curves at several wavelengths for sulfur lake and silicate-flow models of the Loki region as well as the Pearl and Sinton (1982) three-blackbody fit to the IRIS spectra, and compares the results to the 3.8 μm data. It also explores the effect of a change in the sulfur lake temperature on infrared emission. Although both the sulfur and silicate models are published, they have not previously been compared in a single study. The graphs of brightness temperature as a function of viewing area (expressed as equivalent radius) are new. The effect on the infrared emission of the (probably sulfur dioxide) Loki plumes seen in the Voyager images is not considered here. Their contribution to the emission deserves further study but as discussed in Lunine and Stevenson (1985), is (1) hard to quantify and (2) probably small (see also McEwen et al., 1987).

THE MODELS

Three-Temperature Fit

Pearl and Sinton (1982) fitted the IRIS spectra of Loki with three blackbodies, corresponding to temperatures and "equivalent" radii of 450 K, 21 km; 245 K and 121 km; and a background due to solar insolation (in this chapter all radiating areas are reported as equivalent radii). Because the IRIS instrument could not resolve the sources of emission within the Loki region, the spatial distributions are not known. We make the simplest assumption, that the sources are azimuthally symmetric with the highest temperature in the center.

Sulfur Lake

The molten sulfur lake model of Lunine and Stevenson (1985) is powered by an underlying layer of molten silicates, which causes convection and boiling in the molten sulfur. Heat transfer occurs by two mechanisms: (1) direct radiation off the lake at its surface temperature and (2) evaporation of sulfur, expansion of the sulfur vapor beyond the lake, and subsequent condensation of the vapor along the shore (fig. 1 of Lunine and Stevenson, 1985; reproduced in McEwen et al., 1987). Mechanism 2 actually contributes the bulk of the infrared radiation and is loosely identified with the "moderate" temperature component of the Pearl and Sinton (1982). The lake size is set equal to that of Pearl and Sinton (1982) high-temperature component; the lake temperature is tightly constrained to be above ~390 K (to produce the observed power output at Loki), and below ~480 K (above which molten silicates cannot supply sufficient power to the system). This narrow range arises from the sulfur vapor pressure dependence or tempreature, and happens to be just above the sulfur melting point. Additional adjustable parameters are the evaporative and sticking efficiencies for sulfur vapor and condensate, discussed in Lunine and Stevenson (1985).

The temperature profile away from the lake was calculated in Lunine and Stevenson (1985) using simple, cylindrically and spherically symmetric hydrodynamic models. Figure 5 of Lunine and Stevenson (1985) shows two alternative temperature profiles derived from the models. What follows uses the profile that drops inversely as the square root of radial distance from the lake; results of the exponential distribution are similar. We consider as a baseline a lake temperature of 425 K, and show in figure 28 the resulting spectrum compared to the IRIS data, which are represented here by the Pearl and Sinton (1982) three-blackbody fit.

Silicate Flows

Carr's (1986) model postulates exposed molten silicates as the source of the Loki infrared flux. The eruption is assumed to consist of a small area lava channel (highest temperature ~1300 K), an active front (highest temperature ~1200 K), and an inactive flow with temperature decreasing from ~400 K. The temperature-area distribution for the case considered here is given in Carr (1986, table 2). The resulting fit to the IRIS data suggests that the model overestimates the areal fraction at temperatures higher than 500 K and below 200 K (Carr, 1986), which Carr asserts could be corrected by adding sulfur melts.

EFFECT OF VARIABILITY ON THE SPECTRUM

Figure 28 plots the spectrum of the sulfur-lake model with a temperature elevated to 440 K. The consequent increase in vapor pressure results in an overall power increase of ~20–30 percent, and a change in the frequency distribution of the radiance. Carr (1986, figs. 7 and 8) illustrates the effect of changing eruption rates on the spectrum of the silicate-flow model. Earth-based infrared observations of Johnson et al. (1984) are consistent with an increase in power from the Loki region by 50 percent since the Voyager encounters, but may also be due to activity in other hot-spots regions such as Amaterasu Patera (Johnson et al., 1984; Pearl, 1987). Because of the possibility of variability in Loki, we consider two sulfur-lake models in the results presented below: the model fit to the Voyager IRIS data (lake temperature of 425 K), and an "enhanced" lake with a surface temperature of 440 K. The same can be done for the silicate-flow model of Carr; however, this report uses only his temperature distribution from Carr (1986, table 2).

CALCULATION OF AREA-BRIGHTNESS TEMPERATURE RELATION

In this section, we calculate the brightness temperature at several infrared wavelengths accessible to ground-based observers as a function of the areal fraction of the hot spot observed. By this we mean the following: For each of the three models discussed above [3-temperature fit (Pearl and Sinton, 1982), silicate flow

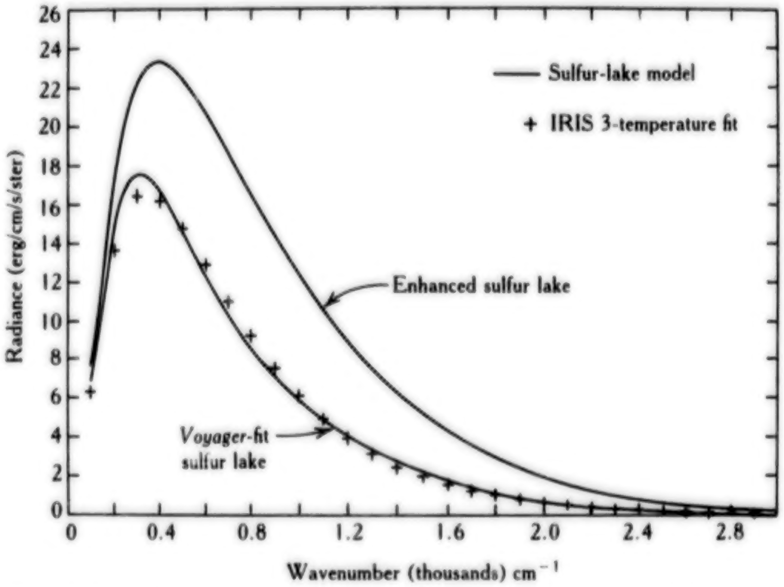

Figure 28. Radiance versus wavenumber for Voyager IRIS data (*crosses*), here represented by the three-temperature fit of Pearl and Sinton (1982), and the sulfur-lake model of Lunine and Stevenson (1985) (*solid line*). The lake temperature is set to 425 K. Also shown is a sulfur-lake model with lake temperature raised to 440 K.

(Carr, 1986), and sulfur lake (Lunine and Stevenson, 1985)], a distribution of kinetic temperatures on the surface has been constructed. If we make the plausible assumption that the hottest temperatures are restricted to the hot-spot center and decrease radially outward along Io's surface (this excludes multiple distributed sources), then at any given wavelength, the hot-spot boundary will be defined by those kinetic temperatures too low to contribute to the flux. Hence a source will appear bigger at longer wavelengths. Any observing technique using a single wavelength, such as occultation of Io by another galilean satellite, will see a certain

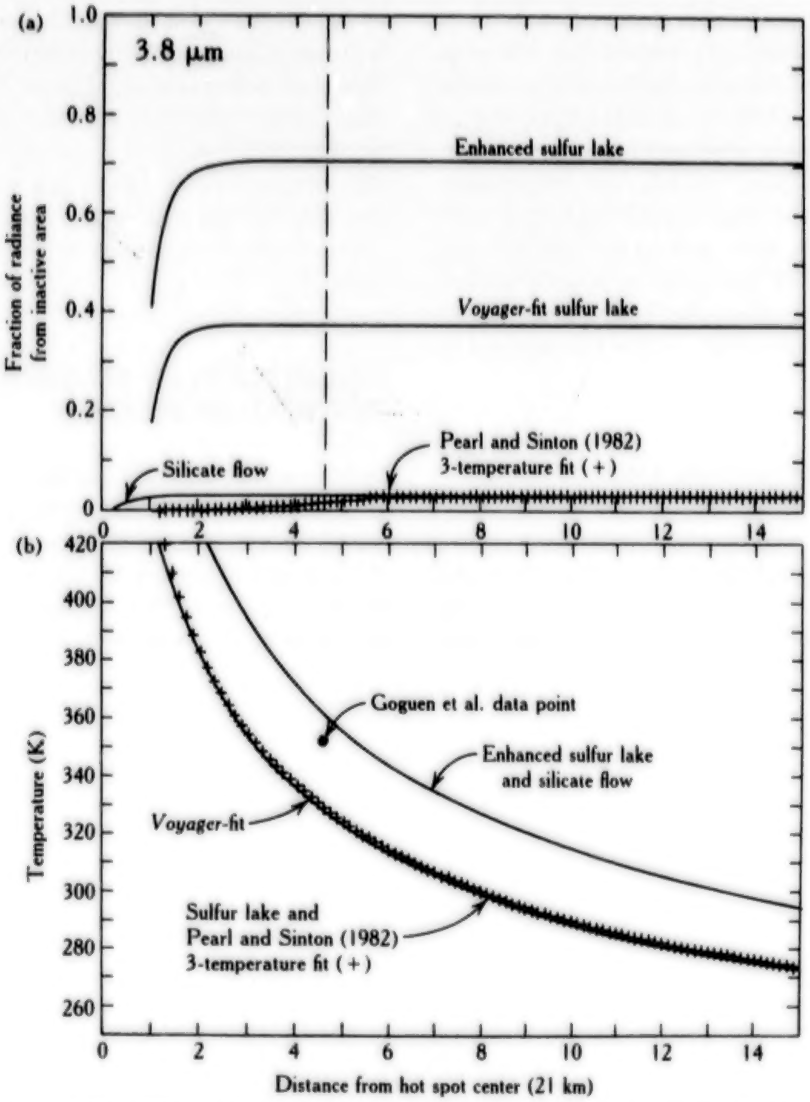

Figure 29. **(a)** Fraction of 3.8-μm thermal emission contributed by inactive area versus distance from the active center of the Loki hot spot. "Inactive" is defined as follows: for the Pearl and Sinton (1982) model, the 245 K component; for the Lunine and Stevenson (1985) model, the sulfur vapor condensation zone, and for the Carr (1986) model, the inactive flow. The predicted observable hot-spot size is given by the distance at which the curves became horizontal. The hot-spot size from the Goguen et al. (1987) data is shown as the *vertical dashed line* **(b)** The brightness temperature of Loki at 3.8-μm as a function of the area observed (expressed as distance from hot-spot center). Reading off the hot-spot size from **(a)**, one can find the predicted brightness temperature from **(b)** for the various models. The data point of Goguen et al. is shown. All distances are normalized to 21 km, the size of the Loki hot component of Pearl and Sinton (1982), and the molten sulfur lake of Lunine and Stevenson (1985).

hot-spot size and brightness temperature standing against the cooler whole disk thermalized sunlight emission. For this report we assume that the Loki hot spot is azimuthally symmetric. We can then calculate at any wavelength, for our model temperature distributions, the distance from the hot spot center beyond which significant flux is no longer contributed. We can also calculate the brightness temperature at that point; both of these quantities can be compared to observations. The brightness temperature is defined as

$$T_b = \frac{hc\nu}{k} \times \frac{1}{\ln\{1 + R^2(\int_0^R 2r\,dr/[\exp[hc\nu/kT(r)] - 1])^{-1}\}}$$

where h is Planck's constant; k is Boltzmann's constant; c the speed of light; ν = wavenumber; T_b = brightness temperature; $T(r)$ = kinetic temperature; a function of radial distance; and R is the equivalent radius of the observed hot-spot area (for each wavelength).

One may question the validity of the concentric circular geometry assumed for hot-spot models, particularly in the case of silicate flows. For multiple distributed sources (i.e., lakes), the assumption is also invalid. As we show below, insufficient data are available to constrain more complicated geometries than single sources.

Figures 29–31 display two types of plots: The first is fractional contribution of "inactive area" to the hot-spot radiation as a function of distance from the hot-spot

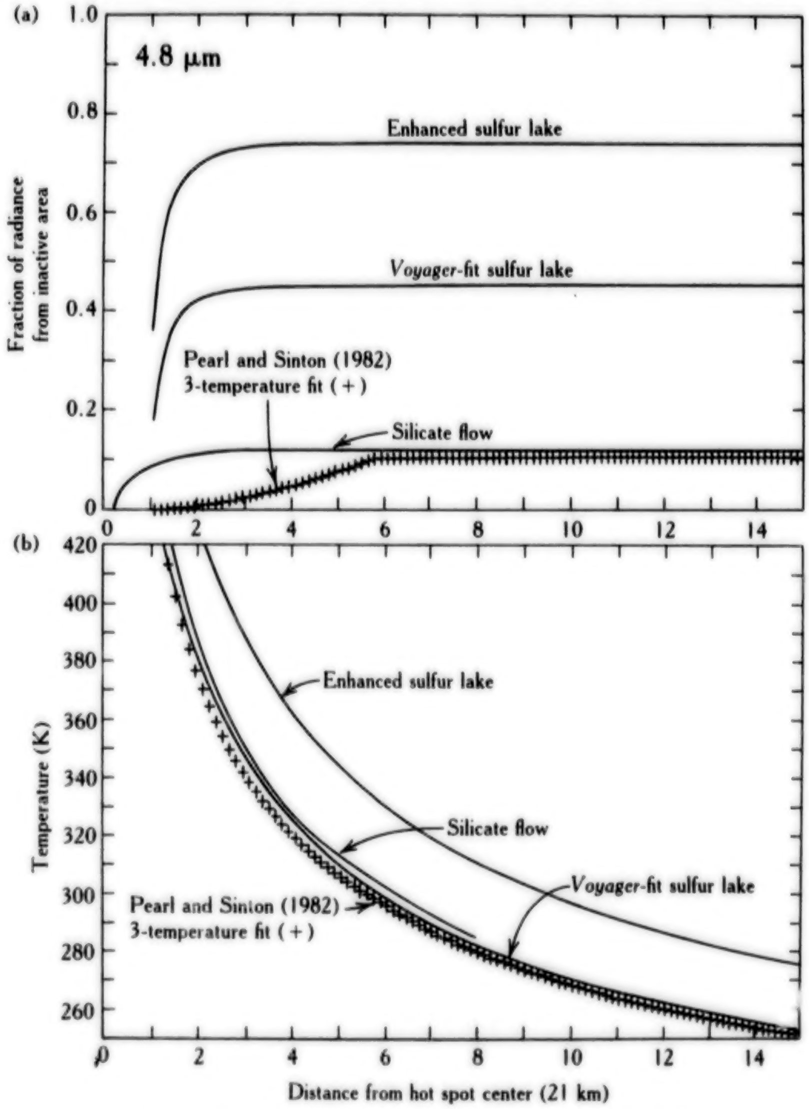

Figure 30. Same as figure 29, for 4.8-µm wavelength.

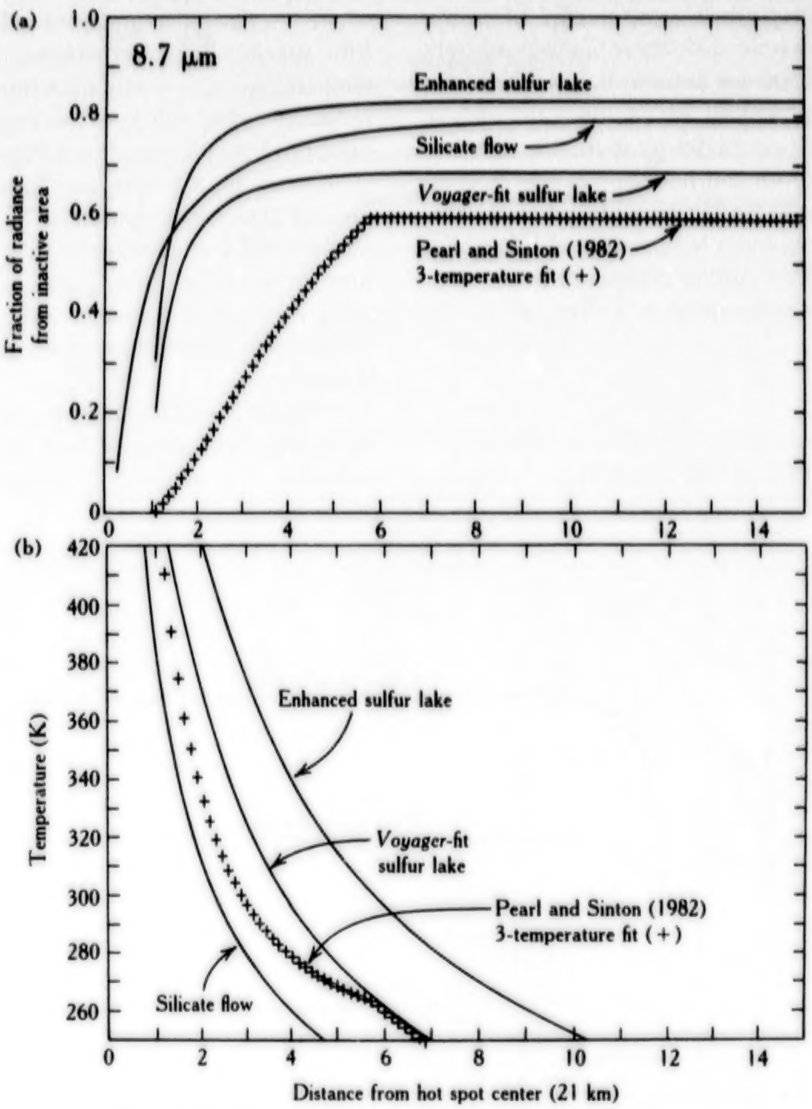

Figure 31. Same as figure 29, for 8.7-μm wavelength.

center. The inactive area, for the three-temperature model, is the 245 K component. For the sulfur lake, it is the region of sulfur vapor condensation, producing temperatures ranging from just below the sulfur freezing point to the thermalized solar ambient. For the silicate-flow model, it is the inactive flow. These figures show not only the differences in relative contribution of the cooler component, but also indicate the "size" of the hot spot for each wavelength considered (3.8, 4.8, 8.7 μm). For the three-temperature model, the size is trivially equal to 121 km, since beyond that the temperature jumps discontinuously to the thermalized solar ambient background. The other models predict different sized spots at different wavelengths, where the curves asymptotically approach horizontal, because of their smoothly radially decreasing temperature distributions.

The second set of figures plot brightness temperature versus radial distance from the hot-spot center, in other words, the brightness temperature of the area enclosed within a specified radius from center. The hot-spot size read off the first set of figures can then be used to determine the predicted brightness temperature at each wavelength.

The different results for each model reflect the different physical distributions of temperature. The Pearl and Sinton (1982) model has only two hot-spot temperatures, plus background. Relative to the Lunine and

Stevenson (1985) sulfur-lake model, the Carr (1986) silicate flow has more area at temperatures above 500 K and below 200 K. Finally, the enhanced sulfur-lake model has a higher radiance overall, and is weighted toward higher temperatures, than the Voyager-fit sulfur lake of Lunine and Stevenson (1985).

INTERPRETATION

Goguen et al. (1987) have presented the results of a mutual events observation at 3.8 microns. They find (preliminary values) a spot size for the Loki hot spot equivalent to 100 km radius, and a brightness temperature of 350 K. Plotted on figure 29, the Loki hot-spot size is intermediate to that predicted by the sulfur-lake model of Lunine and Stevenson (1985) and the three-temperature fit of Pearl and Sinton (1982). The silicate-flow model, having a dearth of temperatures between 200 and 500 K, predicts too small a spot size (but see below). The corresponding brightness temperature is bracketed well by the models, falling closest to the silicate-flow and enhanced sulfur-lake models.

The consistency in brightness temperature and spot size at 3.8 μm between data and models is expected to some extent because all models were fitted to the Voyager IRIS spectra of the Loki region. However, the IRIS field of view on Loki is significantly larger (equivalent radius over 300 km) than the hot-spot size derived from the Goguen et al. (1987) data and predicted by the models. This information is significant. It rules out models in which the Loki hot spot is due to small sources distributed all over the IRIS field of view. Of course, we cannot rule out sources distributed over an area equivalent to the observed 100 km radius, but the consistency between area and brightness temperature seen in the data and simple models suggests that the number of such sources may not be large.

Still, the sulfur-lake and silicate-flow models predict smaller spot sizes than indicated by 3.8-μm data, the sulfur lake by a factor of two and the silicate flows by a factor of four. We might expect multiple active silicate flows in a volcanic area, which would tend to increase the spot size. In the case of the sulfur-lake model, a somewhat flatter temperature (and hence density) distribution for the condensing sulfur vapor is required. (Of course, several sulfur lakes with intersecting sulfur vapor distributions are also possible.) Significantly, the Pearl and Sinton (1982) three-temperature fit predicts somewhat too large a spot size. Hence, the Loki hot spot probably has a kinetic temperature distribution that decreases with increasing distance from hot, active centers.

The results emphasize the importance of having data at several wavelengths. The 8.7-μm band appears particularly diagnostic of the various models, and having both 3.8- and 8.7-μm data could be sufficient to eliminate one or more models. The more complex the assumed geometry (nonazimuthal or distributed sources), the more wavelengths are required. Other factors, including magma composition, fluctuations in eruption rate, and magma outgassing, may complicate the analysis.

CONCLUSIONS

We have synthesized brightness temperatures and spot sizes for various models of the Loki Patera hot spot, including the three-blackbody fit to Voyager data of Pearl and Sinton (1982), the sulfur lake model of Lunine and Stevenson (1985), and the silicate flow model of Carr (1986). Although each model was designed to fit the IRIS data, they predict different spot sizes and brightness temperatures at infrared wavelengths observable in ground-based programs (such as mutual eclipse of galilean satellites). The 3.8-μm data for Loki from the 1985 mutual events is closely bracketed by several models, but none gives a satisfactory fit to spot size. Modifications to the simple physical models such as distributed sources may be required. Multifrequency observations during the next eclipse opportunity are critical to distinguishing between the models. The payoff of such an extensive Earth-based monitoring program is substantial: The Loki region contributes a significant fraction of Io's observed thermal output and understanding its morphology and surface composition will advance our understanding of that object's dynamic crustal processes.

ACKNOWLEDGMENTS

Enjoyable discussions with Al McEwen, Bob Howell and Larry Soderblom are gratefully acknowledged. I would particularly like to thank Jay Goguen for sharing the mutual events data prior to the conference. This work was supported by NASA grant NAGW-1039.

References

Carr, M. H. (1986). Silicate volcanism on Io. *J. Geophys. Res.* 91:3521–3532.

Goguen, J. D., D. Matson, W. Sinton, R. Howell, M. Dyck, G. Veeder, T. Johnson, A. Lane, R. Nelson, and R.

McLaren (1987). Multi-color IR photometry of occultations of Io by Ganymede and Callisto during 1985: Temperatures, areas and locations of major active hot spots and relative satellite astrometry. *Icarus*, submitted.

Johnson, T. V., D. Morrison, D. L. Matson, G. J. Veeder, R. H. Brown, and R. M. Nelson (1984). Volcanic hotspots on Io: Stability and longitudinal distribution. *Science* 226:134–137.

Lunine, J. I., and D. J. Stevenson. Physics and chemistry of sulfur lakes on Io. *Icarus* 64:345–367.

McEwen, A. S., L. A. Soderblom, D. L. Matson, T. V. Johnson, and J. I. Lunine (1985). Calculated occultation profiles of Io and the hot spots. *Geophys. Res. Lttrs.* 13:201–204.

McEwen, A. S., J. I. Lunine, and M. H. Carr (1989). *Dynamic geophysics of Io*. This volume.

Pearl, J. S., and W. M. Sinton (1982). Hot spots of Io. In *Satellites of Jupiter* (D. Morrison, ed.), pp. 724–755. Univ. of Arizona Press, Tucson.

Pearl, J. S. (1987). Io: Amaterasu Patera is hot. *J. Geophys. Res.*, in press.

5

Search for Temperature Effects in the Photometry of the Ionian Dayside

Damon P. Simonelli
NASA/Ames Research Center, Moffett Field
Joseph Veverka
Cornell University, Ithaca

Possible temperature-dependent effects in the photometry of Io, due to the temperature shift exhibited by the absorption shoulder in the spectrum of ordinary sulfur (S_8) and/or the transient condensation-sublimation of atmospheric SO_2, should, if occurring, be detected in (1) eclipse observations (as "posteclipse brightening"), (2) observations of the Jupiter-lit nightside of Io, and (3) observations of the ionian dayside under ordinary diurnal and latitudinal temperature variations (Veverka et al., 1982). Voyager images, and recent Earth-based observations, show no evidence of effect 1 (Veverka et al., 1981; Hammel et al., 1985), and Voyager data are inconclusive regarding effect 2 (Buratti and Terrile, 1985). Effect 3 has not been examined to date because this requires the difficult process of separating temperature effects from "ordinary" photometric effects such as limb darkening. Mechanisms that may change any sulfur present on Io to allotropes other than S_8 (Nash, 1986; Steudel et al., 1986), suggestions of the extreme tenuousness of the ionian atmosphere (e.g., Matson and Nash, 1983), and the lack of posteclipse brightening all weigh indirectly against the presence of dayside temperature effects. However, recent work on determining the photometric behavior of ionian materials with the Hapke function (Simonelli and Veverka, 1986c) now makes *direct* investigation of possibility 3 feasible for the first time.

Due to the location of the S_8 absorption shoulder, and the contrast between any transient SO_2 frost and typical Io surface materials, *either* temperature-dependent process would produce the following effect: images taken in the Voyager violet filter ($\lambda \approx 0.42$ µm) will show, above and beyond ordinary limb-darkening effects, a brightening of Io's surface on going from the warm subsolar point to the colder areas near the terminator—and this brightening will *not* occur in the Voyager orange filter ($\lambda \approx 0.59$ µm). For example, the temperature dependence of the spectrum of S_8 would lead to a brightening in the violet filter by a factor of ≈1.1 on going from 0° to 60° away from the subsolar point (e.g., Veverka et al., 1981). Given the difficulties inherent in working with regions of "similar" photo-

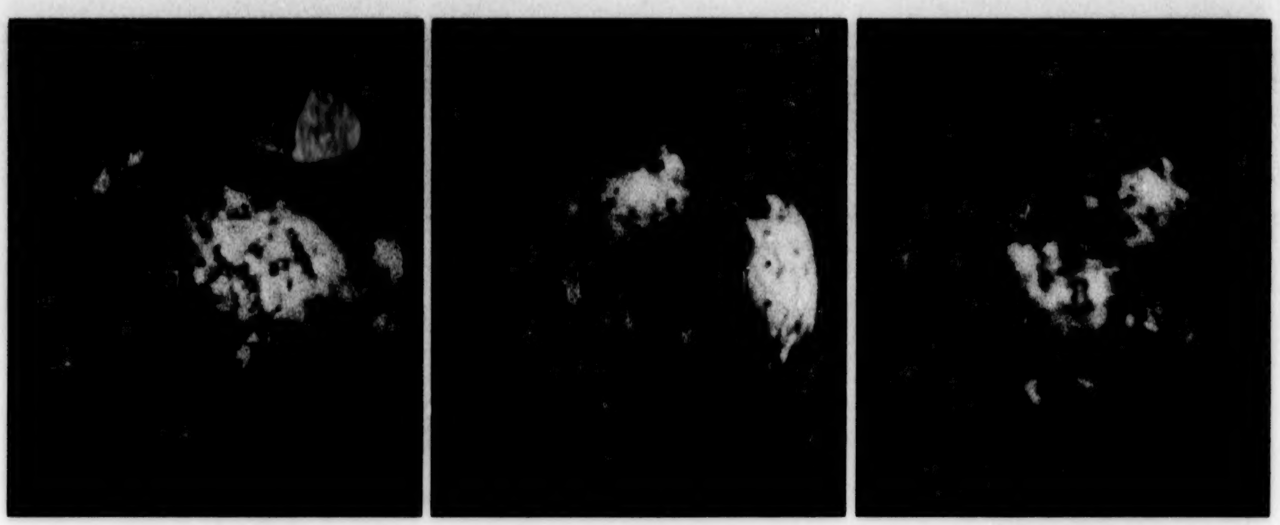

Figure 32. Violet-filter images from left to right, the FDS 16345, FDS 16351, and FDS 16360 Voyager 1 imaging sequences, illustrating the locations of data-taking scans along Media Regio. All scans track along the ionian equator; north is up in all three images.

metric behavior on a surface as heterogeneous as that of Io (Simonelli and Veverka, 1986a), the only viable way to search for such a temperature effect is to observe the *same* region on the satellite at different times of day. We work with images of the equatorial plain Media Regio; this is the largest expanse on Io of so-called average material, the color class from Simonelli and Veverka (1986a, b, c), whose spectrum is closest to that of ordinary S_8-dominated sulfur. In each of three Voyager imaging sequences, showing Media Regio toward the sunrise terminator, subsolar region, and sunset terminator respectively (fig. 32), we (1) take an equatorial scan along Media Regio of reflectance I/F in both the violet and orange filters and (2) make a prediction of the ordinary limb-darkening behavior these reflectance scans *should* show, using the Hapke photometric function (Hapke, 1981, 1984) with Hapke parameters that have been previously derived for mean average material (Simonelli and Veverka, 1986c). The ratio between observed and Hapke-predicted reflectance along a scan shows peaks and valleys that occur at the same points in Media Regio from one imaging sequence to the next; this indicates the presence of *albedo variations* along Media Regio. Finally, the noontime imaging sequence should be free of temperature-related effects; thus the ratio between observed and Hapke-predicted reflectances in this sequence can be used to "correct" the Hapke-predicted reflectances in the near-terminator imaging sequences for albedo variations. Scans from one of the near-terminator imaging sequences showing the ratio between the observed reflectance and "albedo-corrected" Hapke prediction are displayed in figures 33a and 33b.

When using the nominal average-material Hapke parameters from Simonelli and Veverka (1986)—including the average macroscopic roughness for Io as a whole as derived in that reference (mean slope angle $\bar{\theta} = 25°$)—an excess brightness of about the predicted magnitude is seen toward both the sunrise and sunset terminators and in both the violet *and* orange filters. An excess terminator brightness in *both* filters cannot be understood in terms of S_8 or SO_2 effects; such a result must indicate a difficulty in accurately modeling the ordinary limb-darkening behavior of average material close to the terminator. Of the various free parameters in Hapke's function, the parameter that provides the most ready explanation for the observed result is the macroscopic surface roughness. Scans of the ratio between observed reflectance and albedo-corrected Hapke reflectance, produced for different assumptions of the roughness parameter $\bar{\theta}$, indicate that the excess terminator brightness seen in the orange filter is removed by increasing the slope angle to $\bar{\theta} \approx 35$–$40°$, whereas the excess brightness in the violet is not removed until $\bar{\theta} \approx 50$–$60°$ (figs. 33a and 33b). Recent efforts at modeling the globally averaged limb darkening of Io (McEwen, 1987, and the present authors) suggest that the macroscopic roughness of this satellite may be closer to $\bar{\theta} = 30°$ than $\bar{\theta} = 25°$, with $\bar{\theta} = 35°$ still within estimated error bars; a roughness as high as $\bar{\theta} = 50$–$60°$ is *not* physically reasonable, however. Therefore, if one assumes that Media Regio has the

ORIGINAL PAGE
BLACK AND WHITE PHOTOGRAPH

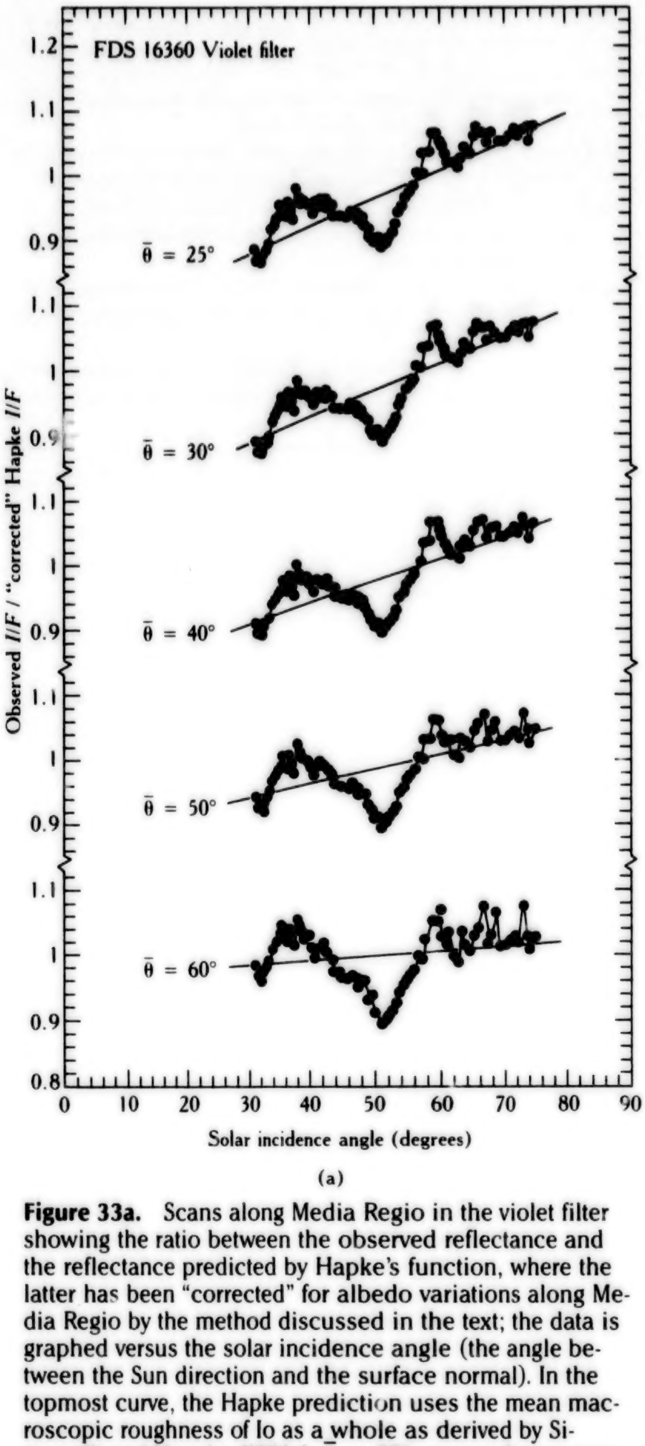

(a)

Figure 33a. Scans along Media Regio in the violet filter showing the ratio between the observed reflectance and the reflectance predicted by Hapke's function, where the latter has been "corrected" for albedo variations along Media Regio by the method discussed in the text; the data is graphed versus the solar incidence angle (the angle between the Sun direction and the surface normal). In the topmost curve, the Hapke prediction uses the mean macroscopic roughness of Io as a whole as derived by Simonelli and Veverka (1986c), $\bar{\theta} = 25°$; succeeding curves show the effects of increasing the value of $\bar{\theta}$. In all curves, the free parameters in Hapke's function other than $\bar{\theta}$ are held constant at values derived for average material in the violet filter (Simonelli and Veverka, 1986c). The displayed data are from the imaging sequence that places Media Regio toward the sunset terminator, FDS 16360 (see fig. 32); results for the sunrise imaging sequence, FDS 16345, are qualitatively similar.

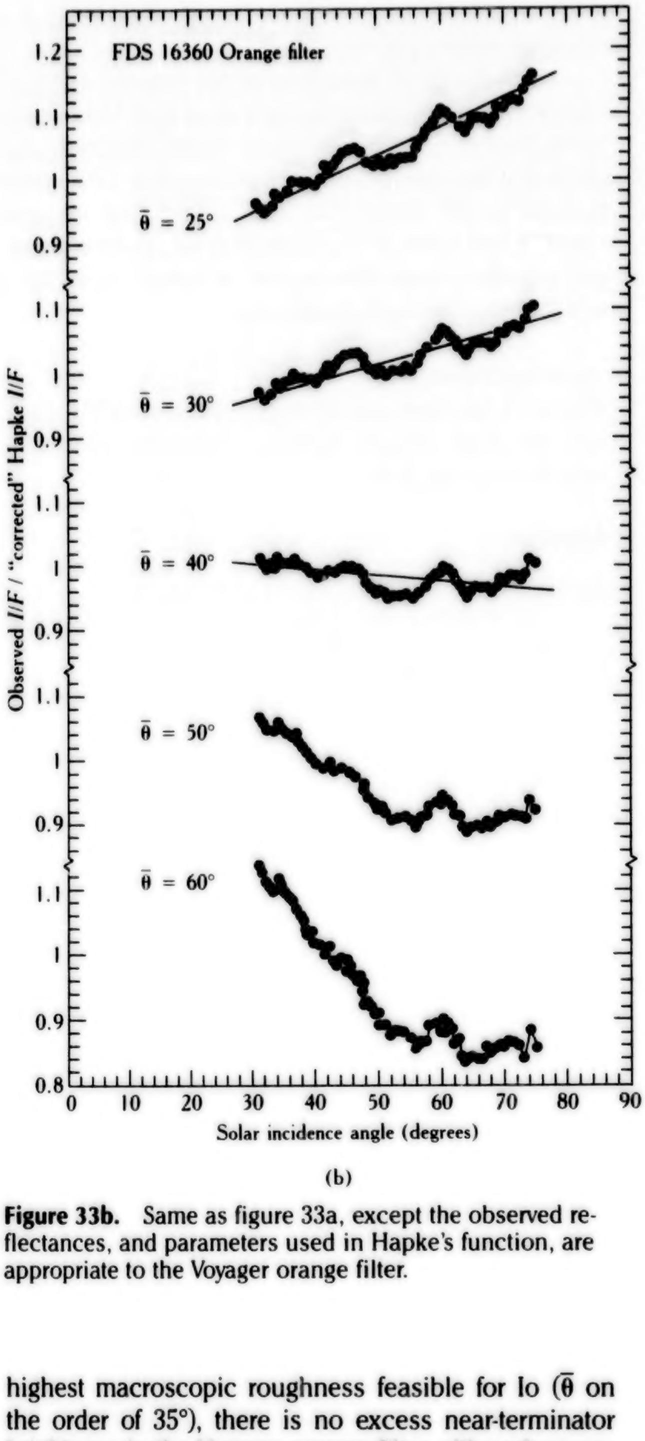

(b)

Figure 33b. Same as figure 33a, except the observed reflectances, and parameters used in Hapke's function, are appropriate to the Voyager orange filter.

highest macroscopic roughness feasible for Io ($\bar{\theta}$ on the order of 35°), there is no excess near-terminator brightness in the Voyager orange filter, although an excess brightness *does* remain in the violet filter.

If further analysis supports the presence of an excess near-terminator brightness in the violet filter only, the most likely explanation is transient condensation of atmospheric SO_2. In order to be consistent with the lack of posteclipse brightening, such condensation must occur in limited, localized areas, possibly those areas in which SO_2 vents are locally thickening the normally tenuous atmosphere.

Since the original writing of this chapter, reevaluation of Io's disk-integrated phase curve by P. Helfenstein using the latest, 1986 version of Hapke's function suggests that the macroscopic roughness $\bar{\theta}$ of the satellite is actually <25° rather than >25°. If borne out, this new result would make it less likely that excess limb brightening in the orange filter can be "removed" by invoking a higher macroscopic roughness.

ACKNOWLEDGMENTS
This work has been supported by NASA grant NSG 7156, and the lead author's National Research Council research associateship.

References

Buratti, B., and R. J. Terrile (1985). Photometric analysis of Jupiter-illuminated images of Io. In *NASA Technical Memorandum* 87563:411–412.

Hammel, H. B., J. D. Goguen, W. M. Sinton, and D. P. Cruikshank (1985). Observational tests for sulfur allotropes on Io. *Icarus* 64:125–132.

Hapke, B. (1981). Bidirectional reflectance spectroscopy. 1. Theory. *J. Geophys. Res.* 86:3039–3054.

Hapke, B. (1984). Bidirectional reflectance spectroscopy. 3. Correction for macroscopic roughness. *Icarus* 59:41–59.

Matson, D. L., and D. B. Nash (1983). Io's atmosphere: Pressure control by regolith cold trapping and surface venting. *J. Geophys. Res.* 88:4771–4783.

McEwen, A. S. (1987). Photometric functions for photoclinometry and other applications. Submitted to *Icarus*.

Nash, D. B. (1986). Sulfur in vacuum: Sublimation effects on frozen melts, and applications to Io's surface and torus. Submitted to *Icarus*.

Simonelli, D. P., and J. Veverka (1986a). Disk-resolved photometry of Io. I. Near-opposition limb darkening. *Icarus* 66:403–427.

Simonelli, D. P., and J. Veverka (1986b). Disk-resolved photometry of Io. II. Opposition surges and normal reflectances. *Icarus* 66:428–454.

Simonelli, D. P., and J. Veverka (1986c). Phase curves of materials on Io: Interpretation in terms of Hapke's function. *Icarus* 68:503–521.

Steudel, R., G. Holdt, and A. T. Young (1986). On the colors of Jupiter's satellite Io: Irradiation of solid sulfur at 77K. *J. Geophys. Res.* 91:4971–4977.

Veverka, J., J. Gradie, P. Thomas, and S. Ostro (1982). How much S_8 (cyclooctasulfur) is there on the surface of Io? *Lunar and Planet. Sci.* 13:823–824.

Veverka, J., D. Simonelli, P. Thomas, D. Morrison, and T. V. Johnson (1981). Voyager search for posteclipse brightening on Io. *Icarus* 47:60–74.

6

Io's Atmosphere and Neutral Clouds

Nicholas M. Schneider
University of Arizona, Tucson
William H. Smyth
AER, Incorporated, Cambridge
Melissa A. McGrath
University of Virginia, Charlottesville

Abstract

Much of our basic understanding of the Io atmosphere, neutral clouds, and plasma torus has come from the study of variations in their morphology, density, and energy distribution. This chapter discusses the time variabilities inherent in the physical processes that govern the behavior of the system, and their relative importance in proposed models of the Io atmosphere. Observations are discussed and compared to model predictions, and new constraints are placed on these models. The variations are then examined in the context of the complete neutral-cloud/plasma torus system, and the unsolved problem of overall system stability is discussed. Several possible mechanisms responsible for the stability are described and evaluated. Future observations of time-variable phenomena show great promise for probing the nature of the atmosphere and its complex interaction with the plasma torus.

OVERVIEW OF THE SYSTEM

This review emphasizes time variabilities of the neutral species in Io's vicinity at the expense of a discussion of our best understanding of the underlying steady-state behavior. The major issues concerning the "average" state of the atmosphere and extended neutral clouds are well reviewed in Brown et al. (1983), Kumar and Hunten (1982), Nash et al. (1986), and Johnson and Matson (1989). Time-variable phenomena have proven to be powerful tools for determining the nature of the atmosphere and neutral clouds, but considerable potential remains untapped.

Nomenclature and Definitions

Figure 34 defines the terminology used in this chapter. The term *lower atmosphere* will refer to atoms and molecules gravitationally bound to Io and confined to an altitude less than or comparable to an Io radius ($R_{\text{Io}} = 1815$ km). It is generally agreed that the dominant atmospheric constituent near the surface is SO_2, but the value of the surface pressure is currently under heated debate (cf., Johnson and Matson, 1989, for a summary). If the column abundance exceeds $\sim(3 \times 10^{14})$ molecules per square centimeter, the atmosphere is considered collisionally thick. The altitude of the transition between the collisionally thick and thin regimes is called the exobase, and the collisionless region, called the corona or exosphere, extends out to $\sim 10^4$ km. Jupiter's gravity dominates outside this radius; atoms and molecules beyond this distance are not considered part of the atmosphere but are considered part of the neutral clouds.

The neutral clouds are huge in comparison, extending out hundreds of thousands of kilometers into the toroidal volume surrounding Io's orbit. To date four neutral gas clouds, as summarized in table 5, have been detected by remote observations of cloud emission lines. A fifth cloud of SO_2 (or S_2) has been proposed as a result of the in situ detection of SO_2^+ (or S_2^+) in the plasma torus. Sodium and potassium are present only in trace amounts but are most readily visible (see table 5). Atoms and molecules in the neutral clouds would form complete gas tori around Jupiter were it not for their finite lifetimes in the plasma torus, which limit their morphologies to partial tori of varying angular extent. The sodium cloud with a short lifetime against electron impact ionization fills only a small portion of the orbital circumference (fig. 34). This short lifetime makes sodium quite responsive to changes in plasma conditions, and the study of changes in the sodium cloud has been instrumental in our remote sensing of the jovian magnetosphere.

Despite their different spatial scales, the neutral clouds are intimately linked to the Io atmosphere through the corotating plasma torus. (See Strobel and Bagenal, this volume, for further discussion of the plasma torus.) The neutral clouds are simultaneously created and destroyed by the torus through a variety of spatially and temporally varying processes. The careful examination of time variabilities is an underutilized tool for probing the interconnection of the surface, atmosphere, corona, clouds, and plasma.

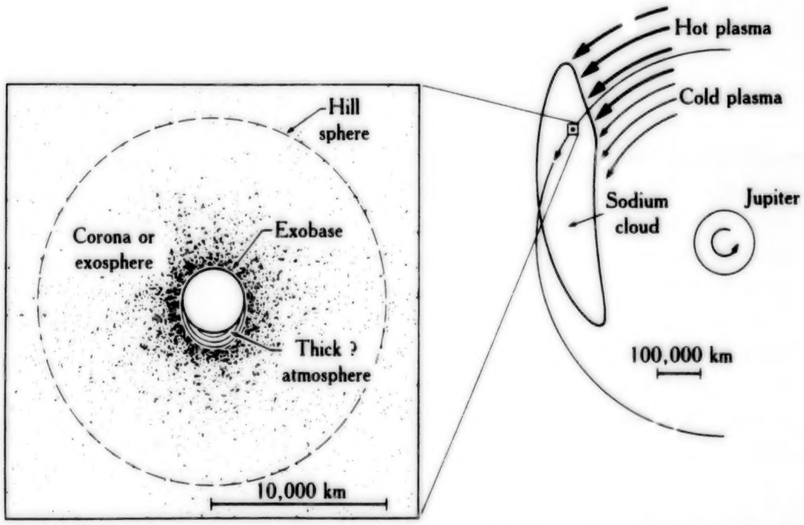

Figure 34. Simplified view of the atmosphere and sodium cloud. The left half illustrates Io's immediate vicinity. The contours schematically show the thick atmosphere, concentrated in this example on the sunlit hemisphere. The thin corona (or exosphere) is represented by the *dots*. The *dashed line* shows the location of the Hill sphere, the effective limit of Io's gravity. The scale of the right half of the figure is reduced by a factor of 40 to show the neutral sodium cloud outline (adapted from Smyth and McElroy, 1978). The corotating plasma, indicated by the *arrows*, travels at 75 km/s, overtaking the neutrals that orbit Jupiter at 17 km/s. The cloud lies preferentially inside Io's orbit because the plasma is cooler there and less able to ionize the sodium. Inside Io's orbit, the cloud extends forward, but not backward, because sodium atoms closer to Jupiter travel faster than Io.

Table 5. Io's Neutral Gas Clouds

	First detection		Cloud emission		
Neutral cloud	**Date**	**Observer**	**Wavelength (Å)**	**Intensity (Rayleighs)**	**Excitation mechanisms**
Sodium	1972	Brown (1974)	5890, 5896	10^3–10^4	Resonance scattering
Potassium	1975	Trafton (1975) Trauger et al. (1976)	7665, 7699	15–300	Resonance scattering
Oxygen	1980	Brown (1981)	6300	~8	Electron impact
Sulfur	1981	Durrance et al. (1983)	1304, 1425	~3	Electron impact

Important Neutral Sources and Sinks

We first discuss the processes responsible for creating and destroying the atmosphere and clouds, and determine their characteristic time scales and amplitudes of variability. Figure 35 shows the important processes schematically. Volcanoes are the initial source of the atmosphere, depositing ejecta on the surface and venting gas directly into the atmosphere. The SO_2 frost sublimates, also supplying the atmosphere. If the atmosphere is collisionally thin, plasma ions may impact the surface and liberate some of the surface atoms and molecules through sputtering. If the atmosphere is collisionally thick, corotating the plasma ions will interact with the gas through a collisional cascade process, transferring some of the energy and momentum of the ions to the neutrals. A fraction of the energized neutrals will escape directly into the distant neutral clouds, and the remainder will create a corona. The neutrals in the collisionally thin regions will be subjected to electron impact ionization, elastic collisions, and charge exchange. All the processes listed are time variable, each with a different amplitude and time scale. Table 6 summarizes the variabilities, and the processes are discussed individually below.

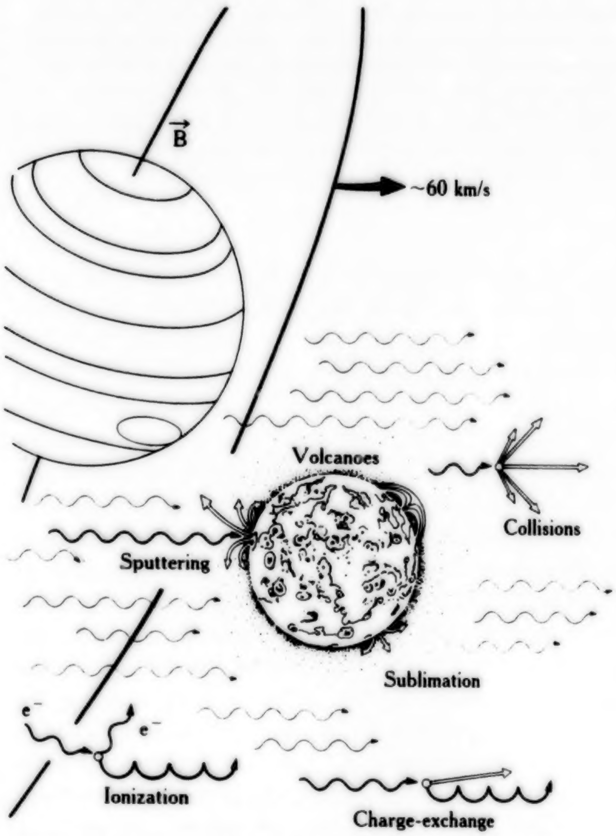

Figure 35. Sources and losses of neutrals at Io. Io is shown embedded in the flow of the corotating plasma. Ions, carried by magnetic field lines, are represented by *wiggly arrows*. Neutrals are shown as *outlined arrows*. The individual processes are discussed in the text.

Plasma Related Processes Ionization, elastic collision, charge exchange, and sputtering rates will all vary systematically with the flux of incident plasma. The plasma density and temperature in the torus is spatially nonuniform, so the flux will depend on Io's position in the magnetosphere. The plasma is confined within ~ ±1 R_J (1 R_J = 71,400 km) of the centrifugal equator, which is tilted 7° with respect to Io's roughly circular orbit. The plasma corotates with Jupiter, making one revolution every ~10 hours. Io orbits Jupiter in ~42.5 hours, which thereby creates a ~13 hour period of the

Table 6. Variability of Important Processes

Process	**Variation amplitude**	**Time scale**
Ionization	2–20	6.5–42 hr
Sputtering	2	6.5–42 hr
Collisions and charge exchange	2–20	6.5–42 hr
Sublimation	large	42 hr
Volcanoes	large	days–years

plasma with respect to Io. The tilt of the plasma plane is the primary cause of systematic variations: Io appears to oscillate in magnetic latitude by $\pm 0.7\, R_J$, with a period of about 13 hours. In addition to these oscillatory effects, more complex but smaller motions of the plasma torus relative to Io's orbit are produced by the offset of the magnetic dipole from the center of Jupiter and the presence of an east-west electric field in the planetary magnetosphere.

The rates for ionization, elastic collisions, and charge exchange are straightforward to calculate in the low-density regions far from Io. The plasma properties will be essentially unchanged by interactions with the atoms and molecules, and plasma-related reaction rates for these neutral gases will vary linearly and instantaneously with the time-varying incident plasma flux. Near Io, however, the incident flux and its effects on the corona and atmosphere may be substantially altered, both by the presence of Io's solid body (Wolf-Gladrow et al., 1987; Barnett, 1986) and by interaction with gas in the extended atmosphere (e.g., Sittler and Strobel, 1987). Although evidence of both types of plasma alteration have been observed, it is difficult to estimate the magnitude of these effects near Io. For the moment we can only say that the situation very near Io is significantly more complicated than elsewhere in the neutral clouds.

We consider first the case of electron impact ionization in the neutral clouds. In this reaction, a torus electron ionizes an atom and thereby removes it from the neutral cloud. The fresh ion is accelerated to corotation velocity with a large gyration velocity, adding mass and energy to the plasma. The lifetime against electron impact ionization depends on the electron density and temperature, and will be shortest when Io passes through the centrifugal equator. Taking the case of sodium, figure 36 shows how the spatial structure of the ionization rate maps into a temporal variation. For sodium near Io's position, the lifetime against ionization varies from ~1.3 hours on the plasma equator to ~4 hours when farthest from the equator. Note that the minimum lifetime occurs twice during a full cycle (ignoring magnetic longitude varations), so the effective period is 6.5 hours if magnetic longitude variations are unimportant. For sodium on trajectories far north or south of Io, the amplitude of variation is much larger. Only one minimum lifetime occurs each cycle, so the period there is 13 hours. Atoms on such out-of-plane orbits move through regions of different ionization lifetime, so more detailed calculations are required to determine the magnitude of the variation.

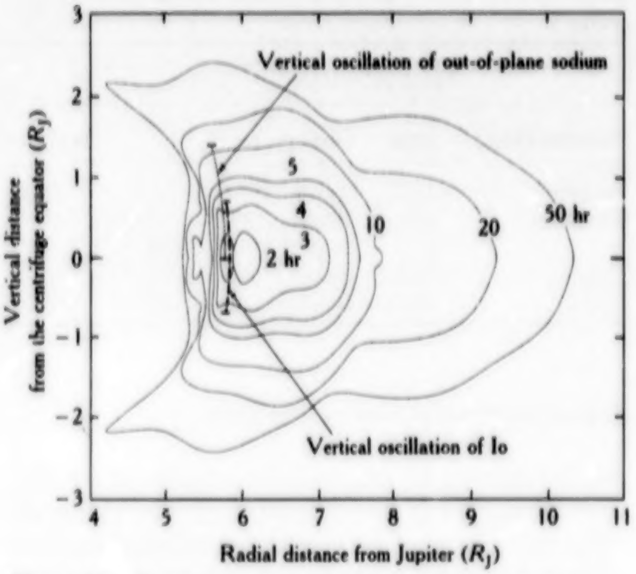

Figure 36. Spatial variation of sodium lifetime against electron impact ionization. Contour labels indicate the lifetime in hours. The rapid rise in lifetime inside about $5.7\, R_J$ is due to a sudden drop in electron temperature. Io's motion, using the tilted dipole approximation to Jupiter's magnetic field, is indicated by the *dashed line*. The *dotted line* shows the range of lifetimes experienced by sodium already out of Io's orbital plane. When the offset of the tilted dipole is included, the lines open up into slightly tilted ovals. When the east-west electric field is incorporated, the contour values also change as a function of orbital longitude. Adapted from Smyth and Combi (1988a).

Io's motion through the plasma is actually more complicated than indicated by the tilted dipole approximation, further modulating the density and temperature of the plasma impacting Io. The axis of the dipole is offset by $\sim 0.13\, R_J$ from Jupiter's rotation axis, so in the magnetic coordinate system Io appears to move inward and outward in addition to its north-south motion. Furthermore, there appears to be an electric field across the entire jovian magnetosphere fixed in Sun-centered coordinates (Barbosa and Kivelson, 1983; Ip and Goertz, 1983; Goertz and Ip, 1984). This field effectively pulls the plasma torus at Io's orbit $\sim 0.15\, R_J$ further away from Jupiter on the east (as seen from the Earth), and toward Jupiter on the west. As a result, the plasma at Io's orbit is on average denser and hotter in the west than in the east. Smyth and Combi (1988a) have constructed a detailed model of the sodium cloud that incorporates these epicyclic offsets. All of these effects operate simultaneously, so variabilities with periods of 6.5, 13, and 42 hours are superposed in the rates of plasma-related processes.

Table 7. Atomic Lifetimes for Plasma-Related Reactions[a]

Atom	Electron impact ionization (hours)	Charge exchange[b] (hours)	Elastic collision[c] (hours)
Sodium	1.3	22	16
Potassium	1.1	11	24
Oxygen	55	18	13
Sulfur	10	13	21

[a] All rates calculated in the centrifugal equator at Io's radial distance. [b] Based on cross sections from Johnson and Strobel (1982). [c] Based on Thomas-Fermi momentum-transfer cross sections with minimum velocity transfer of 2 km/s. The cross section increases for smaller minimum transfers, but a better knowledge of the interaction potential between these ions and atoms is required before more detailed calculations are warranted.

Next we consider elastic collisions and charge-exchange reactions, whose rates depend primarily on the plasma density. In elastic collisions, the incident ions impact the slow neutrals in collisions similar to billiard-ball-type knock-on collisions. Glancing blows are most likely, sending the neutrals off nearly perpendicular to the plasma flow at low velocities. In the less probable head-on collisions, the neutrals are ejected more in the forward direction and at much higher velocities. In charge-exchange reactions, a corotating ion strips an electron from a neutral during a glancing collision, thus becoming a very fast neutral. Forward-directed escaping atoms are the most likely product. Because of the motion of the plasma torus relative to the satellite orbital plane, rates for elastic collisions and charge exchange should show time variations comparable to those of electron impact ionization. The primary difference lies in the fact that ionization acts as a sink of slow neutrals in the clouds, whereas elastic collisions and charge-exchange reactions act primarily as sources of fast neutrals. The relative importance of these processes and electron impact ionizations (based on undisturbed plasma properties at Io's orbit) for each neutral constituent are summarized in table 7. The lifetime of neutrals for these reactions is different for each species. For sodium and potassium, electron impact ionization dominates charge exchange and elastic collisions by order of magnitude, whereas for sulfur and oxygen the three processes have more comparable values. These calculations apply only to plasma properties on the centrifugal equator at Io's distance; the lifetimes vary significantly both radially and normal to the equator.

Sputtering occurs from a collisionally thick target, either Io's surface or the atmospheric exobase. In the simplest analysis, the rate of sputter removal from the target is *SR = incident ion flux × yield per ion × effective area sputtered.* Relative sputtering rates for various conditions on Io are summarized in table 8 and explained below. The single biggest factor controlling the sputter removal rate is the presence or absence of a thick atmosphere on Io. The rate varies roughly as the cube of the exobase radius: two powers for the geometrical increase in the projected size, and one power for the lower gravitational binding energy. Surface sputtering is considerably less efficient since the molecules are more tightly bound in a solid; the tabulated value assumes the entire surface is covered by SO_2, the most easily sputtered Io surface component. For some constituents, especially SO_2, the sputtering rate is a very strong function of temperature (Lanzerotti et al., 1982). The sputtering rate, like the elastic collision rate, depends linearly on the ion density.

The surface sputtering yield also depends on the mass and energy of the incident ions, and the composition of the surface. More massive and energetic ions produce a higher yield, but the flux of such ions on Io may be too low to contribute appreciably to the sputtering rate (Lanzerotti et al., 1982). SO_2 frost is sputtered more efficiently than sulfur, and smooth surfaces allow easier escape than do porous surfaces. Sputtering from

Table 8. Relative SO_2 Supply Rates for Various Atmospheric and Surface Conditions[a]

Exobase at 1800 km altitude[b] (radius = 2 R_{Io})	8.0
Exobase at 900 km altitude[b] (radius = 1.5 R_{Io})	3.4
Exobase at 0 km altitude (radius = 1 R_{Io})	1
Dayside surface only[c] (110 K)	0.22
Nightside surface only[c] (90 K)	0.11

[a] From McGrath and Johnson (1987) and Lanzerotti et al. (1982). [b] Spherically symmetric atmosphere. [c] Maximum possible rate, using 100 percent SO_2 surface coverage and ignoring surface porosity effects.

warmer, dayside surfaces is more efficient than from the nightside; the yield from Io's hot spots is also probably quite high but has not been estimated quantitatively.

Atmospheric sputtering may differ significantly from surface sputtering in a qualitative sense. The atmosphere absorbs an immense momentum flux from the plasma, and only a small fraction goes to the atoms directly sputtered out. The remainder of the input, called ion heating, may be responsible for further ejection from the atmosphere, which may dominate the escape. This process is not well understood, and it may not be subject to the same variations assigned to standard sputtering in the subsequent paragraph. Furthermore, thick atmospheres (and their concomitant ionospheres) are likely to generate a substantial deflection of the plasma flow. This too will strongly modify the atmospheric sputtering process, and the following discussion may not be appropriate. Progress on these issues is relatively recent, and a full analysis of their effects on time variability is premature.

Variabilities in the sputtering rate will be caused primarily by changes in the incident flux, the exobase level, and the temperature of the target. The incident flux for sputtering is subject to exactly the same variations as the collision and charge-exchange rate, and therefore should give rise to variations with periods from 6.5 to 42 hours. Diurnal cycles may affect both the surface temperature and the exobase level, leading to significant variability at the 42-hour orbital period.

One caution should be stressed pertaining to sodium: its physical and chemical state on the surface and in the atmosphere is completely unknown. Unlike SO_2, quantitative measures of its supply rate (akin to table 8) are unavailable, and it is not even clear whether an increase in the exobase level will enhance or decrease the sodium supply rate. If sodium is released only by surface sputtering, a high exobase will diminish the sputtered sodium; if sodium is always present in the atmosphere at a fixed mixing ratio, a high exobase level will lead to an increase in sodium supply. In either case, the sodium supply will still vary with changing atmospheric conditions. We make the assumption that nature does not conspire to equilibrate the release of a trace constituent, and that therefore variations in sodium supply will correlate with those in SO_2, even though a sign of the correlation is unknown. The supply of sodium from the surface is also problematic in its magnitude; current best estimates of the surface sputtering rate for sodium (Chrisey et al., 1987; Sieveka and Johnson, 1984) are well below the levels required to populate the cloud. The problem is alleviated if sodium is always present in a thick atmosphere at about the 1 percent level, but the issue of how sodium is injected into the atmosphere must be addressed.

Sputtering, elastic collisions, and charge exchange eject sodium from Io's vicinity over a large, nonthermal range of velocities. The speed determines the relative importance of the variations in the supply and loss rates. For sodium, slower atoms are most strongly affected by the variable sink. These atoms, generated by sputtering and multiple collision processes, travel at ~3 km/s, and are responsible for filling the region near Io and the forward cloud. The medium-speed sodium (3–30 km/s, the product of one or more elastic collisions) is less sensitive to the variable ionization rate since it travels more quickly out of the plasma, and is more sensitive to the changeable source rate. The highest speed sodium (30–100 km/s, created through charge exchange) is completely unaffected by the changing ionization rate, but responds directly to the variable source rate.

Surface Processes The source of the atmosphere, clouds, and torus is ultimately the extensive volcanic activity on Io. As discussed by McEwen et al. (this volume), the handful of smaller SO_2-driven plumes appear to be long-lived (~years) and fairly constant in number and size. In contrast, only one of the very large plumes is apparently active at any given time, with the eruption lasting only days to months and varying in size during its lifetime. These large plumes may be driven by sulfur vapor instead of SO_2 (McEwen and Soderblom, 1983), so the total volcanic output may change radically in composition as well as amount on this short time scale. The atmosphere, clouds, and torus will subsequently respond according to the strength of their link with the volcanoes.

The small volcanoes also emplace large surface deposits of SO_2 frost that may later sublimate. The equilibrium vapor pressure above these frosts is strongly temperature-dependent, varying by five orders of magnitude over a 40 K change in temperature between the subsolar and antisolar points. As discussed in the next section, this simplified case leads to an atmosphere that is much denser on the dayside than the nightside. As a result, the atmospheric sputtering rates should be higher when the corotating plasma impinges on the sunlit hemisphere, and lower on the dark side, leading to an oscillation in the supply to the neutral clouds during Io's 42-hour orbit around Jupiter.

Despite the compositional difference between the eruptions, the global surface composition has apparently remained fairly constant, as indicated by ground-based photometric data (reviewed by McEwen et al., this volume). The large volcanoes are apparently restricted to a specific longitude range; when they erupt, to first order they overlay the terrain with fresh deposits of the same composition. Therefore, the sublimation and surface sputtering processes, both of which depend on surface composition, would be expected to be relatively insensitive to changes in volcanic activity.

Characteristic Lifetimes of Components of the System

The time scales summarized in table 7 must be placed in the context of the replenishment times of potentially observable features. The replenishment times in table 9 are the ratio of estimated inventory of the regions of interest to the neutral supply rate. The rate used, ~(1.8 × 10^{28}) atoms per second (Smyth and Combi, 1986), is derived by extending the fairly well constrained loss rates from the sodium cloud to models of the oxygen and sulfur clouds.

A change in the region in question will be observable if the replenishment time is comparable to or less than the variation time scale. As table 9 indicates, the replenishment time of the lower atmosphere is too uncertain to determine the likelihood of observable variations. The large range of possible atmospheric lifetimes comes from our ignorance of the atmospheric thickness; an atmosphere with a subsolar pressure of 10^{-7} bar could supply the torus for half a year, ignoring other losses or changes. On the other hand, a thin atmosphere (i.e., a corona) must be regenerated on a time scale of hours. The sodium cloud, extending forward and inside Io's orbit, is composed of survivors of the harsh ionizing plasma near Io. Orbit calculations by Smyth and McElroy (1978) indicate that spatial extent of the observed cloud is consistent with a 20-hour formation time. Finally, the population of the plasma torus is considerably larger than the neutral population, so the lifetime is correspondingly longer. The value for SO_2 frost is included to show that the sputtering process cannot deplete the surface frost on a short time scale; the corona, neutral clouds, and plasma could be supplied for centuries by minimal surface frost.

Table 9. Replenishment Time Scales

SO_2 frost (1 mm)	400 years[a]
Thick atmosphere	2 hours–180 days[b]
Corona	1–2 hours
Extended cloud	~20 hours
Plasma torus	~60 days

[a] Assuming a density of 0.2 g/cm^3 and 100 percent surface coverage.
[b] Assuming a pressure of 10^{-8} bar over the entire dayside hemisphere.

These simplistic calculations show that most of the predicted variations should be visible throughout the sodium cloud and down to the corona. Direct observations of the lower atmosphere would clearly be revealing, but no means of measuring its content on a sufficiently short time scale is currently possible. The long-time constant of the plasma torus suggests that it would respond only to the long-term effects of changing volcanism.

ATMOSPHERIC MODELS

We now examine the three major atmospheric models proposed to date, and determine the dominant time variabilities expected of them. Readers not familiar with these models are urged to consult Johnson et al. (1988). Predictions of the sodium cloud behavior are stressed below, since sodium is the most readily observed neutral constituent. For each atmospheric model, we assume that the neutral clouds and corona are generated by sputtering of the surface or, in the case of a thick atmosphere, sputtering and multiple collisions at the atmospheric exobase. We further assume that sulfur and oxygen ions in the corotating plasma are responsible for sputtering, and that there is no deflection of the plasma flow around Io. Variations on these assumptions are explored in section titled Feedback Loops between Neutrals and Ions.

Sputtered-Corona Model

In the absence of sublimation or volcanic activity, an extended but collisionally thin atmosphere will arise on Io simply from the impact of plasma torus ions on the surface (Watson, 1981). Sieveka and Johnson (1985, 1986) have computed model corona based on the impact of ions into an SO_2 surface. The model assumes a constant flux of ions impacting the trailing hemisphere surface, and does not include loss processes such as ionization. Only about 3 percent of the sputtered molecules directly escape from Io's gravity. Most of the molecules therefore travel on ballistic trajectories around Io, forming a neutral corona. The calculated corona of Sieveka and Johnson (1985) is shown in figure 37. The

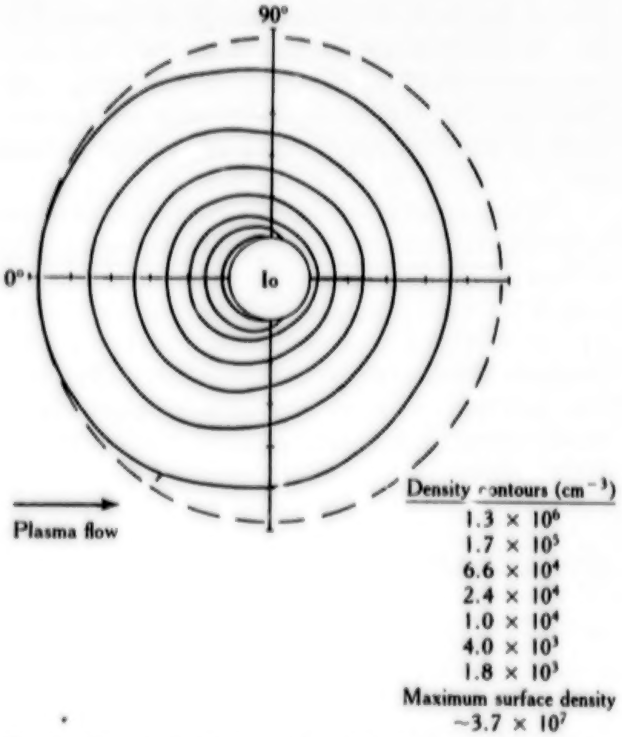

Figure 37. Theoretical model of a sputtered SO_2 corona. From Sieveka and Johnson (1985). The corona is densest above Io's trailing hemisphere.

density is highest over the trailing hemisphere where the incident flux is largest. The column abundance there is $\sim(4.5 \times 10^{14})$ molecules per square centimeter, about unit collisional thickness. The abundance over the leading hemisphere is lower by about an order of magnitude.

The effects of both a time-varying ion flux and neutral lifetime can, however, significantly alter this picture of the corona. The critical parameter that determines the density distribution in the corona is the ratio of the ballistic flight time to the atom-molecular lifetime. The density of atoms and molecules that have relatively long lifetimes in the plasma will be affected primarily by the changing flux of ions to the surface; high ion densities will lead to increased supply of these species. Short-lived species in the corona will not vary as much, since the increased sputtering rate will be approximately offset by the decreased lifetime. In either case, the variations will be fairly small, of the order of the factor of two variations in the plasma density. The strongest variation in the supply rate should have a period of 6.5 hours, but the offset dipole and east/west electric field will generate 13-hour and 42-hour modulations as well.

The temperature difference between the day and night sides will lead to another 42-hour period in SO_2 supply. Sputter yields from dayside SO_2 frosts at 110 K should be about twice the yield from the nightside 90 K frosts (Lanzerotti et al., 1982). Sodium compounds do not exhibit such a larger variation in sputtering rates with temperature, so the supply rate to the sodium clouds will not undergo this diurnal variation. In the absence of a thick atmosphere, changes in volcanic activity do not strongly affect the sputtering rates, so the sputtered-corona model would predict fairly constant densities in the atmosphere, clouds, and torus over the years.

Sublimated Atmosphere

There is considerable (albeit controversial) evidence for a thick SO_2 atmosphere maintained by sublimation, including the detection of gaseous SO_2 over a hot spot (Pearl et al., 1979), identification of SO_2 frost on the surface (Fanale et al., 1979; Hapke, 1979; Smythe et al., 1979), and the presence of a dense ionosphere (Kliore et al., 1975). A number of models have been developed to describe an SO_2 atmosphere in vapor pressure equilibrium with the surface, as reviewed in Johnson et al. (1988). Given the vapor pressure variation of five orders of magnitude over the range of possible Io temperatures, it is clearly essential to identify correctly the region of the surface controlling the equilibrium. Preliminary models (e.g., Pearle et al., 1979) used crude estimates of the average dayside temperatures; more recent studies (Fanale et al., 1982, "regional coldtrapping") have suggested that high-albedo SO_2 patches, much colder than the average surface temperature, dictate a lower atmospheric pressure. In regions lacking SO_2 frosts, coldtrapping in the insulated subsurface layers (Matson and Nash, 1983) may drive the atmospheric pressure lower still. McEwen et al. (1987), using the regional coldtrapping model, suggest that the maximum subsolar pressure is 10^{-8} bar (collisionally thick), with negligible pressure on the night side. This type of atmosphere is illustrated in figure 38.

Earth-based observations can clearly never view Io's night side, but a strong day-night atmospheric asymmetry should produce variations in the sputter-generated neutral clouds (figure 38). When Io is west of Jupiter, the plasma flow impacts the thick dayside atmosphere. Half an orbit (21 hours) later, the plasma strikes the nightside surface. Rough calculations for SO_2 show that the atmospheric sputter removal rate should be a factor of eight higher than the nightside

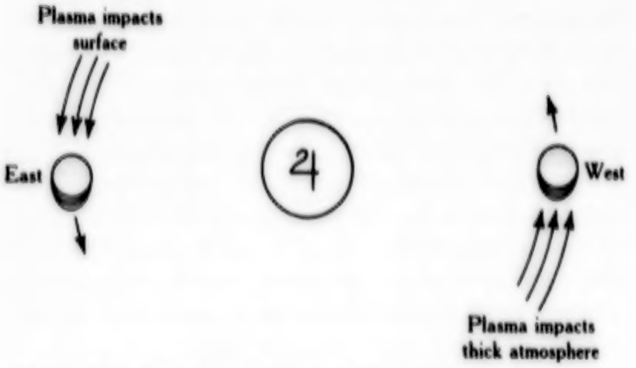

Figure 38. Supply asymmetry of the sublimated atmosphere model. The atmosphere is densest over the warm subsolar point. Ignoring other possible effects, the atmosphere's diurnal asymmetry leads to an orbital asymmetry in the sputtering rate. When Io is west of Jupiter, the plasma impacts the dayside atmosphere. 180° later, the plasma strikes the nightside surface.

surface sputtering rate, not allowing for less than 100 percent SO_2 surface coverage or a high dayside exobase. The formation rate of the neutral clouds of SO_2 and its byproducts should be much greater when Io is west of Jupiter. The level of sodium cloud asymmetry is more difficult to calculate, since we know neither the form sodium takes on the surface nor the process that releases it into the atmosphere. (See the section titled Overview of the System.) Nonetheless, it is unlikely that the supply rate to the sodium cloud could remain constant in the face of large changes in the SO_2 supply rate. In the sublimated atmosphere model, then, the 42-hour diurnal cycle and the plasma-induced variations discussed above should be observable.

Io may have a thick dayside atmosphere and no appreciable nightside atmosphere. This is unique in the solar system. Mechanisms have been proposed for an atmosphere on the dark hemisphere (see Johnson et al., 1988), but all share the feature that the nightside atmosphere is very different from the dayside atmosphere in composition and/or density. If there is a collisionally thick nightside atmosphere, the supply rate asymmetry may be greatly reduced, but probably not eliminated.

Volcano Generated Atmosphere

Volcanoes have been suggested as the direct atmospheric source since the Voyager IRIS experiment detected gaseous SO_2 near an eruption. Only recently has this possibility been quantitatively explored (Moreno et al., 1987, Baumgardner et al., 1987). Their work concludes that even a single volcanic eruption can create a substantial atmosphere. A large Pele-type eruption (typically found in Io's inner trailing quadrant) would form a thick local atmosphere, with an exobase bulging to 500 km over the plume, where the surface pressure nears 10^{-6} bar (figure 39). The exobase level decreases away from the vent, intersecting the surface almost halfway around the planet. Almost all of the erupted gas rapidly condenses onto the cold surface, but the remaining few percent is evidently sufficient to create a thick atmosphere over much of the entire body. In the case of a smaller, Prometheus-type eruption, the exobase reaches only 200 km altitude, and drops to the surface 40° away from the vent.

Supply to the clouds and torus will therefore fall into two regions, dependent on the activity or dormancy of large eruptions. The largest, most variable plumes are favorably situated on Io for sputtering by corotating ions, so the supply rate will be directly linked to the presence or absence of such eruptions. Baumgardner et al. (1987) show that Pele-type eruptions lead to high escape rates characterized by atmospheric sputtering, whereas eruptions lead to a much lower rate characterized by surface sputtering. As table 8 shows, the numerical difference will be at least a factor of four. Baumgardner et al. suggest a factor of 20, including the effects of the high exobase and a more reasonable estimate of the fractional SO_2 surface coverage. Since the large eruptions tend to be short-lived and sporadic, the supply rate may change drastically on a time scale of days to weeks. Furthermore, if the Pele-type eruptions are compositionally different from

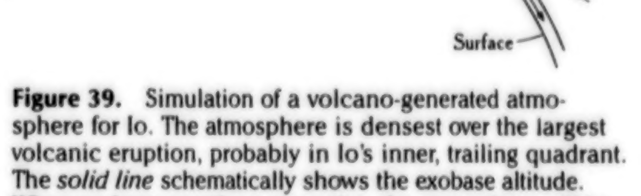

Figure 39. Simulation of a volcano-generated atmosphere for Io. The atmosphere is densest over the largest volcanic eruption, probably in Io's inner, trailing quadrant. The *solid line* schematically shows the exobase altitude. When no large eruptions are active, the atmosphere will be collisionally thin over most of the surface. Adapted from Baumgardner et al. (1987).

the effective surface composition, the clouds and torus may change composition rapidly.

Summary of Predicted Variations

Table 10 summarizes the predicted variabilities of the atmosphere and sodium cloud for each of the models outlined above. The sputtered corona is a fairly stable atmosphere; variations in density above a factor of two would not be expected. The variations should be roughly periodic, with periods ranging from 6.5 to 42 hours, but overlapping variations will distort the regular pattern. The SO_2 supply rate will be higher when the plasma impacts the warm, dayside surface than when it strikes the nightside surface, but the sodium supply rate will probably not vary with surface temperature. A detailed model is necessary to predict the phase lag of the brightness oscillation behind the oscillating supply and loss rates. No large secular changes would be expected.

The dominant variation in the sublimated atmosphere model is caused by the atmosphere's day-night asymmetry. The dayside atmospheric sputtering rate should be a factor of eight higher than the nightside surface value. Some form of orbital asymmetry in the sodium cloud should result, although its exact form is not clear. The presence of a nightside atmosphere will tend to reduce the supply rate variation. Short-term plasma-induced variations will also be present, but at a lower level than the diurnal effect. Again, there are no obvious causes of large secular changes.

The volcano-generated atmosphere would be the most variable on a time scale of days to months. The neutral supply rate may vary by over an order of magnitude, with corresponding changes in composition. These variations would not be periodic, but linked to the erratic eruptions of the large plumes. The compositional change is harder to address quantitatively, but may be quite significant in terms of supply to the plasma torus.

It is, of course, overly simplistic to discuss the models exclusively. Almost certainly, all atmospheric sources are active at some level: Volcanoes create at least a local atmosphere, and the sputtered corona will form above a thick atmosphere regardless of its source. But one of the atmospheric sources, that is, sputtering, sublimation, or volcanic venting, will dominate, and its variability (listed in table 10) will be appropriate.

In the discussion that follows, we compare these predictions with the observed variations, with the goal of determining which model is most consistent with the data, and what additional constraints can be placed on the models if they are to reproduce the observed behavior.

Table 10. Atmospheric Models: Supply Variations

Model	Variation amplitude	Time scale
Sputtered corona	2	6.5–42 hours
SO_2 sublimation	4	42 hours
Volcanic outgassing	4–20	days–years

OBSERVED VARIATIONS

Ideally, one would choose to compare the above predictions against the observed overall state of the atmosphere and neutral clouds. Unfortunately, the dominant constituents, namely SO_2, S, and O, are almost unobservable from Earth or spacecraft. The existing data on these species is limited to mere detection, with little or no information on time variability. Sodium, and the even rarer element potassium, are the only elements sufficiently visible to allow good time-resolved measurements. Although atomic sodium probably makes up only ~1 percent of the atmosphere and neutral clouds, its larger oscillator strength for resonant scattering far outweighs its scarcity. (See Brown and Yung, 1976, for a full discussion of the resonant scattering process.) Since its discovery 15 years ago sodium has been used as a tracer for the atmosphere and clouds of Io. Observations of potassium are scarce, but its behavior is similar in nature to the sodium cloud (Trafton, 1977). In the sections that follow, comments are therefore confined to the behavior of the sodium cloud. We then compare this behavior to the predictions, bearing in mind the caveats outlined in the first section of the chapter concerning the uncertainties about the sodium supply process.

Long-Term Behavior

The sodium cloud is a staple feature of the jovian system; it is always present at approximately the same brightness. To be more quantitative about this apparent constancy requires a comparison of data from a varied suite of instruments, techniques, and observers. Furthermore, the cloud exhibits a number of time variabilities caused by geometrical effects. Figure 34 shows the approximate shape of the cloud; as it orbits about Jupiter its projection on the sky obviously changes. Although such variations are clearly useful in deconvolving the shape of the cloud, they must be separated from true temporal variation in the density of the cloud. Furthermore, the Io-sun Doppler-shift also oscillates with an amplitude of ±17 km/s, varying the solar flux available for resonant scattering by an order of magnitude. Strictly speaking, one can therefore compare only observations obtained at identical orbital and magnetic longitudes. A large body of data and a good modeling capability are clearly required to remove these geometrical effects.

The quantity we use for comparison is the intensity of sodium emission within a radius of ~2.5 arcseconds of Io. This location was chosen as subject to the least dependence on observing geometry and the known short-term variabilities (although there remains a nonnegligible dependence on seeing conditions). Physically, 2.5 arcseconds corresponds to Io's ~10^4-km radius Hill sphere (sometimes called the Lagrange sphere), which encompasses the region where Io's gravity dominates. Observationally, this is slightly larger than the typical seeing disk. It is still necessary to compare emission intensities derived from different observational methods. This requires knowledge of how the emission is distributed in Io's vicinity. In reality, the brightest emission is not generated against Io's one-arcsec disk itself (where sodium is practically invisible due to a lack of contrast [Brown and Yung, 1976]) but from a ring surrounding Io. Under typical seeing conditions, however, the emission is so severely blurred that it covers Io's disk. The measured intensities therefore may be used for relative comparisons, but should not be directly inverted to column abundances without allowance for the effects of seeing.

Table 11 shows emission intensities derived by three methods. Most measurements were made with Io near elongation, but no attempt was made to correct for the dependence of intensity on Doppler shift. The emission intensity near Io can be directly measured by high-resolution spectroscopy (Brown et al., 1983; Schneider et al., 1987) with Io placed on the spectrograph entrance slit. The slit used by Bergstralh et al. (1977) was much larger, and the absolute intensity calibration was performed differently. For imaging studies (Morgan and Pilcher, 1988; Goldberg et al., 1984), where Io's disk must be occulted, the near-Io intensity must be derived from the intensities farther out. Given these limitations, we suspect the accuracy of the intensity calibration between observational methods is only good to the 50 percent level.

The primary result is that no very large variations or secular changes have taken place in the brightness of the Io sodium cloud over a twelve-year period. Given the uncertainties in the relative calibrations and the existence of short-term variations, the intensities in table 11 are consistent with a sodium cloud unchanged within a factor of two through the years. The scatter in the data from Bergstralh et al. (1977), obtained over a two-year period with the same instrumentation, rarely exceeds 50 percent. In addition, the basic shape of the cloud has apparently remained constant since its discovery. Although the actual shape was not successfully deconvolved until 1975 (Murcray and Goody, 1978; Matson et al., 1978), all previous and subsequent observations are consistent with that shape.

Little more can be said at present about the long-term constancy of sodium within Io's Hill sphere. Long-term variations due to plasma properties or volcanic activity are probably present, but the current data are not sensitive to intensity changes smaller than a factor of two. Such variations would be hidden in the broader variations due to imperfect intensity calibration, geometrical effects, changing Doppler shifts, variable seeing conditions, and short-term variations. Through the reduction of old observations and the careful acquisition of new data it will be possible to build a data set sufficient to detect long-term variations.

The constancy of the sodium cloud should be contrasted with the results for the visible sulfur ion emissions. Coverage is not as complete for ion measurements, but Trauger et al. (1980) and Trauger (1984b) present data which demonstrates that the S^+ density in Io's vicinity was lower by an order of magnitude in 1976

Table 11. Stability of the Io Sodium Cloud (≤3" from Io)

Year	Date	Observation	Brightness (kR)	Reference
1974	July–Sept.	slit averaged	30–60	Bergstralh et al. (1975, 1977)
	Nov. 17	1-D profile	~30	Brown et al. (1975)
1975	Nov.–Dec.	slit averaged	30–60	Bergstralh et al. (1977)
1976–1979	(many)	slit averaged	?	Goldberg (1987)
1981	March–June	2-D images	~30	Goldberg et al. (1984)
1984	June	2-D images	~30	Morgan and Pilcher (1988)
1985	Aug.–Sept.	1-D profiles	20–40	Schneider et al. (1987)

than 1981–1983. Curiously, the sodium cloud somehow remained approximately constant (Murcray and Goody, 1978; Goldberg, 1987). Such a situation is clearly intriguing and important, but no explanation for such a juxtaposition has been proposed. We examine several possibilities in the section titled Feedback Loops between Neutrals and Ions.

Short-Term Behavior

On a time scale of hours, numerous periodic changes in the density, shape, and velocity distribution of the sodium cloud become apparent. These variations are primarily sensitive to the interactions between the plasma and the extended neutral clouds, but with care certain variabilities can be used as a probe of the atmosphere itself.

Magnetic Longitude Variations The importance of the plasma equator tilt was first revealed in observations by Trafton (1980, and references therein). They discovered an alternating asymmetry to the extended sodium cloud, with the brightnesses north and south of Io anticorrelated, highly variable, and oscillatory with a 13-hour period (fig. 40). This is precisely the result expected from the preceding discussion of ionization lifetime for sodium out of the orbital plane. From this variation, Trafton was able to determine the speed of the sodium and the electron temperature. Observations of this type provide a relatively simple means of measuring plasma conditions remotely.

Trafton and Macy (1977) also recorded high-resolution spectra of sodium within 10″ (20 Io radii) of Io. All spectra show a skirt to higher velocities, extending up to 18 km/s. Although the number of observations was small, they see a tendency for larger high-velocity populations when the plasma plane passed by Io. Brown and Schneider (1981) report a similar correlation in the appearance of very fast sodium (10–100 km/s) at a distance of 10 R_J from Jupiter. They detected high-speed sodium in only 2 of 17 combinations of Io magnetic and orbital longitudes. Both occurrences traced back to a recent passage of the plasma plane through the sodium cloud, with the cloud situated such that the fast sodium was directed into the field of view. These two types of variation would be expected based on the discussion of the first section of the chapter; collision and charge-exchange products are preferentially ejected when the plasma plane intersects the neutral clouds.

Systematic variations are also apparent in the overall shape of the sodium cloud. Pilcher et al. (1984) and Goldberg et al. (1984) have observed on many occasions the so-called "directional features," which appear north or south outside of Io's orbit. Figure 41 shows an

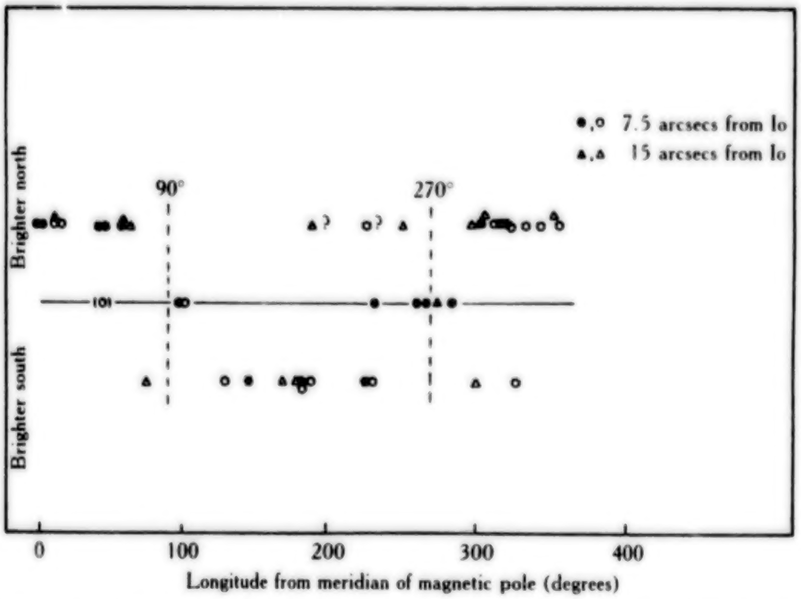

Figure 40. Magnetic longitude variability of the Io sodium cloud. The symbols show the sign of the difference in sodium D-line emission intensity for points symmetrically placed north and south of Io plotted against Io's differential magnetic longitude. In this system, 0° occurs when Jupiter's north magnetic pole is pointed toward Io. Data flagged with "?" may have been subject to an error in the sign of the offset. From Trafton (1980).

ORIGINAL PAGE
COLOR PHOTOGRAPH

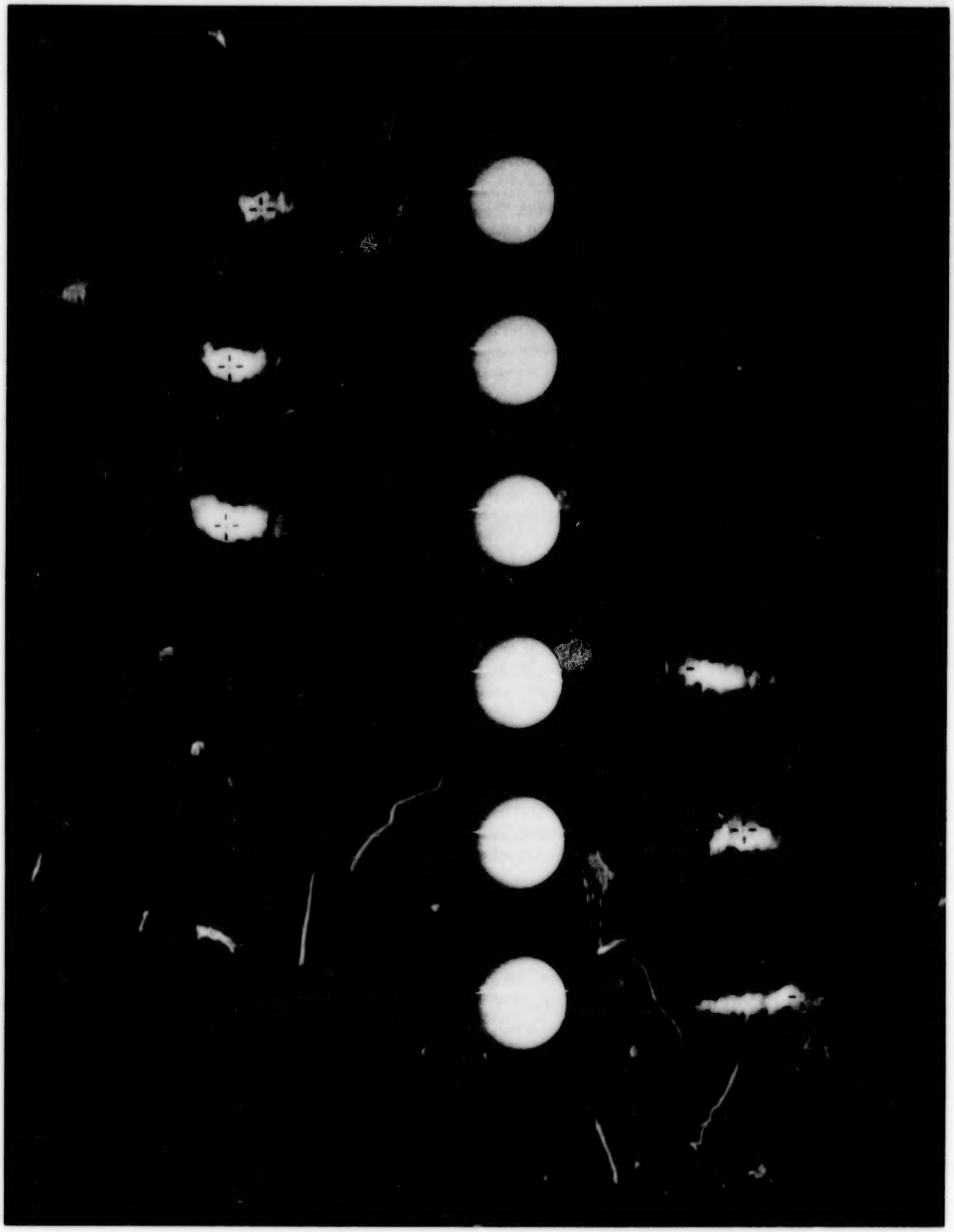

Figure 41. Images of Io's sodium cloud from Goldberg et al. (1984). The top frames show "directional features" extending to the north. A comparison of the third and sixth frames reveals the stretching of the cloud at western elongation due to radiation pressure.

example from Goldberg et al. These features are apparently caused by sodium ejected from Io primarily perpendicular to the orbital motion with velocities of 20 km/s. The north-south asymmetry is caused by preferential ionization at the plasma equator, which oscillates about Io's orbital plane. The Pilcher et al. analysis of the directional features is an excellent example of the power of time-variable phenomena in probing the torus-atmosphere interaction. Modeling of the north-south variation showed that a new population of energetic atoms was required, with a source rate comparable to the previous total source rate. Atomic physics calculations (Sieveka and Johnson, 1984) demonstrated that this could in fact be supplied by a close interaction between Io's atmosphere and the plasma.

Diurnal-Orbital Variations The most extensive published survey of sodium cloud intensities very near Io was performed by Bergstralh et al. (1977) and is shown in figure 42. These data revealed not only the large modulation caused by the effect of Io's Doppler shift through the solar Fraunhofer line, but also a small, yet measurable, tendency toward higher cloud intensities when Io was on the east side of Jupiter. This general trend also appears on a larger spatial scale in the imaging data of Goldberg (1987), but has not yet been quantified.

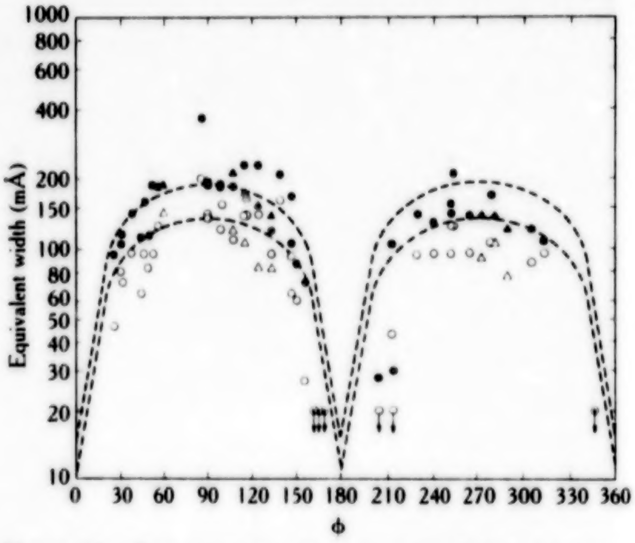

Figure 42. East-west intensity asymmetry of the sodium cloud from Bergstralh et al. (1977). Brightness of the sodium emission as a function of heliocentric orbital longitude. 0° longitude corresponds to superior heliocentric conjunction, with Io behind Jupiter. The *dashed lines* show the predicted variation due to Io's Doppler-shift motion through the deep solar fraunhofer line. *Open circles* show the D_1 line; *closed circles* show the stronger D_2 line. The slit measured 3" by 8" and was centered on Io's disk. Note that the emission east of Jupiter (0–180°) was slightly brighter than that west of the planet.

The east-west asymmetry is not surprising in the context of the processes described in the first section of the chapter, and two explanations have been proposed. Thomas (1986) suggests that the asymmetry is a diurnal effect caused by the large difference between the nightside and dayside atmosphere, as presented in figure 38. In this model, sodium atoms are underabundant in the thick atmosphere. Thus, the supply of sputtered sodium atoms is higher when the corotating plasma strikes the nightside surface (on the east of Jupiter) than when it strikes the dayside atmosphere (on the west). The difference in the sputtering rates results in a brighter sodium cloud when Io is east of Jupiter. Thomas's theory works at a mathematical level, but certain assumptions require confirmation. Although it is certainly plausible that the sodium content in the atmosphere is low (due to inhibited surface sputtering, for example), there is no direct evidence of such an effect. Recent experimental work by Chrisey et al. (1987) has shown that Thomas's calculations of the sodium supply rate from the surface are overly optimistic. It is also probable that the velocity distributions for ejection from the surface and atmosphere would be radically different. But given the uncertainty surrounding the nature of sodium atoms on Io's surface, and the possibility of a large day-night atmospheric asymmetry, a diurnal effect similar to Thomas's cannot be ruled out. Note that for this model, the supply of sulfur and oxygen would be enhanced when that of sodium is diminished.

Smyth and Combi (1987) have developed a model that incorporates the observed east-west asymmetries of the ionized species as well as neutral sodium. Both the Voyager ultraviolet spectrometer (UVS) experiment (Sandel, 1987) and ground-based observations (Morgan, 1985) indicate that the plasma at Io's orbit is hotter and denser on the west of Jupiter than on the east. This has been interpreted as evidence for an east-west electric field of $\sim$3 mV/m, which effectively displaces the plasma inward or outward by $0.15R_J$ on opposite sides of Jupiter. Io is effectively moved to a denser region of the plasma when Io is west of Jupiter. Sodium is ionized more rapidly there, making the cloud fainter when Io is at western elongation. Smyth and Combi suggest that ground-based monitoring of the sodium cloud, especially at certain sensitive longitudes, may yield a direct measurement of the electric field strength, which may also be time-variable. In this model, only the sodium cloud exhibits a strong orbital asymmetry, since only its lifetime (see table 7) is short enough to generate an observable effect.

At a qualitative level, the sodium cloud morphology also varies as a function of orbital longitude. When Io is west of Jupiter, the cloud extends farther along the orbit than at eastern elongation (fig. 41). Smyth (1979, 1983) proposed radiation pressure as the cause, noting that through resonant scattering, the sodium atoms experience an acceleration away from the sun. The radiation pressure effectively stretches the cloud along Io's orbit when Io is west of Jupiter, and compresses it east of Jupiter. Detailed computer modeling can reproduce the general shape variations as long as the most probable velocity of the flux distribution of sodium atoms is ~2.6 km/s.

Recent very long exposures with the International Ultraviolet Explorer (IUE) satellite have yielded the first spectra of neutral oxygen and sulfur in Io's atmosphere and corona (Ballester et al., 1987, discussed further by Strobel, this volume). Although the data cannot be explained by the prevailing view of Io's interaction with the plasma, some rough interpretation is still possible. The four spectra obtained (two each at eastern and western elongation, viewing the downstream and upstream hemispheres, respectively) show no significant differences. The emission may be generated by electron impact excitation; this process should not differ greatly between the upstream and downstream hemispheres since the electron thermal velocities will greatly exceed the corotation velocity. The comparable emission rates therefore argue against a large upstream-downstream atmospheric asymmetry. If the emission region is large compared to Io, this is easily satisfied. Further interpretation of the spectra is required before firm conclusions may be reached.

Variations in Energetic Sodium Jets In addition to the above systematic behavior are some unexplained variations, most notably in the highest-speed sodium. The charge exchange reaction that produces such sodium is quite target-selective; even though sodium is a small percentage of both the atmosphere and torus, the reaction proceeds far more efficiently when a sodium ion collides with a sodium atom (McGrath, 1988). The fast neutral products, at average velocities of ~70 km/s in the Jupiter reference frame, can be observed by ground-based instruments with sufficient sensitivity and velocity resolution.

Trauger (1984b) has obtained velocity-resolved images of a high-speed jet emanating from Io's disk and extending forward along its orbit. These fast neutrals are probably the result of charge-exchange reactions taking place in Io's corona. Figure 43 shows an example of a high-speed jet; the jet is always present in Trauger's data and the vertical shape of the feature is basically a map of Io's extended atmosphere on a scale unobtainable through standard imaging techniques. On other occasions, Trauger (1987) has observed "tilted jets" not attached to Io but recently ejected from it. Both the tilt and the timing may be related to the tilted magnetosphere, but more analysis is required.

Schneider et al. (1987) have obtained high-resolution slit spectra of sodium at moderate distances from Io (~15", or 30 Io radii) and have documented the huge variability of the outer parts of the sodium cloud. Figure 44 shows several examples of high-speed sodium ejection from Io. In some extreme examples, the forward cloud is completely dominated by the rapidly escaping atoms. Note also that the jet typically appears north or south of the slow sodium. Both the directionality and the strength of these jets are highly variable in Schneider's data. This underscores the difficulty in interpretation of sodium cloud images without velocity information: The appearance of the outer parts of the sodium cloud during such bursts of charge-exchange products may have little to do with the behavior of the much slower "normal" cloud.

Several aspects of the high-speed sodium ejection events are unexplained but tantalizing. The jets observed by Trauger extend straight forward from Io and are only a few Io radii in cross section. Those observed by Schneider et al., however, typically extend out of the orbit plane, and are tens of Io radii in cross section. Despite their different morphologies, the velocity distribution of both phenomena indicate charge exchange as the source. Furthermore, there is currently no explanation for the north-south asymmetry of the Schneider observations. At the measured velocities of up to 70 km/s, sodium leaves the hot, dense torus before electron impact ionization can have any measurable effect. The north-south asymmetry may therefore arise from out-of-plane initial ejection velocities, for which there is no clear explanation. Further observations of this bizarre type of event will be required to uncover its significance.

Observed Behavior Versus Predicted Behavior

A host of periodic variations are well established in the extended sodium cloud. Most are adequately explained by the oscillating sink of the hot, dense plasma. These have been and will continue to be useful tools for remote sensing of the extended clouds and plasma.

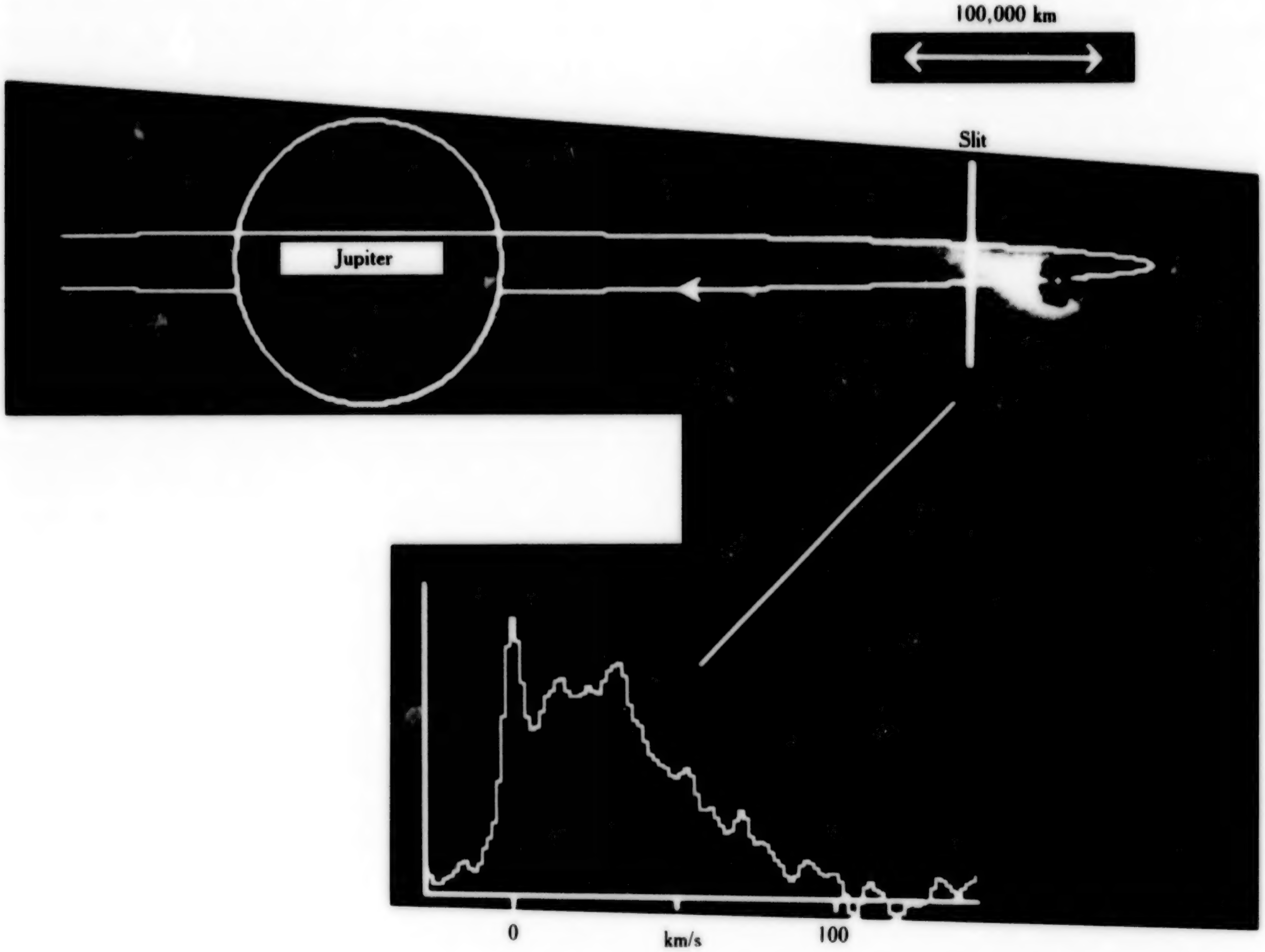

Figure 43. Simultaneous imaging and high-resolution spectroscopy of Io's sodium cloud on 17 June 1984 at 8:45 UT. Image taken by J. S. Morgan at the 2.2-m telescope on Mauna Kea. The white ellipse shows the projection of Io's orbit on the plane of the sky. Io itself is blocked by an occulting disk that is about four Io diameters across. Note that the bulk of the forward cloud does not lie along the projected orbit, but is well north of it. The simultaneous spectrum below by Schneider et al. (1984) obtained at the position of the line labeled "slit" reveals the velocity distribution. About 70 percent of the sodium emission in the region of the slit comes from atoms with velocities above 8 km/s with respect to Io. The spatial cross section of fast sodium feature is much larger than Io itself, unlike the jets observed by Trauger.

Other observed variations (or lack thereof) permit us to apply new constraints to the various atmospheric models. The long-term stability and the east-west orbital asymmetry are the most important results for uncovering the nature of the atmosphere.

The average sodium emission near Io has remained steady within a factor of two, based on two years of consistent monitoring by Bergstralh et al. (1977) and sporadic observations by a number of observers over the 15 years since Brown's discovery of the cloud. Although the relationship between supply to the sodium cloud and the cloud's intensity is under debate (see next section), we interpret the relative constancy of emission as indicative of a fairly steady supply of sodium from Io.

The sputtered corona model easily meets this requirement; it is, in fact, fairly difficult to change the supply rate by large factors. The sublimated atmo-

ORIGINAL PAGE
COLOR PHOTOGRAPH

ORIGINAL PAGE
COLOR PHOTOGRAPH

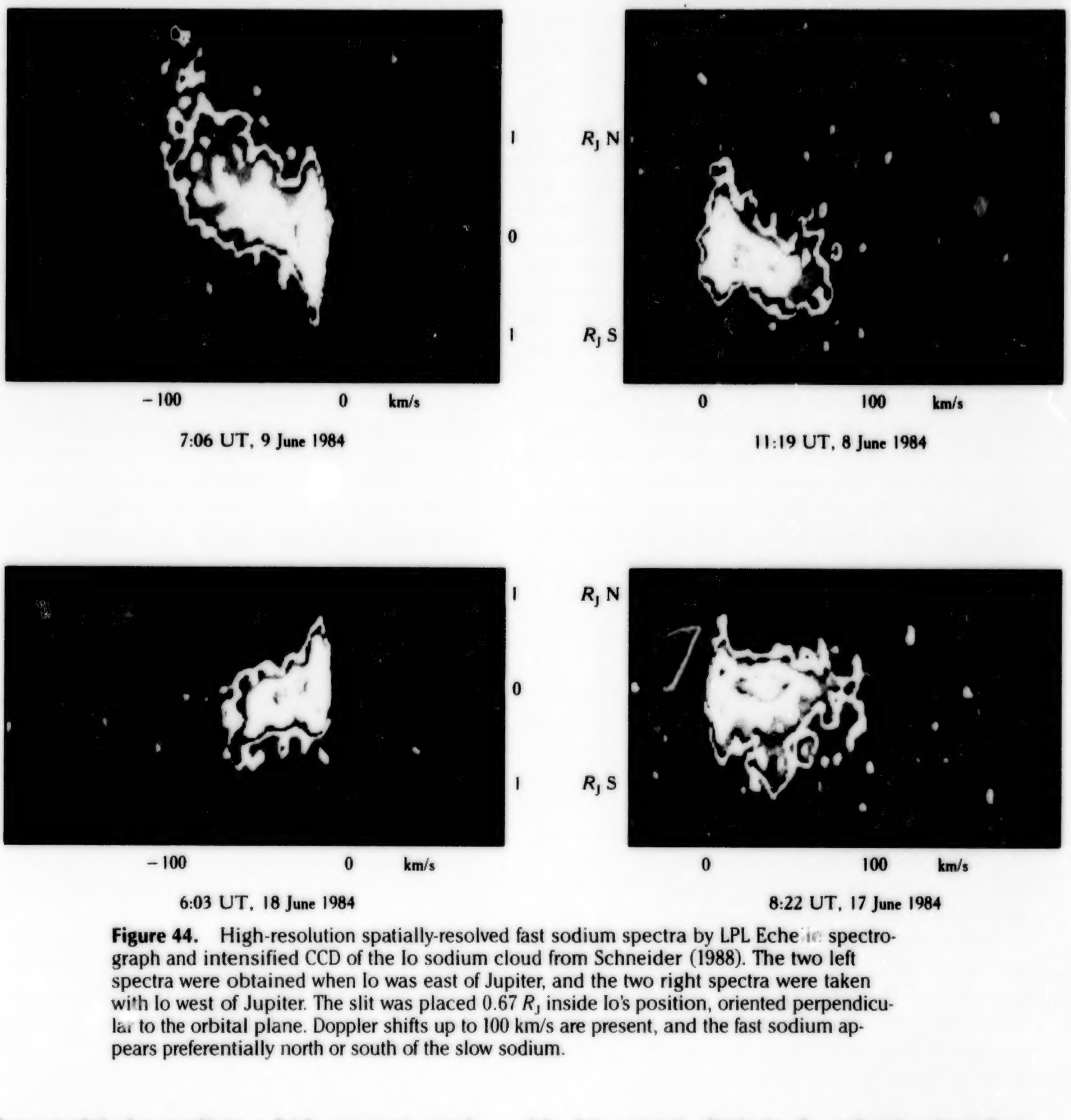

7:06 UT, 9 June 1984

11:19 UT, 8 June 1984

6:03 UT, 18 June 1984

8:22 UT, 17 June 1984

Figure 44. High-resolution spatially-resolved fast sodium spectra by LPL Echelle spectrograph and intensified CCD of the Io sodium cloud from Schneider (1988). The two left spectra were obtained when Io was east of Jupiter, and the two right spectra were taken with Io west of Jupiter. The slit was placed 0.67 R_J inside Io's position, oriented perpendicular to the orbital plane. Doppler shifts up to 100 km/s are present, and the fast sodium appears preferentially north or south of the slow sodium.

sphere model also predicts a fairly constant supply rate, as long as the exobase altitude does not vary with time. We can with some confidence rule out some extreme models, in which the exobase varies from 0 km to 900 km altitude; the supply rate would then vary by an unacceptably large factor of 3.4. The sulfur and oxygen supply from the volcanic atmosphere model proposed by Moreno et al. (1987) would change by a factor of ~4 to 20 with the appearance and disappearance of large plumes; we assume the sodium supply would strongly vary but cannot further quantify it. The available data cannot eliminate the volcanic atmosphere model, but it seem improbable that the sodium cloud would vary at most by a factor of two whereas the other species changed more drastically. We are again limited by our knowledge of the specific source of sodium.

The issue of the east-west orbital asymmetry of the neutral clouds is important in discriminating among atmospheric models, and merits further theoretical and observational work. The data indicate that some process causes a brighter sodium cloud east of Jupiter. Thomas (1986) invokes a time-variable sodium source

C-2

(caused by a day-night atmospheric asymmetry) and a constant sink; Smyth and Combi (1987) use a constant sodium source but a variable sink (caused by the east-west electric field). Each is difficult to refute, and both effects may in fact be active. Based on the figures in table 8, large atmosphere-generated asymmetries are to be expected; the small observed effect may indicate the presence of a significant nightside atmosphere. Further effort must be applied to the sputtered and sublimated atmosphere models, and the cloud asymmetry that would arise from them. The process that liberates atomic sodium is central to this entire issue, and clearly demands further attention in cosmochemical theories and in laboratory experiments.

The symmetry of O and S emissions in the IUE spectra east and west of Jupiter clearly has a strong bearing on this issue, but the apparent inconsistencies of the emission excitation mechanism must be resolved before stronger conclusions can be reached. Ultraviolet observations such as these are difficult but important since they measure the dominant atmospheric constituents. If the atmospheric asymmetry effect dominates, coronal O and S densities should be higher west of Jupiter; the east-west electric field leads to no such asymmetry.

The high-speed jets near Io remain enigmatic. Their unexplained timing and north-south directionality lie outside our current understanding. The relationship between the directional features (which involve medium speed sodium directed at right angles to Io's orbit) and the very-high-speed jets (very fast sodium directed tangent to the orbit) also remains to be established. The sodium jets are more than isolated curiosities, since they imply the existence of similar jets of neutral oxygen and sulfur, greatly enhanced by the increased oxygen and sulfur densities in the atmosphere and plasma. The energy and mass that the oxygen and sulfur charge-exchange jets convey may be comparable to that of the less energetic loss processes (Smyth and Combi, 1986).

FEEDBACK LOOPS BETWEEN NEUTRALS AND IONS

The Problem

In the discussion so far, all the variabilities have been discussed as though the plasma responsible for sputtering, ionization, and the like was unaffected by its interactions with Io and the neutral clouds. The situation is, of course, quite to the contrary: The incident ions were themselves sputtered from Io and ionized only days or weeks before. The ions and neutrals are closely coupled by feedback loops conveying the mass and energy of the system.

In the presence of the variabilities measured and postulated above, one is compelled to ask what mechanism makes the feedback loops stable—what process returns the system to its equilibrium state. At the core of the complex reactions between ions and neutrals is the basic fact that the plasma torus generates itself: The corotating ions lift the neutrals off of Io, and the electrons ionize them. In this narrow view, we have an unstable positive feedback loop, where ions beget more ions, ad infinitum. Although such a scenario may have played a role in the startup of the neutral and ion tori, some mechanism currently limits the progression of mass and energy through the system. At present, there is no general agreement on the limiting process, and the current equilibrium point is not understood. In fact, there is no consensus on the expected effect of, for example, a short- or long-term doubling of the volcanic output.

The identification of this mechanism (or mechanisms) is extremely critical for the correct interpretation of the time-variability of the system. The same processes that keep the ion-neutral tori from blowing up or fading away act to restore the system to equilibrium after perturbations. The nature and time scale of the response to perturbation will be characteristic of the dominant rate-limiting process. Observations of time variations may help identify the process, and a proper mathematical analysis should provide further insights about the system not available through other means.

The purpose of the discussion that follows is not to answer the stability question, but to draw attention to our level of ignorance of this crucial issue. A number of ideas have been put forward, formally or informally, for rate-limiting processes. The following sections outline the basic precepts of each mechanism, derive rough predictions of the system response to supply rate changes, and discuss the shortcomings of the ideas.

Centrifugally Driven Diffusion

Huang and Siscoe (1986, 1987) have developed a mathematical formalism for dealing with simplified ion and neutral tori. They claim that the stabilizing mechanism is centrifugally driven diffusion, a nonlinear process in which the diffusion "constant" is actually proportional to the ion density. Figure 45a demonstrates the nature

C-2

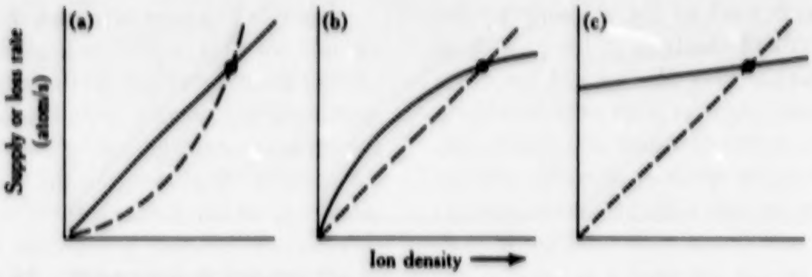

Figure 45. Three types of stability. The supply rate is shown as a *solid line*, and the loss rate by a *dotted line*. A stable equilibrium occurs at the intersection of the supply and loss curves if losses are increasing faster than the supply. (**a**) Nonlinear loss (centrifugally driven diffusion). The supply rate is proportional to the ion flux, and hence ion density. The loss rate varies as the square of the ion density, and always surpasses the supply rate at high densities. (**b**) Dynamic supply limitation (electron cooling, atmospheric buffering, and corotation breakdown). The supply rate is linear at low densities but tails off at higher densities. The linear loss rate is sufficient for system stability. (**c**) Atmospheric shielding. The supply rate is fairly constant with ion density. Linear loss rates can easily match the supply rate.

of the equilibrium. If the ion density increases, both the sputtering flux and the diffusive loss rate increase, but the latter increases faster. A stable equilibrium occurs at the intersection of the supply and loss curves.

The authors have used the equilibrium conditions to place constraints on the impedance of Jupiter's ionosphere and the effective sputter yield. These are difficult quantities to measure directly, which points out the usefulness of stability analysis in probing the torus system.

Huang and Siscoe also predict the response to perturbations in the ion and neutral densities. A transient rise in the neutral supply rate, according to this model, will increase the neutral density, which in turn leads to a marginal increase in the ion density. The excess ions would be dissipated by diffusion with a 60-day time constant, but the neutral excess disappears in about one day. The same calculations indicate that an ion perturbation would not in fact lead to a neutral density perturbation; this counter-intuitive result no doubt stems from the simplifications of the model, and therefore merits reexamination. They further calculate that a secular increase in the neutral supply rate would increase the neutral and ion densities. The unusual state of the torus in 1976 (as described in chapter 2) could not have been long-lived, but might have been due to a transient ion event as described above. The authors maintain that the level of volcanic activity should not affect the density of the ion or neutral tori, but this follows implicitly from their assumption of a strictly constant atmosphere. Eviatar (1987) makes the obvious point that the extent of the atmosphere may respond to the rate of volcanic outgassing. His quantitative estimates of this effect, however, are based on questionable assumptions regarding the importance of atmospheric condensation and the atmospheric area subjected to sputtering.

The key feature of this type of stability is centrifugally driven diffusion. Richardson and McNutt (1987) have recently presented evidence that this mechanism is not important in the Io plasma torus. They maintain that the characteristic signature of this type of flux-tube interchange is missing from the Voyager plasma science experiment data. If only linear diffusion occurs in the Io torus, some other mechanisms must stabilize the system. The other major criticisms of this model stem from the fact that the authors ignore the variability of certain parameters (e.g., the electron temperature and exobase location). The following models have been developed to address these issues.

Supply-Limiting Mechanisms

Stability can also be provided if the supply rate falls below the linear relation used above. In the following three subsections, different means of limiting the supply rate are discussed. In each of them, a linear loss rate (e.g., due to externally driven diffusion) is sufficient for stability.

Electron Cooling Huang and Siscoe assume in their stability model that the plasma temperature (and hence the rate constant for electron impact ionization) is independent of ion and neutral densities. But the Voyager plasma science (PLS) experiment (Sittler and Strobel, 1987) suggests that electrons near Io were significantly cooled, presumably by interaction with Io's dense neutral corona. Two effects lead to the cooling: (1) the energy loss of the incident electron in the process of electron impact ionization, and (2) the addition (from the ionization) of a new electron with negligible gyroenergy. The result is a cooler electron population near Io, less capable of ionizing neutrals than the original population. The electrons may also be cooled through radiative processes, which are very efficient at high densities.

Stability is achieved in this scenario (proposed by Shemansky, 1987) by reducing the ability of the plasma to add fresh ions. In effect, this mechanism stabilizes the supply rate instead of the ion or neutral densities. An increase in the neutral supply rate temporarily boosts the neutral and ion densities, but cools the electrons through ionization and radiative losses so that further ionizations are reduced. Thus the supply rate falls below the linear rate at some value (as shown in figure 45b). Ions are then lost through linear diffusion or other loss processes until the ion density returns to normal. In the meantime, charge exchange and elastic collisions have removed neutrals from the system, and have supplied sufficient energy to the ions to reheat the electrons.

This model is not fully developed, so only qualitative predictions are possible. For both short- and long-term increases in the supply rate the neutral clouds should be denser, and the electron temperature lower. The ion density remains fairly constant. Collisions and charge exchange will become increasingly important, so high-speed jets and directional features should become more pronounced. Without a full mathematical description it is difficult to appraise this stability mechanism critically. This mechanism does offer a solution to the torus "energy crisis" described by Shemansky (1988). He maintains that an additional source of energy (such as charge exchange, enhanced in this scenario) is required to power the torus; it remains to be seen if the amount of energy supplied is sufficient.

Atmospheric Buffering In this scenario, Io's exobase level strikes a balance between the supply from the surface (or volcanoes) and the losses from the top of the atmosphere. Increased volcanic activity, for example, may raise the exobase level, but a higher plasma flux will lower it. Johnson and McGrath (1987) have suggested this mechanism informally, but no calculations have been performed. As discussed in the section titled Overview of the System, the supply rate to the neutral clouds (and torus) depends linearly on the sputtering flux and on the cube of the exobase radius. The supply rate, then, is very sensitive to the exobase level.

Stability is again achieved by controlling the supply rate. At first, a rise in the neutral supply rate increases the neutral and ion densities. But the increased sputtering flux would erode the atmosphere, lowering the exobase and decreasing the supply rate. Note that the exobase must lie above the surface for this mechanism to function. If the exobase lies near the surface, a different mechanism is required. R. E. Johnson (1988) has suggested that a partially thick atmosphere might modulate the incident flux to the surface, and thereby limit both the atmospheric content and the supply rate.

This stability mechanism is difficult to criticize because it has no quantitative basis; the arguments are sound but the magnitude of the effects may not be sufficient to provide stability. Considerable work is required before it can be judged in a satisfactory way.

Corotation Breakdown The supply of ions to the torus (also called the mass-loading rate) causes the Io torus to lag behind corotation slightly, and this lower velocity in turn reduces the mass-loading rate. The observed corotation lag of several percent is due to the finite ability of the jovian magnetosphere to accelerate freshly created ions. A very large mass-loading rate reduces the speed at which ions impact Io; this lowers the sputtering flux, the sputtering yield per incident ion, and the energy input per ionization (or charge exchange). All of these effects serve to lower the ion supply rate and return the system to equilibrium.

Again, detailed predictions are not possible since the mechanism has only been qualitatively examined. The primary response to both temporary and long-term increases in the mass-loading rate is a decrease in the speed of the plasma. The plasma temperature will also be lower, but without further calculations it is impossible to determine how the ion and neutral densities will change. Obviously this mechanism must be studied more fully before its importance to the stability problem can be addressed. Preliminary calculations by Huang and Siscoe (1987b) suggest that the current value for the mass-loading rate is several orders of magnitude below the threshold for this effect. These calculations use many of the simplifications of the centrifugally driven diffusion model, so further examination of the corotation breakdown mechanism is required.

Atmospheric Shielding

The corotating plasma might not impinge directly on the Io atmosphere. The plasma will be deflected (fig. 46) if there are intrinsic magnetic fields, a conducting ionosphere, or electric fields induced by ionization or

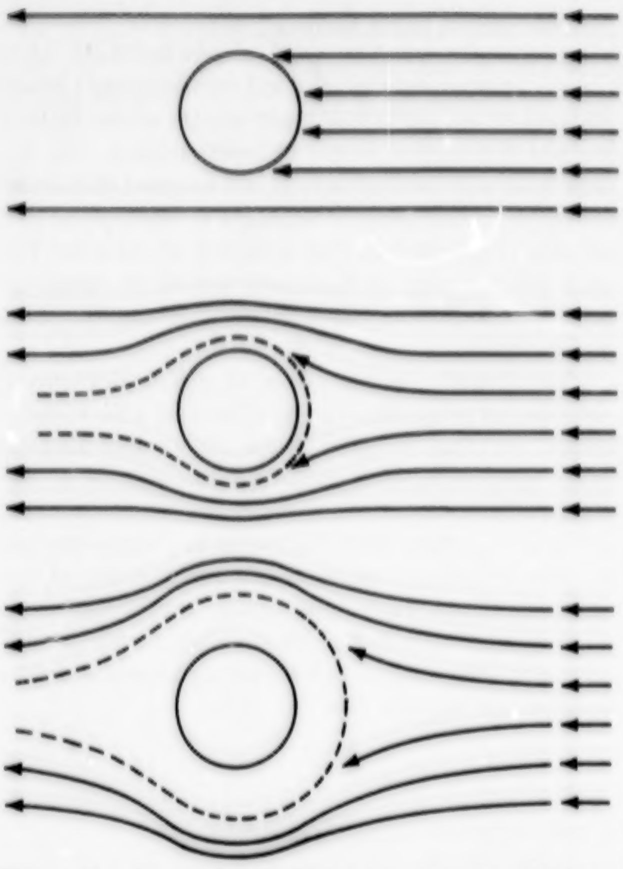

Figure 46. Plasma flow field for various amounts of flow deflection. The plasma can be diverted by an intrinsic magnetic field, a conducting ionosphere, or local electric fields.

charge exchange. Evidence for a deflection of this nature was obtained by the Voyager plasma science experiment (Barnett, 1986). If the flow is held off of Io's atmosphere, the supply to the torus will be determined by the upward flux of atoms and molecules from below the shielded region. For example, thermal escape may control the population of neutrals exposed to the plasma. Thus, as shown in figure 45c, the supply rate will be only weakly dependent on (or conceivably independent of) of the incident corotating flux. The stability problem vanishes: The neutral clouds and torus are driven by escape rates from Io that do not depend on conditions in the torus. Transient ion or neutral events should clearly have little effect on the system. Secular changes, such as an increase in volcanic activity, could affect the level of plasma deflection and/or the escape rate, thereby leading to variations in the supply to and densities of the neutral clouds and torus. The level of change will depend on the physics of the plasma deflection, which is uncertain at present. This scenario cannot be critically appraised without a better understanding of the interaction of the plasma flow and the atmosphere and/or surface. It is appealing, however, since it cleanly explains the stability of the torus system, and the lack of large variations in the sodium cloud.

Stability Summary

It is remarkable that no consensus has emerged on an issue as fundamental as the stability mechanism for the torus, and the diversity of competing idea suggests that no agreement is forthcoming. The correct explanation may not even be on the current list. Each model discussed here requires a considerably more realistic and rigorous treatment, synthesizing the state of knowledge of surface, atmospheric, and magnetospheric physics, and in particular the interaction of the plasma with Io's atmosphere. Each model must be developed sufficiently to make predictions about the individual components (especially the observable components) of the system: the dense atmosphere (if any), the neutral corona, the extended neutral clouds, and the plasma torus. Until this analysis is complete, it is difficult to directly compare predictions of the different models.

One contributing cause to the slow development of stability models is the general lack of data that adequately describe a departure from equilibrium. Observations must capture the full context of the state of the system, at minimum near simultaneous measurements of the neutral and ion densities. A few examples of this essential type of observational coverage do exist. In 1976, for example, the data of Murcray and Goody (1978) and Goldberg (1987) indicate the shape and intensity of the sodium cloud are consistent with the long-term average state of the cloud. Yet Trauger (1984a) reports a substantial difference in the torus density near Io between 1976 and subsequent times. The ion torus was apparently quite different in density and/or temperature; the proposed models of the feedback mechanism are insufficiently developed to compare with this unusual situation in 1976.

CONCLUSIONS AND DISCUSSION

All of the important processes affecting the Io atmosphere and neutral clouds are strongly time-variable, with time constants ranging from hours to years. The study of neutrals near Io has profited dramatically from observations of the changing state of the sodium cloud, allowing remote sensing of the clouds and plasma that would not have been possible in a more constant system. Opportunities abound for further applications of the use of time-variable phenomena in exploring the Io torus system. The conclusions reached below are constrained by two fundamental limitations: (1) we do not know to what extent the plasma is altered or diverted by Io and its atmosphere and (2) we do not know how the process that releases sodium from the surface is related to the process that releases SO_2.

Three widely different atmospheric models have been suggested, and each has its own characteristic variations. Even though the subsolar surface density differs by four orders of magnitude between models, the difference in supply rate to the neutral clouds among models is closer to one order of magnitude, and the time variations within a model may be even smaller. Such differences are at the limit of detectability. The variabilities for the most part have different characteristic time scales: The sputtered corona should show systematic variabilities with periods of 6.5, 13, and 42 hours; the sublimated atmosphere should be driven primarily at 42 hours; and the volcano-generated atmosphere should vary sporadically on a time scale of days to months.

The strongest observational result is the fairly constant level of sodium emission over periods of days to years. This single fact must be accounted for in any atmospheric model and allows limits to be placed on the variations in proposed atmospheres. Large changes in the surface density of Io's atmosphere (determining whether the atmosphere is collisionally thick, and where the exobase is) lead to an unacceptably large sodium cloud variation; if volcanoes are currently driving the exobase level, then the eruption rate has probably endured for at least the 15 years since the discovery of the sodium cloud. Strong variations on the time scales of days to weeks are not observed: Either the exobase level is not strongly dependent on individual volcanic eruptions, or the sodium supply is somehow independent of these eruptions.

Perhaps the most valuable contribution variability analysis can provide is information on the diurnal structure of the Io atmosphere. Since it is virtually impossible to directly measure Io's nightside atmosphere from the Earth, the variability of the neutral clouds may be our best clue. The observed east-west intensity asymmetry of the sodium cloud has been alternately interpreted as evidence for an asymmetric, sublimated atmosphere, or a more uniform global atmosphere affected by an electric field across the magnetosphere. Only combined advances in theory, observation, and laboratory measurement will resolve this question.

The stability of the feedback loops in the torus has effectively been taken for granted over the years. This luxury can no longer be afforded, now that our understanding of the individual components of the system has revealed their complex interdependence. Our review of stability mechanisms is not intended to answer the problem, but rather to highlight it. None of the five scenarios presented can be accepted as it stands, but each demonstrates an important link of the interconnections of the atmosphere, neutral clouds, and plasma torus.

The debate over the nature of the Io atmosphere and the torus-stabilizing mechanism will remain heated for years to come. Observations that attempt direct measurements of important quantities (e.g., the atmospheric column abundance) are clearly needed, but further studies of the time-variable phenomena are a powerful indirect means of answering many of the same questions. Each atmospheric model and each stability mechanism has its own characteristic response to long- and short-term perturbations and may be identified through them.

UNRESOLVED PROBLEMS AND FUTURE WORK

The rich variety and incisive nature of variable phenomena in the atmosphere and neutral clouds warrant a healthy and deliberate monitoring, data reduction, and analysis program. This must be supported by corresponding advances in theory and laboratory work.

Observations

In recent years, observations of the sodium cloud have used advanced instrumentation to address small, well-defined problems. Instrumentation has improved dramatically since the systematic observing programs of the 1970s; application of the same effort with current equipment would provide a vastly more powerful data set. Further measurements of the east-west intensity asymmetry in the cloud are required, with sufficient coverage to determine the effect of magnetic longitude at all orbital longitudes. A concerted effort should be applied to a determination of the orbital longitudes of maximum and minimum sodium brightness; in both proposed asymmetry explanations, supply or loss is maximized at orbital elongation, so the phase lag of the density modulation may be revealing. Systematic coverage will also provide the best measurements of any long-term variability, especially if it is obtained with a fixed instrument configuration.

The mutual eclipses of 1991–1992 provide another opportunity to study the near-Io atmosphere at subarcsec resolution. The radial profile of sodium in the corona is straightforward to measure (Schneider et al., 1987); if enough eclipses are observed, orbital and magnetic longitude effects should be measurable.

Ultraviolet observations provide our best clue about S and O in the vicinity of Io. Observations with IUE (Ballester et al., 1987) should continue, with particular attention to quantifying and explaining any differences between the upstream and downstream hemispheres. The implied possibility of bright visible O auroras (5577 Å, 6300 Å) on Io should be explored. The UV capabilities of the Hubble Space Telescope will be even better suited to address a number of fundamental issues concerning Io's atmosphere. The improved instrumentation and high spatial resolution will permit an accurate mapping of the O and S emissions in Io's vicinity, and their orbital asymmetries. Unambiguous measurements of SO_2 in the atmosphere may be possible. Other Earth-orbital facilities may complement Space Telescope's capabilities.

When feasible, observations of neutral species should be carried out in conjunction with observations of the ionized species; the plasma context is required for correct interpretation of neutral measurements. It has recently become possible (Smyth and Combi, 1988b) to combine the model results from the few existing data sets containing both ion and neutral measurements. This type of data is extremely powerful for deciphering the interaction of the plasma torus and the neutral clouds.

It is critical not to overlook the wealth of existing observations that lies unreduced and unpublished. The power and convenience of modern image processing systems make the task of reduction much more manageable than when the data were taken. The hundreds of unreduced images and spectra are important not only in their own right but also in completing the timeline of sodium cloud behavior over the past decade.

Theoretical Work

We urge a more thorough and uniform development of theoretical models of the atmosphere and of the stability mechanisms to the point of detailed predictions for the atmosphere, corona, neutral clouds, and plasma torus. Our ability to measure changes in the volcanic activity is constantly improving (see Howell and Sinton, this volume), as are our capabilities for detecting small changes in the neutral clouds and plasma torus. How will the system respond to a doubling of the volcanic eruption rate? The lack of a unified theory to explain the combined variations must be addressed. The most difficult link in such a theory is interaction of the corotating plasma with Io's atmosphere. Does the plasma impinge directly on Io's surface or exobase? What causes the flow to stand off of Io, and how might it respond to variable volcanism? What determines the supply rate from Io?

Sodium's easy visibility has been a blessing and a curse, allowing easy measurements of a very minor constituent. Sodium observations tell us little of the atmosphere as a whole if it is released from the surface by totally different means than sulfur and oxygen. What forms may sodium take on Io's surface, and what are the implications for the sputtering process? What is the relative abundance of sodium compounds in the surface and atmosphere? Why have sodium and potassium survived generations of recycling of Io's surface? Does sodium play a role in the thermodynamics of the volcanic eruptions?

Laboratory Work

We have only begun to understand Io's surface and the role it plays in feeding the atmosphere and torus. Further sputtering experiments are called for, employing substances more closely resembling those expected on Io. Sodium-bearing compounds such as Na_2S and NaS_x are of particular interest. Hapke (1986) has recently suggested a mixture of polysulfur oxides, basalt, S_2O, and SO_2, and the sputtering properties of these should be determined. Surface roughness and porosity may also affect the sputtering process, and recent experiments (Nash, 1987; Nash and Moses, 1987) suggest that sulfur deposits may be very filamentary.

Our ability to measure UV emissions from Io has exceeded our ability to interpret them. Laboratory estimates of cross sections for electron-impact excitation, particularly on SO_2 and its byproducts, would greatly aid the interpretation of UV spectra. The advent of the greater resolution and sensitivity of the Hubble Space Telescope will certainly amplify this problem.

References

Ballester, G. E. (1987). Personal communication.

Ballester, G. E., H. W. Moos, P. D. Feldman, D. F. Strobel, M. E. Summers, J.-L. Bertaux, T. E. Skinner, M. C. Festou, and J. H. Lieske (1987). Detection of neutral oxygen and sulfur emissions near Io using IUE. *Astrophys. J.* 319:L33–38.

Barbosa, D. D., and M. G. Kivelson (1983). Dawn-dusk electric field asymmetry of the Io plasma torus. *Geophys. Res. Lett.* 10:210–213.

Barnett, A. S. (1986). In situ measurements of the plasma bulk velocity near the Io flux tube. *J. Geophys. Res.* 91:3011–3019.

Baumgardner, J., M. A. Moreno, G. Schubert, and M. G. Kivelson (1987). Two classes of volcanic eruptions and their corresponding atmospheres on Io. *Bull Am. Astr. Assoc.* 19(3): 856.

Bergstralh, J. T., J. W. Young, D. L. Matson, and T. V. Johnson (1977). Sodium d-line emission from Io: A second year of synoptic observations from Table Mountain Observatory. *Astrophys. J.* 211:L51–55.

Brown, R. A., and N. M. Schneider (1981). Sodium remote from Io. *Icarus* 48:519–535.

Brown, R. A., and Y. L. Yung (1976). Atmosphere and emissions of Io. In *Jupiter* (T. Gehrels, ed.), pp. 197–225. Univ. of Arizona Press.

Brown, R. A., C. B. Pilcher, and D. F. Strobel (1983). Spectrophotometric studies of the Io torus. In *Physics of the jovian magnetosphere* (A. J. Dessler, ed.), pp. 197–225. Cambridge Univ. Press.

Chrisey, D. B., R. E. Johnson, J. W. Boring, and J. A. Phipps (1987). Ejection of sodium from sodium sulfide on the surface of Io. Submitted to *Icarus*.

Eviatar, A. (1987). Volcanic control of the Io atmosphere and neutral plasma torus. *J. Geophys. Res.* 92:8800–8804.

Fanale, F. P., W. B. Banerdt, L. S. Elson, T. V. Johnson, and R. W. Zurek (1982). Io's surface: Its phase composition and influence on Io's atmosphere and Jupiter's magnetosphere. In *The Satellites of Jupiter* (D. Morrison, ed.), pp. 756–781. Univ. of Arizona Press.

Goertz, C. K. and W.-H. Ip (1984). A dawn-to-dusk electric field in the jovian magnetosphere. *Icarus* 32:179–185.

Goldberg, B. A. (1987). Private communication.

Goldberg, B. A., G. W. Garneau, and S. K. LaVoie (1984). Io's sodium cloud. *Science* 226:512–516.

Hapke, B. A. (1986). The surface of Io: A new model. *Bull. Am. Assoc.* 18(3): 774.

Huang, T. S., and G. L. Siscoe (1986). Stability of the Io torus. *J. Geophys. Res.* 91:10163–10166.

Huang, T. S., and G. L. Siscoe (1987a). Types of planetary tori. *Icarus* 70:379–382.

Huang, T. S., and G. L. Siscoe (1987b). Corotation lag limit on mass-loss rate from Io. *Astrophys. J.* 319:1003–1009.

Ip, W.-H., and C. K. Goertz (1983). An interpretation of the dawn-dusk asymmetry of UV emission from the Io plasma torus. *Nature* 302:232.

Johnson, R. E. (1988). Book in preparation.

Johnson, R. E., and M. A. McGrath (1987). Personal communication.

Johnson, T. V., and D. L. Matson (1989). Io's tenuous atmosphere. In *Atmospheres* (S. Atreya, ed.). Univ. of Arizona Press, in preparation.

Kliore, A., G. Fjeldbo, B. Siedel, D. Sweetman, T. Sesplaukis, and P. Woiceshyn (1975). Atmophere of Io from Pioneer 10 radio occultation measurements. *Icarus* 24:407–410.

Kumar, S. (1985). The SO_2 atmosphere and ionosphere of Io: Ion chemistry, atmospheric escape, and models corresponding to the pioneer 10 radio occultation measurements. *Icarus* 61:101–123.

Kumar, S., and D. M. Hunten (1982). Atmospheres. In *Satellites of Jupiter* (D. Morrison, ed.), Tucson. Univ. of Arizona Press.

Lanzerotti, L. J., W. L. Brown, W. M. Augustyniak, R. E. Johnson, and T. P. Armstrong (1982). Laboratory studies of charged particle erosion of SO_2 ice and applications to the frosts of Io. *Astophys. J.* 259:920.

Linker, J. A., M. G. Kivelson, M. A. Moreno, and R. J. Walker (1985). Explanation of the inward displacement of Io's hot plasma torus and consequences for sputtering sources. *Nature* 315:373–378.

Matson, D. L., B. A. Goldberg, T. V. Johnson, and R. W. Carlson (1978). Images of Io's sodium cloud. *Science* 199:531–533.

Matson, D. L., and D. Nash (1983). Io's atmosphere: Pressure control by regolith coldtrapping and surface venting. *J. Geophys. Res.* 88:4771–4783.

McEwen, A. S., and L. A. Soderblom (1983). Two classes of volcanic eruptions on Io. *Icarus* 55:191–217.

McEwen, A. S., L. A. Soderblom, T. V. Johnson, and D. L. Matson (1987). The global distribution, abundance and stability of SO_2 on Io. In preparation.

McGrath, M. A. (1988). Ph.D. dissertation, Univ. of Virginia.

McGrath, M. A., and R. E. Johnson (1987). Magnetosphere plasma sputtering of Io's atmosphere. *Icarus* 69:519–531.

Moreno, M. A., G. Schubert, J. Baumgardner, and M. G. Kivelson (1987). Volcanic eruptions and the atmosphere of Io. In preparation.

Morgan, J. S. (1985). Temporal and spatial variations in the Io torus. *Icarus* 62:389–414.

Morgan, J. S., and C. B. Pilcher (1988). Personal communication.

Murcray, F. J., and R. M. Goody (1978). Pictures of the Io sodium cloud. *Astrophys. J.* 226:327–335.

Nash, D. B. (1987). Sulfur in vacuum: Sublimation effects on frozen melts, and applications to Io's surface and torus. *Icarus* 72:1–34.

Nash, D. B., M. H. Carr, J. Gradie, D. M. Hunten, and C. F. Yoder (1986). Io. In *Satellites* (J. A. Burns, ed.), pp. 629–688. Univ. of Arizona Press, Tuscon.

Nash, D. B., and J. I. Moses (1987). More lab results on vacuum weathering of frozen sulfur: Applications to Io. *Bull. Am. Assoc.* 19(3): 855.

Pearl, J., R. Hanel, V. Kunde, W. Maguire, K. Fox, S, Gupta, C. Ponnamperuma, and F. Raulin (1979). Identification of gaseous SO_2 and new upper limits for other gases on Io. *Nature* 280:757–758

Pilcher, C. B., W. H. Smyth, M. R. Combi, and J. H. Fertel (1984). Io's sodium directional features: Evidence for a magnetosphere-wind-driven gas escape mechanism. *Astrophys. J.* 187:427–444.

Richardson, J. D., and R. L. McNutt (1987). Observational constraints on interchange models at Jupiter. *Geophys. Res. Lett.* 14:64–67.

Sandel, B. R. (1985). Displacement of the center of the plasma torus from Jupiter's magnetic dipole. *Bull. Am. Assoc.* 17:695.

Schneider, N. M. (1987). Velocity structure of the Io sodium cloud. *Bull. Am. Assoc.* 19(3): 854–855.

Schneider, N. M. (1988). Sodium in Io's extended atmosphere. Ph.D. dissertation, Univ. of Arizona.

Schneider, N. M., D. M. Hunten, W. K. Wells, and L. M. Trafton (1987). Eclipse measurements of Io's sodium atmosphere. *Science* 238:55–58.

Shemansky, D. E. (1987). Personal communication.

Shemansky, D. E. (1988). Energy branching in the Io plasma torus; the failure of neutral cloud theory. *J. Geophys. Res.* 93:1773–1784.

Sieveka, E. M., and R. E. Johnson (1984). Ejection of atoms and molecules from Io by plasma-ion impact. *Astrophys. J.* 287:418–426.

Sieveka, E., and R. E. Johnson (1985). Non-isotropic coronal atmosphere on Io. *J. Geophys. Res.* 90:5327–5331.

Sieveka, E., and R. E. Johnson (1986). Correction to "Non-isotropic coronal atmosphere on Io." *J. Geophys. Res.* 91:4608.

Sittler, E. C., and D. F. Strobel (1987). Io plasma torus electrons: Voyager 1. *J. Geophys. Res.* 92:5741–5762.

Smyth, W. H., and M. R. Combi (1986). Understanding the escape of material from Io and its role in the planetary magnetosphere. Paper presented at the Second Neil Brice Memorial Symposium, "Magnetospheres of the Outer Planets," September 1–5, 1986, Iowa City, Iowa. *Bull. Am. Assoc.* 16:663–664.

Smyth, W. H., and M. R. Combi (1987). Correlating east-west asymmetries in the jovian magnetosphere and the Io sodium cloud. *Geophys. Res. Lett.* 14(9): 973–976.

Smyth, W. H. and M. R. Combi (1988a). A general model for Io's neutral gas clouds. II. Application to the sodium cloud. *Astrophys. J.* 328:888–981.

Smyth, W. H., and M. R. Combi (1988b). Personal communication.

Smyth, W. H., and M. B. McElroy (1978). Io sodium cloud: Comparisons of models and two dimensional images. *Astrophys. J.* 226:336–346.

Thomas, N. (1986). An explanation of the east-west asymmetry of Io's sodium cloud. *Nature* 322:343–345.

Trafton, L. (1977). Periodic variations in Io's sodium and potassium clouds. *Astrophys. J.* 215:960–970.

Trafton, L. (1980). An explanation for the alternating north-south asymmetry of Io's sodium cloud. *Icarus* 44:318–325.

Trafton, L., and W. Macy (1977). Io's sodium emission profiles: Variations due to Io's phase and magnetic longitude. *Astrophys. J.* 215:971-976.

Trauger, J. T. (1984a). The jovian nebula: A post-Voyager perspective. *Science* 226:337–341.

Trauger, J. T. (1984b). Photometric images of sulfur ions and sodium neutrals in the Jupiter/Io torus. *Bull. Am. Assoc.* 16:712.

Trauger, J. T. (1987). Private communication.

Trauger, J. T., G. Münch, and F. L. Roesler (1980). A study of the jovian [S II] nebula at high spectral resolution. *Astrophys. J.* 236:1035–1042.

Watson, C. C. (1981). The sputter-generation of planetary coronae: Galilean satellites of Jupiter. *Proc. Lun. Planet. Sci. Conf.* 12:1569–1583.

Wolf-Gladrow, D. A., F. M. Neubauer, and M. Lussen (1987). Io's interaction with the plasma torus: A self-consistent model. *J. Geophys. Res.* 92:9949–9961.

7

Time-Varying Orbits and Tidal Heating of the Galilean Satellites

Richard Greenberg
University of Arizona, Tucson

Abstract

The rapid heat loss from Io due to tidal heating would have quickly damped Io's orbital eccentricity were it not for the Laplace resonance with Europa and Ganymede, which continually pumps the eccentricity. Energy for the on-going heat loss must come from Io's orbit, tending to reduce the semimajor axis and accelerate the mean motion n. That orbital evolution is modified by (1) interchange of energy among the resonant satellites and (2) the unknown rate of energy and angular momentum transported from jovian rotation to Io's orbit due to tidal processes in Jupiter. Most physical models of Jupiter suggest the second source of modification would be negligible. In that case, the Io dissipation rate of 7×10^{13} W (McEwen et al., 1985) would correspond to rapid shrinking of Io's orbit at rate $dn/dt \sim (3 \times 10^{-10})\, n\ \mathrm{yr}^{-1}$. Moreover, the system would be evolving outward from deep resonance, with much greater tidal heating only 10^7 years ago (Greenberg, 1987). In contrast, a model with modification 2 sufficient that the system is at an equilibrium depth in resonance (Yoder, 1979) gives orbital expansion at rate $dn/dt \sim -10^{-10}\, n\ \mathrm{yr}^{-1}$. Either value would shift Io-eclipse times by several minutes over the 300 years of observations. From historical data, Goldstein and Jacobs (1986) found dn/dt near the large positive rate above, but I find that result flawed, due primarily to an incorrect radius assumed for Jupiter, as well as aliasing and clock correction problems. Lieske (1987a) finds much slower dn/dt, which implies significant tides on Jupiter, but evolution still outward from resonance, contrary to the equilibrium model. However, Lieske's comparison with Europa's acceleration supports the equilibrium model. This conflict would be resolved, and the equilibrium model preserved, if the typical dissipation rate in Io over the past 300 years were an order of magnitude smaller than the present thermal radiation rate.

INTRODUCTION

The process of tidal heating in the jovian system and orbital evolution of the galilean satellites are intimately interrelated. The orbital resonance among the satellites is responsible for the continuing energy dissipation in Io. That energy comes out of the orbital motion of the satellites.

If the heat flux presently radiating from Io represents the true rate of tidal dissipation, the orbits are changing in significant ways over a couple of important time scales. First, the nature of the resonance itself may have changed significantly over a time short compared with the age of the solar system; through the tidal connection such changes would have had profound influence on the geology and geophysics of the satellites. Second, orbital evolution may be taking place at a rate fast enough to be detected observationally, for example, in the historical record of satellite eclipse times measured over more than three centuries.

Orbital energy loss reduces the size of orbits and, by Kepler's third law, accelerates the orbital motion. Io's acceleration seems to have been quite slow over the past 300 years; in fact, it has probably been negative. This observation could still be consistent with the fast rate of dissipation in Io if energy were added back to Io's orbit due to tidal effects on Jupiter itself. However, when we include observational constraints on Europa's acceleration as well, we find that the observed orbital changes appear to be inconsistent with continuous dissipation at the rate suggested by infrared radiation from Io.

Thus, although the orbital accelerations are slower than might have been expected from the thermal radiation, the implication is very interesting from the point of view of time-varying phenomena: The typical tidal energy dissipation rate in Io over the past 300 years seems to have been an order of magnitude slower than the energy loss from the satellite during the past decade. Very rapid geophysical and geological changes seem to have taken place in this short time. It appears that either the actual dissipation rate has changed by a factor of ten over a few decades, or the dissipation rate has remained constant whereas the radiational release of energy has been sporadic.

In either case, human history has apparently permitted exploration by spacecraft and ground-based instrumentation at an unusually active time for Io. The indication from study of past orbital motion is that Io was much less active when airplanes and telephones were being invented.

This chapter describes the resonant interaction among the galilean satellites, reviews the theory of tidal evolution and how it couples with resonance dynamics, critically analyzes various determinations of acceleration from the historical observational record, and shows how the results of that analysis lead to the implications described above.

THE LAPLACE RESONANCE

The resonance among the galilean satellites Io, Europa, and Ganymede was described and analyzed by Laplace (1805) two centuries ago, but its implications for the physical properties and history of the satellites have only begun to be appreciated in the past decade. The periods of the three satellites are near a ratio of 1:2:4, so that the effects of mutual perturbations are enhanced by repetitive configurations.

Consider the satellites' motion by pairs. Europa's period is close to twice as long as Io's. Equivalently, the combination of their mean motions, $n_1 - 2n_2 \equiv \nu$, is much smaller than either mean motion (subscripts 1, 2, and 3 refer to Io, Europa, and Ganymede, respectively). Although $n_1 \sim 200°/\text{day}$ and $n_2 \sim 100°/\text{day}$, ν is only 0°.74/day. If the ratio of periods were exactly 1:2, mutual conjunctions of the two satellites would repeatedly occur at the same longitude, an effect that enhances perturbations. In fact, the longitude of conjunction for this pair of satellites migrates slowly at the rate ν.

Similarly, the Europa-Ganymede pair is also near a 1:2 ratio. Moreover, the quantity $n_2 - 2n_3$ equals exactly the same small value ν as for the Io-Europa pair. In other words, the conjunction longitude for Europa-Ganymede migrates at the same rate as for Io-Europa. Therefore the angle ϕ between the two longitudes of conjunction is fixed. The value of ϕ is observed to be 180°.

Because both $n_1 - 2n_2$ and $n_2 - 2n_3$ equal the same small quantity ν, we have the Laplace relation among mean motions:

$$n_1 - 3n_2 + 2n_3 = 0.$$

Integrating the Laplace relation yields the following expression in terms of orbital mean longitudes λ:

$$\lambda_1 - 3\lambda_2 + 2\lambda_3 = \phi,$$

where ϕ is the same constant angle defined above.

The enhanced gravitational perturbations of this resonance have two important effects: First, they maintain ϕ at the stable value 180°. Laplace first demonstrated this stability by showing that $d^2\phi/dt^2$ is proportional to sin ϕ. Second, the resonance forces and maintains significant eccentricities, especially for Io and Europa (0.004 and 0.01, respectively). These forced eccentricities are approximately proportional to $1/\nu$. Remember, ν is a measure of how close the system is to exact resonance: The closer ν is to zero, the closer the ratio of periods would be to exactly 1:2:4, and the larger would be the forced eccentricities.

TIDAL EFFECTS

The eccentricities forced by the oribital resonance are responsible for the tidal working of the bodies of satellites, and the consequent dissipative heating that produces the dramatic volcanism on Io and possibly affected the geophysics of Europa as well (Peale et al., 1979). The bodies are worked because the tidal potential is continually changed, relative to the body of each satellite, as the satellite moves in its eccentric orbit. It is changed in two ways, each of which gives a comparable contribution to the tidal heating: (1) The amplitude of the tidal potential oscillates as the satellite moves between apojove and perijove in its eccentric orbit; the amplitude of the equilibrium tide depends very sensitively on the distance from the tide-raising planet. (2) The orientation of the equilibrium tide changes as the angular velocity of the eccentric orbit oscillates (faster at perijove and slower at apojove); an equilibrium tide would always be oriented symmetrically relative to Jupiter, but the sub-Jupiter point moves back and forth on the satellite's surface. These effects keep each satellite out of equilibrium with the tidal potential, so its body is constantly being worked and distorted, and thus heated.

The tides raised on the satellites by Jupiter also affect the orbits. The energy for tidal heating of a satellite comes out of its orbital motion. Orbital energy is proportional to $-(1/a)$, where a is the orbital semimajor axis, so tidal heating tends to make the satellite's orbit shrink. By Kepler's third law, its mean angular velocity (mean motion n) must increase. The rate of this orbital acceleration is

$$\frac{dn}{dt} \propto +a^{-8}\frac{e^2k}{Q},$$

where k and Q (the Love number and tidal dissipation parameter, respectively) are parameters that essentially lump together the unknown geophysical properties that control the energy dissipation rate.

The process of tidal dissipation described above involves oscillations of a satellite's body relative to the tidal potential. The satellite's mean rotation is assumed to be at an equilibrium rate such that there is no net torque exchanged between the orbital and the rotational motion. Even if the satellite rotated at a different rate it would quickly evolve to equilibrium rotation. The angular momentum of a satellite is too small to have much effect on orbital evolution.

With orbital angular momentum h thus conserved, the orbital eccentricity must decrease because

$$h \propto [a(1 - e^2)]^{1/2}.$$

It follows that

$$\frac{de}{dt} \propto -a^{-6.5}\frac{ek}{Q}.$$

The damping of the orbital eccentricity would tend to stop the evolution because dissipation depends on e (and accordingly e appears in the formulae for both dn/dt and de/dt). Were it not for the effect of the Laplace resonance continually pumping the eccentricities of the galilean satellites, any significant tidal heating would have turned itself off long ago.

It is apparent from the above equations that the evolution depends very strongly on distance, a, from the planet, and might be expected to accelerate as a decreases. However, there are two other processes besides the tidal dissipation in a galilean satellite that govern the rate of change of its mean motion. The first is the interchange of orbital angular momentum and energy among the three resonant satellites. And the second is the effect of tides raised on Jupiter by the satellites.

Tides raised on Jupiter exert a torque on each of the galilean satellite's orbits, because the planet rotates faster than their orbital angular velocities. The tidal bulge raised by each satellite is carried somewhat ahead of the direction of the satellite due to Jupiter's rotation and a lag in its response to the instantaneous tide-raising potential. This lag corresponds to energy dissipation within Jupiter. However, because the orientation of the tidal bulge is ahead of the satellite, it pulls the satellite ahead, adding energy and angular momentum to the orbit. In terms of orbital elements, this effect tends to increase a and slow the mean motion:

$$\frac{dn}{dt} \propto a^{-8}\left(\frac{k}{Q}\right)_{\text{Jupiter}}$$

The actual orbital evolution depends on the combination of the effects of tides raised on and by satellites (principally Io, given the strong dependence on a) with the mutual gravitational interactions enhanced by the Laplace resonance.

EVOLUTION OF THE RESONANCE

Relatively small changes in the mean motions n of the galilean satellites can correspond to very significant changes in the small quantity $\nu = n_1 - 2n_2 = n_2 - 2n_3$. Remember, ν describes how close the system is to exact commensurability, so that a very small change in ν can yield very great changes in forced eccentricities, in tidal heating, and in geophysical evolution. Due to the interchange of energy and angular momentum among the three resonant satellites, the variation of each of the three n's is somewhat different from what would be computed from the equations for tidal variation above. The exact variation rates can be derived using the perturbation equations of classical celestial mechanics (Yoder, 1979; Greenberg, 1982) or, more elegantly, by simply invoking energy and angular momentum constraints (see the chapter appendix).

Roughly speaking, if the dominant tidal process were either dissipation in Io or the effect of tides raised on Jupiter by Io, dm/dt would be comparable to dn_1/dt: ν would increase or decrease, respectively. Suppose the former were the case. As ν increases, the system evolves away from exact resonance and the forced eccentricities decrease. Accordingly, the effect of dissipation in Io diminishes, until it is balanced by the opposite effect of tides raised on Jupiter. For any given ratio of tidal dissipation parameters $(k/Q)_{\text{Jupiter}}(k/Q)_{\text{Io}}$ there is a particular value of e_1 (and corresponding ν) at which the system would be in stable equilibrium with respect to changes in ν (Yoder, 1979).

Equilibrium Hypothesis

Yoder (1979) suggested that the system might be in such a stable equilibrium at present. If it is, then the known value of e_1 combined with a measured dissipation rate in Io and the theoretical value of Jupiter's k (0.38 according to Gavrilov and Zarkov, 1977) would yield a value for Jupiter's tidal dissipation parameter Q_J. Most theoretical estimates of the value of Q_J are greater than $\sim 10^7$; it is difficult to find a convincing mechanism that might give faster dissipation (smaller Q_J) in the planet. But the equilibrium hypothesis requires very small values of Q_J indeed. With a dissipation rate in Io barely sufficient to give volcanism, say, 2×10^{12} W, the value of Q_J implied by equilibrium would be 10^6. The original estimate of heating in Io by Peale et al. (1979) was about 2×10^{13} W, which would require even smaller Q_J of 10^5. Now, the most recent estimate of heat flux for Io based on Voyager and Earth-based infrared measurements (McEwen et al., 1985) is 7×10^{13} W $\pm$ 25 percent; with such a dissipation rate in Io, resonance equilibrium would require rapid dissipation in Jupiter as well, with $Q_J \sim (3 \times 10^4)$.

Such small values of Q_J, especially the last one, have been rather difficult to justify in the context of physical models of tidal dissipation within Jupiter. Models of atmospheric dissipation gave values of Q_J from 5×10^{13} to 5×10^7 (Goldreich and Nicholson, 1977; Houben and Gierasch, 1980, respectively). Dermott (1979) suggested that dissipation in Jupiter's core might give $Q_J = 10^6$, but that estimate was changed to 10^7 by Hubbard. If correct, these values argue against the resonance equilibrium idea proposed by Yoder.

Perhaps the strongest constraint on the value of Q_J was noted by Goldreich and Soter (1966). If Q_J were smaller than $\sim 10^5$, then the transfer of energy from Jupiter's spin to Io's orbit would have moved Io well beyond its present jovian distance by now, even if it had started at the Roche limit on Jupiter's surface 4.5×10^9 years ago. In Goldreich and Soter's paper, this limit was only evaluated to an order of magnitude. In order to determine whether the equilibrium model violates this limit, we need to compute it to greater precision. For example, as noted by Schubert (comments at this workshop and in Schubert et al., 1986), Goldreich and Soter used $k_J = 1.5$, rather than the currently accepted value 0.38. I find that correction is partially offset first by a 30 percent correction to their arithmetic and second by an adjustment of the degree to which acceleration is modified by the exchange of orbital energy among the resonant satellites (see the chapter appendix). With these refinements, the lower limit on Q_J becomes 6.5×10^4, over twice the value implied by the equilibrium hypothesis.

Goldreich and Soter did not include the possibility that tidal dissipation in Io could be strong enough to remove significant orbital energy from the satellite; no one had thought of that idea before 1979 (Peale et al., 1979). In principle, this loss of energy could relax Goldreich and Soter's constraint. But as shown in the chapter appendix, if the ratio of dissipation in Io to that in Jupiter is balanced to give $d\nu/dt = 0$ as in the Yoder equilibrium hypothesis, then dissipation in Jupiter still dominates the change in Io's semimajor axis and mean motion. That is why my refined value of the Q_J limit is not very different from Goldreich and Soter's estimate.

Based on these considerations, the equilibrium hypothesis seems inconsistent with the high present heat flux from Io. However, they could be reconciled if the value of Q_J has only relatively recently become small enough to balance, because the constraint by Goldreich and Soter really only applies to the average value of Q_J. The only problem then is to find a physical process that could have permitted slow dissipation for a long time and then reduced Q_J to 3×10^4. In fact, the only physical process so far suggested to give such rapid dissipation would probably be transitory: It involves condensation of helium clouds deep in Jupiter's interior (Stevenson, 1983). The model is highly speculative because it depends sensitively on such unknowns as the amount of helium at the appropriate depth, the density of droplet nucleation sites, and the size of the helium droplets. The phenomenon might be transitory, ending when the helium rains out of the clouds. Although this mechanism could give Q_J as small as 10^2, it is not at all certain whether its time-variability and present value for Q_J fits the requirements of the equilibrium hypothesis, or even whether this speculative process has occurred at all.

Disequilibrium Models

Given all the above difficulties with the equilibrium hypothesis, Greenberg (1980, 1982) suggested that the system may not be in equilibrium at all. If the effect of tides raised on Jupiter is small compared with the known strong effect of dissipation in Io, then the value of ν may simply be increasing. Its present value may be where it happens to be today, and not the result of evolution to stable equilibrium. If ν is increasing, then it must have been smaller in the past; the system would be evolving outward from deep resonance (small ν and large forced eccentricities) toward larger ν and smaller forced eccentricities.

Two possible evolutionary scenarios were proposed by Greenberg (1980, 1982), which both fit a present disequilibrium model. In the first, it is assumed that tides on Io have always dominated the evolution, so that the system has monotonically evolved outward from deep resonance. With the present value of (k/Q) for Io as determined from observation, the system would have evolved from very small ν to its present value of ν in $<10^7$ year (see the chapter appendix; also Yoder and Peale, 1981). Therefore, an implication of this hypothesis is that the system may have started on the other side of exact commensurability ($\nu < 0$), evolved through exact commensurability ($\nu = 0$), and is now on its way out of resonance altogether ($\nu > 0$).

In the second disequilibrium scenario, Io's interior alternately melts and refreezes in a feedback cycle coupled to orbital evolution. When Io melts, the higher amplitude of its tidal distortion allows greater heat production (as described by Peale et al., 1979), so ν can increase. The corresponding decrease in Io's orbital eccentricity then reduces the heating rate, so Io freezes again and the process can reverse and then repeat itself. In this model, the system is presently at a point in the cycle where dissipation in Io dominates ($d\nu/dt > 0$), rather than in the equilibrium state ($d\nu/dt = 0$).

As originally proposed by Greenberg, this episodic scenario was admittedly speculative particularly in its geophysical assumptions, but it did avoid the difficulties with the equilibrium model. It also avoided the somewhat improbable aspect of the simple disequilibrium model that the system must have come through deep resonance very recently compared with the age of the solar system. More recently, Ojakangas and Stevenson (1984, 1986) have shown that the episodic scenario is indeed plausible from a geophysical standpoint.

Yoder and Peale (1981) demonstrated an apparently serious difficulty, however, with any scenario that involves deep resonance in the past. Although analysis to first order in orbital eccentricities had indicated that the Laplace relation is stable for small values of ν as well as the present value (Greenberg, 1981), Yoder and Peale's third-order analysis showed that ϕ is not stable at 180° for ν less than about ⅕ of its present value. For such small ν, eccentricities are sufficiently large that the higher-order terms can destabilize the configuration. In fact, this instability can also be shown with a second-order analysis (Greenberg, 1987).

The present stable configuration of the Laplace relation, with $\phi = 180°$, is also known to be unstable for negative values of ν. There, the resonant system could nevertheless be stable with $\phi = 0°$ (Sinclair, 1975; Yoder and Peale, 1981). Thus, any evolution of the system from negative ν (as in the first, nonepisodic, disequilibrium scenario) would have had to cross the uncharted wilderness of deep resonance, where ϕ is stable at neither 0° nor 180°. Even the episodic heating model would be suspect to the extent that it involves dipping into this "unstable" region.

More recently it has been shown that although ϕ is not stable at either 0° or 180°, it is stable at intermediate values that vary with ν (Greenberg, 1987). In other words, there are stable evolutionary paths in deep resonance, along the ν, ϕ plane, even where $\phi = 0°$ or 180°

is unstable. By stable paths, we mean paths through phase space that are analogous in terms of stability to level paths along the bottoms of valleys; the system is stable at any point along such a path, but it can slowly evolve through the valley. These paths are described in detail by Greenberg (1987). For positive m these paths branch (at a bifurcation point) from the stable line $\phi = 180°$, providing an unbroken evolutionary track for the episodic scenario in which the system periodically dips toward deep resonance (small ν).

EVOLUTION FROM DEEP RESONANCE

Unlike the episodic scenario, the scenario of simple passage through and out of resonance still suffers from two major weaknesses: (1) As discussed under the heading Evolution of the Resonance (and in the chapter appendix), that evolution would have taken place very rapidly; such recent short-lived behavior seems rather improbable. (Note that as discussed above, the equilibrium hypothesis may have similar difficulties.) (2) The rapid evolution means that the system would have had to have come from the other side of exact resonance ($\nu < 0$). Although Greenberg has now demonstrated that there are stable evolutionary paths in deep resonance, the dynamics of passage though the exact resonance ($\nu = 0$) are not yet understood.

Both of these difficulties are avoided, while still retaining the disequilibrium hypothesis, if we adopt the episodic scenario. Dissipation in Io alternately turns on and off, so that rapid recent evolution outward from deep resonance could be interpreted as only part of a periodic cycle. Recall that the advantage of this idea over the equilibrium hypothesis is that it does not require improbably small values for Q_J. On the other hand, the episodic model cannot work for arbitrarily large values of Q_J. If Q_J is much greater than 10^7, the phase of the cycle with Io turned off would last for the age of the solar system—hardly episodic. With $Q_J = 10^7$ that phase would last $\sim 10^9$ years; the probability that we would observe Io during its 10^7-year hot phase would be only 1 percent. Perhaps $Q_J \sim 10^6$ provides an acceptable compromise, being not too far from most jovian models, while giving a reasonable probability (10 percent) in the context of the episodic model for a presently active Io with evolution outward from resonance.

Rapid evolution out of deep resonance provides a mechanism for stimulating the present free eccentricity of Ganymede. Suppose the evolution has progressed from deep resonance ($\nu < 0\overset{\circ}{.}175$/day), through the bifurcation point to its present state $\nu \sim 0\overset{\circ}{.}74$/day. Continuous energy dissipation corresponds to continuous variation of $S\nu$. But for continuous variation of ν there must be a discontinuous jump in ϕ at the bifurcation point. This would have induced free eccentricity superimposed on the forced eccentricity, and this would have happened $\sim 10^7$ years ago (Greenberg, 1987).

Tides raised on a satellite generally tend to damp orbital eccentricity (Goldreich, 1963). For the galilean satellites, the orbital resonance keeps eccentricities up to the forced value, whereas tides damp the free (or oscillatory) component of the eccentricity. The rate of damping is the same as given in the section titled Tidal Effects. For Io with its rapid dissipation, Q/k is effectively <10, so the time scale τ for damping e is $<10^4$ years. Its free eccentricity must be damped shortly after stimulation. For Europa, assuming the reasonable value $Q/k \sim 500$ (Cassen et al., 1982), $\tau \sim 10^7$ years, most of the free e_2 (whether primordial or induced at the bifurcation point) would be damped, consistent with the low present value.

For Ganymede, with the rigidity of ice and $Q \sim 100$, free eccentricity would damp in $\tau \sim 10^8$ years. Even with rigidity an order of magnitude greater than ice (like rock), τ would be less than the age of the solar system. Any primordial free eccentricity would probably have decayed away by now. But if the system has passed through the bifurcation point on its way out from deep resonance, the free eccentricity thus stimulated $\sim 10^7$ years ago would still remain. Thus, a substantial free eccentricity would be expected at present. That state is exactly what is observed. For Ganymede, the free eccentricity is more than twice the present forced component; its value is very close to (and may be a fossil of) the forced value at the bifurcation point.

Similarly, the stimulation of oscillations at the bifurcation point could explain the present free libration of ϕ as well. There could be other ways to explain it, but the present free oscillations in the system are consistent with evolution from deep resonance.

There also are geological and geophysical properties of the satellites that seem consistent with substantially greater heating rates in the past than at present. This evidence also supports the disequilibrium hypothesis with evolution outward from deeper resonance, because in deeper resonance the forced eccentricities, and hence tidal heating rates, for all three satellites would have been enhanced. First, Ganymede with its grooved terrain has clearly undergone greater endogenic evolution than the otherwise similar Callisto. Resonant tidal heating would have contributed to this difference, although the greater radioactive heating of

Ganymede also may have been important (Cassen et al., 1982).

Second, the very smooth surface of Europa suggests a significant tidal heating. Past residence in deep resonance would have allowed melting of a thick water layer, which would have tended to level the thin ice layer above it. Once such melting occurred, it would tend to promote increased dissipation due to the higher amplitude of tidal distortion, and would thus sustain a liquid water layer even as forced e_2 decreased to its present value. If the system evolved from outside resonance (smaller e_2), as in Yoder's hypothesis, melting would probably have been unable to get underway (Cassen et al., 1982).

Third, the removal of sulfur, which is so much in evidence near the surface of Io, from FeS in the interior likely occurred early in the geophysical history, before core formation that would have carried sulfur into the depths. Such removal would have required an early heat source. The extreme tidal heating in deep resonance could have served that purpose.

The disequilibrium hypothesis seems to fit the relevant observable characteristics of the galilean satellite system. It avoids some of the problems with the equilibrium model, especially the need for very rapid tidal energy dissipation in Jupiter. It does require recent passage out of deep resonance. The stable evolutionary paths in deep resonance described in this chapter eliminate a major objection to such models. There remains uncertainty about behavior in very deep resonance. These difficulties are avoided in the episodic model, with present evolution outward from deep resonance representing one phase of periodic evolution. Although the episodic model contradicts the equilibrium hypothesis, it does not necessarily preclude earlier capture into resonance.

MEASUREMENTS OF ORBITAL EVOLUTION

The competing equilibrium and disequilibrium hypotheses make distinct predictions regarding the present rates of orbital acceleration. Greenberg et al. (1986) combined various assumptions about the ratio of dissipation in Io to that in Jupiter, with equations for rates of total orbital energy and angular momentum dissipation in the system, to obtain equations relating orbital acceleration to dissipation in Io. If Io were not involved in a resonance, and if dissipation in Jupiter were negligible, energy dissipation in the satellite at rate $\dot{E}$ would be related to orbital acceleration by

$$\frac{\dot{E}}{E_1} = \frac{2}{3}\frac{\dot{n}_1}{n_1}.$$

Here E_1 is Io's orbital energy (see the chapter appendix). This equation follows from Kepler's third law. Note that both $\dot{E}$ and E_1 are negative. Because Io shares orbital energy and angular momentum with the other satellites by way of the Laplace resonance, this expression must be modified slightly to

$$\frac{\dot{E}}{E_1} = 0.56\frac{\dot{n}_1}{n_1},$$

as derived in the chapter appendix. In that case, with negligible dissipation in Jupiter, the system would be evolving rapidly outward from deep resonance. Now if tidal dissipation in Jupiter is sufficiently great to give the equilibrium hypothesized by Yoder (1979), we have the very different relation

$$\frac{\dot{E}}{E_1} = -1.54\frac{\dot{n}_1}{n_1}$$

(see the chapter appendix; also Greenberg et al., 1986), where $\dot{E}$ still represents dissipation in Io.

For the observed value of $\dot{E}$ (McEwen et al., 1985 and in this volume), the assumption of little dissipation in Jupiter (disequilibrium with evolution outward from deeper resonance) gives $\dot{n}_1/n_1 \sim 3 \times 10^{-10}\,\mathrm{yr}^{-1}$ (from the second equation above). This value is in good agreement with determinations of $\dot{n}_1$ from the historical observational record by DeSitter (1928) and by Goldstein and Jacobs (1986). Goldstein and Jacobs found $\dot{n}_1/n_1 = 4.6 \times 10^{-10}\,\mathrm{yr}^{-1} + 20$ percent. However, Lieske (1987a) finds the value $\dot{n}_1/n_1 = (-7.4 + 8.7) \times 10^{-12}\,\mathrm{yr}^{-1}$ consistent with the negative sign predicted by the equilibrium hypothesis (third equation above) but too slow by more than an order of magnitude. Lieske's value thus implies that dissipation in Jupiter is too slow to maintain Yoder's proposed equilibrium model. Thus, either determination of $\dot{n}_1$ (Goldstein and Jacobs' or Lieske's) combined with the measured Io heat flux indicates disequilibrium, with evolution outward from deep resonance.

The logical solution is summarized schematically in figure 47. The equilibrium hypothesis requires a specific ratio between the tidal dissipation rates (diagonal solid line). The rate of dissipation in Io is known, perhaps, from the heat flux. The intersection of these requirements predicts a dissipation rate in Jupiter. The latter rate is faster than produced by most interior models, with the exception of Stevenson's (1983) helium clouds. The value of $\dot{n}_1$ found by Goldstein and

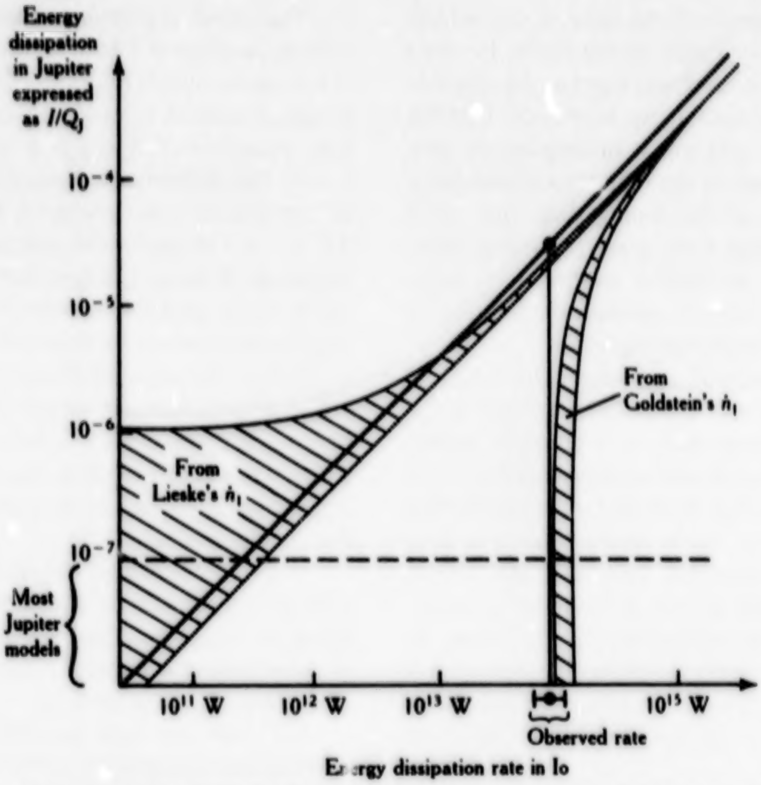

Figure 47. Relationships among tidal dissipation rates in Io and in Jupiter, Io's orbital acceleration $\dot{n}_1$, and the rate $\dot{\nu}$. Observational determination of the thermal radiation from Io (McEwen et al., 1985) is shown, as are the constraints due to the two determinations of $\dot{n}_1$, by Lieske (1987a) and by Goldstein and Jacobs (1986), the latter now shown in this chapter to be spurious. In the equilibrium model, the system is constrained to the diagonal line $\dot{\nu} = 0$. Most models of Jupiter's interior suggest that dissipation is so slow that $\dot{\nu} < 0$, except for Stevenson's (1983) speculative model. Lieske's (1987a) determination of ν shows that the system lies on the $\dot{\nu} = 0$ line, which is inconsistent with his value of $\dot{n}_1$ unless the average dissipation rate in Io has been $<10^{13}$ W over the past 300 years.

Jacobs (1986) is consistent with very little dissipation in Jupiter, and hence evolution outward from resonance. The value of $\dot{n}_1$ found by Lieske (1987a) requires much more dissipation than is given by most interior models, but distinctly less than is consistent with the equilibrium model. Neither determination of $\dot{n}_1$ would be consistent with equilibrium.

In order to resolve the different determinations by Lieske and by Goldstein and Jacobs, I have carefully investigated the data bases and analytical methods of these researchers. This investigation has required exciting detective work, wading through exotic centuries-old data and interviewing remarkable characters.

My personal prejudices were somewhat divided. On one hand, I found the results of Goldstein and Jacobs attractive because they fit the disequilibrium hypothesis so well. (In fact Goldstein and Jacobs' original, prepublication, interpretation of their determination of dn_1/dt had been incorrect, because they did not properly account for the exchange of energy and angular momentum among the satellites. They thought that it did not fit any tidal evolution model well; this gave additional credibility to their result when I showed that their value of dn_1/dt did agree very well indeed with the expected rate given the measured dissipation in Io and the disequilibrium model with negligible dissipation in Jupiter, as shown in figure 47.) On the other hand, Lieske's results were based on a much more extensive data set, on a more complete theoretical model, and on a more conventional method for estimating the clock correction ΔT = ET − UT.

These determinations of acceleration are based on a record of eclipse timings (when satellites enter the shadow of Jupiter) that dates back over 300 years. This datum is recorded in terms of the time of day, which was known quite precisely even in the 1600s. In other words, the rotation of the Earth was used as the clock in timing these events. Of course, we now know that the Earth's rotation is not uniform. It undergoes its own tidal deceleration, as well as significant rotational irregularities. In order to use the timing data, one must relate the rather irregular time scale (universal time, UT) that is based on the Earth's rotation to a more uniform time scale, such as ephemeris time (ET), which is based on planetary ephemerides.

An ideal way to relate UT to ET throughout history would be to compare the computed behavior of an astronomical body whose motion is perfectly understood with the historical record of observations in UT. Any discrepancies could be attributed to nonuniformity of UT. Unfortunately, the body whose motion is best documented in the historical record is the Moon, whose motion is complicated by its tidal deceleration. The latter is reasonably understood by now thanks to modern measurements, and assuming it is reasonably uniform, astronomers can use the Moon's historical record to evaluate UT − ET (Lieske, 1986a; Brouwer, 1952).

Goldstein (1985) introduced a rather unconventional determination of UT − ET based on assumptions about the Earth's rotation, specifically that it decelerates sufficiently uniformly that UT − ET can be derived by extrapolating backward from recent motion. Goldstein attributes differences between his determination of UT − ET and others to some putative error in the lunar theory. More plausibly, it is due to irregularities in the Earth's rotation, which are known to occur. Hence Goldstein's UT − ET is not widely accepted.

Nevertheless, the determination of Io's acceleration by Goldstein and Jacobs was based on that unconventional clock correction, and for that reason their result was suspect (Lieske, 1986d). More recently, Lieske (1987b) has pointed out that the difference in clock corrections could only explain a small fraction of the difference between the two determinations of dn_1/dt.

That result is shown as follows: The shift in longitudinal position of Io due to an acceleration of its motion is given by $0.5(dn_1/dt)t^2$. This expression gives the longitude relative to what it would be at time t if motion was unaccelerated starting at some arbitrary time $t = 0$. The difference between the two determinations of acceleration is about $4.7 \times 10^{-10} n_1$/yr or 3.5×10^{-5} deg/yr², which would give a difference in longitude of about 1.5° over the 300-year interval under study. Such an error in orbital longitude would affect eclipse event times by about 10 minutes. However, the difference between Goldstein's (1985) evaluation of UT − ET and Brouwer's more conventional one is only about 2 minutes for a few hundred years ago, a small fraction of the discrepancy due to differences in dn_1/dt. Apparently, the clock correction is at most a small portion of the problem.

Next, I investigated the method used by Goldstein and Jacobs to evaluate the acceleration. Their method involved comparing the mean motions and longitudes at three different epochs t during the past 300 years. These are shown in table 12.

The first two lines in table 12 show n_1 and L as determined by Goldstein (1975) from the historical data sets shown. The last line gives orbital elements from the theory of Sampson, which was constructed to fit data from the period listed. Goldstein and Jacobs' tabulation of Sampson's n_1 has a confusing typographical error, but they probably used the correct value shown here in their analysis. The error on the seventeenth-century n_1 is +0.°000016/day and on the "Innes" n_1 is +10–6°/day (Goldstein, 1975).

Exactly how Goldstein and Jacobs derived dn_1/dt is not very clear in their paper, but it is possible to follow their general approach and get to the same answer in a way that reveals some very serious shortcomings. First, compare the seventeenth-century data with the Innes values. The seventeenth-century values predict that at the Innes epoch 88400 days later,

$$L = L_{17thC} + n_{17thC} \times 88400 = 234^{\circ}\!.14.$$

Table 12.

Data set (name)	**Dates of observations (years)**	**n_1 (degrees/day)**	**Longitude, L (degrees)**	**t (Julian)**
Picard-Roemer	1668–1678	203.4889192	293.675	2332540
Innes	1908–1928	203.48895936	237.2752	2420940
Sampson	1878–1906	203.48895422	142.5999	2415020

Using Goldstein's acceleration of the UT clock,

$$\text{Time correction} = 4 \times 10^{-13}\ \text{day}^{-1}\, t^2 = 0.0031\ \text{day},$$

which gives a longitude correction $0.0031 n_1 = 0\overset{\circ}{.}63$. Thus the seventeenth-century data would predict $L = 234.14 + 0.63 = 234\overset{\circ}{.}77$ at the Innes epoch. Compare that with the actual L at the Innes time, $237\overset{\circ}{.}28$ from table 12. Suppose this difference of $2\overset{\circ}{.}51$ were due to acceleration of Io. In that case,

$$0.5\left(\frac{dn_1}{dt}\right) \times (88400\ \text{days})^2 = 2\overset{\circ}{.}51 \Rightarrow \frac{dn_1}{dt} = 11.5 \times 10^{-10}\,\frac{n_1}{\text{yr}}.$$

This result is somewhat more than twice the acceleration found by Goldstein and Jacobs, and nowhere near Lieske's result. This calculation seems to confirm roughly the Goldstein and Jacobs value.

However, there are two points to notice about this result. First, it strongly depends on the seventeenth-century value of n_1. If we take into account the uncertainty in the determination given by Goldstein (1975) and quoted above, we obtain an uncertainty in dn_1/dt of $+6 \times 10^{-10}\ n_1/\text{yr}$, six times greater than the formal error quoted by Goldstein and Jacobs. The second point is that we have not used the value of n_1 for the Innes epoch in this calculation. We can use it by simply reversing the above procedure and projecting the Innes-epoch results backward to the seventeenth-century epoch for comparison with the longitude at that time. That calculation gives $dn_1/dt = -1.1 \times 10^{-10}\ n_1/\text{yr}$, a value much closer to Lieske's result, and much more precise thanks to the smaller uncertainty of the Innes mean motion.

If we average the result obtained by projecting the seventeenth-century values forward to the Innes epoch (11.5×10^{-10}), with that obtained by projecting the Innes values backward (-1.1×10^{-10}), we get $5 \times 10^{-10}\ n_1/\text{yr}$, Goldstein and Jacobs' value. This averaging is essentially equivalent to their procedure. However, I have shown that their fairly large positive value depends on the very uncertain seventeenth-century n_1. Certainly, the inconsistency between the two results (projecting the seventeenth-century motion forward and the Innes motion backward) shows that the uncertainty is very large.

Goldstein and Jacobs also compared the seventeenth-century motion with the behavior at the Sampson epoch. When I repeat the procedure described above for these two epochs, I find $dn_1/dt = 12.9 \times 10^{-10}\ n_1/\text{yr}$ and $-2.8 \times 10^{-10}\ n_1/\text{yr}$, for the forward and backward projection, respectively. Just as before, the forward projection gives a fast positive acceleration and the backward projection gives a slower negative acceleration. Again, the average of these two values gives the result reported by Goldstein and Jacobs. However, all the evidence for a positive value depends on the seventeenth-century mean motion. I have shown that both the Innes and the Sampson motions, projected back to the seventeenth-century longitude, imply small negative acceleration.

The above analysis suggested that there might be something wrong with Goldstein and Jacobs' seventeenth-century mean motion. Careful examination of Goldstein's (1975) solution for the seventeenth-century mean motion shows two significant errors.

The first comes from Goldstein's evaluation of the "great inequality" in Io's motion. In celestial mechanics the term *inequality* refers to the oscillatory acceleration and deceleration of angular velocity during each period of an eccentric orbit; it is the difference between the true orbital longitude and the "mean longitude" computed by assuming uniform motion ("mean motion"). For Io, the great inequality refers to the periodic oscillation in longitude that corresponds to the forced eccentricity, the effect of the Laplace resonance. The perijove of the forced eccentric motion is aligned with the longitude of Io's conjunction with Europa. Therefore, Io moves fastest at conjunction and is farthest ahead of mean motion 90° after conjunction, and farthest behind mean motion 90° before conjunction. The amplitude of this oscillation, determined by the mass of Europa and the value of ν, is $0\overset{\circ}{.}47$; its frequency is simply $n_1 - \nu$, approximately the same as n_1; its phase is well defined by the longitudes of Io and Europa.

Rather than use the known amplitude and phase of the great inequality, Goldstein chose to adjust these along with the unknown parameters (mean motion and longitude at epoch) in his least squares fit to the seventeenth-century data. His fit gave an amplitude of $0\overset{\circ}{.}4936$ and a phase 3° off the correct known values. This error introduces an artificial oscillation of $\sim 0\overset{\circ}{.}02$ in Io's longitude. Such an error might be expected to have negligible effect on the mean-motion determinations, because it has such a short period compared with the ten-year interval of observations (1668–1678).

However, there is an unfortunate aliasing effect due to the way that the measurements were made. Remember, all these data are from eclipse measurements, so during a given observation season (the few months before and after opposition of Jupiter with respect to the

Earth) all longitude determinations were made on one side of Jupiter, and at a roughly constant phase of the great inequality. This longitude varies slowly over the course of Jupiter's orbital period, which is comparable to the interval of observation. Thus an error of ~0°.02 per 10 years is not out of the question, and would be quite significant considering that an error in n_1 of only about 10^{-5} deg/day would explain Goldstein and Jacobs' putative acceleration value. When this correction is made, it introduces a slope to the residuals that corresponds to an increase in the seventeenth-century n_1 of about 3×10^{-6} deg/day, as shown in figure 48.

I have found an even more serious error in Goldstein's (1975) determination of n_1 from the seventeenth-century data. Apparently he used an equatorial radius for Jupiter of 70,650 km, instead of the known, correct value of 71,400 km. It seems that he chose this value in order to minimize the residuals of his orbital fit to the eclipse data, although the exact method is not clear and the reason for rejecting the known value was not given.

The error in planetary radius should not have been a serious problem if the data set included both immersion and emersion eclipse events distributed well over time. These data would have canceled any systematic errors in longitude due to the radius error.

However, inspection of the data set used by Goldstein shows that most of the data in the first half of the decade of observations (1668–1673) were immersion events, whereas most in the second half were emersions (figure 49; also see Goldstein's, 1975, table I). This means that, with his too small radius, Goldstein thought Io was ahead of its correct position early in the decade, and behind late in the decade. The 750 km error in radius corresponds to about 0°.1 in longitude. When this correction is made to Goldstein's residuals as shown in figure 48c, I find a least-squares slope that corresponds to an increase in n_1 of 10^{-5} deg/day. This correction, combined with the significant range of uncertainty in the evaluation of n_1, means that the seventeenth-century mean motion can be projected forward without acceleration to fit later longitudinal positions.

I conclude that the acceleration determined by Goldstein and Jacobs is spurious. But is Lieske's value any better? As far as I can tell it is, although I have not checked all the details of his work. The theory certainly seems more complete and accurate. Also it is based on a much more extensive data set (Lieske, 1986b, c), including for example six times as much seventeenth-century data, which would help eliminate some of the

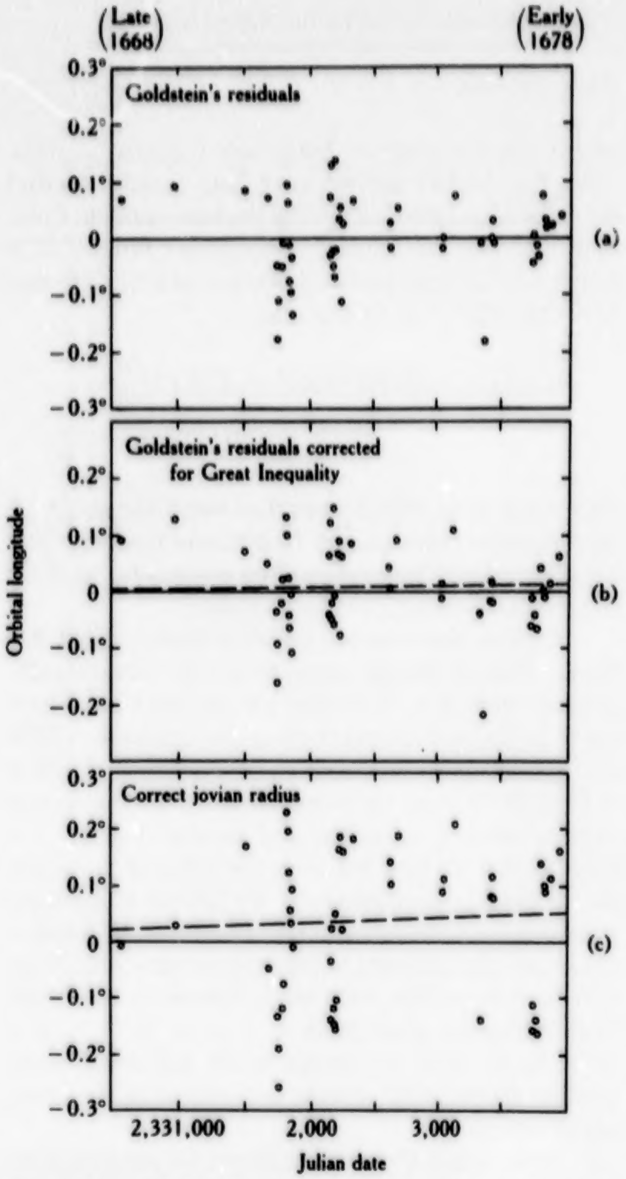

Figure 48. (**a**) Residuals in the eclipse timing data given Goldstein's (1975) solution for orbital acceleration. He gave residuals in terms of event time; here they are converted to orbital longitude. (**b**) Goldstein's residuals adjusted to correct effect of "great inequality," Europa's short-period perturbation. Here the correct mass and orbital position of Europa is used. The straight-line fit (*dashed line*) shows a slight correction to the seventeenth-century mean motion. (**c**) The additional correction of using the true radius of Jupiter further changes the residuals as shown. The straight-line fit shows a correction of 10^{-5} deg/day compared with the mean motion given by Goldstein for that epoch. Note that scatter is greater in (**c**) compared with (**a**), which is why Goldstein selected a small radius for Jupiter. However, the radius of Jupiter is so well known by other measurements that Goldstein's choice is not justified.

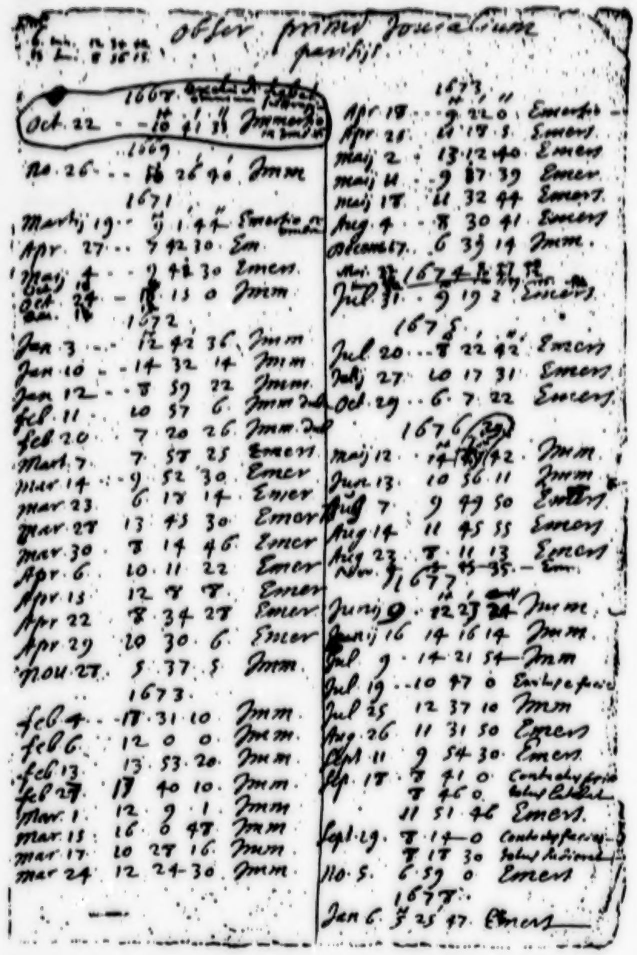

Figure 49. Roemer's eclipse data from 1668 to 1678 at Observatoire de Paris. "*Imm*" shows Immersion or disappearance events; "*Emer*" shows Emersion or reappearance events. Reproduced from Nielsen (1944).

problems that Goldstein had. Therefore, it seems reasonable to conclude that Lieske's value for the acceleration of Io is correct: It is slow and probably negative (i.e., Io is spiraling outward from Jupiter).

DISCUSSION

The conclusion that Lieske's value of the acceleration is the preferred one has important implications. I have already discussed how Lieske's result that $dn_1/dt < 0$ still does not indicate enough tidal dissipation in Jupiter to counteract the increase in ν due to dissipation in Io. Lieske's value still indicates a system evolving towards larger ν, rather than an equilibrium condition. The equilibrium condition could only have held if the true energy dissipation rate in Io, time averaged over the past 300-year orbital observation history were at least an order of magnitude less than the value implied by the thermal flux.

In fact, there are two aspects of Lieske's work that suggest the system has indeed been in equilibrium ($\nu = 0$) on average over the past 300 years. First, although his value for Io's acceleration supports disequilibrium, it requires a value for Q_J comparable to (but not quite as small as) the value needed for equilibrium. It seems rather a coincidence that the value should be so close to the surprisingly small value needed for equilibrium, but not quite be there.

Second, Lieske has also determined limits on the acceleration of Europa, which, when combined with that for Io, show that $d\nu/dt$ is in fact very small, less than $0.5 \times 10^{-11}\ n_1$/yr in absolute value. In terms of the diagram in figure 47, this means that the system lies within the width of the diagonal equilibrium line ($d\nu/dt = 0$). We see from that figure that, if the measured heat flux of 7×10^{13} W truly represents the average dissipation rate over the past 300 years, Lieske's determination of dn_1/dt is inconsistent with his determination of $d\nu/dt$.

This difference seems to be statistically real. The ranges shown in figure 47 correspond to Lieske's stated formal uncertainties. Lieske (1987a) does write that these uncertainties could be multiplied by a factor of two or three to account for possible errors in astronomical constants and the dynamic theory. However, the determinations of dn_1/dt and $d\nu/dt$ could only be consistent if the actual errors were at least six times the formal uncertainties.

The only other way to reconcile these results would be to conclude that over the past 300 years, while the relevant eclipse data were being collected, the average dissipation rate on Io was 10^{13} W or less to be consistent with this result; only in that range are Lieske's two results consistent according to figure 47. This dissipation rate is an order of magnitude less than the heat flux from Io.

Thus, the implication of Lieske's acceleration values is that for the past 10 or 15 years heat has been coming out of Io at a rate 10 times faster than the average over the past 300 years. This increase might be due either to an actual increase in the dissipation rate or short-lived release of pent-up heat. Either case speaks of very great geophysical and/or geological changes in Io on time scales of years. Also, the arrival of Voyager and the advent of Earth-based infrared detection has come by chance in an unusually active decade on Io.

ORIGINAL PAGE IS
OF POOR QUALITY

If the change represents a real increase in the dissipation rate, rather than a sudden release, then the resonant system must be out of equilibrium in the 1980s. It is ironic that the implication of sudden change on very short time scales follows from a measurement that shows that over a longer time scale (centuries) the system is apparently in equilibrium. Moreover, this observational evidence for equilibrium suggests (as would even near-equilibrium) that internal structure and tidal dissipation in Jupiter is time variable. This implication follows from the fact that the only interior model so far able to give sufficient dissipation for equilibrium is Stevenson's (1983) helium-cloud model, which as discussed earlier is likely to be only a temporary phenomenon.

I conclude that Lieske's determination of orbital acceleration for the satellites, and the resonance equilibrium hypothesis that it supports, imply strong, sudden changes in the heat flux from Io and in Jupiter's interior. They also imply that the present time is rather special in regard to those kinds of changes.

One might reject these conclusions on philosophical grounds, either because of uniformitarian bias or the improbability that special things happen just as people happen to be looking, but this would require that something be wrong with Lieske's results. If that were the case, the scenario of long-term disequilibrium of the resonance would become viable. That scenario has some very attractive elements as discussed in the section titled Evolution from Deep Resonance, but it certainly would not satisfy a uniformitarian: It implies great changes in the satellite's orbits and tidal heating over the past few million years.

On the basis of evidence from the observed heat flux from Io, orbital acceleration, and theory of the interrelations of dynamic and geophysical processes, there seems to be an inescapable conclusion: There have been and continue to be dramatic short-time-scale changes in the jovian system, including changes in the galilean satellites' orbits, geology, and geophysics, and in the planet's internal structure.

APPENDIX
CONSTRAINTS FROM ENERGY AND ANGULAR MOMENTUM

Many of the essential relationships among tidal effects, depth in resonance ν, and orbital acceleration used in this chapter can be derived simply from consideration of energy and angular momentum constraints. The orbital energy of each satellite is

$$E_i = -\frac{1}{2} m_i n_i^2 a_i^2 < 0. \tag{7.1}$$

The variation of total energy ($E \equiv \Sigma E_i$) is found by differentiating and using Kepler's third law ($n^2 a^3 = GM$):

$$dE = -\Sigma E_i \frac{da_i}{a_i} = \frac{2}{3} \Sigma E_i \frac{dn_i}{n_i}.$$

Orbital angular momentum is

$$L_i = m_i [GMa_i(1 - e_i^2)]^{1/2},$$

where M is Jupiter's mass. The variation of total orbital angular momentum ($L \equiv \Sigma L_i$) is

$$dL = -\Sigma (GMa_i)^{1/2} m_i \times \left[\frac{1}{3}(1 - e_i^2)^{1/2} \frac{dn_i}{n_i} + (1 - e_i^2)^{-1/2} e_i de_i\right]. \tag{7.2}$$

The resonance constraints give $n_1 - 2n_2 = n_2 - 2n_3 = \nu$, so

$$dn_1 - 2dn_2 = d\nu \tag{7.3}$$

and

$$dn_2 - 2dn_3 = d\nu. \tag{7.4}$$

For a given total energy change dE/dt and net torque dL/dt, eqs. (7.1)–(7.4) can be solved for the three orbital accelerations dn_i/dt and for $d\nu/dt$. To get such a solution, the variation of the eccentricities can be eliminated by invoking their dependence on ν due to the resonance or by showing that such variation is negligibly small.

Before solving these four equations, I first numerically evaluate the coefficients in eq. (7.1). With the satellites' known mass values and with the mean motion ratio 1:2:4, corresponding to semimajor axis ratios 1:0.63:(0.63)^2, one obtains $E_2 = 0.34E_1$ and $E_3 = 0.66 E_1$. (I have been repeatedly surprised that these two coefficients add up to unity, but I cannot think of any particular physical significance to it.) Thus,

$$dE = \frac{2}{3} E_1 \left(\frac{dn_1}{n_1} + 0.34 \frac{dn_2}{n_2} + 0.66 \frac{dn_3}{n_3}\right).$$

The three dn_i/n_i can be eliminated from this equation by using eqs. (7.2)–(7.4) and further simplification comes from using $e_i^2 \ll 1$, yielding

$$dE = \frac{2}{3}E_1\left[-0.66de_1^2 - 0.44de_2^2 - 1.74de_3^2 + 0.84\frac{d\nu}{n_2} - 1.38\frac{dL}{(GMa_1)^{1/2}m_1}\right].$$

Yoder and Peale (1981) derived a version of the above formula for the special case $dL = 0$ (their eq. 96). They used it to show that the scenario with negligible tidal torque from Jupiter implies that the system must have been near exact resonance a relatively short time ago. I summarize their argument as follows. In this scenario, the only energy change is that due to dissipation in Io, so dE/dt appears to be -7×10^{13} W or -7×10^{20} erg/sec. We can further simplify the above equation by noting that, at least at present, all $de_i \ll d\nu/n_2$. The energy variation equation thus takes the form

$$\frac{dE}{dt} = \frac{2}{3}E_1 \times 0.84\frac{(\Delta\nu/\Delta t)}{n_2}.$$

With the numerical value $E_1 = -1.34 \times 10^{38}$ erg, we find that the time for ν to change from near zero (exact resonance) to its present value $\sim 0\overset{\circ}{.}8$/day is $\Delta t = 2 \times 10^7$ yr, as found by Yoder and Peale.

In fact, although all de_i are small for the present value of ν, for very small ν the variation in e_i can be significant because e_i is roughly proportional to $1/\nu$. Inspection of the dE equation above shows that for constant dE/dt, inclusion of the de_i terms would slow the evolution somewhat compared with the calculation above. On the other hand, the dissipation rate dE/dt would also be larger when ν is small and e_i are correspondingly large, because of the additional tidal heating in the satellites; this effect would increase the rate of change of ν. Thus, the time for evolution from ν near 0 to its present value could be somewhat different from 2×10^7 yr. However, these effects involving eccentricities are negligible except in deep resonance, so the conclusion that evolution from deep resonance ($\nu \sim 0\overset{\circ}{.}2$/day) took less than -10^7 yr is still valid (see the section titled Evolution of the Resonance).

For the remainder of this discussion, I will restrict myself to consideration of values of ν close enough to the present value or larger, so that the terms with de_i are negligible. Thus the dE equation becomes

$$0.75\frac{dE}{E_1} = 0.42\frac{d\nu}{n_2} - 0.69\frac{dL}{(GMa_1)^{1/2}m_1}. \quad (7.5)$$

Similarly, the equations for dn_i become

$$\frac{dn_1}{n_1} = 0.99\frac{d\nu}{n_2} - 0.69\frac{dL}{(GMa_1)^{1/2}m_1} \quad (7.6)$$

$$\frac{dn_2}{n_2} = 0.49\frac{d\nu}{n_2} - 0.69\frac{dL}{(GMa_1)^{1/2}m_1} \quad (7.7)$$

$$\frac{dn_3}{n_3} = -0.51\frac{d\nu}{n_2} - 0.69\frac{dL}{(GMa_1)^{1/2}m_1}. \quad (7.8)$$

Note that eqs. (7.5)–(7.8) are simply rearranged and simplified versions of eqs. (7.1)–(7.4).

Next, I incorporate the rates of changes of E and L due to tides on Io and on Jupiter into these equations. Following the notation of Yoder (1979; see also Greenberg, 1982), we have for the orbital acceleration of Io due to tides raised on Jupiter

$$\frac{\dot{n}_1}{n_1} = -\frac{9}{2}k_J(R_J/a_1)^5(m_1/M)\frac{n_1}{Q_J} \equiv -c,$$

where k_J is Jupiter's Love number, R_J is its radius, m_1 is Io's mass, and Q_J is the tidal dissipation parameter. Thus, the effect of jovian tides on orbital energy is

$$\frac{dE_1}{dt} = -\frac{2}{3}E_1c, \qquad \text{[Tides on Jupiter]}$$

and the same tidal torque changes the orbital angular momentum at the rate

$$\frac{dL_1}{dt} = (GMa_1)^{1/2}\frac{m_1c}{3}, \qquad \text{[Tides on Jupiter]}$$

where terms of order e_2 have been neglected. (This angular momentum and energy comes from Jupiter's rotation, of course.) Similarly, tides raised on Io by Jupiter tend to accelerate Io at the rate

$$\frac{\dot{n}_1}{n_1} = 7Dce_1^2,$$

where D is the product of ratios:

$$D \equiv \frac{k_1}{k_J}\left(\frac{R_1}{R_J}\right)^5\left(\frac{M_J}{m_1}\right)^2\left(\frac{Q_J}{Q_1}\right).$$

Thus the effect on orbital energy is

$$\frac{dE_1}{dt} = \frac{14}{3}E_1Dce_1^2. \qquad \text{[Tides on Io]}$$

As mentioned in the main text, these tides produce no change in orbital angular momentum

$$\frac{dL_1}{dt} = 0. \qquad \text{[Tides on Io]}$$

Now, let us consider orbital evolution rates under various assumptions. First, for reference, consider the simple case where Io is uncoupled from any gravitational interactions with the other satellites and where tides raised on Jupiter are negligible. From Kepler's third law we have the relation

$$\frac{\dot{n}_1}{n_1} = \frac{3}{2}\frac{(dE/dt_{\mathrm{in\,Io}})}{E_1}. \tag{7.9}$$

Of course the satellites are gravitationally coupled through the resonance. But if we retain the assumption that tides on Jupiter are negligible, eqs. (7.5) and (7.6) give

$$\frac{\dot{n}_1}{n_1} = 1.18 \times \frac{3}{2}\frac{(dE/dt_{\mathrm{in\,Io}})}{E_1}. \tag{7.10}$$

Acceleration would be 18 percent faster than if gravitational coupling were negligible.

Next, consider the most general case with resonant coupling and significant tides on both Io and Jupiter. If we insert the effects on energy and angular momentum into eq. (7.5) we find

$$\frac{d\nu}{dt} = 0.32 n_1 c (13De_1^2 - 1). \tag{7.11}$$

Inspection of eq. (7.11) shows that ν would be in equilibrium at

$$D = \frac{1}{13e_1^2}.$$

Moreover this equilibrium is stable, because $e_1 \propto 1/\nu$. This result was obtained by Yoder (1979) from consideration of equations of variation of orbital elements, but I have shown here that it follows from energy and angular momentum considerations as well. This equilibrium value of the ratio D defines the ratio of Q_J to the tidal dissipation rate in Io as discussed in the section titled Evolution of the Resonance.

For this equilibrium case ($d\nu/dt = 0$), we can use eq. (7.6) to evaluate Io's acceleration:

$$\frac{\dot{n}_1}{n_1} = -0.43 \times \frac{3}{2}\frac{(dE/dt_{\mathrm{in\,Io}})}{E_1}. \tag{7.12}$$

The implications of eqs. (7.9), (7.10), and (7.12) are discussed in the section titled Measurements of Orbital Evolution.

Finally, I find an expression for dn_1/dt by using eq. (7.5) to eliminate $d\nu$ from eq. (7.6). Then eq. (7.6), with the variation in E and L due to tides on both Io and Europa, gives

$$\frac{dn_1}{dt} = 0.86 n_1 c (9.5De_1^2 - 1). \tag{7.13}$$

This equation is used to generate the curves in figure 47 for various values of dn_1/dt. Note that $dn_1/dt = 0$ for a somewhat larger value of D than the one that gave equilibrium of ν (c.f., eq. [7.11]) (i.e., for a higher ratio of dissipation in Io compared with dissipation in Jupiter). Thus the line in figure 47 for $dn_1/dt = 0$ is just below the line for equilibrium ($d\nu/dt = 0$).

ACKNOWLEDGMENTS

I thank Jay Lieske for several enlightening discussions. This work is supported by Grant No. NAGW-944 from NASA's Planetary Geology and Geophysics Program.

References

Cassen, P., S. J. Peale, and R. T. Reynolds (1982). Structure and thermal evolution of the galilean satellites. In *Satellites of Jupiter* (D. Morrison, ed.). Univ. of Arizona Press, Tucson.

Dermott, S. F. (1979). Tidal dissipation in the solid cores of the major planets. *Icarus* 37:310–321.

DeSitter, W. (1928). Orbital elements determining the longitudes of Jupiter's satellites, derived from observations. *Leiden Annals* 16, Part 2.

Gavrilov, S. V., and V. N. Zharkov (1977). Love numbers of the giant planets. *Icarus* 32:443–449.

Goldreich, P. (1963). On the eccentricity of satellite orbits in the solar system. *Mon. Not. Roy. Astron. Soc.* 126:257–268.

Goldreich, P., and P. D. Nicholson (1977). Turbulent viscosity and Jupiter's tidal Q. *Icarus* 30:301–304.

Goldreich, P., and S. Soter (1966). Q in the solar system. *Icarus* 5:375–389.

Goldstein, S. J. (1975). On the secular change in the period of Io, 1668–1926. *Astron. J.* 80:532–539.

Goldstein, S. J. (1985). On the slow changes in the Earth's rotation. *Astron. J.* 90:1900–1905.

Goldstein, S. J., and K. C. Jacobs (1986). The contraction of Io's orbit. *Astron. J.* 92:199–202.

Greenberg, R. (1980). Presentation at the Satellites of Jupiter Conference, Kona, Hawaii.

Greenberg, R. (1981). Tidal evolution of the galilean satellites: A linearized theory. *Icarus* 46:415–423.

Greenberg, R. (1982). Orbital evolution of the galilean satellites. In *Satellites of Jupiter* (D. Morrison, ed.). Univ. of Arizona Press, Tucson.

Greenberg, R. (1987). Galilean satellites: Evolutionary paths in deep resonance. *Icarus* 70:334–337.

Laplace, P. S. (1805). *Mecanique Celeste*, vol. 4, Courcier, Paris. (Translation by N. Bowditch, reprinted 1966 by Chelsea, New York.)

Lieske, J. H. (1986a). The possibility of estimating tidal perturbations of Jupiter's galilean satellites. In *Relativity in celestial mechanics and astronomy* (J. Kovalevsky and V. A. Brumberg, eds.), p. 117. Reidel, Dordrecht.

Lieske, J. H. (1986b). A collection of galilean satellite eclipse observations. *Astron. Astrophys.* 154:61.

Lieske, J. H. (1986c). A collection of galilean satellite eclipse observations, 1652–1983: II. *Astron. Astrophys. Suppl.* 63:143–202.

Lieske, J. H. (1986d). Private communication.

Lieske, J. H. (1987a). Galilean satellite evolution: Observational evidence for secular change in the mean motion. *Astron. Astrophys.* 176:146–158.

Lieske, J. H. (1987b). Private communication.

McEwen, A. S., D. L. Matson, T. V. Johnson, and L. A. Soderblom (1985). Volcanic hotspots on Io. Correlation with low albedo calderas. *J. Geophys. Res.* 90:12345–12379.

Nielsen, A. V. (1944) *Ole Roemer, en skildring af hans liv og gerning* (Aarhus Observatory).

Ojakangas, G. W., and D. J. Stevenson (1984). Episodic heatflow in tidally heated satellites. *Bull. Amer. Astron. Soc.* 16:661.

Ojakangas, G. W., and D. J. Stevenson (1986). Episodic volcanism of tidally heated satellites with application to Io. *Icarus* 66:341–358.

Peale, S. J., P. Cassen, and R. T. Reynolds (1979). Melting of Io by tidal dissipation. *Science* 203:892–894.

Schubert, G., T. Spohn, and R. T. Reynolds (1986). Thermal histories, compositions, and internal structures of the moons of the solar system. In *Satellites* (J. Burns and M. S. Matthews, eds.), pp. 224–292. Univ. of Arizona Press, Tucson.

Sinclair, A. T. (1975). The orbital resonance amongst the galilean satellites of Jupiter. *Mon. Not. Roy. Astron. Soc.* 171:59–72.

Stevenson, D. J. (1983). The origin and evolution of the great resonance in the jovian satellite system. *J. Geophys. Res.* 88:2445–2455.

Yoder, C. F. (1979). How tidal heating in Io drives the galilean orbital resonance locks. *Nature* 279:767–769.

Yoder, C. F., and S. J. Peale (1981). The tides of Io. *Icarus* 47:1–35.

8

Anticipated Time Variations in (Our Understanding of) Jupiter's Ring System

Mark R. Showalter
NASA/AMES Research Center, Moffett Field

Abstract

Jupiter's ring system comprises three rather distinct components, identified as the main ring, halo, and exterior "gossamer" ring. The Voyager data set places significant constraints on each of these components, but leaves many questions unanswered. The system appears to interact in a complex, dynamic manner with the planet's magnetic field, and also with several embedded satellites. Many subtleties of these interactions will require higher-quality data, such as the Galileo orbiter can provide, in order to be understood fully. Some analogous processes are undoubtedly at work in the ring systems of Saturn, Uranus, and Neptune as well.

INTRODUCTION

Jupiter's ring system was first discovered in 1979, in a single long exposure by the Voyager 1 camera, which was specifically intended to search for a possible faint ring system. Following the ring's discovery, Voyager 2 was programmed to take a closer look during its passage through the planetary system. To date, virtually all that is known about Jupiter's ring system comes from the analysis of the 25 images returned by Voyager.

Given the faintness of the ring, one should not be surprised that it placed a considerable strain on the capabilities of the Voyager cameras. Most of the exposure times required were roughly 100 times longer than those more typical for the planet and its satellites. As a result, these images are characterized by a number of flaws, including smear, low signal-to-noise ratio (SNR), background light contamination, confused geometry, and uncertain pointing, which make their interpretation unusually difficult. Sadly, this set of images predates the innovation of "image motion compensation," which was shown to be so valuable during the Voyager 2 fly-by of Uranus.

The original intention of this chapter was to address some of the possible time-variable processes in Jupiter's ring system. However, given the current state of our knowledge, it seems quite premature to isolate and discuss only those aspects that might be time-variable. The amount of data in hand, and the incompleteness of our understanding, simply do not permit such a narrow approach. Perhaps it is appropriate to draw an analogy with our knowledge of the saturnian rings following the Pioneer 11 encounter in 1979. Certainly, an enormous amount was learned about the system. Nevertheless, we had to await the arrival of Voyager at Saturn to discover spoke activity, kinks, clumps and "braids" in the F ring, shepherding satellites, fine structure, sharp edges, spiral density and bending waves, moonlet wake patterns, and eccentric features. The phenomena just listed represent the vast majority of subjects of ongoing ring studies.

In the future, the Galileo mission will arrive at Jupiter and subject the entire system to two years of intensive scrutiny. Undoubtedly, when we place data from Galileo and Voyager side by side we will see enormous changes. However, most of these variations will not be intrinsic to the system, but will simply illustrate the vast improvement in data quality. One is far more likely to observe subtle time variations over the two years of the Galileo mission than over the ~15 years between Voyager and Galileo.

In this chapter, I have chosen to survey some of the more significant potential contributions of Galileo to our understanding of Jupiter's diaphanous ring system. The first section will summarize the state of our knowledge, and discuss some of the ongoing physical processes as we currently understand them. The second section will place particular emphasis on a number of the system's more puzzling aspects, including some features that are hinted at in the data, but that are especially difficult to explain at this time.

PROPERTIES AND PHYSICAL PROCESSES

Our understanding of Jupiter's ring system has evolved rather substantially over the years since its discovery. The most thorough analysis of the Voyager images has been performed recently by Showalter et al. (1985, 1987; see also Showalter, 1985), and most of the results summarized below originate therein. Nevertheless, previous investigators (Smith et al., 1979a, b; Owen et al., 1979; Jewitt and Danielson, 1981; Jewitt, 1982) have all made crucial contributions to the subject. Several Earth-based detections at visible (Smith and Reitsema, 1980; Jewitt et al., 1981) and infrared (Neugebauer et al., 1981) wavelengths complement the image data, as do a few significant nondetections (Hanel et al., 1979;

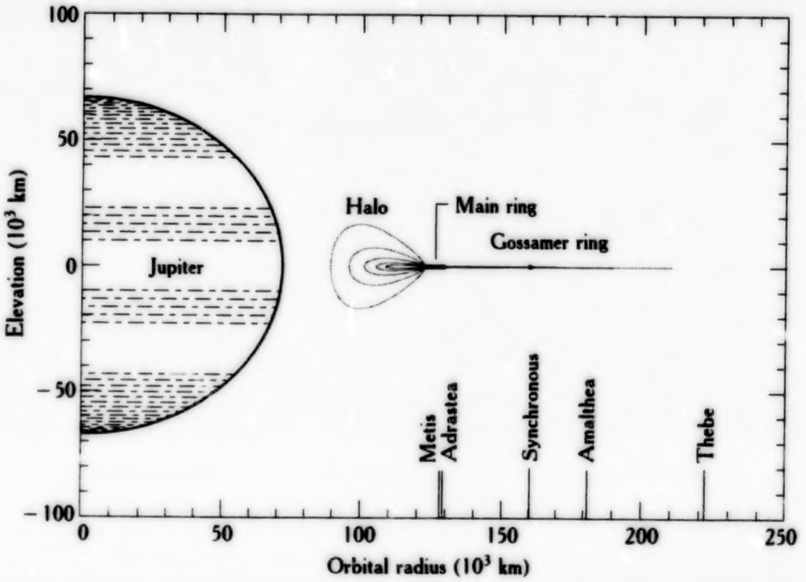

Figure 50. A cross-sectional view of Jupiter and the three main components of its ring system, drawn approximately to scale. The locations of the inner satellites (from Synnott, 1984) and synchronous orbit are also shown.

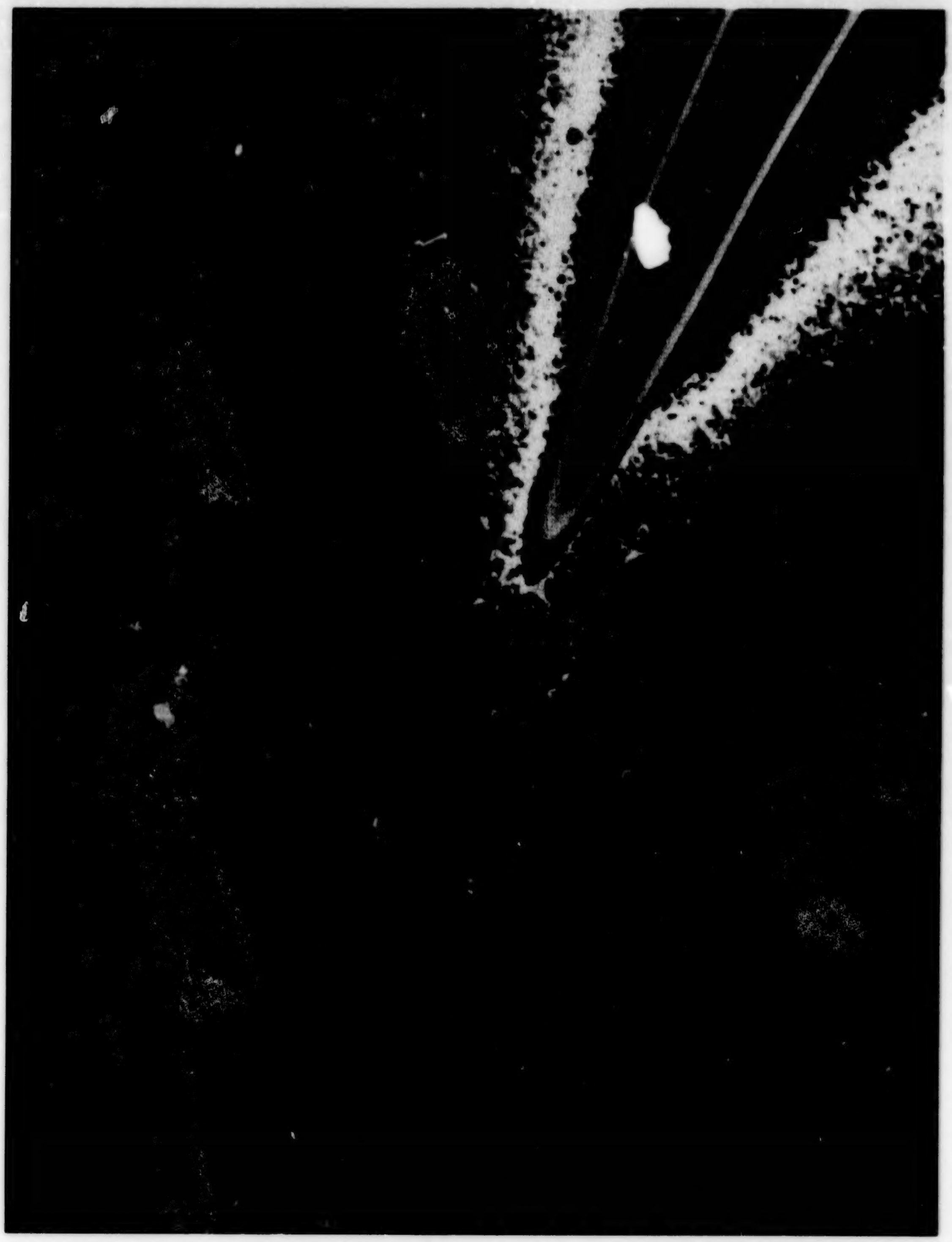

Figure 51. A specially enhanced version of wide-angle Voyager image FDS 20693.02, showing the three main ring components. The faintest features in the image are shaded using a secondary grayscale that runs from black to white. The main ring ansa is shown at upper right, in a rather standard black and white view. The excess light surrounding and interior to it is from the diffuse, vertically extended halo, which arises at the main ring's inner edge and appears to be crudely lens-shaped here. The halo is outlined in white by the transition from the secondary grayscale to the primary. Using this enhancement, the exceedingly faint gossamer ring is visible as a broad stripe extending outward from the ansa, toward the lower right.

ORIGINAL PAGE
BLACK AND WHITE PHOTOGRAPH

Tyler et al., 1981; Dunham et al., 1982), Also, a dip in the number of charged particles detected by Pioneer 11 near its closest approach to the planet (Acuña and Ness, 1976) was apparently caused by the ring, as were impact events recorded by the meteoroid detector (Elliot and Kerr, 1985, p. 95).

Jupiter's ring system is now known to comprise three rather distinct components: the main ring, the inner halo, and the exterior gossamer ring. These components are shown in figures 50 and 51. They are each discussed in turn below.

The Main Ring

The most prominent component of Jupiter's ring system, and the first to be discovered, is the main ring. Its outer boundary falls at an orbital radius of 129,130 ± 100 km, slightly beyond the orbit of the tiny satellite Adrastea. The boundary is unresolved ($\lesssim$200 km in radial width) and does not deviate in any measurable way from circularity (eccentricity, $e \lesssim 10^{-3}$). The main ring's inner edge is located near a radius of 122,000 km and appears to be much more gradual, fading into the halo (discussed below) over a radial distance of ~2000 km.

Based on its marked increase in brightness between low- and high-phase angles, the ring appears to contain a substantial population of micron-sized grains. The phase function and color properties near forward-scatter (scattering angles θ between 3° and 6°) suggest that this population is well modeled by a power law size distribution of the form $n(r) \propto r^{-p}$ with $p = 2.5 \pm 0.5$, where $n(r)dr$ is defined as the number of particles per unit ring area with radii between r and $r + dr$. These grains account for an optical depth of a few $\times 10^{-6}$ if the distribution extends up to $r = 100$ μm. Based on the light scattering behavior in backscatter, the ring appears to contain a comparable optical depth in macroscopic bodies, which are rough, dark, and red, much like the surface of Amalthea. These larger bodies must also be the cause of the charged particle depletion detected by Pioneer 11.

Although most of the main ring's ~7000 km radial expanse appears rather uniform, its outer 2000 km is dominated by three evenly spaced bright features. Metis and Adrastea orbit just outside the first and third of these, and may be associated dynamically; the second is not associated with any known body. Interestingly, these three features appear to be much narrower and (in a relative sense) brighter in backscatter than they are in forward-scatter. Since the two lighting angles emphasize opposite ends of the size distribution, this observation seems to indicate a segregation of particle sizes with radius. Perhaps what we are seeing are narrow bands of boulders (in backscatter) surrounded by clouds of their own micron-sized ejecta (in forward-scatter). This appealing dynamic model will be discussed further below.

The vertical thickness of the main ring is quite difficult to constrain from the imaging data. Nevertheless, from a single edge-on view in backscatter, it appears to be <30 km thick. In forward-scatter the ring can only be constrained to a thickness of <300 km.

The Halo

The halo arises at the main ring's inner boundary, and grows thicker and ever more diffuse inward from there. Showalter et al. (1987) have been able to generate a false cross section of the halo, showing the distribution of material with radius and elevation, based on specialized processing of certain Voyager images that show the jovian shadow cutting across the ring system. They find that the halo vanishes from sight fully 20,000 km above the jovian cloudtops, at an orbital radius of ~90,000 km. It reaches a maximum full thickness of ~20,000 km, but is not measurably asymmetric about the ring plane. The amount of material in the halo appears to diminish exponentially with elevation, having a maximum scale height of ~3000 km, near a radius of 110,000 km. Interestingly, the halo's brightness integrated normal to the ring plane appears to be similar to that of the main ring, implying that the two components are of comparable optical depth.

The light-scattering properties of the halo are very difficult to constrain, owing to its uncertain, vertically extended geometry. Nevertheless, its phase function appears to be slightly flatter in forward-scatter than that of the main ring, whereas its color properties are the same. This suggests that the particle size distributions in the two systems, at least at micron sizes, are similar but not identical; the halo probably has fewer large grains. However, the halo's phase function slope and color both rule out the possibility that it contains a significant population of very tiny ($\lesssim$0.1 μm) Rayleigh scatters. The halo has not been reliably detected in backscattered light, implying a very small population of macroscopic bodies.

The "Gossamer" Ring

The third known component of Jupiter's ring system is an exceedingly faint outward extension to the main ring, dubbed the "gossamer" ring by Showalter et al. (1985), since it is far fainter than the other two (already faint) components. It was discovered in a single wide-angle (WA) Voyager frame (FDS 20693.02; see fig. 51) after careful reprocessing of the background. Confirming evidence for it was found subsequently in an overlapping narrow-angle (NA) frame (FDS 20693.01). The gossamer ring extends outward from the main ring to a limiting radius of ~210,000 km, which is well beyond the orbit of Amalthea. Its brightness appears to diminish almost linearly with radius, disappearing into the background noise near the orbit of the tiny satellite Thebe. The only known exception to this trend is a narrow 20 percent enhancement in brightness, which falls at a radius of 160,000 ± 2000 km, but has been only marginally detected at the 4σ level. It may well be associated dynamically with Jupiter's synchronous orbit at 160,200 km. The ring appears to increase in brightness by nearly a factor of two between the scattering angles of 7° and 6° over which it is observed, suggesting the diffraction of light by tiny grains of radius $r \approx 1.5$ μm. Although this strongly implies a large population of micron-sized grains (as in the main ring), it is not possible to significantly constrain the population of particles either much larger or much smaller than a micron. If one makes the questionable assumption that the micron-sized grains obey a distribution similar to that in the main ring, then this ring's normal optical depth $\tau \sim 10^{-7}$, comparable to Saturn's E ring. This value is compatible with $\tau \gtrsim 10^{-8}$, determined from a single Pioneer 10 impact detection near the ring's outer boundary, and applying to particles larger than $r \approx 6$ μm. From the nondetection of the ring in backscattered light, one can infer that the ring has fewer macroscopic bodies relative to the fine dust than does the main ring.

A Survey of Physical Processes

As our understanding of jovian ring-system properties has varied over the years since its discovery, so have our conjectures about the ongoing physical processes. Many investigators have contributed to this discussion, including Burns et al. (1980, 1984, 1985), Consolmagno (1983), Grün et al. (1980), Johnson et al. (1980), Morfill et al. (1980a–d), and Schaffer and Burns (1984, 1986, 1987a).

As noted above, micron-sized dust grains constitute a major component of the ring system and are responsible for its marked brightening at high-phase angles. A number of processes act to limit the lifetimes of such tiny grains, including sputtering, meteoroid erosion, Poynting-Robertson drag, and plasma drag. It is believed (Burns et al., 1984) that the dominant evolutionary force acting is plasma drag. This force arises from collisions between dust grains and the plasma, which is tied to the planet's rotating magnetic field; it transports material away from the synchronous orbit, either outward or inward, on time scales of $10^{2\pm1}$ years for micron-sized grains. The dominant destruction process, sputtering, is thought to erode away these tiny grains on a somewhat longer time scale ($10^{3\pm1}$ yr).

Given such brief lifetimes, ring material must be continually replenished from some source for the ring to persist. Universally, it has been assumed that the fine dust particles arise as impact ejecta from a belt of larger parent bodies. The inferred power law size distribution of the fine dust even matches that expected from hypervelocity impacts, after subsequent evolution under plasma drag (Showalter et al., 1987). The parent bodies have apparently been observed in backscattered light. Adrastea and Metis may be nothing more than the largest of these, sharing with the others a common origin; alternatively, the macroscopic bodies may have originated as the ejecta from a major impact into one (or both) of the ring moons. The three bright features in the main-ring features provide some evidence for this model, since the fine dust seems to reflect the distribution of the larger bodies.

The source of the projectiles impacting the larger ring bodies has been a matter of some dispute. Burns et al. (1980, 1984) estimate that the local micrometeoroid flux is sufficient to maintain the ring, whereas Grün et al. (1980; see also Morfill et al., 1980a–d) invoke an additional flux of dust grains released by volcanoes on Io. The flux from etiher source is highly uncertain, and the latter may not exist at all (Burns et al., 1984). The Io source was originally proposed because incoming volcanic projectiles would be expected to obey a narrow size distribution, which could explain a peculiarity of the size distribution inferred by Jewitt and Danielson (1981) for the main ring. However, now that the ring population is thought to satisfy a simple power law, this additional source may no longer be needed. The Galileo dust detector should help to settle this issue once and for all, by accurately measuring the micrometeoroid influx at Jupiter.

Eventually, the orbits of micron-sized grains decay past the main ring's inner boundary and into the halo region. If grains evolve through the system much more rapidly than they sputter away (as rough time-scale estimates indicate), then the particle size distribution will not change markedly from the ring to the halo. This is consistent with the crude halo photometry that has been performed. Jupiter's inclined magnetic field undoubtedly than disperses the halo particles into the broad cloud we observe. Integrations of the equations of motion (Consolmagno, 1983; Schaffer and Burns, 1984, 1987a) yield thicknesses that are consistent with the halo's 20,000-km vertical expanse, based on plausible charge-to-mass ratios for the grains.

Nevertheless, these studies do not account for several halo features, most notably its disappearance fully 20,000 km above the jovian atmosphere. Here, the theory of Lorentz resonances introduced by Burns et al. (1985) undoubtedly plays an important role. Particles that orbit at a radius of 101,000 km circle the planet exactly twice every time the magnetic field rotates once. Hence the Lorentz force (arising from a charged grain's motion relative to the rotating magnetic field) contains a component with the same period as the orbital motion. Relatively large vertical and horizontal excursions may then arise from the small but repetitive Lorentz perturbations. Accordingly, when halo grains evolve into the region of the 2:1 Lorentz resonance, they will be rapidly dispersed so far that they can no longer be seen and perhaps are even lost into the jovian atmosphere. This simple description appears to explain the halo's inner boundary quite satisfactorily.

Other such resonances may also play an important dynamic role in the ring system. For example, the 3:2 resonance lies very near the transition zone between the main ring and the halo; perhaps it is this driving force that first scatters the inward-evolving grains into the halo region. Figure 52 (adapted from Schaffer and Burns, 1987a) shows the relative strengths of the most important Lorentz resonances in the jovian system. This explanation, however, is not entirely adequate for the transition from main ring to halo, because the resonant effects are not expected to be quite as localized as what is observed. Furthermore, integrations indicate that typical elevations in the resonance zones are only ~10 times larger than those outside the zones, whereas the observed ratio is much greater.

Hence, some other changes in ring properties must be occurring as well. We do know that the inner edge of the main ring is marked by a rapid reduction in the number of large particles. The absence of these may play an important role. Goertz and Ip (1984) describe how dust particles within a ring may be "shielded" by densely packed larger bodies, so that they do not attain the electric charges that they would in free space. This suggests that the halo may begin when the grains evolve inward beyond the protection of the macroscopic bodies and are then rapidly charged to a much higher potential. However, in a ring of such low optical depth it is uncertain that particles can be

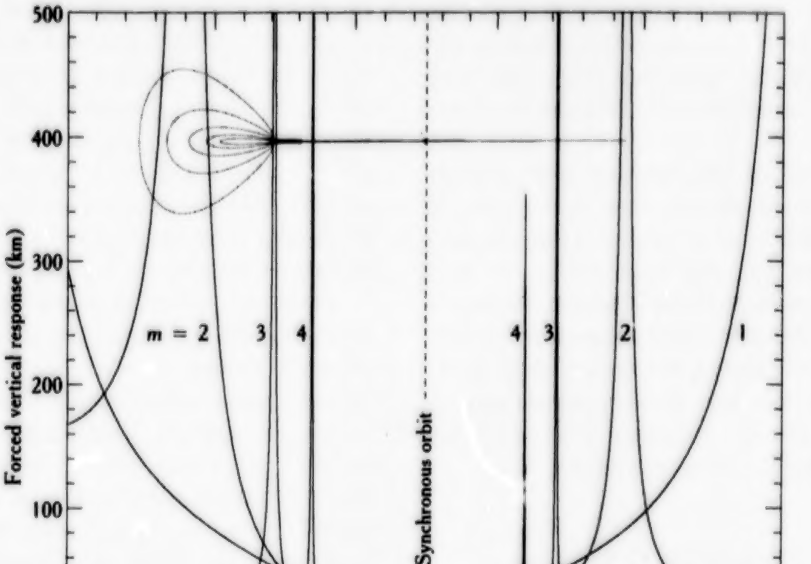

Figure 52. A plot of the vertical response of a ring particle charged to −1 V/μm, driven by the *m*th moment of Jupiter's magnetic field (based on Schaffer and Burns, 1987a, fig. 51). This response becomes quite large in the neighborhood of Lorentz resonances. A cross-sectional view of the ring system (cf. fig. 50) is shown for comparison.

packed at sufficient spatial density to effectively shield the dust grains.

It should be noted that we have just presented two independent explanations for the ring-halo transition, neither of which seems to be adequate by itself. Perhaps both processes are working in synergy to create the halo. This is initially troubling because there is no reason why both should act at the same location; it appears to be simply coincidental that the population of large bodies peters out at the location of a strong Lorentz resonance. If this has happened by mere chance, then the jovian halo would appear very different if the large bodies were to have fallen at a different location. Alternatively, the large bodies may cease here because they are more rapidly abraded away in the vicinity of a strong Lorentz resonance.

Considering how little is known about the gossamer ring, it should not be surprising that it remains somewhat mysterious. Once again, the observed population of micron-sized grains must be replenished continually from some unseen source. If sputtering and plasma drag act on comparable time scales here, then particles will move outward from synchronous orbit and erode away at similar rates. Hence, we would expect to see a steady decrease in ring brightness with increasing distance from the source region. This is consistent with the ring's observed linear decay outside synchronous orbit, implying that the sources are confined to a somewhat narrower radial region than are the visible grains. The brightness variations inside synchronous orbit are harder to explain; they may more closely reflect the underlying distribution of parent bodies.

The bright feature at synchronous orbit appears surprising at first, since plasma drag drives material away from this location, not toward it. However, here the plasma corotates with ring material, so its drag force vanishes. Hence, material injected into the ring at this location will evolve away much more slowly (probably under the weak Poynting-Robertson drag force) than that introduced elsewhere. If the source body population extends across synchronous orbit, then this brightness enhancement is to be expected.

PUZZLES OF THE JOVIAN RING SYSTEM

One might get the impression from the previous section that, at least in general terms, the ring system of Jupiter is well understood. Plausible theories have now been put forward to explain a number of the ring's most prominent characteristics. Nevertheless, one should not be lulled into a false sense of security; the rings of Saturn also made a great deal more sense to theoreticians when much less was known about them. The following section will highlight several ring properties that tend to undermine our confidence.

AZIMUTHAL ASYMMETRY

One of the most puzzling aspects of Jupiter's ring system is a marked azimuthal asymmetry, which is visible in several images. This property was first noted by Jewitt and Danielson (1981) and is discussed in greater detail by Showalter et al. (1987). It is apparent in figure 51 (FDS 20693.02), in which the ring's far (upper) arm appears to be consistently about 10 percent brighter than its near (lower) arm. Since the same effect is also seen in several frames of an overlapping NA mosaic (FDS 20692.45–.53), it is quite definitely not an instrumental effect or a flaw in the data. Even more puzzling is the fact that this asymmetry spills over into the halo, which is also seen to be roughly 10 percent brighter surrounding the far arm than the near in both the WA frame and in the overlapping NA mosaic.

One possibility worth considering is that this additional brightness arises from secondary light reflected off the planet. However, since these images were taken looking back from inside Jupiter's shadow, the ring particles would have to backscatter the light from the planet to Voyager, and this they do far too inefficiently to account for the observed enhancement. Furthermore, one would expect the light from Jupiter to increase toward the planetary limb, since ring particles here would see a greater fraction of the lit jovian disk; this is contradicted by the fact that the asymmetry is greatest near the ansa and vanishes near the limb. Whatever the explanation for this strange feature, it appears to be intrinsic to the ring system itself.

A recent meteoroid impact into one of the larger jovian ring bodies might account for the enhancement, since the sudden burst of ejecta would brighten a localized region, which would then take some time to spread in longitude. Brightening 45° of the ring by 10 percent requires an extra ~1 percent of the total ring cross section in micron-sized grains. Material that is ejected from a ring moon will have typical velocities of 10–100 m/s (see Burns et al., 1984, fig. 17) and so will span 45° of arc in 4–40 days. If this were a typical impact event, then the ring's entire complement of micron-sized grains could be regenerated in ~100 times as long, or 1–10 years. Estimates of grain removal time scales are all somewhat longer than this (Burns et al., 1984), so the scenario seems unlikely. If the excess brightness was caused by a recent impact, then our observation of it was very unlikely. Further, it is difficult to understand how this sort of an event would lead to a similar brightness asymmetry in the nearby halo, since ejecta could not scatter that far in radial distance.

This phenomenon may be reminiscent of the well-documented quadrant asymmetry found within Saturn's A ring (Thompson et al., 1981; Franklin et al., 1987; see also Cuzzi et al., 1984, and references therein). Indeed, additional forward-scattered Voyager images seem to be consistent with this hypothesis; the near ring quadrant tends to be brighter adjoining the "left" limb (in FDS 20691.27, .31), whereas the far quadrant is brighter next to the "right" limb (in FDS 20691.35, .39). However, scaling and background uncertainties in these frames are large enough to make the conclusions questionable. For example, the right limb images show a marked asymmetry that is not confirmed by the overlapping higher-quality NA frames (including FDS 20692.37). Nevertheless, if the phenomenon is real, then both its amplitude and sense are comparable to that which has been detected at Saturn.

This asymmetry has not been entirely explained for the A ring. It is widely attributed to mutual shadowing by clumps of particles in the density "wakes" of larger ring members (Colombo et al., 1976; see also Cuzzi et al., 1984). Dones (1987) has refined this model by noting that vertical corrugations in the ring arising from these wakes will be more important than any shadowing. However, an explanation of this sort cannot work at Jupiter, where optical depths are far too low for shadowing or ring surface effects to be important.

An alternative explanation for the asymmetry involves elongated particles locked into some preferential orientation, and so showing a variable cross section when viewed from different angles (Ferrín, 1974; Lumme and Irvine, 1976). This is untenable at Saturn, where collisions reorient particles often. However, it deserves closer scrutiny in this case because collisions between jovian ring particles are very infrequent. Since the magnetic field is inclined by ~10°, the ring particles experience a rapidly varying field as they orbit, which may be capable of imparting a preferential orientation and/or spin onto tiny, elongated grains. This could be similar to the process whereby magnetic fields orient particles in the interstellar medium, as detected by the polarization of starlight. This is a very complex dynamic problem, but worthy of further study.

Vertical Asymmetry

The possibility that the jovian halo is not symmetric about the ring plane has been the subject of some controversy. Jewitt and Danielson (1981) reported a vertical offset of some 300 km in the one image of the ring ansa (see fig. 51), but this was not confirmed by Showalter et al. (1987). The original detection may have been caused by the image's background light, which is not a small fraction of the halo's brightness. Alternatively, it may have arisen from the small genuine asymmetry, which Showalter et al. ascribe to variations with azimuth rather than elevation. Several other Voyager WA images capture a large enough piece of the halo to place significant constraints on vertical asymmetry, but do not provide conclusive answers. One pair of frames taken near the jovian limb (FDS 20691.27, .31) do not show any measurable offset, whereas another pair taken at the opposite limb (FDS 20691.35, .39) show a marked asymmetry. However, Showalter et al. (1987) note that the halo only appears near a corner in these latter frames, and it is here that both the background level and the absolute calibration are most uncertain. Hence, it is possible to ascribe the asymmetry here to flaws in the data. In summary, although no conclusive evidence exists for vertical asymmetry in the jovian halo, the possibility cannot be ruled out definitively.

As was discussed previously, the broad vertical expanse of the halo probably arises from perturbations by Jupiter's inclined magnetic field, which are able to lift grains out of the ring plane far faster than collisions can damp them back down. The absence of a substantial observed asymmetry was at first quite surprising, since dynamic simulations of perturbed particle trajectories within the halo always showed marked asymmetries (Consolmagno, 1983; Schaffer and Burns, 1984, 1987a). However, more recent work by Schaffer and Burns (1987b) nullifies this conclusion. Their newer integrations include drag forces in addition to the time-reversible gravitational and electromagnetic forces treated previously. They have found that this makes a crucial difference; as grains evolve through resonances they suffer significant jumps in inclination and eccentricity, but emerge from the zones distributed symmetrically. The asymmetries reported previously were a consequence of specialized initial conditions. Nevertheless, Schaffer reports that asymmetries should still exist very near to the resonance zones. In the future, Galileo may be able to observe the halo continuously over periods comparable to a jovian day, and thereby detect any subtle "flapping" of the halo under the magnetic field's influence.

Fine Radial Structure

The only fine structures detected thus far in Jupiter's ring system are the three bright features described under the heading Properties and Physical Processes.

One should be particularly cautious, however, in asserting that the ring is generally featureless; the features we do see are at about the resolution limit of the data (~200 km), owing to smear and low SNR. Upon closer inspection by Galileo, the ring could show a wealth of unexpected structure.

Theoreticians can offer many reasons why the ring should not contain a great deal of structure in the fine dust. Each localized source region would simply add a small increment to the dust population evolving inward across it, yielding a rather smooth ring profile in forward-scatter. Crudely, this is consistent with what we have seen. However, many similar reasons exist as to why we should not see fine structure in the uranian ring system. Nevertheless, one long exposure taken by Voyager as it looked back from within the uranian shadow (FDS 26852.19; see Smith et al., 1986) shows a great deal of structure in the fine dust. Indeed, this image was taken with a viewing geometry and exposure time quite similar to many of the jovian ring images; the only major difference was that in this frame the smear was limited by careful planning. This image is particularly puzzling because structure is visible on radial scales that are finer than the expected noncircularities of dust particle orbits, when electromagnetic perturbations are considered (Burns, 1987). As in the main jovian ring, some sort of shielding is needed to limit charges on the tiny grains.

One must therefore consider seriously the possibility that similar fine structure will be found when Galileo arrives at Jupiter. It might reflect shepherding, wake formation, or other effects that are normally associated with rings of much higher optical depth. Regardless, it could have important ramifications for the other planetary ring systems as well.

Arcs, Clumps, and Idle Speculation

As we learn more about them, planetary ring systems continue to confound us with new and ever more bizarre solutions to a set of rather simple dynamic equations. The newly discovered neptunian ring arcs are a case in point, being completely unanticipated, difficult to explain, and unquestionably real.

Recently, Cuzzi and Burns (1987) have cited evidence for what may be a similar phenomenon at Saturn: clumps of low optical depth material between the orbits of Pandora and Prometheus, in the neighborhood of the F ring. They base their conclusions on the fact that Pioneer 11 detected several localized depletions of trapped magnetospheric electrons in the area, which do not correspond to known rings or satellites. Such clumps are envisioned as transitory clouds of debris, arising occasionally from collisions among an unseen band of boulders. The physics that Cuzzi and Burns invoke here is quite applicable to the situation in the jovian ring. Certainly, a band of boulders is present, within which collisions must occasionally take place. When they do, clouds of surface debris will undoubtedly be released. Voyager was not capable of detecting stochastic variations of this sort at Jupiter, but the Galileo camera may be capable of doing so.

Several other Saturn ring phenomena are known or believed to be time-variable, such as B ring spokes and the "braids" of the F ring. Although neither is understood on theoretical grounds, it is surely not coincidental that they both involve populations of fine dust; such tiny grains tend to respond much more rapidly to small transitory effects than do the larger ring members. On the basis of its particle population alone, therefore, Jupiter's ring system appears to be a likely contender for time-variations. Aside from some of the analogies already drawn, I would not want to speculate on the form that these variations might take. Nevertheless, as Galileo returns its data, the changes that take place in the ring system at Jupiter may not be exclusively within our Earth-based understanding.

ACKNOWLEDGMENTS

I wish to thank Joe Burns, Jeff Cuzzi, Luke Dones, Phil Nicholson, and Les Schaffer for helpful discussions and comments. I am particularly grateful to Les Shaffer for the opportunity to discuss some of his as-yet-unpublished results.

References

Acuña, M. H., and N. F. Ness (1976). The complex main magnetic field of Jupiter. *J. Geophys. Res.* 81:2917–2922.

Burns, J. A. (1987). Private communication.

Burns, J. A., L. E. Schaffer, R. J. Greenberg, and M. R. Showalter (1985). Lorentz resonances and the structure of the jovian ring. *Nature* 316:115–119.

Burns, J. A., M. R. Showalter, J. N. Cuzzi, and J. B. Pollack (1980). Physical processes in Jupiter's ring: Clues to its origin by Jove! *Icarus* 44:339–360.

Burns, J. A., M. R. Showalter, and G. E. Morfill (1984). The ethereal rings of Jupiter and Saturn. In *Planetary Rings* (R. Greenberg and A. Brahic, eds.), pp. 200–272. Univ. of Arizona Press, Tucson.

Colombo, G., P. Goldreich, and A. Harris (1976). Spiral structure as an explanation for the asymmetric brightness of Saturn's A ring. *Nature* 264:344–345.

Consolmagno, G. J. (1983). Lorentz forces on dust in Jupiter's ring. *J. Geophys. Res.* 88:5607–5612.

Cuzzi, J. N., J. J. Lissauer, L. W. Esposito, J. B. Holberg, E. A. Marouf, G. L. Tyler, and A. Boischot (1984). Saturn's rings: Properties and processes. In *Planetary Rings* (R. Greenberg and A. Brahic, eds.), pp. 73–199. Univ. of Arizona Press, Tucson.

Cuzzi, J. N., and J. A. Burns (1987). Charged particle depletion surrounding Saturn's F ring: Evidence for a moonlet belt. *Icarus,* in press.

Dones, L. (1987). *Dynamical and photometric studies of Saturn's rings*. Ph.D. dissertation, Univ. of California, Berkeley, 196 + vii pp.

Dunham, E., J. E. Elliot, D. Mink, and A. R. Klemola (1982). Limited on possible narrow rings around Jupiter. *Astron. J.* 87:1423–1427.

Elliot, J., and R. Kerr (1985). *Rings: Discoveries from Galileo to Voyager*. MIT Press, Cambridge, Mass.

Ferrín, I. R. (1974). Saturn's rings I. Optical thickness of rings A, B, D, and the structure of ring B. *Icarus* 22:159–174.

Franklin, F. A., A. F. Cook II, R. T. F. Barrey, C. A. Roff, G. E. Hunt, and H. B. de Rueda (1987). Voyager observations of the azimuthal brightness variations in Saturn's rings. *Icarus* 69:280–296.

Goertz, C. K., and W.-H. Ip (1984). Limitation of electrostatic charging of dust particles in a plasma. *Geophys. Res. Ltrs.* 11:349–352.

Grün, E., G. Morfill, G. Schwehm, and T. V. Johnson (1980). A model of the origin of the jovian ring. *Icarus* 44:326–338.

Hanel, R., B. Conrath, M. Flasar, L. Herath, V. Kunde, P. Lowman, W. Maguire, J. Pearl, J. Pirraglia, R. Samuelson, D. Gautier, P. Gierasch, L. Horn, S. Kumar, and C. Ponnamperuma (1979). Infrared observations of the jovian system from Voyager 2. *Science* 206:952–956.

Jewitt, D. C. (1982). The rings of Jupiter. In *Satellites of Jupiter* (D. Morrison, ed.), pp. 44–64. Univ. of Arizona Press, Tucson.

Jewitt, D. C., and G. E. Danielson (1981). The jovian ring. *J. Geophys. Res.* 86:8691–8697.

Jewitt, D. C., G. E. Danielson, and R. J. Terrile (1981). Ground-based observations of the jovian ring and inner satellites. *Icarus* 48:536–539.

Johnson, T. V., G. E. Morfill, and E. Grün (1980). Dust in Jupiter's magnetosphere: An Io source? *Geophys. Res. Ltrs.* 7:305–308.

Lumme, K., and W. M. Irvine (1976). Azimuthal brightness variations in Saturn's rings. *Astrophys. J.* 204:L55–L57.

Morfill, G. E., E. Grün, and T. V. Johnson (1980a). Dust in Jupiter's magnetosphere: Physical processes. *Planet. Space Sci.* 28:1087–1100.

Morfill, G. E., E. Grün, and T. V. Johnson (1980b). Dust in Jupiter's magnetosphere: Origin of the ring. *Planet. Space Sci.* 28:1101–1110.

Morfill, G. E., E. Grün, and T. V. Johnson (1980c). Dust in Jupiter's magnetosphere: Time variations. *Planet. Space Sci.* 28:1111–1114.

Morfill, G. E., E. Grün, and T. V. Johnson (1980d). Dust in Jupiter's magnetosphere: Effect on magnetospheric electrons and ions. *Planet. Space Sci.* 28:1115–1123.

Neugebauer, G., E. E. Becklin, D. Jewitt, R. Terrile, and G. E. Danielson (1981). Spectra of the Jovian ring and Amalthea. *Astron. J.* 86:607–610.

Owen, T., G. E. Daneilson, A. F. Cook, C. Hansen, V. L. Hall, and T. C. Duxbury (1979). Jupiter's rings. *Nature* 281:442–446.

Schaffer, L., and J. A. Burns (1984). Dust motion in Jupiter's tilted magnetic field. *Adu Space Research* 4:107–110.

Schaffer, L. E., and J. A. Burns (1986). Dynamics of weakly charged grains passing through Lorentz resonances: Implications for jovian ring topology. *Bull. Am. Astron. Soc.* 18:777–778.

Schaffer, L., and J. A. Burns (1987a). The dynamics of weakly charged dust: Motion through Jupiter's gravitational and magnetic fields. *J. Geophys. Res.* 92:2264–2280.

Schaffer, L. E., and J. A. Burns (1987b). Private communication.

Showalter, M. R. (1985). Jupiter's ring system resolved: Physical properties inferred from the Voyager images. Ph.D. dissertation, Cornell Univ., 213 + xiii pp.

Showalter, M. R., J. A. Burns, J. N. Cuzzi, and J. B. Pollack (1985) Discovery of Jupiter's "gossamer" ring. *Nature* 316:526–528.

Showalter, M. R., J. A. Burns, J. N. Cuzzi, and J. B. Pollack (1987). Jupiter's ring system: New results on structure and particle properties. *Icarus* 69:458–498.

Smith, B. A., and H. J. Reitsema (1980). CCD observations of Jupiter's ring and Amalthea. Presented at IAU Colloquium 57, Kona, Hawaii.

Smith, B. A., L. A. Soderblom, T. V. Johnson, A. P. Ingersoll, S. A. Collings, E. M. Shoemaker, G. E. Hunt, H. Masursky, M. H. Carr, M. E. Davies, A. F. Cook II, J. Boyce, G. E. Danielson, T. Owen, C. Sagan, R. F. Beebe, J. Veverka, R. G. Strom, J. F. McCauley, D. Morrison, G. A. Briggs, and V. E. Suomi (1979a). The Jupiter system seen through the eyes of Voyager 1. *Science* 204:951–972.

Smith, B. A., L. A. Soderblom, R. Beebe, J. Boyce, G. Briggs, M. H. Carr, S. A. Collins, A. F. Cook II, G. E. Danielson, M. E. Davies, G. E. Hunt, A. Ingersoll, T. V. Johnson, H. Masursky, J. McCauley, D. Morrison, T. Owen, C. Sagan, E. M. Shoemaker, R. Strom, V. E. Suomi, and J. Veverka (1979b). The galilean satellites and Jupiter: Voyager 2 imaging science results. *Science* 206:927–950.

Smith, B. A., L. A. Soderblom, R. Beebe, D. Bliss, J. M. Boyce, A. Brahic, G. A. Briggs, R. H. Brown, S. A. Collins, A. F. Cook II, S. K. Croft, J. N. Cuzzi, G. E. Danielson, M. E. Davies, T. E. Dowling, D. Godfrey, C. J. Hansen, C. Harris, G. E. Hunt, A. P. Ingersoll, T. V. Johnson, R. J. Kraus, H. Masursky, D. Morrison, T. Owen, J. Plescia, J. B. Pollack, C. P. Porco, K. Rages, C. Sagan, E. M. Shoemaker, L. A. Sromovsky, C. Stoker, R. G. Strom, V. E. Suomi, S. P. Synnott, R. J. Terrile, P. Thomas, W. R. Thompson, and J. Veverka (1986). Voyager 2 in the uranian system: Imaging science results. *Science* 233:43–64.

Synnott, S. P. (1984). Orbits of the small inner satellites of Jupiter. *Icarus* 58:178–181.

Thompson, W. T., K. Lumme, W. M. Irvine, W. A. Baum, and L. W. Esposito (1981). Saturn's rings: Azimuthal variations, phase curves and radial profiles in four colors. *Icarus* 46:187–200.

Tyler, G. L., E. A. Marouf, and G. E. Wood (1981). Radio occultation of Jupiter's ring: Bounds on optical depth and particle size, and a comparison with infrared and optical results. *J. Geophys. Res.* 86:8699–8703.

PART II

MAGNETOSPHERIC PHENOMENA, IO'S TORUS, AND AURORAE

PRECEDING PAGE BLANK NOT FILMED

9

Possible Time Variations of Jupiter's Magnetic Field

E. H. Levy
University of Arizona, Tucson

Abstract

Planetary magnetic fields are apparently generated by magnetohydrodynamic dynamos in the highly electrically conducting fluid interiors of the planets. Temporal variations in such dynamo magnetic fields occur directly as a result of the motions of the electrically conducting fluid in which the field lines are embedded and as a result of the overall temporal behavior of the dynamo's regenerative modes. Thus, the observed variations, of internal origin, in a planetary magnetic field yield clues about the characteristics and motions of the planet's interior. This chapter briefly reviews the basic physical processes leading to magnetic field variations of internal origin in planets and surveys the implications of such variations as may be observed at Jupiter for our understanding of that planet.

INTRODUCTION

Planets have strong, large-scale magnetic fields because their interiors are composed of electrically conducting fluids that convect, because the planets rotate, and because there are few, if any, free magnetic charges to magnetically short-circuit the fields (Parker, 1970a).

To the extent that an electrically conducting fluid creates an effective electric short circuit between any two points in the fluid, the fluid cannot sustain an electric field within itself. However, a moving magnetic field is equivalent to an electric field, through the standard Lorentz transformation. Therefore, a highly electrically conducting fluid cannot tolerate the motion of a magnetic field within it, and the field and the fluid are constrained to move together. We say that the magnetic field lines are frozen into the fluid (Alfvén, 1950). Magnetic field lines can move through such a fluid only to

PRECEDING PAGE BLANK NOT FILMED

the extent allowed by the finite value of the electrical resistivity, which allows an electric field to be sustained.

As a consequence of the magnetohydrodynamic behavior described above, variations of a planetary magnetic field, of internal origin, reflect the motions of the fluid in which the magnetic field lines are embedded—either directly, as the magnetic field lines are dragged around by the fluid, or indirectly, as a consequence of the magnetic-field generation process acting on the average, large-scale field.

Apparently, planetary magnetic fields are generated by the action of magnetohydrodynamic dynamos (Parker, 1955, 1970b, 1979; Braginskii, 1964; Steenbeck, et al., 1966; Krause and Rädler, 1980). This same dynamo process also seems to account for the generation of magnetic fields in a wide variety of other cosmic objects.

The two cosmic magnetic fields that are the most completely studied are those of the Earth and the Sun. Most of our ideas about the generation and behavior of cosmic magnetic fields have been provoked and shaped by our knowledge of these two objects. Therefore, we will begin this brief overview with a review of the terrestrial and solar magnetic fields and we will apply the lessons learned from those examples, and from the basic properties of the magnetohydrodynamic equations, to explore the possible magnetic behaviors of Jupiter. At our present state of understanding, both of the internal dynamics of Jupiter and of the general behavior of magnetohydrodynamics (MHD) systems, this seems like a more useful approach than the detailed exploration of some particular model. Also, because the rudiments of magnetic field generation are unfamiliar to many of the workers at whom this volume is directed, we will couch the discussion in terms of a basic review of the theory.

THE TERRESTRIAL AND SOLAR MAGNETIC FIELDS

The Geomagnetic Field

To a first approximation, the geomagnetic field is centered, axially aligned dipole with a surface strength of about one half gauss. The *poloidal* magnetic field lines, which we observe outside of the planet's core, extend down through the mantle and penetrate into the core, there constituting one component of the core magnetic field—the poloidal component, with an intensity of 5–10 gauss.

Examining Earth's surface magnetic field more closely, one sees substantial departures from the idealized axial dipole. The dipole moment is offset from Earth's center by several hundred kilometers and the dipole axis is tilted some 11.5° from the axis of rotation. Of the total surface magnetic field, only about 80 percent is attributable to the dipole component; the remaining 20 percent consists of higher-order multipoles. Subtracting away the dipole and looking only at the higher components of the field, one finds that the residual field is arranged in about a dozen continental-size patches of magnetization scattered about the surface.

Neither the geomagnetic dipole nor the pattern of higher-order field components is invariant. The magnetic dipole axis wanders westward and the tilt angle varies randomly through time, as no doubt, does the central offset. The higher-order field components (namely, the large surface patches of magnetization) drift westward at a rate of about one fifth of a degree of longitude per year; other variations aside, the westward drift would carry the pattern completely around the globe in about 2000 years. However, the scattered magnetization patches do not constitute a rigid pattern. The individual patches seem to develop and evanesce with lifetimes typically lasting some 10^3 years.

The overall magnetic field strength also varies substantially with time. Paleomagnetic studies indicate that the total field strength varies randomly with time scales of 10^3 to 10^4 years and with the amplitude of variation being some one half of the average amplitude.

Perhaps the most spectacular variation in the geomagnetic field is the geomagnetic reversal. Occasionally, and apparently suddenly and spontaneously, the geomagnetic field reverses its polarity (Runcorn, 1955). The individual polarity intervals are of random duration and follow a Poisson distribution with the average length of a polarity interval being about 200,000 years (Cox, 1975). Individual polarity intervals may be as short as 10,000 years and as long as many millions of years.

The Solar Magnetic Field

Upon first look, the Sun's magnetic field appears disordered and entirely unlike the far smoother geomagnetic field. This is, in part, because we look directly onto the generation region of the solar magnetic field—the solar convection zone, where the magnetic field is still locked into a highly dynamic fluid—whereas the geomagnetic field's generation region is hidden from view more than 3000 kilometers beneath a static, non-electrically conducting mantle. However, careful examination reveals the Sun's magnetic field to have a highly ordered structure.

At low and middle latitudes, the Sun's surface magnetic field is highly irregular in structure and distribution; at high latitudes the field has a more regular, polar structure. Overall, the solar magnetic field has the odd spatial symmetry of a dipole. Small-scale magnetic structures at low and middle latitudes on the Sun—sunspot pairs and bipolar regions—systematically have the same polarity sense in one hemisphere of the Sun (north or south), with one polarity consistently leading the other in the direction of the Sun's rotation. In the other hemisphere, the polarities have the opposite ordering. The small-scale magnetic structures tend to rotate faster than the surface layers of the Sun itself; in addition, the rotation rate varies with solar latitude, decreasing toward the poles. The magnitudes of these rotational variations seems to substantially exceed 10 percent of the solar rotation rate.

The Sun's magnetic field undergoes a regular oscillation with a full period of about 22 years. After each 11-year half-period (corresponding to periods of high sunspot activity), the entire magnetic structure of the Sun changes polarity. The polar fields (the dipolelike parts) change sign and the polarity relationships in the lower-latitude, small-scale fields also reverse. This regular oscillatory behavior is distinctly different from the reversal behavior of the geomagnetic field. The geomagnetic field has long periods of quasi-stationary magnetic field, interspersed by sudden polarity reversals after random intervals of time. (For more details about the complicated behavior of the Sun's magnetic field, see Parker, 1979, and references therein; also Howard, 1977; Zwaan, 1987.)

MAGNETIC FIELD BEHAVIOR AND DYNAMOS

Under conditions where the classical laws of physics apply, magnetic fields in fluids are described by Maxwell's equations and Newton's laws. In a highly electrically conducting fluid, slowly evolving magnetic fields are described by the magnetic induction equation, derived from Maxwell's equations (Alfvén, 1950; Parker, 1970a; Roberts, 1967):

$$\frac{\partial \mathbf{B}}{\partial t} = \nabla \times (\mathbf{v} \times \mathbf{B}) + \eta \nabla^2 \mathbf{B}, \qquad (9.1)$$

where $\eta = c^2/4\pi\sigma$ is the so-called magnetic diffusivity, whereas σ is the fluid's electrical conductivity, here taken to be homogeneous. The two terms on the right-hand side of eq. (9.1) correspond respectively to the convection of magnetic field lines with the moving fluid and to diffusion of magnetic field lines through the fluid. Both of these effects contribute to the total time variation of a planetary magnetic field.

The fluid velocity is given by the equation of motion,

$$\rho \frac{\partial \mathbf{v}}{\partial t} + \rho \mathbf{v} \cdot \nabla \mathbf{v} = -\nabla p + \frac{1}{4\pi} (\nabla \times \mathbf{B}) \times \mathbf{B} + \cdots \qquad (9.2)$$

Equations (9.1) and (9.2), supplemented by ancillary constitutive relations and boundary conditions, describe the behavior of a cosmic dynamo magnetic field. The magnetic fields of planets correspond to solutions of these equations that have the magnetic field, **B**, nonvanishing after long times.

Planetary Dynamos

A variety of specific types of fluid motion have been put forward for planetary dynamos. Because the dynamic problems of planetary fluid motion remain largely unsolved, there is uncertainty about the detailed character of the fluid motion within planets. However, the essential aspects of fluid motion that seem to be responsible for magnetic field generation in a variety of cosmic objects, including planets, include nonuniform rotation and cyclonic, or helical, convection (fig. 53). The dynamo regeneration of such a magnetic field occurs as a result of a closed-cycle process. The nonuniform rotation generates, from the poloidal part of the field, a toroidal magnetic field confined to the electrically conducting parts of a planet (fig. 54). The helical convection interacts with the toroidal magnetic field to produce new poloidal magnetic field (fig. 55), thus closing the regeneration cycle as shown in figure 56. Although this schematic is somewhat simplified, leaving aside higher-order effects, it captures the essential features of the regeneration process (Parker, 1955, 1970b; Moffatt, 1978; Krause and Rädler, 1980).

Mathematically, this simplified magnetic field regeneration cycle can be written in the form of a set of dynamo equations (see, for example, Parker, 1955, 1979; Levy, 1976).

$$\frac{\partial B_\phi}{\partial t} - \eta\left(\nabla^2 - \frac{1}{r^2 \sin^2\theta}\right) B_\phi = \left(\frac{\partial v_\phi}{\partial r} - \frac{v_\phi}{r}\right) B_r + \cdots, \qquad (9.3)$$

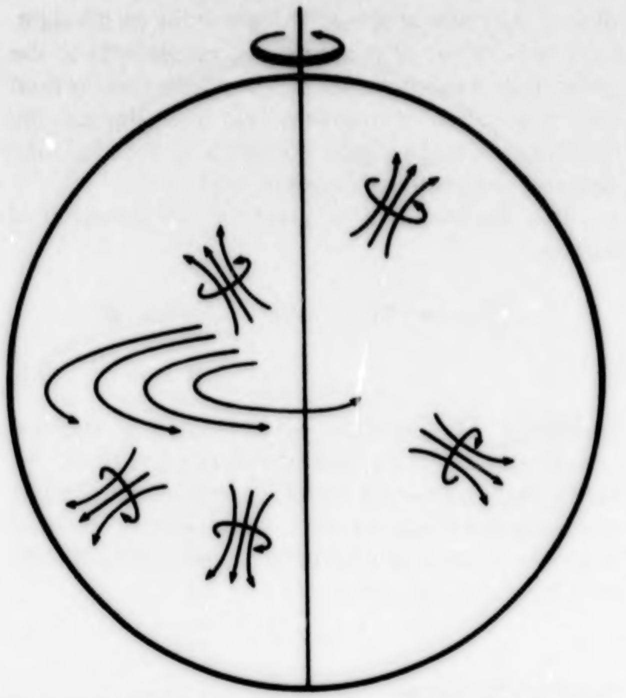

Figure 53. The fluid motions that make for efficient magnetic field generation in cosmic systems, including planets, consist of large-scale nonuniform rotation and cyclonic, or helical, convection. In the cyclonic convection, $[\nabla \times \mathbf{v}] \times \mathbf{v} \neq 0$ locally.

$$\frac{\partial A_\phi}{\partial t} - \eta\left(\nabla^2 - \frac{1}{r^2 \sin^2\theta}\right)A_\phi = \Gamma B_\phi, \qquad (9.4)$$

and

$$\mathbf{B}_\mathrm{p} \equiv (B_r, B_\theta) = \nabla \times A_\phi \mathbf{e}_\phi. \qquad (9.5)$$

In eq. (9.3), only the source term resulting from the radial gradient in the fluid's angular velocity is shown on the right-hand side; a similar source term, resulting from the latitudinal gradient is left out. In eq. (9.4), the quantity Γ is the cyclonic component of the convective flow, to within a multiplicative geometrical filling factor of the order of unity.

The Character of the Generated Fields—Stationary Modes

Taking eqs. (9.3) through (9.5) in dimensional form, and considering first stationary magnetic fields for which $\partial/\partial t \equiv 0$, we have

$$-\eta \frac{B_\phi}{R^2} \sim \gamma B_\mathrm{p} \qquad \left[\sim \frac{\Delta v_\phi}{R} B_\mathrm{p}\right], \qquad (9.3a)$$

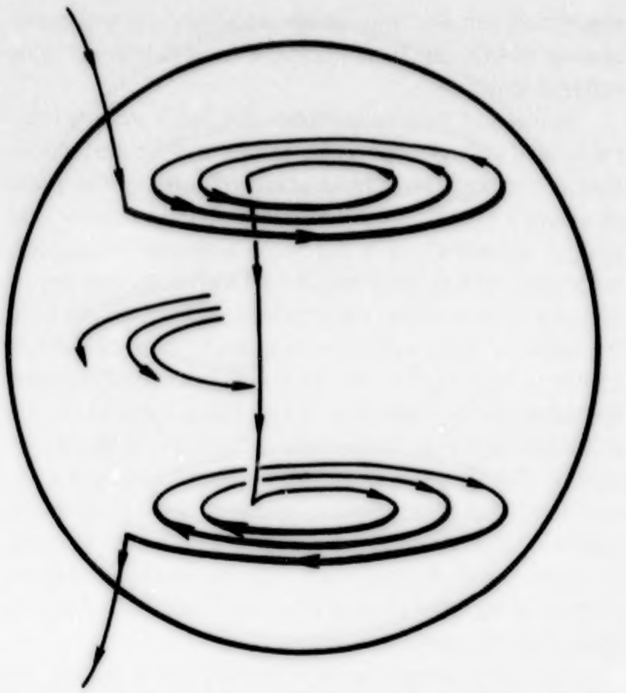

Figure 54. Nonuniform rotation, in the highly electrically conducting fluid of a planetary dynamo, winds the poloidal magnetic lines of force around the rotation axis. This produces a strong toroidal magnetic field that is confined entirely to the electrically conducting interior.

$$-\eta \frac{A_\phi}{R^2} \sim \Gamma B_\phi \qquad [\sim V_\mathrm{cyc} B_\phi], \qquad (9.4a)$$

and

$$B_\mathrm{p} \sim \frac{A_\phi}{R}. \qquad (9.5a)$$

These three homogeneous algebraic equations have a solution in the case that the determinant of their coefficients vanishes; thus a solution requires that

$$N \equiv \frac{\gamma \Gamma R^3}{\eta^2} = 1. \qquad (9.6)$$

The so-called "dynamo number," N, is a measure of the overall vigor of the regenerative fluid motion, measured in terms of the magnetic dissipation rate; it can easily be seen to be the product of the *magnetic Reynolds numbers* corresponding to the differential rotation and to the cyclonic part of the convection. The criterion that $N = 1$ for a stationary solution of the dynamo equations corresponds to the requirement that the rate of magnetic field generation by the fluid motion balances the rate of the field's dissipation by electrical resistance. Rigorous calculations lead to results that are similar to those of this crude analysis except that a hierarchy of stationary solutions is found to exist: Stationary solutions occurring with larger amplitudes of the fluid velocity (namely, larger N) are typically found, as expected, to have smaller spatial scales. Moreover, in formal solutions to the dynamo equations, the most easily excited stationary state usually has $N \simeq 10^2$, as a result of the various geometrical factors that are neglected in the simple dimensional analysis given here (Levy, 1972a, c; Roberts, 1972; Stix, 1973).

The dynamo equations also have solutions with amplitudes that grow or decay monotonically. For example, if the dynamo number of a fluid flow is slightly below the smallest critical value that corresponds to a stationary state, the magnetic field amplitude will decay exponentially. On the other hand, if the dynamo number is slightly larger than this smallest critical value, the magnetic field amplitude will grow exponentially. In both cases the *e*-folding time of the field variation depends on the actual value of the dynamo number, increasing in magnitude for larger deviations of the dynamo number away from the stationary-state value—at least in the immediate neighborhood of the stationary state (Parker, 1971).

It is also worth pointing out that the dynamo equations are homogeneous in the magnetic-field quantities, so that neither the amplitude nor the overall polarity of the magnetic field is specified by these

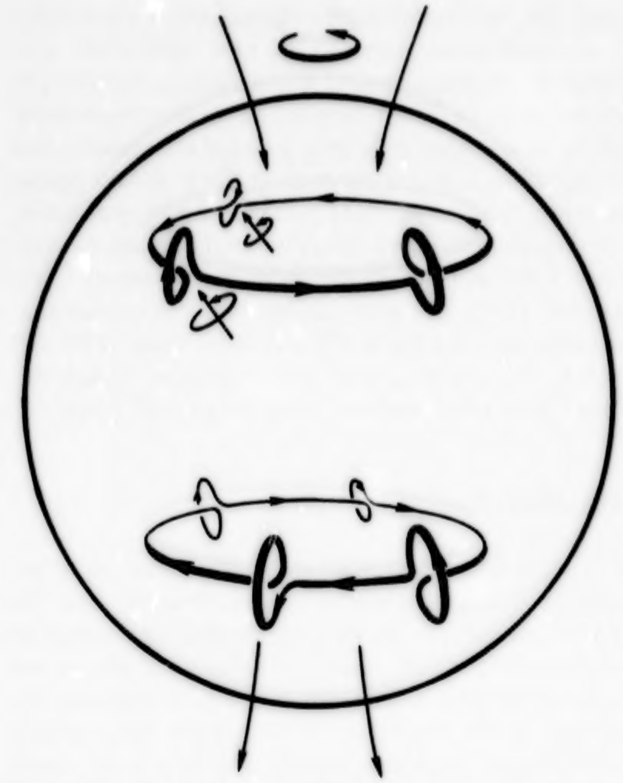

Figure 55. The cyclonic convection raises loops in the strong toroidal magnetic field lines and twists the loops toward the local meridional plane to generate a source of poloidal magnetic field that reinforces the original poloidal magnetic field.

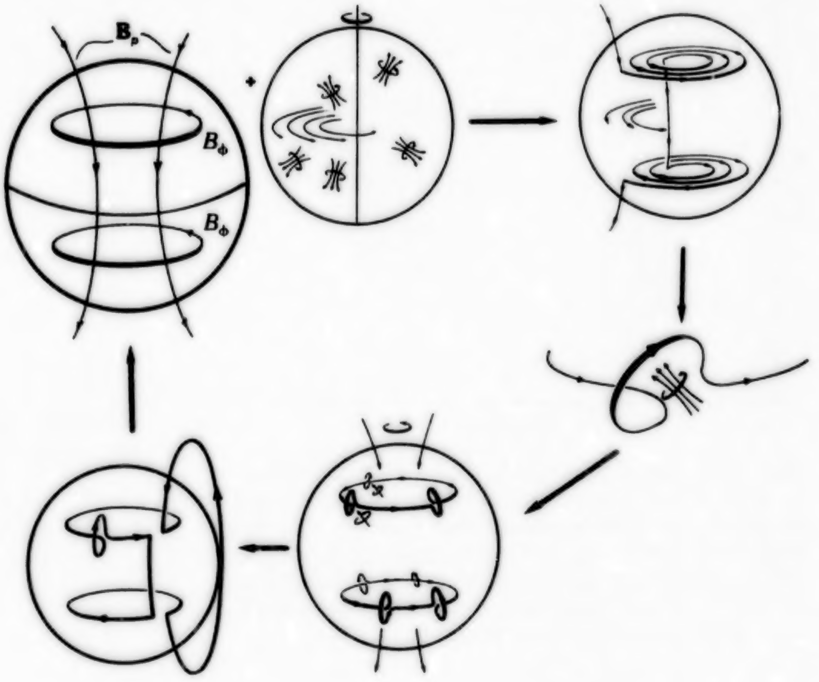

Figure 56. Altogether the magnetic field is regenerated by a self-consistent closed cycle in which the nonuniform rotation generates toroidal magnetic field from the poloidal magnetic field and the cyclonic convection generates poloidal magnetic field from the toroidal magnetic field. The illustration here is highly schematic, but it captures the essential features of the dynamo regeneration process.

kinematic equations. Either polarity of the magnetic field is equally well generated by such a dynamo; replacing all of the magnetic field quantities in eqs. (9.3) through (9.5) or, equivalently, reversing the directions of all of the magnetic field vectors in the illustrations, leaves the dynamo regeneration process unchanged. The magnetic field amplitude attained by a dynamo system is, in the end, determined by the dynamics of the fluid motion. Specifically the Lorentz force from the magnetic field must ultimately alter the fluid motion through eq. (9.2) and cause the magnetic field intensity to saturate. This difficult nonlinear problem has still not been solved. However, because the Lorentz force is second order in the magnetic field, inclusion of the dynamic considerations does not alter the symmetry of the dynamo with respect to the magnetic field's polarity.

Dynamo stationary states may be either dynamically stable or unstable (Levy, 1974). Inasmuch as the dynamically unstable states will not be observed in real bodies, they need not be considered further here. In real systems, the dynamo stationary states will actually be observed as quasi-stationary variations of the field about a stable stationary equilibrium. Although the idealized linear perturbation example illustrated in figure 57 shows the magnetic field variation as a regular oscillation, in the real case such a quasi-stationary magnetic field will likely vary chaotically in the vicinity of an equilibrium attractor. The time scale of the very small oscillations around the stationary equilibrium shown in figure 57 can be quite rapid, the period being of the order of the geometric mean of the resistive free decay time and the dynamo regions' Alfvén speed crossing time (Levy, 1974). Such rapid—approximately 10^2 years—very small amplitude field variations may have been detected in the geomagnetic record (Braginskii, 1970). The geomagnetic field also varies randomly by about a factor of two on time scales of 10^3–10^4 years. The geomagnetic dipole amplitude has decreased by a few percent during the past 100 years.

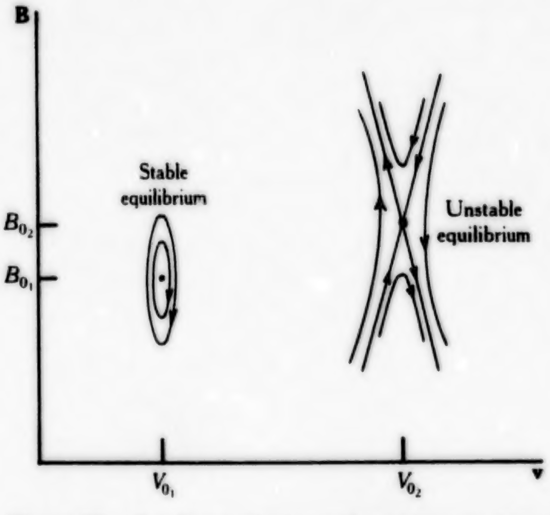

Figure 57. Small perturbations of a stationary dynamo magnetic field from its equilibrium state produce dynamic oscillations around the equilibrium (shown as the closed trajectories on the left in this **B-v** phase-space plot). Some dynamo equlibrium states may be dynamically unstable (shown on the right with open phase-space trajectories) and will not be observed in real objects.

Oscillatory Modes

On paper, oscillatory magnetic modes occur more frequently than do stationary modes. However, only for Earth and the Sun do we have enough information to know whether the magnetic fields oscillate or are quasi-stationary; we observe one of each. Consider the nature of the oscillatory modes. Following Parker's (1971) simple analysis, consider a dynamo occurring in a flattened, Cartesian-coordinate dynamo. In these coordinates, the dynamo equations take the following elementary form:

$$\frac{\partial B_y}{\partial t} - \eta\nabla^2 B_y = \gamma B_x;$$

$$\frac{\partial A_y}{\partial t} - \eta\nabla^2 A_y = \Gamma B_y;$$

$$B_x = -\frac{\partial A_y}{\partial z}. \tag{9.7}$$

The oscillating magnetic field can be thought of as wave mode in a resonant cavity formed by the dynamo region. To obtain a dispersion relation for the waves, write

$$\begin{pmatrix} A_y \\ B_y \end{pmatrix} = \begin{pmatrix} A \\ B \end{pmatrix} \exp\,(ikz - i\omega t). \tag{9.8}$$

Using the ansatz in eq. (9.8), we find the solution to eqs. (9.7) as

$$\begin{pmatrix} A_y \\ B_y \end{pmatrix} = \begin{pmatrix} A \\ B \end{pmatrix} \exp i \left[kz \pm \sqrt{\frac{|\gamma\Gamma|}{2}}\, t\right]$$
$$\exp\left[-\eta k^2 \sqrt[4]{\frac{|\gamma\Gamma|}{2}}\right] t. \tag{9.9}$$

Equation (9.9) describes the basic behavior of an oscillating dynamo mode. If L is the length scale of the magnetic mode generated in the dynamo cavity—usually the linear size of the dynamo region for the lowest order mode—then $k = 2\pi/L$. Note that, for a constant amplitude oscillation, the second exponent in eq. (9.9) must vanish, that is to say $Im(\omega) = 0$. Comparing the first and second exponents, we then find that the period of a constant amplitude oscillatory mode is given by

$$Re(\omega) = \eta k^2. \qquad (9.10)$$

Equation (9.10) states that the period of an oscillatory mode should be of the same order as the dissipative decay time of the mode. This is a useful result; the diffusivity, η, generally is easier to estimate than is the quantity $\gamma\Gamma$ in eq. (9.9), inasmuch as the latter quantity involves difficult-to-calculate dynamic factors.

As an example of the application of eq. (9.10) in a real object, consider the oscillation period of the Sun. Using an effective average electrical conductivity of 10^{15} s^{-1} for the fluid in the solar convection zone and 10^{11} cm for the length scale, one finds an oscillation period, $\mathcal{P} = L^2/(2\pi\eta)$, of about 5×10^8 years—clearly in disagreement with the observed 22-year solar magnetic cycle. This discrepancy illustrates the role of turbulent transport in enhancing magnetic-field dissipation rates. In the solar convection zone, and probably also in Jupiter, the dissipation of the magnetic field is dominated by turbulent and other macroscopic transport processes, resulting in time scales for variations of the global-scale magnetic-field components that are far faster than would be predicted on the basis of classical electrical resistance alone.

In the solar convection zone, magnetic-field transport and dissipation are dominated by the turbulent convective motions. Crudely, the effective turbulent diffusion coefficient for magnetic fields can be written (Steenbeck et al., 1966; Leighton, 1969; Parker, 1979, and references therein) as $\eta_t = 0.1 v_t \lambda_t$, where v_t is the fluid velocity in the large turbulent eddies and λ_t is the length scale of the largest turbulent eddies. Taking, for the Sun, $v_t \sim 0.5$ km s^{-1} and $\lambda_t \sim 10^9$ cm, corresponding to the observed properties of the supergranulation, then $\eta_t \sim 10^{13}$ cm^2 s^{-1}. Using this turbulent magnetic diffusion coefficient in eq. (9.10), one finds a value of about 10 years for the period of the solar magnetic cycle, a result that is in good agreement, for such a crude analysis, with the observed value of 22 years.

JUPITER

There is not enough evidence in hand at present to judge whether Jupiter's magnetic field is quasi-stationary, as is the geomagnetic field, or oscillatory, as is the solar magnetic field. Both possibilities must be considered in anticipating possible magnetic-field variations of internal origin in that planet.

Time Variations of a Quasi-stationary Field

There are four major varieties of time variations that should be considered: changes in the overall amplitude of the magnetic field (e.g., in the magnitude of the dipole moment), the growth and decay of small-scale field components, the longitudinal drift and shear of small-scale structures, and field polarity reversals.

Overall Amplitude Variations

Large variations of the magnetic field's overall amplitude can occur on the time scale of the field's free decay time, determined by the classical electrical resistance decay time or by the turbulent transport time, whichever is the smaller. For Earth, the resistive magnetic diffusion coefficient η_r, and the turbulent magnetic diffusion coefficient, η_t, are comparable: $\eta_r \sim \eta_t \sim 10^5$ cm^2 s^{-1}. The magnetic diffusion time for the dipole mode is $\tau_d = R^2/4\eta$; for the values of the relevant variable corresponding to Earth's core, $\tau_d \sim 10^4$ years.

For Jupiter's metallic interior, $\sigma \sim 10^{17}$ s^{-1} (Hubbard, 1973), so that $\eta_r \sim 10^3$ cm^2 s^{-1}, and the radial extent of the dynamo region is probably in the range near 5×10^9 cm, leading to a decay time for the dipole component, based on classical electrical resistivity, of 2×10^8 years. However, Jupiter is thought to have vigorous, thermally driven convection in its interior, with typical convective velocities of about 10 cm s^{-1}. The effective mixing length scale of the convection that we will guess to be in the range of 10^7 to 10^9 cm depends on the details of the convection, which are not understood, especially with respect to the effect of rotation and a strong magnetic field on the effective mixing length scale. Thus $\eta_t \sim 10^7$–10^9 cm^2 s^{-1}, leading to a dipole-mode decay time of $\tau_d \sim 10^4$–10^2 years. In Jupiter, turbulent transport probably dominates the magnetic field dissipation, as it does in the Sun. Depending on the effective mixing scale of the convective motions, then, the overall time scale of large changes in Jupiter's magnetic field strength would be in the range of 100 to 10,000 years. Over the approximately 20 years of observation time encompassing the Pioneer, Voyager, and Galileo spacecraft projects, one might expect the change in the overall magnetic moment of Jupiter to be in the range of a few tenths of 1 percent to perhaps as large as 10 percent, even if the jovian magnetic field operates in a stationary dynamo mode. However, the absence of a striking change between the times of the Pioneer and Voyager spacecraft measurements and limitations imposed by general stability of radio emissions leave a low likelihood for variations at the high end of that range.

Growth and Decay of Small-Scale Field Components

The time scale for the growth and decay of small-scale field components is of the order of $\tau_{ss} \sim \lambda/v_c$, where λ is the length scale of the convective eddies, and v_c is the fluid velocity. For Earth, $\lambda \sim 3 \times 10^8$ cm and $v_c \sim 10^{-2}$ cm s^{-1}. This leads to $\tau_{ss} \sim 10^3$ years, which is consistent with the observations, but then again both λ and v_c are derived from those observations, so that the agreement is inevitable.

For Jupiter, with a convection velocity of the order of 10 cm s^{-1}, the interior fluid turnover time is as short as a few tens of years. Thus, if the pattern of dynamo regenerative fluid motions in Jupiter were similar to that in Earth (where the coherence length of the major convective eddies seems to be of the order of the radius of the electrically conducting core and the coherence time of the individual eddies seems to be of the order of the fluid turnover time) one might expect major variations in the magnetic field on a time scale as short as one or a few decades, with length scales of a few times 10^9 to 10^{10} cm. However, the presence of such rapidly varying field structures in the internal magnetic field is by no means guaranteed. If the convective motions were organized into persistent, long-lived convection rolls as in the scenario suggested on the basis of a geostrophic-balance dynamic model of planetary magnetic-field generation (Busse, 1976, 1977), then even the rapid fluid velocities would not give rise to rapid field variations. In that case, the field variations would be governed by the coherence time of the pattern of convection rolls, something that is not known.

Very rapid variations of the small-scale magnetic field components would be partially shielded by intervening matter of finite electrical conductivity. The degree to which this effect would mask rapid variations in the small-scale field depends on the detailed distribution of convective motions and electrical conductivity within Jupiter. If externally detectable variations in the internal field are indeed measured, these would provide a potent tool for probing some of Jupiter's internal structure and dynamics. Unfortunately, the large distance from Jupiter at which the Galileo spacecraft will orbit will limit that spacecraft's ability to make decisive measurements of the planet's smaller-scale magnetic field features.

Drift and Shear of the Field—Motion of the Dipole

As pointed out above, Earth's magnetic field drifts westward at about one fifth of a degree longitude per year on the average, lagging the rotation of the mantle. The magnetic pole also wanders in a generally westward direction at about 0°.05 per year and wanders in inclination, presently at about the rate of 0°.02 per year toward the rotational pole (Nagata, 1965). The longitudinal drift of the Sun's magnetic field is probably better characterized than is that of the Earth's; this is because the rate of drift is much larger and because the Sun has very small-scale and well-defined magnetic structures that can be seen from afar and the motions of which can be relatively well characterized. The Sun's magnetic field tends to drift eastward with respect to the photosphere, leading the rotation of the Sun's surface layers. The Sun's latitudinal variation in rotation rate—involving a latitudinal shearing of at least some components of the field structure—probably has an analog in the behavior of Earth's magnetic field. But the time during which detailed global observations of Earth's magnetic field have been carried out, roughly 400 years, has spanned only slightly more than one radian of rotational displacement of the magnetic field, roughly the size of a single large surface magnetic feature. Thus many details of the geomagnetic field's secular behavior remain fuzzy.

The presence of latitudinal variations in the rotation rate of Jupiter's magnetic field would not be surprising. The question remains open, although the possible detection of alternate rotation systems for the jovian magnetic field (Sandel and Dessler, 1988) may indicate the presence of shearing motions in the magnetic field. It worth noting that a several percent difference in rotation periods corresponds to a differential rotation speed somewhat in excess of 10^4 cm s^{-1}; this is of the order of, or smaller than, the differential rotation speed that is indicated by the latitudinal differential rotation seen in the Sun. The observational analysis of rotational inhomogeneities in Jupiter's magnetic field is made difficult by the absence of a rigidly rotating reference frame fixed to the planet, a role played for the Earth by the crust; the fluid body of Jupiter does not have a well-defined rotation of its own against which the magnetic field can be measured. As a result, the shearing motions of the magnetic field must be calibrated internally against the field structure itself.

Altogether, there is *no* reason to expect that Jupiter's magnetic field will rotate as a rigid structure and every reason to expect the opposite. The shearing of the magnetic field should provide a powerful clue as to the character of Jupiter's internal fluid motions. The challenge is to determine the shearing motions. Because the predominant shearing will be found in the smaller-scale field components, the diagnostic ability of a spacecraft such as Galileo, confined as it is to orbits relatively distant from the planet, is generally limited in this area. The use of proxy measures such as periodicities in radio emissions may be a useful tool; but it remains to be understood why such phenomena pick out a few specific rotational frequencies from a shearing structure that is likely to have a distribution of rotation rates that is more or less continuous over some range. One problem in the interpretation of such data is to ascertain the extent to which the secondary mechanisms that are actually measured may act as a filter to pass only a subset of the frequencies that characterize the magnetic field itself.

Polarity Reversals

Quasi-stationary dynamo modes are susceptible to polarity reversals as a result of transient fluctuations in the distribution of convection (Parker, 1969; Levy, 1972b, c), and the occasional polarity reversals of Earth's quasi-stationary magnetic field seem to be at least explicable on that basis, without appealing to more complicated magnetohydrodynamic behaviors that are not presently understood. On this basis, the reversals of Earth's magnetic field occur because the regenerative convection is distributed over a relatively small number (~10 or 20) of randomly distributed convection cells; it is fluctuations in this distribution that induce the magnetic polarity reversals in the cited scenarios. In a much larger object, such as the Sun, there are many more individual convection cells contributing to the generation of the magnetic field. Thus, a large random fluctuation in the distribution is far less likely and polarity reversals of a quasi-stationary field—at least through this mechanism—are also far less likely than for Earth. The convection patterns in Jupiter are not known, but they may be analogous to those in Earth with convective length scales comparable to the size of the dynamo region. Because the convective fluid motions in Jupiter are some 10^3 times faster than in Earth, and the effective magnetic-field diffusion coefficient consequently much larger, the time scale for a polarity reversal, if one were to occur, could be expected to be shorter than in Earth by as much as one or two orders of magnitude. Thus, if a polarity reversal did occur, it could be completed over a time span of a hundred years of less.

It cannot be ruled out that Jupiter's magnetic field will reverse polarity during a period of observation spanning the next several hundred years. However, determining whether such a polarity reversal were an episodic reversal of a quasi-stationary mode or a regular reversal of an oscillatory mode would require observations extending over a period of time substantially longer than R^2/η, the magnetic field's "free" decay time.

Regular Oscillations of the Magnetic Field

The lowest order dynamo mode in Jupiter would have a length scale of the order of 10^{10} cm. As discussed above, the turbulent diffusivity is likely to be in the range $\eta_t \sim 10^7$–10^9 cm^2 s^{-1}. Using these values in eq. (9.10), we find that the expected oscillation period of Jupiter's magnetic field, if it were to operate in an oscillatory mode, would be in the range of 10^4–10^2 years (Levy, 1976; see also Hathaway and Dessler, 1986). The latter value of about 10^2 years assumes that the mixing length scale of the convection in Jupiter is 10^9 cm; inasmuch as that is within a factor of a few of the maximum possible mixing length scale (the radial extent of Jupiter's dynamo region), 100 years must be within a factor of a few of an absolute lower bound on jovian magnetic field oscillation period, within the constraints of present theory.

CONCLUSIONS

This chapter has briefly summarized the variety of major temporal variations that may be exhibited by dynamo magnetic fields. We have been guided by our understanding of the kinds of fluid motions that seem to efficiently generate magnetic fields in cosmic objects, by the basic mathematical properties of the dynamo equations and their solutions, which seem to describe the generation of such magnetic fields, and by the observed behavior of the Earth's and the Sun's magnetic fields, the two best studied of cosmic magnetic fields.

Owing to the relatively high convective velocities in Jupiter, the fluid turnover time in the electrically conducting interior may be as short as a decade, two orders of magnitude shorter than in Earth. Over a time span of decades, relevant to the subject matter of this volume, Jupiter's magnetic field could exhibit a number of variations of internal origin, including changes in the field's overall amplitude, variations in the small-scale structures, longitudinal shearing motions, and variations in magnetic pole position; polarity reversals—either episodic or regular oscillations—probably cannot be ruled out over intervals exceeding 10^2 years. Some such variations are sure to be discovered if the magnetic field can be measured with enough sensitivity to small-scale components. However, the orbit of the Galileo spacecraft will impose a severe limitation in that respect. Important information about variations in Jupiter's magnetic field—or limits on such variations—remain also to be extracted from continuing radio observations. A challenge is to separate observed changes due to changes in the magnetic field from other effects, extraneous from that point of view (Hide and Stannard, 1976, and references therein; de Pater, this volume). The detection of magnetic field variations of internal origin would provide a powerful diagnostic as to the state of fluid motions within Jupiter. The objective of obtaining high quality magnetic field measurements close to Jupiter (as well as close to other planets) should play a role in the planning of investigations, both for Galileo and for missions that follow it.

ACKNOWLEDGMENTS

I am grateful to W. B. Hubbard for a useful discussion. This work was supported by the U.S. National Aeronautics and Space Administration under grant NSG-7419.

References

Alfvén, H. (1950). *Cosmical electrodynamics*, 1st edition, Clarendon Press, Oxford.

Braginskii, S. I. (1964). Kinematic models of the earth's hydrodynamics dynamo. *Geomagn. i Aeron.* 4:732–744.

Braginskii, S. I. (1970). Oscillation spectrum of the hydrodynamics dynamo of the earth. *Geomagn. i Aeron* 10(3): 221–232.

Busse, F. H. (1976). Generation of planetary magnetism by convection. *Phys. Earth Planet. Int.* 12:350–358.

Busse, F. H. (1977). An example of non-linear dynamo action. *J. Geophy.* 43:441–452.

Cox, A. (1975). The frequency of geomagnetic reversals and the symmetry of the nondipole field. *Rev. Geophys. Space Phys.* 13(3): 35–51.

Hathaway, D. H., and A. J. Dessler (1986). Magnetic reversals of Jupiter and Saturn. *Icarus* 67:88–95.

Hide, R., and D. Stanndard (1976). In *Jupiter* (T. Gehrels, ed.). Univ. of Arizona Press, Tucson.

Howard, R. (1977). Large-scale solar magnetic fields. *Ann. Rev. Astron. Astrophys.* 15:153–173.

Hubbard, W. B. (1973). Interiors of Jupiter and Saturn. *Ann. Rev. Earth Planet. Sci.* 1:85–106.

Krause F., and K.-H. Rädler (1980). *Mean-field magnetohydrodynamics and dynamo theory*, Pergamon Press, New York.

Leighton, R. B. (1969). Transport of magnetic fields on the Sun. *Astrophys. J.* 140:1559–1562.

Levy, E. H. (1972a). Effectiveness of cyclonic convection for producing the geomagnetic field. *Astrophys. J.* 171:621–634.

Levy, E. H. (1972b). Kinematic reversal schemes for the geomagnetic dipole. *Astrophys. J.* 171:635–642.

Levy, E. H. (1972c). On the state of the geomagnetic field and its reversals. *Astrophys. J.* 175:573–581.

Levy, E. H. (1974). Dynamical stability of stationary dynamo magnetic fields. *Astrophys. J.* 187:361–367.

Levy, E. H. (1976). Generation of planetary magnetic fields. *Ann. Rev. Earth Planet. Sci.* 4:159–185.

Moffatt, H. K. (1978). *Magnetic field generation in electrically conducting fluids*, Cambridge Univ. Press, Cambridge.

Nagata, T. (1965). Main characteristics of recent geomagnetic secular variations. *J. Geomag. Geoelect.* 17:263.

Parker, E. N. (1955). Hydromagnetic dynamo models. *Astrophys. J.* 122:293–314.

Parker, E. N. (1969). The occasional reversal of the geomagnetic field. *Astrophys. J.* 158:815–827.

Parker, E. N. (1970a). The origin of magnetic fields. *Astrophys. J.* 160:383–404.

Parker, E. N. (1970b). The generation of magnetic fields in astrophysical bodies. I. The dynamo equations. *Astrophys. J.* 162:665–681.

Parker, E. N. (1971). The generation of magnetic fields in astrophysical bodies. II. The solar and terrestrial dynamos. *Astrophys. J.* 164:491–509.

Parker, E. N. (1979). *Cosmical magnetic fields*, Clarendon Press, Oxford.

Roberts, P. H. (1967). *An introduction to magnetohydrodynamics*, American Elsevier Publishing Company, New York.

Roberts, P. H. (1972). Kinematic dynamo models. *Phil. Trans. Roy. Soc.* 272:663–698.

Runcorn, S. K. (1955). Rock magnetism—geophysical aspects. *Adv. Phys.* 4:244–291.

Sandel, B. R., and A. J. Dessler (1988). *J. Geophys. Res.*, submitted.

Steenbeck, M., F. Krause, and K.-H. Rädler (1966). Berechnung der Mittleren Lorentz-Feldstarken $\mathbf{v} \times \mathbf{B}$ fur ein Elektrisch Leitendes Medium in Turbulenter, durch Coriolis-Krafte Beeinflusster Bewegung. *Z. Naturforsch. A.* 21:369–376.

Stix, M. (1973). A non-axisymmetric α-effect dynamo. *Astron. Astrophys.* 13:203–208.

Zwaan, C. (1987). Elements and patterns in the solar magnetic field. *Ann. Rev. Astron. Astrophys.* 25:83–111.

10

Time Variability in Jupiter's Synchrotron Radiation

Imke de Pater
University of California, Berkeley
Michael J. Klein
Jet Propulsion Laboratory, Pasadena

Abstract

This chapter presents an overview of possible time variability in the decimetric radio emission from Jupiter. It investigates the presence or absence of fluctuations with time in different synchrotron radiation characteristics: the total intensity, the position angle of the electric vector, the degree of linear and circular polarization, the angular separation of the radiation peaks projected on the sky, and the longitudinal asymmetry of the radiation peaks. Variations in time, other than those caused by the changing viewing aspect of the planet, are only apparent in the total flux density and the angular separation of the radiation peaks. The longitudinal asymmetry of the radiation peaks changed once between 1967 and 1973. In the same period a large decrease was detected in the total flux density, and the centroid of the radiation peaks (the standoff distance) moved closer to the planet. The spectrum of the synchrotron radiation hardened slightly.

INTRODUCTION

Earth-based radio observations of Jupiter carried out in the fifties and early sixties revealed the existence of a magnetic field surrounding the planet. Radiation at decametric wavelengths was attributed to cyclotron emission, whereas a decimetric component was suggested to be due to synchroton radiation. The latter suggestion was based upon the presence of linear polarization and the extent of the emission region as inferred from interferometric observations by Radhakrishnan and Roberts (1960) and Morris and Berge (1962). This radiation would be emitted by energetic electrons trapped in a magnetic dipole field, similar to the Earth's Van Allen belt. The peak-to-peak variation in the position angle of the electric vector implied a misalignment of the magnetic and rotational axes of ~10°. This misalignment could also explain the variation in total intensity and other emission parameters during one jovian rotation (the so-called "beaming" effect), if most electrons are confined to the magnetic equatorial plane (pitch angles near 90°).

Soon it became apparent that a pure dipole field was oversimplified. Warwick (1963) proposed a displacement of the dipole from the center of the planet to explain the dynamic spectrum of the decametric radiation. Warwick (1964) further suggested that the asymmetric behavior of Jupiter's beaming curves at decimetric wavelengths implied a magnetic-field configuration more complex than that of a pure dipole field, the simplest case being an offset dipole field. Berge and Morris (1964) made some position measurements of Jupiter's synchrotron radiation, and showed that their results could be interpreted in terms of such an offset dipole field. They also suggested that the fit to the beaming curves could be improved by including the blocking effect of the planet on such an offset dipole field.

Other refinements were required to explain the longitudinal asymmetries (hot spot) in radio images, first detected by Branson (1968) and confirmed by de Pater and Dames (1979). In-situ measurements by the Pioneer spacecraft led to models with multiple rather than dipole magnetic field configurations. Radio images of Jupiter's circularly polarized flux density (de Pater, 1980b) showed the quadrupole moments in Jupiter's field. The contribution of these terms transforms the magnetic equatorial "plane" into the "warped" surface observed by the Pioneer and Voyager spacecraft. The microwave data could be modeled well (de Pater, 1981b, c) with help of the octupole magnetic field configuration derived from data taken with the magnetometer aboard Pioneer 11 (Acuña and Ness, 1976; Smith et al. 1976).

Excellent review papers on Jupiter's decimetric radiation are written by Berge and Gulkis (1976) and Carr et al. (1983). From these and other papers we conclude that many details of Jupiter's synchrotron radiation are understood. However, we still do not know the source of the relativistic electrons in the planet's radiation belts, and we do not know what their mode of transport is. These issues are important to explain the time variability in the various characteristics of Jupiter's synchrotron radiation.

The following will discuss the Earth-based radio astronomy data and assess the presence or absence of time variability in six parameters: the total flux density, S; the position angle, PA, of the electric vector averaged over the emission region; the degree of linear and circular polarization, PL and PC; the standoff distance of the radiation peaks from the planet, and the asymmetry (formerly called the "hot" region) in Jupiter's radiation belts.

THE OBSERVATIONS

The Beaming Curves

To search for time variations in Jupiter's flux density, one must account for the modulation caused by Jupiter's rotation. The beaming curve of the total intensity exhibits two maxima and two minima each period. The maxima occur when the Earth is in the plane of the magnetic equator (i.e., when $\varphi_m = 0$, where φ_m is the magnetic latitude of the Earth). The beaming curve minima occur when φ_m reaches a maximum, and one of the poles is facing the Earth. Figure 58 shows an example of the beaming curves in the different radiation parameters S, PA, PL, and PC; the bottom panel shows φ_m. The orientation of Jupiter's magnetosphere is indicated at the top. One can see that the maxima and minima in S indeed occur at approximately the expected values of φ_m; small deviations are attributed to the higher-order terms in Jupiter's magnetic field. Note that the beaming curve of PL is similar to that of S. The beaming curve of the circular polarization, PC, crosses zero where S and PL show maxima, and reaches a positive or negative maximum where S and PL show minima.

The magnetic latitude of the earth can be calculated with: $\varphi_m = D_E + \beta \cos(\lambda - \lambda_0)$, with D_E the declination of the earth, β the angle between Jupiter's magnetic and rotational axes, λ the longitude and λ_0 the longitude of the magnetic north pole. Since D_E varies from $-3\overset{\circ}{.}3$ to $+3\overset{\circ}{.}3$ during one jovian year, the longitude at which $\varphi_m = 0$ varies with D_E. Consequently, the longitudes at which S and PL show their maxima and PC = 0 vary in a systematic way: one will see the peaks move closer together when D_E changes from $+3\overset{\circ}{.}3$ to $-3\overset{\circ}{.}3$. Also the depth of the minima is influenced by the variation in D_E, as can be seen in figure 58. The difference in height between the two maxima in the S and PL data can be explained by the nondipolar character of the field. This difference is typ-

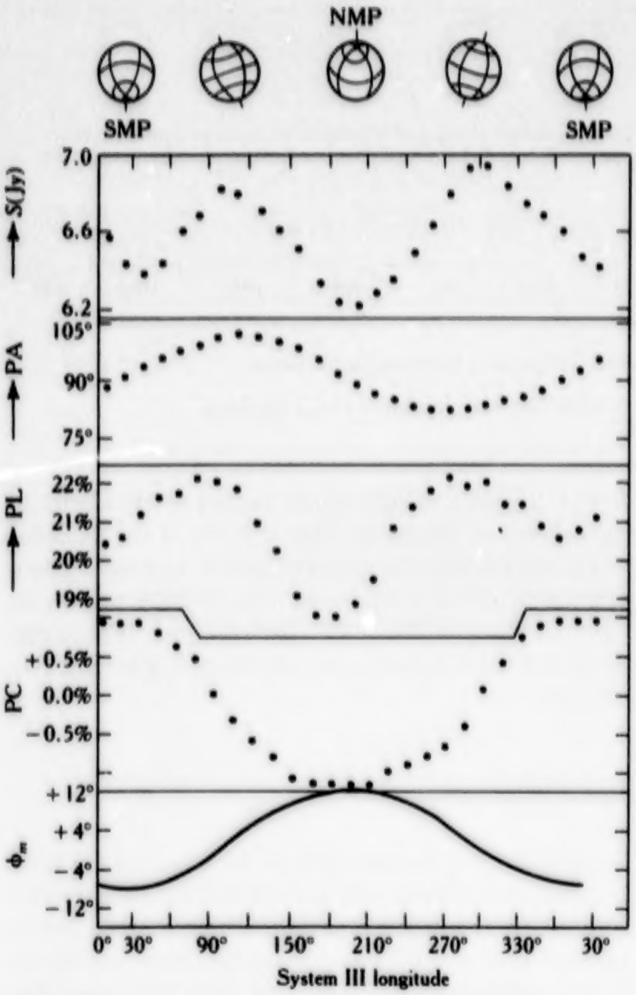

Figure 58. An example of the modulations of the synchrotron radiation due to Jupiter's rotation. The orientation of the planet is indicated at the top; the different panels show subsequently the total flux density S, the position angle of the electric vector PA, the degree of linear polarization PL, the degree of circular polarization PC, and the magnetic latitude of the Earth φ_m (after de Pater, 1980b).

ically 1–2 percent (Berge and Gulkis, 1976, and references therein), with extreme fluctuations of up to 5 percent (de Pater and Dames, 1979). The peak near 300° usually is slightly larger than that near 100°.

Total Intensity

Only a few years after the first detection of Jupiter's synchrotron radiation in 1958 (Sloanaker, 1959), Roberts and Huguenin (1962) reported data that suggested that the intensity of Jupiter's radiation was correlated with solar activity. The reality of the fluctuations was much debated due to possible confusion with background radio sources. However, subsequent observations by Gerard (1970), Klein et al. (1972), Gerard (1976), and Klein (1976) showed that long-term variations occurred in the planet's flux density, but that they were not correlated with the solar 10.7 cm flux. Gerard (1970, 1976) reported the existence of irregular short-term variations. A typical time scale for these fluctuations was about one week. Gulkis et al. (1973) reported that the 13-cm flux density beaming curve observed in 1969 was different in shape from the 11-cm beaming curve measured in 1964.

Since 1971, the planet has been monitored with the 26 meter Goldstone antenna in California (Klein et al., this volume). The data are obtained for a few hours several times a month with low noise receiving systems and circularly polarized feeds operating at 2295 MHz (wavelength = 13.1 cm). To account for the periodicity in the flux density due to Jupiter's rotation, the average of the two peak intensities in the beaming curve is determined for each observing session. Relative error estimates range from about 2 percent near jovian opposition to about 5 percent near superior conjunction. These estimates include the confusion effects of weak background radio sources.

Figure 59 shows the observations as a function of time (Klein et al., this volume). The data base is extended with 11–13 cm observations taken prior to 1969 from the Parks (Australia) and Nançay (France) telescopes (see Klein, 1976). A clear long-term variation in the flux density can be distinguished, with several irregular shorter-term variations. Between 1967 and 1972 the intensity decreased by ~25 percent. In the same period the flux density at 20 cm dropped by ~35 percent (Klein, 1976). Between 1972 and 1977 the 11–13 cm flux density increased to the old level.

Besides variations in peak intensity, which can be caused by planetwide changes in the electron density or, perhaps, the field strength, we are also interested in the question of time variability in the shape of the beaming curve. If such changes occur, they would likely be caused by localized changes in the magnetic field configuration or changes in the precise location of the radiating electrons within Jupiter's multipole field. Since observed parameters are affected by changes in the viewing geometry (see above), we must account for observations made at different phases in the orbital period of Jupiter, when the apparent sub-Earth latitude, D_E, changes from $+3\overset{\circ}{.}3$ to $-3\overset{\circ}{.}3$. It appears that this is a major cause of the observed changes in the shape of the quasi-sinusoidal beaming curves.

In order to address questions concerning the

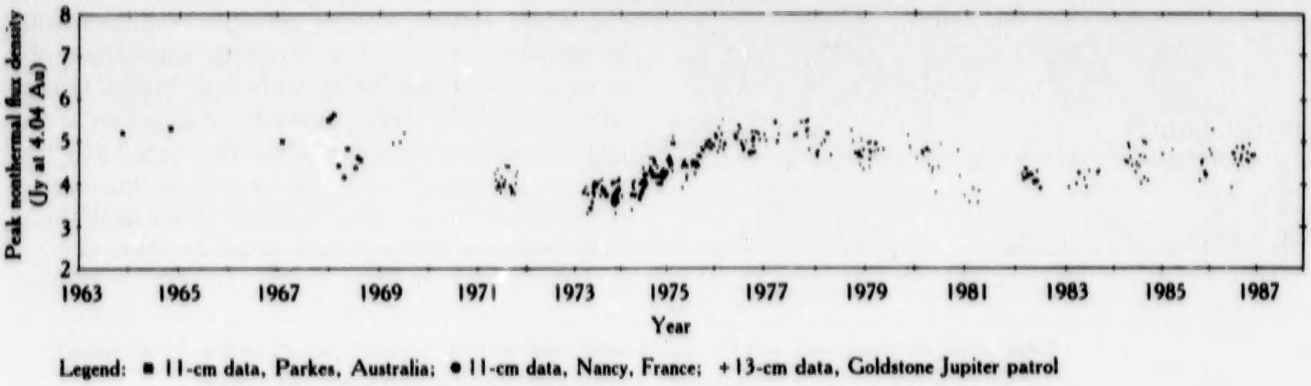

Figure 59. The total flux density history by synchrotron from Jupiter at 11–13 cm as a function of time (from Klein et al., this volume).

shape of curves, it is convenient to model the curves by a Fourier series:

$$Y(\lambda) = A_0 - \Sigma A_n \sin[n(\lambda - \lambda_n)], \quad (10.1)$$

where $Y(\lambda)$ is the observed quantity at longitude λ; A_0, A_n, and λ_n are the constants to be fitted in the nth term. Series like these can be applied to express the shape of the beaming curves in the total intensity, the position angle of the electric vector, the circular polarization, and the like. In general, the term A_0 is a constant, equal to the mean value of the beaming curve over one rotation. To first approximation, since the higher-order moments of the magnetic field get progressively smaller, the parameters A_n are related to the strength of each multipole moment (e.g., see equations by Roederer, 1972; de Pater, 1981b; and Komesaroff and McCulloch, 1981). The longitude λ_n is the corresponding phase angle with respect to the reference meridian $\lambda = 0$ (System III, 1965 coordinates).

The coefficients A_n and λ_n are determined most accurately from data when Jupiter is in opposition and the flux density received at Earth is strongest. The observational data taken near the oppositions of 1964, 1969, and 1971 through 1976 were analyzed by Klein et al. (this volume) to compare the recent data with the early data of Roberts and Komesaroff (1965). The A-values for the total flux density, S, were normalized to A_0 to bring out changes in the beaming curve rather than fluctuations in the average flux density level and eq. (10.1) was rewritten (with arbitrary changes in sign):

$$S(\lambda) = A_0[1 + \Sigma A_n \sin[n(\lambda + \lambda_n)]]. \quad (10.2)$$

Figure 60, from Klein et al. (this volume), shows the coefficients A_n and λ_n plotted as a function of D_E for $n = 1$, 2, and 3. A full orbital period of the planet is represented in the figure. The stability of the A-coefficients implies that the magnetosphere as a whole gets brighter or dimmer when the flux density plotted in figure 59 changes. The linear decrease in λ_1 reflects the motion of the maxima in the beaming curve when D_E changes.

Linear Polarization

A collection of measurements of the maximum degree of linear polarization was assembled by Klein (1976) and plotted as a function of time. These PL data, taken between 1963 and 1975 at wavelengths from 10.4 cm to 21 cm, appeared to be constant with time near the mean value of 24.5 percent during that particular jovian year. We extended this data set with additional data from Neidhofer et al. (1977), Gardner and Whiteoak (1977), de Pater and Dames (1979), and de Pater (1980b). The results are shown in figure 61, plotted as a function of D_E. The data at 10–13 cm are indicated by crosses and at 18–21 cm by filled circles. A negative correlation in the polarization degree with D_E might be present in the data, but the scatter is large enough that no variation is also consistent with the observations. We did not attempt to fit a Fourier series through the beaming curves due to the large uncertainties in the individual beaming curves.

Position Angle of the Electric Vector

Measurements of the position angle of the electric vector of the polarized synchrotron flux, averaged over the disk, represent an average of the direction of the magnetic field on the sky. This is a consequence of the fact

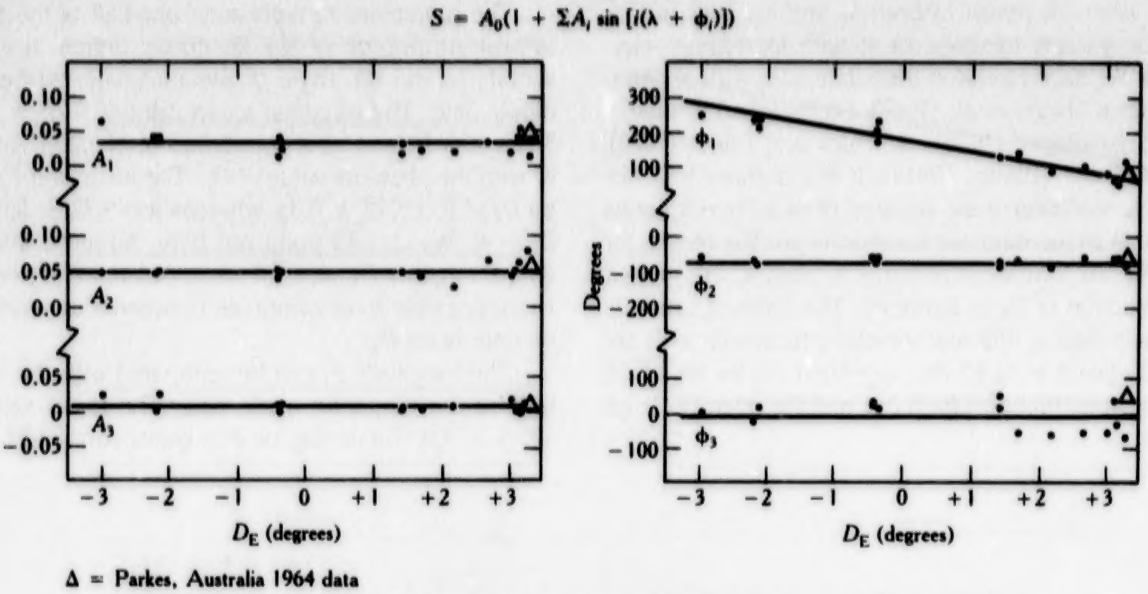

Figure 60. Stability of the 13-cm beaming curve coefficients for the total flux density: the Fourier terms A_n and φ_n are shown as a function of D_E for data taken when Jupiter was at opposition, in the period 1969–1978 (after Klein et al., 1987). Note that $\varphi_n = -\lambda_n$ in the text.

that the synchrotron emission pattern for each electron is beamed in the forward direction and linearly polarized perpendicular to the line of sight and the magnetic field line. The observed synchrotron emission arises from all electrons that move toward the observer along the line of sight. For the special case of equatorially confined electrons in a pure dipole field, the measured angle, PA, would be inclined 90° from the direction of the magnetic axis. If the field is multipolar rather than dipolar in shape, with a warped rather than flat magnetic surface, the measured angle, PA, is a spatially integrated average of the direction of the magnetic field within the emitting volume. The measurement is weighed most heavily by the areas from which most radiation is received, which is approximately from an annulus centered between 1.2 and 1.6 R_J. Since higher-order moments in the field are significant at this distance, the PA data will respond to the higher-order moments of Jupiter's field. Komesaroff and McCulloch (1981) show that the beaming curve in PA can best be explained if both dipole and quadrupole terms of the magnetic field (e.g., as measured by Pioneer 11) are taken into account, and if the effects of planetary shadowing are included. Komesaroff et al. (1980) also found that the precise shape of the beaming curve also depends upon the declination of the Earth, D_E; hence real time variations in this shape can be found only by comparing data over several Jupiter orbits. A change in the shape might then be interpreted as a change in the magnetic-field configuration, or in the radial position of the radiating particles.

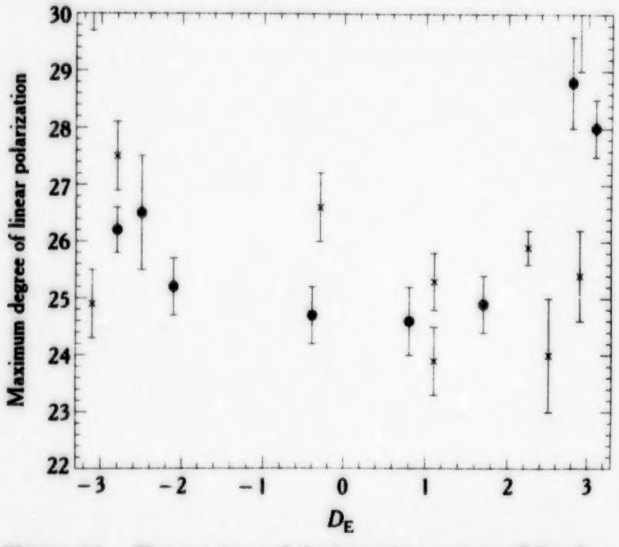

Figure 61. The maxima of the beaming curves of the degree of linear polarization as a function of D_E. The *crosses* are for data taken at 10–13 cm, the *filled circles* for 18–21 cm (see text for list of references).

Komesaroff et al. (1980) examined the position angle of the electric vector from polarization data of the planet over a time period of 16 years. They noticed a linear increase with D_E in the first fundamental term, and a linear decrease in both λ_1 and λ_2. They further noticed a slight increase in A_1 with increasing wavelength. We have extended their data base with observations from Morris et al. (1968), Gardner and Whiteoak (1977), Neidhofer (1978), de Pater and Dame (1979), and de Pater (1980b, 1981a). If the authors had not made a nonlinear least squares fit of a Fourier series (eq. 10.1) to the data, we have done so. The results for the first two fundamental terms A_n with λ_n are plotted as a function of D_E in figure 62. The different symbols represent data at different wavelengths: the crosses are for data taken at 11–13 cm, the filled circles for 18–21 cm, the open triangles for 6 cm, and the open circle for 50 cm.

The parameter A_1 represents one-half of the peak-to-peak amplitude of the PA curve; hence, it corresponds to the tilt angle of the magnetic axis of the dipole field. The weighted mean value is 9.72 ± 0.50. There may indeed be a correlation of A_1 either with D_E or with the absolute value of D_E. The mean value of PA for $D_E < 0$ is 9.42 ± 0.33, whereas it is 9.77 ± 0.50 for $D_E > 0$. We should point out here, however, that the data at negative D_E were all taken before 1972; hence it is not possible to discriminate between a dependence on time or on D_E.

The longitude λ_1 can be compared with the longitude of the magnetic north pole. The mean value is 195.6 ± 3.0. There may be a negative correlation with

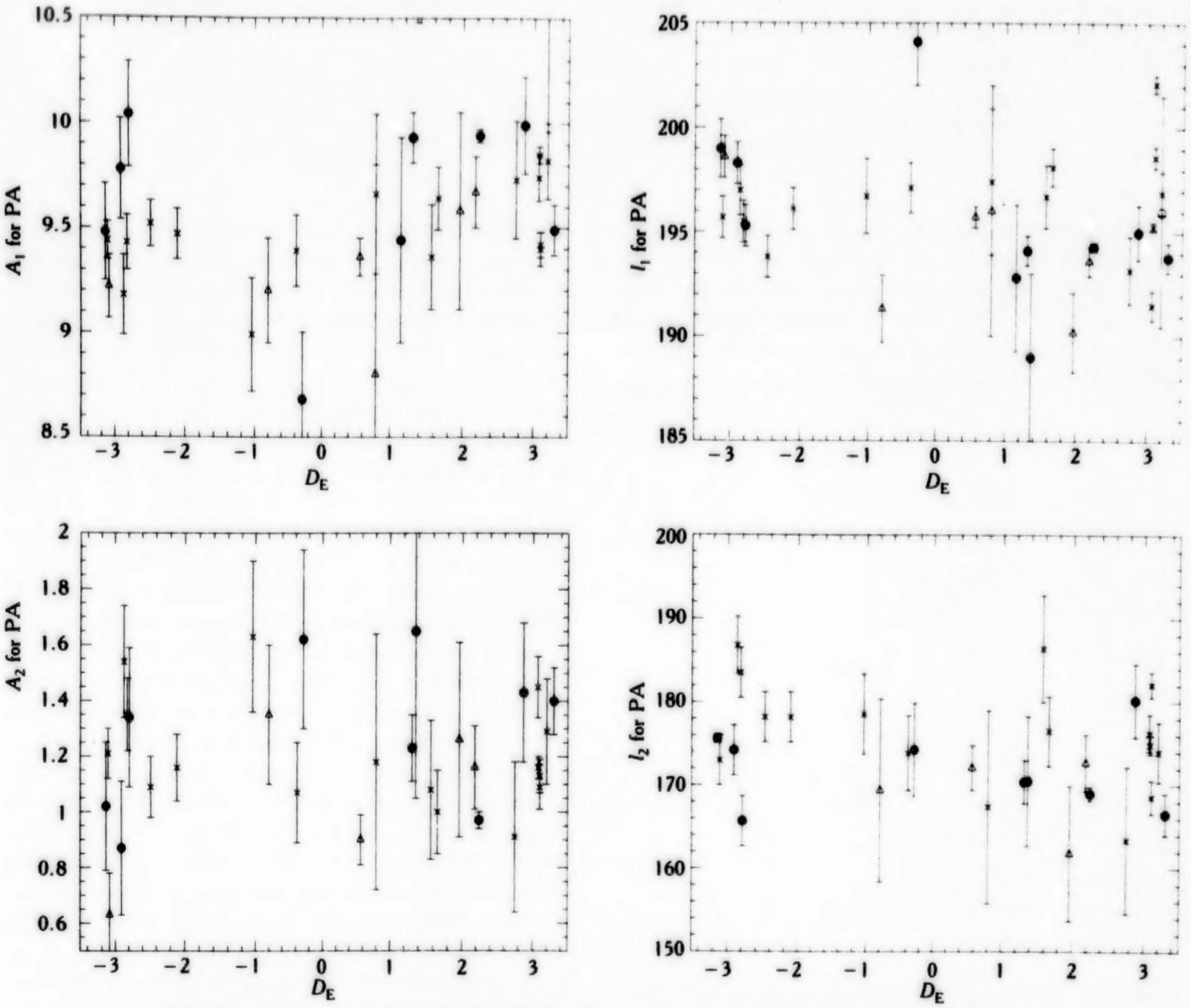

Figure 62. Beaming curve coefficients for the position angle of the electric vector, PA: the Fourier terms A_n and λ_n are shown as a function of D_E (see text for list of references). The different symbols refer to data taken at different wavelengths: the *crosses* are for data at 10–13 cm, the *filled circles* for 18–21 cm, the *open triangles* for 6 cm, and the *open circle* for 50 cm.

D_E, but we cannot exclude time variations (see comment above). The weighted mean value of λ_1 at $D_E < 0$ is 196.5 ± 2.9, and at $D_E > 0$ it is 195.5 ± 3.0. No variation with time other than the possible negative correlation with D_E can be found. This implies that there is no drift in the longitude of the magnetic north pole, as would be expected if the rotation period of the planet was in error. Hence, the rotation period of $9^h 55^m 29.71^s$ (System III, 1965) is consistent with the expanded data set.

The changes in A_1 and λ_1 with D_E are a manifestation of the higher-order terms of the magnetic field. In a pure dipole field λ_1 would be constant, and A_1 as good as constant.

The second-order harmonics are caused primarily by the quadrupole terms of the magnetic field. No variation with D_E or with time, larger than the uncertainty of the data, is apparent in either A_2 or λ_2.

No study of the fundamental term A_0 has been performed. The value of this parameter is related to the geometry of the observing system and the tilt of Jupiter's disk on the sky. Deviations from the calculated (expected) values of A_0 are typically very small, and they are usually consistent with the uncertainties in the corrections applied for Faraday rotation in the Earth's ionosphere.

Circular Polarization

The circularly polarized flux density is a measure of the magnetic-field strength of the field vector along the line of sight and of the precise latitudinal distribution of the electrons. For a pure dipole field, one expects a maximum when one of the magnetic poles is turned toward us, and zero flux density when the line of sight intersects the magnetic equator. We measure left-handed circular polarization (indicated by a negative sign) when the north pole is facing us, and right-handed (positive sign) when the south pole is turned toward us. The sign is chosen to follow the astronomer's convention (IEEE Standard, No. 211, 1969). Deviations in the PC beaming curve from a pure sine wave reflect the existence of higher-order terms in Jupiter's magnetic field. Unfortunately, the data are not yet of high enough quality that these higher-order terms can be derived from the existing beaming curves. High-resolution images of the circularly polarized flux density, however, clearly show the multipole character of the field; an example is shown in figure 63. The data show features consistent with those expected from field models derived from the Pioneer 11 data (de Pater, 1981b, c).

A least squares fit to the data at different epochs provides us with the mean level of the polarization, A_0,

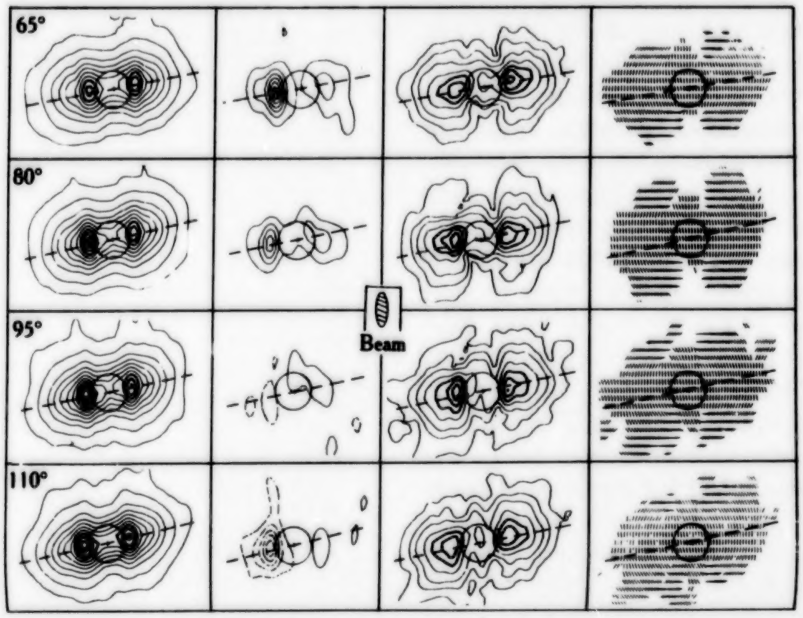

Figure 63. An example of radio images of Jupiter's synchrotron radiation: the images from left to right are for Jupiter's total intensity, circularly and linearly polarized flux density, and a vector diagram of the magnetic field direction; the latter is obtained by adding 90° to the vector diagram of the position angle of the electric vectors on the source. The jovian longitude (System III, 1965) is indicated in the upper left corner, and the size of the beam is indicated at the center (after de Pater, 1980b).

the half peak-to-peak amplitude, A_1, and the longitude of the pole, λ_1 (actually 90° away from it with eq. 10.1). Synchrotron radiation theory shows that the circular polarization is proportional to the inverse square root of the frequency. We, therefore, multiplied the A_1's with $\sqrt{[\nu_0/\nu_1]}$, to normalize them. We chose the frequency $\nu_0 = 1.4$ GHz. The results for A_0, A_1, and λ_1 as a function of D_E are shown in figure 64. The observations are taken from Neidhofer et al. (1977, 1980), Biraud et al. (1977), Roberts and Komesaroff (1976), Berge (1974), de Pater (1980b), and de Pater and Jaffe (1984). The data show a negative correlation with D_E in A_0. The parameters A_1 and λ_1 do not show any variation in time larger than their uncertainties. The mean A_1 value is 1.07 ± 0.15 with a mean λ_1 of 289.5 ± 5.4. The latter value implies a longitude of the magnetic north pole of $199.5 \pm 5.^\circ4$. This corresponds well with the longitude of $195.7 \pm 3.^\circ1$ as derived from the measurements of the position angle of the electric vector. Small differences are to be expected from the nondipolar character of the field.

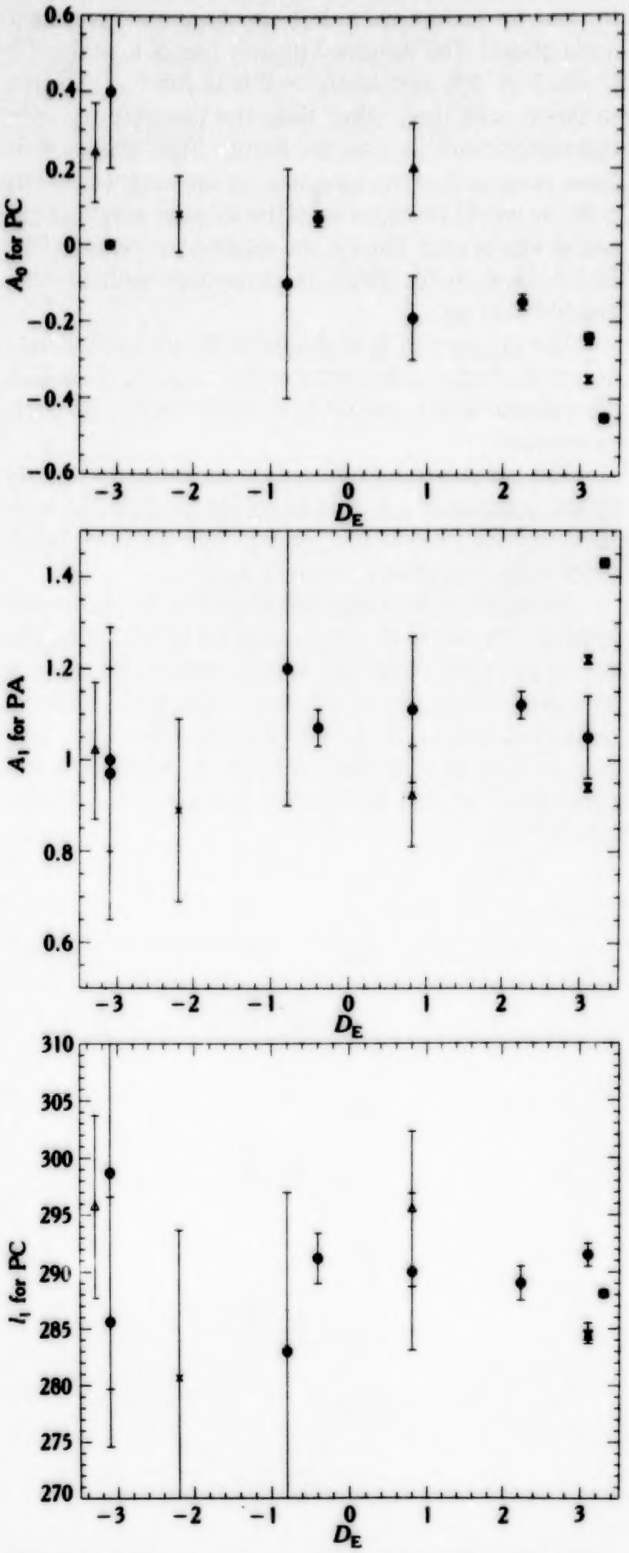

Figure 64. Beaming curve coefficients for the degree of circular polarization, PC: The Fourier terms A_0, A_1, and λ_1 are shown as a function of D_E (see text for list of references). The different symbols refer to data taken at different wavelengths: the *crosses* are for data at 10–13 cm, the *filled circles* for 18–21 cm, and the *open triangles* for 6 cm.

High Resolution Images

The first radio image of Jupiter was obtained by Berge (1966) from model fits to visibility data. The data were obtained with the Owens Valley interferometer at a wavelength of 10.8 cm. His two-dimensional image shows the two radiation peaks at a distance of 1.6 R_J from the center of the planet. In 1967, Branson (1968) constructed a map from 20-cm data obtained with the Cambridge one-mile telescope. His map, which was obtained by a direct Fourier transform of the data without the use of models, shows the radiation peaks at the same distance. The most surprising result was an asymmetry in the maps: One of the peaks was slightly more intense than the other one. In his three images, the appearance of the asymmetry changed with Jupiter's rotation. The east side was brightest when the longitude of the central meridian was 135°, the west side was brightest at a central meridian of 255°, and the peaks were equal when the longitude of the central meridian was 15°. This implied that the hot spot had to be close to the longitude of the magnetic north pole.

In 1972–1974 several observers (Olsen, in Berge and Gulkis, 1976; de Pater and Dames, 1979) obtained images of the planet with good east-west resolution (one-dimensional stripscans). The radiation peaks were at a distance of 1.3 R_J rather than 1.6 R_J, at wavelengths of 3.7, 11, and 21 cm. At the latter wavelength all rotational aspects of the planet were observed, and the asymmetry between the radiation peaks clearly showed up. When interpreted in terms of a hot spot, or hot region, the region appeared to have migrated to a longitude of 255 ± 10°. Even though Branson's maps were smeared over 120° in longitude by observing and reduction processes, the difference in the measured position of the hot region between the two epochs is real. This has been verified by creating maps of one of de Pater's data sets, smeared over the same longitude range as Branson's maps. The hot region then appears to have moved about 60° in longitude, in the time interval between 1967 and 1973.

Complete sets of maps were obtained in 1977 and 1978 with the Westerbork array (the Netherlands; de Pater, 1980b, 1981a). Since 1981 de Pater has accumulated data with the very large array (VLA) at 20 and 6 cm, every 15 months, when the array is in a suitable configuration. Unfortunately, the data reduction of the latter data sets has not been finished yet. The first of the series of images was published by de Pater and Jaffe (1984).

Figure 65 shows a graph of the standoff distance of the radiation peaks as a function of time. The numbers are obtained from data published by Berge (1966), Branson (1968), de Pater and Dames (1979), de Pater (1980b, 1981a), de Pater and Jaffe (1984), de Pater and Dickel (1986), Olsen (in Berge and Gulkis, 1976), Kenderdine (1980), Roberts et al. (1984), de Pater et al. (1982). The peaks have slowly moved outward from 1.3 R_J in 1973 to 1.45 R_J in the early 1980's, when there may be a tendency toward stabilization near that value.

The asymmetry, first indicated with the term hot spot, is probably caused by the multipole character of the magnetic field, although this alone cannot entirely explain the magnitude of the asymmetry (de Pater, 1981c). The longitude of the maximum asymmetry has been very stable since 1973. Since 1977 the asymmetry of the radiation belts has been measured quite precisely as a function of jovian longitude. Figure 66 shows the asymmetry in the total flux density as a function of jovian longitude. The curve is from VLA data taken in 1981 (de Pater and Jaffe, 1984). De Pater (1983) shows a comparison of this data set with that obtained with the Westerbork telescope in 1977 (de Pater, 1980b), after the VLA data were convolved with a Gaussian beam that matched the Westerbork data. No obvious differences between the curves were found. With the higher resolution of the VLA data, a much more precise measure will be obtained in the future.

DISCUSSION

From the above it is clear that many of the time variations detected to date in Jupiter's synchrotron radiation characteristics can be explained by the changing viewing geometry of the planet. Only a few phenomena appear to be caused by physical changes in the magnetosphere. Examples detected so far are the long-term fluctuations in the total intensity, the variation in the standoff distance of the radiation peaks, and changes

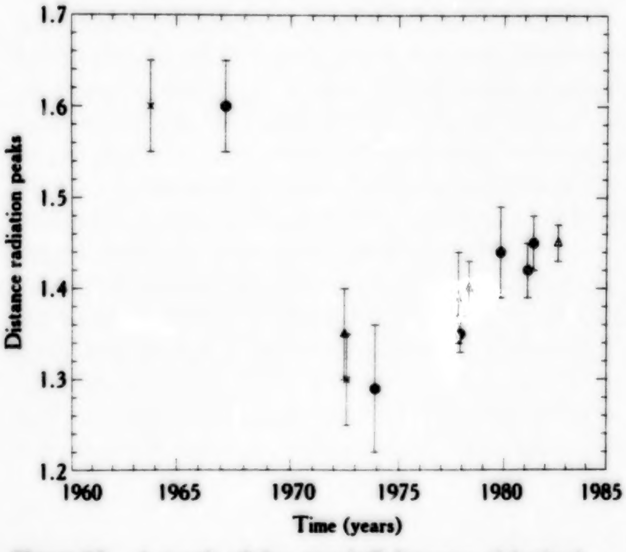

Figure 65. A graph of the standoff distance of Jupiter's radiation peaks as a function of time. The *crosses* are for data at 10–13 cm, the *filled circles* for 18–21 cm, the *open triangles* for 6 cm, and the *filled triangle* for 3.7 cm (see text for list of references).

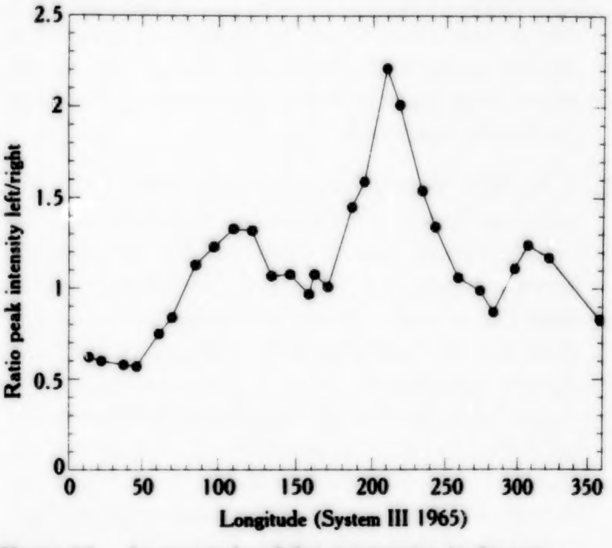

Figure 66. An example of the asymmetry in the synchrotron radiation from the radiation belt. The ratio S_{left}/S_{right} of the emission peaks at the two sides of the planet is indicated as a function of jovian longitude. The data are from de Pater and Jaffe (1984).

in the asymmetry and synchrotron spectrum that were observed between 1967 and 1973. Short-term fluctuations in the total intensity with time scales of weeks or even days may also be present. Temporal variations in the polarization parameters may have occurred, but further observations are needed to improve the confidence and/or discriminate between D_E and time variations.

The discussion below divides the data into two periods: (1) 1967 to 1973 and (2) 1972 to 1977. In the first period, the magnetic field configuration may have changed; in the second period, the configuration appeared to be stable.

1. 1967–1972: During this period the total flux density and standoff distance of the radiation peaks decreased, the hot spot migrated 60° in longitude and the synchrotron spectrum may have hardened. There is also some evidence that the Fourier coefficients A_1 and λ_1 in the fit of the position angle of the electric vector may have changed between 1970 and 1974. One plausible explanation for this combination of hot-spot migration and the change in the PA data involves a possible change in the magnetic field (de Pater, 1980a). If the higher-order moments of the magnetic field configuration changed, the diffusion parameters and wave-particle interactions would all be influenced. This, for example, can cause an increased loss of particles into the atmospheric loss cone, which would result in a corresponding decrease in the synchrotron emission. Of course, the electron spectrum may have changed as well, since wave-particle interactions are generally energy dependent. It may be difficult to sort out the various explanations until new results can be obtained from Earth-based observations and/or from the Galileo spacecraft.

2. 1972–1977: During this period in time, the radio emission from Jupiter increased steadily and the radiation peaks moved outward. The fact that the beaming curves in S, PA, and PC remained constant during these years (except for changes with D_E) suggests that the magnetic field configuration did not change significantly. Hence, the slow increase in Jupiter's flux density and in the standoff distance of the radiation peaks is probably caused by fluctuations in the particle density and/or the diffusion parameters. Fluctuations in the overall magnetic field intensity cannot be excluded.

De Pater and Goertz (1988) performed numerical calculations on diffusion of energetic electrons into the radiation belts. They calculated the effect of changes in the diffusion parameters on the synchrotron radiation characteristics, as well as the effect of an increased influx of particles. We can summarize some of their results as follows: An increase in radial diffusion and/or a decrease in particle losses causes the radiation peaks to move inward, and the level of the synchrotron radiation to increase. This is just opposite to what is observed. A small increase in the incoming electron flux will not influence the position of the radiation peaks, but it will, of course, enhance the synchrotron emission in linear proportion with the increase of electrons. Hence, one scenario that would explain the increase in synchrotron radiation with the simultaneous outward motion of the radiation peaks is to combine a decrease in the radial diffusion with an increase in the electron density in the radiation belts. The model predicts that an enhancement of the electron density by a factor of 10 during 10 days at $L = 6$ (Io's orbit) will cause the synchrotron radiation to increase by 20–25 percent after 200–400 days (more precise numbers depend on the choice of the diffusion parameters); the radiation does not stabilize again before 2–2.5 years have passed. Bursts of particles inserted at larger L-shells will be smeared out even more. Hence, only slow variations in Jupiter's radio emission can be caused by changes at Io's orbit or beyond (e.g., solar-wind boundary). Short-term variations are more difficult to explain. If indeed diffusion is the primary mode of transport of energetic electrons, this model predicts that the mechanism responsible for short-term variations must originate within the belts.

In 1976 Klein (1976) searched unsuccessfully for a correlation between the fluctuations in the intensity of Jupiter's radio emission with Earth-based indices of solar activity. In 1986 Bolton (Klein et al. this volume) assembled solar-wind data from about a dozen spacecraft and began a correlation study with the 13-cm Jupiter data. A tentative result from this work is a possible positive correlation in the long-term variation of Jupiter's radio emission with the ion number density in the solar wind. If this result is proved correct, it will be the first evidence that the solar wind is at least one major source of energetic electrons in Jupiter's radiation belts. It also supports the theory that diffusion is a major mode of transport in the jovian magnetosphere.

SUMMARY

In table 13 we summarize the synchrotron radiation characteristics examined in this chapter and indicate

Table 13. Jovian Synchrotron Radiation Characteristics

Synchrotron parameter	Periodic dependence on D_E	Nonperiodic fluctuations in time
Total intensity		
Maximum intensity	n	y
Beaming curve: A1	n	n
I1	y	n
A2	n	n
I2	n	n
A3	n	n
I3	n	n
Degree of linear polarity		
Maximum polarity degree	p	n
Beaming curve[a]		
Position angle, PA		
Beaming curve:[a] A0		
A1	p	p
I1	p	p
A2	n	n
I2	n	n
Degree of circular polarity		
Beaming curve: A0	y	n
A1	n	n
I1	n	n
Standoff distance		
Radiation peaks	n	y
Asymmetry (hot spot)		y
Spectrum decimetric radiation		y

[a] Parameters have not been determined due to large uncertainties in the data. n = not detected; y = detected; p = possibly detected.

the presence or absence of time variability. The latter is divided into periodic variations with D_E and nonperiodic fluctuations in time. With the high spatial resolution obtainable with the VLA it may be of interest in the future to examine PL, PA, and PC of the two radiation peaks separately.

FUTURE WORK

In order to obtain the information necessary to study and interpret time variations in Jupiter's synchrotron radiation, we strongly recommend the following studies:

1. Continue the ongoing microwave monitoring programs—the 13-cm total flux density observations with the NASA Deep Space Network antennas (~ weekly).
2. The VLA high-resolution observations in all four Stokes parameters (~ annually).
3. Expand the microwave observations—expand total flux monitoring to additional wavelengths, measure the synchrotron spectrum (~ annually), measure the polarization (I, Q, U, V) at various microwave wavelengths, and initiate periods of intensive monitoring to study and verify the short-term variability.
4. Continue correlation studies between the time variability in Jupiter's radio emission and, for example, solar wind parameters, solar ultraviolet (UV) and extreme ultraviolet (EUV) emission, Io's plasma torus, and Io's volcanism.
5. Develop improved models of jovian magnetospheric phenomena; include detailed diffusion theory and consider alternative particle-transport mechanisms.

ACKNOWLEDGMENTS

This research, in part, was supported by NASA grant NAGW-776 and NSF grant AST-8405358 to the University of California in Berkeley, and the Alfred P. Sloan foundation. Part of the research described in this chapter was performed by the Jet Propulsion Laboratory, California Institute of Technology, under contract with the National Aeronautics and Space Administration.

References

Acuña, M. H., and N. F. Ness (1976). Results from the GSFC fluxgate magnetometer on Pioneer 11. In *Jupiter* (T. Gehrels, ed.), pp. 830–847. Univ. of Arizona Press, Tucson.

Berge, G. L. (1966). An interferometric study of Jupiter's decimetric radio emission. *Astrophys. J.* 146:767–798.

Berge, G. L., and S. Gulkis (1974). The position and Stokes parameters of the integrated 21 cm radio emission of Jupiter and their variation with epoch and central meridian longitude. *Astrophys. J.* 191:775–784.

Berge, G. L., and S. Gulkis (1976). Earth based radio observations of Jupiter: Millimeter to meter wavelengths. In *Jupiter* (T. Gehrels, ed.), pp. 621–692. Univ. of Arizona Press, Tucson.

Berge, J. L., and D. Morris (1964). Decimetric measurements relating to the possible displacement of Jupiter's magnetic dipole. *Astrophys. J.* 140:1330–1332.

Biraud, F., J. C. Ribes, J. D. Murray, and J. A. Roberts (1977). Circular polarization of Jupiter's 1.4 GHz radio emission. *Astron. Astrophys.* 58:433–435.

Branson, N. J. B. A. (1968). High resolution radio observations of the planet Jupiter. *Mon. Not. Roy. Astron. Soc.* 139:155–162.

Carr, T.D., M. D. Desch, and J. K. Alexander (1983). Phenomenology of magnetospheric radio emissions. In *Physics of the jovian magnetosphere* (A. J. Dessler, ed.), pp. 226–284. Cambridge Univ. Press, Cambridge.

de Pater, I. (1980a). *Observations and models of the decimetric radio emission from Jupiter*, Ph.D. Thesis, Leiden University.

de Pater, I. (1980b). 21 cm maps of Jupiter's radiation belts from all rotational aspects. *Astron. Astrophys.* 88:175–183.

de Pater, I. (1981a). Radis maps of Jupiter's radiation belts and planetary disk at $\lambda = 6$ cm. *Astron. Astrophys.* 93:370–381.

de Pater, I. (1981b). A comparison of radio data and model calculations of Jupiter's synchrotron radiation, I. The high energy electron distribution in Jupiter's inner magnetosphere. *J. Geophys. Res.* 80:3397–3422.

de Pater, I. (1981c). A comparison of radio data and model calculations of Jupiter's synchrotron radiation, II. East-west asymmetry in the radiation belts as a function of jovian longitude. *J. Geophys. Res.* 86:3423–3429.

de Pater, I. (1983). Synchrotron radiation as a probe of the inner magnetosphere of Jupiter. *Adv. Space Res.* 3(3): 31–37.

de Pater, I., and H. A. C. Dames (1979). Jupiter's radiation belts and atmosphere. *Astron. Astophys.* 72:148–160.

de Pater, I., and J. R. Dickel (1986). Jupiter's zone-belt structure at radio wavelengths: I. Observations. *Astrophys. J.* 308:459–471.

de Pater, I., and C. K. Goertz (1988). *Radial diffusion of energetic electrons and Jupiter's synchrotron radiation*, in preparation.

de Pater, I. and W. J. Jaffe (1984). VLA observations of Jupiter's non-thermal radiation. *Astrophys. J. Suppl.* 54:405–419.

de Pater, I., and W. J. Jaffe, R. A. Brown, and G. L. Berge (1982). Radio emission from Io. *Astrophys. J.* 261:296–401.

Gardner, F. F., and J. B. Whiteoak (1977). Linear polarization of Jupiter at 6, 11, and 21 cm wavelengths. *Astron. Astrophys.* 60:369–375.

Gerard, E. (1970). Long term variations of the decimetric radio emission of Jupiter. *Radio Science* 5:513–516.

Gerard, E. (1976). Variation of the radio emission of Jupiter at 21.3 and 6.2 cm wavelengths. *Astron. Astrophys.* 50:353–360.

Gulkis, S., B. Gary, and M. Klein (1973). Observations of Jupiter at 13 cm wavelength during 1969 and 1971. *Icarus* 18:181–191.

Kenderdine, S. (1980). A study of Jupiter at 2.7 GHz with the 5 km telescope. I. Observations. *Mon. Not. Roy. Astron. Soc.* 191:925–931.

Klein, M. J. (1976). The variability of the total flux density and polarization of Jupiter's decimetric radio emission. *J. Geophys. Res.* 81:3380–3382.

Klein, M. J., S. Gulkis, and C. T. Stelzried (1972). Jupiter: New evidence of long-term variations of its decimetric flux density. *Astrophys. J.* 176:L85–L88.

Komesaroff, M. M., and P. M. McCulloch (1981). The position angle of Jupiter's linearly polarized synchrotron emission and the jovian magnetic field configuration. *Mon. Not. Roy. Astron. Soc.* 195:775–785.

Komesaroff, M. M., P. M. McCulloch, G. L. Berge, and M. J. Klein (1980). The position angle of Jupiter's linearly polarized synchrotron emission—observations extending over 16 years. *Mon. Not. Roy. Astron. Soc.* 193:745–759.

Morris, D. and G. L. Berge (1962). Measurements of the polarization and angular extent of the decimetric radiation of Jupiter. *Astrophys. J.* 136:276–282.

Morris, D., J. B. Whiteoak, and F. Tonking (1968). The linear polarization of radiation from Jupiter at 6 cm wavelength. *Austr. J. Phys.* 21:337–340.

Neidhofer, J. (1978). *Die Polarization der Dezimeterstrahlung und das zugrundeliegende Magnetfeld des Jupiter*, Ph.D. dissertation, University of Bonn, West Germany.

Neidhofer, J., R. S. Booth, D. Morris, W. Wilson, F. Biraud, and J.-C. Ribes (1977). New measurements of the Stokes parameters of Jupiter's 11 cm radiation. *Astron. Astrophys.* 61:321–328.

Neidhofer, J., D. Morris, and W. Wilson (1980). Observations of the jovian radiation at 11 and 18 cm wavelength. *Astron. Astrophys.* 83:297–302.

Radhakrishnan, V., and J. A. Roberts (1960). Polarization and angular extent of the 960 Mc/sec radiation from Jupiter. *Phys. Rev. Lett.* 4:493–494.

Roberts, J. A., G. L. Berge, and R. C. Bignell (1984). High resolution maps of the 1.5 GHz emission from Jupiter's disk and radiation belt. *Astrophys. J.* 282:345–358.

Roberts, J. A. and G. R. Huguenin (1962). La Physique des planets. *Mem. Soc. R. Sci. Liege* 7:569–587.

Roberts, J. A., and M. M. Komesaroff (1965). Observations of Jupiter's radio spectrum and polarization in the range from 6 cm to 100 cm. *Icarus* 4:127–156.

Roberts, J. A., and M. M. Komesaroff (1976). Circular polarization of the 1.4 GHz emission from Jupiter's radiation belts. *Icarus* 29:455–461.

Roederer, J. G. (1972). Geomagnetic field distortions and their effects on radiation belt particles. *Rev. Geophys. Space Phys.* 10:599–629.

Sloanaker, R. M. (1959). Apparent temperature of Jupiter at a wavelength of 10 cm. *Astron. J.* 64:346.

Smith, E. J. L., L. Davis, Jr., and D. E. Jones (1976). In *Jupiter* (T. Gehrels, ed.), pp. 788–829. Univ. of Arizona Press, Tucson.

Warwick, J. W. (1963). The position and sign of Jupiter's magnetic moment. *Astrophys. J.* 137:1317–1318.

Warwick, J. W. (1964). Radio emission from Jupiter. *Ann. Rev. Astron. Astrophys.* 2:1–22.

11

Systematic Observations and Correlation Studies of Variations in the Synchrotron Radio Emission from Jupiter

M. J. Klein
T. J. Thompson
Jet Propulsion Laboratory, Pasadena

S. Bolton
Jet Propulsion Laboratory, Pasadena
University of California, Berkeley

Abstract

A long-term observational program to monitor the time variations of the microwave radio emission from Jupiter has been in progress since April 1971. The measurements are made several times each month with the NASA Deep Space Network (DSN) antennas operating at 2295 MHz (13.1 cm). The data set, when combined with measurements by other observers, provides a record that extends over two 11-year solar cycles. The combined data set shows considerable variability that may be directly related to high-energy electron population of the inner magnetosphere. Preliminary results of a study to search for plausible correlations between the jovian synchrotron emission and solar-related phenomena reveal that a positive correlation may exist with the ion number density in the solar wind.

Time variability in the synchrotron radio emission from Jupiter's magnetosphere has been widely reported in the literature (see e.g., de Pater and Klein, this volume). Early attempts to relate these variations with solar phenomena or with jovian system parameters were not successful.

Following the confirmation of the long-term variability in the 13-cm flux density (Klein et al., 1972) we initiated a long-term observational program, the DSN Jupiter Patrol, to study the jovian microwave radio emission at 2295 MHz (wavelength = 13.1 cm). The program is designed to measure the time scale of the variability and to establish a large data base suitable for correlation studies.

Jupiter Patrol measurements are made several times each month with the NASA DSN antennas equipped with circularly polarized feeds and low-noise receiving systems. The jovian flux density is calibrated during each observing session from a list of a dozen sources distributed around the sky. These sources have in turn been calibrated against the primary calibration radio source Virgo A (3C 274). The flux density of Virgo A is assumed to be 140 Jy (1 Jy = 1 jansky = 10^{-26} W m^{-2} Hz^{-1}) at 2295 MHz (Baars et al., 1977).

The Jupiter Patrol observations reported here are scheduled, on a noninterference basis, as part of the ongoing research and development activity of the 26-m antenna at the Venus Development Station, Goldstone, California. The 64-m antenna at Goldstone was scheduled a few nights each year to measure linear polarization (reported in Komesaroff et al., 1980) and to augment the beaming-curve data described below.

The history of the observed variations in the synchrotron emission in the 11–13 cm wavelength range extends over 23 years when the DSN Jupiter Patrol results are combined with the early measurements of Roberts and Komesaroff (1965), Roberts and Ekersk (1968), Komesaroff and McCulloch (1967), Gerard (1970), and Gulkis and Gary (1971). The results are plotted in figure 67 as a function of date. The data points represent the peak values of the nonthermal flux density, S_p, normalized to a standard distance of 4.04 AU for each date. Long-term variations are clearly evident. Variations with time scales as short as weeks, or even days, may be present. Relative error estimates for the jovian peak flux-density determinations range from about 2.5 percent near jovian opposition to about 5 percent near superior conjunction. This estimate includes the confusion effects of weak background radio sources. The long-term variations are approximately 40 percent (peak-to-peak) and the short-term variations may be as large as 20 percent.

The combined effects of the beaming pattern of the synchrotron emission, which is strongly peaked toward Jupiter's magnetic equator, and the tilt of the magnetosphere with respect to the planet's rotation axis, produce the double-humped beaming curve shown in figure 68. Very few of the patrol observations span the entire 9-hour 55-minute rotation period. Consequently, peak flux-density values must be derived from various segments of the beaming curve. Our analysis shows that the beaming curve can be adequately represented by a Fourier series expansion of the form

$$S = A_0[1 + \Sigma_i^n A_i \sin[i(\lambda + \phi_i)]], \qquad (11.1)$$

where the coefficients A_i and ϕ_i are either constants or well-behaved functions of D_E, the declination of the

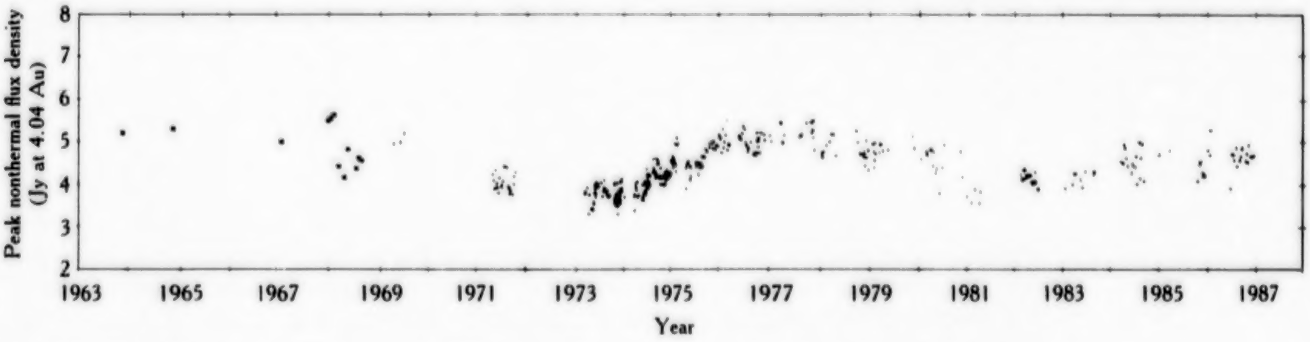

Legend: ■ 11-cm data, Parkes, Australia; ● 11-cm data, Nancy, France; + 13-cm data, Goldstone Jupiter patrol

Figure 67. The history of the observed variations in the Jupiter's synchrotron emission near 13 cm wavelength. The data represent the peak values of the nonthermal flux density, S_p, normalized to a standard distance of 4.04 AU for each date. Long-term variations are clearly evident. Variations with time scales as short as weeks, or even days, may be present.

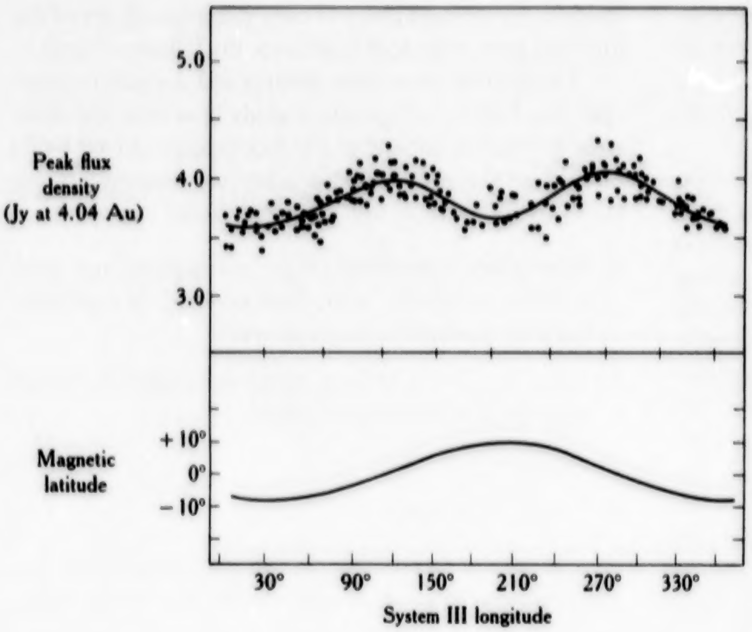

Figure 68. The combined effects of the beaming pattern of the synchrotron emission and the tilt of the magnetosphere with respect to the jovian rotation axis produce the double-humped beaming curve shown in the figure. Very few of the patrol observations span the entire 9-hour 55-minute rotation period, and peak flux-density values must be derived from various segments of the beaming curve.

Earth in the jovicentric coordinate system. Using the Fourier series with $n = 3$, one can derive the average of the two peak flux values from sparsely populated beaming curve data.

The long-term stability of the Fourier coefficients is indicated in figure 69. The coefficients were derived from least squares solutions to ensembles of data collected over several weeks. Observations with the highest signal-to-noise ratios (SNR) were selected for this analysis. About 30 percent of the composite beaming-

$$S = A_0(1 + \Sigma A_i \sin [i(\lambda + \phi_i)])$$

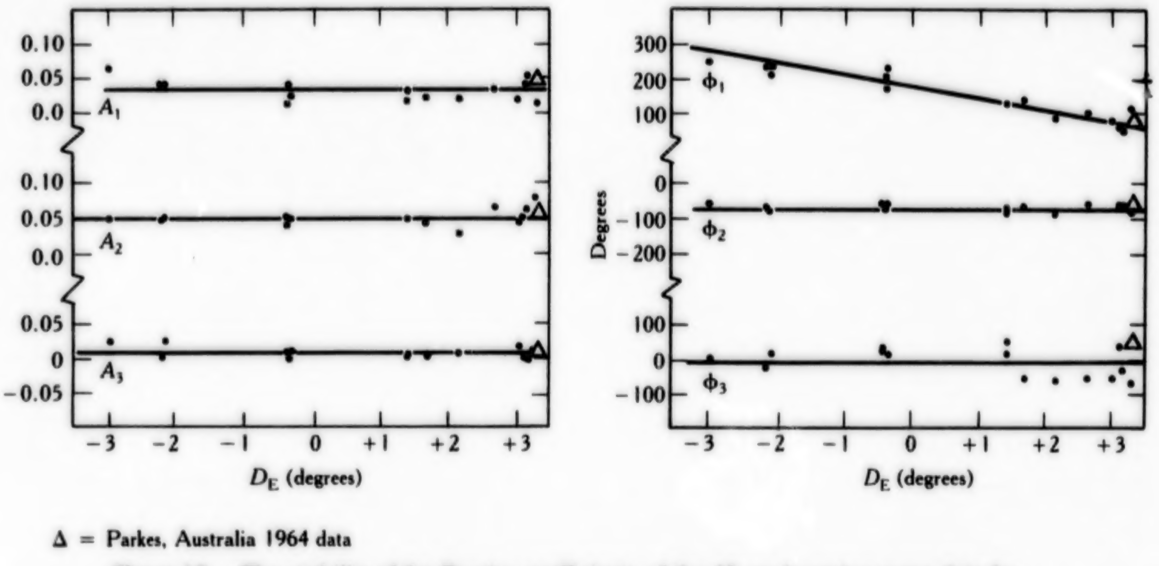

Figure 69. The stability of the Fourier coefficients of the 13-cm beaming curve data for 1964–1978. The coefficients were derived from least squares solutions to ensembles of data collected over several weeks. Observations with the highest SNR were selected for this analysis. Note the excellent agreement near $D_E = +3°$ between the Goldstone results and the Parkes data taken 12 years earlier.

curve data were taken with the 64-meter antenna, which enhances the SNR by a factor of seven over the 26-m observations. Note the excellent agreement near $D_E = +3°$ between the Goldstone results and the Parkes data taken 12 years earlier.

It is generally believed that the high-energy electrons (>1 MeV) responsible for the jovian synchrotron radio emission are produced by adiabatic diffusion of low-energy electrons from regions of weak to strong magnetic field intensity. Both the driving force for the diffusion process and the source of the realistic electrons are presently unknown. It has been suggested that interior regions of Jupiter's strong magnetic field are probably insulated from fluctuations in the solar wind. However, electron injection processes far out in the magnetic field could be influenced by the solar wind, whereas the driving mechanisms responsible for the diffusion process could be influenced by other solar phenomena. If plausible correlations can be found and verified, they would provide new information about the physical processes that influence the radiation belts.

Using solar-wind data from about a dozen spacecraft, we began a correlation study to search for solar-wind relationships. The study has expanded to include other plausible correlations. Several parameters are currently included in this ongoing study:

1. Solar-wind parameters (e.g., ion density, ion temperature, magnetic field, flow velocity) or combinations of parameters (e.g., ρv; ρv^2)
2. Solar flux (e.g., 10.7-cm flux; ultraviolet (UV) and extreme ultraviolet (EUV) flux)
3. Sunspot cycle
4. Io and the Io torus

One of the parameters showing a tendency for correlation with jovian synchrotron emission is the solar-

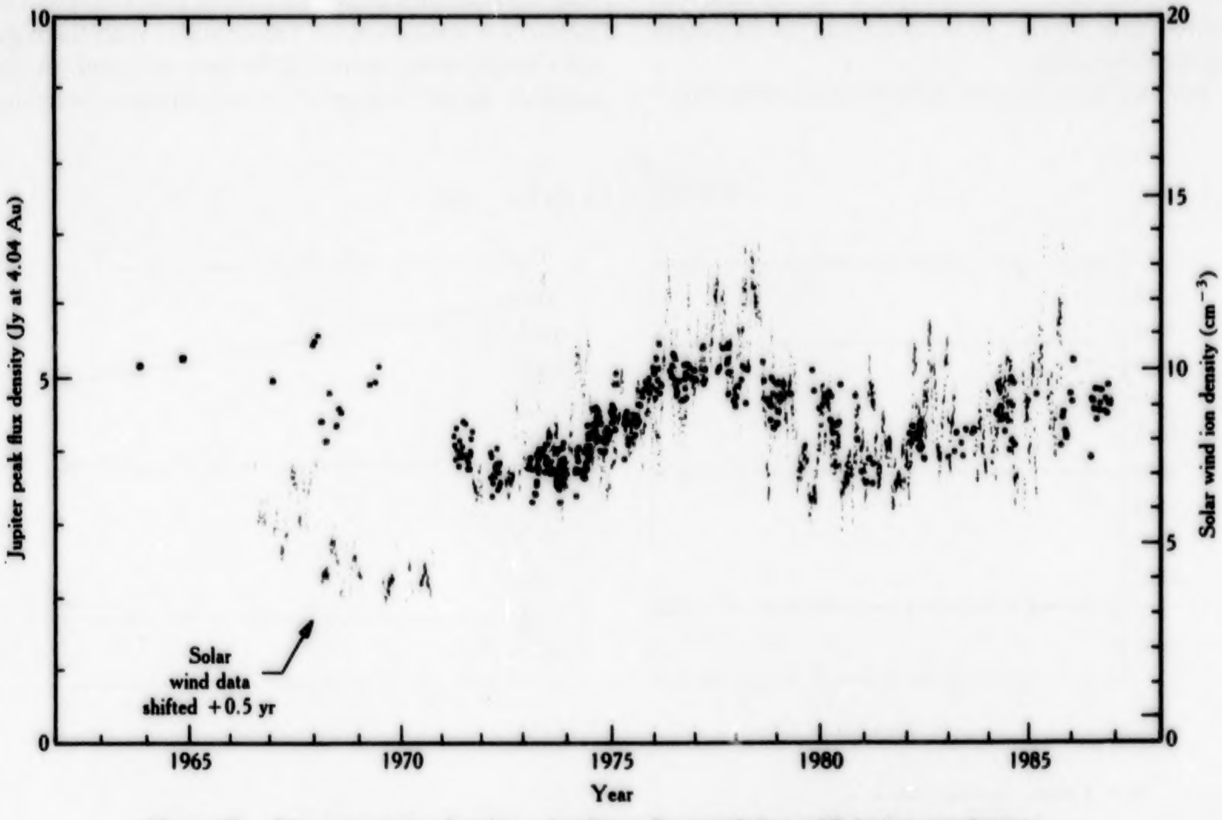

Figure 70. One parameter showing a tendency for correlation with jovian synchrotron emissions *(heavy dots)* is the solar-wind ion density *(light grey data)* from Jupiter Patrol. The gap in the solar wind data near 1970 may be important, because there appears to be a discontinuity in the spacecraft calibration data taken before and after that date. Further analysis of this potential correlation is planned.

wind ion density. Comparison with the jovian results is shown in figure 70. The gap in the solar-wind data near 1970 is important because there is a discontinuity in the spacecraft calibration data taken before and after that date. Indications are that the early values of the ion density are biased by as much as a factor of two with respect to the later data. Further analysis of this potential correlation is planned.

If this tentative result is proved correct, it will be the first evidence that the solar wind is at least one major source of energetic electrons in Jupiter's radiation belts.

ACKNOWLEDGMENTS

The research described in this chapter was performed by the Jet Propulsion Laboratory, California Institute of Technology, under contract with the National Aeronautics and Space Administration. Work by S. J. Bolton was supported, in part, by NASA grant NAGW-776 to the University of California, Berkeley.

References

Baars, J. W. M., R. Genzel, I. I. K. Pauliny-Toth, and A. West (1977). *The absolute spectrum of Cas A; An accurate flux density scale and a set of secondary standards*, 99–106.

Gerard, E. (1970). Long term variations of the decimeter radiation of Jupiter. *Radio Sci.* 5:513–516.

Gulkis, S., and B. Gary (1971). Circular-polarization and total flux measurements of Jupiter at 13.1-cm wavelength. *Astron. J.* 12–16.

Klein, M. J., S. Gulkis, and C. T. Stelzried (1972). Jupiter: New evidence of long-term variations of its decimeter flux density. *Astrophys. J. Lett.* 176:L85–L88.

Komesaroff, M. M., and P. M. McCullough (1967). The radio rotation period of Jupiter. *Astrophys. Lett.* 1:39–41.

Komesaroff, M. M., P. M. McCulloch, G. L. Berge, and M. J. Klein (1980). The position angle of Jupiter's linearly polarized synchrotron emission: Observations extending over 16 years. *Mon. Not. Roy. Astron. Soc.* 193:745–759.

Roberts, J. A., and R. D. Ekers (1968ts). Observations of the beaming of Jupiter's radio emission at 620 and 2650 MHz. *Icarus* 8:160–165.

Roberts, J. A., and M. M. Komesaroff (1965). Observations of Jupiter's radio spectrum and polarization in the range from 6 cm to 100 cm. *Icarus* 4:127–156.

12

Jupiter Decametric Radiation

Françoise Genova
Philippe Zarka
A. Lecacheux
Observatoire de Paris, Meudon

Abstract

The ground-based and Voyager radio observations of Jupiter show that the emission in the decametric and hectometric frequency ranges is extremely variable. Many kinds of fluctuations are seen, on time scales of milliseconds to days or longer, and the spectrum of the emission is also very fluctuating. After a brief review of the general characteristics of the emission, this chapter describes first its dominant periodicities—the planetary rotation and the control by Io—then, the short-term modulations—the S-bursts, with durations of some tens of milliseconds, and other fluctuations with time scales shorter than several minutes, in particular the arcs, the effects of propagation close to the source, and, in the case of ground-based observations, those between Jupiter and the radiotelescope. Finally, the search for long-term fluctuations of the emission, and the difficulties found in correlating them with the variations of other parameters of the jovian environment, the solar wind, the auroras, and the like are discussed. As a conclusion, the perspectives and needs for observational as well as theoretical work are discussed, especially for long-term observations and correlations with observations at other wavelengths.

INTRODUCTION

It has been known since the observations by Burke and Franklin (1955) that Jupiter is a powerful emitter of radio waves in the decameter wavelengths. Since then, Jupiter decametric radiation has been regularly observed from the ground, at fixed frequency, and with narrow- or broad-band receivers, as well as from space. In particular, the two Voyager spacecraft, which encountered the planet in 1979, allowed observation of the radiation down to hectometer and kilometer wavelengths. These spacecraft also discovered the kilometric emissions from Saturn and Uranus. Subsequent studies showed many similarities in the characteristics of these emissions, together with that of the Earth's "auroral kilometric radiation," suggesting a same basic mechanism for their generation. The understanding of the jovian decametric emission is thus closely linked to that of the other planetary radio emissions. It is the only one that can be observed from the ground, and also the one that possesses the richest (and most complicated) phenomenology. The studies of the jovian emission show, in particular, its great variability. Many kinds of fluctuations of the emission spectrum are observed, with time scales from milliseconds to days. Some of these fluctuations are well understood, others are not; all of them will be discussed in this chapter. We present first the general characteristics of the jovian radiation. We deal in particular with the periodicities that dominate the rotation and Io's revolution, and with the effect of the periodicities linked to the Earth motion (in the case of ground-based observations). We describe afterward the short-term variations of the radiation: the so-called S-burst emission and the modulations observed in the more frequent smoother emission with time scales of seconds to minutes, in particular the arcs, which structure the whole dynamic spectrum of the emission, and, on the ground-based observations, the effects of the wave propagation between the source and the Earth. Finally, the importance of the search for long-term fluctuations of the emission, and correlation with the variation of other parameters at Jupiter or in the jovian environment (solar wind, auroras), is put forward. As a conclusion, the perspectives and needs for observational as well as for theoretical works are discussed.

GENERAL CHARACTERISTICS OF JUPITER'S RADIATION

Intensity and Spectrum

The jovian emissions are nonthermal and very intense: The brightness temperature is greater than 10^{12} K, with the hypothesis of a source covering the whole planetary disc (which leads to an important underestimation of the temperature). The peak flux density (measured at 4 AU) is about 3×10^{-19} W m^{-2} Hz^{-1} at 10 MHz, which is approximately the frequency of the maximum of the average spectrum. It is difficult to evaluate the total emitted power, since the emission pattern (necessary for converting flux densities into power) is poorly known. Carr et al. (1983) give a power of 6×10^9 W at 10 MHz, if the emission pattern is a thin hollow cone (which is probable), with an upper limit of 3×10^{11} W for an isotropic source.

The emission covers a very broad frequency range, from ≤100 kHz to 40 MHz for both hectometric and decametric radiations (figure. 71). The ground-based observations are limited to frequencies higher than the ionospheric cutoff ($9\sqrt{n_e}$, in kHz, where n_e is the peak ionospheric electron density in cm^{-3}), which varies with the season, hour, and location, but is in general close to 10 MHz, although in some circumstances it can be as low as ~4 MHz. Observations in the hectometric range are thus possible from spacecraft only, and the wide frequency range and good frequency coverage of the planetary radio astronomy (PRA) experiment aboard the two Voyager spacecraft allowed very useful observations of the hectometric component of the emission.

The hectometric emission (HOM) is thought to be the low-frequency extension of the activity in the decametric range (DAM) (Boischot et al., 1981). This has been difficult to establish, since the two frequency ranges were observed on Voyager by two receivers with different frequency resolutions, channel bandwidths, and sensitivities (Warwick et al., 1977). A firmer observational indication of a relationship between the two emissions is given by a recent comparison of six months of Voyager hectometric data with simultaneous ground-based decametric observations recorded at Nançay, France (Genova et al., 1987).

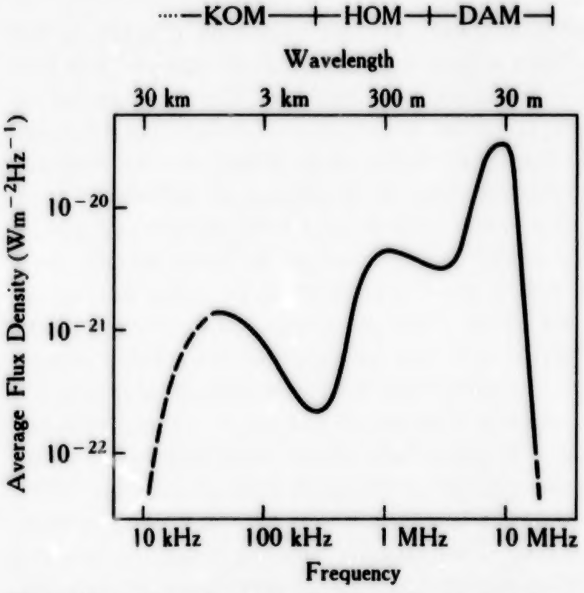

Figure 71. Schematic view of the average power flux-density spectrum of Jupiter's nonthermal magnetosphere radio emissions (averaged over active and nonactive periods). Flux densities are normalized to a distance of 4.04 AU. Adapted from Carr et al., 1983.

Other components have been discovered by Voyager, in the kilometric range: the broad-band and narrow-band kilometric radiations (respectively, bKOM and nKOM). These emissions are probably more directly linked to the Io torus itself, or to its close environment, than the decametric and hectometric emissions, and they will not be studied in detail here (for more information, see the reviews by Carr et al., 1983, and Kaiser and Desch, 1984, and the more recent papers by Leblanc and Daigne, 1985, Daigne and Leblanc, 1986, and Jones, 1986).

The maximum emitted frequency (about 39.5 MHz) corresponds well to the maximum surface electron gyrofrequency (Barrow and Alexander, 1981), computed from the multipolar magnetic field models deduced from the observations by the Pioneer spacecraft (Acuña and Ness, 1976; Smith et al., 1976; a review can be found in Acuña et al., 1983). More generally, the observations are in accordance with an emission close to the local gyrofrequency (f in MHz equals about $2.8 \times B$ in gauss). Then, the emission frequency, for a source along a given magnetic field line, corresponds to the altitude of the source. From the above values for the maximum and minimum frequencies, we deduce that the source extends from the surface up to altitudes higher than 4 jovian radii.

Dynamic Spectra

As already mentioned, an important property of the emissions is to be highly variable on many time scales. The instantaneous bandwidth of the emission, for instance, is almost always much smaller than the maximum frequency range given above, and the intensity and spectrum vary much during an individual event. The time scales of the fluctuations can be roughly studied by recording the emission in one or several channels with a narrow-frequency bandwidth. But, as we will see below, some phenomena with different physical origins can have comparable characteristic times, which make them difficult to separate at fixed frequencies, whereas they can be distinguished relatively easily through broad-band spectral observations. Moreover, the causes of emission modulations are better understood when their effects on the whole spectrum are known. This explains why the record of dynamic spectra (intensity against time and frequency) is a privileged tool with which to study the modulations of the emission. Large bandwidth dynamic spectral observations (between the ionospheric cutoff and the emission maximum frequency) were carried on at Boulder between 1960 and 1975, and have been performed at Nançay since 1978 (Boischot et al., 1980, figure 72). A small array of broad-band antennas is also operating in Tsuge, Japan. Similarly, dynamic spectra recorded by Voyager in the hectometric and decametric ranges are invaluable to complement and extend the study of the properties of the emission. Because of the limited amount of transmitted data, they are mainly restricted to the study of fluctuations slower than 12 s (although it was also possible to study the general appearance and organization of very short bursts in the dynamic spectra). Examples of dynamic spectra of Jupiter's emission recorded from Voyager and at Nançay are shown on figures 73a and b, and 79, 81, and 84, respectively. The arc structure of the whole emission appears well in figure 73b.

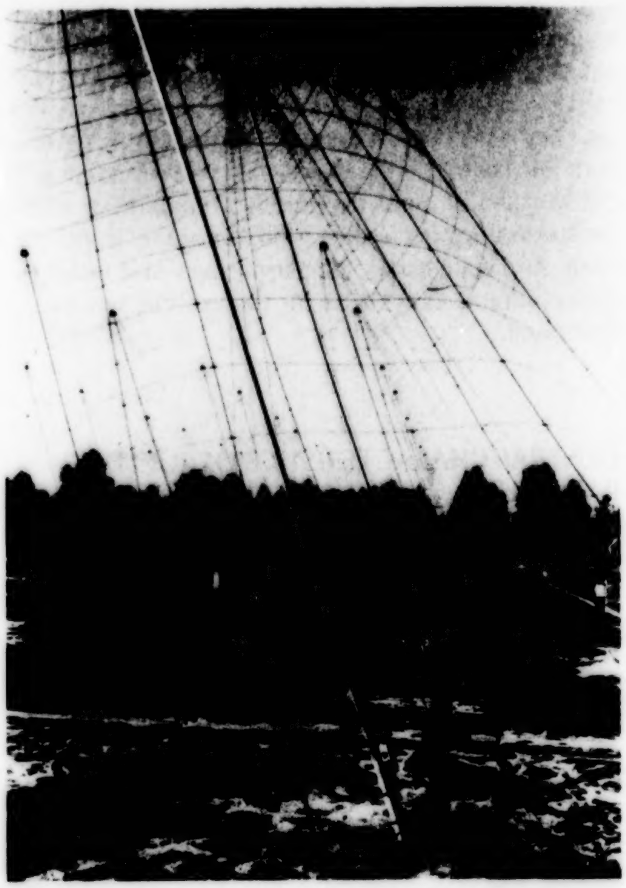

Figure 72. The decametric array at Nançay (France). The array is composed of 144 spiral antennas; half of them measure one circular polarization component. It has been used since 1978 to observe the jovian decametric radiation, 8 hours daily, between 10–15 and 40 MHz. From Boischot et al., 1980.

ORIGINAL PAGE
BLACK AND WHITE PHOTOGRAPH

ORIGINAL PAGE
BLACK AND WHITE PHOTOGRAPH

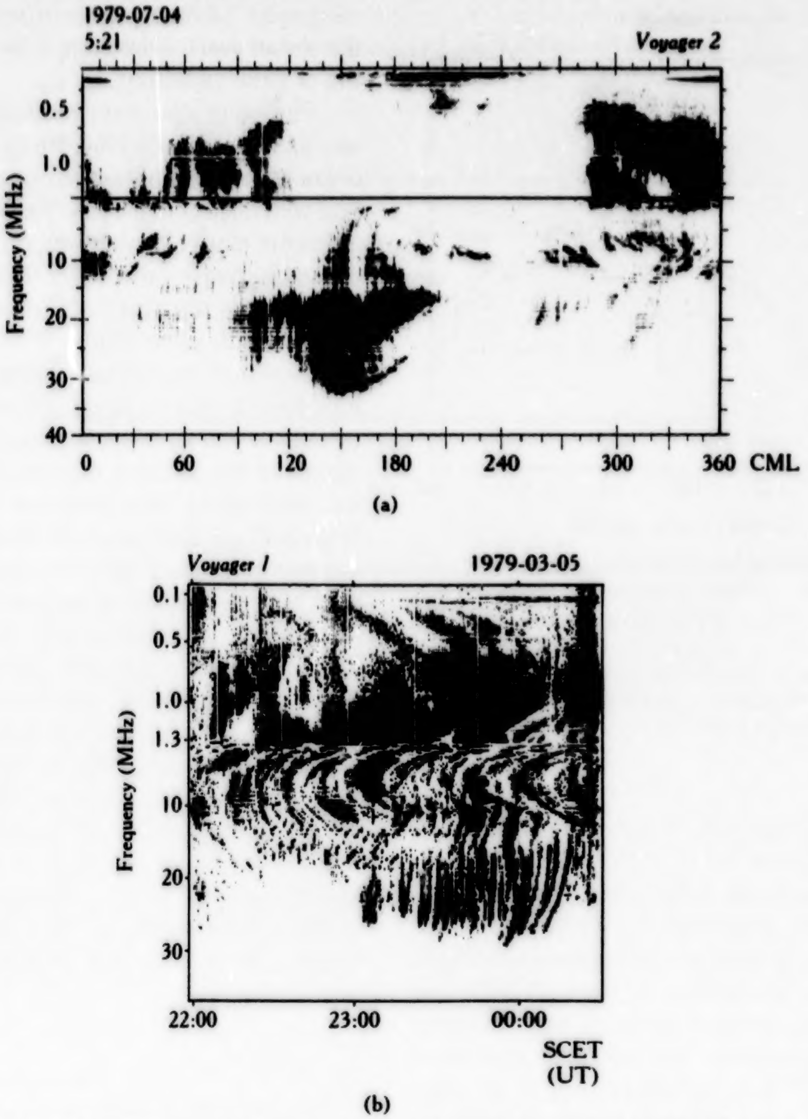

Figure 73. Dynamic spectra of Jupiter decametric emissions observed by Voyager. The intensity is shown in a gray shading scale. Black means here higher-intensity levels. The emission was observed by two different receivers, one covering the frequency range between 1 kHz and 1.3 MHz, and the other from 1.2 to 40 MHz. (**a**) Emission observed during one planetary rotation. Two "storms" appear at high frequencies. Kilometric emissions are seen at low frequencies. nKOM events appear for central meridian longitudes close to 0°, bKOM events around 200°. (**b**) Nested arc families compose most of the emission.

Modulation by the Planetary Rotation and Control by Io

At frequencies higher than about 15 MHz, the jovian activity does not occur continuously. The events appear as "storms," which generally last from one to several hours. The emission pattern is organized principally as a function of the observer's longitude in a jovicentric coordinate frame (central meridian longitude or CML), that is, the observer's position with respect to the planetary magnetic field (figure 74). Synoptic decametric observations over long time intervals give the most precise estimate of the rotation period of the core of the planet: $9^h 55^m 29.71^s \pm 0.01$ s (Carr et al., 1970; Duncan, 1971; Kaiser and Alexander, 1972; Alexander, 1975; Riddle and Warwick, 1976). The fact that the radiation visibility is principally controlled by the magnetic field in the source is quite in accordance with an emission close to the local gyrofrequency. Because the jovian magnetic dipole axis is tilted from the rotation axis (high multi-

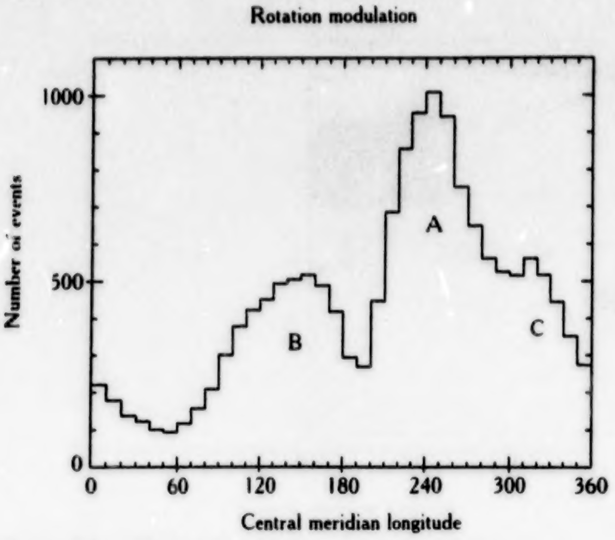

Figure 74. Modulation by the planetary rotation—histogram showing the number of emissions observed at Boulder from 1960 to 1975 and at Nançay from 1978 to 1984 (Warwick et al., 1975; Leblanc et al., 1981, 1983; Leblanc and Gerbault, 1987), as a function of the central meridian longitude. Three peaks appear, conventional names of which are indicated by A, B, and C.

polar terms are also present), it is not surprising that the dominant periodicity found in the data is the rotation period of the magnetic field—the observer's position in the emission lobe changes while the planet rotates. In particular, gyrofrequencies corresponding to the highest radiation frequencies (above ~27 MHz) are encountered only in a limited region, at high latitudes in the northern hemisphere. The two-lobe pattern of figure 74 corresponds to emissions coming from either side of this unique source region only seen during one planetary rotation, when the observer is in the emission lobe. This lobe behaves like a corotating "searchlight beam" (Maeda and Carr, 1984; Riihimaa, 1986). This suggests that the emission lobe is a hollow cone. Its aperture, about 70–80°, has been estimated through direct interpretation of the observed emission pattern (Dulk, 1967; Green, 1984; Genova and Aubier, 1985), ray tracing calculations (Menietti et al., 1984b), observations from different directions (Poquerusse and Lecacheux, 1978), as well as theoretical considerations (see e.g., Hewitt et al., 1981). This conical sheet is narrow, its thickness being probably of the order of a few degrees (although Green, 1984, found cone edges as broad as 30° in some cases). These conclusions are supported by the dramatic changes in DAM occurrence (Lecacheux, 1974; St. Cyr, 1985) and HOM morphology (Alexander et al., 1979) as a function of the observer's jovigraphic latitude (which varies by only ±3°.3 during the jovian year), suggesting a strong latitudinal beaming of these emissions.

The other dominant modulation of the radiation was found by Bigg in 1964. He discovered that the DAM occurrence probability depends on the observer's position with respect to the satellite Io. This appears clearly when the emission occurrence is displayed as a function of Io phase—the angle Φ between the direction opposite to the direction of observation and the Jupiter–Io direction (figure 75)—or in the usual two-dimensional coordinate system central meridian longitude–Io phase (figure 76), where the modulations by both Io and the planetary rotation appear. The usual names of the different regions of enhanced emission occurrence in this diagram (incorrectly called "sources") are also shown in figure 76. The "Io control" appears as low as 2 MHz (Alexander et al., 1981), but is much more evident at higher frequencies; the Io-dependent emissions reach very high frequencies much more often than the Io-independent ones (Genova and Aubier, 1987), and these were thought for years to be confined to frequencies below 27 MHz (see e.g., Carr and Desch, 1976; Goldstein and Eviatar, 1979). However, Barrow and Desch (1980), Barrow and Alexander (1981), and Genova and Aubier (1987) showed that the high-frequency limits of the two kinds of emissions are very similar (above 35 MHz). The Io-controlled emissions are also more intense than the others (Desch et al., 1975; Desch, 1980), and the shape

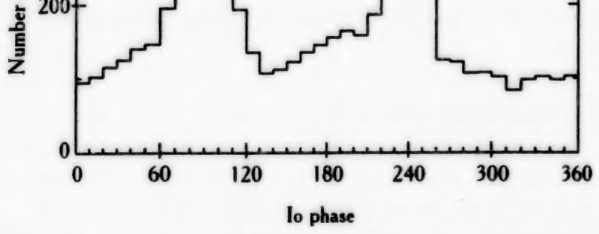

Figure 75. Io control. Histogram of the number of emissions observed at Boulder and at Nançay, as a function of Io phase.

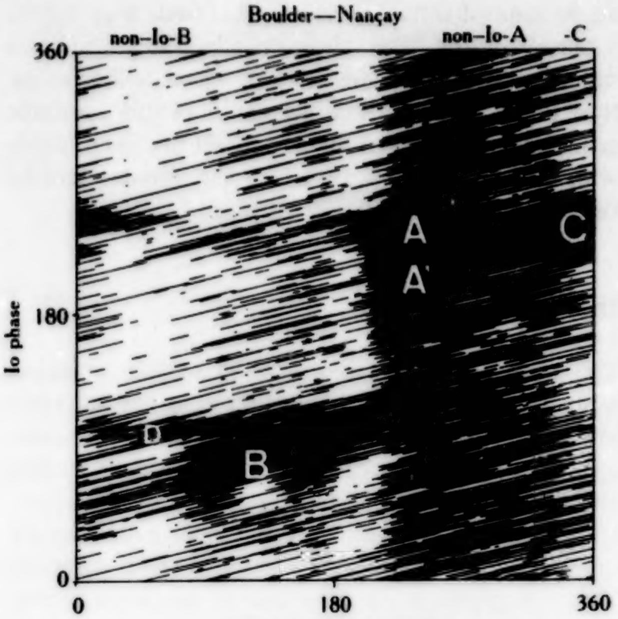

Figure 76. Central meridian longitude and Io phase of the decametric emissions observed at Boulder and at Nançay. The Io-independent emissions appear in *vertical bands*, the Io-dependent ones draw *irregularly shaped areas* in the diagram (*labeled with white letters*).

of their arcs is different from that of the arcs of the Io-independent emissions (Leblanc, 1981).

More generally, the shape and aspect of the dynamic spectrum is a very powerful tool with which to organize the different kinds of emissions. Different quasi-permanent "dynamic spectral landmarks," which are repeatable even at intervals of many years, correspond to the different regions of the CML-Φ diagram of figure 76 (Dulk, 1965; Leblanc, 1981; Carr et al., 1983). The shape of the arcs is a very sensitive criterion for sorting the Io-dependent and Io-independent emissions (Leblanc, 1981; Genova and Aubier, 1985). This allows us to study the properties of each type of emission on more properly sampled data, and increases the statistical significance of the results (see e.g., Barrow et al., 1986).

No effect from the other satellites was found (see Carr and Desch, 1976, and the references therein; St. Cyr, 1985).

The strong control of part of the jovian emissions by Io shows well the unique role of Io in the jovian magnetosphere. This has long suggested that the source region of the Io-dependent emissions was along the Io magnetic flux tube, or close to it. Winglee (1986) recently discussed an enhancement in the density of the energetic component in the Io plasma torus correlated with certain jovian longitudes. He attributes the Io-controlled emissions to enhanced emission from the heated electrons moving down the Io field line. The electrons could be accelerated by Alfvén waves associated with Io motion (Goertz, 1980; Neubauer, 1980; Acuña et al., 1981). Qualitative attempts to localize the source of the Io emissions (Genova and Boischot, 1981; Calvert, 1983) were in accordance with the hypothesis of an emission at or close to the Io field line. In a quantitative statistical study, Genova and Aubier (1985) have shown that, with the Pioneer multipole magnetic field models, some of the Io emissions that appear as isolated arcs in the dynamic spectra can come from the southern and northern feet of the Io flux tube (see also, Riddle, 1983). But most of the high-frequency Io-dependent emissions come from a field line that crosses the equator ~70° behind Io (see also Thieman and Smith, 1979). If the magnetic field models close to the surface are correct, it will be necessary, for explaining this delay, to understand better the interaction between Io and Jupiter's inner magnetosphere. One has to induce acceleration of energetic particles, which are thought to be the energy source for the emission, not only directly between Io and the ionosphere, but also on field lines behind Io. One possible mechanism, where the acceleration takes place by way of a pattern of kinetic Alfvén waves, from the model of Gurnett and Goertz (1981), has been proposed by Hashimoto and Goldstein (1983). But, as discussed by Genova and Calvert (1987), the problem remains open.

Why One Has to Be Careful with Statistics

The jovian emissions are so multiple that, in general, one cannot define their characteristics from one or a small number of examples: It is most often necessary to use the largest possible number of events and to study their properties statistically. Moreover, for instance, the solar-wind influence on the emission, or the interplanetary scintillation seen on the ground-based observations, have time scales of days or months. All this shows the importance of long-term synoptic observations, and thus the need for long-term observational programs from the ground. Some additional statistical work is also possible with the Voyager data, which were recorded continously for several months.

But one also has to be careful when handling this kind of data. Ground-based observations are contaminated by the presence of periods linked to the Earth's diurnal or annual rotation, and by beats between these periods and the emission periodicities (see e.g., Sastry,

ORIGINAL PAGE
BLACK AND WHITE PHOTOGRAPH

1968). For instance, due to the presence of interferences during daytime, which sometimes prevent identification of emissions below ~20–25 MHz, many more emissions are observed at night (figure 77). Moreover, the inspection of several years of ground-based data shows that there are more interferences at some particular times, for example, in November during late afternoon and the beginning of the night, up to 1:00 AM, in Nançay. This kind of effect has to be searched for and eliminated to avoid bias in statistical occurrence studies.

Another problem is encountered in all kind of data sets, obtained from the ground as well as from space. It arises from beats between the intrinsic periods of the emissions and the nonuniform coverage of the CML–Io phase plane of the observations. This is particularly important, for instance, in the case of the Voyager PRA observations in the high-frequency range, which covered only a few weeks around each encounter with the planet, with a varying noise level due to the rapid change in the distance between the source and spacecraft (figure 78a). This is true even for very long term synoptic observations (figure 78b, c, d), and has always to be taken into account as soon as statistical occurrence studies are concerned.

SHORT-TERM VARIABILITY

During some jovian events, a specific kind of emission composed of brief narrow-band bursts with duration of some tens of milliseconds is observed. It is called S-burst emission (S for "short") (Gallet, 1961), and has a different aspect from the more usual, smoother radiation (figure 79). The characteristics of this sporadic emission will be given first. Then, all the fluctuations with time scales from ~1 s to a few minutes will be briefly described.

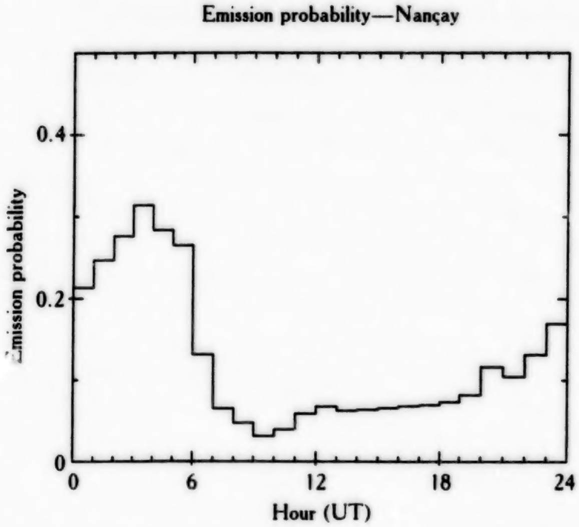

Figure 77. Probability of observing an emission at Nançay (number of observed emissions divided by the number of observations) as a function of the hour in day. Very few emissions are observed during daytime.

The S-Burst Emission

The brief bursts that compose the S-burst emission have an instantaneous bandwidth of a few hundred kHz, and appear generally scattered in the dynamic spectra (figure 79b, c). These bursts occur during storms lasting from about half an hour to a few hours. Like the more common, smoother emissions, they are organized into arcs with duration of some minutes. They can appear at the same time as the smooth emission (at the same or different frequencies), or alone (Leblanc et al., 1980b). The S-burst emission seems to be strictly organized with respect to Io (figure 80) (see e.g., Riihimaa, 1977; Leblanc et al., 1980b; Alexander and Desch, 1984; Genova and Calvert, 1987). At high frequencies, it has the same source region as most of the northern hemisphere Io-dependent emissions, as described above (Genova and Calvert, 1987). The regions where high-frequency S-bursts occur in the CML-Φ diagram is contained in the one where the northern hemisphere high-frequency smooth emissions appear, but is narrower (figure 80). Thus, the S-burst emission is more directive than the smoother emission from the same source region. At lower frequencies, the S-bursts are strictly controlled by Io, and the influence of the planetary rotation is far less effective; for instance, S-bursts are observed at almost all longitudes for $70^\circ \leq \Phi \leq 110^\circ$ at frequencies lower than 15 MHz (Alexander and Desch, 1984), with occasional events at higher frequencies in the same region (Genova and Calvert, 1987). Preliminary polarization observations suggest that there also exist S-bursts coming from the southern hemisphere (Riihimaa, 1976).

Ellis (1979) published an atlas displaying the shape of many S-burst events recorded at low frequencies. Most (but not strictly all) of the S-bursts drift rapidly with time toward low frequencies. This frequency drift is often intepreted as being due, for an emission close to the local gyrofrequency, to the motion along the magnetic field lines of electron beams that would produce the emission (Ellis, 1974). The frequency decrease implies then that the electrons are moving upward, in the direction of decreasing magnetic field

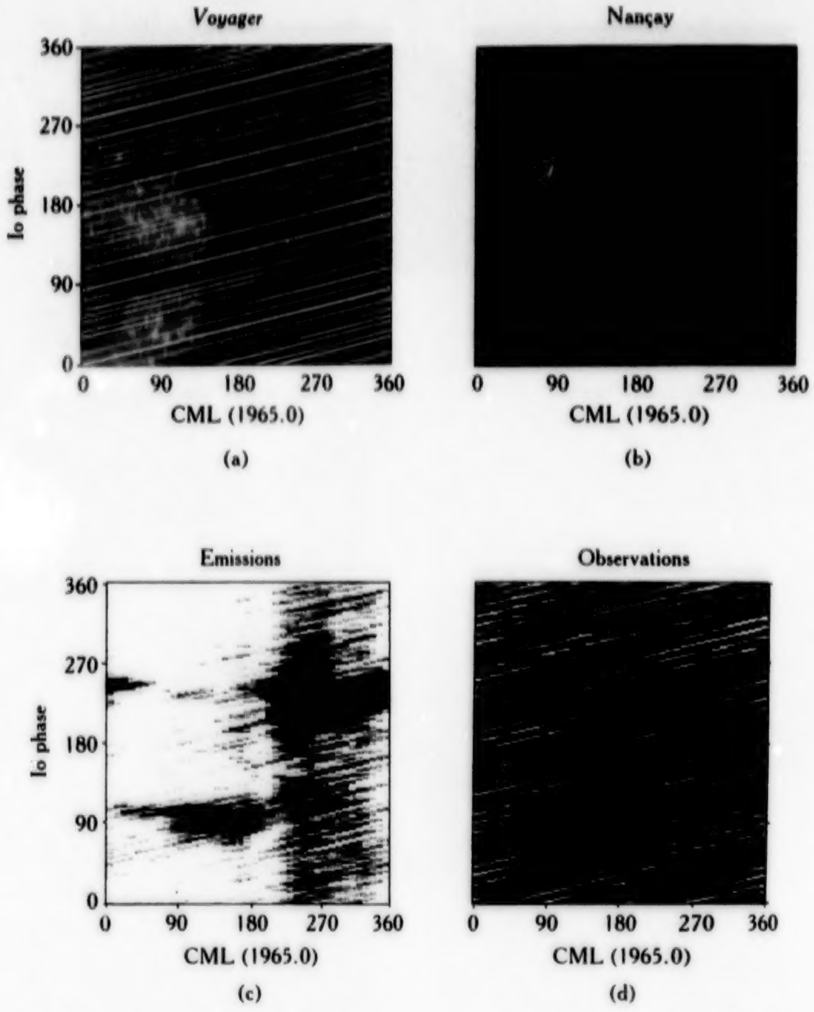

Figure 78. Central meridian longitude and Io phase (**a**) of Voyager 1 and 2 observations for the short period around encounters during which the decametric emissions were observed with sufficient signal to noise ratio, taken from the catalogue of Aubier and Genova (1985) (the duration of usable observations is much longer for the hectometric band); and (**b**) of Nançay observations from 1978 to 1984. The sampling of the CML-Φ plane is not complete, even in the second case of Boulder observations (**d**) and emissions observed (**c**) from 1960 to 1975 (in *gray levels*). *White regions* have been observed less than 30 times, *black regions* more than 60 times. The coverage of the CML-Φ_{Io} plane is obviously not uniform. Moreover, the Io-B region was sampled more often during some years (which is not the case at Nançay). The structures found in the non-Io-A region (for CML ≥ 200° out of the Io-A region (i.e., for $\Phi \leq 180°$) and $\Phi \geq 270°$) are artifacts due to the observation coverage.

magnitude. It has been shown, by measuring the frequency drift and consequently the electron speed along the field lines, that these electrons cannot be trapped. They have a very small equatorial pitch angle (~3°.5), and during their adiabatic motion along the field lines, they reach the ionosphere where they are lost through collisions (Desch et al., 1978; Leblanc et al., 1980a; Ellis, 1980). If this interpretation is correct, the electrons should then be accelerated close to the ionosphere, at least in the northern hemisphere. The source extent of one burst is estimated to a few hundred kilometers.

The precise mechanism that produces the S-burst emission is still somewhat uncertain. The conditions of excitation by Io are probably similar to those for the smoother emission (Genova and Calvert, 1987), but the mechanism is probably not exactly the same as the generation mechanism for the smoother emission (see e.g., Staelin and Rosenkranz, 1982; Zaitsev et al., 1986; Melrose, 1986). Some of these authors suggest that the

ORIGINAL PAGE
BLACK AND WHITE PHOTOGRAPH

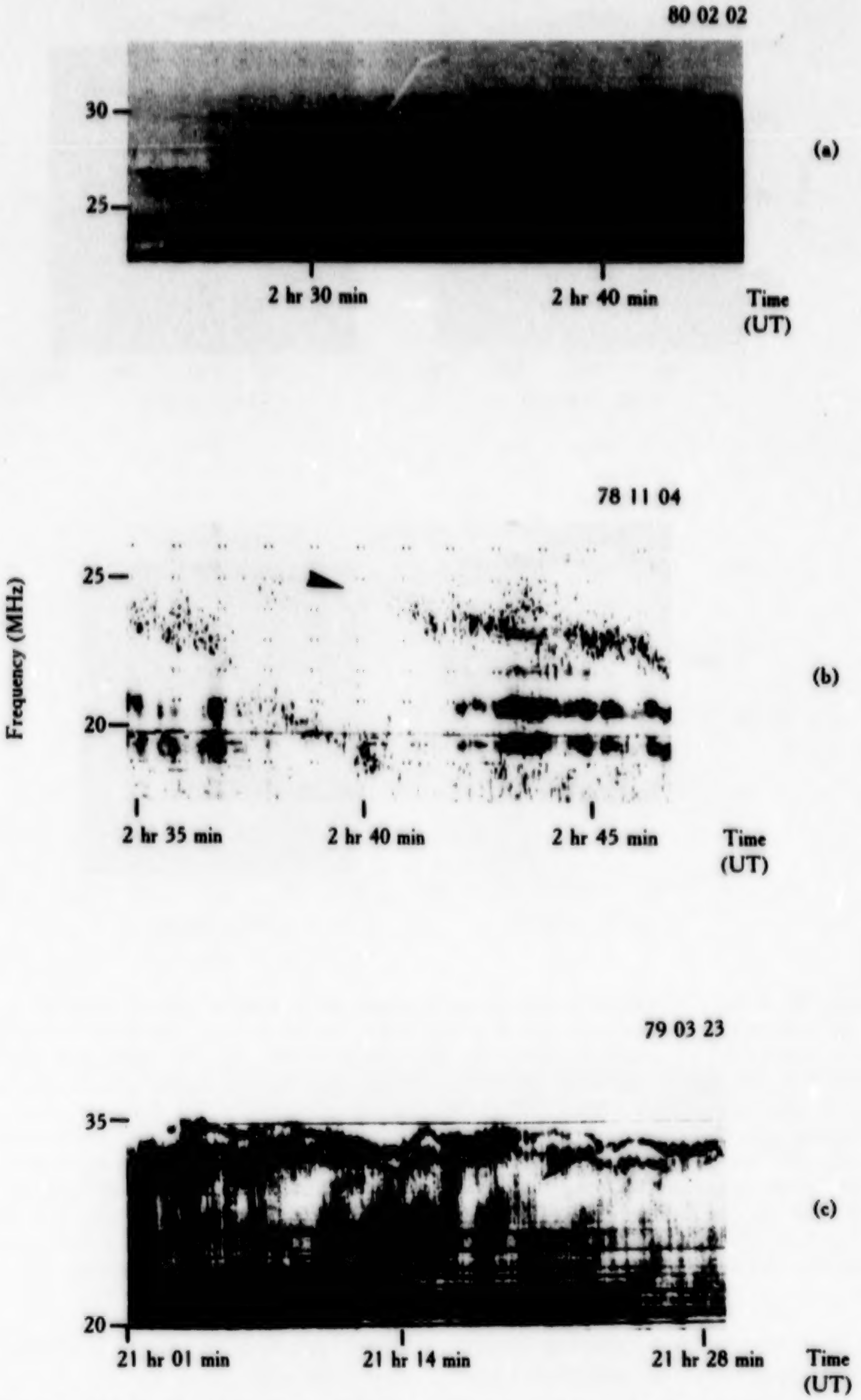

Figure 79. Intrinsic structure of the dynamic spectrum of the jovian emission, observed at Nançay. (**A**) Smooth emission. The vertical patterns are due to ionospheric and interplanetary scintillation. (**B**) S-burst emission. Each dot corresponds to an S-burst, through which the receiver sweeps slowly. (**C**) Superimposed smooth and S-burst emissions. "Splitting" appears at the high-frequency limit of the emission.

ORIGINAL PAGE
BLACK AND WHITE PHOTOGRAPH

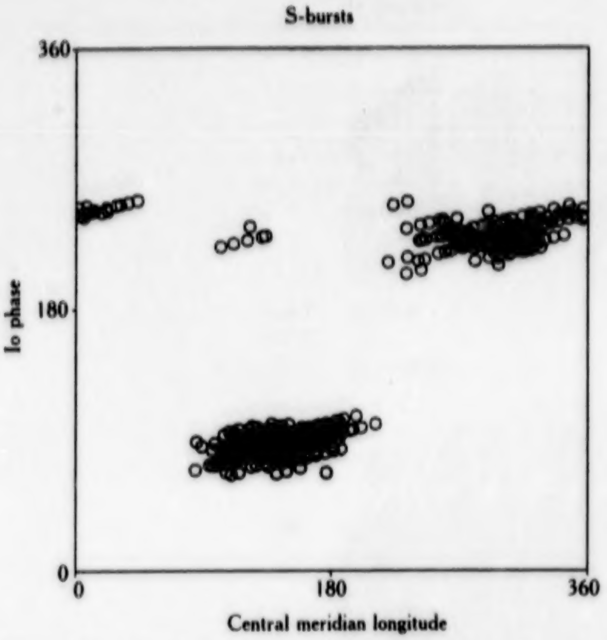

Figure 80. Central meridian longitude and Io phase of S-burst emission observed at Nançay, above 15 MHz. The regions of occurrence found by Alexander and Desch (1984) below 15 MHz would appear as two horizontal bands centered at $\Phi_{Io} \sim 90°$ and 230°. From Genova and Calvert, 1987.

negative drift could be intrinsic to the proposed mechanism and independent of the particle movement. Zaitsev et al. (1986) suggest, for instance, that plasma waves excited by loss-cone electrons near the upper-hybrid frequency could convert to electromagnetic waves, and interpret the negative drift rate as due to the group delay of extraordinary waves during their propagation in regions with low-refractive index. Melrose (1986) proposes a phase-bunching mechanism adapted from the theory for discrete very low frequency (VLF) emissions (Helliwell, 1967), which could also be driven by loss-cone electrons.

Propagation Effects Far from the Source

The decametric emissions observed from the ground have propagated through inhomogeneous media, which modulate their spectrum and intensity. The effect of the interplanetary medium is to produce the so-called interplanetary scintillation, due to the electron density inhomogeneities convected by the solar wind, which cross the line of sight. Out of the periods of Earth-Jupiter conjunction and opposition, this scintillation produces modulations with a large bandwidth, and time scale of about 1 s (figure 81a). It was first identified from fixed frequency records by Douglas and Smith (1967) and by Slee and Higgins (1968) and was later studied on dynamic spectra by Riihimaa (1978) (with a 2-MHz bandwidth) and by Genova and Leblanc (1981). The interplanetary scintillations have been used to determine the position of the source of jovian DAM by Genova and Boischot (1981), followed by Boischot et al. (1987).

Broad-band fluctuations, slowly drifting in frequency in the dynamic spectra, are also produced by the Earth's ionosphere, with time scales of some 10 seconds (figure 81b) (Warwick, 1964; Riihimaa, 1979; Genova et al., 1981). This kind of fringe system tends to occur at certain periods (at night and in winter, at Nançay) and could be linked to spread-F ionospheric phenomena.

Finally, the traveling ionospheric disturbances (TID) act as lenses with a focal length at decameter wavelengths close to their distance to the radio telescope. They produce caustic patterns in the dynamic spectra (figure 81c). Meyer-Vernet et al. (1981) and Genova and Aubier (1983) described the effects observed on solar decametric radiation (see also Mercier, 1986). All these modulations, which are superimposed to the radiation leaving the jovian magnetosphere, have been characterized through long-term ground-based observations. They have been used both to study the inhomogeneous media that produce them, and in some cases, to study the properties of the radio emission itself.

Intrinsic Modulations

As seen earlier (figure 23), the jovian emission is made of arc patterns, or sometimes isolated arcs, with very few exceptions (Leblanc, 1981; Carr et al., 1983; Genova and Aubier, 1987). The arc patterns appear as series of nested curved structures in the dynamic spectra. One individual arc lasts for a few minutes at a given frequency, and has an instantaneous frequency range of a few MHz (on the properties of arcs, see Boischot et al., 1981, and references therein). The sense of curvature of the arcs depends on the central meridian longitude of observation. Many papers dealt with the origin of the arcs (Boischot and Aubier, 1981; Goldstein and Thieman, 1981; Gurnett and Goertz, 1981; Lecacheux et al., 1981; Pearce, 1981; Staelin, 1981; Warwick, 1981; Menietti et al., 1984b). For example, Gurnett and Goertz (1981) suggest that the emission originates from electrons accelerated by kinetic Alfvén waves produced by the motion of Io in the planetary magnetic field. These

ORIGINAL PAGE
BLACK AND WHITE PHOTOGRAPH

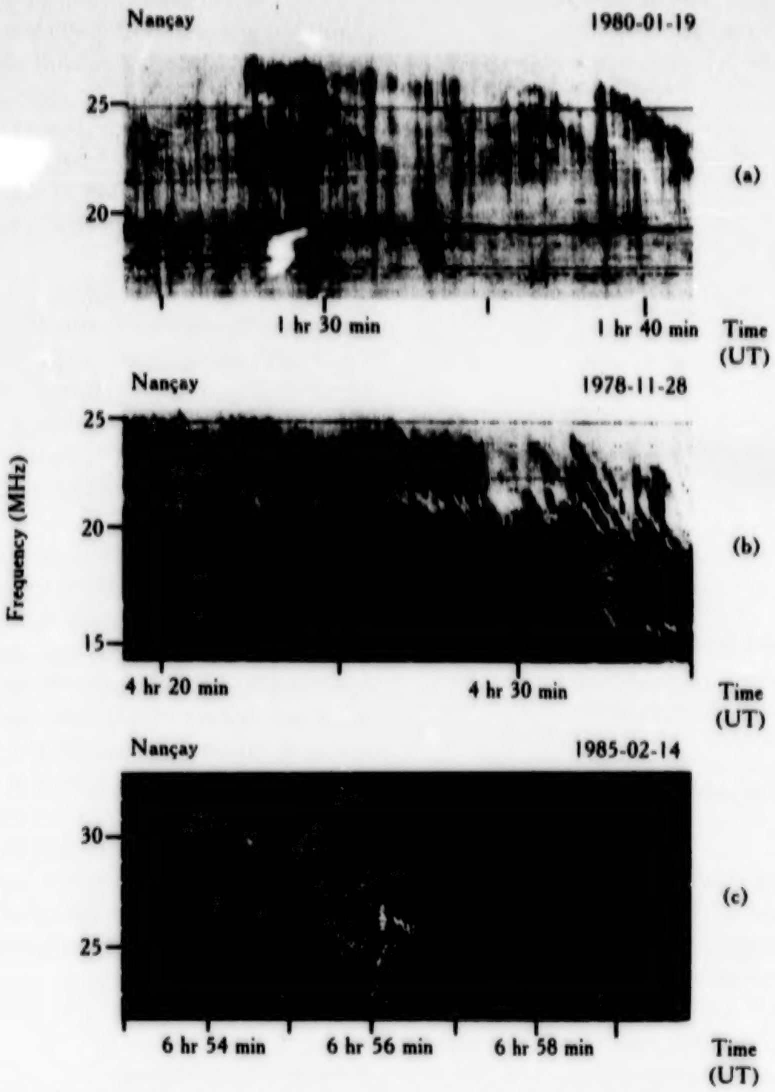

Figure 81. Effects of propagation between Jupiter and the Earth, observed at Nançay. (**a**) Interplanetary scintillation. It produces the regular, vertical pattern, with a quasi-period of about 1 s. (**b**) Ionospheric fringes. They are observed in Nançay at night, in winter. (**c**) Ionospheric caustics. The caustic envelops the emission. As the source is very small, two fringe systems, approximately parallel to the two branches of the caustic, are also seen (see fig. 83 for a model of the phenomenon). From Genova, 1987.

waves bounce from one hemisphere to the other, and the Alfvén waves pattern follows Io's motion. The arcs could then be seen when the observer successively intersects an emission cone produced at each successive discrete triggered source, at the foot of each Alfvén "wing" (figure 82). Lecacheux et al. (1981) propose a very different mechanism where the arcs are diffraction fringes produced when the wave propagates through an isolated plasma irregularity, which might be found in the Io plasma torus (figure 83).

Other modulations appear very often in the dynamic spectra. The modulation "lanes" are regular, almost parallel, lines that last for a few seconds to a few tens of seconds (i.e., sometimes with time scales very close to that of the ionospheric fringes) and drift in frequency (figure 84) (Riihimaa, 1970, 1974, 1976, 1979; Genova et al., 1981). The sense of the drift is mainly related to the observer's position in central meridian longitude (i.e., with respect to the planetary magnetic field). The lanes could be fringes due to large-scale diffraction in the Io plasma torus (Meyer-Vernet et al., 1981).

An intense narrow-band emission called *splitting* can also be observed at the high-frequency limit of Io-

ORIGINAL PAGE
BLACK AND WHITE PHOTOGRAPH

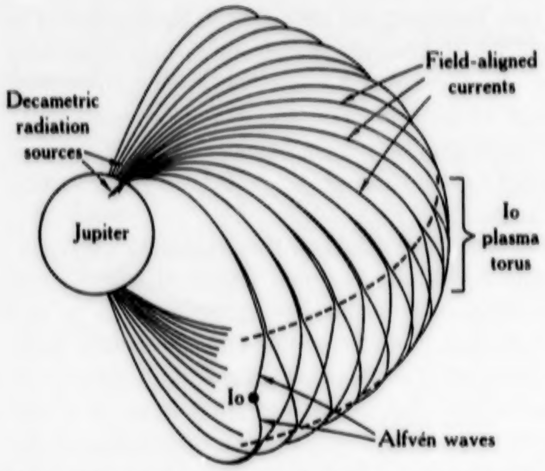

Figure 82. Schematic sketch of the standing Alfvén wave pattern excited by the motion of Io through the plasma torus. From Gurnett and Goertz, 1981.

dependent events, with sometimes one or several parallel patterns at lower frequency (figure 79c) (Leblanc and Rubio, 1983). It occurs almost always in a small, well-defined region of the CML-Φ diagram, and is thus strongly Io-controlled. More generally, narrow-band events, which are called *N* events by Carr et al. (1983), were studied by Krausche et al. (1976), Flagg et al. (1976), and Riihimaa (1977, 1985). They are perhaps, at least sometimes, made of trains of successive S-bursts. There is no complete theory for the origin of these phenomena (Lecacheux et al., 1981; Meyer-Vernet et al., 1981; Zaitsev et al., 1986).

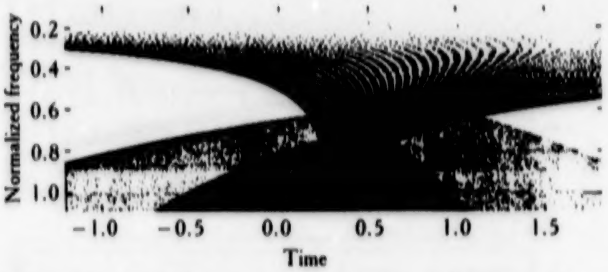

Figure 83. Arcs due to diffraction. This theoretical dynamic spectrum shows a caustic and two fringes systems, produced by an isolated phase-changing plasma "blob" encountered along the ray path. One of the fringe systems is identified by the authors as the pattern of jovian arcs. From Lecacheux et al., 1981.

LONG-TERM VARIABILITY

The observations of the decametric radiation are, in a certain sense, repeatable: The occurrence and characteristics of most of the patterns observed in the dynamic spectra are found in well-defined ranges of CML (for the rotation-controlled patterns), and/or Io phase (for the Io-controlled ones), as seen earlier. Moreover, the study of the Io-dependent emissions shows the great similarity of the shapes of the dynamic spectra recorded in similar geometrical conditions of CML and Io phase (figure 85) (Barrow et al., 1982). A perfect repeatability would imply an overall stability of the source location and beaming, given the geometry of observation with respect to the magnetic field and Io position. Although there is no systematic study of the

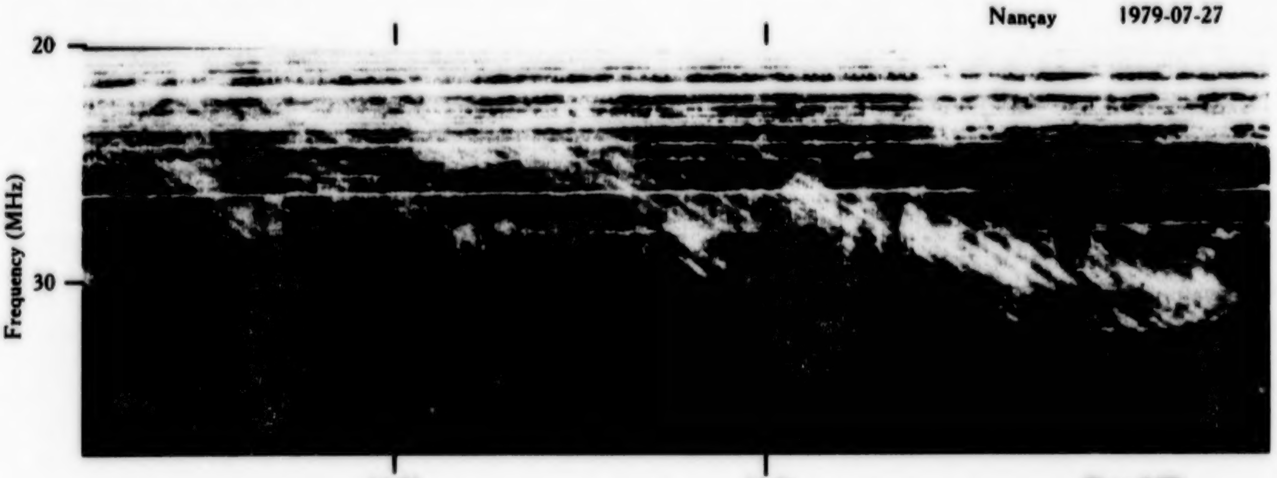

Figure 84. Modulation lanes. Two patterns of drifting modulation lanes cross the dynamic spectra. Adapted from Genova et al., 1981.

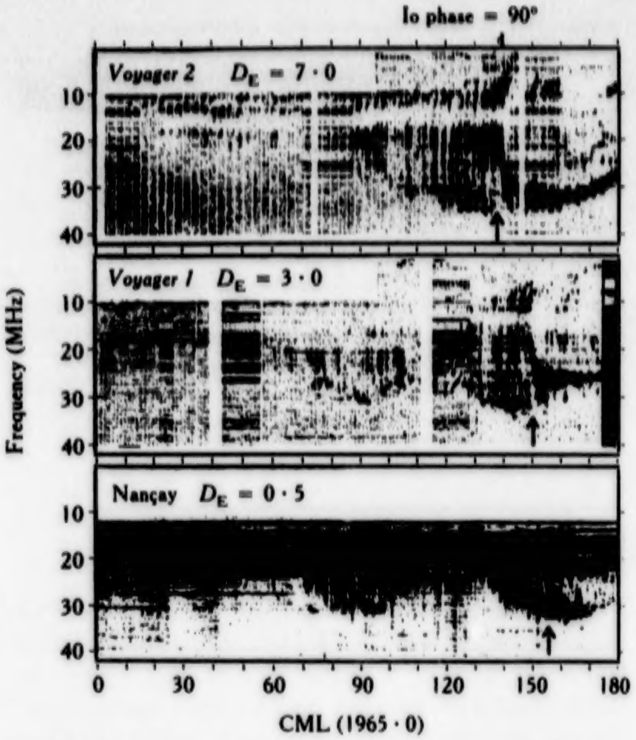

Figure 85. Comparison of Io-B emissions observed from the Earth and from Voyager 1 and 2, for the same CML and Φ. The global shapes of the dynamic spectra are very similar. The small gap (*arrow*) moves with the jovigraphic latitude of the observer. From Barrow et al., 1982.

variability of the dynamic spectrum, it seems that a certain stability exists, but no exact repeatability is found, in general. For example, the highest frequency limit of the emission, corresponding to the altitude extent or position of the source, seems to vary. Similarly, the intensity can be very different from one storm to another. This is particularly striking for the Io-independent events for which "occurrence probability" (i.e., roughly the ratio of the number of emissions observed to the number of observations in given conditions) is far lower than unity for both sensitive ground-based and Voyager observations. It is not possible to know whether this is due to intensity fluctuations only (emissions with too low intensity to appear above the background count as no emission in terms of probability of occurrence), variable beaming, or if there is sometimes no emission at all, due to conditions not favorable to wave growth in the source. In conditions favorable to observation, it seems that the occurrence probability at the "center" of the Io-controlled regions of the CML-Io phase diagram is closer to 100 percent, but the overall probability for the global Io-dependent regions, as observed from Nançay for instance, is about 40 percent. Moreover, the strong latitudinal beaming of the emission mentioned above leads to a long-term periodic variation of the average occurrence probability of DAM (at all frequencies), and of the positions of Io-controlled regions in CML, at Jupiter's revolution period (11.9 years) (see Carr et al., 1983, and references therein).

Aside from the effect of the planetary magnetic field rotation, which, as noted earlier, dominates the whole emission, its long-term variability can be the sign of external controls of the emission. With reference to the other similar planetary radio emissions (i.e., the auroral kilometric radiation from the Earth and Saturn's kilometric radiation), a relationship is expected between the radio radiation and the auroral activity, considered as an index of particle precipitation, and also with the solar-wind fluctuations at Jupiter. In fact, the situation is much more intricate at Jupiter, because of the role of Io in the magnetosphere. For instance, a relationship between the density variations in the torus and the radio emission could be expected also. On the other hand, Calvert (1985a) has suggested that some hectometric jovian radio emissions could be triggered by weaker radio waves from the Sun, which has given rise to a hot controversy (Desch and Kaiser, 1985; Calvert, 1985b). Calvert interprets his results as indicating that natural radio lasers, such as those that he proposes to explain the Earth's auroral kilometric radiation (Calvert, 1982), could be at the origin of the jovian emission.

As a general rule, the statistical study of the long-term fluctuations of the jovian emission is made difficult by the presence of the Io period in the data. Another problem arises because the exact position of the source of all the events is not known; it is almost certain that the source of the Io-dependent radiation is along field lines that intersect Io's orbit, or very close to them. But there is no direct observational evidence about the position of the source of the Io-independent radiation. This source is certainly located at high latitudes, but it could be on field lines that intersect Io orbit or the outer regions of the Io torus, or at higher latitudes, for instance, on open field lines linked to the magnetic tail of the planet. The exact latitude of the source of radio emission is also linked to the possibility or not for the emission to be subject to the solar-wind influence. The field lines that intersect Io's orbit are deeply embedded in the inner jovian magnetosphere, in regions dominated by the rotation of the jovian magnetic field, where the solar-wind effect is probably negligible. But, for eventual radiation from higher latitudes, the emissive field lines could be in

ORIGINAL PAGE
BLACK AND WHITE PHOTOGRAPH

regions linked to the outer magnetosphere, where the solar-wind effect would become significant. The most intense component of the ultraviolet (UV) auroral emission, indicating a region of strong particle precipitation, seems to lie in a region on the surface intermediate between the foot of the Io and tail field lines (Herbert et al., 1987), but it is possible that particle precipitation, producing weaker auroras, occur at the foot of the Io torus or tail field lines. Nevertheless, the determination of the exact latitude of auroral UV emission, and especially of the northern limit of the emitting zone, is not a simple problem (see e.g., Skinner et al., 1984). On the other hand, enhancements in the infrared emission of NH_3, CH_4, and C_2H_2 are observed in a well-localized region at high latitude, near 180° of longitude (Kostiuk et al., 1977; Caldwell et al., 1980, 1983; Drossart et al., 1986). They are interpreted as due to atmosphere modification by auroral electron precipitation. No study has been made of the radio emission in connection with this possibly emissive region. Quite generally, observations of UV and infrared (IR) emissions over long periods of time would be necessary for correlation with the radio data.

No study of possible correlation of the jovian radiation with auroral UV or IR emission, or with torus parameters, has been published to date, to the author's knowledge, but many papers deal with its correlation with the solar wind. This latter will be discussed in some detail in the following, since it illustrates well recent progress due to space observations, and also the complementarity between ground-based and spacecraft observations.

The study of the correlations between the solar wind and jovian radiation is not an easy one, especially when ground-based data are to be used, because of the presence of interfering Earth periodicities (see e.g., Sastry, 1968) and due to the necessity to extrapolate the solar-wind measurements from the Earth to Jupiter's orbit. Nevertheless, several pre-Voyager studies strongly suggested an association between the fluctuations of the Io-independent jovian radiation and the sector structure of the solar wind (see e.g., Terasawa et al., 1978; Barrow, 1978, 1979; Oya and Morioka, 1981; Pokorny, 1982). Although no detailed analysis was published for the Io emissions, Barrow (1978) indicated that they did not seem to be influenced by the solar wind. But the most recent review paper about the phenomenology of the jovian radiation noted: "There is not yet general agreement as to the nature and, indeed, even the existence of a solar influence" (Carr et al., 1983).

The analysis of the Voyager radio data, free of Earth-linked periods, and continuous in time, allowed most of the difficulties to be removed. Moreover, solar-wind measurements were also possible aboard the spacecraft, much closer to Jupiter, which permits more reliable extrapolations. It was shown first that the hectometric radiation (for which the influence of Io is very small or null) presents large intensity fluctuations, with the same periodicities as the solar-wind magnetic sector structure, during six months when this pattern remained very stable (Zarka and Genova, 1983). It was concluded that the jovian hectometric emission should have its source in a magnetospheric region subject to the solar-wind influence, and thus probably not as deep in the inner magnetosphere as the Io torus field lines. Also for hectometric data, Desch and Barrow (1984) found a correlation with the solar-wind density at Jupiter, measured by Voyager, and perhaps an association with the solar-wind sector structure. In the decametric range, a correlation of the non-Io emission with the solar-wind density and velocity, and with the interplanetary magnetic field magnitude was found, with no effect for the Io-dependent emission (Barrow et al., 1986). The link between emissions in the two wavelength ranges was established by comparing long duration Nançay ground-based observations of the decametric radiation with simultaneous Voyager measurements in the hectometric range (Genova et al., 1987). One side result of these studies is that the probability of occurrence of jovian Io-independent decametric events, observed from the ground, fluctuates in response to the solar-wind effect on the emission.

Thus, the complementary use of space- and ground-based observations shows a basic difference between the Io and non-Io emissions of Jupiter. The results are well in accordance with the source of the Io-dependent emissions being close to the Io field line, shielded from the solar wind in the rotation-dominated inner magnetosphere; they suggest that the Io-independent emissions could be at higher latitudes—for instance, on field lines connected to the magnetospheric tail, or close to them—except if the solar-wind influence, for instance on energetic particles, can exist deeper in the inner magnetosphere, down to the Io torus field lines. It would probably be fruitful to relate these conclusions to the fact that Io-dependent emissions are observed at similar central meridian longitudes with similar characteristics when seen from different local times (by Voyager before and after the encounters), whereas this is not true for the Io-independent events (Alexander et al., 1981; Leblanc, 1981). This means that the source of Io-dependent events is certainly not fixed in local time; it remains to be studied if the observations of the Io-independent events are consistent with a source in a fixed local time range (which is the case for the Earth and Saturn kilometric radiations). In any case, the precise mechanism responsible for the solar-wind influence on the Io-independent radiation and, more generally, on the dynamics of the high-latitude magnetosphere, is far from being well understood.

CONCLUSION

Unlike in many other domains, the importance of long-term systematic "routine" observations, as continuous in time as possible, of the jovian radio emissions, has long been recognized. Some experience has been acquired of the problems raised by the maintenance of routine equipment, by systematic handling of large amounts of data, in analog and digitized form, and by their statistical analysis.

In this domain also, the complementarity between space- and ground-based observations appears well. Of course, Voyager observations were unique in the sense that they gave access to the whole emission frequency range, down to hectometer wavelengths, and also to new viewing angles, from the night and early morning sides of the planet. But ground-based observations, which can be as sensitive as the Voyager ones, for instance with the Nançay instrument, are essential for elaborate studies of the short-term variations of the emission. The most useful information is drawn from dynamic spectra, recorded with high time and frequency resolution, which require data transmission capabilities too large for a spacecraft experiment. In particular, the fine structure of the very short and narrow-band S-bursts is accessible only from the ground. Observations from the ground also allow study of the inhomogeneous media between the source and the radio telescope, such as the interplanetary medium and the Earth ionosphere, and sometimes give important information about the emission itself. Moreover, the simultaneous use of ground-based and space data has proven to be a valuable tool for study of the directivity of the emission, and the relationship between the decametric and hectometric radiations. This will be absolutely necessary in the future, since the plasma and radio receivers aboard Galileo and Ulysses cover only the low-frequency part of the jovian emission, up to 1 MHz for Ulysses and 5.6 MHz for Galileo, whereas the emission extends up to 40 MHz; it is probable that no Io-dependent emission will be observed with Ulysses. Finally, the long-term synoptic ground-based observations are essential to the study of the variability of the jovian emission over long time scales (together with a very careful data analysis).

From the study of all these observations, an appreciable knowledge was gained of many of the physical parameters necessary to understand the generation mechanism of the emission and to relate it to other phenomena in the jovian magnetosphere. In particular, the spectrum and its variations are well known, the control by the planetary magnetic field is generally understood, and the role of Io has been thoroughly investigated, the next step being to determine how Io triggers the Io-dependent emissions. Important information has been gathered already about the emission lobe (but at present time only from the accessible directions, that is, a very limited latitude range around the equatorial plane), the localization of the sources of the emissions, the S-bursts and their relationship to the more usual smooth emission, and the polarization of the emission. However, the available studies need to be somewhat complemented, in particular concerning the polarization. Similarly, the study of the intrinsic fine spectral and temporal structure of the emission, (understanding of which is linked to that of the small-scale phenomena in the source region) and/or the propagation in the jovian environment must be carried on. This means that ground-based spectral observations, continuous in time, and if possible with a wide spectral coverage, must go on. The data from the future space missions (Galileo in orbit around Jupiter and Ulysses, that will probe higher jovian latitudes), that have direction finding and polarization measurement capabilities, are also eagerly waited for, in spite of the frequency-range limitations mentioned above. Moreover, before the end of the millenium, Cassini should fly by Jupiter en route for Saturn, we hope during Galileo's operating lifetime, allowing invaluable stereoscopic observations of the jovian radio emission, especially after encounter, with Cassini departing from Jupiter in the midnight direction.

From the point of view of theoretical studies, during the last years, much progress has been made in the understanding of the origin of the Earth's auroral kilometric radiation. Most of the recently published papers deal with the cyclotron maser instability mechanism, also named maser synchrotron instability (MSI), through which the free energy of an energetic electron population is directly converted into escaping electromagnetic waves (Wu and Lee, 1979; see e.g., the review of Wu, 1985, and references therein; and the more recent works of Hayes and Melrose, 1986; Pritchett, 1986a, b; Strangeway, 1985, 1986; and Zarka et al., 1986, among others). The striking similarities between the Earth's radiation and Jupiter's decametric and hectometric emissions (and also with Saturn's and Uranus' kilometric radiations), together with their different morphologies (frequency ranges, spectral arcs, and the like) suggest that they are produced by the same basic type of instability, but probably with different magnetospheric contexts (magnetic field magnitude, plasma distribution in the source, presence of Io, geometry, and the like). The next step is to try to apply the mechanism developed for the Earth to the case of the other planets. The main obstacle is that, unlike for the Earth, there are no in-situ measurements of the plasma environment and particle distribution functions in the source regions for the outer planets; one has to rely on models extrapolated from near-equatorial measurements to study the generation mechanism and its efficiency in these different physical conditions. The case of Saturn is beginning to be investigated. Lecacheux and Le Quéau (1984) have shown the relevance of the MSI for generating this emission, and Galopeau et al. (1987) have calculated a maximum spectrum for Saturn's kilometric radiation, consistent with the observations. The case of Uranus is too recent to have motivated elaborate theoretical studies.

Goldstein and Goertz (1983) reviewed the possible mechanisms for the generation of the jovian emission. Due to the presence of Io, the interaction of which with the surrounding medium could excite electron beams more easily than loss-cone type features, they conclude that indirect (beam driven) mechanisms are preferred to direct (loss-cone driven) ones. However, other authors have shown that the MSI is relevant to the DAM generation. In particular, this mechanism predicts that the emission is beamed in a thin hollow cone, in good agreement with the observational constraints (Hewitt et al., 1981). Moreover, Le Quéau (1982) estimated, from the MSI mechanism saturated by electron nonlinear trapping, a peak intensity about 10^{-18} W m^{-2} Hz^{-1} at 4 AU for the decametric emission, close to that observed. Thus, the question remains open. One can speculate that both types of mechanisms coexist at Jupiter, the Io-dependent emissions being generated by a beam-driven type instability, whereas the non-Io decametric and hectometric emissions, more similar to the other planetary radio emissions, would be emitted like these last ones by a direct loss-cone driven instability (as the MSI). Alternatively, the same mechanism could be operating in different conditions, for instance, driven by different features of the electron population, or in different regions of the high-latitude magnetosphere. The investigations about the origin of S-bursts must also be carried on.

Finally, a fine future can be predicted for studies of the connections between radio-radiation and other phenomena taking place in the vicinity of Jupiter. One has to go on in the investigation of the correlation between the Io-independent emission and the solar-wind parameters at Jupiter, and more generally of the interaction of the jovian outer magnetosphere with the solar wind, in particular by extending the time basis of the study. This means obtaining new simultaneous observations of the radio emission and of the solar wind at Jupiter. On the other hand, with reference to the case of the Earth's auroral kilometric radiation, for which the problem is now well documented, it would be useful to begin studying the possible relation between the radio emission and the auroras, taken here as the signature of particle precipitation. The relationship between the auroral regions, seen in UV and IR, and the position of the radio source field lines, must be investigated; also, it would be useful to compute a global index of auroral activity, regularly enough for correlation with both the solar-wind parameters and the radio emission. Unfortunately, all these studies could be plagued by the lack of latitude resolution of the auroral data. Similarly, it could prove interesting to correlate the radio observations to the torus fluctuations, provided that these latter could be recorded for long enough durations, with a sufficient self-coherence in the data. For all these problems, one can expect nice input from the International Jupiter Watch.

References

Acuña, M. H., and N. F. Ness (1976). Results from the GSFC fluxgate magnetometer on Pioneer 11. In *Jupiter* (T. Gehrels, ed.), pp. 830–847. Univ. of Arizona Press, Tucson.

Acuña, M. H., K. W. Behannon, and J. E. P. Connerney (1983). Jupiter's magnetic field and magnetosphere. In *Physics of the jovian magnetosphere* (A. J. Dessler, ed.), pp. 1–50. Cambridge Univ. Press, Cambridge.

Acuña, M. H., F. M. Neubauer, and N. F. Ness (1981). Standing Alfvén wave current system at Io: Voyager 1 observations. *J. Geophys. Res.* 86:8515–8522.

Alexander, J. K. (1975). Note on the beaming of Jupiter's decameter-wave radiation and its effect on radio rotation period determination. *Astrophys. J.* 195:227–233.

Alexander, J. K., and M. D. Desch (1984). Voyager observations of jovian millisecond radio bursts. *J. Geophys. Res.* 89:2689–2697.

Alexander, J. K., T. D. Carr, J. R. Thieman, J. J. Schauble, and A. C. Riddle (1981). Synoptic observations of Jupiter's radio emissions: Average statistical properties observed by Voyager. *J. Geophys. Res.* 86:8529–8545.

Alexander, J. K., M. D. Desch, M. L. Kaiser, and J. R. Thieman (1979). Latitudinal beaming of Jupiter's low frequency radio emissions. *J. Geophys. Res.* 84:5167–5174.

Aubier, M. G., and F. Genova (1985). A catalogue of the high frequency limit of the jovian decameter emission observed by Voyager. *Astron. Astrophys. Suppl. Ser.* 61:341–351.

Barrow, C. H., (1978). Jupiter's decametric radio emission and solar activity. *Planet. Space Sci.* 26:1193–1199.

Barrow, C. H. (1979). Association of corotating magnetic sector structure with Jupiter's decameter-wave radio emission. *J. Geophys. Res.* 84:5366–5372.

Barrow, C. H., and J. K. Alexander (1981). Maximum frequency of the decametric radiation from Jupiter. *Astron. Astrophys.* 90:L4–L7.

Barrow, C. H., and M. D. Desch (1980). Non-Io decametric radiation from Jupiter at frequencies above 30 MHz. *Astron. Astrophys.* 86:339–341.

Barrow, C. H., M. D. Desch, and F. Genova (1986). Solar wind control of Jupiter's decametric radio emission. *Astron. Astrophys.* 165:244–250.

Barrow, C. H., A. Lecacheux, and Y. Leblanc (1982). Arc structures in the jovian decameter emission observed from the Earth and from Voyager. *Astron. Astrophys.* 106:94–97.

Bigg, E. K. (1964). Influence of the satellite Io on Jupiter's decametric emission. *Nature* 203:1008–1010.

Boischot, A., and M. G. Aubier (1981). The jovian decametric arcs as an interference pattern. *J. Geophys. Res.* 86:8561–8563.

Boischot, A., A. Lecacheux, M. L. Kaiser, M. D. Desch, and J. K. Alexander (1981). Radio Jupiter after Voyager: An overview of the planetary radio astronomy observations. *J. Geophys. Res.* 86:8213–8226.

Boischot, A., C. Rosolen, M. G. Aubier, G. Daigne, F. Genova, Y. Leblanc, A. Lecacheux, J. de la Noë, and B. M. Pedersen (1980). A new high gain, broadband, steerable array to study jovian decametric emissions. *Icarus* 43:399–407.

Boischot, A., J. H. Sastri, and P. Zarka (1987). Localization of Io and non-Io sources of jovian decameter emission. *Astron. Astrophys.* 175:287–288.

Burke, B. F., and K. L. Franklin (1955). Observations of a variable radio source associated with the planet Jupiter. *J. Geophys. Res.* 60:213–217.

Caldwell, J., A. T. Tokunaga, and F. C. Gillet (1980). Possible infrared aurorae on Jupiter. *Icarus* 44:667–675.

Caldwell, J., A. T. Tokunaga, and G. S. Orton (1983). Further observations of 5 μm polar brightening of Jupiter. *Icarus* 53:133–140.

Calvert, W. (1982). A feedback model for the source of auroral kilometric radiation. *J. Geophys. Res.* 87:8199–8214.

Calvert, W. (1983). The source location of certain jovian decametric radio emissions. *J. Geophys. Res.* 88:6165–6170.

Calvert, W. (1985a). Triggered jovian radio emission. *Geophys. Res. Lett.* 12:179–182.

Calvert, W. (1985b). Affirmation of triggered jovian radio emission and their attribution to corotating radio lasers. *Geophys. Res. Lett.* 12:625–626.

Carr, T. D., and M. D. Desch (1976). Recent decametric and hectometric observations of Jupiter. In *Jupiter* (T. Gehrels, ed.), pp. 693–735. Univ. of Arizona Press, Tucson.

Carr, T. D., M. D. Desch, and J. K. Alexander (1983). Phenomenology of magnetospheric radio emissions. In *Physics of the jovian magnetosphere* (A. J. Dessler, ed.), pp. 226–284. Cambridge Univ. Press, Cambridge.

Carr, T. D., A. G. Smith, F. F. Donovan, and H. I. Register (1970). The twelve-year periodicities of the decametric radiation of Jupiter. *Radio Sci.* 5:495–503.

Daigne, G., and Y. Leblanc (1986). Narrow-band jovian kilometric radiation: Occurrence, polarization, and rotation period. *J. Geophys. Res.* 91:7961–7969.

Desch, M. D. (1980). Io control of the jovian radio emission. *Nature* 287:339–340.

Desch, M. D., and C. H. Barrow (1984). Direct evidence for solar wind control of Jupiter's hectometer wavelength radio emission. *J. Geophys. Res.* 89:6819.

Desch, M. D., T. D. Carr, and J. Levy (1975). Observations of Jupiter at 26.3 MHz using a large array. *Icarus* 25:12–17.

Desch, M. D., R. S. Flagg, and J. May (1978). Jovian S bursts observations at 32 MHz. *Nature* 272:38–40.

Desch, M. D., and M. L. Kaiser (1985). On the proposed triggering of the jovian radio emission. *Geophys. Res. Lett.* 12:621–624.

Douglas, J. N., and H. J. Smith (1967). Interplanetary scintillation in jovian decametric radiation. *Astrophys. J.* 148:885–903.

Drossart, P., B. Bézard, S. Atreya, J. Lacy, E. Serabyn, A. Tokunaga, and T. Encrenaz (1986). Enhanced acetylene emission near the north pole of Jupiter. *Icarus* 66:610–618.

Dulk, G. A. (1965). *Io related radio emission from Jupiter.* Ph.D. thesis, Univ. of Colorado, Boulder.

Dulk, G. A. (1967). Apparent changes in the rotation rate of Jupiter. *Icarus* 7:173–182.

Duncan, R. A. (1971). Jupiter's rotation. *Planet. Space Sci.* 19:391–398.

Ellis, G. R. A. (1974). The Jupiter radio bursts. *Proc. Astron. Soc. Austr.* 2:1–8.

Ellis, G. R. A. (1979). *An atlas of selected spectra of the Jupiter S-bursts.* Univ. of Tasmania, Hobart, Australia.

Ellis, G. R. A. (1980). The source of the Jupiter S-bursts. *Nature* 283:48–50.

Flagg, R. S., D. S. Krausche, and G. R. Lebo (1976). High resolution spectral analysis of the jovian decametric radiation, II. The band-like emission. *Icarus* 20:477–482.

Gallet, R. M. (1961). Radio observations of Jupiter. In *Planets and satellites* (G. P. Kuiper and B. M. Middlehurst, eds.), pp. 500–533. Univ. of Chicago Press, Chicago.

Galopeau, P., P. Zarka, and D. Le Quéau (1987). to be submitted.

Genova, F. (1987). Les émissions radio "aurorales" des planètes. *Ann. Phys. Fr.* 12:57–107.

Genova, F., and M. G. Aubier (1983). Terrestrial ionospheric effects on solar decameter spectra. *Annales Geophys.* 1:415–424.

Genova, F., and M. G. Aubier (1985). Io-dependent sources of the jovian decameter emission. *Astron. Astrophys.* 150:139–150.

Genova, F., and M. G. Aubier (1987). High frequency limit and visibility of the non-Io and Io dependent jovian decameter radio emission. *Astron. Astrophys.* 177:303–309.

Genova, F., M. G. Aubier, and A. Lecacheux (1981). Modulations in jovian decametric spectra: Propagation effects in terrestrial ionosphere and jovian environment. *Astron. Astrophys.* 104:229–239.

Genova, F., and A. Boischot (1981). Structure of the source of jovian decametric radiation and interplanetary scintillation. *Nature* 293:382–383.

Genova, F., and W. Calvert (1987). Location of the source of the jovian millisecond radio bursts. *J. Geophys. Res.*, submitted.

Genova, F., and Y. Leblanc (1981). Interplanetary scintillation and jovian DAM emission. *Astron. Astrophys.* 98:133–139.

Genova, F., P. Zarka, and C. H. Barrow (1987). Voyager and Nançay observations of the jovian radio emission at different frequencies: Solar wind effect and source extent. *Astron. Astrophys.* 182:159–162.

Goertz, C. K. (1980). Io's interaction with the plasma torus. *J. Geophys. Res.* 85:2949–2956.

Goldstein, M. L., and A. Eviatar (1979). An emission mechanism for the Io-independent jovian decameter radiation. *Astrophys. J.* 230:261–273.

Goldstein, M. L., and C. K. Goertz (1983). Theories of radio emissions and plasma waves. In *Physics of the jovian magnetosphere* (A. J. Dessler, ed.), pp. 317–352. Cambridge Univ. Press, Cambridge.

Goldstein, M. L., and J. R. Thieman (1981). The formation of arcs in the dynamic spectra of jovian decametric bursts. *J. Geophys. Res.* 86:8569–8578.

Green, J. L. (1984). The Io decametric emission cone. *Radio Sci.* 19:556–570.

Gurnett, D. A., and C. K. Goertz (1981). Multiple Alfvén wave reflections excited by Io: Origin of the jovian decametric arcs. *J. Geophys. Res.* 88:2010–2020.

Hashimoto, K., and M. L. Goldstein (1983). A theory of the Io phase asymmetry of the jovian decametric radiation. *J. Geophys. Res.* 88:2010–2020.

Hayes, L. M., and D. B. Melrose (1986). Generation of ordinary mode auroral kilometric radiation by extraordinary waves. *J. Geophys. Res.* 91:211–217.

Heliwell, R. (1967). A theory of discrete VLF emissions from the magnetosphere. *J. Geophys. Res.* 72:4773.

Herbert, F. H., B. R. Sandel, and A. L. Broadfoot (1987). Observations of the jovian UV aurora by Voyager. *J. Geophys. Res.* 92:3141–3154.

Hewitt, R. G., D. B. Melrose, and K. G. Rönmark (1981). A cyclotron theory for the beaming pattern of Jupiter's decametric radio emission. *Proc. Astr. Soc. Austr.* 4:221–226.

Jones, D. (1986). Io plasma torus and the source of the jovian kilometric radiation (bKOM). *Nature* 324:40–42.

Kaiser, M. L., and J. K. Alexander (1972). The jovian decametric notation period. *Astrophys. Lett.* 12:215–217.

Kaiser, M. L., and M. D. Desch (1984). Radio emissions from the planets Earth, Jupiter and Saturn. *Rev. Geophys. Space Phys.* 6:373–384.

Kostiuk, T., M. J. Mumma, J. J. Hillman, D. Buhl, L. W. Brown, and J. L. Faris (1977). NH_3 spectral line measurements on Earth and Jupiter using 10 μm superheterodyne receiver. *Infrared Phys.* 17:431–439.

Krausche, D. S., R. S. Flagg, G. R. Lebo, and A. G. Smith (1976). High resolution spectral analyses of the jovian decametric radiation. I. Burst morphology and drift rates. *Icarus* 29:463–475.

Leblanc, Y. (1981). On the arc structure of the DAM Jupiter emission. *J. Geophys. Res.* 86:8546–8568.

Leblanc, Y., and G. Daigne (1985). Broadband jovian kilometric radiation: New results on polarization and beaming. *J. Geophys. Res.* 90:12073–12080.

Leblanc, Y., and A. Gerbault (1987). A catalogue of the jovian decametric radio emission from January 1982 to December 1984. *Astron. Astrophys. Suppl. Ser.* to be submitted.

Leblanc, Y., and M. Rubio (1983). A narrow-band splitting at the jovian decametric cutoff frequency. *Astron. Astrophys.* 111:284–294.

Leblanc, Y., M. G. Aubier, C. Rosolen, F. Genova, and J. de la Noë (1980a). The jovian S-bursts. II Frequency drift measurements at different frequencies throughout several storms. *Astron. Astrophys.* 86:349–354.

Leblanc, Y., J. de la Noë, F. Genova, A. Gerbault, and A. Lecacheux (1981). A catalogue of jovian decametric radio emission from January 1978 to December 1979. *Astron. Astrophys. Suppl. Ser.* 46:135–149.

Leblanc, Y., F. Genova, and J. de la Noë (1980b). The jovian S-bursts. I Occurrence with L bursts and frequency limit. *Astron. Astrophys.* 86:342–348.

Leblanc, Y., A. Gerbault, M. Rubio, and F. Genova (1983). A catalogue of the jovian decametric radio observations from January 1980 to December 1981. *Astron. Astrophys. Suppl. Ser.* 54:135–148.

Lecacheux, A. (1974). Periodic variations of the position of jovian decameter sources in longitude (system III) and phase of Io. *Astron. Astrophys.* 37:301–304.

Lecacheux, A., and D. Le Quéau (1984). *Saturnian kilometric radio emission*. Invited paper, XXIth URSI General Assembly, Florence, Italy.

Lecacheux, A., N. Meyer-Vernet, and G. Daigne (1981). Jupiter's decametric radio emission: A nice problem of optics. *Astron. Astrophys.* 94:L9–L12.

Le Quéau, D. (1982). *Emissions radioélectriques dues á des faisceaux d'électrons se propageant dans l'environnement ionosphérique et magnétosphérique*. Thèse d'état, Université Paris VII.

Maeda, K., and T. D. Carr (1984). Beam structure of Jupiter's decametric radiation. *Nature* 308:166–169.

Melrose, D. B. (1986). A phase-bunching mechanism for fine structure in auroral kilometric radiation and jovian decameter radiation. *J. Geophys. Res.* 91:7970–7980.

Menietti, J. D., J. L. Green, S. Gulkis, and N. F. Six (1984a). Three-dimensional ray tracing of the jovian magnetosphere in the low frequency range. *J. Geophys.* 89:1489–1495.

Menietti, J. D., J. L. Green, S. Gulkis, and N. F. Six (1984b). Jovian decametric arcs: An estimate of the required wave normal angles from three-dimensional ray tracing. *J. Geophys. Res.* 89:9089–9094.

Mercier, C. (1986). Effects of atmospheric gravity waves on radioastronomical observations. *Annales Geophys.* 4:469–480.

Meyer-Vernet, N., G. Daigne, and A. Lecacheux (1981). Dynamic spectra of some terrestrial ionospheric effects at decametric wavelengths. Application in other astrophysical contexts. *Astron. Astrophys.* 96:296–301.

Neubauer, F. M. (1980). Non linear standing Alfvén wave current system at Io: Theory. *J. Geophys. Res.* 85:1171–1178.

Oya, H., and A. Morioka (1981). Effect of turbulent region of interplanetary magnetic field on jovian decametric radiation emitted from the main source. *Planet. Space Sci.* 29:783–791.

Pearce, J. B. (1981). A heuristic model for jovian decametric arcs. *J. Geophys. Res.* 86:8579–8580.

Pokorný, Z. (1982). Decametric emission of Jupiter and solar activity. *Bull. Astr. Inst. Czech.* 33:193–201.

Poquerusse, M., and A. Lecacheux (1978). First direct measurement of the beaming of Jupiter's decametric radiation. *Nature* 275:111–113.

Pritchett, P. L. (1986a). The electron-cyclotron maser instability in relativistic plasmas. *Phys. Fluids* 29:2919–2930.

Pritchett, P. L. (1986b). Cyclotron maser radiation from a source structure localized perpendicular to the ambient magnetic field. *J. Geophys. Res.* 91:13569–13581.

Riddle, A. C. (1983). Identification of radio emission from the Io flux tube. *J. Geophys. Res.* 88:455–458.

Riddle, A. C., and J. W. Warwick (1976). Redefinition of System III longitude. *Icarus* 27:457–459.

Riihimaa, J. J. (1970). Modulation lanes in the dynamic spectra of jovian L bursts. *Astron. Astrophys.* 4:180–188.

Riihimaa, J. J. (1974). Modulation lanes in the dynamic spectra of Jupiter's decametric radio emission. *Ann. Acad. Sci. Fenn.* A 6:1–38.

Riihimaa, J. J. (1976). Polarization patterns in the dynamic spectra of Jupiter's decametric radio bursts. *Astron. Astrophys.* 53:121–129.

Riihimaa, J. J. (1977). S-bursts in Jupiter's decametric radio spectra. *Astrophys. Space Sci.* 51:363–383.

Riihimaa, J. J. (1978). L-bursts in Jupiter's decametric radio spectra. *Astrophys. Space Sci.* 56:503–518.

Riihimaa, J. J. (1979). Modulation lanes in the dynamic spectra of Jupiter's decametric radio bursts. *Astron. Astrophys.* 78:L21–L23.

Riihimaa, J. J. (1985). Bursts of type N in Jupiter's decametric radio spectra. *Earth, Moon, Planets* 32:9–19.

Riihimaa, J. J. (1986). Beaming of Jupiter's decametric emission. *Earth, Moon, Planets* 34:133–138.

St. Cyr, O. C. (1985). *Jupiter's decameter and kilometer emissions: Satellite effects and long term periodicities*. Ph.D. Thesis, Univ. of Florida.

Sastry, Ch. V. (1968). Decameter radio emission from Jupiter and solar activity. *Planet. Space Sci.* 16:1147–1153.

Skinner, T. E., S. T. Durrance, P. D. Feldman, and H. W. Moos (1984). IUE observations of longitudinal and temporal variations in the jovian auroral emission. *Astron. Astrophys.* 278:441–448.

Slee, O. B., and C. S. Higgins (1968). The solar wind and jovian decameter radio emission. *Aust. J. Phys.* 21:341–368.

Smith, E. J., L. Davis, Jr., and D. E. Jones (1976). Jupiter's magnetic field and magnetosphere. In *Jupiter* (T. Gehrels, ed.), pp. 788–829. Univ. of Arizona Press, Tucson.

Staelin D. H. (1981). Character of the jovian decametric arcs. *J. Geophys. Res.* 86:8581–8584.

Staelin, D. H., and P. W. Rosenkranz (1982). Formation of jovian decametric S bursts by modulated electron streams. *J. Geophys. Res.* 87:10401–10406.

Strangeway, R. J. (1985). Wave dispersion and ray propagation in a weakly relativistic electron plasma: Implications for the generation of auroral kilometric radiation. *J. Geophys. Res.* 90:9675–9687.

Strangeway, R. J. (1986). On the applicability of relativistic dispersion to auroral zone electron distributions. *J. Geophys. Res.* 91:3152–3166.

Terasawa, T., K. Maezawa, and S. Machida (1978). Solar wind effect on Jupiter's non-Io related radio emission. *Nature* 273:131–132.

Thieman, J. R., and A. G. Smith (1979). Detailed geometrical modeling of Jupiter's Io-related decametric radiation. *J. Geophys. Res.* 84:2666–2674.

Warwick, J. W. (1963). Dynamic spectra of Jupiter's decametric emission. *Astrophy. J.* 137:41–60.

Warwick, J. W. (1964). Radio star scintillations from ionospheric waves. *Radio Sci. J. of Res. N. B. S.* 68D:179.

Warwick, J. W. (1981). Models for Jupiter's decametric arcs. *J. Geophys. Res.* 86:8585–8592.

Warwick, J. W., G. A., Dulk, and A. C. Riddle (1975). Jupiter radio emission: January, 1960; March, 1975. Radio Astronomy Observatory of the University of Colorado, Report PRA 3.

Warwick, J. W., J. B. Pearce, R. G. Peltzer, and A. C. Riddle (1977). Planetary radioastronomy experiment for Voyager missions. *Space Sci. Rev.* 21:309–327.

Winglee, R. M. (1986). On Io's control of jovian decametric radio emissions. *J. Geophys. Res.* 91:1405–1416.

Wu, C. S. (1985). Kinetic cyclotron and synchrotron maser instabilities: Radio emission by direct amplification of radiation. *Space Sci. Rev.* 41:215–298.

Wu, C. S., and L. C. Lee (1979). A theory of the terrestrial kilometric radiation. *Astrophys. J.* 230:621–626.

Zaitsev, V. V., E. Y. Zlotnik, and V. E Shaposhnikov (1986). The origin of S-bursts in Jupiter's decametric radio spectra. *Astron. Astrophys.* 169:345–354.

Zarka, P., and F. Genova (1983). Low frequency jovian emission and solar wind magnetic sector structure. *Nature* 306:767–768.

Zarka, P., D. Le Quéau, and F. Genova (1986). The maser synchrotron instability in an inhomogeneous medium: Determination of the spectral intensity of auroral kilometric radiation. *J. Geophys. Res.* 91:13542–13558.

13

Solar Wind Effect on Jovian Low-Frequency Magnetospheric Radio Emissions from Ground-Based and Spacecraft Observations

Philippe Zarka
Françoise Genova
Observatoire de Paris, Meudon

Abstract

The Fourier analysis of the intensity fluctuations of jovian radio emission at hectometer wavelengths, observed by the Voyager spacecraft, has allowed a demonstration of the influence of the solar wind, particularly of its magnetic sector structure, on this emission. On the other hand, the jovian decametric emission observed by Voyager appears to be well correlated with the hectometer emission. Finally, the probability of observing Io-independent decameter emission from the ground (with the decameter array in Nançay, France) presents strong time variations that correspond well to the fluctuations of hectometer activity, influenced by the solar wind. This suggests that the hectometer and Io-independent decameter events originate from the same source

regions, at high latitude in the jovian magnetosphere, and that the altitude extent of the source covers several planetary radii, as for the source of Saturn kilometric radiation. No similar effect is found for the Io-dependent decameter emission, which is consistent with a source close to the Io field line. This work illustrates the complementarity between spacecraft low-frequency and ground-based high-frequency observations of the jovian radio emissions.

The kilometric radio emissions of the Earth and Saturn, observed from spacecraft-borne receivers, are known to fluctuate with time scales of several days, in correlation with variations of the solar wind or related phenomena at these planets (Kaiser and Alexander, 1977a, b; Voots et al., 1977; Gallagher and d'Angelo, 1981; Desch, 1982; Desch and Rucker, 1983). The case of the decametric radio emission from Jupiter (DAM), observed from ground-based radiotelescope, is complicated by the presence of undesirable periodicities in the data. These are due to the control of part of the emission (called Io-DAM) by the position of the satellite Io relative to the observer (the component independent of Io being called non-Io-DAM) and to the periodicities linked to the Earth motion, combined with that of Jupiter. Moreover, the different components of the jovian emission may correspond to solar-correlated and uncorrelated types of DAM.

Almost since its discovery in 1954, the jovian DAM was searched for a solar influence. An historical outline of these early studies is given in a review by Barrow (1985). Kaiser and Alexander (1973) published the negative results of a search of solar-related periodicities in 17 years of data at 22 MHz, by power spectrum analysis. Carr and Desch (1976) summarized the situation by noting that little or no agreement existed then on solar-jovian correlations. Oya and Morioka (1981), Terasawa et al. (1978), Barrow (1978, 1979), Leviitski and Vladimirski (1979), and Pokorny (1982) showed the possible control of non-Io-DAM by solar-wind parameters or interplanetary magnetic field (IMF) structure through correlations with geomagnetic indices of activity or solar-wind measurements close to the Earth orbit, extrapolated to Jupiter. But these works involved heavy mathematical tools and uncertain solar-wind extrapolation from Earth to Jupiter. The data were mainly obtained at fixed frequencies, in limited time intervals. The Io-DAM was only addressed by Barrow (1978) who cited an absence of correlation with the geomagnetic index A_p. The results could have been affected by beaming effects and the like. In the most recent review of the phenomenology of Jupiter's radio emissions, Carr et al. (1983) concluded that there was "not yet general agreement as to the nature and, indeed, even the existence of a solar influence" on jovian radio emissions.

However, the data from the Voyager 1 and 2 spacecraft, which encountered Jupiter in 1979 and allowed observation of its radio emissions up to hectometer (HOM) and kilometer (KOM) wavelengths, brought considerable help to solve this problem, which can be summarized by the following three questions:

1. Is there a solar wind (or IMF) influence on jovian HOM, Io-DAM, and/or non-Io-DAM?
2. Is there a relation between the hectometric and the decametric components? This is not evident because these emissions were observed by Voyager with two receivers with different characteristics (see for example, Boischot et al., 1981). The KOM emission probably comes from the vicinity of the Io plasma torus (see e.g., Leblanc and Daigne, 1986), and will not be addressed here, whereas the HOM and DAM have many characteristics in common with the "auroral" emissions of the Earth, Saturn, and possibly Uranus.
3. What will be the consequences of the answers to the above questions about the location of the source of the emissions?

The first study of the solar-wind influence on Voyager radio data, which are free from the Earth-linked periodicities, was made in the hectometer wavelength range, where the influence of Io is negligible. Zarka and Genova (1983) studied a 6.7-month time-interval of continuous HOM data (15 December 1978) obtained simultaneously by Voyager 1 and 2, by power spectrum analysis. They found significant peaks in both power spectra at ~10.5, ~14.5, and 29 ± 2 days, this last value being consistent with the solar rotation period. For most of the time studied, the solar magnetic field polarity pattern showed a well-defined structure (Solar Geophysical Data, 1979). Beginning on 6 February 1979, after a disturbed period, there were two unequal sectors whose durations evolved slowly in the ranges 14–

16.5 and 9–11 days, respectively, corresponding well to the peaks in HOM power spectra.

Later, Desch and Barrow (1984) studied the relation between the HOM energy and the solar-wind speed and density measured by Voyager 1 and extrapolated at Jupiter's orbit (i.e., with extrapolations much more reliable than from the Earth orbit), through cross-correlation analysis over 2.5 months of Voyager 1 data and $\sim$6 months of Voyager 2 data, included in the above interval. They found a correlation at $>3\sigma$ between HOM energy and solar-wind density, but no significant correlation between HOM and solar-wind speed. The autocorrelation of their data sets confirmed the results of Zarka and Genova (1983).

The influence of the solar wind on Voyager data at decametric wavelengths was established by Barrow et al. (1986). They showed, through superposed epoch and cross-correlation analyses over $\sim$20-day intervals just before Voyager 1 and 2 encounters with Jupiter, that the non-Io-DAM was related to the solar-wind density and velocity, and to the IMF magnitude, as observed by Voyager close to the planet, although the Io-DAM was not. The correlations were very well defined for the Voyager 2 data although only marginal for the Voyager 1 data. The authors gave a possible explanation of this difference: The IMF structure was very "turbulent" at the time of Voyager 1 observations of DAM, whereas it exhibited a stable two-sector structure during Voyager 2 observations.

A relation between HOM and DAM emissions was then demonstrated by Genova et al. (1987), who found a $>4\sigma$ correlation between the energies measured by the Voyager spacecraft in the frequency bands (0.5–1 MHz) for the HOM and ($\sim$16–20 MHz) for the DAM, during $\sim$1-month intervals before the encounters. Finally, as the DAM observations by Voyager are not well suited for further study, since they do not cover a sufficiently long period (because of a high interference level in the high-frequency band at decameter wavelengths), these authors used the ground-based DAM observations recorded at Nançay, France, together with the Voyager HOM observations, to study the solar-wind effect in the two frequency ranges. As in the study of Barrow et al. (1986), the DAM observations were sorted in Io-DAM and non-Io-DAM types through their spectral characteristics (Aubier and Genova, 1985), which was shown to be the best available criterion. A two-level index of HOM activity was defined from the fluctuations of this emission, correlated in Voyager 1 and 2 observations (Zarka and Genova, 1983). It was then found that the occurrence probability of non-Io-DAM events was much higher in periods of high-HOM activity (8.1 percent) than in periods of low-HOM activity (2.5 percent), whereas that of Io-DAM events was independent of HOM activity (respectively, 38.6 percent and 36.2 percent).

All these results allow us to answer the above questions:

1. There is a solar wind influence on HOM and non-Io-DAM emissions. This influence appears mainly through the sector structure of the IMF polarity, and related parameters, such as the IMF magnitude, the solar-wind density (which is known to be higher near the sector's boundary), and perhaps speed. The solar-wind control of these jovian emissions is much weaker than that of the terrestrial and saturnian radio emissions, and it remains secondary to the role of Jupiter's rotation.

2. As a consequence, the HOM and non-Io-DAM are very probably the low-frequency and high-frequency parts of the same radio emission, coming from the same source regions spread along the magnetic field lines, the Io-DAM being a separated component.

3. Observational studies suggest that the source of Io-DAM is on field lines intersecting the Io orbit (see e.g., Genova and Aubier, 1985, and references therein). This localization is consistent with the absence of solar modulation of the Io-DAM, the field lines in question being deeply embedded in the inner jovian magnetosphere, where the influence of the rotating magnetic field of the planet is certainly dominant.

4. On the other hand, the global HOM modulation observed by Voyager 1 and 2 from very different viewing geometries, and the linked modulations of non-Io-DAM, imply global changes of the radiating region due to solar-wind variations. Such magnetospheric regions, where the solar-wind influence is possible, should be located at higher latitudes than the field lines intersecting Io's orbit. The source field lines could be close to the cusp region (as in Saturn's case), or linked to the magnetospheric tail (as in the case of Earth), which is known to be controlled by the solar wind (Lepping et al., 1983). Alternatively, if the source of the HOM and non-Io-DAM is at lower latitudes, on field lines intersecting the Io torus or the Io orbit, one has to find a mechanism to allow the solar wind to influence the inner magnetosphere of the planet. For emission close to the

local gyrofrequency, and with the Pioneer models of the jovian magnetic field (Acuña et al., 1983), the source of the jovian HOM and non-Io-DAM extends from very close to the surface up to altitudes >4 jovian radii.

Of course, this deserves further work, in particular to gain more precise understanding of the nature of the interaction between the solar wind and the radio emissions. This work illustrates the complementarity between spacecraft low-frequency and ground-based high-frequency observations of the jovian radio emissions, and its usefulness in solving a long-standing problem. Systematic monitoring of the jovian emissions over a wide spectral range (from the ionospheric cutoff ~10 MHz, to the highest observed frequency of the emission, 40 MHz) has proven to be necessary for the study of their properties (see Genova et al., this volume). The ground-based long-term observations have been complemented by those from the Voyager spacecraft, which gave access to frequencies below the ionospheric cutoff, and to data free of Earth-linked bias. The study should be pursued in the frame of the International Jupiter Watch program: Reliable simultaneous observations of the radio-emission and solar-wind parameters, over long periods of time, and also of auroral precipitations, are necessary to understand better the relationship between the magnetosphere of Jupiter and its solar-wind environment.

References

Acuña, M. H., K. W., Behannon, and J. E. P. Connerney (1983). Jupiter's magnetic field and magnetosphere. In *Physics of the jovian magnetosphere* (A. J. Dessler, ed.), pp. 1–50. Cambridge Univ. Press, Cambridge.

Aubier, M. G., and F. Genova (1985). A catalogue of the high frequency limit of the jovian decameter emission observed by Voyager. *Astron. Astrophys. Supp. Ser.* 61:341–351.

Barrow, C. H. (1978). Jupiter's decametric radio emission and solar activity. *Planet. Space Sci.* 26:1193–1199.

Barrow, C. H. (1979). Association of corotating magnetic sector structure with jupiter's decameter-wave radio emission. *J. Geophys. Res.* 84:5366–5372.

Barrow, C. H. (1985). The influence of the Sun on Jupiter's radio emission. In *Planetary radio emissions* (H. O. Rücker and S. J. Bauer, eds.), pp. 148–182. Verlag der Osterr. Akademie der Wissenschaften, Graz, Austria.

Barrow, C. H., M. D. Desch, and F. Genova (1986). Solar wind control of Jupiter's decametric radio emission. *Astron. Astrophys.* 165:244–250.

Boischot, A., A. Lecacheux, M. L. Kaiser, M. D. Desch, and J. K. Alexander (1981). Radio Jupiter after Voyager: An overview of the planetary radio astronomy observations. *J. Geophys. Res.* 86:8213–8226.

Carr, T. D., and M. D. Desch (1976). Recent decametric and hectometric observations of Jupiter. In *Jupiter* (T. Gehrels, ed.), pp. 693–735. Univ. of Arizona Press, Tucson.

Carr, T. D., M. D. Desch, and J. K. Alexander (1983). Phenomenology of magnetospheric radio emissions. In *Physics of the jovian magnetosphere* (A. J. Dessler, ed.), pp. 226–284. Cambridge Univ. Press, Cambridge.

Desch, M. D. (1982). Evidence for solar wind control of Saturn radio emission. *J. Geophys. Res.* 87:4549–4554.

Desch, M. D., and C. H. Barrow (1984). Direct evidence for solar wind control of Jupiter's hectometer-wavelength radio emission. *J. Geophys. Res.* 89:6819–6823.

Desch, M. D., and H. O. Rucker (1983). The relationship between Saturn kilometric radiation and the solar wind. *J. Geophys. Res.* 88:8999–9006.

Gallagher, D. L., and N. D'Angelo (1981). Correlations between solar wind parameters and auroral kilometric radiation intensity. *Geophys. Res. Lett.* 8:1087–1089.

Genova, F., and M. G. Aubier (1985). Io-dependent sources of the jovian decameter emission. *Astron. Astrophys.* 150:139–150.

Genova, F., P. Zarka, and C. H. Barrow (1987). Voyager and Nançay observations of the jovian radio emission at different frequencies: Solar wind effect and source extent. *Astron. Astrophys.* 182:159–162.

Kaiser, M. L., and J. K. Alexander (1973). Periodicities in the jovian decametric emissions. *Astrophys. Lett.* 14:55–58.

Kaiser, M. L., and J. K. Alexander (1977a). Terrestrial kilometric radiation. 3. Average spectral properties. *J. Geophys. Res.* 82:3273–3280.

Kaiser, M. L., and J. K. Alexander (1977b). Relationship between auroral substorms and the occurrence of terrestrial kilometric radiation. *J. Geophys. Res.* 82:5283–5286.

Leblanc, Y., and G. Daigne (1986). The radio sources at the boundaries of the Io plasma torus. In *The solid bodies of the outer solar system*, Proc. Conf. Vulcano, Italy, ESA SP-242, pp. 143–148.

Lepping, R. P., M. D. Desch, L. W. Klein, E. C. Sittler, Jr., J. D. Sullivan, W. S. Kurth, and K. W. Behannon (1983). Structure and other properties of Jupiter's distant magnetotail. *J. Geophys. Res.* 88:8801–8815.

Leviitski, L. S., and B. M. Vladimirski (1979). Influence of sector structure of interplanetary magnetic field on Jupiter's decameter radio emission. *Izv. Krymsk. Astrofiz. Obs.* 59:104.

Oya, H., and A. Morioka (1981). Effect of turbulent region of interplanetary magnetic field on jovian decametric radio emission from the main source. *Planet. Space Sci.* 29:783–791.

Pokorny, Z. (1982). Decametric emission of Jupiter and solar activity. *Bull Astr. Inst. Czech.* 33:193–201.

Terasawa, T., K. Maezawa, and S. Machida (1978). Solar wind effect on Jupiter's non-Io related radio emission. *Nature* 273:131–132.

Voots, G. R., D. A. Gurnett, and S.-I Akasofu (1977). Auroral kilometric radiation as an indicator of auroral magnetic disturbances. *J. Geophys. Res.* 82:2259–2266.

Zarka, P., and F. Genova (1983). Low frequency jovian emission and the solar wind magnetic sector structure. *Nature* 306:767–768.

14

New Longitude System for the Jovian Magnetosphere

B. R. Sandel
University of Arizona, Tucson

A. J. Dessler
Rice University, Houston

Phenomena in Jupiter's magnetosphere are commonly organized in System III longitudes, but several of these phenomena drift regularly in System III. These phenomena include the brightness of the hot plasma torus at SIII 685 Å and at SIII 9531 Å (Sandel, 1983; Roesler et al., 1984) and the narrow-band kilometric radio emission (nKOM) (Kaiser and Desch, 1980), which is simultaneously modulated at the System III period (Daigne and Leblanc, 1986). Other ground-based observations show brigtness variations that are not fixed in System III. We have extended the analysis of periodicities of the second kind to find whether they can be organized into a single new longitude system that we call System IV (Sandel and Dessler, 1987). Principally we use data from the 1979 Voyager flybys of Jupiter. In order to lengthen the time base to improve the accuracy of the System IV rotation period, we also utilize available ground-based observations of the Io torus of Brown and Shemansky (1982) and Roesler et al. (1984). The data of Brown and Shemansky contain 53 observations obtained over a 64-day interval, and the data of Roesler et al. contain 71 observations obtained over a 19-day interval. The Voyager radio observations extended over nearly a full year, whereas Voyager ultraviolet spectrometer (UVS) observations of the torus covered a 41-day interval.

Periodograms computed for Voyager UVS measurements of the extreme ultraviolet (EUV) brightness of the torus by the procedure described by Scargle (1983) imply the presence of modulation at the System IV period. The probability of finding by chance the power measured at the System IV period is 4×10^{-18} for the receding ansa and 3×10^{-3} for the approaching ansa (Sandel and Dressler, 1987). Voyager UVS measurements define the phase of System IV, and for convenience we place the EUV brightening at a System IV longitude of 180° (figure 86). The UVS observations and nKOM measurements define a narrow range of periods about 3 percent greater than the System III period. By assuming that optical brightenings of the torus ob-

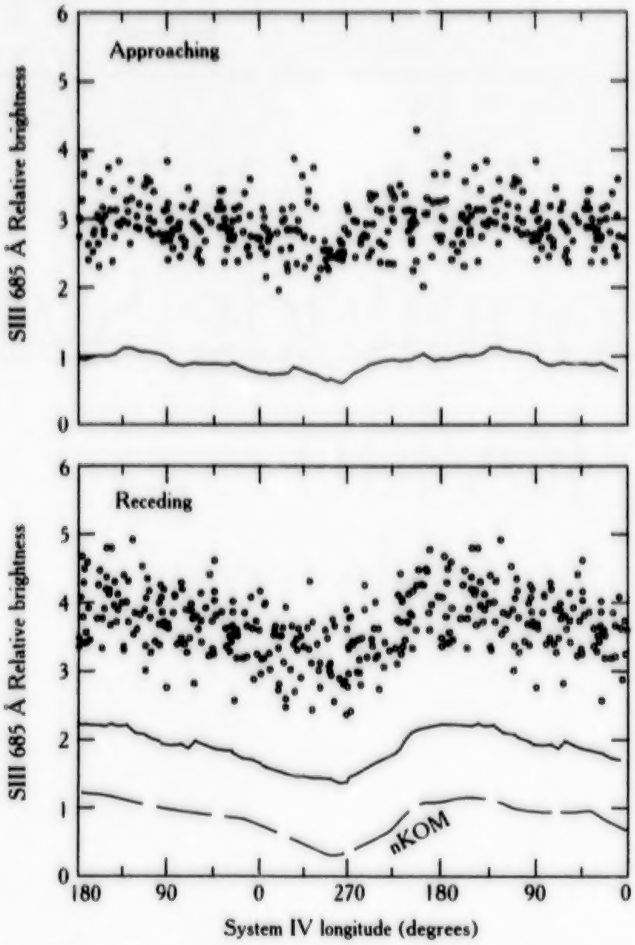

Figure 86. Relative brightness of the approaching (*top*) and receding (*bottom*) ansa of the plasma torus as a function of System IV longitude. We show the brightness of the S III 685 Å feature, the brighest in the EUV spectrum of the torus. The abscissa refers to the System IV longitude of the observed ansa. The *solid curves* below the data points are sliding averages of the data computed using a triangular function of 30° FWHM and displaced downward by two units. The brightness at both ansa is modulated at the System IV period, with the modulation at the receding ansa stronger than at the approaching, where the modulation is barely apparent in this figure. The *dashed curve* in the bottom panel is a scaled and phase-shifted plot of the nKOM probability from figure 88a. The EUV brightness and the nKOM probability change with System IV in qualitatively the same way. These plots should be compared with figure 9 of Sandel and Broadfoot (1982), which shows the absence of modulation when the same data are plotted as a function of System III longitude.

served from Earth in 1981 and 1982 occurred at the same System IV phase as the EUV brightenings, we can select a period consistent with all observations. The periods allowed by the various data sets are shown in figure 87. This leads to the preliminary transformation between System III and System IV:

$$\lambda_{IV} = \lambda_{III} + 338 - 25.486t,$$

where t is measured in days and decimal fractions from 00:00 UT on 1 January 1979.

Presently, all the data in hand are organized by this system (for example, see figures 86, 88, 89, and 90). Note that the brightenings all fall near 180°. That System IV organizes the optical and EUV measurements better than does System III can be verified by examining the figures cited in the captions for our figures 86, 89, and 90.

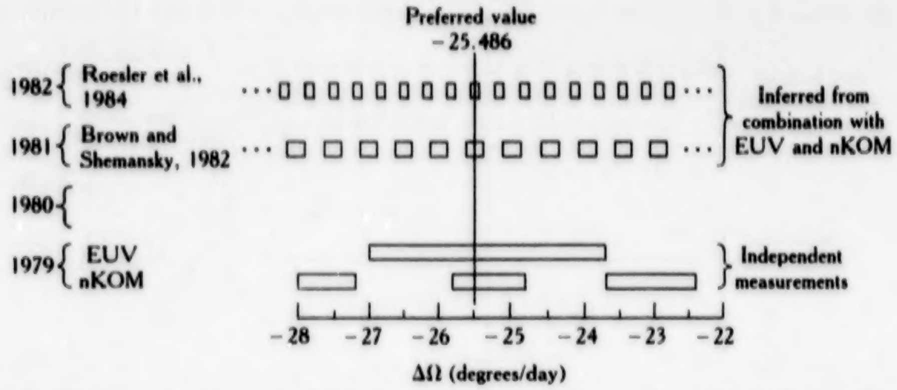

Figure 87. Ranges of values of ΔΩ, the angular rate of System IV relative to System III, that are acceptable on the basis of several subsets of the data. The ranges determined from the EUV and nKOM observations are independent. Neither the data of Roesler et al. nor of Brown and Shemansky limit ΔΩ within the range of the abscissa. The ranges shown for those sets of observations were inferred by combining them separately with the EUV and nKOM measurements. Several values of ΔΩ are consistent with the nKOM, the EUV, and one or the other of the sets of ground-based observations, because of the ambiguity introduced by the possibility of changing the rotation of System IV relative to System III by an integral number of complete rotations in the years between the Voyager and ground-based measurements. Discrete ranges of values of ΔΩ are acceptable, as shown here. The interval between the ranges differs for the two sets of ground-based data because of the different lengths of time separating them from the Voyager observations.

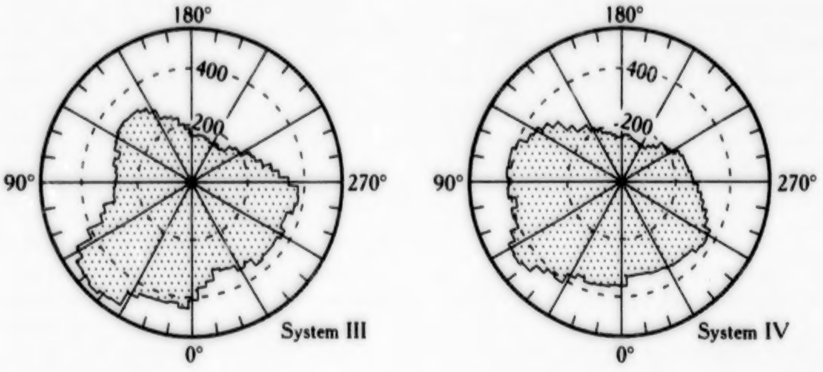

(a) (b)

Figure 88. Relative probability of observing nKOM as a function of the longitude of the central meridian of Jupiter as seen from Voyager. **(a)** Probability in System III. **(b)** Probability in System IV. In both systems, the probability has well-defined peaks and varies by more than a factor of two with longitude. The nKOM probability thus has components modulated at each of the two periods.

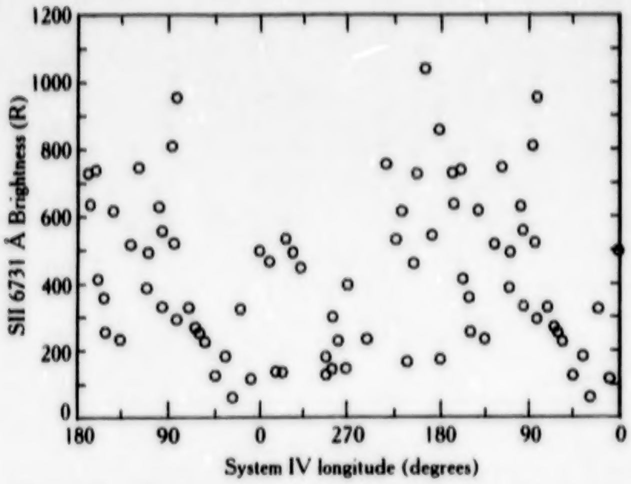

Figure 89. Measurements of the S II 6731 Å brightness of the ansae of the plasma torus obtained in 1981 (Brown and Shemansky, 1982). The abscissa refers to the longitude of the ansa. The brighter measurements are generally confined to longitudes near 180°. This graph should be compared with figure 2 of Brown and Shemansky (1982), which shows the increased scatter when the same data are plotted as a function of System III longitude.

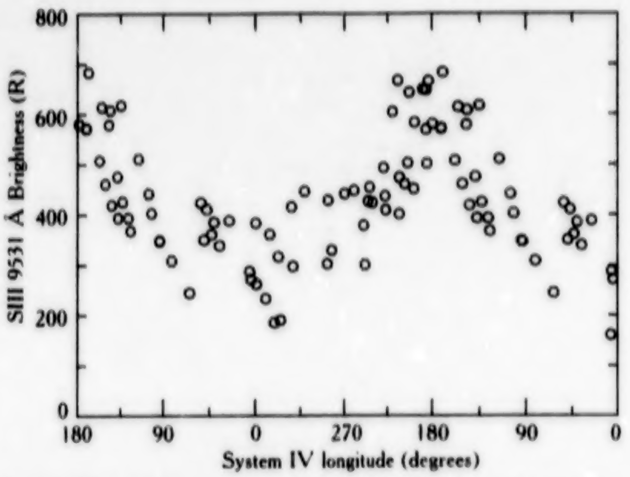

Figure 90. Measurements of the S III 9531 Å brightness of the receding ansa of the torus obtained in 1982 (Roesler et al., 1984). The abscissa refers to the longitude of the ansa. The brightness is strongly modulated at the System IV period, with a peak near λ_{IV} = 180°. This graph should be compared with figure 1 of Roesler et al., which shows the increased scatter when the same data are plotted as a function of System III longitude.

We expect that continuing analysis will further refine the definition of System IV. It is therefore important for others to add existing observations to the base of the data, both to refine the definition of the coordinate system, and, most important, to test the idea that a single longitude grid is appropriate for the several phenomena that drift at nearly the same rate in System III.

References

Brown, R. A., and D. E. Shemansky (1982). On the nature of SII emissions from Jupiter's hot plasma torus. *Astrophys. J.* 163:433–442.

Daigne, G., and Y. Leblanc (1986). Narrow-band jovian kilometric radiation: Occurrence, polarization, and rotation period. *J. Geophys. Res.* 91:7961–7969.

Kaiser, M. L., and M. D. Desch (1980). Narrow-band jovian kilometric radiation: A new radio component. *J. Geophys. Res. Lett.* 7:389.

Roesler, F. L., F. Sherb, and R. J. Oliversen (1984). Periodic intensity variation in [S III] 9531 Å emission from the Jupiter plasma torus. *Geophys. Res. Lett.* 11:128.

Sandel, B. R. (1983). Corotation lag in the Io plasma torus—Evidence from Voyager EUV observations. *B.A.A.S.* 15:810.

Sandel, B. R., and A L. Broadfoot (1982). Io's hot plasma torus—A synoptic view from Voyager. *J. Geophys. Res.* 87:212.

Sandel, B. R., and A. J. Dessler (1987). Dual periodicity of the jovian magnetosphere. In preparation.

Scargle, J. D. (1983). Studies in astronomical time series analysis II. Statistical aspects of spectral analysis of unevenly spaced data. *Astrophys. J.* 263:835.

15

Energetics, Luminosity, and Spectroscopy of Io's Torus

Darrell F. Strobel
The Johns Hopkins University, Baltimore

Abstract

This chapter gives a review of the Io torus on the following topics: composition, temperature, luminosity, energetics, interaction of Io's atmosphere corona with the plasma torus, time constants, and variability. Convergence is finally being reached on the steady-state composition and temperature of the plasma torus. The luminosity of the torus during the Voyager encounters was larger (0.4–0.8 eV cm^{-3} s^{-1}) than originally inferred as a consequence of improved atomic physics. The energy crisis may have been finally resolved by including heating of the thermal plasma by inflowing energetic (~1–20 keV) ions from the outer magnetosphere, but more quantitative calculations and direct measurement of these ions are needed. There is significant variability in torus plasma properties with the extreme conditions being represented by the periods of the Pioneer and Voyager encounters when the average electron density may have differed by as much as a factor of 25.

INTRODUCTION

It has been approximately seven years since the review articles of Pilcher and Strobel (1982) and Brown et al. (1983a) were published. In that period of time, considerable progress has been made, although at a pace somewhat slower than would have been predicted then. The Io torus in all of its ramifications has proven to be elusive in the diagnosis of the essential physical processes that control its behavior, evolution, and structure in spite of the measurements by Pioneer and Voyager spacecrafts and continued ground-based and International Ultra-Violet Explorer (IUE) observations.

As scientists, we were ill prepared to deal with the phenomena associated with the Io torus. The Pioneer measurements were interpreted conventionally by preconceived notions that did not alert us to the wealth of scientific phenomena awaiting discovery. An additional clue was reported by Brown (1974) shortly after the Pioneer 10 encounter, namely sodium D-line emission in the vicinity of the innermost galilean satellite, Io. This was followed by the detection of emission from forbidden red lines of SII (Kupo et al., 1976) and the interpretation by Brown (1976) of a plasma in the inner magnetosphere of Jupiter around Io with temperature of $\sim(2.5 \times 10^4)$ K and density of 3200 cm^{-3}. From an historical point of view, it is interesting that these observations and their interpretation had little, if any, impact on planning the Voyager 1 encounter in terms of expected scientific results.

The discovery of active volcanism on Io during the Voyager 1 encounter, which amply illustrated the old saying that "one picture is worth a thousand words," provided the ultimate clue and revolutionized the study of the inner jovian magnetosphere. Progress from the spectroscopist's perspective was still slow because much of the atomic physics needed to interpret the Voyager ultraviolet spectrometer (UVS) and ground-based data was either uncertain or unknown. As an example, the energy levels of SII ion were incorrectly assigned above 14 eV (Brown and Shemansky, 1982), which resulted in the prediction of strong emission from the SII ($3p^3\ {}^4S^0$–$3p^2 3d\ {}^4P$) multiplet at 863 A rather than the correct wavelength of 765 A. Accurate theoretical collision strengths (normalized electron impact excitation cross sections) for almost all of the important multiplets in the extreme ultraviolet (EUV) spectra of the Voyager UVS experiment were not available in 1979. Only a dedicated effort by Henry and his colleagues (Ho and Henry, 1983, 1984, 1985; and Tayal and Henry, 1987) has rectified this situation in recent years. However, there are no experimental measurements to verify the accuracy of these calculated collision strengths, although experimental measurements of oscillator strengths for allowed transitions provide some verification in the asymptotic limit of the Born approximation.

Although the international workshop was on *Time-Variable Phenomena in the Jovian System*, it is important before addressing such phenomena to establish what we think we know for sure in a steady-state sense or, more specifically, at the time of the Voyager 1 encounter when we have the most comprehensive data set available. Our confidence in our knowledge of the structure of the Io torus at that time will dictate how bold we can be in characterizing time-dependent phenomena.

COMPOSITION

Perhaps the most accurately known and most agreed upon property of the Io plasma torus is the electron and total ion charge density as a function of radial and latitudinal position. It is based on measurements of the plasma science experiment (PLS) and the planetary radio astronomy (PRA) experiment with concurrence from the UVS experiment and is illustrated in figure 91 along with the trajectory of the Voyager 1 spacecraft. To first order outside of Io's orbit (5.9 R_J) the mixing ratio of individual ion densities to electron densities is a conserved quantity with radial distance out to about 7.5 R_J. During the Voyager 2 encounter, four months later, the UVS spectra suggest that the electron density increased by ~50 percent to an average "spectroscopic" value of 3000 cm^{-3} (Shemansky, 1987).

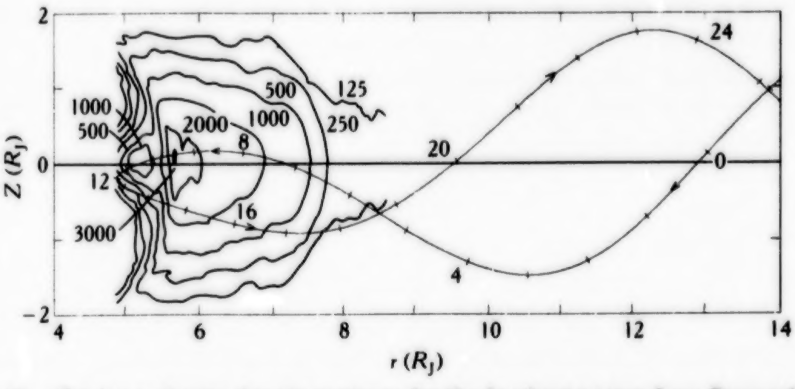

Figure 91. Total ion charge density contours for the Io plasma torus from Bagenal et al. (1985) superimposed on the Voyager 1 trajectory plotted as a function of radial distance from Jupiter's center and vertical distance Z relative to the centrifugal equator. After Sittler and Strobel (1987). Copyright by the American Geophysical Union.

In contrast, the actual ion densities or mixing ratios are probably the least accurately known property of the torus over the last eight years as figure 92 demonstrates. Here the ion densities normalized to an electron density of 2000 cm^{-3} are shown for conditions in the hot, outer torus (5.9–7.5 R_J) at the Voyager 1 encounter as a function of essentially our learning curve. For example, in the 30-day science report Broadfoot et al. (1979) reported only OIII with no mention of OII, whereas after Brown et al. (1983b) placed an upper limit of 5 cm^{-3} on OIII in the post-Voyager epoch this constraint has generally been regarded to be applicable also to the Voyager 1 encounter period. However, the only measured constraint on OIII density is an upper limit of 110 cm^{-3} from IUE observations during the encounter period (Moos and Clarke, 1981). This sad state of affairs (figure 92) resulted from the inability of the UVS experiment to distinguish OII from OIII, which have their principal spectral signatures at 833–835 A and the inability of the PLS experiment to separate OII from SIII because of their equal mass to charge ratios. The initial lack of accurate atomic physics parameters and nondetection of the OII 539 A multiplet (see discussion by Shemansky, 1987) were also contributing factors to the inability to obtain accurate ion composition from in situ and remote observations (figure 92).

The current and hopefully correct values of the ion densities at the time of the Voyager 1 encounter may be

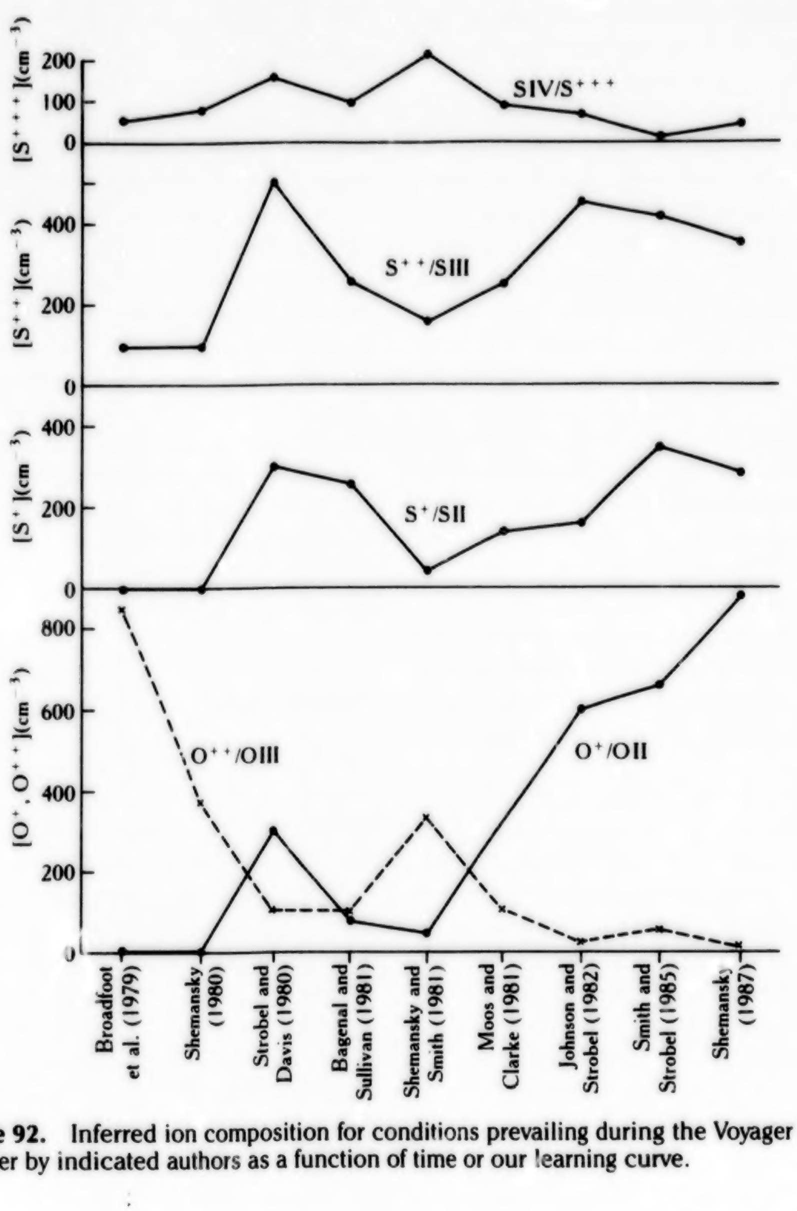

Figure 92. Inferred ion composition for conditions prevailing during the Voyager 1 encounter by indicated authors as a function of time or our learning curve.

obtained from the last two entries in figure 92: calculations of Smith and Strobel (19835) and Shemansky (1987) constrained by UVS spectra. The principal differences are in the partitioning of OII relative to SII and SIII and the calculated electron temperature. Smith and Strobel (1985) did not attempt to do a detailed spectral fit of the data, whereas Shemansky (1987) did. In spite of this difference, there is now fairly good agreement in their results when compared to the earliest analyses in figure 92. It must be remembered that these results are applicable to the hot, outer torus where ion mixing ratios are approximately invariant with radial positions and latitude. With the aid of figure 91, the respective ion density contours can be approximately constructed by exploiting this invariance. In a chapter by Bagenal (this volume) the equivalent PLS results (in table 14) may be compared with figure 92. It can be seen that these two independent techniques for determining ion composition are finally converging to similar mixing ratios.

Beyond the outer boundary of the hot torus (7.5 R_J) there is evidence for a transition to more highly ionized oxygen and sulfur in the UVS spectra at 8 R_J (Shemansky and Strobel, unpublished work). This coincides with the rapid rise of the thermal electron temperature from 5 to 20–30 eV. Unfortunately low plasma densities at these radial distances produce weak radiation and hence poor signal to noise for remote ultraviolet (UV) sensing of this region.

The cold, inner torus (5–5.6 R_J) does not generate a detectable UV signature by virtue of its cold electron temperature. Our primary means of probing this region are the in-situ PLS measurements reviewed by Bagenal and ground-based observations, of which the CCD imaging measurements of Trauger (1984) have provided the most definite results but have received only preliminary analysis. The latter technique allows remote sensing of the forbidden lines of SII and SIII and retrieval of electron densities in the 5.3–5.6 R_J region in the range of 1000 cm^{-3} and ion temperatures which are typically ~2 eV.

In the post-Voyager epoch Trauger (1984) found a thin (0.2 R_J), ribbonlike structure extended along the flux tubes at ~5.8 R_J with ~50 eV SII and SIII ions superimposed with 7–35 eV SII ions, which he called the hot inner torus. Electron densities are typically in the range of 3000–4000 cm^{-3} in this structure with SII and SIII densities in the range of 500–800 cm^{-4}. This high density structure is evident in the Voyager data shown in figure 91, where it is the 3000 cm^{-3} contour at 5.8 R_J just above $z = 0$. System III variations were reported by Trauger.

TEMPERATURE

In the hot outer torus, the primary measurement of electron temperature comes from the PLS experiment (Sittler and Strobel, 1987) and indicates an effective electron temperature of 5–6 eV with the thermal core (cold component) at $T_c \sim 5$ eV and a hot component with $T_H \sim 100\ T_c$ and density $n_H \sim 2$–3 cm^{-3}. The hot component is extremely important in the ionization of ions with large ionization potentials, but does not contribute significantly to the electron excited radiative output of the torus. The calculations of Smith and Strobel (1985) and Shemansky (1987) give average electron temperatures of 4.75 and 5.3 eV, respectively, and in the latter calculation the cold component is 5 eV. Thus, there is good agreement on the temperature of the cold, thermal component, in spite of the difficulty in deducing it from the primary measured quantities in the PLS experiment. These in-situ temperatures were measured and inferred during the Voyager 1 encounter only, as Voyager 2 did not pass through the hot, outer torus. Analysis of Voyager 2 UVS spectra suggests that the average electron temperature was nearly 2 eV colder (Shemansky, 1987).

In the cold, inner torus the electron temperature is too low to be measured directly and must be inferred from the ion temperature. Sittler and Strobel (1987) displayed values of $T_e = T_i$, which is only valid in the absence of significant heat sources in the inner torus, such as charge exchange of cold ions with neutrals and corotation electric field acceleration of new ions to pickup gyroenergies. Their values may only be upper limits as a consequence. In the ribbon structure region at ~5.8 R_J, Sittler and Strobel (1987) suggest $T_e \sim 2$–3 eV, whereas at 5 R_J, $T_e \sim 1$ eV.

LUMINOSITY

The Io plasma torus radiates copious amounts of energy in the EUV, UV, and visible parts of the spectrum through electron impact excitation of the principal ions SII, SIII, and OII with smaller contributions from SIV and OIII, whose concentrations are considerably less. For conditions at the Voyager 1 encounter the total radiative power loss was ~0.4 eV cm^{-3} s^{-1} (~[3 × 10^{12}] W), whereas during the Voyager 2 encounter it was approximately twice as large (Shemansky, 1987). The most accurate and detailed radiative cooling rates for individual ions were calculated by Shemansky (1988a) as a function of electron temperature. In the case of SII, it is necessary to include a very large number of lines, many of which were unknown at the time of the Voyager 1 encounter, to get an accurate result. In the hot, outer torus cooling is dominated by OII, SII, and SIII ions. At the cold electron temperatures in the inner torus the forbidden red lines of SII, the dominant ion, are an important mechanism for cooling this region.

ENERGETICS

Given the copious amounts of UV radiation emitted by the Io plasma torus (~[3–6 × 10^{12}]W) a source of at least this magnitude is required to maintain a steady state energy balance. The fuel for this power loss suggested by Broadfoot et al. (1979) and based on theoretical ideas of Siscoe and Chen (1977) is mass loss from Io followed by either electron impact or charge exchange ionization and subsequent acceleration by the $\mathbf{v} \times \mathbf{B}$ corotation electric field to attain a gyroenergy of ~0.25–0.6 keV. The details of the precise mechanism(s) for injection of neutral or ionized material from Io into the torus is still uncertain. Candidates are sputtering by torus ions from the surface if the atmosphere is "thin" (Matson et al., 1974) and from the atmosphere if it is "thick" (Haff et al., 1981; McGrath and Johnson, 1987), thermal escape from the exosphere of a thick atmosphere (Kumar, 1984; Summers et al., 1988), and ionization of neutral species in the corona by electron impact or charge exchange. A number of authors, since the original suggestion by Broadfoot et al. (1979), have advocated that sufficient neutrals escape Io, are ionized, and are energized by the corotation electric field to account for all the required energy to fuel the plasma torus (e.g., Brown, 1981; Barbosa et al., 1983; Smith and Strobel, 1985). This theory, called neutral cloud theory, has been pronounced a failure by Shemansky (1988a) on the basis of his more accurate and much larger radiative cooling rates. A characteristic feature of previous models, in particular the Smith and Strobel (1985) model, is that with their smaller, now incorrect, atomic physics parameters SIII had the largest radiative cooling rate per ion along with a large collisional heating rate of electrons per ion. According to the results of Smith and Strobel the preferred equilibrium state of the torus is one with SIII as the dominant sulfur ion, in which case it is the dominant electron heater and the dominant radiator. With the radiative cooling rates of Shemansky (1988a) SII is the dominant radiator at typical electron temperatures in the torus (~1–5 eV). It is so efficient that in a neutral cloud theory model the electron temperature is suppressed and never attains a sufficient value to produce significant SII density by electron impact ionization. This violates the inferred density ratio of SII:SIII ~0.7 from ground-based observations (Trauger, 1984; Pilcher and Morgan, 1985) and Voyager UVS data. Local, homogeneous models of the torus that incorporate the most accurate radiative cooling rates cannot produce this ratio if corotation electric field acceleration of ions is the only energy source, because they predict essentially a singly ionized plasma (Shemansky, 1988a).

Shemansky (1988a) suggests a solution to this problem by introducing an ad hoc heat input to the electrons to solve the energy crisis of insufficient electron temperature. He suggests two possibilities: dominance of charge exchange over electron impact ionization in the torus interaction with Io's corona and/or a heterogeneous source of energetic electrons. The model results of Smith and Strobel (1985) in conjunction with Voyager PLS data (Bagenal, this volume) can eliminate the first suggestion. In figure 93 from Smith and Strobel (1985) it is noted that injection of ions at the pickup energy and a power rate of 0.35 eV cm^{-3} s^{-1} drives the ion velocity distribution so non-Maxwellian that the predicted PLS and actual PLS data would bear no resemblance to each other. Given the fact that the Smith and Strobel (1985) work has approximately the "correct" composition and temperatures one can deduce from their results that the maximum amount of power transferred by the pickup mechanism to the ions is in the range 0.15–0.2 eV cm^{-3} s^{-1} (figures 12 and 13 in Smith and Strobel, 1985). Any additional amount of power input to and flowing through the ions would produce ion velocity distribution functions with suprathermal tails inconsistent with PLS data. Thus, additional energy must be supplied to the ions.

Smith et al. (1988) propose a solution to this energy crisis from the same source as the solution to the jovian auroral energy crisis, namely inward diffusing energetic oxygen and sulfur ions (Gehrels and Stone, 1983; Thorne, 1983). These ions were created in the outer magnetosphere by electron impact ionization of fast neutrals produced by charge-exchange reactions in the Io plasma torus and energized by magnetic pumping (Goertz, 1978) and other acceleration mechanisms. The most energetic ions are scattered by wave-particle interactions in the strong diffusion limit down the magnetic field lines and precipitate in Jupiter's auroral zones. There is a threshold energy resonance $E_{\mathrm{res}} \sim B^2/8\pi n_{\mathrm{e}}$, where B is the magnetic field strength and n_{e}

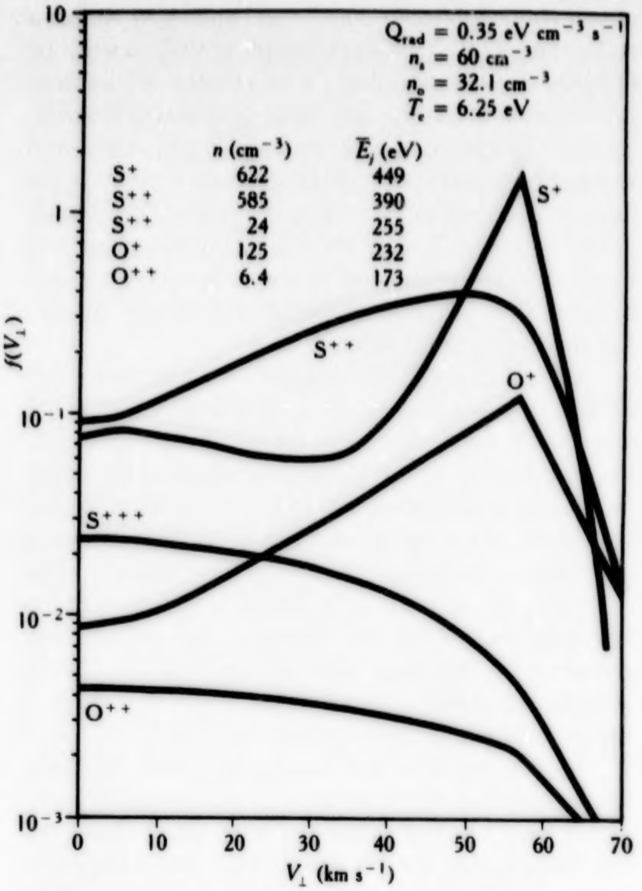

Figure 93. Ion velocity distribution for a case where the radiative power loss is 0.35 eV cm^{-3} s^{-1} with indicated ion composition and average energies. After Smith and Strobel (1985). Copyright by the American Geophysical Union.

is the electron density. At $L \sim 8$, $E_{\text{res}} \sim$ 6–20 keV for typical torus parameters. Thus ions with less energy diffuse inward to the hot torus where they collisionally transfer their energy preferentially to the electrons, as shown in figure 94 by the fact that the ion collisional cooling time constant is independent of energy down to ~100 eV. This power ($\sim[1 - 15 \times 10^{12}]$W) can be transferred in sufficient quantities within the lifetime of these energetic ions against charge exchange. Direct measurements and more quantitative calculations are needed to put this explanation of the energy crisis on a convincing basis.

It thus appears that the failure of previous neutral cloud theories was the myopic view that the Io plasma torus was self-contained and that all ions were energized within the torus by the pickup mechanism (corotation electric field acceleration). The neutral clouds are the source of the mass, but the energization takes place equally within the torus by the pickup mechanism and in the outer magnetosphere by other mechanisms. Clearly the magnetosphere must be viewed as a whole, and processes occurring in remote regions can have pronounced consequences elsewhere in the magnetosphere.

Interaction of Io's Atmosphere-Corona with the Plasma Torus

Sittler and Strobel (1987) observed a symmetrical decrease in the cold, thermal electron temperature by ~0.7 eV in an Io-centered coordinate system with maximum decrease occurring at closest approach and the nominal passage through the predicted Io flux tube. They attributed the observed localized cooling of electrons to thermal conduction along magnetic flux tubes intersecting a dense corona and suggested that plasma interaction with Io's neutral corona should produce an observable UV signature. The existence of a dense corona around Io was also required theoretically by Summers et al. (1988) to account for the high-velocity sodium (Na) jets observed by Trauger (1984). Further support for a neutral corona is provided by the remarkable measurement of the Na density distribution around Io by Schneider et al. (1987) and further discussed in Schneider et al. (1988).

Ballester et al. (1987) on the basis of these interferences performed two 14-hour IUE observations, which resulted in the first detection of emission from neutral oxygen and sulfur UV multiplets at or near Io, $\leq 5\,R_{\text{Io}}$ in radius (figure 95). Their observations and two subsequent ones display remarkable symmetry, independent of whether Io is viewed on the upstream or downstream side of torus plasma flow past Io. The observation of the OI 1356 A and SI 1900, 1914 A semiforbidden (^{3}P–^{5}S^0) multiplets implies electron impact excitation. The fact that the UV emission is symmetrical in spite of the geometry of the impacting torus plasma with Io implies that the excitation electrons have much larger velocities than the relative (to Io) corotation velocity of the impacting plasma. For example, 5 eV electrons have an average velocity of $\sim 10^8$ cm s^{-1}, which is a factor of ~20 greater than relative corotation velocity and hence would impact Io almost isotropically.

The absence of the SI 1429 A multiplet, which was detected by Durrance et. al (1983) in the torus away from Io where it was presumably produced by electron impact on sulfur atoms, and the presence of the SI 1479

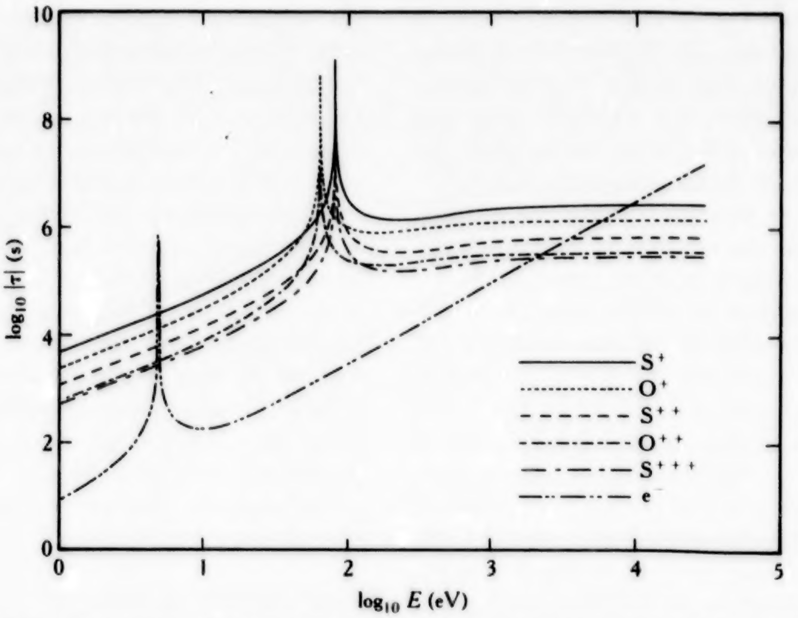

Figure 94. Time constants for test electrons or ions at a given energy to initially approach thermal equilibrium. Assumed composition is [e] = 2000, [SI] = 6, [SII] = 280, [SIII] = 400, [SIV] = 25, [OI] = 30, [OII] = 800, [OIII] = 15 cm^{-3}, T_e = 5, and T_i = 100 eV.

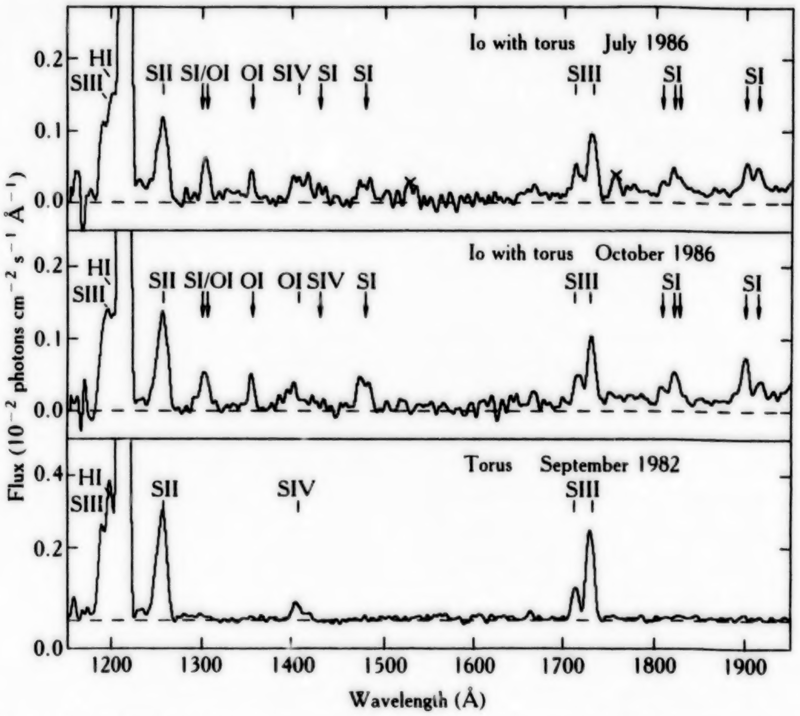

Figure 95. IUE spectra of Io and torus (*top and center*) from the 1986 observations, together with a comparison torus spectra. *Arrows* mark Io emission features, *ticks* mark torus emission features (and the geocoronal HI Lyman alpha), and features marked with an *X* are camera artifacts. After Ballester et al. (1987). Copyright by the American Astronomical Society.

A multiplet (not detected by Durrance et al.) in the IUE spectra clearly implies the observation of a plasma interaction more complex than simple electron impact on oxygen and sulfur atoms in Io's corona. According to theoretical calculations by Ho and Henry (1985) the SI 1479 A multiplet is extremely weak and the SI 1429 A multiplet should be a prominent feature of electron impact spectra unless the electron temperature is extremely cold. In fact, only in laboratory spectra of electron impact on SO_2 gas at 50–200 eV does the 1479 A multiplet appear prominently. But the observed IUE spectra are not consistent with the spectra of electron impact on SO_2 either, because the SI 1429 A and SI 1814 A multiplets are ~60 percent of the intensity of the SI 1479 A multiplet (Ajello, 1987) and thus not compatible with the observed upper limits on SI 1429 A: SI 1479 A and SI 1429 A: SI 1814 A intensity ratios of ~0.4 and 0.3, respectively. It must also be kept in mind that the threshold energy to produce the SI 1479 A multiplet is ~20 eV, as the SO_2 molecule must be split into three atoms. Given the brightness of this feature it seems that the exciting electrons must be hotter than 5 eV, if it is due to electron impact of SO_2.

Recent experimental work by Doering and Gulcicek (1987) suggests that the shape resonance calculated theoretically by Rountree and Henry (1972) and Rountree (1977) is a real feature in the OI 1304 A cross section. It also appears in the OI 1356 A cross section. The consequence of these resonances is to substantially enhance the electron impact rates of OI at very low electron temperatures and reduce the required OI column density by an order of magnitude over the values given in Ballester et al. (1987), if plasma interaction with a neutral corona were the correct description of the observations.

Given the uncertainty in the interpretation of these IUE observations, it is legitimate to ask what we know for sure. The ratio of the lines in the SI 1814 A multiplet are not in the optically thin ratio of 5:3:1. The line corresponding to the transition to the lowest fine structure level ($J = 2$) of the ground state (^{3}P) is depleted in intensity and indicative of optical thickness effects. Thus the minimum SI column density sampled by UV photons is at least 2×10^{12} cm^{-2}. The intensity ratio of SI 1429 A:SI 1814 A constrains the temperature of the exciting electrons to be no more than 2 eV to the extent that most of the SI 1814 A intensity is produced by electron impact on SI. Approximately 50 percent of its intensity should be due to this source based on the intensity predicted by scaling the SO_2 laboratory cross sections to the observed SI 1479 A intensity to infer the maximum contribution from electron impact on SO_2. Until accurate cross sections are available for $e + SO_2$ over a considerable energy range further progress cannot be made. Based on the observed IUE intensities it is improbable that electron impact ionization in the Io corona is a major source of mass loading of the Io plasma torus (<2 percent of the required amount).

It should also be noted that self-consistent numerical models of the interaction between the plasma torus and Io predict large current flows in the ionosphere of Io (~[1 − 2 × 10^6]A, Wolf-Galdrow et al., 1987). If plasma instabilities result from such large currents it may be possible that local acceleration of plasma to sufficient energy in the atmosphere-ionosphere is partially responsible for the observed IUE spectra and the auroral-like emissions detected by the Voyager camera on Io's nightside (Cook et al., 1981).

TIME CONSTRAINTS

Before the discussion of time-dependent and time-variable phenomena in the Io torus it is a good idea to get some feel, based on known physical processes, for the rates or time constants with which the torus plasma properties can respond to external and internal perturbations. The following composition is assumed for the torus: [e] = 2000, [SI] = 6, [SII] = 280, [SIII] = 400, [SIV] = 25, [OI] = 30, [OII] = 800, [OIII] = 15 cm^{-3}, $T_e = 5$, and $T_i = 100$ eV. Time constants can be appropriately scaled for other total charge and neutral densities. To the extent that plasma rigidly rotates with the planet as a result of the corotation electric field, an observer in an inertial frame of reference would see a $9^h55^m29.7^s$ periodicity. Due to the finite torque that the atmosphere can exert on the plasma, eventually the plasma must cease corotating. The resulting slippage increases its period with increasing radial distance (Hill, 1980). The period of Io around Jupiter is 42.5 hr and thus the plasma sweeps by Io with an effective period of ~13 hr.

Approximately 50 percent of the energy input to the torus is ionization of neutrals and acceleration of the new ions by the corotation electric field to gyroenergies ~270 eV for O+ and 540 eV for S+ (Shemansky, 1988a; Smith et al., 1988). From figure 95 the time constant for collisional energy loss to cool these ions and heat the electrons is 1 × 106 and 2 × 106 s, respectively. Thus, the addition of more hot ions will require approximately a week to affect the electron temperature unless the plasma density is substantially increased. In contrast the newly created electrons acquire only ~10^{-2} eV, but are quickly heated by ambient electrons with a time constant of <100 s. The fresh ions also have a "pancake" pitch angle distribution, which gets isotropized with a time constant of (T_i/T_e) times the collisional energy loss time constant or $\sim 10^7$ s (Smith and Strobel, 1985, Barbosa and Moreno, 1988). Thus, the ions would be expected to be anisotropic for confinement or residence times shorter than 10^7 s.

Lifetimes against electron impact ionization in the hot torus range from $\sim(5 \times 10^4)$ for SI and 5×10^5 for OI to 5×10^7 s for SIV and OIII. These time constants should be compared with those of charge-exchange processes, although the distribution of neutral O and S atoms is not well known in the hot torus. For the five dominant ions in the torus (SII, SIII, SIV, OII, and OIII) typical time constants for charge exchange are in the range of $2\text{–}7 \times 10^6$ s. Charge-exchange processes are dominant for highly ionized species in the hot torus and for all ions in the cold, inner torus where the lower electron temperature renders electron impact ionization uncompetitive.

The energy content of the plasma torus is $\sim(1.5 \times 10^5)$ eV cm^{-3} s^{-1}. With a radiative power loss of $\sim.04$ eV cm^{-3} s^{-1} (Shemansky, 1988a) the radiative time constant is $\sim(4 \times 10^5)$ s. This implies that in the absence of a continuous energy source the electrons would cool down substantially in about five days. Of course the radiative time constant would substantially increase as the electrons cool down and the plasma becomes a less efficient radiator. The radiative time constant is thus one of the shortest time constants governing plasma processes in the torus.

The mechanism(s) for radial diffusion in the plasma torus is severely constrained by Voyager PLS data (Richardson and McNutt, 1987), but the observationally inferred values of the radial diffusion coefficient are in the range of $D_{LL} \sim (1\text{–}4 \times 10^{-6})$ s^{-1}, for which one nominally would derive a radial diffusion time constant of $(\Delta L)^2/D_{LL}$. A more rigorous analysis by Cheng (1986) gives $N/(d/dL((D_{LL}/L^2)dNL^2/dL))$ or 6×10^6 s for the radial diffusion time constant defined from the continuity equation. This is also the time constant for net ion mass loss from the hot outer torus, because the radial outward flow is the dominant loss process for ion mass in this region and is balanced by electron impact ionization of SI and OI plus those charge-exchange reactions that generate a net increase in ion mass. One can also introduce a time constant for energy generation by ionization of neutrals by both electron impact and charge-exchange and subsequent acceleration by the corotation electric field. According to the results of Smith and Strobel (1985) the total charge-exchange rate is twice the magnitude of total electron-impact rate in the hot torus and the ratio of the average ion temperature to initial gyroenergy of fresh ions is ~ 0.25. Thus the time constant for energy generation is $\sim(4 \times 10^5)$ s, precisely equal to the radiative time constant.

VARIABILITY

Neutral and plasma properties of the torus are inferred to be variable on the basis of observable properties such as spectroscopic intensities and in-situ measurements of plasma composition and temperatures. In general, the shorter-lived species exhibit more variability than longer-lived species, in particular at visible wavelengths in contrast to EUV wavelengths. For example, the forbidden red line emission has been reported to be much more variable than the EUV emission of SIII (Sandel and Broadfoot, 1982a). In addition to time variability, torus properties vary with longitude, latitude, and radial distance (e.g. figure 91). From in-situ measurements (e.g., electron temperature) along the Voyager 1 trajectory, it is extremely difficult to distinguish radial, longitudinal, and latitudinal variations. In the absence of further in-situ measurements it is almost impossible to make significant progress on local variations in Jupiter's rotating frame of reference, as remotely sensed plasma properties involve averaging along the line of sight. The focus in this section, as a consequence, will be on time variations in an inertial frame of reference.

Persistent System III longitudinal variations in SII brightness in the inner and outer torus were reported very early by Pilcher and Morgan (1980), Trafton (1980), and Trauger et al. (1980). However, Brown and Shemansky (1982) found no evidence for variation in the intensity of SII red lines with System III longitude or the intensity ratio of the red lines, which is proportional to electron density, with System III longitude. In addition, the EUV brightnesses from the Voyager UVS were initially reported to show no obvious System III longitude variation (Sandel and Broadfoot, 1982a, Shemansky and Sandel, 1982). Roesler et al. (1984), however, discovered that the brightnesses of the torus in the visible and EUV do have a periodicity with a period ~3 percent longer than the System III period. Sandel and Dessler (1988) have proposed a System IV longitude system whose period is almost precisely 3 percent longer than System III's. This coordinate system successfully organizes the data of Roesler et al. (1984) and Brown and Shemansky (1982) with brightness peaks at 180° longitude. In addition, it is consistent with the narrow-band

C-3

kilometric radio emission, which also exhibits a period longer than System III by 3 percent (Kaiser and Desch, 1980). The theory of torus-plasma slippage in response to mass loading was developed by Hill (1979, 1980) and is one possible explanation for the existence of the System IV period. An alternate explanation for the System IV period has been advanced by Dessler (1985) who argues that Jupiter's magnetic field possesses a high-latitude component that rotates 3 percent slower than the low-latitude, System III magnetic field.

The situation appears to be more complex than this according to Pilcher and Morgan (1985). They observed brightness peaks in the 180–230° System III longitude region for both SII and SIII visible emissions. These two ions account for approximately 30–50 percent of the total ion density and thus their observations suggest increased mass in the "active sector" longitudes, as designated by the magnetic anomaly model of Dessler and Hill (1975). In addition, they interpret their observations to require a local plasma source in the active sector that apparently drifts to higher magnetic longitudes and produces the observed temporal variations in the distribution of SII emission with longitude. Sandel (1988) notes that the available SIII 9532 A emission data of Pilcher and Morgan (1985) are for times when the System III and IV coordinates are aligned. Thus, for the short duration of their observations, it is impossible to distinguish between them. For Sandel and Dessler (1988), it is important that the Roesler et al. (1984) SIII data that exhibits System IV periodicity not be in conflict with the similar Pilcher and Morgan data. However for the SII visible radiation Pilcher et al. (1985) and Pilcher and Morgan (1985) present a strong case for System III longitude variation. However OII emissions show substantially smaller or negligible longitudinal variations in intensity (Morgan, 1985a). It is clear that further observations are needed to clarify the nature of the observed SII and SIII brightness variability and whether the local (restricted ranges of longitude) plasma source is a characteristic feature of the plasma torus and whether the torus oscillates among a number of quasi-stable states that lead to the complex observed temporal variations.

Sandel and Broadfoot (1982a, b) discovered a local time variation or asymmetry in the EUV luminosity of the torus with peak brightness at 1900 LT and modulated by the position of Io. The luminosity is brighter downstream from Io. Shemansky and Sandel (1982) concluded this asymmetry must be due to a variation in electron temperature rather than plasma composition and mass. Barbosa and Kivelson (1983) and Goertz and Ip (1983) proposed the existence of a dawn-to-dusk electric field to produce the local time asymmetry. Electron temperature changes are also responsible for the Io-related enhancement in EUV emission (Sandel and Broadfoot, 1982b) by ~(4×10^{11}) W or ~20 percent of the total radiative power loss of the torus. This power is a factor of two larger than an estimate by Sittler and Strobel (1987) from the Io-related decrease in electron temperature.

There is some evidence for variations in plasma properties on a longer time scale. The Voyager 1 and 2 encounters were separated by about four months and Shemansky (1987) has inferred from the UVS spectra an increase in the average electron density from 2000 to 3000 cm^{-3} and a decrease in the average electron temperature by 1.7 eV from the Voyager 1 to Voyager 2 encounter. The Trauger (1984) observations in the post-Voyager epoch also support a case for increased electron density by at least 30 percent. Likewise Morgan (1985b) found that his 1981 ground-based observations of SII and OII emissions required an electron density profile in the hot outer torus about 1.5–2 times the Voyager 1 profile to fit the SII and OII line ratios. In addition, Morgan deduced that the SII ion temperatures were approximately a factor of two colder than observed by Bagenal et al. (1985) during the Voyager 1 encounter and that the OII density to electron density ratio was significantly reduced in 1981. Another feature of Morgan's (1985a) data is the occasional observation of extreme line ratios for SII 6716 A: SII 6731 A in the range of 0.02–0.22, which can best be understood in terms of high density clumping of torus plasma ($n_e > 5 \times 10^4\ \mathrm{cm}^{-3}$), which constitutes approximately 3 percent of the volume (Morgan, 1985a). The time scale for the appearance of high density clumps is short, apparently less than a day according to table III of Morgan (1985a).

The only long-term monitoring of the UV emission of the hot, outer torus has been by IUE, from which spectra in the 1100–1800 A region have been obtained since the Voyager 1 encounter period in early 1979. Typical brightness of SII, SIII, and SIV multiplets in this wavelength region varied by a factor of three over the period 1979 to 1985 (Moos et al., 1985). Part of this variability may be due to observing geometry effects. In fact, Moos et al. (1985) computed the ratio of SII:SIII and SIII:SIV brightnesses and found that these ratios vary substantially less (~30 percent). It is tempting to argue that taking ratios removes the geometry effects and thus the variability of torus emissions over a half of a solar cycle is small. But it must be remembered that the spectral features monitored by IUE do not directly yield either electron density (OII has no spectral signature in this wavelength interval) or electron temperature. From an intercomparison of the Voyager 1 and 2 encounter EUV data Shemansky (1987) deduced an increase in electron density with an accompanying decrease in electron temperature. The brightness of a UV multiplet would increase in response to this density change, but decrease in response to the temperature change. Thus the absence of variability in the ratio of emission brightnesses does not necessarily imply that plasma properties are constant. Moos et al. (1985) constructed a "zero-dimensional" model with a number of assumptions including a negligible variation in electron temperature with time and concluded that the variability of the electron density over the six year period was only 14 percent. However, the actual electron density variation could have been substantially greater if electron temperature variability were included.

The other important evidence for long-term variability in the Io plasma torus is a comparison of UV measurements made by Pioneer 10 (Judge and Carlson, 1974) and Voyager 1 and 2 (Broadfoot et al., 1979, Sandel et al., 1979). A reanalysis of the Pioneer 10 data shows that the torus luminosity was a factor of ~25 weaker than during the Voyager encounters and that the torus was not continuous with longitude in that there were gaps in its luminosity during the Pioneer encounter (Shemansky, 1988b). The substantially reduced torus brightness suggests that the average electron density was reduced to $\sim 500\ \mathrm{cm}^{-3}$ at the time of the Pioneer encounter (Shemansky, 1988b). Stated another way, there is no possibility by virtue of intercomparisons with other measurements of interplanetary HI-Lyman alpha and HeI-584 A radiation that the Io plasma torus had the same luminosity during the Pioneer and Voyager encounters. Additional support for lower electron densities during the Pioneer encounter is provided by magnetic field perturbation observations associated with the passage of the spacecrafts through standing Alfven wave patterns. Walker and Kivelson (1981) found the Alfven Mach number to be ~0.03 during the Pioneer 10 encounter, which is 0.2 times the Voyager 1 encounter value. Because the Alfven speed is inversely proportional to the square root of the electron density, this would imply an increase in the electron density by a factor of 25 from the Pioneer to the Voyager epoch. Although this is not in good agreement with the density inferred by Shemansky, it can be brought in much better agreement by noting that the luminosity scales linearly with electron density rather than the square of the electron density when the electron-ion collision frequency significantly exceeds the reciprocal of the ion residence time (see eq. [28] and figure 8 in Smith and Strobel, 1985).

CONCLUDING REMARKS

There is strong evidence for significant variability in plasma composition, temperature, and mass in the Io torus on both the short- and long-time scales. Most of these variations are not understood in a quantitative, let alone predictive manner. Particularly perplexing are apparent multiple periodicities displayed by SII red line intensities. Equally perplexing are the indications of severe inhomogeneities in the torus concentrations and temperature (i. e., the high-density clumps or sheets of plasma). Is this an infrequent occurrence or does this phenomenon play a central role in the structure of the plasma torus? Do the implied severe depletions of plasma mass during the Pioneer encounters relative to the Voyager encounters suggest that volcanism on Io was substantially less active then? Clearly more observations are needed to address these and other questions which are necessary to unravel the mysteries of the variable jovian systems.

ACKNOWLEDGMENTS
This effort was supported by NASA grant NAGW-648 and the Voyager mission.

References

Bagenal, F., and J. D. Sullivan (1981). Direct plasma measurements in the Io torus and inner magnetosphere of Jupiter. *J. Geophys. Res.* 86:8447–8466.

Bagenal, F., R. L. McNutt, Jr., J. W. Belcher, H. S. Bridge, and J. D. Sullivan (1985). Revised ion temperatures for Voyager plasma measurements in the Io plasma torus. *J. Geophys. Res.* 90:1755.

Ballester, G. E., H. W. Moos, P. D. Feldman, D. F. Strobel, M. E. Summers, J. L. Bertaux, T. E. Skinner, M. C. Festou, and J. H. Lieske (1987). Detection of neutral oxygen and sulfur emissions near Io using IUE. *Astrophys. J. Lett.* 319:33–38.

Barbosa, D. D., F. V. Coroniti, and A. Eviatar (1983). Coulomb thermal properties and stability of the Io plasma torus. *Astrophys. J.* 274:429–442.

Barbosa, D. D., and M. G. Kivelson (1983). Dawn-dusk electric field asymmetry of the Io plasma torus. *Geophys. Res. Lett.* 10:210–213.

Barbosa, D. D., and Moreno, M. A. (1988). A comprehensive model of ion diffusion and charge exchange in the cold Io torus. *J. Geophys. Res.* submitted.

Broadfoot, A. L., et al. (1979). Extreme ultraviolet observations from Voyager 1 encounter with Jupiter. *Science* 206:979–982.

Brown, R. A. (1974). Optical line emission from Io. In *Exploration of the planetary system*. In (A. Woszczyk and C. Iwaniszewska, eds.), pp. 527–531. D. Reidel, Hingman, Mass.

Brown, R. A. (1976). A model of Jupiter's sulfur nebula. *Astrophys. J. Lett.* 206:179–183.

Brown, R. A. (1981). The Jupiter hot plasma torus: Observed electron temperature and energy flows. *Astrophys. J.* 263:433–442.

Brown, R. A., and D. E. Shemansky (1982). On the nature of SII emission from the Io plasma torus. *Astrophys. J.* 263:433–442.

Brown, R. A., C. B. Pilcher, and D. F. Strobel (1983a). Spectrophotometric studies of the Io torus. In *Physics of the jovian magnetosphere* (A. J. Dessler, ed.), pp. 197–224. Cambridge Univ. Press, Cambridge.

Brown, R. A., D. E. Shemansky, and R. E. Johnson (1983b). A deficiency of OIII in the Io plasma torus. *Astrophys. J.* 264:309–323.

Cheng, A. F. (1986). Radial diffusion and ion partitioning in the Io torus. *Geophys. Res. Lett.* 13:517–520.

Cook, A. F., E. M. Shoemaker, B. A. Smith, G. E. Danielson, T. V. Johnson, and S. P. Synnott (1981). *Science* 211:1419.

Dessler, A. J. (1985). Differential rotation of the magnetic fields of gaseous planets. *Geophys. Res. Lett.* 12:299–302.

Dessler, A. J., and T. W. Hill (1975). High-order magnetic multipoles as a source of gross asymmetry in the distant jovian magnetosphere. *Geophys. Res. Lett.* 2:567–570.

Doering, J. P., and E. E. Gulcicek (1987). Direct electron excitation cross sections for atomic oxygen transitions at low energies. *EOS* 68:1392.

Durrance, S. T., P. D. Feldman, and H. A. Weaver (1983). Rocket detection of ultraviolet emission from neutral oxygen and sulfur in the Io torus. *Astrophys. J. Lett.* 125–129.

Gehrels, N., and E. C. Stone (1983). Energetic oxygen and sulfur ions in the jovian magnetosphere and their contribution to the auroral excitation. *J. Geophys. Res.* 88:5537–5550.

Goertz, C. K. (1978). Energization of charged particles in Jupiter's outer magnetosphere. *J. Geophys. Res.* 83:3145–3150.

Goertz, C. K., and W. H. Ip (1983). A dawn-to-dusk electric field in the jovian magnetosphere. *Planet Space Sci.* 32:179.

Haff, P. K., C. C. Watson, and Y. K. Yung (1981). Sputter ejection of matter from Io. *J. Geophys. Res.* 86:6933–6938.

Hill, T. W. (1979). Inertial limit on corotation. *J. Geophys. Res.* 84:6554–6558.

Hill, T. W. (1980). Corotation lag in Jupiter's magnetosphere: A comparison of observation and theory. *Science* 207:301–302.

Ho, Y. K. and R. J. W. Henry (1983). Oscillator strengths and collision strengths for OII and OIII. *Astrophys. J.* 264:733–739.

Ho, Y. K. and R. J. W. Henry (1984a). Oscillator strengths and collision strengths for SIII. *Astrophys. J.* 282:816–819.

Ho, Y. K. and R. J. W. Henry (1984b). Oscillator strengths for λ1199 and λ1729 of SIII. *Astrophys. J.* 284:435–437.

Ho, Y. K. and R. J. W. Henry (1985). Oscillator strengths and collision strengths for neutral sulfur. *Astrophys. J. Lett.* 205:51–53.

Johnson, R. E., and D. F. Strobel (1982). Charge exchange in the Io torus and exosphere. *J. Geophys. Res.* 87:10385–10393.

Judge, D. L., and R. W. Carlson (1974). Pioneer 10 observations of the ultraviolet glow in the vicinity of Jupiter. *Science* 183:317–318.

Kaiser, M. L., and M. D. Desch (1980). Narrow-band jovian kilometric radiation: A new radio component. *Geophys. Res. Lett.* 7:389–392.

Kumar, S. (1984). Sulfur and oxygen escape from Io and a lower limit to atmospheric SO_2 at Voyager 1 encounter. *J. Geophys. Res.* 89:7399.

Kupo, I., Y. Mekler, and A. Eviatar (1976). Detection of ionized sulfur in the Jovian magnetosphere. *Astrophys. J. Lett.* 205:51–53.

Matson, D. L., T. V. Johnson, and F. P. Fanale (1974). Sodium D-line emission from Io: Sputtering and resonant scattering hypotheses. *Astrophys. J. Lett.* 192:43–46.

McGrath, M. A., and R. E. Johnson (1987). Magnetospheric plasma sputtering of Io's atmosphere. *Icarus* 69:519–531.

Moos, H. W., and J. T. Clarke (1981). Ultraviolet observations of the Io torus from earth orbit using the IUE Observatory. *Astrophys. J.* 247:354–361.

Moos, H. W., T. E. Skinner, S. T. Durrance, P. D. Feldman, M. C. Festou, and J. L. Bertaux (1985). Long-term stability of the Io high-temperature plasma torus. *Astrophys. J.* 294:369–382.

Morgan, J. S. (1985a). Temporal and spatial variations in the Io torus. *Icarus* 62:389–414.

Morgan, J. S. (1985b). Models of the Io torus. *Icarus* 63.243–265.

Pilcher, C. B., and J. S. Morgan (1980). The distribution of [SII] emission around Jupiter. *Astrophys. J.* 238:375–380.

Pilcher, C. B., and D. F. Strobel (1982). Emissions from neutrals and ions in the jovian magnetosphere. In *Satellites of Jupiter* (D. Morrison, ed.), pp. 807–845. Univ. of Arizona Press, Tucson.

Pilcher, C. B., J. H. Fertel, and J. S. Morgan (1985). [SII] images of the Io torus. *Astrophys. J.* 291:377–393.

Pilcher, C. B., and J. S. Morgan (1985). Magnetic longitude variations in the Io torus. *Adv. Space Res.* 5:337–345.

Richardson, J. D., and R. L. McNutt, Jr. (1987). Observational constraints on interchange models at Jupiter. *Geophys. Res. Lett.* 14:64–67.

Roesler, F. L., F. Sherb, and R. J. Oliversen (1984). Periodic intensity variation in [SIII] 9531 A emission from the Jupiter plasma torus. *Geophys. Res. Lett.* 11:128–130.

Rountree, S. P. (1977). Electron-impact excitation of atomic oxygen: $^3P - 3s^5S^0$ and $^3P - 3s^3S^0$. *J. Phys. B: Atom. Molec. Phys.* 10:13, 2719–2725.

Rountree, S. P., and R. J. W. Henry (1972). Electron-impact excitation cross sections for atomic oxygen: $^3P - 3s^3S^0$. *Phys. Rev.* 6 (A 6):2106–2109.

Sandel, B. R. (1988). Private communication.

Sandel, B. R., and A. L. Broadfoot (1982a). Io's hot plasma torus—a synoptic view from Voyager. *J. Geophys. Res.* 87:212–218.

Sandel, B. R., and A. L. Broadfoot (1982b). Discovery of an Io-correlated energy source for Io's hot plasma torus. *J. Geophys. Res.* 87:2231–2240.

Sandel, B. R., and A. J. Dessler (1988). Dual periodicity of the jovian magnetosphere. *J. Geophys. Res.*, submitted.

Sandel, B. R. et al. (1979). Extreme ultraviolet observations from Voyager 2 encounter with Jupiter. *Science* 206:962–966.

Schneider, D. M. Hunten, W. K. Wells, and L. M. Trafton (1987). Eclipse measurements of Io's sodium atmosphere. *Science* 238:55–58.

Shemansky, D. E. (1980). Radiative cooling efficiencies and predicted spectra of the Io plasma torus. *Astrophys. J.* 236:1043–1054.

Shemansky, D. E. (1987). Ratio of oxygen to sulfur in the Io plasma torus. *J. Geophys. Res.* 92(A6): 6141–6146.

Shemansky, D. E. (1988a). Energy branching in the Io plasma torus; the failure of neutral cloud theory. *J. Geophys. Res.* 93:1773–1784.

Shemansky, D. E. (1988b). Private communication.

Shemansky, D. E., and G. R. Smith (1981). The Voyager EUV spectrum of the Io plasma torus. *J. Geophys. Res.* 86:9179–9192.

Shemansky, D. E., and B. R. Sandel (1982). The injection of energy into the Io plasma torus. *J. Geophys. Res.* 87:219–229.

Siscoe, G. L., and C. K. Chen (1977). Io: A source for Jupiter's inner plasmasphere. *Icarus* 31:1–10.

Sittler, E. C., Jr., and D. F. Strobel (1987). Io plasma torus electrons: Voyager 1. *J. Geophys. Res.* 90(A10): 9469–9493.

Smith, R. A., and D. F. Strobel (1985). Energy partitioning in the Io plasma torus. *J. Geophys. Res.* 90(A10): 9469–9493.

Smith, R. A., F. Bagenal, A. F. Cheng, and D. F. Strobel (1988). On the energy crisis in the Io plasma torus. *Geophys. Res. Lett*, submitted.

Strobel, D. F., and J. Davis (1980). Properties of the Io plasma torus inferred from Voyager EUV data. *Astrophys. J. Lett.* 238:49–52.

Summer, M. E., D. F. Strobel, Y. L. Yung, J. T. Trauger, and F. Mills (1988). The structure of Io's atomic corona and implications for atmospheric escape. *Astrophys. J.*, submitted.

Tayal, S. S., and R. J. W. Henry (1987). Effective collision strengths for electron impact excitation in SII. *Astrophys. J.* 313:487–493.

Thorne, R. M. (1983). Microscopic plasma processes in the jovian magnetosphere. In *Physics of the jovian magnetosphere* (A. J. Dessler, ed.), pp. 454–488. Cambridge Univ. Press, Cambridge.

Trafton, L. (1980). Jovian SII torus: Its longitudinal asymmetry. *Icarus* 42:111–124.

Trauger, J. T. (1984). The jovian nebula: A post-Voyager perspective. *Science* 236:337–341.

Trauger, J. T., G. Munch, and F. L. Roesler (1980). A study of the jovian [SII] nebula at high spectral resolution. *Astrophys. J.* 236:1035–1042.

Walker, R., and M. Kivelson (1981). Multiply reflected standing Alfven waves in the Io torus: Pioneer 10 observations. *Geophys. Res. Lett.* 8:1281–1284.

Wolf-Gladrow, D. A., F. M. Neubauer, and M. Lussem (1987). Io's interaction with the plasma torus: A self-consistent model. *J. Geophys. Res.* 92:9949–9961.

16

Torus–Magnetosphere Coupling

Fran Bagenal
Massachusetts Institute of Technology, Cambridge

Abstract

To understand temporal variability of the jovian magnetosphere, it is necessary to study the coupled system of the Io plasma torus, the magnetosphere, and Jupiter's ionosphere. At present, efforts have been concentrated on separate elements of the system.

Progress has been made in both measuring and modeling the plasma conditions in the cold and warm regions of the torus. Models of the warm torus developed by Shemansky (1987b) show that the observed plasma conditions require an additional source of energy in the torus, comparable to that picked up by the ions in plasma production (3×10^{13} W). Estimates of mass-loading on the ionosphere and the concomitant perturbation in the plasma flow suggest it may not be possible to produce this much power in a small region such as Io's atmosphere, as Shemansky proposes. A fully self-consistent, three-dimensional plasma model of the magnetosphere-atmosphere interaction is urgently required. A recent analysis of the Voyager plasma science data in the region between the warm torus and the plasma sheet ($L = 6$ to 12) indicates that there is an additional source of plasma between 9 and 11 R_J, possibly the ionization of neutral material from Europa or recycling of material from the Io torus. In addition to a thermalized ion population with $T_i \sim 50$ eV there is a hot population with temperatures > 1 keV that comprises up to 35 percent of the total charge density. To ascertain if this hot population could be acting as an intermediary and transferring energy from the inwardly diffusing energetic particles to provide the 10^{13} W to the torus, we need a comprehensive model of the region between the torus and the plasma sheet, including ionosphere-magnetosphere coupling.

INTRODUCTION

The Io plasma torus is the main source of plasma for the jovian magnetosphere. At the same time, it is the interaction of the streaming magnetospheric plasma with Io (or its atmosphere/ionosphere) that may be the source mechanism. The magnetosphere is coupled to Jupiter (the "flywheel") by field-aligned currents that close in the ionosphere (the "clutch"). Thus, the ionosphere tries to enforce corotation throughout the magnetosphere. Conversely, mass-loading and radial motion in the magnetosphere drive currents in the ionosphere. In the outer regions of the magnetosphere, particles are accelerated to high energies (by some as yet undetermined mechanism). The energetic particles diffuse inward toward the torus and "disappear" between $L \sim 12$ and $L \sim 6$. Some of these particles precipitate into the ionosphere, where they cause intense auroral emissions. Particle precipitation may in turn modify the electrical conductivity of the ionosphere and hence affect the rate of radial motion in the magnetosphere. Particle precipitation will also generate secondary electrons that could be a significant source of energy for the torus plasma and supply a background population of protons. The remaining energetic particles continue to diffuse inward through the torus, where they may heat the torus plasma. This complicated three-way coupling between the torus, magnetosphere, and ionosphere is sketched in figure 96. The main elements of the system are reasonably well understood: (1) The cold inner torus has been explored both from ground-based observations (Trauger, 1984) and by Voyager 1 (Bagenal, 1985). Recent work by Barbosa and Moreno (1987) has provided a fairly comprehensive theoretical model. (2) The composition of the warm outer torus has been well determined by Voyager and International Ultraviolet Explorer (IUE) ultraviolet (UV) observations (Shemansky, 1987b; Moos et al., 1985). The Voyager plasma science (PLS) instrument has provided good determinations of the ion (Bagenal et al., 1985) and electron (Sittler and Strobel, 1987) temperatures. The data have led to considerable theoretical work on centrifugally driven radial diffusion (Summers and Siscoe, 1985) and steady-state models of the torus plasma with a source cloud of neutral sulfur and oxygen atoms (Barbosa et al., 1983; Smith and Strobel, 1985; Moreno et al., 1985; Shemansky, 1987b). (3) The properties of the plasma sheet have been well determined by Voyager PLS (McNutt et al., 1981), and the radial forces on the plasma in the plasma sheet seem to be reasonably balanced (Vasyliunas, 1983; McNutt, 1984; Mauk et al., 1986). (4) The energetic particle populations have been measured extensively by the Pioneer and Voyager spacecraft (Schardt and Goertz, 1983). In particular, Gehrels and Stone (1983) show a dramatic decrease in oxygen and sulfur ions at 10s MeV energies between $L \sim 12$ and $L \sim 6$ (with the strongest losses outside $L \sim 8$). (5) The auroras have been measured by rocket-borne detectors, IUE and Voyager (see Clarke et al., this volume). Herbert et al. (1987) have reviewed the evidence for 3–8 × 10^{12} W of emission from an oval skirting the $L \sim 6$ field lines at the time of the Voyager 1 encounter.

However, there remain important elements of the system that are not well determined: (1) To understand the coupling between the torus and the magnetosphere

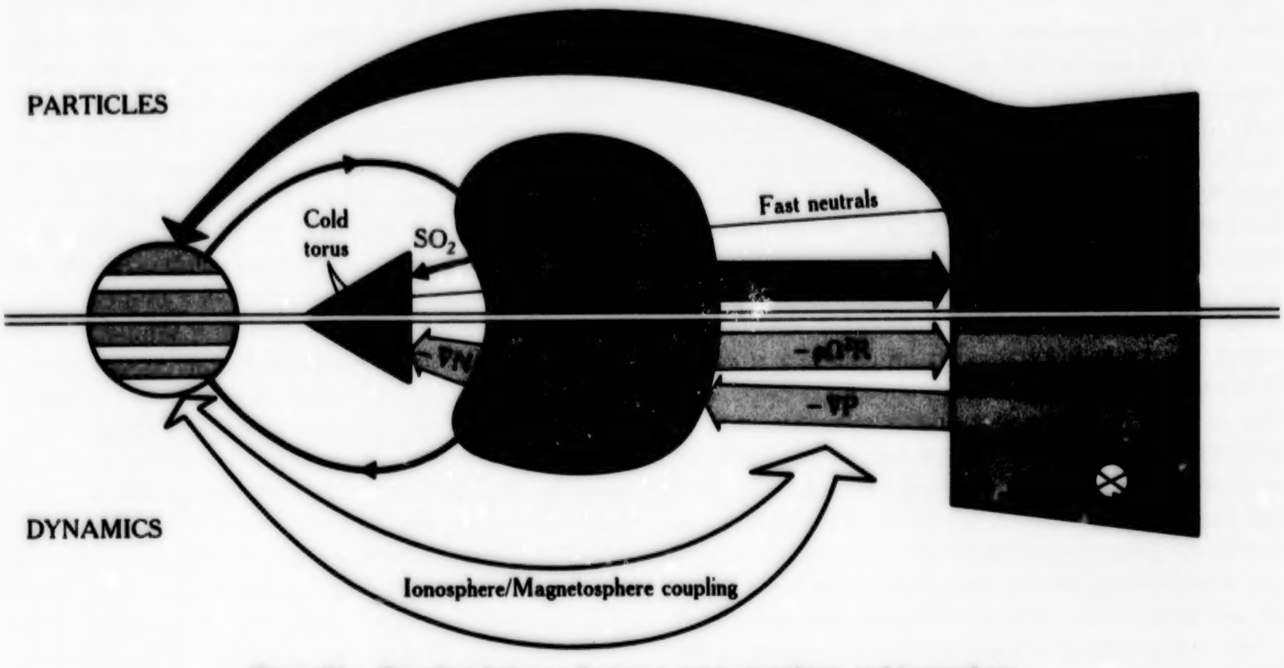

Figure 96. Coupling between the torus, magnetosphere, and ionosphere.

we need to know the properties of the plasma between $L = 6$ and 15. The extraction of plasma parameters from the PLS data, which has been particularly difficult in this region, is the major subject of this chapter. (2) It is important to know the electrical conductivity of Jupiter's ionosphere for determining the degree to which the magnetosphere is coupled to the planet's rotation. Estimates range from 0.1 mho to 10 mho (Strobel and Atreya, 1983). (3) Whether the source of the aurora is electron or ion precipitation is a topic of current debate (see Clarke et al., this volume). The resolution of this matter has important implications for both particle transport and the ionospheric conductivity. (4) Cheng et al. (1983) show Voyager low energy charged particle (LECP) data for their upper energy channels (>0.2 MeV) but the lower-energy channels (30–200 keV) of the LECP detectors were heavily saturated inside $L \sim 10$. There were no Voyager measurements of ions between 6 keV and 30 keV; we will have to wait for Galileo to reveal the particle properties in this important intermediate energy range.

The elements of this torus-magnetosphere-ionosphere system are usually studied separately but the strong coupling between them requires that the system be studied as a whole. Clearly, the system will suffer temporal variability, and the study of how each element varies will give clues of the coupling processes. Unfortunately, many aspects of the magnetosphere can be measured only locally. We have two Pioneer plus two Voyager passes through the jovian magnetosphere but it is hard to separate temporal variations from longitudinal, latitudinal, and radial variations. As far as the Voyager PLS data are concerned, Voyager 1 to Voyager 2 comparisons are limited to outside 10 R_J and have revealed considerable differences in the middle magnetosphere due to changes in the solar-wind conditions (McNutt et al., 1987). Because of the nature of the PLS data inside 12 R_J, we are only just beginning to understand the Voyager 1 inbound pass, even after eight years' work. Luckily, we are not confined to local measurements; valuable information about the magnetosphere can be obtained remotely. Although somewhat limited in spatial coverage, to a line of sight measurement and in coverage of ionic species, UV and optical measurements of the torus emissions will always be the major means of monitoring plasma conditions in the torus. Radio emissions also reveal properties such as electron density and temperature (see chapters by Zarka and Genova, and DePater and Klein in this volume). Of particular importance to the torus-magnetosphere coupling problem, Jones (1987) reports a possible means of monitoring the radial density gradient over the several months of the two Voyager encounters. The time is now ripe for a synthesis of the results from various Voyager and Pioneer experiments, in combination with theoretical models, to study the whole torus-magnetosphere-ionosphere system.

COLD TORUS

It was from the cold, inner region of the torus that emission was first detected and the cold torus remains the best-understood part of the jovian magnetosphere, but it is rather a backwater since only about 2 percent of plasma (and a much smaller fraction of energy) diffuses inward from Io. Hence, although its effect on the inner radiation belts, Amalthea, and the rings may be significant, its net influence on the magnetosphere is small.

Remote observations of S^+ and O^+ show the cold torus to be persistent but having variations in n_e and T_e and with longitude and time (Brown et al., 1983; Trauger, 1984). The Voyager PLS instrument made detailed measurements of S^+, O^+, S^{2+}, O^{2+}, and SO_2^+ ions and their temperature, T_i in to 4.9 R_J (Bagenal, 1985). Nevertheless, some aspects of the cold torus remained puzzling: Why did the ratio of oxygen to sulfur not decrease inward as one would expect (Johnson and Strobel, 1982); why was there so much O^{2+} when T_e is <1 eV; and how did the SO_2^+ ions survive so far from Io? Moreover, the presence of a hot component to the ion distribution indicated a local source of pick-up ions (Bagenal, 1985). Richardson and Siscoe's (1983) models of plasma diffusing inward from Io could not generate radial profiles of both density and temperature that were compatible with the data. Many of these questions may have been resolved by Barbosa and Moreno (1987), who have considered the photodissociation of SO_2 and the reactions of the dissociation products and the surrounding plasma. A key reaction in their model is a near-resonant charge-exchange reaction between SO and S^+, which may account for the removal of sulfur inward of Io. This fairly comprehensive model needs to be fully tested on details of the Voyager data, but it may prove to be a valuable tool for exploring possible explanations of the longitudinal and temporal variability of the inner torus.

The transition from the warm to the cold torus is very sharp: There is a clear change in the nature of the PLS spectra between consecutive measurements on both the inbound and outbound legs of the Voyager 1 trajectory. The high-resolution spectra in figure 97 show

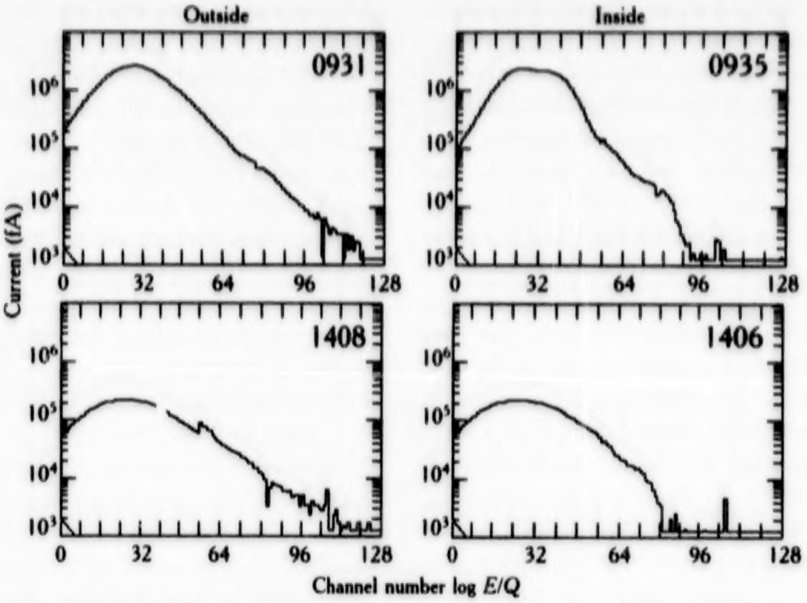

Figure 97. Voyager 1 PLS energy-per-charge spectra obtained on 5 March 1979 near the boundary between the warm and cold regions of the Io torus. The fluxes measured inbound (*below*) were much lower than on the inbound leg (*above*) because the spacecraft was farther from the centrifugal equator and the detector was pointed away from the corotating flow.

how the tail to the ion distributions at higher energies is greatly reduced inside the boundary. More precise timing of the boundary crossings can be obtained from the low-resolution data obtained between the spectra shown in figure 97. In figure 98 the magnetic L-shell values have been plotted for the times of the inbound and outbound crossings using the full O4 (Acuña), and offset tilted dipole (OTD) approximation to the O4 magnetic field model (Acuña et al., 1983). For both magnetic field models the L-shells of the inbound and outbound crossings are remarkably close, the separation ΔL being less than 0.07 and 0.04, respectively, for the

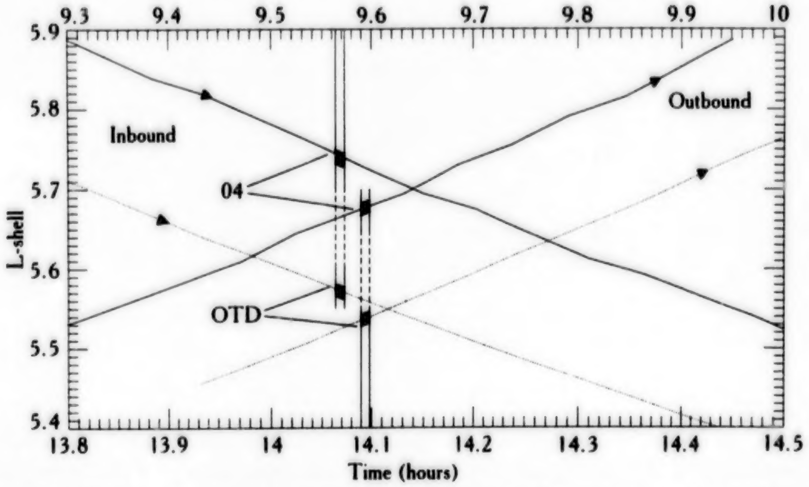

Figure 98. Magnetic L-shell of Voyager 1 for the inbound (*upper time axis*) and outbound (*lower time axis*) crossings of the inner torus boundary for the full O4 (*full lines*) and OTD (*dotted lines*) magnetic field models. The vertical lines attached to the upper (lower) axis correspond to the times of consecutive measurements on the inbound (outbound) passes.

O4 and OTD models. In both cases, the inbound crossing was at a larger L-value, which is consistent with an asymmetry in the ion drift paths due to a dawn-dusk electric fields but the magnitude is rather less than the value of ~0.1 derived for the Voyager 1 trajectory from the estimates of the electric field by Barbosa and Kivelson (1983) and Ip and Goertz (1983). The boundary L-shell ($L = 5.711 \pm 0.032$ for the full O4 model and $L = 5.557 \pm 0.017$ for the OTD model) coincides with the location of the maximum in flux tube content (NL^2, where N is the total number of ions per unit L-shell) and the location of a sharp decrease in temperature (Bagenal, 1985). It is the torus divide: the separation between inward and outward diffusion. Linker et al. (1985) have been able to produce such a boundary well inside Io's orbit by including the effects of Jupiter's gravitational potential on the trajectories of low-velocity neutral atoms sputtered from Io.

WARM TORUS

Moos et al. (1985) have reported that five years of IUE observations indicate the temporal variability of the warm torus is small. The mixing ratios of S^+, S^{2+}, and S^{3+} appear to vary less than 28 percent and the electron density and temperature are inferred to vary by only ±10 percent and ±14 percent, respectively. On the other hand, Shemansky (1987a) reports considerable variation in the torus conditions between Voyager 1 and Voyager 2, inferred from ultraviolet spectrometer (UVS) data. He reports a relatively small change in composition (toward lower ionization states, compatible with a slightly reduced electron temperature), but he infers a 50 percent increase in electron density. Certainly, measurements of the variability will enhance our understanding of the processes. But at present we need to understand the Voyager 1 epoch.

Table 14 shows the composition of the warm torus as derived from various observations and theoretical models. It seems quite extraordinary that it has taken eight years for a general consensus to have been reached on the composition of the warm torus. There are several factors that have contributed to this delay, but the main issues have been (1) the lack of accurate atomic data for the interpretation of UV data and theoretical models (Brown et al., 1982; Shemansky, 1987a) and (2) the need to calculate the response of the PLS instrument to trans-sonic flows. From the IUE and UVS data the best-determined parameter is the ratio $S^+/$

Table 14. Composition of Warm Torus

	H^+	O^{2+}	S^{3+}	O^+	S^{2+}	S^+	N_e	T	T_{hot} 16	T_{hot} S^+	$\dot{T}$
UVS Voyager 1[a]			**16**	**39**	**32**	**13**	2250				
IUE[b]			**4**	**50**	**40**	**6**					
DES[c]		**<1**	**<1**	**49**	**5**	**46**	2000				
DES[d]		**3**	**6**	**42**	**36**	**13**	2000				
B&M[e]		**9**	**6**	**40**	**34**	**11**	2000				
UVS Voyager 2[f]		**<1**	**2**	**45**	**36**	**17**	3000				
PLS1[g]											
Thermal	50	51	75	652	250	217	2149	55			
	±23	**±42**	**±21**	**±96**	**±39**	**±59**		**±13**			
Hot				384		20.4			O^+173	980	
				±79		**±25**			**±29**		
No hot S^{2+}	**2.3**	**4.7**	**10.5**	**48.3**	**23**	**11**					92.6
35 percent S^{2+}	**2.3**	**4.7**	**10.5**	**36.3**	**35**	**11**			S^{2+}346		100
PLS2[h]											
Thermal	50	15	45	553	393	258	2260	62			
	±30	**±54**	**±27**	**±137**	**±52**	**±69**		**±18**			
Hot				427		20.4			O^+184	980	
				±88		**±27**			**±33**		
No hot S^{2+}	**2.2**	**1.3**	**6**	**43.5**	**35**	**11.4**					99.5

Bold numbers are percentages of charge density. Densities are in *ions* cm^{-3} and temperatures are in eV. [a] Shemansky (1987b) Voyager 1 spectrum at 5.75 R_J. [b] Moos et al., (1986) standard model with 1.17 R_J scale height. [c] Shemansky (1987b) model from neutral cloud theory. [d] Shemansky (1987b) modified theory with electron heating. [e] Barbosa and Moreno (1987). [f] Shemansky (1987a) Voyager 2 spectrum. [g] Fit to PLS data at $L = 6.0$. [h] Fit to PLS data with reduced O^{2+} and S^{3+}.

S^{2+}, which is 0.6–0.7 by number (0.3–0.35 by charge). Shemansky (1987a) now claims that the ratio S^{2+}/O^{+} is well determined at 0.4 by number (0.8 by charge). Unfortunately, there are no detectable O^{+} emission lines in the IUE spectral range. When it comes to higher ionization states there may be some disagreement over S^{3+} with Shemansky (1987b) reporting larger abundances from the Voyager 1 UVS measurements (16 percent by charge) than measured by IUE (4 percent by charge) and predicted by various theoretical models (Shemansky, 1987b; Barbosa and Moreno, 1987). There are not direct measurements of O^{2+} abundance since the O^{2+} line at 833 Å is swamped by a near coincident O^{+} line in the UVS spectra (which has 30 Å resolution) and again there are no O^{2+} lines in the IUE range. The lack of O^{2+} emission at 5007 Å reported by Brown et al. (1982) puts an upper limit on the abundance of O^{2+} ions (1 percent) that is even less than the low densities from theoretical models. This may be true temporal variability and further ground-based observations of the 5007 Å line would be particularly useful. Note that the theoretical model of Barbosa and Moreno (1987) includes as much as 9 percent O^{2+} (by charge) to account, in part, for the large abundance of O^{2+} observed in the cold torus (Bagenal, 1985).

In analysis of the PLS data in the warm torus, we have been guided by the above constraints on the ion composition. The plasma flow is trans-sonic and the individual spectral peaks of the different ionic species cannot be resolved. The lack of a unique determination of plasma parameters in the warm torus has been acknowledged from the beginning, and our recent efforts have been to derive levels of uncertainty in the parameters. First of all, the broad, central maximum in the spectra is consistent with corotating ions with an atomic mass-to-charge ratio (A/Z) of 16 dominating the plasma. We therefore constrained the plasma flow velocity to that of corotation, assumed the bulk of the ions to have the same temperature, and started with a composition that is roughly consistent with the UV emissions.

To match the PLS data at lower energies we included a small percentage of protons (at the same temperature as the bulk of the ions). To match the PLS data at higher energies we had to introduce hot components at A/Z equal to 16 and 32. Even with all the above constraints, we are left with 11 free parameters to fit rather featureless spectra. Furthermore, there is the underlying problem that the velocity distribution of each ionic species is probably not the Maxwellian function we must assume for our analysis (as discussed below).

In table 14 we show the results of two fits to a spectrum obtained at $L = 6.0$ (PLS1 and PLS2). In both cases, the uncertainties are quite large for the minor species (O^{2+}, S^{3+}, and S^{+}). Although the differences between the two cases are within the uncertainties for each parameter, it is interesting to note that when the fraction of ions at higher ionization state (i.e., O^{2+} and S^{3+}) are reduced (in the second case, PLS2) the fraction of $A/Z = 16$ ions and the ion temperature T_i increase. The temperatures of the thermal component, T_i are consistent with the earlier estimates that were corrected by Bagenal et al. (1985). However, in both cases the hot component contributes about 20 percent of the total charge density and nearly doubles the average ion temperature. At $L \sim 6$ Sittler and Strobel (1987) report an electron temperature of 5 eV. The issue we must now address is how the torus maintains these temperatures.

Brown's (1974) detection of neutral sodium and the Pioneer detection of UV emission from what was thought to be a hydrogen cloud near Io (Judge and Carlson, 1974) (now known to have probably been emission from heavy ions) led Hill and Michel (1976) to suggest that the ionization of neutral material near Io's orbit could produce centrifugally confined plasma in the inner magnetosphere of Jupiter. Siscoe (1977) derived the pick-up (so-called "tin-can") velocity distribution and suggested the heavy ions should have temperatures on the order of a few hundred eV. Siscoe and Chen (1978) and Siscoe (1978) developed models of a plasmasphere, including heavy ions, produced by a source at Io. Thus, it was initially puzzling when Voyager found ion temperatures of only a few 10s of eV. Goertz (1980) then proposed that the lower ion temperatures might be explained if the ions could be produced in a small region close to Io. To see why this would be so let us consider the pickup process in more detail (figures. 99–101).

The rest frame of the plasma is by definition that where

$$\mathbf{E} = -\mathbf{V} \times \mathbf{B} = 0. \qquad (16.1)$$

In the case of the jovian magnetosphere the conductivity of the ionosphere and the plasma conductivity parallel (but not perpendicular) to the magnetic field is sufficiently high to ensure that magnetic field lines are equipotentials and any plasma injected into the magnetosphere will be accelerated up to corotation with the planet (which becomes the rest frame of the plasma). On the ionization of a neutral the new ion and electron have a velocity close to that of the original neutral

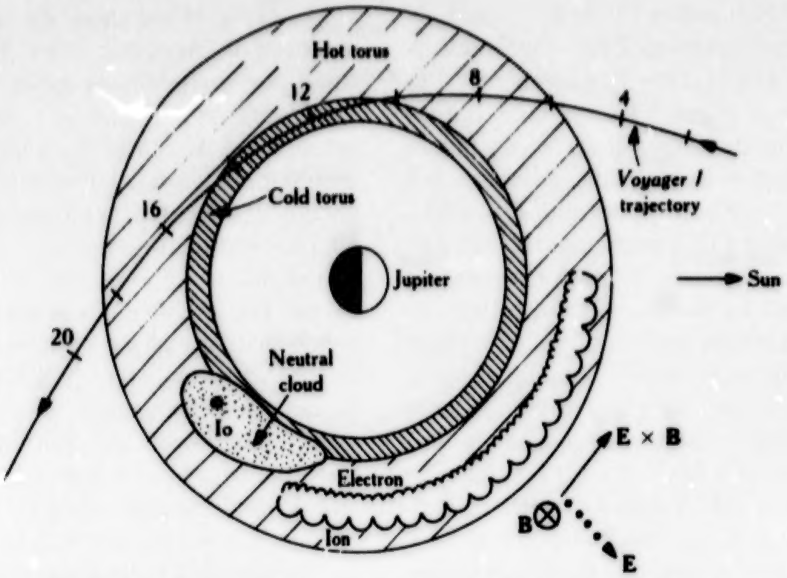
Hot torus
12
8
4
Voyager I trajectory
16
Cold torus
Jupiter
Sun
20
Neutral cloud
Io
E × B
Electron
B
Ion
E

Figure 99. Ion pick-up in the Io plasma—the equatorial plane.

(close to the orbital velocity of Io ~ 57 km^{-1} relative to the corotating rest frame of the plasma). The new ion and electron therefore see an electric field

$$\mathbf{E}_{\mathrm{co}} = -\mathbf{V}_{\mathrm{co}} \times \mathbf{B}.$$

This electric field causes the ion and electron to drift with a velocity

$$\mathbf{V}_{\mathrm{drift}} = \frac{\mathbf{E}_{\mathrm{co}} \times \mathbf{B}}{B^2}$$

(in the same sense) around the planet. The newly picked-up ions and electrons also commence to gyrate (in opposite directions) perpendicular to the local magnetic field direction. The difference in their gyroradii ($r \equiv mV_i/qB = mV_{\mathrm{co}}/qB$) causes a small radial displacement, giving rise to a radial current. This can be thought of as a pick-up current (that connects to the ionosphere by way of field-aligned currents) and the $\mathbf{J} \times \mathbf{B}$ force on the new plasma that enforces corotation (figure 100). However, the initial charge separation produces an electric field in the opposite direction to the corotational electric field. If there is enough ionization in a small enough region, this polarization electric field will cancel a significant fraction of the corotational electric field. The corotating plasma then sees

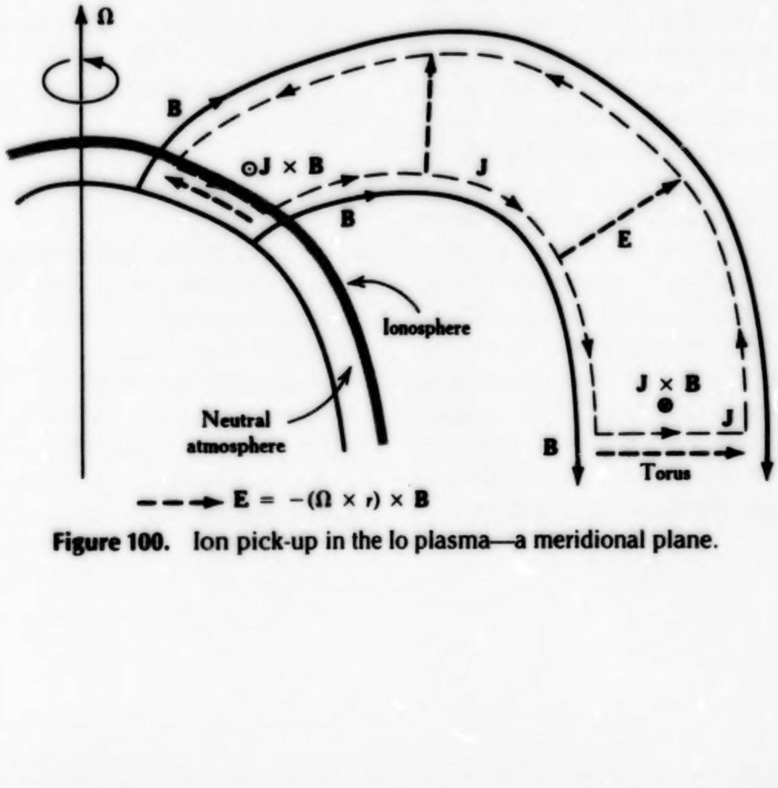
Ω
B
⊙J × B
J
B
E
Ionosphere
J × B
Neutral atmosphere
B
J
Torus
E = −(Ω × r) × B

Figure 100. Ion pick-up in the Io plasma—a meridional plane.

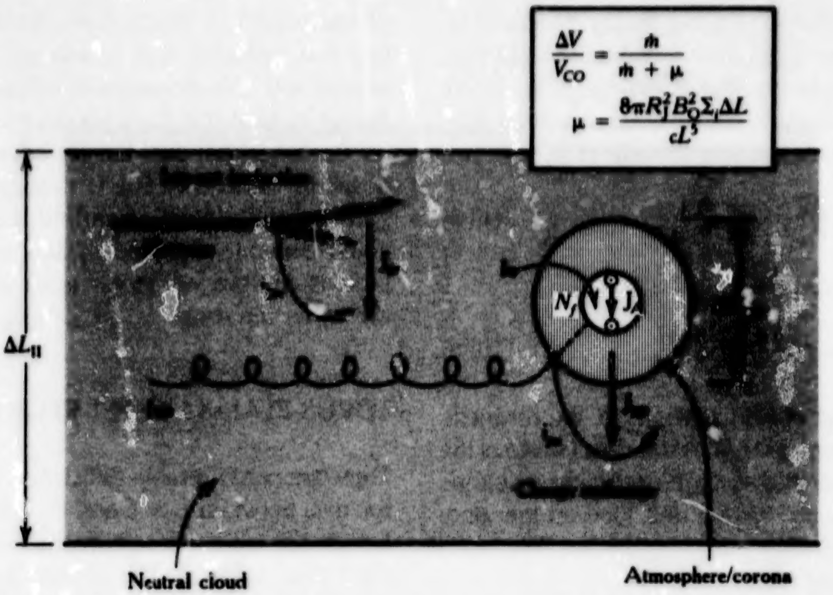
$\frac{\Delta V}{V_{CO}} = \frac{\dot{m}}{\dot{m} + \mu}$
$\mu = \frac{8\pi R_J^2 B_O^2 \Sigma_i \Delta L}{cL^5}$
$\Delta L_{\parallel}$
N_f
J_r
Neutral cloud
Atmosphere/corona

Figure 101. Ion pick-up in the Io plasma. Pick-up currents and mass-loading due to (1) impact ionization (II) in an extended neutral cloud and (2) charge exchange (CX) in Io's atmosphere.

this (polarization) electric field and slows down to satisfy eq. (16.1) in the plasma rest frame. Hence, considerable local ionization screens out the corotational electric field and the gyro energy of the locally picked-up ions is correspondingly reduced. Goertz (1980) proposed that ionization of material in the small region of Io's atmosphere might explain why the torus ions have temperatures considerably less than the full 540 and 270 eV pick-up energies for oxygen and sulfur ions. However, it was then realized that the plasma radiates a considerable fraction of its energy (Broadfoot et al., 1979). Initial calculations of the energy injection rate from ionization of new material at the full pick-up energy could reasonably balance the radiation output (Barbosa et al., 1983; Smith and Strobel, 1985), but Shemansky (1987b) has recently calculated, using more accurate values for the radiated power, diffusive loss time, and atomic data, that an appreciable additional source of energy is required to explain the observed plasma parameters (specifically, T_e, n_e and the S^+/S^{2+} ratio). Shemansky calculates that 0.3 eV cm^{-3} s^{-1} is required, corresponding to a total power of 7×10^{13} W for a torus volume of $2\pi 6 \times 1 \times 1R_J^3$.

Shemansky points out that increasing the source strength and decreasing the diffusive loss time (to maintain the observed density) actually lead to a lower electron temperature. Although each ionization produces a hot ion, it also produces a cold electron ($T_{e,\ \text{pick-up}} < 0.01$ eV). Furthermore, there is insufficient time for the ion to transfer its energy by way of Coulomb collisions to the electrons. A mechanism is therefore required that adds energy to the system without increasing the total density. Shemansky proposes that this could be done with charge-exchange reactions in a dense atmosphere of Io. The high density is required to increase the probability of a charge-exchange reaction toward unity. Very low electron temperatures are also probably required to reduce the chances of electron impact ionizations. The charge-exchange mechanism would also conveniently produce fast neutrals that could heat up Io's atmosphere. However, there could be a serious problem with Shemanky's suggestion. Let us return to the pick-up process illustrated in figures 99–101.

The pick-up current is given by (Hill et al., 1983)

$$\mathbf{J}_{pu} = q_i S \mathbf{r}_i, \qquad (16.2)$$

where S is the ion source strength (ions m^{-3} s^{-1}) and $r_i = m_i E / q_i B^2$ is the local ion gyro radius. Thus,

$$\mathbf{J}_{pu} = \frac{m_i S}{B^2} \mathbf{E}, \qquad (16.3)$$

where $\dot{m}$ is the rate of mass production (g m^{-3} s^{-1}). If each ion picks up a gyro speed of $V_{co} - \Delta V$, then the total power gained by the torus (and lost by Jupiter) is

$$P = \frac{1}{2} \dot{m} (V_{co} - \Delta V)^2. \qquad (16.4)$$

However, we must balance the net torque generated by the addition of mass against the counter torque supplied by the ionosphere's conductance (Hill, 1979). This leads to an expression for the local deviation from corotation due to mass-loading (Eviatar et al., 1983)

$$\frac{\Delta V}{V_{\text{co}}} = \frac{\dot{m}}{\dot{m} + \mu}, \tag{16.5}$$

where

$$\mu = \frac{8\pi\Sigma R_J^2 B_o \Delta L}{c^2 L^5}, \tag{16.6}$$

Σ is the ionospheric conductivity, B_o is the magnetic field in the ionosphere, and ΔL is the radial width of the source region. Note that charge-exchange reactions draw the same pick-up current and load on the ionosphere as impact ionization ($r_e \ll r_i$) (figure 101). Combining eqs. (16.4) and (16.5) we have

$$P = \frac{1}{2}\dot{m}V_{\text{co}}^2\left[1 - \frac{\dot{m}}{\dot{m} + \mu}\right]^2. \tag{16.7}$$

This equation says that if μ is small (e.g., Σ and ΔL small), then there is a large deviation from corotation in the source region ($\Delta V \rightarrow V_{\text{co}}$) and little power is extracted (i.e., leading to T_i small). Conversely, if μ is large, the deviation from corotation is small and the maximum power is extracted and the ions have the full pick-up energy. For Jupiter at $L \sim 6$

$$\mu = 3.2 \times 10^{8}(\Delta L)\left[\frac{\Sigma}{1\ \text{mho}}\right] \text{g s}^{-1}. \tag{16.8}$$

The total mass-loading on the torus is estimated to be 10^{30} amu s^{-1}, or 2×10^6 g s^{-1}. Thus, for an extended cloud of $\Delta L \sim 1R_J$ the conductivity has to be less than 5×10^{-4} mho for there to be appreciable deviation of the plasma flow from corotation and the full power of $1/2\,\dot{m}\,V_{\text{co}}^2 \sim 3 \times 10^{13}$ W is provided to the pick-up ions. However, if we try to extract the same sort of power from a small region in Io's atmosphere, as suggested by Shemansky (1987b), then for $\Delta L \sim 0.025$ (1 R_{Io}) and $\Sigma = 1$ mho, $\mu = 8 \times 10^6$ and $\Delta V \sim 20$ percent V_{co}. The plasma is slowed down appreciably and the energy extracted is much less than the pick-up energy. Moreover, the effect of the field-aligned (Birkeland) currents that close the current loop between the radial pick-up currents and the ionosphere must be taken into consideration when calculating the deflection of the plasma flow. The effect will be qualitatively the same as Io's Alfven currents (Goertz, 1980; Neubauer, 1980) to deflect the plasma around the source region. Thus a proper self-consistent, three-dimensional plasma calculation is needed to model the interaction of the torus plasma with Io's atmosphere. We must also conclude that it is unlikely that charge-exchange of corotating plasma with Io's atmosphere will provide the necessary energy to heat the torus electrons. One energy source for the torus that has largely been forgotten was proposed by Thorne (1980), who suggested that the energetic particles that stimulate the auroral emission could generate (hot) secondary electrons and (cold) protons. Below we propose an alternative source of energy for the torus.

TORUS-PLASMA SHEET REGION

There are considerable difficulties in analyzing the PLS ion data between $L = 6$ and 11. The most serious problem is that we do not know the velocity distribution of each ionic species. The plasma is not fully collisional and therefore the distribution functions probably deviate appreciably from a Maxwellian. Newly picked-up ions are expected to have a ring distribution in velocity space, whereas the interaction with a population of energetic particles is expected to produce a tail to the distribution that would fall off as a power law at higher energies. With trans-sonic magnetospheric plasma flowing obliquely into the detectors, the instrumental response cannot be simplified and its calculation for even Maxwellian functions is very time-consuming. Moreover, with a hot, multi-species plasma the spectral peaks of the ionic species are not resolved, and hence the ion bulk velocity and composition cannot be determined independently. The strategy has been to look for constraints on the composition. At $L \sim 6$ we used the ratios S^+/S^{2+} and S^{2+}/O^+ determined from UV observations (discussed above). At radial distances $>11.5\,R_J$, there are regions where the plasma is sufficiently cold that the composition and velocity are well determined from resolved peaks in the ion spectra. Thus, between 6 and 11.5 R_J we made an educated first guess at the composition and then investigated the range of parameters (velocity, temperature, and ion densities) that produce a reasonable fit to the data. In each case, a resolution matrix can be calculated and shows the degree to which the parameters are independent and how well the parameters are resolved in the data at a particular location in parameter space (which can be up to 15 dimensions). But it is impossible to tell if there is another equally good solution some distance away. This problem of nonuniqueness is exacerbated by the underlying limitations of not knowing the true distribution function. As if this were not enough, we are plagued with the quirk of nature that gives the two most abundant ions in the torus, O^+ and S^{2+}, the same atomic A/Z ratio of 16. Since the PLS detector differentiates by energy-per-charge, the corotating O^+ and S^{2+} ions produce superposed peaks in the PLS ion spectra. The situation is improved somewhat by making the probably reasonable assumption that most of the heavy ions are thermalized (with T_i the same for all species) comprising what we call the thermal component. The high-energy part of the spectrum is modeled with a sum of two or three Maxwellian functions corresponding to O^+, S^{2+}, and S^+ ions at much higher temperatures. However, the composition of the ions that make up this, the hot component, is not well constrained.

The ionic composition that is derived from our analysis is shown in figure 102. Remember that the composition is well determined inside $L \sim 6$ and outside $L \sim 11.5$. The significant changes in the composition between these two locations are (1) the fraction of the total positive charge density provided by the $A/Z = 16$ species drops from ~0.7 at $L = 6$ to something between 0.3 and 0.55 in the plasma sheet; (2) the charge fraction of each of the higher-ionization states, O^{2+} and S^{3+}, increases from about 10 percent at $L \sim 6$ to ~15 percent or more in the plasma sheet. However, the charge fraction of S^+ remains about 10 percent outside the cold torus (where it is the dominant species). These results are qualitatively consistent with the increased ionization over the time the plasma takes to diffuse away from the source near Io and as the electrons heat up outside $L \sim 7$ (Sittler and Strobel, 1987). Note that both Trauger (1984) and Moos et al. (1985) have reported a reduction in the S^+/S^{2+} ratio between $L = 6$ and $L = 7$, whereas Moos et al (1985) also reported a slight increase in S^{3+}/S^{2+}.

Despite the difficulties analyzing the data between $L = 6$ and 11.5 we have been able to extract some important plasma properties. The first major result is that the mean ion temperature reaches 1 keV in the transition region between the torus and the plasma sheet. Figure 103 shows that not only does the temperature of the thermal component rise from 50–60 eV at $L \sim 6$ to 400–500 eV at $L \sim$ 9–11, but the existence of a substantial hot component (~30 percent of the charge density), which is at least five times hotter, raises the average ion temperature considerably. The "high" temperature of $1.4 \pm 0.6 \times 10^6$ K (120 ± 51 eV) for S^{2+} ions at 6.5 R_J reported by Roessler et al. (1982) is quite consistent with the Voyager values of $\bar{T}$ at 6.5 R_J. The

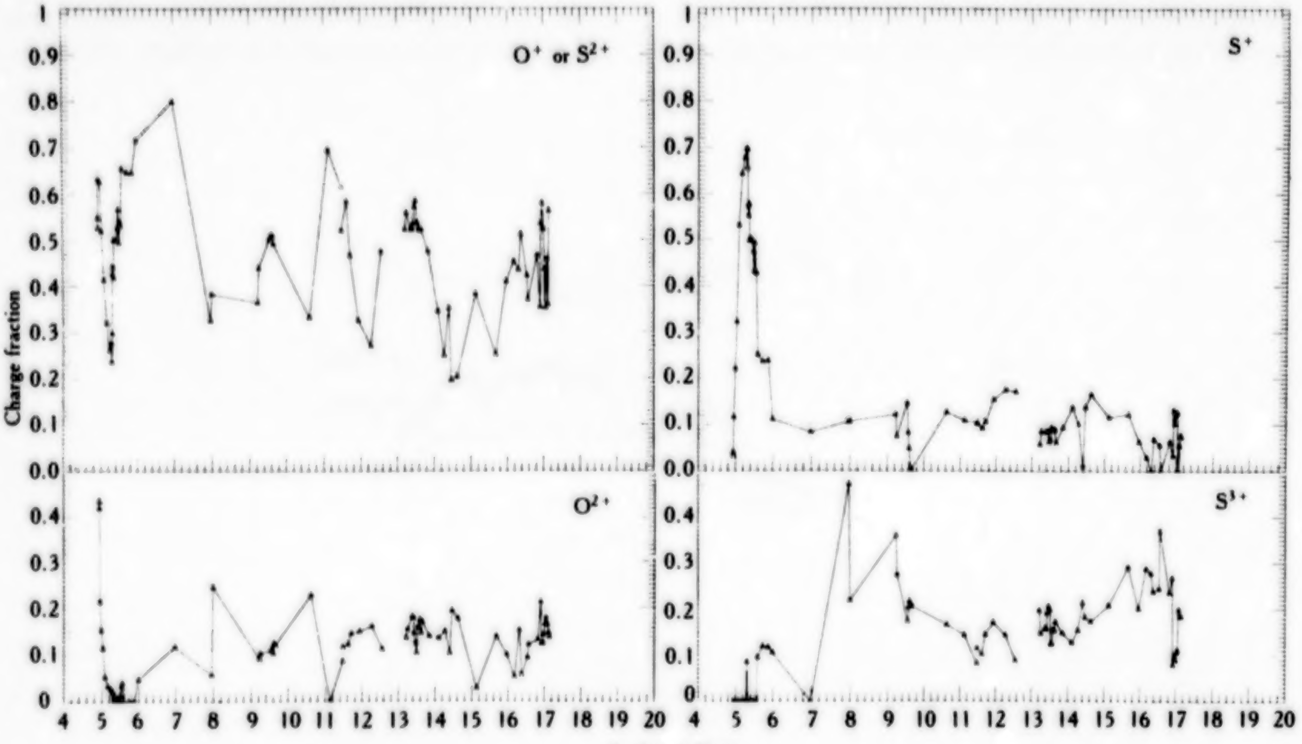

Figure 102. Ion composition from analysis of the PLS ion data on the Voyager 1 inbound pass.

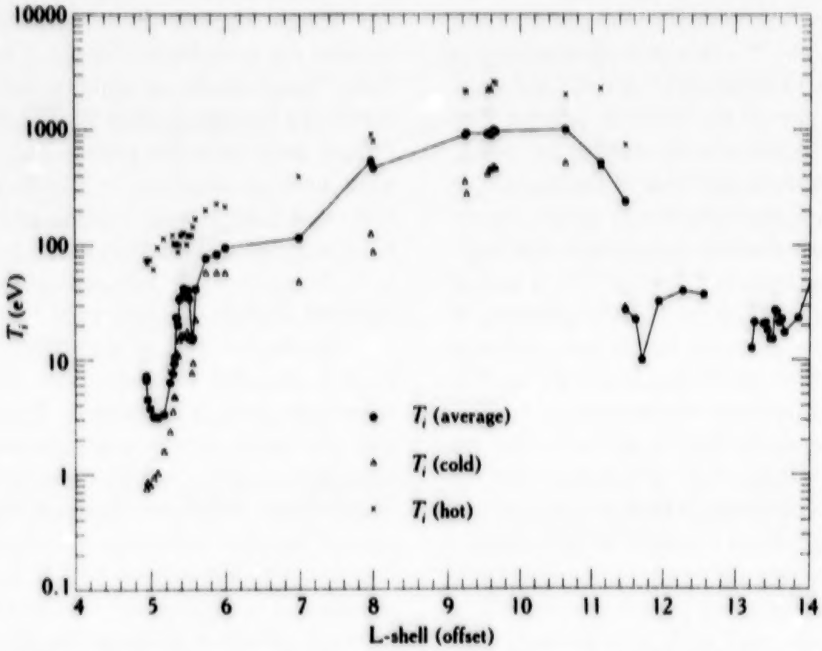

Figure 103. Ion temperatures derived from the PLS data on the Voyager 1 inbound pass.

Voyager PLS detectors were pointed roughly perpendicular to the ambient magnetic field and therefore these ion temperatures are $T_{i\perp}$. The thermal component is probably fairly isotropic but the hot component, a large proportion of which is presumably recently picked-up ions, could have very large thermal anisotropies with $T_{i\parallel} \ll T_{i\perp}$ (e.g., calculations by Barbosa and Moreno, 1987).

In figure 104 the temperatures of the electrons derived by Sittler and Strobel (1987) are plotted for the Voyager 1 inbound pass. The first thing to note is that the average electron temperature remains ~10 times

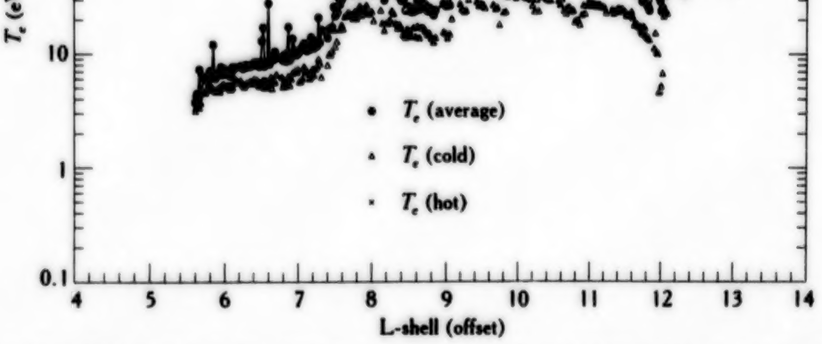

Figure 104. Electron temperatures derived from the PLS data on the Voyager 1 inbound pass. From Sittler and Strobel (1987).

less than the average ion temperature, except outside $L \sim 12$, where $T_e > T_i$. (Note that the hot component has not been included in the fits to the ion data outside 11.5 R_J.) The ratio T_i/T_e remains roughly constant while the density drops by over two orders of magnitude from the dense, almost collisional regime at $L \sim 6$ to $L \sim 11$. Second, there is a sharp rise in both T_e and T_i at the outer boundary of the warm torus between $L \sim 7$ to 8. (Further work is needed to determine if the dip in T_e between $L = 8$ and 9 is matched by a drop in T_i.) Not surprisingly, the electrons are more thermalized than the ions with the hot electrons comprising a small fraction of the total density. It is interesting to note that there is a sharp change in the fraction of hot electrons at about $L \sim 9$, outside (inside) of which n_{hot}/n_e is ~ 10 percent (<1 percent). This is the very location ($L \sim 9$ to 11) where we find we are unable to find a satisfactory fit to the ion data unless we allow the azimuthal component of the bulk velocity to have a substantial (~40 percent) lag behind corotation. The innermost well-resolved spectrum in the plasma sheet shows only a 20–25 percent lag at 11.5 R_J. Thus, there must be considerable mass-loading and/or radial transport between 9 and 11 R_J, but by 11.5 R_J the ionosphere has been able to torque the magnetospheric plasma back up toward corotation.

For investigations of the radial transport of plasma we have calculated the quantity NL^2 (where N is the total number of ions per unit L-shell) using ambipolar diffusion of a multi-species plasma for the latitudinal distribution along the (OTD) magnetic field (Bagenal and Sullivan, 1981; Bagenal, 1985). Our preliminary results suggest the radial profile of NL^2 flattens between $L \sim 8$ and 11. This implies there is either a local source of material or enhanced radial transport, consistent with the substantial deviation from corotation at the same radial distance. Previous analyses of the plasma data (using crude approximations to the instrument response) indicated a sharp drop in NL^2 between $L \sim 7$ and 8. This "ramp" was interpreted by Siscoe et al. (1981) as the outer boundary to the torus where outwardly diffusing torus plasma was impounded by the pressure gradient forces of the inwardly-diffusing energetic particles. Summers and Siscoe (1985) later inferred that a population of <3.8 keV ions would be required to produce the ramp. Our recent analysis certainly reveals that there is a substantial population of keV ions outside $L \sim 8$ but further work is needed to determine if the torus plasma is indeed impounded.

We conclude that between the torus and the plasma sheet there are three main ion populations, which are schematically illustrated in figure 105. First, there is a thermal population ($T_i \sim 50$ eV) that dominates the plasma in the torus. This population diffuses outward (possibly cooling semiadiabatically) to the plasma sheet were the cold ions are centrifugally confined to the equator. Second, there is a hot population that consists of mainly pick-up ions at $L \sim 6$ (with $T_i \sim$ 300 eV and $T_\parallel \ll T_i$). Between $L \sim 7$ and 8 the hot population begins to dominate the ion distribution, swamping the thermal population in the PLS spectra (though the actual number density remains <35 percent). Between $L \sim 7$ and 12 possible sources of these hot ions could be (1) charge exchange with fast neutrals from the torus (Barbosa et al., 1984); (2) ionization-charge exchange of neutral material from Europa; and (3) Coulomb (or wave induced) interaction with energetic particles that are diffusing inward. Outside $L \sim 12$ the hot population is not confined to the equator but spread over a large region. For the third population we lumped together all particles with energies above the 6 keV threshold of the PLS instrument. The most energetic particles (>20 MeV/nucleon-gauss, i.e., >3 MeV heavy ions at $L \sim 8$) have to be produced by an acceleration mechanism in the outer magnetosphere (reviewed by Hill et al., 1983; Barbosa et al., 1984). Heavy ions with energies <3 MeV (at $L = 8$) could have been generated by the re-ionization of fast neutrals produced by charge-exchange reactions in the torus. The ions pick up large gyro-motions in the outer magnetosphere and are heated futher (adiabatically) as they diffuse inward. Gehrels and Stone (1983) estimated the >200 MeV/gauss (~1.6 MeV at $L \sim 8$) particles could carry 10^{13} W across $L \sim 10$ (10 times more power than that carried out by the outwardly-diffusing torus particles). Paonessa (1985) has also calculated that the LECP particles between 40 and 500 MeV/gauss (~500 keV at $L \sim 8$) could carry 5×10^{12} W inward. It has generally been assumed that the remainder of the 10^{14} W needed to power the aurora is provided by less energetic particles. The trouble is that we do not have radial profiles of particles with energies between 6 and 200 keV from which to calculate the power they could deliver to the aurora and to calculate any remaining energy that could be available to heat the torus plasma.

Furthermore, even if there is enough energy available, the problem is transferring the energy from the inwardly diffusing energetic particles to the electrons at $L \sim 6$. We argue that the hot population observed by PLS could act as the intermediary. Although the ions are actually diffusing slowly outward, they interact with the inwardly diffusing energetic particles and energy is cascaded through the ion populations to the electrons that in turn stimulate the UV emissions in the torus.

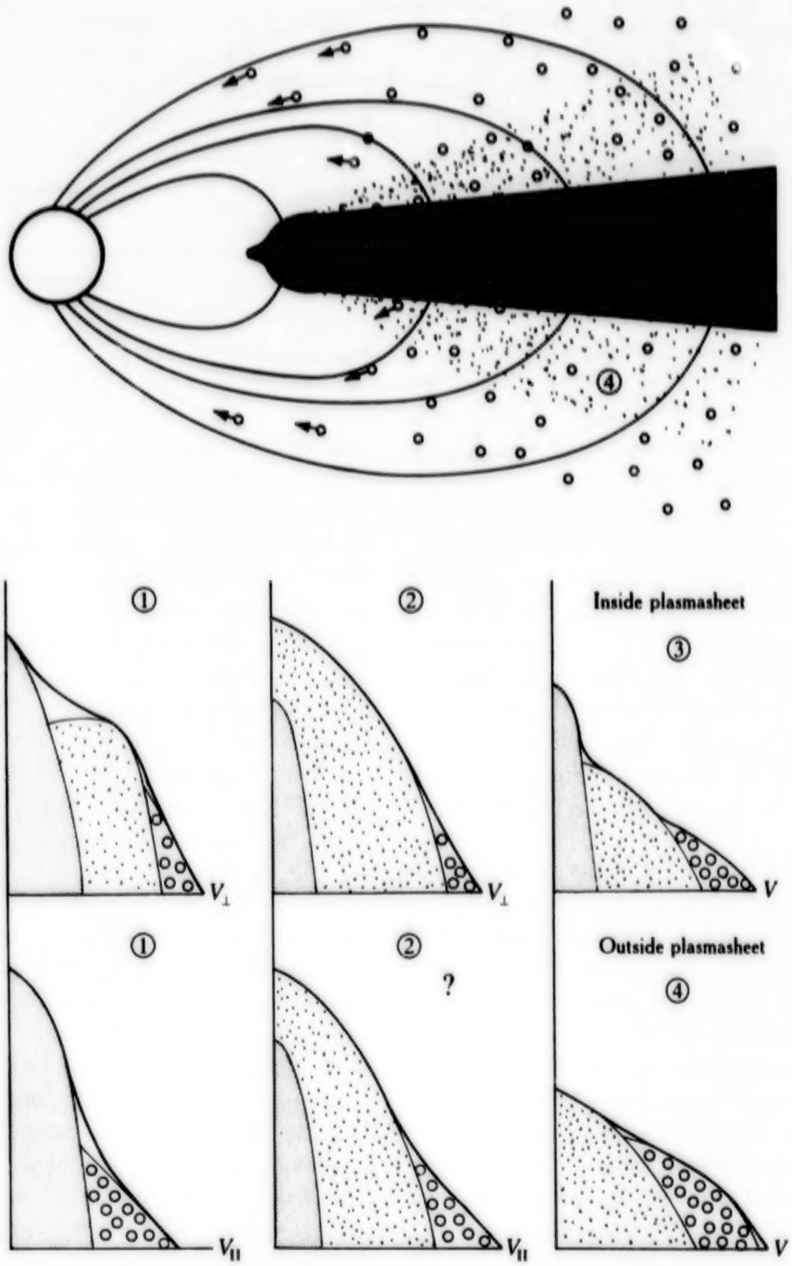

Figure 105. The three ion populations in the torus-plasma sheet region. The numbered regions are (1) the warm torus, (2) $L = 8$–12, (3) inside the plasma sheet ($<12\ R_J$), and (4) outside the plasma sheet in the middle magnetosphere.

Barbosa and Moreno (1987) show time scales for the energy transfer by Coulomb collisions between keV particles to be of the same order as diffusive time scales (i.e., ~30 days). Thus, energy could be transferred inward at the same rate as the plasma is diffusing outward. If we take the energy density of the hot component at $L \sim 8$ ($nkT \sim (6 \times 10^4)$ eV cm^{-3}), a diffusive velocity of 0.5 km s^{-1}, and an area of $2\pi 8 \times 4R_J^2$, then we find a power of ~(5×10^{12}) W would be transferred into the torus. If the energy rates are faster, then the source could be much larger.

SUMMARY

1. The torus, magnetosphere, and ionosphere are strongly coupled; to understand time-variable phe-

nomena in the jovian magnetosphere, we need to look at the whole system.

2. The cold, inner torus is well described for the Voyager 1 epoch, and Barbosa and Moreno (1987) have provided a reasonably comprehensive model. We now need to apply such a model to details of the Voyager data and to understand the observed longitudinal and temporal variations.

3. Agreement has been reached on the composition of the warm torus at the time of the Voyager 1 encounter. To obtain the observed conditions with a steady-state neutral cloud source an additional energy source of $\sim 10^{13}$ W is needed (Shemansky, 1987b).

4. There may be a problem with Shemansky's mechanism for providing a heat source by charge-exchange reactions in Io's atmosphere because a concentrated source screens out the corotational electric field. We need a full three-dimensional model of plasma-neutral interaction near Io.

5. Plasma parameters determined from PLS data provide evidence of source of plasma at $L \sim 9$. Possible sources are the ionization of neutral material from Europa or recycling of torus material.

6. There are three ion populations: (a) thermal ions ($T_i \sim 50$ eV) from Io plasma torus which diffuse out to plasma sheet; (b) a hot population ($T_i \sim 300$ eV), which could be (i) local pick-up ions from Europa material, (ii) recycled torus fast neutrals, (iii) torus ions heated by interaction with an energetic population; (c) an energetic population that has diffused inward from the outer/middle magnetosphere.

7. We need a detailed theoretical model that includes (a) centrifugally driven radial diffusion; (b) the effect of changes in ionospheric conductivity due to precipitating particles on the rate of radial diffusion (Summers, 1987); (c) an accurate (nondipolar) magnetic field model; (d) at least two dimensions, because of latitudinal separation of ion populations; (e) interactions between the many populations: (i) neutrals from Io, Europa, and charge-exchange reactions (ii) thermal, hot, and energetic ion and electron populations.

ACKNOWLEDGMENTS
The author would like to thank John Richardson, Richard Selesnick, and Ralph McNutt for their collaboration in work for this paper (which was supported under JPL/NASA contract number 957781).

References

Acuña, M. H. Private communication.

Acuña, M. H., K. W. Behannon, and J. E. P. Connerney (1983). Jupiter's magnetic field and magnetosphere. In *Physics of the jovian magnetosphere* (A. J. Dessler, ed.), pp. 1–50. Cambridge Univ. Press, New York.

Bagenal, F. (1985). Plasma conditions inside Io's orbit: Voyager measurements. *Geophys. Res.* 90:311.

Bagenal, F., R. L. McNutt, J. W. Belcher, H. S. Bridge, and J. D. Sullivan (1985). Revised ion temperatures for Voyager plasma measurements in the Io plasma torus. *J. Geophys. Res.* 90:1755.

Bagenal, F., and J. D. Sullivan (1981). Direct plasma measurements in the Io torus and inner magnetosphere of Jupiter. *J. Geophys. Res.* 86:8447.

Barbosa, D. D., F. V. Coroniti, and A. Eviatar (1983). Coulomb thermal properties and stability of the Io plasma torus. *Astrophys. J.* 274:429.

Barbosa, D. D., A. Eviatar, and G. L. Siscoe (1984). On the acceleration of energetic ions in Jupiter's magnetosphere. *J. Geophys. Res.* 89:3789.

Barbosa, D. D., and M. Kivelson (1983). Dawn-dusk electric asymmetry of the Io plasma torus. *Geophys. Res. Lett.* 10:210.

Barbosa, D. D., and M. Moreno (1987). A comprehensive model of ion diffusion and charge exchange in the cold Io torus. *J. Geophys. Res.* submitted.

Brown, R. A. (1974). Optical line emission from Io. In *Exploration of the solar system* (A. Woszczyk and C. I. Iwaniszewska, eds.), pp. 527–531. D. Reidel, Hingham, Mass.

Brown, R. A., C. B. Pilcher, and D. F. Strobel (1983). Spectrophotometric studies of the Io torus. In *Physics of the jovian magnetosphere* (A. J. Dessler, ed.) pp. 197–225. Cambridge Univ. Press, New York.

Brown, R. A., D. E. Shemansky, and R. E. Johnson (1982). A deficiency of O III in the Io plasma torus. *Astrophys. J.* 264:309.

Cheng, A. F., C. G. Maclennan, L. J. Lanzerotti, M. T. Paonessa, and T. P. Armstrong (1983). Energetic ion losses near Io's orbit. *J. Geophys. Res.* 88:3936.

Eviatar, A., R. L. McNutt, J. D. Sullivan, and G. L. Siscoe (1983). Heavy ions in the outer kronian magnetosphere. *J. Geophys. Res.* 88:823.

Gehrels, N., and Stone (1983). Energetic oxygen and sulfur ions in the jovian magnetosphere and their contribution to the auroral excitation. *J. Geophys. Res.* 88:5537.

Goertz, C. K. (1980). Io's interaction with the plasma torus. *J. Geophys. Res.* 85:2949.

Herbert, F., B. R. Sandel, and A. L. Broadfoot (1987). Observations of the jovian UV aurora by Voyager. *J. Geophys. Res.* 92:3141.

Hill, T. W. (1979). Inertial limit on corotation. *J. Geophys. Res.* 84:6554.

Hill, T. W., A. J. Dessler, and C. K. Goertz (1983). In *Physics of the jovian magnetosphere* (A. J. Dessler, ed.), pp. 353–395. Cambridge Univ. Press, New York.

Hill, T. W., and C. F. Michel (1976). Heavy ions from the galilean satellites and the centrifugal distortion of the jovian magnetosphere. *J. Geophys. Res.* 81:4561.

Ip, W.-H., and C. K. Goertz (1983). An interpretation of dawn-dusk asymmetry of UV emission from the Io plasma torus. *Nature* 302:232.

Jones, D. (1987). Io plasma torus and the source of jovian narrow-band kilometric radiation. *Nature* 327:492.

Judge, D. L., and Carlson (1974). Pioneer 10 observations of the ultraviolet glow in the vicinity of Jupiter. *Science* 183:317.

Linker, J. A., M. Kivelson, M. Moreno, and R. J. Walker (1985). Explanation of the inward displacement of Io's hot plasma torus and consequences for sputtering sources. *Nature* 315:373.

Mauk, B. H., and S. M. Krimigis (1987). Radial force balance within Jupiter's dayside magnetosphere. *J. Geophys. Res.* 92:9931.

McNutt, R. L. (1984). Force balance in the outer planet magnetospheres. In *Physics of space plasmas* (T. Cheng, ed.), pp. 179–210. Scientific Publishers, Cambridge, Mass.

McNutt, R. L., J. W. Belcher, and H. S. Bridge (1981). Positive ion observations in the middle magnetosphere of Jupiter. *J. Geophys. Res.* 86:8319.

McNutt, R. L., P. S. Coppi, R. S. Selesnick, and B. Coppi (1987). Plasma depletions in the jovian magnetosphere: Evidence of transport and solar wind interaction. *J. Geophys. Res.* 92:4377.

Moos, H. W., T. E. Skinner, S. T. Durrance, P. D. Feldman, M. C. Festou, and J.-L. Bertaux (1985). Long-term stability of the Io high-temperature plasma torus. *Astrophys. J.* 294:369.

Moreno, M. A., W. I. Newman, and M. Kivelson (1985). Ion partitioning in the hot Io torus: The influence of S_2 outgassing. *J. Geophys. Res.* 90:12065.

Neubauer, F. (1980). Nonlinear standing Alfven wave current system at Io: Theory. *J. Geophys. Res.* 85:117.

Johnson, R. E., and D. F. Strobel (1982). Charge exchange in the Io torus and exosphere. *J. Geophys. Res.* 87:385.

Paonessa, M. (1985). Voyager observations of ion phase space densities in the jovian magnetosphere. *J. Geophys. Res.* 90:521.

Richardson, J. D., and G. L. Siscoe (1983). The problem of cooling the cold Io torus. *J. Geophys. Res.* 88:2001.

Roessler, F. L., R. J. Oliversen, F. Scherb, J. Lattis, T. B. Williams, D. G. York, E. B. Jenkins, J. L. Lowrance, P. Zucchino, and D. Long (1982). Fabry-Perot/CCD observations of [SIII] and [SII] emissions from the Jupiter plasma torus. *Astrophys. J.* 259:900.

Schardt, A. W., and C. K. Goertz (1983). In *Physics of the jovian magnetosphere* (A. J. Dessler, ed.), pp. 157–191. Cambridge Univ. Press, New York.

Shemansky, D. E. (1987a). Ratio of oxygen to sulfur in the Io plasma torus. *J. Geophys. Res.* 92:6141.

Shemansky, D. E. (1987b). Energy branching in the Io plasma torus: Failure of neutral cloud theory. *J. Geophys. Res.*, submitted.

Siscoe, G. L. (1977). On the equatorial confinement and velocity space distribution of satellite ions in Jupiter's magnetosphere. *J. Geophys. Res.* 82:1641.

Siscoe, G. L. (1978). Jovian magnetosphere. *J. Geophys. Res.* 83:2118.

Siscoe, G. L., and C. K. Chen (1978). Io: A source for Jupiter's inner plasma sphere. *Icarus* 31:1.

Sittler, E. C., and D. F. Strobel (1987). Io plasma torus electrons: Voyager 1. *J. Geophys. Res.* 92:5741.

Smith, R. A., and D. F. Strobel (1985). Energy partitioning in the Io plasma torus. *J. Geophys. Res.* 90:9469.

Strobel, D. F., and S. K. Atreya (1983). Ionosphere. In *Physics of the jovian magnetosphere* (A. J. Dessler, ed.), pp. 51–68. Cambridge Univ. Press, New York.

Summers, D., and G. L. Siscoe (1985). Coupled low-energy ring current plasma diffusion in the jovian magnetosphere. *J. Geophys. Res.* 90:2665.

Summer, D., R. M. Thorne, and Y. Mei (1987). A model of plasma diffusion in the inner jovian magnetosphere incorporating precipitation induced conductivity. *Astrophys. J.*, submitted.

Thorne, R. M. (1980). Jovian auroral secondary electrons and their influence on the Io plasma torus. *J. Geophys. Res. Lett.* 8:509.

Trauger, J. T. (1984). The jovian nebula: A post-Voyager perspective. *Science* 226:337.

Vasyliunas, V. M. (1983). Plasma distribution and flow. In *Physics of the jovian magnetosphere* (A. J. Dessler, ed.), pp. 395–454. Cambridge Univ. Press, New York.

17

The Aurora and Airglow of Jupiter

John Clarke
NASA/Goddard Space Flight Center, Greenbelt

John Caldwell
York University, Toronto

Tom Skinner
University of Colorado, Boulder

Roger Yelle
University of Arizona, Tucson

Abstract

We define the aurora as atmospheric emission induced by precipitating magnetospheric particles (or secondary electrons), and airglow as scattered solar radiation and/or emissions from the polar regions of Jupiter, which include extreme ultraviolet (EUV) and far ultraviolet (FUV) emissions of H and H_2, soft X rays most likely produced by sulfur and oxygen K-shell excitation, and localized stratospheric infrared (IR) emissions. Outstanding questions about the aurora include the composition and energies of the precipitating particles (i.e., electrons, protons, and O and S ions), the source regions and energization mechanism within the magnetosphere, contributions by ionospheric electric fields to particle acceleration, and the effects of the deposited energy in heating and ionizing the upper atmosphere. Airglow processes include resonant scattering of incident solar H L_α direct photoelectron excitation of H and H_2, a potentially significant level of H_2 fluorescence, and the phenomenon of electroglow. Electroglow has been defined as soft charged particle excitation of atmospheric gas in the presence of sunlight, although ideas about the electroglow process are rapidly evolving beyond the initial definition. Important questions include the nature of the additional energy source beyond direct photoelectron and ion excitation, the role of sunlight in producing electroglow, and the associated contributions to heating and ionization of the upper atmosphere.

INTRODUCTION

The study of aurora and airglow from Jupiter has evolved rapidly over the last decade from a period of initial discoveries, which will not be reviewed here, to its present state of multiwavelength studies that emphasize the physical processes involved in the production and control of the emissions. Future studies will address the mechanisms of particle acceleration, ionospheric processes related to aurora and electroglow, the degree of solar control, and the effects on the atmosphere of the deposited energy. We will attempt to review and define the problems to be studied, in the hope that by defining the problems we may move closer to the answers.

This chapter is organized about a selection of key questions regarding the radiation observed from the upper atmosphere of Jupiter:

- Aurora—Are the incoming particles electrons, protons, ions, or some combination of these? Where in the magnetosphere do they originate? What are the chemical and thermal effects on the atmosphere?
- Airglow—What produces the H L_α bulge? How much of the dayside H L_α is scattered sunlight? What produces the bright dawn-crescent H L_α? How much H_2 emission is produced by fluorescence?
- Electroglow—What are its characteristics? What are the proposed mechanisms? What is the relationship to heating and ionization? What new observations can test the theories?

AURORA

Jupiter's aurora requires an input energy of nearly 10^{14} W to produce the observed FUV emissions, compared to roughly 10^{11} W from the Earth's aurora. This corresponds to a planet-averaged ratio of auroral:solar radiation inputs that is 20–50 times higher at Jupiter than at the Earth. We study Jupiter as an extreme case of the effect that a planetary magnetosphere can have on the upper atmosphere.

Precipitation of electrons, protons, and sulfur and oxygen ions have all been hypothesized for Jupiter's aurora: electron precipitation based on arguments for wave-particle scattering in the Io torus (Thorne and Tsurutani, 1979), protons based on their copious abundance in the jovian magnetosphere and the difficulties in explaining the energy required to power the aurora with just electrons (Goertz, 1980), and sulfur and oxygen ions from the composition of the Io torus and evidence for heavy ion acceleration and loss near 8 R_J based on phase space calculations of in situ ion density measurements (Gehrels and Stone, 1983). Observationally, the FUV auroral spectra of H L_α and H_2 bands are well fit by laboratory spectra of H_2 excited by 10–100 KeV electrons modified by a modest amount of hydrocarbon absorption (Yung et al., 1982). Since the emission spectrum does not change greatly for electron energies higher than roughly 100 eV, secondary electrons collisionally produced by incident ions or protons could equally well explain the spectra. However, protons and ions would create other unique spectral signatures.

Soft X-ray observations of Jupiter by the Einstein X-ray Observatory (Metzger et al., 1983) have revealed localized emission from the polar regions with very soft energy spectra (200 eV to 1 KeV). Potential mechanisms for the X rays are electron bremsstrahlung and S and O K-shell emission. Because electron bremsstrahlung would require a total energy of 10^{15} to 10^{16} W, which is unreasonably larger than the 10^{13} W deduced from the

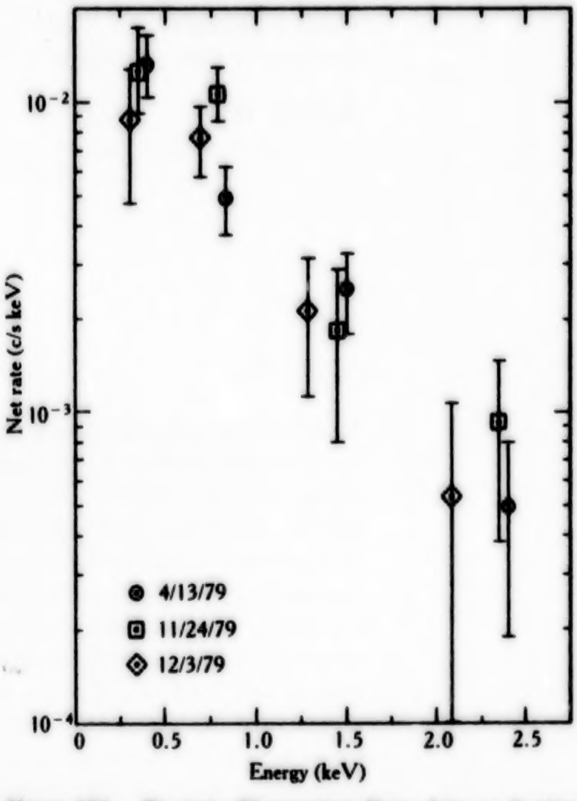

Figure 106. Einstein Observatory X-ray data on Jupiter's aurora by Metzger et al. (1983). "The X-ray count rate spectra from Jupiter for the three imaging proportional counter observations. Channels 3 through 8 have been paired." See table 15 for a tabulation of count rates (counts/s) for the three Einstein X-ray observations.

Table 15. Net Source Rates[a]: 0.2-3.0 keV

UT		Exposure Time (s)	Source (counts/s)	Background (counts/s)	Net (counts/s)
Time	Start stop				
13 April 1979	0100 0639	5986	0.018 ± 0.002	0.006 ± 0.001	0.012 ± 0.002
24 November 1979	0222 1710	5276	0.025 ± 0.002	0.012 ± 0.001	0.013 ± 0.002
2 December 1979	0213 0749	8338	0.041 ± 0.002	0.029 ± 0.001	0.012 ± 0.002

[a] After Metzger et al., 1983

FUV fluxes, Metzger et al. prefer the S and O K-shell mechanism (see fig. 106). If this is correct, the individual K-shell features should be resolvable at higher resolution, unlike the bremsstrahlung continuum. However, if ions are precipitating from the Io torus region, they will be slowed down by collisions in the atmosphere and also produce recombination radiation. Recently Waite et al. (1988) have obtained high signal international ultraviolet explorer (IUE) spectra in a search for lines of OI, SI, SII, and SIII and have set upper limits to their detection at levels (compared to the H_2 fluxes) significantly lower than expected for precipitating ions. The most stringent limit was set for OI 1304 Å, which was not detected at a limit 30 times less than predicted for a pure ion aurora. However, the X-ray data provide strong evidence for ion precipitation. A consistent picture is obtained for both data sets if electrons of 10–100 KeV energies produce the FUV emission observed, whereas the ions are sufficiently energetic to penetrate below the homopause where resulting FUV emissions are absorbed by hydrocarbons before leaving the atmosphere. This requires a systematically higher energy for the ions than electrons, roughly 100–300 KeV/nucleon or greater, and this in turn suggests different acceleration processes for the ions and electrons. Finally, there are few constraints on a population of more energetic electrons that penetrate into the FUV-absorbing regions below the homopause, so that the observed FUV emissions may represent only the tip of the auroral iceberg.

Proton precipitation has been observed spectroscopically in the Earth's aurora since the early 1950s by Doppler shifted Balmer alpha line emission excited by charge exchange of incident fast (roughly 50 KeV) protons (Meinel, 1951), as shown in the upper panel of figure 107. This same asymmetric line profile should be observed at high resolution in Jupiter's H L_α emission if protons are precipitating, since protons of a few MeV energy are needed to penetrate to the assumed auroral emission altitude. Initial high-resolution IUE observations in a program to study this phenomenon (Clarke and Waite, unpublished) have revealed a very pronounced lack of any strongly Doppler-shifted emission

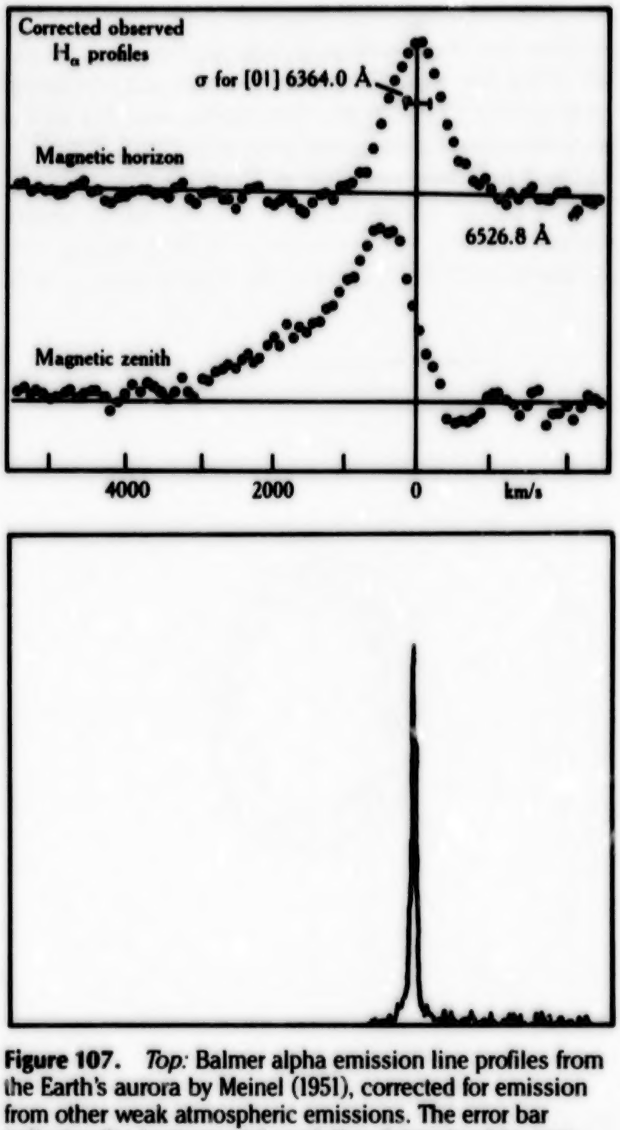

Figure 107. *Top:* Balmer alpha emission line profiles from the Earth's aurora by Meinel (1951), corrected for emission from other weak atmospheric emissions. The error bar indicates the instrumental resolution determined by measurement of the [OI] line, and the maximum observed field-aligned blueshift corresponds to a proton energy of roughly 50 KeV. *Bottom:* HL_α auroral spectrum of Jupiter from the IUE Observatory (Clark and Waite, unpublished), plotted at the same velocity scale as the Meinel data. The high-energy proton precipitation so evident in the Earth's aurora is clearly not present on Jupiter, although the line is broadened over the instrumental resolution (see text).

(lower panel of fig. 107), although the auroral H L_α line appears broadened by an energy equivalent of 10–100 eV proton motions. The lack of proton precipitation is surprising, given the wealth of protons in the magnetosphere. This further supports the picture of electron excitation of the observed FUV emission. The low-energy Doppler broadening that is observed may be due to ionospheric current systems, similar to those in the Earth's auroral zones, and the strength of this emission will indicate the relative contribution to the total auroral budget of ionospheric processes.

The magnetospheric location of the auroral acceleration and precipitation is best studied by spatially resolving the auroral zones. This was accomplished best during the Voyager encounters, leading to the identification of auroral emission at the latitudes of the Io torus field lines, as seen in figure 108 (Broadfoot et al., 1981). The extent of the auroral emission toward higher latitudes (greater L-shells) is less tightly constrained, and precipitation may extend over a large range of field lines from the torus outward. Further spatial information about the FUV emission has been derived by comparing the observed variation in intensity with longitude to a modeled brightness distribution (by Skinner and Moos, 1984 and Skinner et al. 1984 using IUE and Herbert et al., 1987 using the Voyager ultraviolet spectrometer [UVS]). Both studies indicate a longitudinally confined bright region in the northern auroral zone, centered near 180° longitude, and a more uniform southern auroral zone with an apparent brightness maximum near 0° longitude. These longitudinal patterns are consistent features over time scales of years, although the brightness of the aurora varies over days and months. Herbert et al. have pointed out that these intensity maxima are at longitudes where the mirror point altitude is decreasing with time for particles drifting in longitude, in the sense that they are either electrons or positive ions whose motion is dominated by the corotation lag of the host region of the Io torus (i.e., drifting opposite to the electrons). Higher spatial resolution observations of the auroral zones will greatly assist identifying the precipitation regions in the magnetosphere.

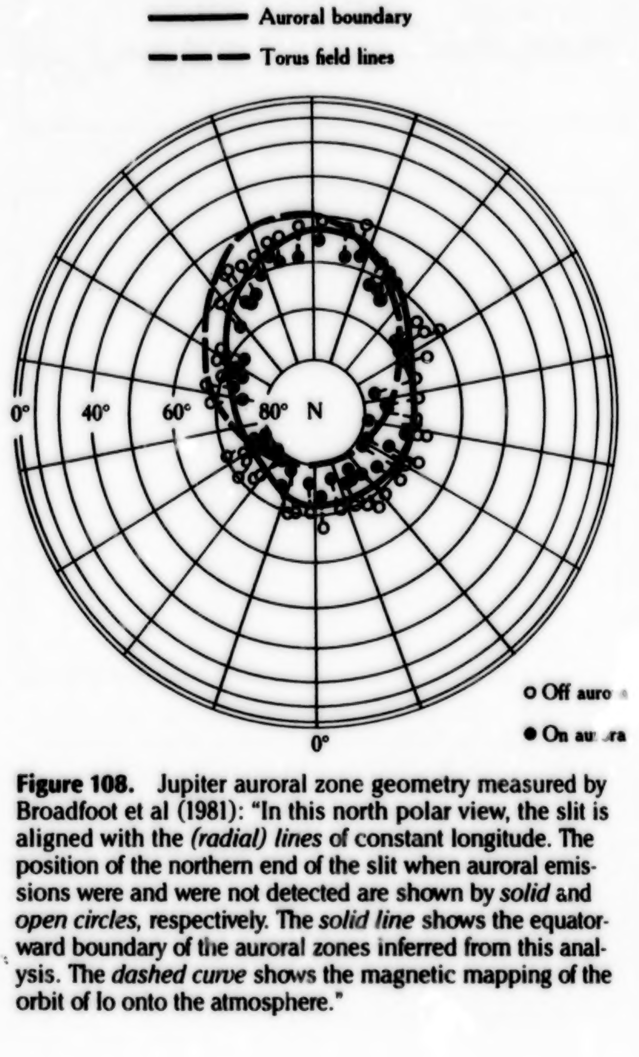

Figure 108. Jupiter auroral zone geometry measured by Broadfoot et al (1981): "In this north polar view, the slit is aligned with the *(radial) lines* of constant longitude. The position of the northern end of the slit when auroral emissions were and were not detected are shown by *solid* and *open circles*, respectively. The *solid line* shows the equatorward boundary of the auroral zones inferred from this analysis. The *dashed curve* shows the magnetic mapping of the orbit of Io onto the atmosphere."

Additional information about both the location of the energy deposition and the effects on the atmosphere is derived from near-IR observations from ground-based telescopes. Several independent groups have identified enhanced molecular emission from the auroral bright regions: in ammonia at 10.3 μm (Kostiuk et al., 1977), stratospheric methane at 7.8 μm (Caldwell et al., 1980), acetylene at 13 μm (Drossart et al., 1986), and a decrease in ethane emission at 12 μm (Kostiuk et al., 1987).

The northern IR hot spot is more localized than the FUV bright region and is somewhat extended in longitude. It has consistently been observed at 8 μm wavelength at System III longitude 180°, latitude 60° N, since and including the first Voyager encounter in 1979 (Caldwell et al., 1988). It is always on or inside the auroral arc (i.e., magnetotail field lines), which is distinctly different from the ultraviolet geometry described above. There is, therefore, an indication that the magnetospheric sources for the auroral emission in various spectral regions may be different. The southern IR hot spot is also localized, but it drifts. It may be found anywhere from System III longitude 300° to 90°, and when tracked for a period of an hour or so, is observed to drift toward higher latitudes. Its motion is not understood.

The infrared observations also indicate that particle precipitation modifies the chemistry of the upper atmosphere in the auroral regions. Enhanced emission from CH_4 demonstrates an increased temperature there. Consistent with this, enhanced emission from C_2H_2 suggests an increased abundance of C_2H_2 there, but the C_2H_6 observations are only consistent with a decrease in C_2H_6. Also, some extremely rare gases, with abundance on the order of parts per billion, are uniquely observed in the north polar hot spot and nowhere else on Jupiter. These include C_2H_4, C_3H_4, and C_6H_6 (Kim et al., 1985).

CH_4 is the expected species for carbon in chemical equilibrium in the atmosphere of Jupiter. Elsewhere on the planet, photochemical processes lead to various disequilibrium hydrocarbons at high altitudes. In the hot spots, it appears as if energetic particles produce somewhat different disequilibrium products than does photochemistry. If there is considerable penetration of incident particles below the homopause, the resulting stratospheric FUV auroral emission would create a locally "hot" photochemical balance, and the question arises as to whether the IR emission traces these more energetic "FUV-hidden" particles, or just reflects the impact of the particles previously observed. Auroral precipitation also leads to enhanced ionization and production of H atoms by dissociation of H_2. The enhanced ionization and auroral currents may be reflected in the turbulent proton motions previously mentioned, and production of H has implications for the airglow discussed below.

Multiwavelength observations closely spaced in time could greatly elucidate the relationships between the various emissions and their production mechanisms. As examples, do the FUV and IR bright regions vary together? Does the auroral brightness follow observable changes in Io torus density and/or temperature? Would an enhancement in localized atmospheric emissions from Io be followed by auroral activity? Do the X-ray intensities correlate with FUV and/or IR brightness? Is the appearance of bright X-ray emission accompanied by sulfur and oxygen line emission in the FUV? Does the degree of proton precipitation increase under certain circumstances? To answer these questions we will need more consistent multiwavelength coverage rather than much higher quality data.

AIRGLOW

We limit our discussion of airglow to radiative scattering processes, as distinguished from diffuse charged particle excitation, which is discussed as electroglow.

Diffuse H L_α He 584Å, and H_2 Lyman- and Werner-band emissions are observed throughout the sunlit atmosphere of Jupiter (see fig. 109, taken from Shemansky, 1985). No H_2 emission has been detected from the dark atmosphere (upper limit roughly 1/10 the sunlit

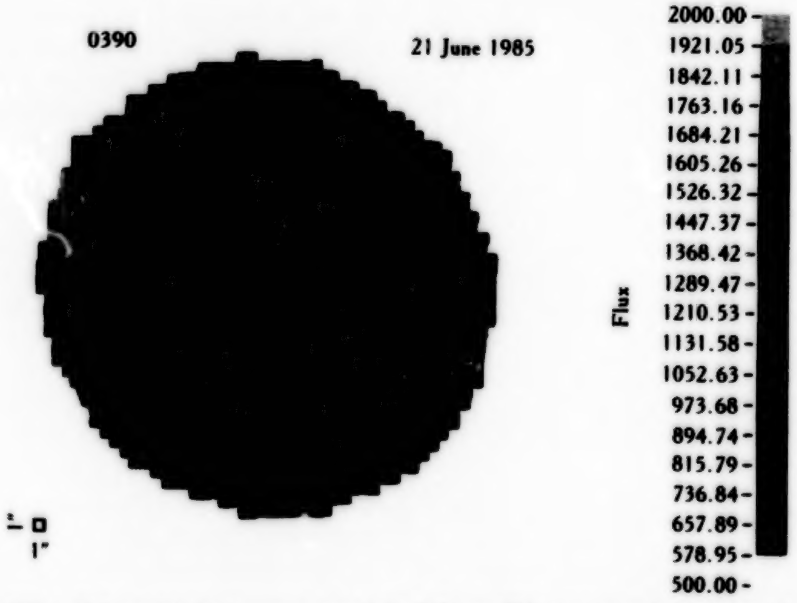

Figure 109. Color-added intensity map of the 7.8 μm CH_4 emission from Jupiter's north polar auroral zone from Caldwell et al. (1987): "The thick lines are the 180° system III longitude and the equator. The longitude lines are distorted by the planet's rotation during data acquisition. The dark green *curves* near the poles represent the auroral arc (*inner*) and the magnetic foot-print of Io's orbit. The north polar hot spot, visible at 180° longitude and 60° N latitude, has been observed to be fixed at this position for over 6 years."

ORIGINAL PAGE
COLOR PHOTOGRAPH

brightness, Broadfoot et al., 1981), although H L_α covers the dark atmosphere with a similar spatial distribution to the dayside but reduced brightness (roughly 5–10 percent of the dayside brightness). One exception is bright (2–5 kR) H L_α from the dark equatorial atmosphere up to 20–30° beyond the dawn terminator, as shown in figure 110 (McConnell et al., 1980). The observed H L_α is likely to be a combination of airglow (resonantly scattered solar H L_α) and electroglow, whereas the H_2 band emissions have been interpreted as signatures of soft electron excitation (photoelectrons or a comparable process) until a recent suggestion that resonance fluorescence may contribute substantially (Yelle et al., 1987). On Jupiter the H L_α is limb-darkened, consistent with resonant scattering from an optically thick layer of H atoms, and also shows an equatorial brightening above the level expected from resonant scattering from a plane parallel layer of H atoms (Clarke et al., 1980; Sandel et al., 1980). This equatorial brightening occurs at all longitudes and peaks near 100° and is called the "H L_α bulge." It is also fixed in magnetic rather than atmospheric coordinates, and this same spatial pattern occurs in the dark atmosphere at a reduced brightness. The He 584Å dayglow appears throughout the sunlit atmosphere from resonant scattering of solar emission. McConnel et al. found a spatial variation in the emission that anticorrelates with the H L_α pattern, although Shemansky (1985) contested this result.

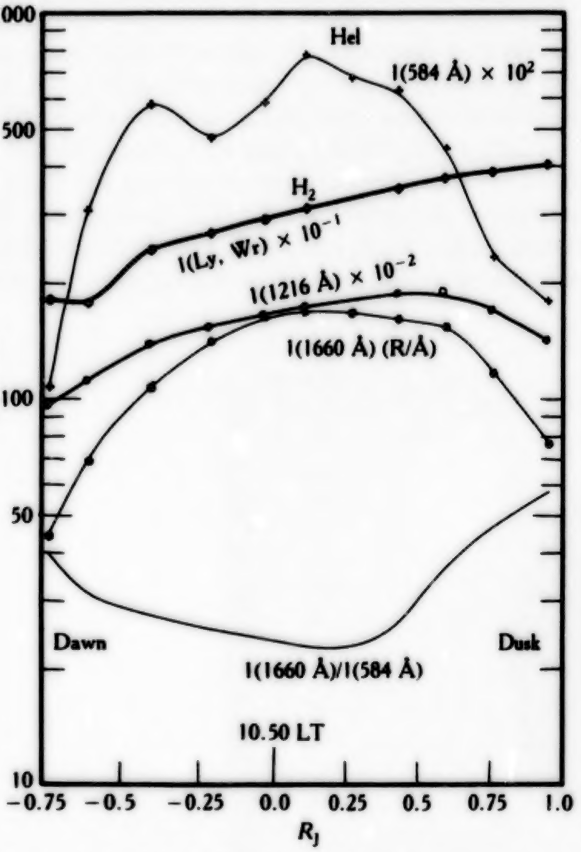

Figure 110. Spatial distribution of Jupiter's airglow and electroglow emissions from Voyager UVS data of Shemansky (1985): "Emission rates as a function of position along the equatorial belt of Jupiter obtained from Voyager 2 E-W map data averaged over all magnetic longitudes. The curvature shown in the H_2 (Lyman + Werner) emission plot in the −0.75 to −0.4 R_J is considered to be real, but the fine structure in the He (584 Å) curve may be statistical in nature.

The questions of the relative importance of resonant scattering to the dayside H L_α and production of the H L_α bulge are related. Monitoring the H L_α emission since 1979 with IUE (fig. 111) has shown that the dayside brightness at both bulge and nonbulge longitudes is proportional to the solar flux at H L_α (Skinner et al., 1988). Pure resonant scattering would thus require a constant reflectivity, or constant H column density (i.e., independent of solar photodissociation, which varies with solar cycle). This is plausible if the global H abundance is driven by auroral dissociation of H_2, which may be a sufficient source of H atoms (Yung and Strobel, 1980). Although the general equatorial brightening might be explained by an enhanced H column, the time scale for maintaining an enhanced H column at a specific longitude is short, unless there is a local driving mechanism, such as enhanced H_2 dissociation or a local temperature increase consistent with the magnetic connection. If a combination of electroglow and resonant scattering (which decreases somewhat faster than the solar H L_α, in line with a decreasing H production) is invoked, to be consistent with the data the electroglow portion must increase toward solar minimum by the same amount. Alternately, both components could follow the solar variation, but the simplest explanation appears to be that the majority of Jupiter's dayside H L_α is due to resonant scattering.

One alternate explanation for the bulge involves deposition of energy and modification of the ionosphere preferentially at bulge longitudes (Shemansky, 1985). Another alternate explanation for the bulge emission is that it represents a process similar to the tropical arcs on the Earth (Clarke et al., 1987). Independent evidence for such an equatorial anomaly has been presented, based on ionospheric profiles from radio occultation data (Mahajan, 1981). Important observations to distinguish these theories would include determining the altitude of the bulge emission in the atmo-

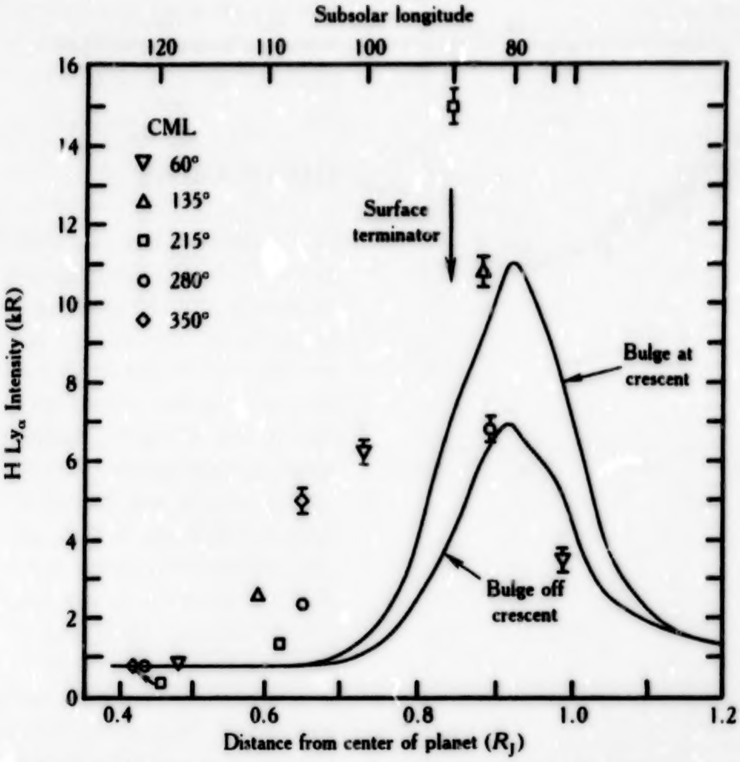

Figure 111. Jupiter's illuminated crescent and darkside (dawn) H L_α emission spatial distribution from McConnell et al. (1980): "The five separate scans shown here were taken within 8° of the equator, but at different central meridian longitudes (CML). For the scans at CML 60°, 280°, and 350°, the L_α bulge region was not on the crescent, but for the scans at CML 135°, and 215° the bulge overlapped the crescent. The *solid curves* show the apparent intensity calculated by averaging over the slit for the L_α bulge present and not present on the crescent. The nightside was assumed to have a uniform intensity of 1400 R."

sphere, higher spatial resolution maps of the bulge distribution (tropical arcs on the Earth exhibit double peaks at roughly 15 magnetic latitude, although this depends on the direction of the thermospheric winds), and high spectral resolution line profile measurements to measure the optical depth of the H column and/or fast protons through charge exchange.

Roughly 50 percent of the "dark" atmosphere H L_α can be explained by scattering of H L_α from the interplanetary H L_α glow. McConnell et al. (1980) suggest that the additional emission may be excited by precipitating particles, although the similarity to the dayside spatial distribution and difficulty in generating hemispherically diffuse particle precipitation both argue against this possibility. It may be that the extra emission is a weaker version of the dayside electroglow. The dawn crescent emission cannot be explained by scattering processes, but occurs in a region where local magnetic field lines may map into sunlit conjugate regions with much higher ionospheric densities. Field-aligned currents from the conjugate regions could lead to this emission, and this is part of the dynamo theory for the electroglow discussed below.

The dayside H_2 emission is greater by a factor of four to five than calculated photoelectron excitation rates, although apart from the energy requirement photoelectron excitation fits the spectral and spatial observations well (Prange, 1986). This emission falls under the original definition of electroglow, and Shemansky (1985) has obtained good fits to the H_2 spectra with laboratory spectra of H_2 excited by 10–50 eV electrons. Recently Yelle et al. (1987) have suggested that the emission is not electron excited, but has other characteristics suggesting a direct solar input. They show particularly (fig. 112) that the H_2 bands below 1100 Å scale in brightness as $1/r^2$ from Jupiter to Saturn to Uranus. (For reference, the flux below 1100 Å represents roughly one-third of the total H_2 flux, and the H L_α flux may be one to two times the integrated H_2 flux.) They further suggest that the H_2 bands may be largely produced by resonance fluorescence. Initial calculations of the fluorescent intensity suggest that roughly one-half of the

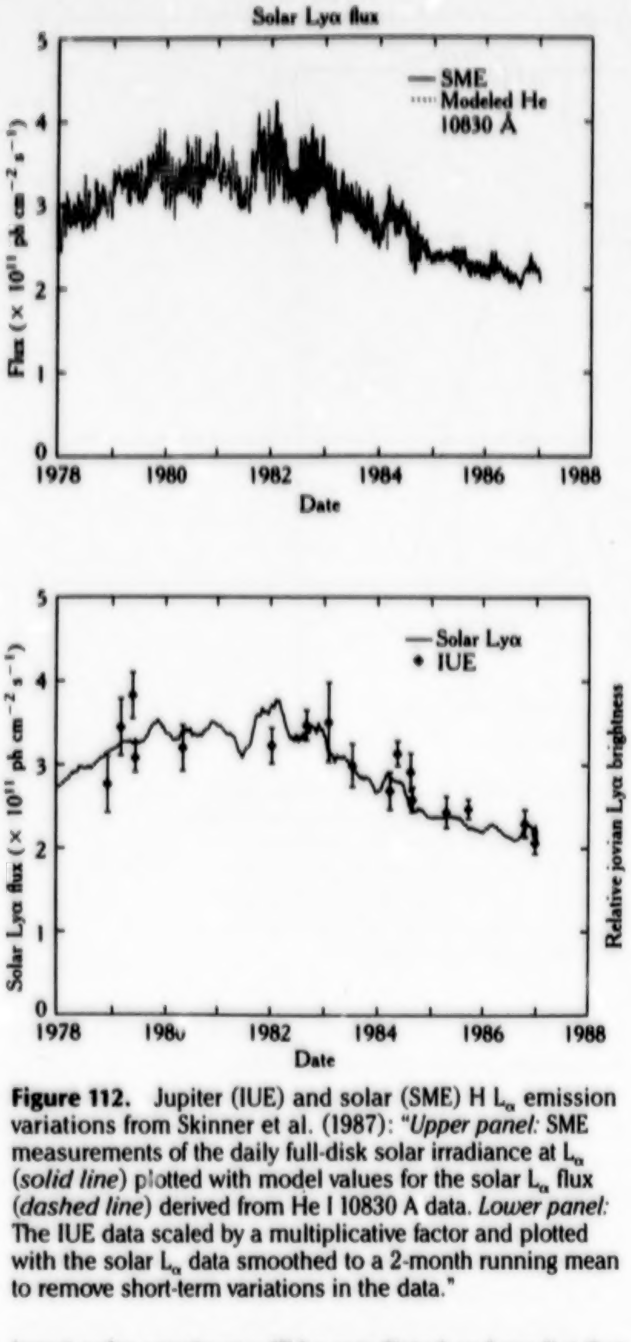

Figure 112. Jupiter (IUE) and solar (SME) H L_α emission variations from Skinner et al. (1987): "*Upper panel:* SME measurements of the daily full-disk solar irradiance at L_α (*solid line*) plotted with model values for the solar L_α flux (*dashed line*) derived from He I 10830 A data. *Lower panel:* The IUE data scaled by a multiplicative factor and plotted with the solar L_α data smoothed to a 2-month running mean to remove short-term variations in the data."

input solar spectrum will be reradiated and predict that roughly two-thirds of the observed H_2 band emission at Jupiter may result from this process. This mechanism depends on the optical depth of the H_2 column above the hydrocarbon layers. One limitation of this process is that it will not follow the observed $1/r^2$ dependence since the H_2 column varies from planet to planet. Calculations remain to be worked out for the predicted spectrum and altitude distribution of H_2 fluorescence emission, which will depend on the convolution of the H_2 spectrum with the incident solar spectrum. Moderately high resolution spectra of the diffuse H_2 emission bands may distinguish between charged particle excitation and fluorescence.

ELECTROGLOW

Electroglow has been defined by Broadfoot et al. (1986) as soft (3–50 eV) electron excitation of the sunlit atmosphere (H and H_2) peaking at altitudes just above the homopause. The energy required to produce these emissions is 10–100 times the solar EUV input available for photoelectron excitation at Uranus and a factor of four to five at Jupiter, strongly indicating an intrinsic emitting mechanism. Clearly, there is some process common to Jupiter, Saturn, and Uranus that produces diffuse emissions of H L_α and H_2 bands in the sunlit atmospheres (first suggested by Shemansky and Smith, 1986). However, it is not clear that the airglow processes discussed above can resolve this energy deficit, which would imply alternate charged particle excitation scenarios. The same process may be responsible for the very high upper atmospheric temperatures and enhanced ionospheric densities. The interpretation of this process, however, is very controversial.

The emission is largely confined to the sunlit atmosphere, with contributions from the dark atmosphere limited to 5–10 percent of the dayside intensities or less. The altitude of the emission has been measured at Saturn and Uranus, but not Jupiter, and peaks rather low in the atmosphere around neutral densities of 10^{12} to 10^{13} cm^{-3} (where the mean free path for a low-energy electron is on the order of 1 m). The emission extends at a much lower level up to the exobase. The observed peaks for H and H_2 occur at the same altitude on Saturn and Uranus, and both planets show limb brightening by similar fractions in the two emissions. Both emissions decrease in the shadow of Saturn's rings. Since they do not decrease along L-shells passing through Saturn's rings, where trapped particle populations are depleted, they are unlikely to be caused by precipitating particles. The optically thin H L_α from deep in the H column implies a Doppler spread of the emitted photons, as would be produced by fast protons and/or H atoms. Ruling out precipitation, this implies particle acceleration in situ (comparable to the Earth's E and F regions), and any mechanism that accelerates protons will also accelerate electrons.

There are differences of opinion among the authors of this chapter about the degree of relationship between the H L_α and H_2 band emissions. There are processes for producing H L_α that will not produce H_2

bands (discussed above); however, the spatial and altitude profiles of the two emissions are similar (except for the H L_α bulge). The production of the emissions by radiation processes alone (i.e., no unique process involving diffuse charged particle excitation and related to heating and ionization) is discussed above. Below we discuss the evidence for an electron-excited glow.

One model has been suggested to explain in-situ acceleration of photoelectrons and ions at the observed altitudes (Clarke et al., 1987). In the Earth's ionosphere electric fields and field-aligned currents are produced by the action of the ionospheric dynamo (see fig. 113). Any planet with a substantial magnetic field, an ionosphere, and thermospheric winds will also have such a dynamo. Field-aligned currents can lead to preferential acceleration of the high-energy photoelectrons and ions by both anomalous and classical resistivity. These currents may be induced by an ionospheric dynamo acting as a current generator, dayside-nightside ionospheric density differences, or magnetospheric convection. The diffuse nature of the electroglow suggests a dynamo process, which is based on neutral thermospheric winds in the presence of a magnetic field and is diffuse over the sunlit hemisphere. Calculations of the electron acceleration against collisional losses show that the mechanism is plausible even at the distance of Uranus (Hudson et al., 1987), and the calculated altitude of this process matches the observed altitude of the optically thin emissions on Saturn and Uranus. The $1/r^2$ scaling over a period of declining solar EUV flux is consistent with the more constant longer-wavelength FUV solar flux that contributes to thermospheric winds. This general picture is also consistent with the bright dawn crescent H L_α on Jupiter and tropical arc generation of the H L_α bulge through the action of an equatorial anomaly. The most often cited weakness of the dynamo picture is that by analogy to the Earth it would seem to imply latitudinal structure, which has been observed at H L_α but not in the H_2 bands.

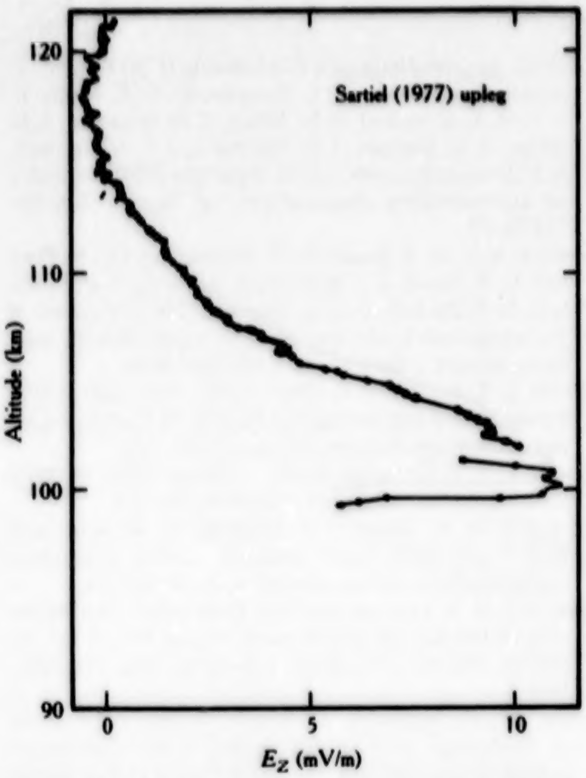

Figure 114. The Earth's E-region daytime vertical electric field (equatorial electrojet) measured at Thumba, India by Sartiel (1977).

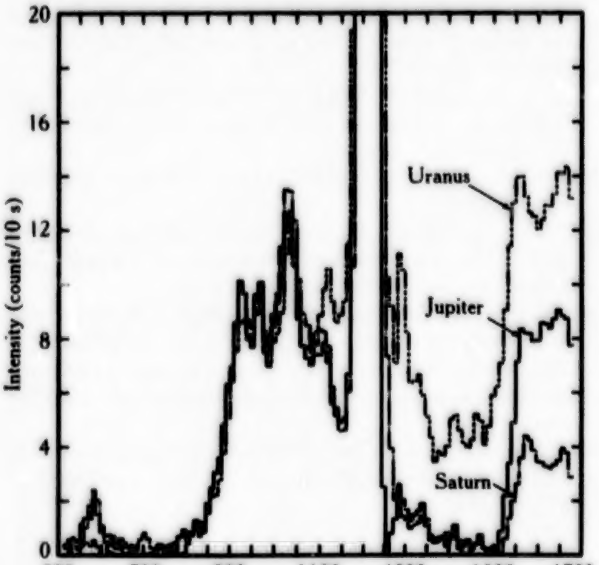

Figure 113. Voyager 2 UVS equatorial spectra from Yelle et al. (1987): "An overplot of the Jupiter, Saturn, and Uranus spectra. The Saturn and Uranus spectra have been scaled to the Jovian spectrum assuming an r^{-2} (r = heliocentric distance) intensity variation."

In terms of new observations to test the different ideas, much can be accomplished at Jupiter. Measurements of the altitude distribution are very important. Measurements of other parameters required for modeling atmospheric processes include the solar EUV flux and spectrum, thermospheric winds, and the magnitude and direction of proton acceleration. Higher-signal level H_2 spectra and spatial-variation measurements are very important. Finally, what we discover at Neptune may tell us a lot about the electroglow at Jupiter.

References

Broadfoot, A. L., F. Herbert, J. B. Holberg, D. M. Hunten, S. Kumar, B. R. Sandel, D. E. Shemansky, G. R. Smith, R. V. Yelle, D. F. Strobel, H. W. Moos, T. M. Donahue, S. K. Atreya, J. L. Bertaux, J. E. Blamont, J. C. McConnell, A. J. Dessler, S. Linick, and R. Springer (1986). Ultraviolet spectrometer observations of Uranus. *Science* 233:74–79.

Broadfoot, A. L., B. R. Sandel, D. E. Shemansky, J. C. McConnell, G. R. Smith, J. B. Holberg, S. K. Atreya, T. M. Donahue, D. F. Strobel, and J. L. Bertaux (1981). Overview of the Voyager ultraviolet spectrometer results through Jupiter encounter. *J. Geophys. Res.* 86:8259–8284.

Caldwell, J., R. Halthorne, G. Orton, and J. Bergstralh (1988). Infrared polar brightenings on Jupiter. IV. Spatial properties of methane emission. *Icarus* 74:331–339.

Caldwell, J., A. T. Tokunaga, and F. C. Gillett (1980). Possible infrared aurorae on Jupiter. *Icarus* 44:667–675.

Clarke, J. T., H. A. Weaver, P. D. Feldman, H. W. Moos, and W. G. Fastie (1980). Spatial imaging of hydrogen Lyman-α emissions from Jupiter. *Astrophys. J.* 240:696–701.

Clarke, J. T., M. K. Hudson, and Y. L. Yung (1987). The excitation of the far ultraviolet electroglow emissions on Uranus, Saturn and Jupiter. *J. Geophys. Res.* 92:15139–15147.

Drossart, P., B. Bezard, S. K. Atreya, J. Lacy, E. Serabyn, A. Tokunaga, and Th. Encrenaz (1986). Enhanced acetylene emission near the north pole of Jupiter. *Icarus* 66:610–618.

Gehrels, N., and E. C. Stone (1983). Energetic oxygen and sulfur ions in the jovian magnetosphere and their contribution to the auroral excitation. *J. Geophys. Res.* 88:5537–5550.

Goertz, C. K. (1980). Proton aurora on Jupiter's nightside. *Geophys. Res. Lett.* 7:365–368.

Herbert, F., B. R. Sandel, and A. L. Broadfoot (1987). Observations of the jovian UV aurora by Voyager. *J. Geophys. Res.* 92:3141–3154.

Hudson, M. K., J. T. Clarke, and J. Warren (1987). *J. Geophys. Res.*, submitted.

Kim, S. J., J. Caldwell, A. R. Rivold, R. Wagener, and G. Orton (1985). Infrared polar brightening on Jupiter. III Spectrometry from the Voyager IRIS experiment. *Icarus* 64:233–248.

Kostiuk, T., F. Espenek, M. Mumma, D. Deming, and D. Zipoy (1987). *Icarus,* in press.

Kostiuk, T., M. J. Mumma, J. J. Hillman, D. Buhl, L. W. Brown, and J. L. Faris (1977). NH_3 spectral line measurements on Earth and Jupiter using a 10 μm superheterodyne receiver. *Infrared Phys.* 1:431–439.

Mahajan, K. K. (1981). Equatorial anomaly in the jovian ionosphere. *Geophys. Res. Lett.* 8:66–68.

McConnell, J. C., B. R. Sandel, and A. L. Broadfoot (1980). Airglow from Jupiter's nightside and crescent: Ultraviolet spectrometer measurements from Voyager 2. *Icarus* 43:128–142.

McConnell, J. C., B. R. Sandel, and A. L. Broadfoot (1981). Voyager UV spectrometer observations of the He 584Å dayglow of Jupiter. *Planet. Space Sci.* 29:283–292.

Meinel, A. B. (1951). Doppler shifted auroral hydrogen emission. *Astrophys. J.* 113:50–54.

Metzger, A. E., D. A. Gilman, J. L. Luthey, and K. C. Hurley (1983). The detection of X-rays from Jupiter. *J. Geophys. Res.* 88:7731–7741.

Prange, R. (1986). New evidence for the role of photoelectrons in the H_2-dayglow of the giant planets. *Astron. Astrophys.* 161:L1–L4.

Sandel, B. R., A. L. Broadfoot, and D. F. Strobel (1980). Discovery of a longitudinal asymmetry in the H Lyman-α brightness of Jupiter. *Geophys. Res. Lett.* 7:5–8.

Sartiel, J. (1977). *Champs Electriques dans la region de l'Electrojet Equatorial.* Ph.D. Thesis, Univ. of Paris.

Shemansky, D. E. (1985). An explanation for the H Ly-α longitudinal asymmetry in the equatorial spectrum of Jupiter. *J. Geophys. Res.* 90:2673–2694.

Shemansky, D. E., and G. R. Smith (1986). The implication of the presence of a magnetosphere on Uranus in the relationship of EUV and radio emission. *Geophys. Res. Lett.* 13:2–5.

Skinner, T., and H. W. Moos (1984). Comparison of the jovian north and south pole aurorae using the IUE observatory. *Geophys. Res. Lett.* 11:1107–1110.

Skinner, T. E., S. T. Durrance, P. D. Feldman, and H. W. Moos (1984). IUE observations of longitudinal and temporal variations in the jovian auroral emission. *Astrophys. J.* 278:441–448.

Skinner, T. E., M. T. Deland, G. E. Ballester, K. A. Coplin, P. D. Feldman, and H. W. Moos (1988). Temporal variation of the jovian HI Lyman-alpha emission (1979–1986). *J. Geophys. Res.* 93:29–34.

Thorne, R. M., and B. J. Tsurutani (1979). Diffuse jovian aurora influenced by plasma ejection from Io. *Geophys. Res. Lett.* 6:649–652.

Waite, J. H., J. T. Clarke, and T. E. Cravens (1988). *J. Geophys. Res.*, in press.

Yelle, R. V., J. C. McConnell, B. R. Sandel, and A. L. Broadfoot (1987). The dependence of electroglow on the solar flux. *J. Geophys. Res.* 92:15110–15124.

Yung, Y. L., G. R. Gladstone, K. M. Chang, J. M. Ajello, and S. K. Srivastava (1982). H_2 fluorescence spectrum from 1200 to 1700 Å by electron impact: Laboratory study and application to jovian aurora. *Astrophys. J. Lett.* 254:L65–L69.

Yung, Y. L., and D. F. Strobel (1980). Hydrocarbon chemistry and Lyman alpha albedo of Jupiter. *Astrophys. J.* 239:395–402.

18

Spectral Analysis of Jovian Auroral Emissions

G. R. Gladstone
University of Colorado, Boulder
T. E. Skinner
University of Colorado, Boulder

Abstract

Beginning in early 1981, a comprehensive set of 14 International Ultraviolet Explorer (IUE) observations of the jovian aurora, each comprised of ~10 spectra, has been devoted to mapping the north and south pole emissions over complete rotations of the planet. The long-term nature of this study makes the IUE data set especially valuable, since they augment and extend our knowledge of the jovian aurora derived from the Voyager "snapshot." In addition, the resolution of the IUE short-wavelength spectrograph is ~3 times better than that of the Voyager ultraviolet spectrometer (UVS). Using a detailed model for electron-impact excitation of H_2 together with an up-to-date model jovian atmosphere and an accurate radiative transfer code, we are able to determine the column density of CH_4 above the auroral emission layer to very high precision. This provides an important constraint on the structure of the auroral atmosphere and the energy spectrum of the precipitating particles. Preliminary results determined from applying the model to two spectra representing the brightest and the weakest auroral emissions observed with IUE are presented. The sensitivity of the model to changes in the auroral particle energies and the composition of the atmosphere is also examined.

INTRODUCTION

Auroral processes play an important role in the upper atmosphere of Jupiter. Since their discovery by the Voyager UVS instruments (Broadfoot et al., 1981), the auroral H_2 Lyman- and Werner-band emissions in the spectral region from 1200 Å to 1700 Å have been extensively monitored by the IUE observatory (e.g., Clarke et al., 1980; Durrance et al., 1982; Skinner et al., 1984). In addition to the ultraviolet emissions, auroral "hotspots" are observed in the infrared bands of methane (e.g., Caldwell et al., 1980; Caldwell, this volume) and acetylene (e.g., Drossart et al., 1986) (though ethane band emissions either show no brightenings or actually get dimmer in the auroral regions [e.g., Kostiuk et al., this volume; Bjoraker et al., this volume]).

The power required to produce these emissions has been estimated to be ~10^{14} W (e.g., Gérard and Singh, 1982; Yung et al., 1982), which is approximately equal to the power in the total solar flux incident on Jupiter at wavelengths below about 2100 Å. A large fraction of this energy must go into heating of the upper atmosphere. Large amounts of H_2 must be dissociated and/or ionized in the auroral region, and, if the precipitating particles are energetic enough to penetrate the homopause, the resultant ion-neutral chemistry will greatly modify the hydrocarbon abundances in the region.

The identity of the particles that power the aurora is not known, although three possibilities—electrons, protons, or heavy ions (most likely oxygen and sulfur from the Io torus)—have been suggested. The leading candidates are energetic O and S ions, which are scattered into the auroral regions while diffusing in toward Io (picking up lots of energy in the process), from the outer magnetosphere. These ions had originally escaped from Io by recombining with electrons to form a "neutral wind," but some were photoionized before they could escape the jovian magnetosphere (Eviatar and Barbosa, 1984; Gehrels and Stone, 1983). The emissions expected from these precipitating ions have not been positively identified in the ultraviolet (UV) spectra of the aurora, although Kim (1987) discusses a tentative identification of the O I triplet at 1304 Å.

Extending the approach of Yung et al. (1982), we have modeled two IUE auroral spectra to look for the effects of hydrocarbon absorption on the H_2 Lyman- and Werner-band emissions. Since the Yung et al. study was made, both data and models have improved considerably. By fitting the amount of hydrocarbon absorption in the IUE spectra we can determine very accurately the mean energy of the precipitating particles, if the structure of the atmosphere is well known. This will greatly assist in the identification of the particles. Alternatively, if the energy spectrum of the precipitating particles is given, we can determine very accurately the atmospheric structure in the auroral regions. This will provide important constraints on the effect of the aurora on the chemistry in the polar regions of Jupiter.

Since, at present, neither the auroral atmospheric structuren or the energy spectrum of the precipitating particles are independently known, our results can be used only to constrain which combinations of these two items are allowable. However, it may be possible to determine the atmospheric composition in the auroral region independently. This might be accomplished, for example, by studying the reflected contribution (at wavelengths longer than ~1650 Å) to the IUE auroral spectra.

OBSERVATIONS

The geometries of the two IUE spectra we have chosen to model in this study are shown in figure 115. Both spectra were obtained using the large aperture of the short-wavelength prime (SWP) camera of the spectrograph in low-dispersion mode. The auroral zones shown in the figure are the footprints of the Io torus mapped along magnetic field lines into the upper at-

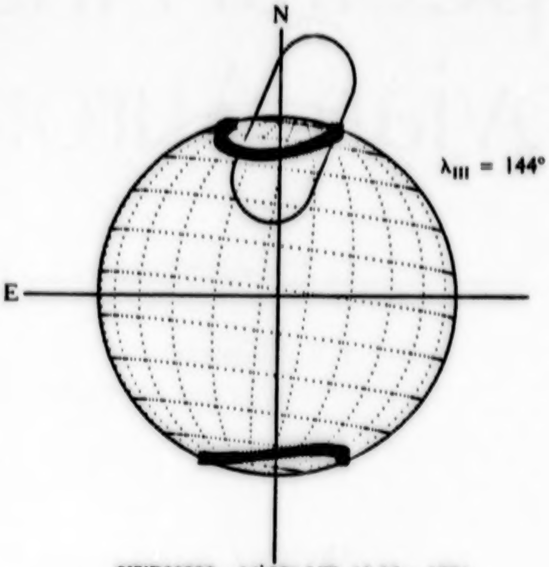

SWP22998—16^h38^m UT; 12 May 1984

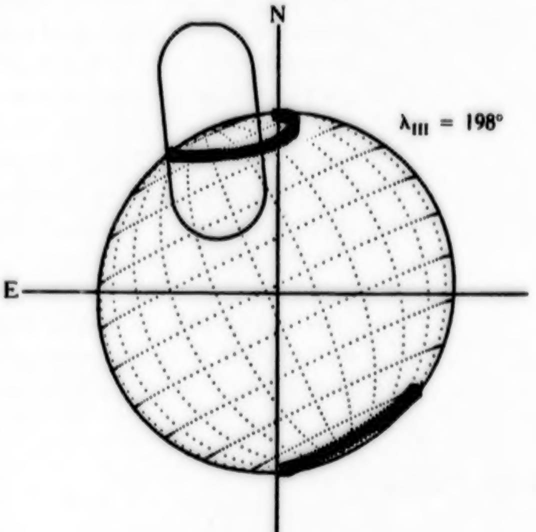

SWP11111—7^h00^m UT; 20 January 1981

Figure 115. The geometry of the observations projected onto the celestial sphere, showing the large aperture field of view of the IUE SWP spectrograph, the Io torus footprint at the north and south poles, and the orientation of Jupiter. Planetographic latitudes and longitudes are shown at 15° intervals.

mosphere (Connerney et al., 1981). One of the strongest auroras yet observed by the IUE (SWP 22998) was recorded on 12 May 1984, at a central meridian longitude (CML) of λ_{III} = 144°. The weakest aurora observed by the IUE (SWP 11111) was recorded on 20 January 1981, at a CML of λ_{III} = 198°. Both spectra were 15 minute exposures, with the large aperture offset by 15″ toward the north pole of Jupiter. The spectral resolution of the SWP for an extended object is approximately 10 Å. The spectra presented here have had a background of reflected sunlight and grating-scattered light from longer wavelengths subtracted to leave behind only those emissions that are due to the aurora. Further details of the data reduction are described by Skinner et al. (1984).

MODELS

The model atmosphere used in this study was provided by M. Allen and is a preliminary photochemical-diffusive equilibrium model of the jovian upper atmosphere in the region of the north equatorial belt (NEB). The number density profiles of several important species from this model atmosphere are shown in figure 116. At present, there are no models of the upper atmosphere in the auroral regions, and this represents the major uncertainty in our modeling. The most important difference between our model atmosphere and the actual auroral atmosphere is likely to be the value of the eddy diffusion coefficient at the homopause, K_h. Other differences, including large changes in hydrocarbon abundances and temperature profiles, are also very important but have less impact on the results of this study. In our NEB model atmosphere, $K_h = 3.0 \times 10^6$ cm^2 s^{-1}, but it is possible that in the auroral regions that K_h is much larger than this. We will discuss the implications of this in the next section.

We used a simple Chapman profile to represent the initial volume emission rates, $V(z)$, for the aurora-produced H_2 Lyman- and Werner-band emissions. The profile that corresponds to our best fit of the IUE spectra is shown for comparison with the model atmosphere in figure 116. With this initial volume excitation rate profile, plus the absorption cross sections as a function of wavelength for CH_4 and C_2H_2 (shown in figure 117), we calculated the "transmission" of the model atmosphere as a function of wavelength at 1 Å intervals in the region from 1200 Å to 1700 Å. The transmission is defined by us to be the ratio of the multiply scattered intensity, emergent at a zenith angle of 60° (as determined from the auroral zone geometry at the time of the observations; see figure 115), to the intensity that would result if the atmosphere were optically thin. This

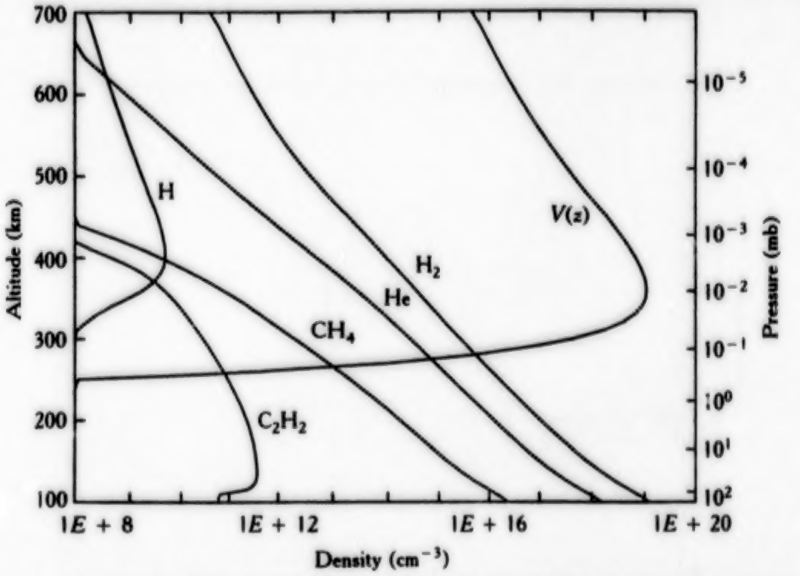

Figure 116. Altitude profiles for the main constituents of the jovian model atmosphere (NEB) used to fit the IUE data. The altitude scale refers to the height above the 6 bar level. The altitude profile of the best-fit volume emission rate (in relative units) is superimposed for comparison. This profile peaks at a vertical column density of $N_s = 1.8 \times 10^{21}$ cm^{-2}, corresponding to auroral particle energies equivalent to ~95 keV electrons. If the auroral atmosphere is highly disturbed, so that $K_h \gg 10^6$ cm^2 s^{-1}, then the required column density and particle energies will be lower.

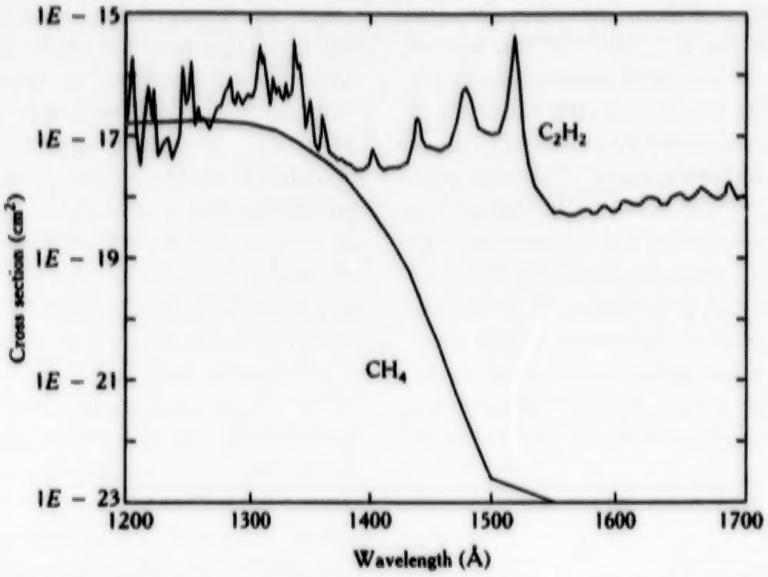

Figure 117. Wavelength dependence of the absorption cross sections for methane and acetylene, the primary absorbers of auroral emissions in the 1200–1700 Å wavelength range.

quantity is plotted as a function of wavelength in figure 118. The transmission is dominated by absorption by CH_4 below ~1450 Å, with three large absorption features of C_2H_2 also showing up strongly at 1440 Å, 1480 Å, and 1520 Å. Longward of the 1520 Å absorption feature Rayleigh scattering by H_2 and He manage to raise the transmission just slightly above unity.

An H_2 Lyman- and Werner-band modeling program (written in large part by Y. L. Yung and the late T. L. Kwok) was used to model the expected spectral distribution of the optically thin H_2 emissions. This model calculates the intensities of each rotational line of each vibrational band in both the B-X (Lyman) and C-X (Werner) bands, and includes cascading into the B

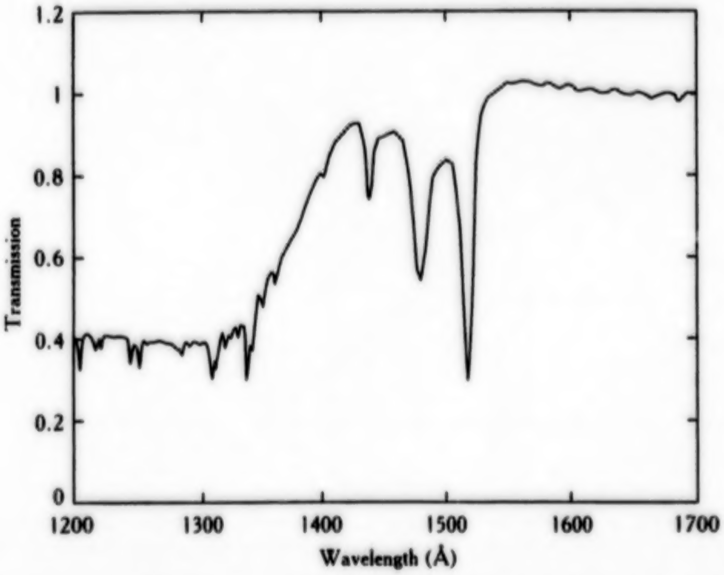

Figure 118. Effective Jupiter auroral transmission (defined in text) for the volume emission rate profile shown in figure 116. The zenith look angle used in the calculations was 60°, as determined from the observing geometry of figure 115.

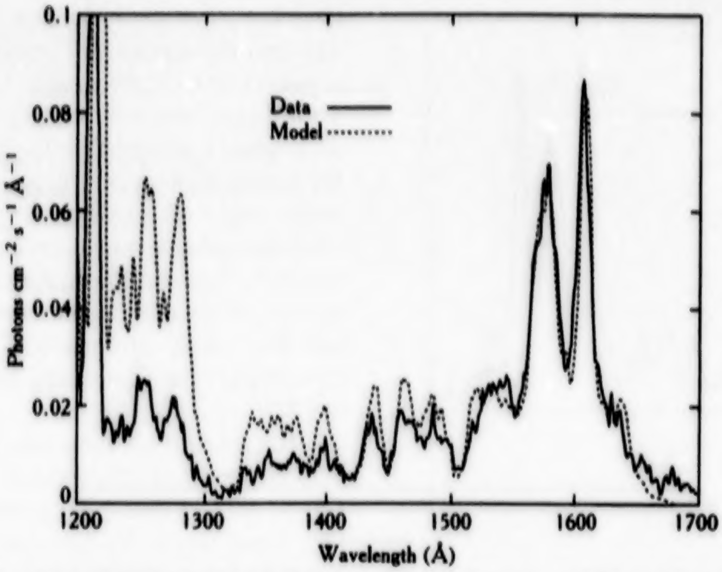

Figure 119. Auroral emissions from H Lyα and the H_2 Lyman- and Werner-bands are shown as a function of wavelength (*solid line*) for the brightest aurora observed by IUE (SWP 22998). A synthetic (model) H_2 spectrum (*dashed line*) for 100 eV electron impact has been smoothed to the IUE resolution of ~10 Å and superimposed on the IUE spectrum.

state from the higher energy *E,F* state. We assumed that the majority of the excitation of the H_2 bands is due to secondary electrons, and we have used the results of Shemansky et al. (1985) at 100 eV to represent the excitation cross sections of these secondaries. The model "laboratory" spectrum, smoothed to IUE resolution, is shown in figure 119 together with the strong (SWP 22998) aurora spectrum for comparison. The model H_2 spectrum has been normalized to the IUE spectrum at longer wavelengths where the transmission is approximately unity. It is seen that there is a general divergence of the two spectra toward shorter wavelengths (where hydrocarbon absorption is strongest), with the intensity of the observed spectra becoming progressively weaker. The weakening of the observed auroral spectra at shorter wavelengths has also been observed in Voyager UVS spectra of the jovian auroral regions (Shemansky, et al., 1985), although the data have not yet been modeled in detail. Finally, the model H_2 spectrum is multiplied by the transmission curve of figure 118, smoothed to IUE resolution, and scaled to both the strong and weak auroras. The resulting model spectra and data are shown in figure 120.

DISCUSSION

The fits that we have obtained to both auroral spectra in this way are excellent. The large-scale features are all nicely reproduced and we expect in future studies to be able to model small-scale features as well (such as the three strong C_2H_2 absorption bands). The slight shift in registration of features below 1300 Å is puzzling, but is probably due to miscalibration of the IUE wavelengths dispersion (currently being investigated by the IUE project). The main point to be made here is that the auroras on Jupiter are most definitely penetrating he homopause. This was a conclusion of Yung et al. (1982), however it was questioned by Durrance et al. (1982), who compared the jovian aurora with a laoratory spectrum of discharge-excited H_2. By varying the operating pressure of the discharge lamp, they were able to obtain a spectrum that provided a good match to the jovian auroral spectrum. However, these pressure effects have not been seen by other experimenters (see, for example, Shemansky et al., 1985), and are most likely due to edge effects in the discharge tube (J. Ajello, 1987). Therefore, an investigation into the role of hydrocarbon absorption in shaping the auroral spectra is important. Since the precipitating particles are penetrating the homopause, ion-neutral chemistry is a dominant factor in determining the hydrocarbon abundances in the auroral regions. As for the energy of the incoming particles, if our NEB model atmosphere is a good approximation of the actual auroral region atmosphere, then the average energy of the precipitating particles is the equivalent of ~95 keV electrons. The column depth of penetration by the particles is N_s ~

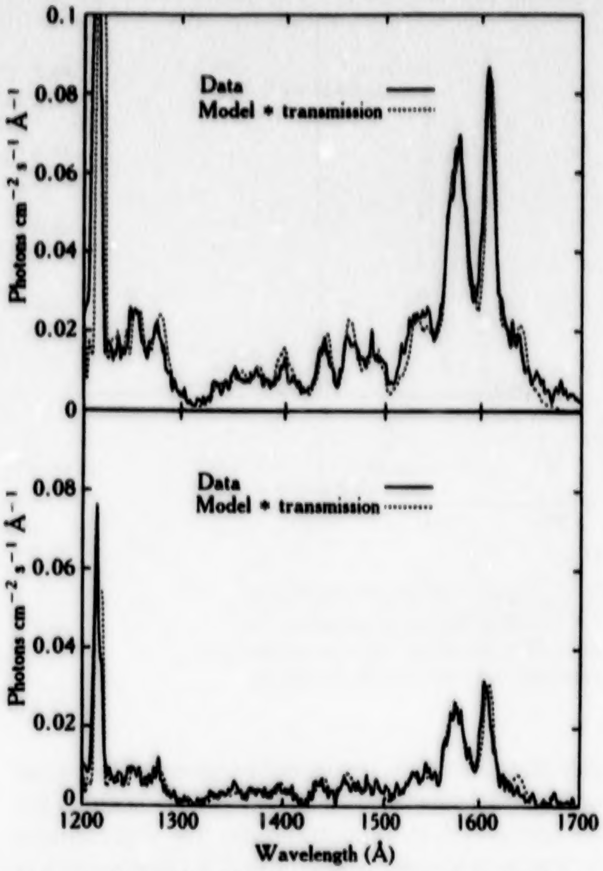

Figure 120. Our model auroral spectrum (*dashed line*), consisting of the synthetic spectrum of figure 119 multiplied by the transmission function of figure 118, is shown superimposed on the brightest (*upper panel*) and weakest (*lower panel*) auroras observed by IUE.

(1.8 × 10^{21}) cm^{-2}. If the precipitating particles are protons, then their mean energy must be ~3.3 MeV (however, Clarke et al., this volume, do not see a broadened auroral Lyman-α line profile that would accompany energetic proton precipitation). If the precipitating particles are oxygen or sulfur ions, their mean energy must be ~6–7 MeV/nucleon, and they penetrate to much greater depths than ions with the energy spectrum derived by Gehrels and Stone (1983). However, if the NEB model atmosphere is not an accurate representation of the auroral atmosphere (a likely possibility), then the best we can do is to relate the energy of the precipitating particles to the value of K_h in the auroral region. This relationship will be explored in a future paper. At present, we can say with certainty only that the column of CH_4 above the level at which the peak emission rate for the H_2 bands occurs is ~(5 × 10^{16}) cm^{-2}. Our simple Chapman profile approach to the particle transport-volume emission rate problem does not allow us to accurately determine the energy flux into the aurora (the angular size of the emitting region is also problematic). However, from previous studies (e.g., Waite et al., 1983; Gérard and Singh, 1982) we crudely estimate that the particle energy flux into the auroral regions is ~40 erg cm^{-2} s^{-1} for the strong aurora and ~16 erg cm^{-2} s^{-1} for the weak aurora. Given the ephemeral nature of auroras as we are accustomed to them on Earth, it is remarkable that the two auroras we have chosen to study, separated in time by over three years, are produced by particles having the same mean energy and only differing in input flux by a factor of ~2.5.

The method we have used is very sensitive to this column density of CH_4 above the peak emitting level, as can be seen in figure 121 in which the model spectra that result when N_s (the total column atmosphere above the peak emission level) are varied by a factor of two in either direction about the value used to obtain the fits to the data. To fit the slope of the Lyman bands in the 1300 Å to 1500 Å region and to get the peaks of the Werner bands in the 1230 Å to 1300 Å region requires N_s to be accurate to ~20 percent. Finally, we note that in future work it may be possible to obtain the column density of C_2H_2 above the peak emission level, in addition to the CH_4 column. The model spectra that result when the abundance of acetylene is increased and decreased by a factor of five relative to the standard model are shown in figure 122. Knowing the column densities of these two major hydrocarbons will greatly assist in constraining models of auroral region ion-neutral chemistry in the upper atmosphere on Jupiter.

CONCLUSIONS

We have demonstrated that the auroral spectra taken by the IUE can be modeled with a high degree of accuracy to yield information on both the structure of the atmosphere in the auroral regions on Jupier as well as the flux and mean energies of the particles responsible for the aurora. This study may be considerably improved by the addition of an auroral electron (or ion) transport model to replace our simple Chapman profile approach. Topics for future study include examining the dependence of the mean energy and flux of the precipitating particles on magnetic longitude (or perhaps on local time, if the emission comes mainly from one hot spot). A model auroral atmosphere would be especially useful in our analyses, and would help tie in the UV observations with the infrared (IR) observations referred to in the introduction.

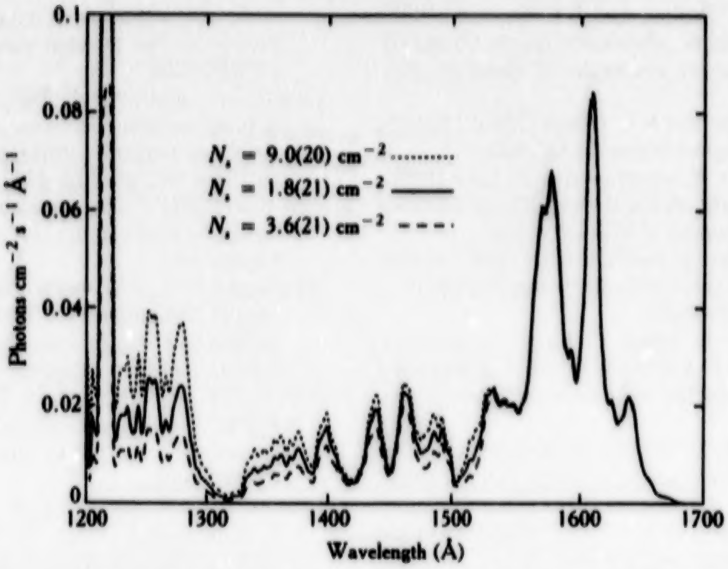

Figure 121. In this model of H_2 bands to peak source column sensitivity comparison, model auroral spectra are plotted for different values of the atmospheric column abundance (N_s) above the peak auroral emission rate level. The extreme sensitivity of the transmitted intensity to N_s indicates that the derived energy for the precipitating particles is accurate to ~20 percent. The *solid line* is the best-fitting case from figure 120.

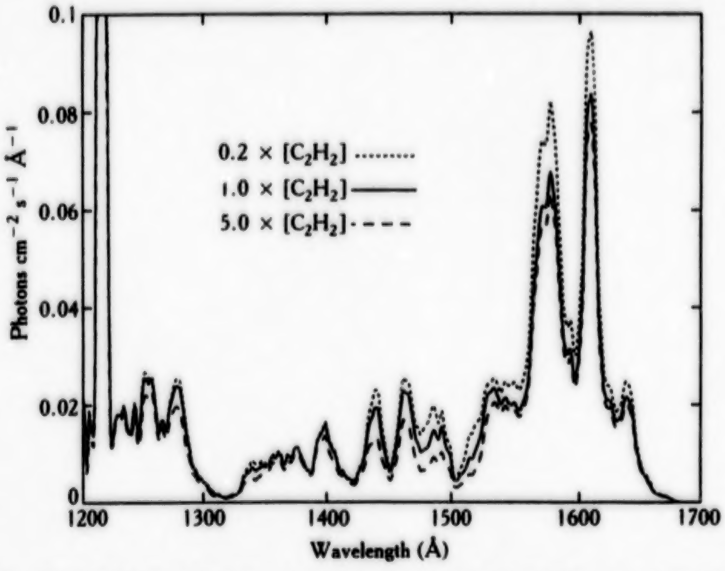

Figure 122. Model (H_2 band) auroral spectra are plotted for different values of the acetylene abundance, illustrating the sensitivity of the model to the C_2H_2 absorption features at 1440 Å, 1480 Å and 1520 Å. The *solid line* is the best-fitting case from figure 120.

ACKNOWLEDGMENTS

We would like to thank J. T. Clarke, J. C. McConnell, H. W. Moos, D. E. Shemansky, D. F. Strobel, and R. J. Yelle for helpful discussions. This work was supported in part by NASA grants NAGW-197 and NAGW-389.

References

Ajello, J. (1987). Private communication.
Allen, M. ( ). Private communication.
Broadfoot, A. L., B. R. Sandel, D. E. Shemansky, J. C. McConnell, G. R. Smith, J. B. Holberg, S. K. Atreya,

T. M. Donahue, D. F. Strobel, and J. L. Bertaux (1981). Overview of the Voyager ultraviolet spectrometry results through the Jupiter encounter. *J. Geophys. Res.* 86:8259–8284.

Caldwell, J., A. T. Tokunaga, and F. C. Gillett (1980). Possible infrared aurorae on Jupiter. *Icarus* 44:667-675.

Clarke, J. T., H. W. Moos, S. K. Atreya, and A. L. Lane (1980). Observations from Earth orbit and variability of the polar aurora on Jupiter. *Astrophys. J.* 241:L179–L182.

Connerney, J. E. P., M. H. Acuña, and N. F. Ness (1981). Modeling the jovian current sheet and inner magnetosphere. *J. Geophys. Res.* 86:8370–8384.

Drossart, R., P. Bézard, S. Atreya, J. Lacy, E. Serabyn, A. Tokunaga, and T. Encrenaz (1986). Enhanced acetylene emission near the north pole of Jupiter. *Icarus* 66:610–618.

Durrance, S. T., P. D. Feldman, and H. W. Moos (1982). The spectrum of the jovian aurora 1150–1700 Å. *Geophys. Res. Lett.* 9:652-655.

Eviatar, A., and D. D. Barbosa (1984). Jovian magnetospheric neutral wind and auroral precipitation flux. *J. Geophys. Res.* 89:7393–7398.

Gehrels, N., and E. C. Stone (1983). Energetic oxygen and sulfur ions in the jovian magnetosphere and their contribution to the auroral excitation. *J. Geophys. Res.* 88:5537–5550.

Gérard, J.-Cl., and V. Singh (1982). A model of energy deposition of energetic electrons and EUV emission in the jovian and saturnian atmospheres and implications. *J. Geophys. Res.* 87:4525–4532.

Kim, S. J. (1987). Poster presentation at workshop on *Time-variable phenomena in the jovian system*, Lowell Observatory.

Shemansky, D. E., J. M. Ajello, and D. T. Hall (1985). Electron impact excitation of H_2: Rydberg band systems and the benchmark dissociative cross section for H Lyman-Alpha. *Astrophys. J.* 296:765–773.

Skinner, T. E., S. T. Durrance, P. D. Feldman, and H. W. Moos (1984). IUE observations of longitudinal and temporal variations in the jovian auroral emission. *Astrophys. J.* 278:441–448.

Yung, Y. L., G. R. Gladstone, K.-M. Chang, J. M. Ajello, and S. K. Srivastava (1982). H_2 fluorescence spectrum from 1200 to 1700 Å by electron impact: Laboratory study and application to jovian aurora. *Astrophys. J.* 254:L65–L69.

19

Jupiter's Aurora: Detection of Quadrupole H_2 Emission

L. Trafton
J. Carr
D. Lester
P. Harvey
University of Texas, Austin

Abstract

We apparently have detected a weak emission feature in Jupiter's northern and southern aurora at 2.12 μm, the wavelength of the $S_1(1)$ H_2 quadrupole line. We observed an intensity varying with position from 0.5×10^{-3} to 1.9×10^{-3} erg cm^{-2} s^{-1} averaged over 3.8-arcsec diameter beam. This may be the auroral H_2 emission predicted by Kim and Maguire (1986) but it is only 3 to 12 percent of the predicted value.

INTRODUCTION

The existence of jovian auroral emission in the ultraviolet and thermal infrared is well documented (Broadfoot et al., 1979; Caldwell et al., 1983; Drossart et al., 1986). Until very recently, no emission had been detected at intermediate wavelengths. Kim and Maguire (1986) calculated that the intensities of the fundamental H_2 quadrupole lines in Jupiter's aurora should be comparable to the intensities of infrared objects in the Orion nebula. They suggested that the H_2 emission may be observable by ground-based telescopes through the 2-μm atmospheric window. In response, Trafton et al. (1987) searched for this emission and reported a possible detection of emission in the $S_1(1)$ H_2 line in the northern aurora. We have since obtained additional observations at twice the spectral resolution that confirm our previous result and show that emission at the wavelength of the $S_1(1)$ line of H_2 also occurs in the southern auroral region and probably at other locations on the disk. We summarize our most recent results here.

OBSERVATIONS

The observations were made on 7 and 9 July 1987 at the McDonald Observatory using the infrared Grating Spectrometer (Harvey, Lester and Carr, in preparation) at the cassegrain focus on the 2.7-m telescope. The instrument is a cooled-grating spectrograph with a 32-element InSb self-scanned detector array developed by Cincinnati Electronics, Inc. The K-band filter served as order separator and the spectral resolution was $R = 1200$.

Alternating exposures of Jupiter and a region of the sky corresponding to an offset of 60 arcsec north were recorded (30–40 exposures were used in each position). The pattern was Jupiter-sky-sky-Jupiter. Jupiter's polar radius was 18.2 arcsec and the equatorial radius was 19.5 arcsec. Pointing was accomplished with the aid of a large television viewing screen. The observations of July 9 were obtained during the morning twilight when the sky background was changing rapidly. However, the observations were short enough for this variation to be approximately linear over each pair of observations. Therefore, summing, pairs of Jupiter-sky observations allowed the sky subtractions to average out correctly.

We obtained spectra with System III longitudes ranging from 220 to 350°. Figure 123 shows the positions on Jupiter of the spectra. Table 16 summarizes the observations and results. We have not yet had an opportunity to observe the active region of the northern aurora near λ_{III} (1965) = 180°, at high-spectral resolution. The notation NNW and NNE corresponds to positions within 3 arcsec of the northern limb with abscissa half the equatorial radius from the center toward the west and east limbs, respectively. The seeing on July 7 averaged 4–5 arcsec and 4 arcsec on July 9; these values are slightly larger than the aperture. If the emission comes from a smaller area, then the true emission intensities would be larger than the values we derive here. The air mass ranged from 1.35 to 1.15 on July 7 and 1.28 to 1.16 on July 9. Slight miscancellations of telluric features are therefore possible. We used the G8 III star BS437 for the flux standard and BS432 as a secondary standard. Therefore, residual features from

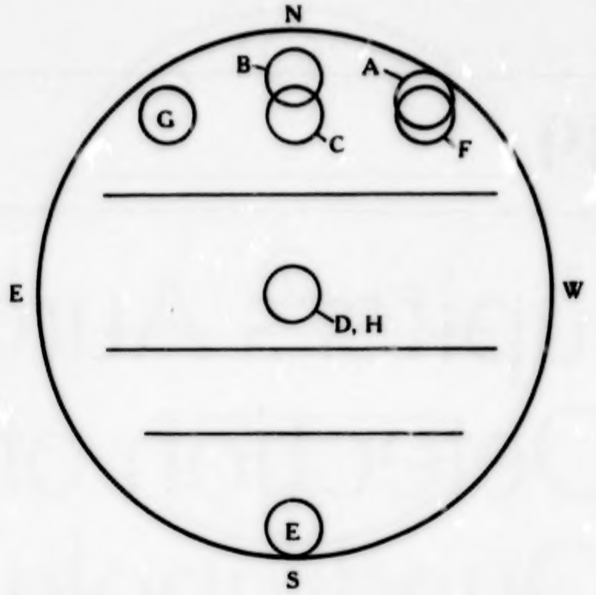

Figure 123. Schematic showing location of observations on Jupiter's (circularized) disk. The *circles* also indicate the size of the aperture. (*A*) Northern auroral region (approximate); (*B*) 3 arcsec from north limb; (*C*) 5.5 arcsec from north limb; (*D*) Jupiter's center, λ_{III} = 270°; (*E*) south polar region; (*F*) "NNW"; (*G*) "NNE"; (*H*) Jupiter's center, λ_{III} = 309°.

Table 16. Observations

UT	Exposure (minutes)	λ_{III} (1965) (degrees)	Location	Flux × 10^{16} (W m^{-2})	Intensity × 10^{6} (W m^{-2} sr^{-1})
			7 July 1987		
10:53	14	~252	NNW	2.5 ± 0.04	0.67 ± 0.01
11:06	8	~350	NNE	1.8 ± 0.02	0.46 ± 0.01
11:14	6	309	Center of disk	3.1 ± 0.02	~0.81 ± 0.01
			9 July 1987		
11:40	4	~220	Northern aurora (NNW)	4.9 ± 0.1	1.3 ± 0.03
11:32	6	260	3 from northern limb	3.4 ± 0.1	0.9 ± 0.02
11:24	6	256	5.5 from northern limb	1.5 ± 0.03	0.39 ± 0.01
11:48	6	270	Center of disk	~3.3 ± 0.1	~0.9 ± 0.02
11:53	4	272	Southern aurora	6.3 ± 0.1	1.5 ± 0.04

Tabulated errors do not include the uncertainty of the absolute calibration and continuum placement; the true errors are larger.

the ratio of a G2 V star (the Sun) to a G8 III star are expected; however, these should also be weak.

The absolute magnitudes for the standard stars were obtained from Johnson et al. (1966), Koorneef (1983), and Wamstecker (1981). We approximated the stellar energy distribution by a black body having a temperature appropriate to the star's spectral class. Since Jupiter filled the aperture for most observations, we approximated the average intensity over the beam as

$$I = \frac{0.75C_R}{A_{eff}C}, \qquad (19.1)$$

where C_R is observed count rate, A_{eff} is the effective solid angle, 2.3×10^{-10} sr, and C is the ratio of the observed count rate from the standard star to the flux of the star at this wavelength (Trafton et al., 1987).

RESULTS

Figure 124 shows the strongest emission that we have so far observed from Jupiter in the vicinity of the $S_1(1)$ H_2 line. Monochromatic flux is plotted versus wavelength. It was located at NNW at λ_{III} (1965) = 220°; that is 40° from the hot spot at λ_{III} (1965) = 178°. This spectrum is dominated by the fundamental pressure-induced H_2 band (Martin et al., 1976), which is most apparent in figure 124D, the center of the disk. The standard deviations depicted in the figure do not include the uncertainty of the absolute calibration. We determined the relative uncertainties empirically as described by Trafton et al. (1987) by dividing the first object-sky observation by the second object-sky observations and computing the rms deviation over all channels. We halved this to obtain the error of the summa-

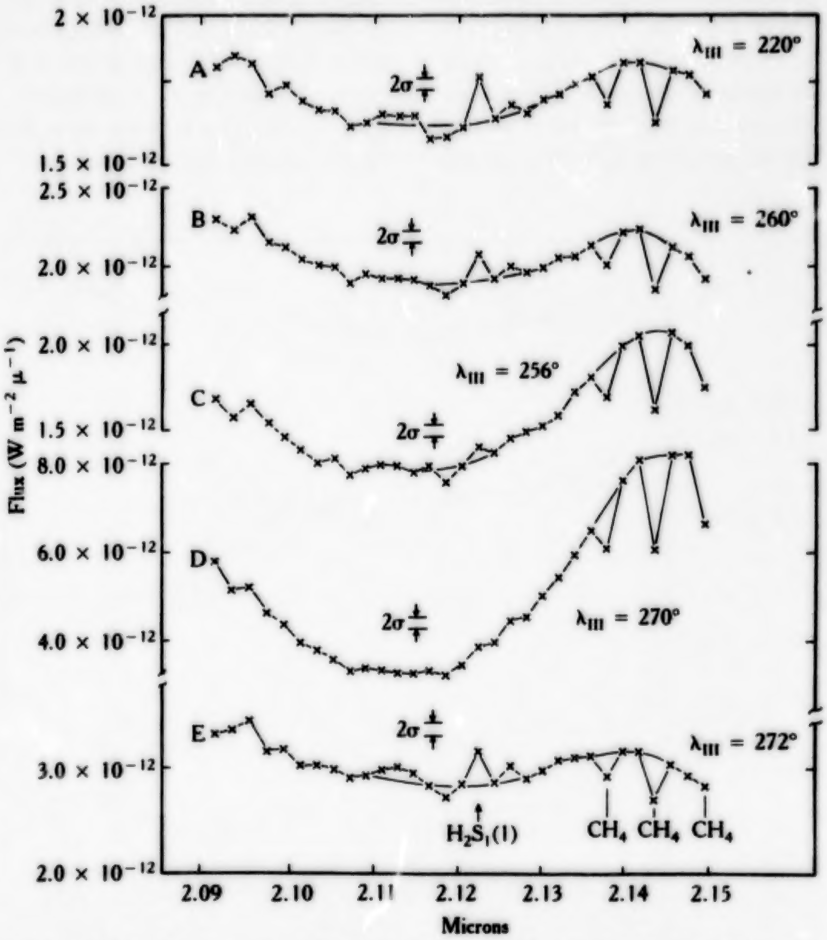

Figure 124. Calibrated spectra of Jupiter for 9 July 1987 showing the H_2 $S_1(1)$ emission feature. The positional codes indicated on the *left* of each spectrum are the same as for figure 123; the sequence is roughly from north to south on Jupiter. The System III longitude (1965) of each midexposure is shown on the *right*. Also shown are interpolated local continua levels and neighboring methane absorptions.

tion observation (one square root of 2 for twice the counts and another for not taking the ratio). The noise from the stellar calibration spectrum adds another 1.8 percent uncertainty for the July 9 spectra only; this error is included in the error given on the graphs. This error is negligible for the July 7 data owing to the lack of necessity for a secondary standard on that night (which had a spectrum of lower signal to noise ratio than the primary standard spectrum). The equivalent width of the emission feature in this spectrum is 2.2 ± 0.03 A. This corresponds to a flux of (4.9 ± 0.01) × 10^{-16} W m^{-2} or to an intensity averaged over the effective beam of (1.6 ± 0.3) × 10^{-6} W m^{-2} sr^{-1}. These errors do not include the uncertainty in the absolute calibration.

Figure 124 shows a sequence from Jupiter's northern aurora to the southern aurora. All but the first are located on the central meridian. Figures 124B, C, and D are located 3 arcsec and 5.5 arcsec from the northern limb and at the center of the disk, respectively. The strong features on the right are due to CH_4 and are strongest when the background pressure induced absorption is strongest (i.e., when the aerosol scattering is least). In contrast, the H_2 emission is least when the H_2 background absorption is greatest (i.e., the emission is greatest in the auroral regions as should be the case if the identification is correct). We evidently have detected the H_2 quadrupole emission in both the northern and southern aurora.

Figures 125F and G show the emission on July 7 at the locations NNW and NNE, respectively, for comparison at different longitudes. The different continuum levels and CH_4 absorptions reflect the slightly different distances from the limb and the strong limb brightening. Emission to some extent is visible on all of our spectra at this resolution, even at the center of the disk on July 7, where the error bars are smaller than the plotting symbol. A weak emission is evident at the proper wavelength.

We have neglected the quadrupole H_2 absorption in our measurements of the emission intensity; our values assume that the local continuum is valid in the emission line. The strength of the absorption depends on the visibility of the background H_2 and should be strongest in the center of the disk where the pressure-induced absorption is strongest. It is not evident in figure 125H, so it is probably at most a small correction for the auroral emission values.

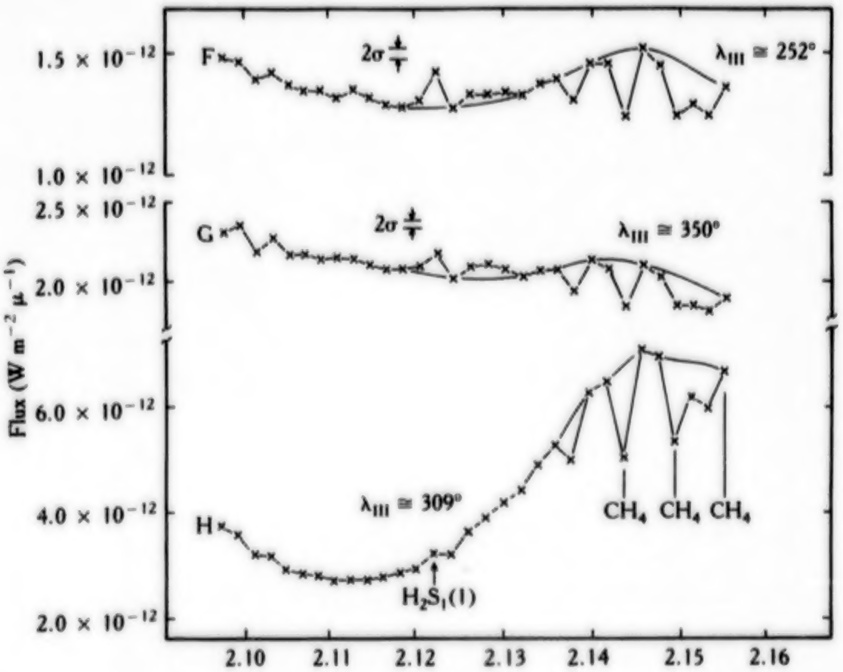

Figure 125. Calibrated spectra of Jupiter for 7 July 1987 showing the H_2 $S_1(1)$ emission feature. The positional codes indicated on the *left* of each spectrum (center of the disk) are smaller than the plotted symbols. The System III longitude (1965) of each midexposure is shown on the *right*. Also shown are interpolated local continua levels and neighboring methane absorptions.

Kim and Maguire (1986) predicted that the intensity of the auroral $S_1(1)$ H_2 emission should be detectable assuming no significant decrease in jovian auroral activity since the 1979 Voyager encounter. They calculated that 5 keV electrons precipitating 100 erg cm^{-2} s^{-1} over several square arcsecs (corresponding to our aperture size) should cause an emission intensity for this H_2 line of 1.3×10^{-5} W m^{-2} sr^{-1}. Our observations range from 3 to 12 percent of this value. Greater than expected nonradiative deexcitation of the H_2 molecules by way of collisions with H may be the result of an uncertain H density in the aurora.

To further confirm the identification of this emission and to interpret its strength, time variation, and distribution among rotational levels, we plan further observations to obtain spectra of this line and to attempt detection of the other vibrational-rotational lines of H_2 in the overtone band.

ACKNOWLEDGMENTS

This research was supported by NASA grant NGR 44-012-152. Construction and development of the Infrared Grating Spectrometer was made possible by NSF grant AST-8414652 and NASA grant NGR 44-012-152. We thank S. Kim for helpful discussions.

References

Broadfoot, A. L., M. J. S. Belton, P. Z. Takacs, B. R. Sandel, D. E. Shemansky, J. B. Holberg, J. M. Ajello, S. K. Atreya, T. M. Donahue, H. W. Moos, J. L. Bertaux, J. E. Blamont, D. F. Strobel, J. C. McConnell, A. Dalgarno, R. Goody, and M. B. McElroy (1979). Extreme ultraviolet observations from Voyager 1 encounter with Jupiter. *Science* 204:979–982.

Caldwell, J., A. T. Tokunaga, and G. S. Orton (1983). Further observations of 8 μm polar brightenings of Jupiter. *Icarus* 53:133–140.

Drossart, P., B. Bezard, S. Atreya, J. Lacy, E. Serabyn, A. Tekunaga, and T. Encrenaz (1987). Enhanced acetylene emission near the north pole Jupiter. *Icarus* 66:610–618.

Johnson, H. L., R. I. Mitchell, B. Iriarte, and W. Z. Wisniewski (1966). UBVRIJKL photometry of the bright stars. *Comm. of the Lunar and Planetary Lab.* No. 63:99–110.

Kim, S., and W. Maguire (1986). Two micron quadropole line emission of H_2 from the jovian auroral zone. In *The jovian atmospheres*, NASA Conference Publication 2441:95–98.

Koorneef, J. (1983). Near-infrared photometry II. Intrinsic colors and the absolute calibration from one to five microns. *Astron. Astrophys.* 128:84–93.

Trafton, L., J. Carr, D. Lester, and P. Harvey (1987). An upper limit to and a possible detection of Jupiter's northern auroral $S_1(1)$ H_2 quadrupole line emissions. *Icarus*, submitted.

Wamstecker, W. (1981). Standard stars and calibration for JHKLM photometry. *Astron. Astrophys.* 97:329–333.

20

Is Ethane Varying in the Jovian North Polar "Hot Spot"?

Theodor Kostiuk
Fred Espenak
Michael J. Mumma
NASA/Goddard Space Flight Center, Greenbelt

Abstract

Several ground-based observations have revealed increased emission intensity in the spectra from methane and acetylene in the jovian polar stratosphere near 180° longitude and 60° latitude. Increased stratospheric temperature was suggested as at least partly responsible for the observed methane and acetylene enhancements. Observations (in 1982, 1983, and 1986) of individual lines of ethane using Doppler-limited spectral resolution showed no increase in emission and on one occasion a decrease in the observed line intensities.

We modeled the behavior of ethane emission as a function of jovian temperature profile and stratospheric ethane abundance. Our results suggest that ethane emission in the north polar "hot spot" cannot be explained by reasonable temperature changes alone, and thus, hydrocarbon density (and therefore chemistry) must be altered in this region.

INTRODUCTION

Existing one-dimensional models (Yung and Strobel, 1980; Gladstone, 1983; Allen, 1986; Atreya, 1986) for hydrocarbon photochemistry on Jupiter do not consider spatial or temporal variability of the resultant species. Observational results show an increase in the C_2H_2/C_2H_6 mole fraction ratio from south to north on Jupiter (Maguire et al., 1985). In the north polar stratosphere at 60° N latitude and 180° longitude (System III, 1965) enhanced emission of CH_4 at 7.8 mm was observed by Caldwell et al. (1980). Analysis of Voyager infrared interferometer spectrometer (IRIS) spectra on this hot spot also showed enhanced molecular-band emission from CH_4 and C_2H_2 as well as band emission from previously undetected minor hydrocarbon constituents (Kim et al., 1985). Enhancement of line intensities of C_2H_2 was also observed by Drossart et al. (1986) as well as a significant C_2H_2 enhancement relative to C_2H_6 (Drossart et al., 1985) in the hot spot. Bjoraker et al. (1987) found north-south acetylene variability on Jupiter with a large C_2H_2/C_2H_6 emission ratio at the hot spot. We investigated the ethane stratospheric abundance and variability in this hot-spot region by measuring and modeling single lines of C_2H_2. Measurements were made using sub-Doppler spectral resolution infrared heterodyne spectroscopy near 12 mm (cf., Kostiuk et al., 1983; Kostiuk et al., 1987). Results from two measurement sets taken at the McMath Telescope at the National Solar Observatory on Kitt Peak, Arizona, in April and May 1982, with a 2-arcsec field of view, positioned at 60° N latitude and on the central meridian longitude (CML) of Jupiter, showed no significant change in the ethane emission and, thus, mole fraction near 180° longitude. The resultant C_2H_6 mole fractions are plotted versus System III, 1965, longitude in figure 126. They remained approximately constant at $2.9 \pm 0.8 \times 10^{-6}$ through longitudes of 184°. Observations at the NASA Infrared Telescope Facility on Mauna Kea, Hawaii, in October 1986 with a 1-arcsec field of view also failed to reveal any increase in ethane line emission near the north polar hot spot, as shown in figure 127a. Bjoraker et al. (1987) also found no enhancement in north polar ethane.

Data taken in April, 1983 at the McMath Telescope (Kostiuk et al., 1987) showed a decrease in C_2H_6 emission near the hot spot (fig. 127b). The mole fraction value of $\sim(1.8 \times 10^{-6})$ was retrieved from 80° to 165° CML (fig. 126). Near 180° there was a sharp drop in the retrieved C_2H_6 abundance, consistent with the disappearance of the emission. The mole fraction again increased above 200° CML, rising to a somewhat larger value of 6×10^{-6} at 235° CML. The latitudinal range per point (due to integration time used per point) is shown in figure 126. From 160° on, the measurement was continuous and the points represent the centers of a moving average of approximately half-hour stacks of data. Since measurements were made continuously during the decrease in emission and the field-of-view on Jupiter was tracked visually throughout the observation, simple guiding errors cannot explain the observations results. A discussion on the effects of guiding

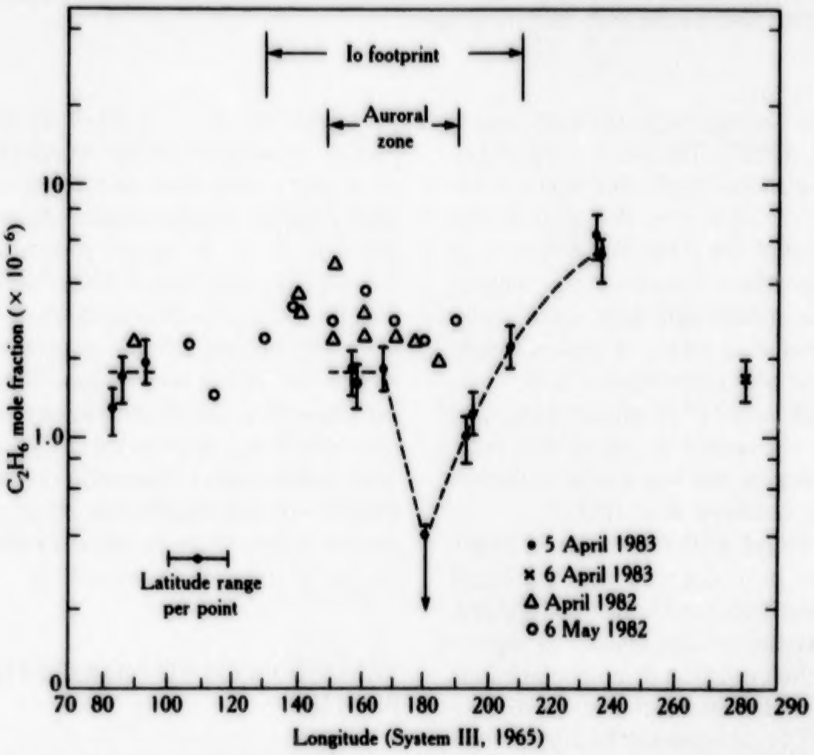

Figure 126. Retrieved C_2H_6 mole fractions versus longitude on Jupiter. The field-of-view was positioned at 60° N latitude. Note the lack of change in mole fraction in April and May 1982 and the decrease in C_2H_6 in April 1983.

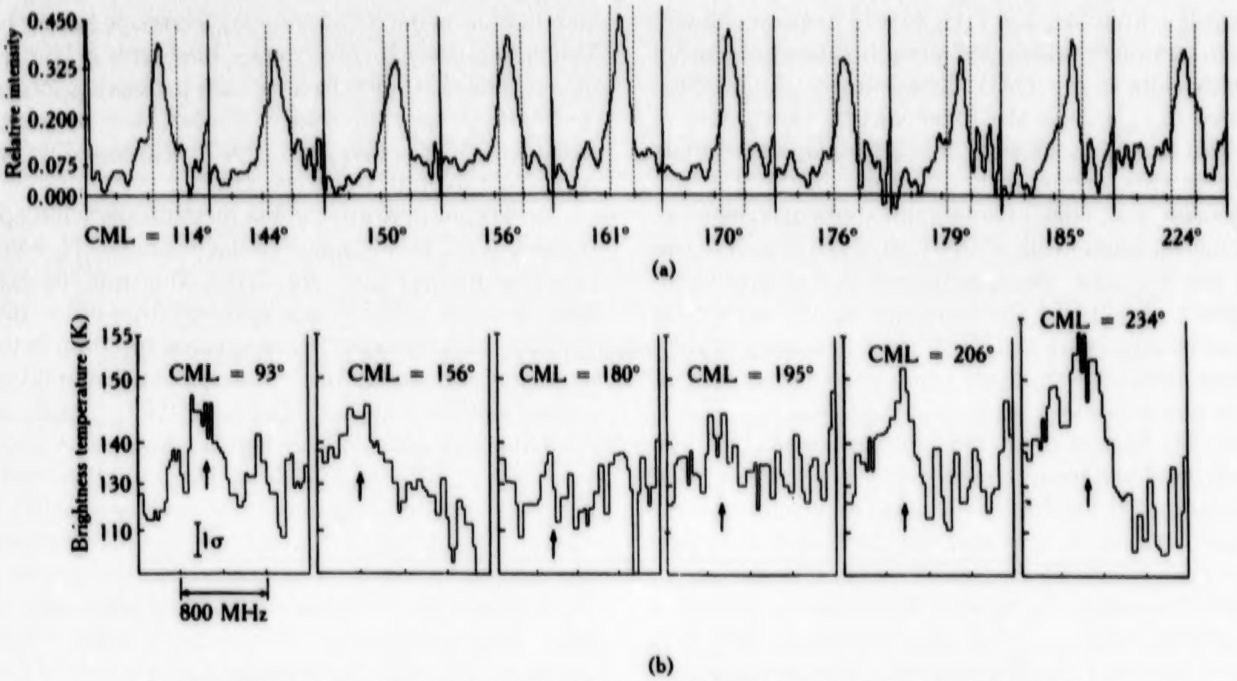

Figure 127. **(a)** Ethane emission line (RR [5,11]; 851.5051 cm^{-1}) measured on Jupiter in October 1986 with the 1-arcsec instrument beam positioned at 60° N latitude and CML as indicated. Note that near CML 180° no increase of C_2H_6 emission is observed. **(b)** Measurements of the RR (6,14) line taken in April 1983 with a 2-arcsec field of view at 60° N latitude and CML on Jupiter. Each spectrum represents about 18° in longitudinal coverage. The expected position of the ethane line is indicated by the *arrow.* The line disappears at CML = 180° (see Kostiuk et al., 1987 for details).

errors and atmospheric seeing on the retrieved data is given in Kostiuk et al. (1987). The same temperature profile and atmospheric model were used at 60° N latitude for analysis of all the data sets. The vertical error bars in figure 126 represent the precision of fit ($\sim \pm 20$ percent). The accuracy of the retrieved values is dependent on the atmospheric model and molecular parameters used and is limited to a factor of approximately two. The rapid decrease and reemergence of the C_2H_6 emission near 180° CML and 60° N latitude indicate a localized phenomena <4 arcsec in extent. The location and extent of this region are very similar to the hot spot region reported by Caldwell et al. (1980).

Kim et al. (1985) found a 10 K increase in stratospheric temperature to be consistent with enhanced CH_4 polar band emission found in Voyager IRIS spectra, but an increase in abundance was needed to explain observed increases in the emission of molecular bands of other species (e.g., C_2H_2). Drossart et al. (1986) proposed an increase in C_2H_2 abundance to explain their observations, but do not rule out thermal or nonthermal effects.

Halthore et al. (1987) developed a thermal-equilibrium model for the north polar hot spot based on Voyager IRIS data requiring upper stratospheric (pressures less than 1 mbar) temperatures between 220 and 250 K. Their model reproduces the enhanced 7.8-μm CH_4 emission. It also can be made consistent with the observed enhancement of 13.6-μm C_2H_2 emission, but requires that the acetylene abundance be increased in the hot spot region. Since Halthore et al. do not observe a significant increase in ethane emission, they infer a depletion in the hot spot of ~80 percent. In search of a single explanation consistent with all observations, we investigated the effect of changes in atmospheric temperature profiles on ethane emission lines formed in the jovian stratosphere.

VARIATION OF STANDARD TEMPERATURE PROFILE

The absolute temperature scale in our jovian measurements was established by comparison to measurements on the Moon and on a calibrated black-body reference. The uncertainty in the absolute temperature calibration was less than ±5 K. Therefore, changes in the brightness temperature $> \pm 5$ K of the measured C_2H_6 lines would be observable by us (see Kostiuk et al., 1987).

Line profiles were modeled starting with a fixed C_2H_6 mole fraction and various temperature profiles (fig. 128). The temperature at the tropopause was fixed, and the maximum incremental temperature change was assumed to occur at the top of our model atmosphere (~0.14 mbar), since heat is presumably deposited from above. Analytic continuation was used to establish temperatures at intermediate pressure levels. The modeled emergent line profiles (for RR [6,14] are shown in figure 129a. An increase (decrease) in stratospheric temperature at ~5 K at 2 mbar (~10 K at 0.14 mbar) would increase (decrease) the line brightness temperature by ~5 K. This is about the uncertainty in our temperature calibration. Greater changes in stratospheric temperature are, therefore, outside our experimental uncertainty. Thus, a simple increase in stratospheric temperature would cause a commensurate increase in the C_2H_6 line emission (fig. 129a), yet no significant increase in emission was observed in our data (at the 10 K level). In order for the line to be undetectable at our signal-to-noise ratio (and the fixed mole fraction) the stratospheric temperature at 2 mbar would have to be decreased by ~30 K (peak line brightness temperature ≤ 135 K), which is physically unrealistic (fig. 129a).

VARIATION IN C_2H_6 ABUNDANCE AND MIXING PROFILE

Figure 129b illustrates the dependence of ethane line intensity on C_2H_6 mole fraction, for a given temperature profile. The mole fractions were varied from one-quarter to four times the value (2.6×10^{-6}) retrieved from the measured spectra (fig. 129a, b), using the nominal temperature profile (fig. 128). From figure 129b it is seen that a two-fold change in C_2H_6 mole fraction would exceed our absolute uncertainty in the brightness temperature scale (~5 K).

Comparing peak brightness temperatures to those in figure 129a, an 8 K decrease in line intensity could be consistent with a two-fold decrease in C_2H_6 abundance or an ~15 K decrease in the upper stratospheric temperature profile (~8 K at 2 mbar). For the nominal temperature profile the retrieved C_2H_6 mole fraction would

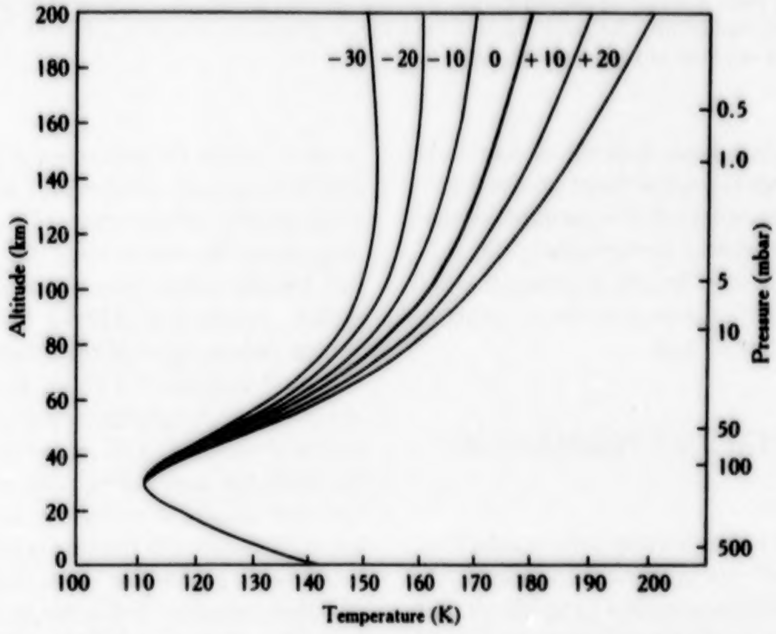

Figure 128. Model jovian temperature profiles varied by 10 K increments at the top of our model (0.14 mbar). The altitude scale is for the standard temperature profile (0). These profiles were used to investigate the sensitivity of jovian ethane emission to changes in the stratospheric temperature (see figure 129).

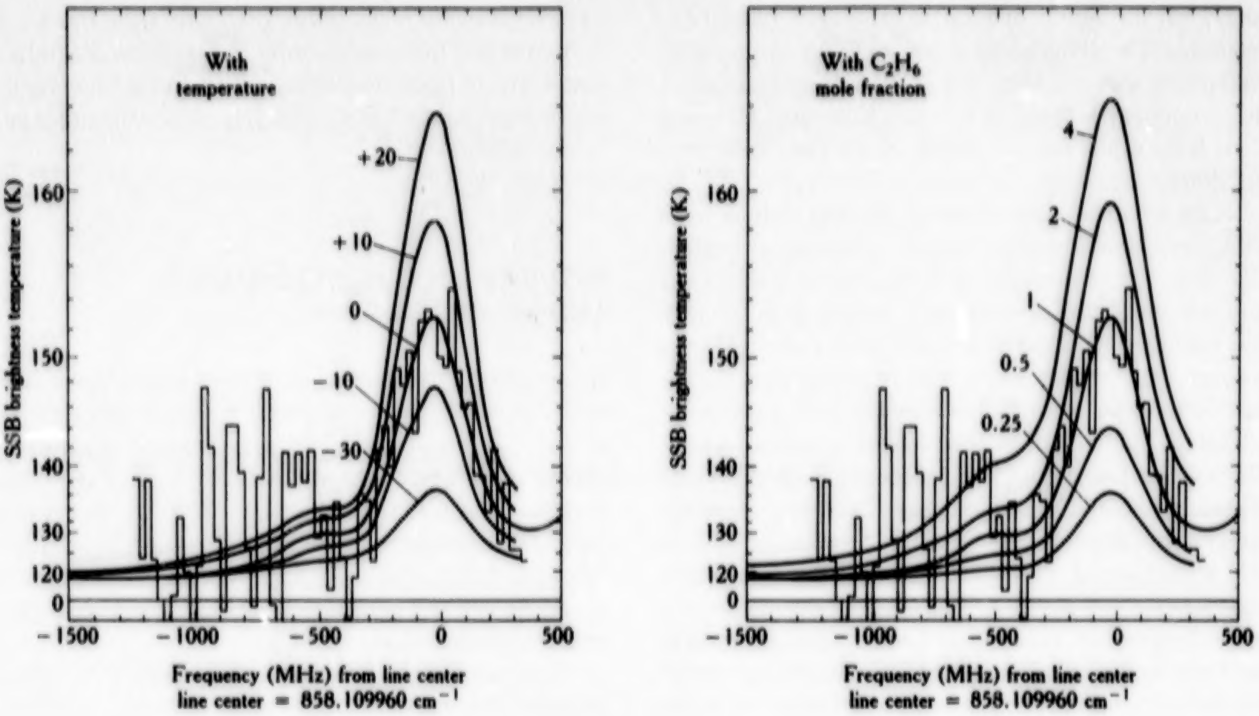

(a) (b)

Figure 129. **(a)** Stratospheric RR (6,14) lines on Jupiter (60° N) (CML = 88°) as modeled using the temperature profiles on figure 128 and a constant C_2H_6 mole fraction of 2.6×10^{-6}. Each *curve* is labeled by the incremental temperature change at 0.14 mbar of the respective temperature profile. Actual measured data are also plotted for comparison.
(b) Changes in the RR (6,14) jovian line profile (60° N) (CML = 88°) as a function of changing C_2H_6 mole fraction of Jupiter for the standard temperature profile. The *lines* are labeled by factors multiplying the mole fraction value retrieved from observations, 2.6×10^{-6}. Measured data are also plotted for comparison.

have to decrease by more than a factor of four to be undetectable at the observed noise level on the data.

If the measured line emission is to remain constant with increasing stratospheric temperature, the C_2H_6 mole fraction must decrease. To compensate for a 30 K temperature increase the ethane abundance must be reduced by nearly a factor of four.

VARIATION WITH "EXOTIC" TEMPERATURE PROFILE

In the case of a normal jovian atmospheric model (e.g., Kostiuk et al., 1983, 1987) the major contribution to the observed C_2H_6 line profile comes from regions of pressures above 1 mbar.

In an attempt to relate the hot, upper stratospheric model of Halthore et al. (1987) to observations of ethane emission, the ethane spectrum was modeled using two-layer jovian atmospheric models—a standard temperature profile for pressures > 1 mbar, an isothermal profile for pressures between 1 and 150 mbar, and a hot stratospheric temperature (T_S = 200–250 K) at altitudes above the 1 mbar level (fig. 130). We first modeled the ethane lines using an extreme temperature profile—isothermal (110 K) from the tropopause to 1 mbar (where most of the ethane is present) and hot (T_S) for pressures > 1 mbar (where CH_4 emission is observed). Such a profile would minimize ethane emission and maximize CH_4 emission, as was observed in the north hot spot region. The ethane RR (6,14) emission line modeled using the various T_S is shown in figure 131 along with the line modeled using a standard temperature profile (fig. 131a). The vertical bars on the standard emission line indicate the expected peak-to-peak noise on measured data. Note that for the exotic temperature profile in figure 130 with T_S > 220 K the expected emission line would be measurably brighter and thus observable by us. With T_S = 250 K, the line would exhibit a brightness temperature of over 170 K. At

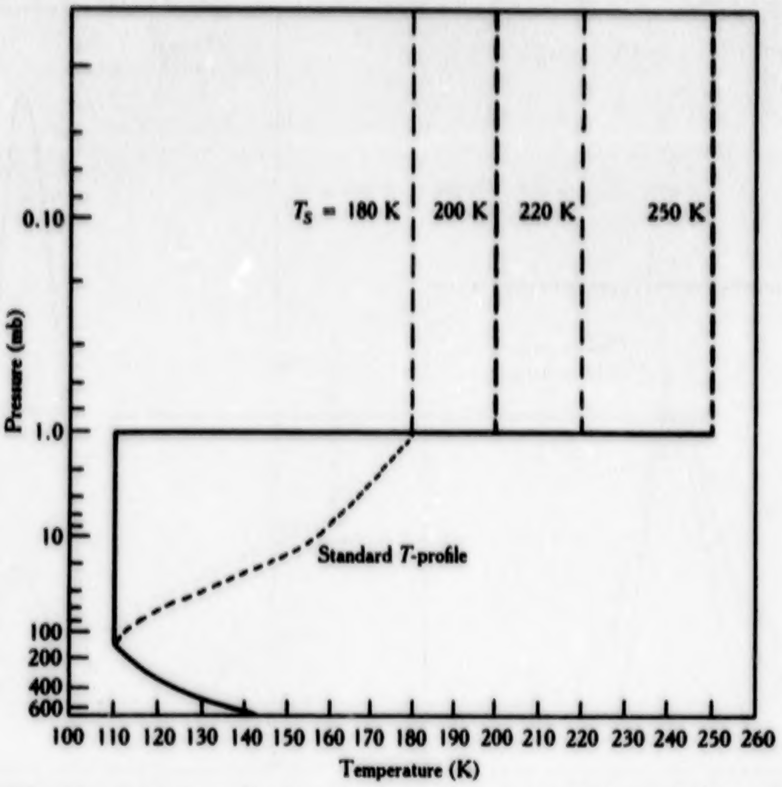

Figure 130. Temperature profiles used to test the hot-stratospheric model for enhanced CH_4 and C_2H_2 emission (see text).

T_S = 200 K, the C_2H_6 emission would have a 146 K brightness temperature and this change would be measurable. If the upper stratospheric temperature were 220 K the line brightness would be comparable to that from the standard profile. The line width, however, would be significantly different (fig. 131a). In fact, all lines formed with the exotic hot stratospheric temperature profile would be narrow, since the lines are formed at pressures below 1 mbar, where pressure broadening is greatly reduced. The off-line continuum intensity is also lower because the temperature profile in the lower stratosphere has been artificially reduced. This difference in widths would also be observable by us, even at the measured signal-to-noise ratio seen in figure 131a.

The isothermal lower stratosphere could not eliminate the ethane emission for the proposed hot T_S. With such a profile, T_S would have to be $\leq$180 K (approximately standard) in order to reduce the C_2H_6 line below the measured noise level. A more realistic standard lower stratospheric temperature profile (fig. 130) only enhanced the modeled emission lines further.

In the ethane measurements we made, there is no evidence of such line enhancements or narrowing and, thus, of temperature distributions shown in figure 130. Therefore, the observations of stratospheric C_2H_6 emission on Jupiter cannot be made consistent with an elevated upper stratospheric temperature model alone (if the mixing ratio is taken to be constant with altitude above the 100 mbar level).

CONCLUSIONS

The above analyses shows that, if ethane model fraction remains constant, changes >5 K in the standard stratospheric temperature on Jupiter would be observable as increased emission in infrared heterodyne spectroscopic measurements of C_2H_6 lines. For a fixed temperature profile, a two-fold change in C_2H_6 mole fraction on Jupiter would also be observable. The effects of an exotic hot stratospheric temperature profile ($T_s \gtrsim$ 200 K) in the hot spot would also be observable in our measurements. No such effects or significant C_2H_6 line enhancement was observed in the hot-spot region.

The disappearance of ethane emission near CML = 180° in the April 1983 measurements (Kostiuk et al., 1987) can be explained by a large reduction of

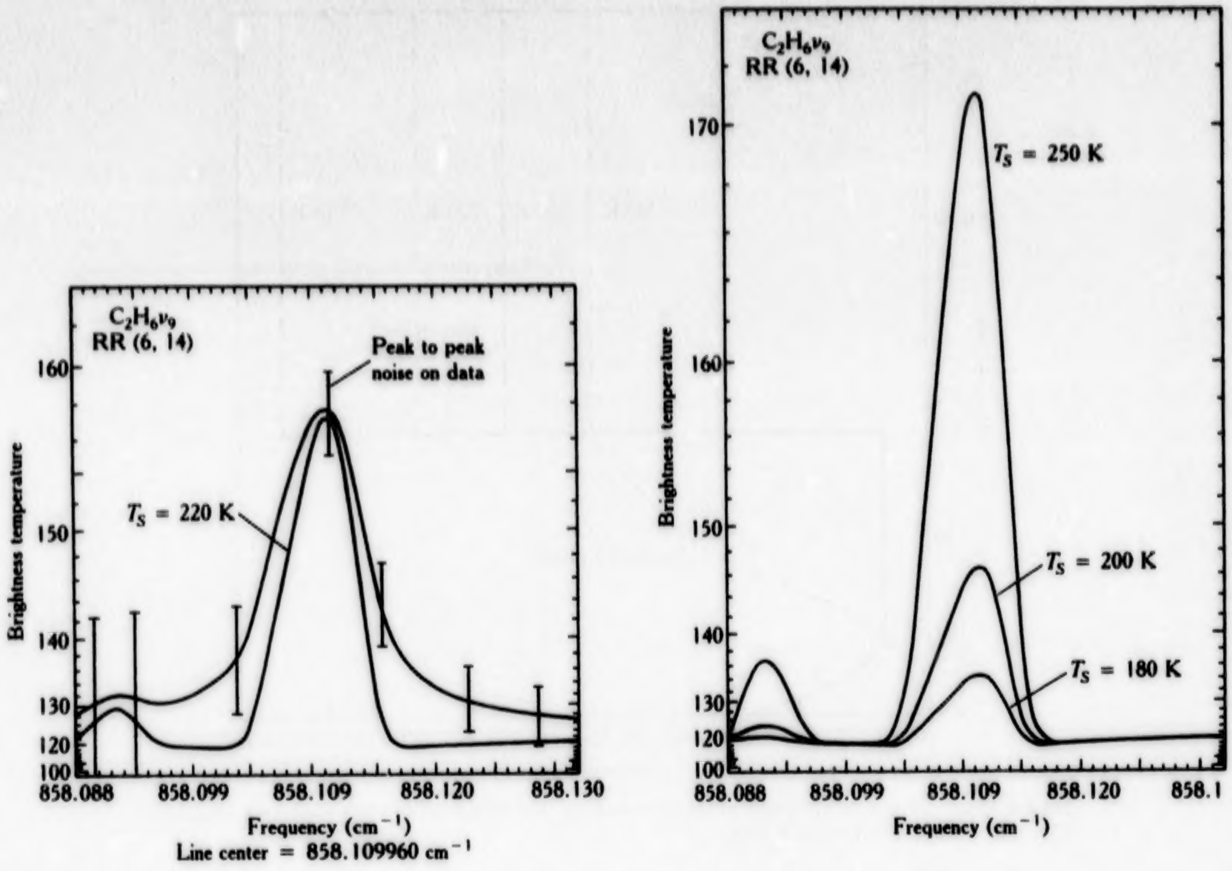

(a) (b)

Figure 131. Modeled ethane emission lines for the exotic temperature profiles of figure 130. Note that even with no C_2H_6 contribution from the lower stratosphere, effects of $T_S >$ 220 K would be observable on the measured line profile, the curve with error bars in **(a)**.

ethane abundance or an extremely cold stratospheric temperature. Both of these possible explanations are inconsistent with our present knowledge of the quiescent jovian atmosphere.

We conclude that temperature changes alone cannot explain both the observed enhanced emission from CH_4 and C_2H_2 and the lack of observed change or decrease in the measured C_2H_6 emission lines in this polar region. A decrease in stratospheric ethane is required to compensate for the increased temperature, indicating altered hydrocarbon chemistry in the hot spot (e.g., the formation of C_2H_2 at the expense of C_2H_6). Photochemical models must be developed that account for effects of precipitating charged particles, secondary ultraviolet emissions, thermal effects on photochemical and diffusion time constants of the various hydrocarbons, possible nonthermal effects, and possible effects of dynamics.

ACKNOWLEDGMENTS

The authors were guest investigators at the National Solar Observatory, a division of the National Optical Astronomy Observatories, which is operated by the Association of Universities for Research in Astronomy, under contract to the National Science Foundation. T. Kostiuk and F. Espenak were visiting astronomers at the Infrared Telescope Facility, which is operated by the University of Hawaii under contract from the National Aeronautics and Space Administration.

References

Allen, M. (1986). Private communication.
Atreya, S. K. (1986). *Atmospheres and ionospheres of the outer planets and their satellites*. Springer-Verlag, New York.
Bjoraker, G. L., D. E. Jennings, and G. R. Wiedemann (1987). *High spectral resolution observations of ethane and*

acetylene in the polar regions of Jupiter. International Workshop on Time-Variable Phenomena in the Jovian System, August 25–27, Flagstaff, Ariz.

Caldwell, J., A. T. Tokunaga, and F. C. Gillett (1980). Possible infrared aurorae on Jupiter. *Icarus* 44:667–675.

Drossart, P., B. Bezard, S. Atreya, J. Lacy, E. Serabyn, A. Tokunaga, and T. Encrenaz (1986). Enhanced acetylene emission near the north pole of Jupiter. *Icarus* 66:610–618.

Drossart, P., E. Serabyn, J. Lacy, S. Atreya, B. Bezard, and T. Encrenaz (1985). Acetylene, ethane and polar infrared brightening on Jupiter. *Bull. Am. Astron. Soc.* 17:708.

Gladstone, G. R. (1983). *Radiative transfer and photochemistry in the upper atmosphere of Jupiter*. Ph.D. thesis, California Institute of Technology, Pasadena.

Halthore, R., A. Burrows, and J. Caldwell (1987). Infrared polar brightenings on Jupiter V. A thermal equilibrium model for the north polar hot spot. *Icarus*, submitted.

Kim, S. J., J. Caldwell, A. R. Rivolo, and R. Wagener (1985). Infrared polar brightening on Jupiter III. Spectrometry from Voyager 1 IRIS experiment. *Icarus* 64:233–248.

Kostiuk, T., F. Espenak, M. J. Mumma, D. Deming, and D. Zipoy (1987). Variability of ethane on Jupiter. *Icarus* 72:384–410.

Kostiuk, T., M. J. Mumma, F. Espenak, D. Deming, D. E. Jennings, W. Maguire, and D. Zipoy (1983). Measurements of stratospheric ethane in the jovian south polar region from infrared heterodyne spectroscopy of the ν_9 band near 12 microns. *Astrophys. J.* 265:564–569.

Maguire, W. C., R. E. Samuelson, R. A. Hanel, and V. G. Kunde (1985). Latitudinal variation of acetylene and ethane in the jovian atmosphere from Voyager IRIS observations. *BAAS* 17:708.

Yung, Y. L., and D. F. Strobel (1980). Hydrocarbon photochemistry and Lyman alpha albedo of Jupiter. *Astrophys. J.* 239:395.

PART III

PHENOMENA IN THE JOVIAN ATMOSPHERE

PRECEDING PAGE BLANK NOT FILMED

21

Time-Variable Nature of the Jovian Cloud Properties and Thermal Structure: An Observational Perspective

R. F. Beebe
New Mexico State University, Las Cruces
G. S. Orton
R. A. West
Jet Propulsion Laboratory, Pasadena

Abstract

This chapter reviews observations of the temporal behavior of jovian cloud properties and thermal structure of the upper troposphere and stratosphere. Changes in the albedo and color of belt and zones have been reported in the literature for well over a century. We discuss the north-south asymmetry of the equatorial zone, contrast between the north and south equatorial belts and the role of south equatorial belt disturbances, the asymmetric behavior of the north and south tropical

PRECEDING PAGE BLANK NOT FIL[illegible]

PRECEDING PAGE BLANK NOT FILMED

zones, and the variable nature of north and south temperate belts. Smaller-scale features exhibit a variety of evolutionary patterns. We describe the long-term behavior of "white" features near 20° N, small "red" spots near 18° N, "convective systems" originating at 15° N, "dark brown" cyclonic systems in the north equatorial belt, a long-lived "white" cloud system in the southern equatorial zone, the great red spot, the white ovals at 25°5 S, and cyclonic-anticyclonic systems at 37° S. Information on time variability of cloud vertical structure and particle density comes from thermal emission in deeply probing spectral windows, and from hydrogen and methane absorption in the visible and near-infrared. A long-lived steady haze layer permeates the upper troposphere. Clouds near the base of the ammonia condensation level or deeper are responsible for the variations seen primarily at 5 μm. Seasonal behavior in the temperature structure of the stratosphere is observed and correlates with the expected radiative response to insolation. Nonseasonal behavior has only recently been observed, with spatial scales ranging from global to the limit of resolution (7000 km), and with time scales ranging from a few years to days. Large-scale tropospheric temperature fields have been observed to be stable since a monitoring program began in 1980. Many important questions remain to be answered. A concerted effort involving several techniques, systematic observations covering time scales from days to years, and improvements over present methods to achieve higher signal-to-noise and better spatial resolution are needed to provide the data base for a more realistic and detailed understanding of the coupled dynamic, chemical, and cloud-physical processes operating in the jovian atmosphere.

INTRODUCTION

Most studies of the jovian cloud patterns have attempted to provide insight into steady-state processes operating on large scales. A commonly held notion is that anticyclonic zones are regions of upwelling where white condensation clouds form, and cyclonic belts are downwelling regions having little cloudy material. Yet such a generalization ignores well-documented albedo changes that make some cyclonic regions bright, and some anticyclonic regions dark. Basic questions about the composition, microphysical characteristics, distribution, and transport of chromophores remain unanswered. To gain a more realistic understanding of chemical, microphysical, and dynamic processes operating in the upper troposphere and stratosphere, it is necessary to go beyond the simple concepts of upwelling and downwelling and to examine cloud, chemical, temperature, and wind data in a detailed, three-dimensional, time-dependent context.

This chapter reviews observations of the time-variable nature of cloud albedo and morphology, cloud vertical structure, and thermal structure. These topics are intimately related on a physical basis, but it is not yet clear how they are related on an observational basis. Accordingly, this chapter is divided into three major sections that reflect the historical development of each of the subfields. Studies of cloud albedo and morphology have a long, rich history compared to studies of cloud vertical structure, which require sophisticated spectrometers or infrared detectors. Thermal studies are the newest subfield among the disciplines discussed here.

In companion chapters, Drossart and Courtin discuss the temporal behavior of chemical constituents, and Flasar (this volume) reviews dynamic and meteorological concepts for the jovian atmosphere.

CLOUD ALBEDO AND MORPHOLOGY PATTERNS

Because Jupiter is readily accessible through a small telescope the observational record extends over more than 300 years. Cassini and his group at the Paris Observatory carried out detailed observations from 1665 to 1713 and determined that the equatorial period of rotation was about five minutes less than that at midlatitudes. The British Astronomical Association continued the tradition and published annual summaries of the condition of the cloud deck in the *Journal of the British Astronomical Association (BAA).* By the beginning of the twentieth century the *BAA* had standardized their nomenclature and established procedures for integrating the data and presenting a systematic report. Previous to this integrated effort, much of the data exists in the format preferred by the individual observer, has been haphazardly archived, and is difficult to interpret.

The organized efforts of the *BAA* led to adoption of a nomenclature that is an extension of the climatic nomenclature on Earth (Peek, 1958). Although this terminology has been in use for many decades, it encompasses two weaknesses: (1) The nomenclature is cumbersome—although "equatorial" and "polar" are useful generic terms, terms such as "tropical zone" and "north north temperate belt" are less appropriate. (2) The regions are differentiated in large part on the basis of albedo variations, thus, latitudinal positions assigned to the belt edges are subject to the effects of poor visibility through Earth's atmosphere and albedo changes in adjacent regions.

A better way to designate features is to specify their planetocentric latitude, a fundamental coordinate system that defines the angular distance from the planetary equator. We will use planetocentric coordinates throughout this article. Use of terms such as equatorial zone, north or south equatorial belt, and polar region should cause little confusion; however, continued use of the high-latitude nomenclature of the *BAA* can lead to confusion. The *BAA* data set is a unique and useful collection, and modification of *BAA* high-latitude nomenclature system to fit the Voyager results would lead to confusion in the future. In table 17 we specify which latitudinal region corresponds with any *BAA* terminology that we use.

Table 17 is a tabulation of maximum and minimum wind speeds derived from the 1979 Voyager 1 and 2 data sets. Planetographic latitudes are given in parenthesis. An additional column assigns the traditional *BAA* nomenclature, according to Peek (1958), with zones assigned to anticyclonic regions bounded on the poleward side by an eastward jet. Beginning in the north, the sequence is north polar region (NPR), north north temperate zone (NNTZ), north north temperate belt (NNTB), north temperate zone (NTZ), north temperate belt (NTB), north tropical zone (NTropZ or NTrZ), north equatorial belt (NEB), north half of the equatorial zone (EZn), and equatorial belt (EB). Parallel notation is assigned to the southern hemisphere. The table has been symmetrically laid out in terms of the albedo features and *BAA* nomenclature. Comparison with tables in Peek (1958) indicate that *BAA* nomenclature overlays the velocity structure within 32° of the equator. Poleward of that, anticyclonic zones display more longitudinal structure, and at ground-based resolution frequently do not appear as a high-albedo zone. Consequently, there is confusion present in the historical data at high latitudes.

All velocities are reduced to the standard Voyager Jupiter reference system, which assumes that the equatorial radius is 71,400 km at the visible cloud deck ($P \sim 500$ mbar) and the ratio of the equatorial to polar axis is 1.0693. System III longitude is defined with longitude increasing with time within a system that is referenced

Table 17. Maxima and Minima Zonal Wind Velocities

Northern hemisphere				**Southern hemisphere**			
Planetocentric latitude (degrees)	**Planetographic latitude (degrees)**	**Maximum zonal velocity (m/s)**	**BAA**	**Planetocentric latitude (degrees)**	**Planetographic latitude (degrees)**	**Maximum zonal velocity (m/s)**	**BAA**
0.0	(0.0)	90	EB	0.0	(0.0)	90	EB
			EZn				EZs
6.0	(6.8)	112	—	6.5	(7.5)	153	—
			NEB				SEB
15.0	(17.0)	−37	—	17.5	(19.8)	−71	—
			NTrZ				STrZ
20.0	(22.5)	168	—	24.5	(28.5)	57	—
			NTB				STB
26.8	(30.0)	−38	—	29.5	(33.0)	−44	—
			NTZ				STZ
31.8	(35.2)	40	—	34.0	(37.5)	41	—
			NNTB				SSTB
34.5	(38.2)	−27	—	36.8	(40.5)	−12	—
			NNTZ				SSTZ
38.2	(42.0)	29	—	39.8	(43.5)	54	—
			NPR				SPR
40.5	(44.5)	−12		45.8	(49.5)	−17	
43.8	(47.5)	32		50.2	(54.0)	43	
47.2	(50.0)	−30					

to a zero point that corresponds to the longitude that was coincident with Earth-based observers' central meridian at 0 h UT, 1 January 1965 (Julian day = 2438761.5). The rotation rate of the planet is defined as 870°.536 day. This system is based on periodicity of decimetric and decameteric radiation, and is assumed to be corotating with the interior of the planet (Riddle and Warwick, 1976). Clouds drifting eastward toward decreasing longitudes as a function of time have a net eastward velocity relative to the solid-body angular velocity and are defined as having a positive velocity.

Time-Dependent Behavior of the Belts and Zones

Variability of cloud systems occurs on time scales from minutes to years, depending on the length scale. Turbulent eddy velocity, which can potentially modify the existing cloud structure, is usually 10 to 20 m s^{-1} at horizontal scale of 130 km (Ingersoll et al., 1981; Limaye, 1986). In general, the more sharply defined the feature, the more predictable the drift rate and the less likely the feature is located near a wind maxima. Some regions become bright suddenly, as if a local strong convection cell is bringing ammonia vapor to high altitude where it condenses and forms thick white clouds. We refer to these as "convective sites." The term *convective* is intended to be purely descriptive of the morphology and activity, since we do not have any other evidence suggesting that convection is in fact any stronger at these sites than elsewhere. Growth rates of actively convective regions can be derived from data sets that span a few hours, whereas detection of shrinkage rates of long-lived features may require data sets spanning many years. These kinds of features are seen to play an important role in modifying the large-scale appearance of belts and zones. We begin with an historical introduction.

Visually, the color contrast on Jupiter is subtle, and the observer is strongly influenced by the reflectivity of the surrounding regions (see Young, 1985). Early observations of the planet were hampered by the inability to obtain objective data. Until the development of equatorially mounted reflectors with improved primary mirrors and color-corrected eyepieces, reports of color are of questionable reliability. Nineteenth-century observers used terms such as crimson lake, a well-known pigment of the day. Few designated the relative surface brightness of the region in question. Early twentieth-century observers developed a more useful terminology that not only specifies the color, but also assigns a number representing the relative brightness of the region.

Historical positional measurements are more reliable than reported colors. The latitudinal position of a well-defined cloud system can be determined by using a filar micrometer on an equatorially mounted telescope (Peek, 1958). Individual observers selected specific regions and determined the central meridian crossings of selected cloud patterns over a period of several weeks. As a result, the rotation of features that were large enough and possessed an easily detectable contrast with their surroundings were accurately mapped. Data were integrated and cylindrical maps were constructed, yielding reliable results. However, these data cannot be used to infer changes in the zonal wind currents because the data base consists of a collection of drawings, and latitudes were not measured (e.g., with a micrometer or scored eyepiece) with sufficient accuracy.

In a hand-written memoir, N. E. Green (1887) reviewed the appearance of the cloud deck of Jupiter from 1860 to 1887. He divided the general appearance of the planet into four eras:

1. 1860–1868: The equator was white with dark belts on either side, with the southern belt "the stronger marked."
2. 1869–1872: The equator was "a decided coppery hue" and the north and south belts were less obvious.
3. 1873–1878: The equator was becoming whiter and the north and south belts had returned to prominence. The north belt was coppery in color and considerable small-scale detail was recorded in the southern hemisphere.
4. 1879–1887: This was "the great red spot period." The south belt was redder than the north belt near the end of this period. The beginning was dominated by high-albedo clouds surrounding a very well-defined great red spot (GRS).

The time scales associated with these changes are typical of the atmosphere of Jupiter. There are several patterns of behavior that grossly alter the surface brightness of large regions of the planet:

1. The change in color and structure of cloud systems in the equatorial zone.
2. Albedo changes and observable convection in the cyclonic belts between 7° and 18° latitude (north

and south). Convective activity in the southern belt adversely affects the visibility of the GRS.

3. The appearance of convective structures in the eastward jet at 20° N and a subsequent decrease in the albedo in the cyclonic region northward to 27° N, the NTB.
4. Positioning of the white ovals located at 30° latitude, relative to disturbances in the zone to the north of them, the south tropical zone (STrZ), and the GRS.

Equatorial Activity

Historically, the coppery hue reported by Green is observed when a few large white clouds are present in a portion of the equatorial zone. The cloud structure in the northern and southern regions varies with time. The asymmetry in the Pioneer and Voyager data is typical (Gehrels et al., 1974; Gehrels, 1976; Smith et al., 1979a, b). (See fig. 132, which shows the typical plume structure along the northern edge of the zone, whereas along the southern edge are typically small chevron structures.)

The plumes are bounded on the north by blue-gray regions and at ground-based resolutions are most detectable in photographs obtained through a red filter. Figure 133 presents a comparison of blue and red images obtained in 1972 with those from 1979 and 1982. In 1972, the equatorial region was relatively free of white cloud structures and reflected the tawny or orange color that is historically documented. In 1979, the region showed the north-south asymmetry that has been frequently noted. The lower-albedo region along the equator marks the location of the local velocity minimum, that has been called the equatorial belt. In 1982, the equatorial region displayed a high reflectivity, typical of periods in the past when observers described the detail as being veiled.

Normalized scans of surface brightness versus latitude derived from New Mexico State University (NMSU; see Hockey, 1985) broad-band blue plates for a period from 1967 to 1984 show a north-south gradient across the EZ except during 1967 when the south was brightest, 1972 when the zone was dark and tawny, and 1982 when the zone was white. For the last 20 years, the structures along the northern edge of the zone have displayed the plume pattern. The southern portion of the zone tends to have fewer and more diffuse bright regions.

There is observational evidence that the GRS and the convection pattern in the south equatorial belt (SEB) have considerable effect on the southern portion of the equatorial zone. In 1971, a south equatorial belt disturbance interacted with the GRS. Material moving eastward encountered the flow pattern associated with the northern perimeter of the GRS and spilled into the southern portion of the equatorial zone (Reese, 1972). In 1975, another major south equatorial belt disturbance occurred and material again spilled into the equatorial zone. This material formed a white cloud system that remained visible through the Voyager encounters. We will refer to this cloud system as the south equatorial feature. Its zonal velocity of 94.3 m s^{-1} was determined from the pre-encounter Voyager 1 images. This velocity contrasts with values of 105 to 150 m s^{-1} for plume features along the northern edge of the equatorial zone.

Behavior of the equatorial zone at visible wavelengths is consistent with the idea that aperiodic convection inserts high-albedo cloud systems into the prevailing zonal flow, causing weak anticyclonic systems to form. These systems appear to shear apart, dissipate, or mix with their surroundings. Time scales for zonal brightness increases are on the order of five years, although the time scale from bright to dark is usually shorter (Hockey and Beebe, 1983).

The North and South Equatorial Belts

The north and south equatorial belts have traditionally been divided into north and south components based on the appearance of regions of higher reflectivity within the belts. High-resolution Voyager data shows that much of the structure has a latitudinally dependent component and that the albedo variations have a spiral structure. Leovy (1986) proposed that this may be evidence for breaking waves in the atmosphere. Peek (1958) summarized the historical record of reported position, color, and surface brightness of the belts. Not only have the measured latitudinal extent, color, and reflectivity of the belts varied in an aperiodic manner, but also the appearance of either belt has changed within intervals of weeks. At ground-based resolution, sites of active convection are observable in both belts.

The activity that was visible in the NEB during the Voyager encounters is typical of the region. During the Voyager 1 encounter the convective site was at nearly the same longitude as the GRS and visible in the blue-filtered Voyager 1 movie. It is south of the westward maxima at 15° N latitude. In the interval between the

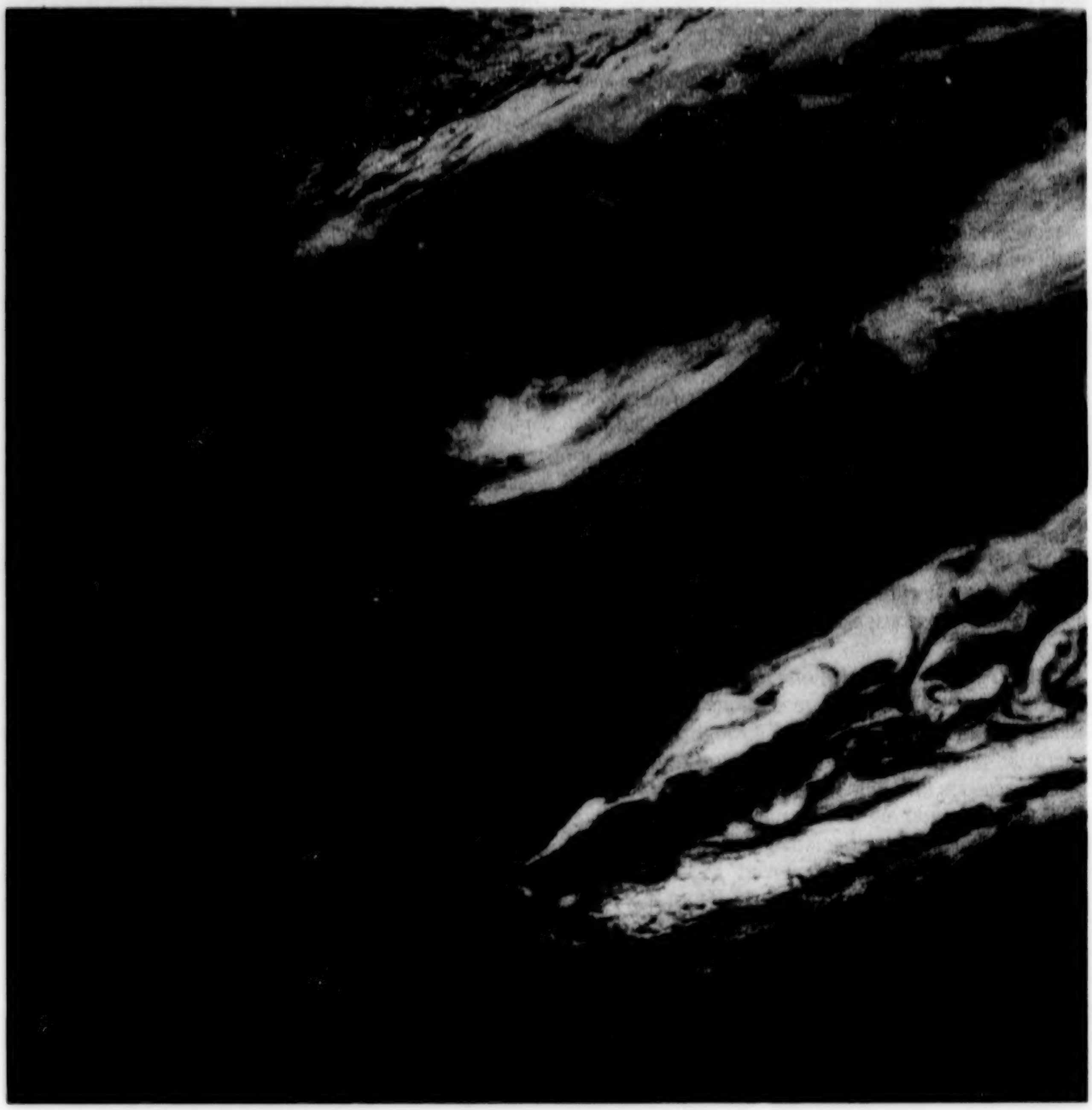

Figure 132. A false-color, contrast-enhanced, Voyager 2 composite image. This image has been strongly enhanced to accent the color differences of the equatorial zone. The plumelike white structures are seen in the northern portion of the zone, whereas the small chevron features along the south edge of the zone define the eastward jet. Anticyclonic flow is suggested by the morphology of the clouds; however, few tracers are available for direct determination of rotation rates. The maximum eastward jet at 20°0 N is located along the narrow band above the "barge," whereas the white region in the lower right is the cyclonic region associated with GRS.

ORIGINAL PAGE
COLOR PHOTOGRAPH

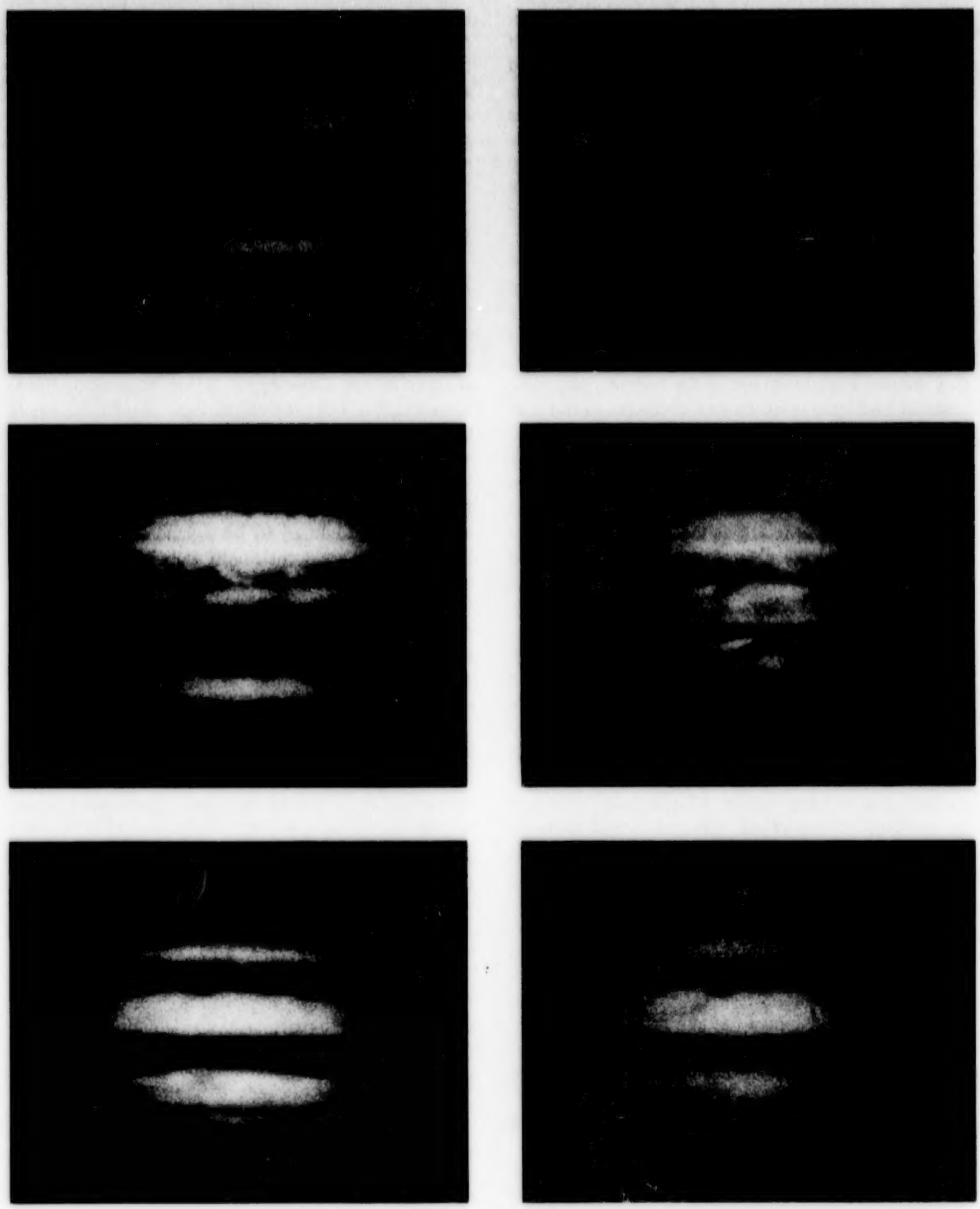

Figure 133. Variation of the albedo of the equatorial region. These images were obtained at NMSU. The left images are in blue (Kodak emulsion III-O/Schott filter GG-395), and the right images are in red (III-F/OG-570) light. The upper images were obtained on October 1972, and reveal an orange equatorial zone; the center images, from 14 March 1982, show the equatorial zone bright in both red and blue.

ORIGINAL PAGE
BLACK AND WHITE PHOTOGRAPH

Voyager 1 and 2 encounters, the site moved eastward about 75° in longitude, as seen in figure 134 (Smith et al., 1979b). White clouds emerge from the site, expand southward, and are drawn out in the meridional shear of the zonal wind, forming turbulent diagonal features that become more east-west trending as they move away from the site. NMSU photographic data indicate that the lifetime of a convective site is on the order of years and that more than one site, at widely spaced longitudes, may be present.

Dark brown cyclonic structures are located near 12°5 N latitude within a diagonal streak of brighter material extending toward the equator as shown in figure 134. The eastward velocity of these features is less than the eastward velocity of the convective sites, hence, they are frequently obscured by the encroaching white material leading to considerable variability in the contrast and apparent latitudinal extent of the belt.

Convection of the SEB has frequently been the most visible activity on the planet. This belt undergoes a process where the reflectivity increases to the point that the region is as bright as the adjacent STrZ. The GRS becomes sharply defined and dark in violet and blue light (Reese, 1972; Gehrels, 1976). This aspect of the SEB was present when Pioneers 10 and 11 encountered Jupiter in 1973 and 1974.

The inverse process, a major SEB disturbance, occurred in July 1975. Peek (1958, chapter 17) described the characteristics of similar disturbances. A very white cloud, preceded by a dark border, appeared 50° west of the GRS. The cloud expanded and was sheared out into an S-like structure (cf., Reese, 1972), extending across the SEB in a NE-SW direction. White clouds formed in the northern portion of the SEB and moved eastward toward the GRS and eddies developed in the westward jet along the poleward side of the disturbance. The eddies circled the planet and encountered the GRS from the east, carrying white material around the perimeter of the spot. The contrast between the GRS and its surroundings decreased rapidly. Within weeks, convection at two additional sites had occurred and the belt had apparently mixed to the extent that the white reflective material was removed from, or dark material added to, a major portion of the belt (cf., Sanchez-Lavega and Rodrigo, 1985). At the present (mid-1987) the belt appears similar to that seen during the Voyager encounters.

The first report of a major disturbance was recorded in 1919 in the *Journal of the British Astronomical Association.* Subsequent events were reported by the *BAA* in 1928, 1943, 1949, 1952, 1955, 1958, 1962, and 1964. Reese (1972) presented a detailed report of a 1971 disturbance, which was followed by the major disturbance in 1975. The sites of the convective disturbances are almost stationary in System III; hence, the possibility of a uniformly rotating source has been considered (Chapman and Reese, 1968). Voyager images indicate there is an enhanced tendency for convection near the following end of the cyclonic region to the west of the GRS.

The Tropical Zones

The high albedo north tropical zone is the region of the strongest anticyclonic shear on the planet. At Voyager resolution, the zone contains a series of white diagonal cloud structures with a northeast-southwest inclination of about 10° and a spacing of 750 km. Maxworthy (1984) argued that if these structures were passive tracers of the mean flow, meridional velocities near 40 m s^{-1} would be required to sustain the observed morphology. He suggested that the prevailing texture of the zone may be due to roll vortices since measured meridional velocities are too small to be accurately determined. Larger vortices are occasionally embedded in the zone. Voyager 2 images show two white and one brown oval (Beebe and Hockey, 1986, figure 135). Pioneer 10 observed a red oval (Pioneer 10, 1973, 10:23:36), similar to the one observed in 1976 (see fig. 135a, b). The east-west axes of these features are inclined in the direction of the zonal shear, and the average period that they are detectable at Earth-based resolution is two to three years.

In contrast, the south tropical zone lies along the poleward side of the GRS. Relative to the northern zone, it is displaced poleward, extending from 17°5 to 24°5 S latitude, with zonal winds increasing from approximately -70 to 60 m s^{-1}. Along the equatorward side, anticyclonic eddies, about 4000 km in length, form south of the westward wind maximum and cause albedo variations that appear as dark notches at ground-based resolution. This activity is enhanced when there are active convection sites in the SEB. From time to time anticyclonic oval structures appear in the zone (see fig. 135c, d). These features have lifetimes of a few years and appear to be similar to their northern counterparts.

A second characteristic behavior is associated with this zone. This is called the south tropical disturbance. At ground-based resolution the foremost characteristic of this disturbance is that a longitudinal region of the zone undergoes a decrease in albedo. During the 1977–1978 apparition, the zone appeared as a white band around the planet in blue light. A south tropical disturbance was apparent in 1978–1979 (cf., Sanchez-Lavega

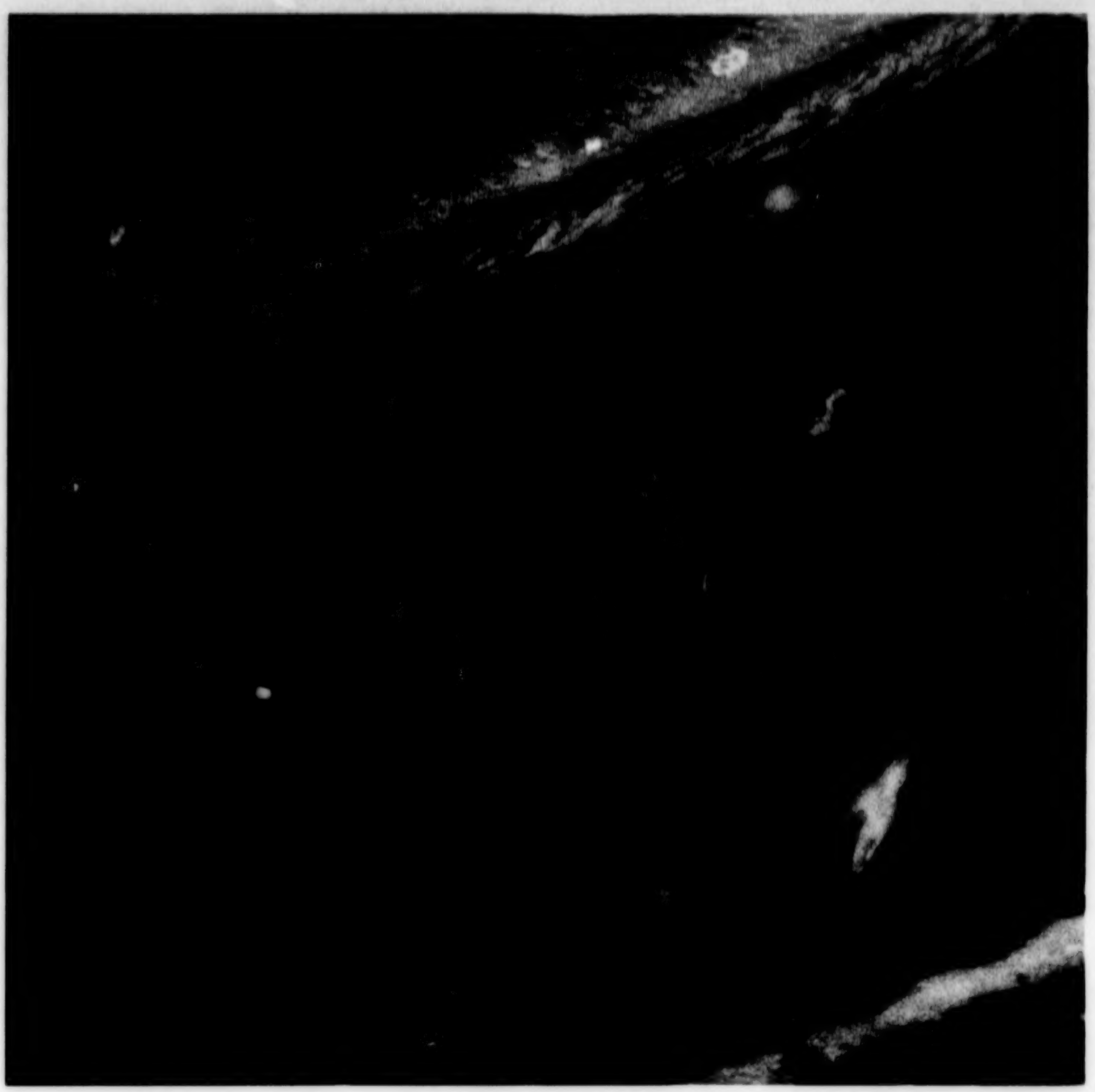

Figure 134. A north equatorial belt cyclonic feature. This feature, historically called a barge, is located in a high-albedo region that follows a diagonal trend across the belt. A smaller cyclonic feature is visible at the east edge of the figure, whereas the bright white cloud to the northeast of the large cyclonic feature is located in the northern anticyclonic zone. The westward jet at 26°8 N and the eastward jet at 20°0 N are located in the upper left, whereas the cyclonic region to the west of the GRS is at the lower right. An "active" plume is located south of the cyclonic feature. Note that the maximum eastward jet at 6°0 N is indicated by the morphology and that convective structures lie to the north of the jet.

and Rodrigo, 1985). When Voyager 1 arrived the following end of the disturbance was approaching the west end of the GRS. East of the GRS, the zone contained convective structure and had a lower reflectivity. The leading edge was not well defined. By the Voyager 2 encounter, the following end of the disturbance had moved beyond the GRS and was creating an obstacle to the westward motion of the eddies along the equatorward edge of the zone. These eddies were deflected poleward and moved back to the east near the pole-

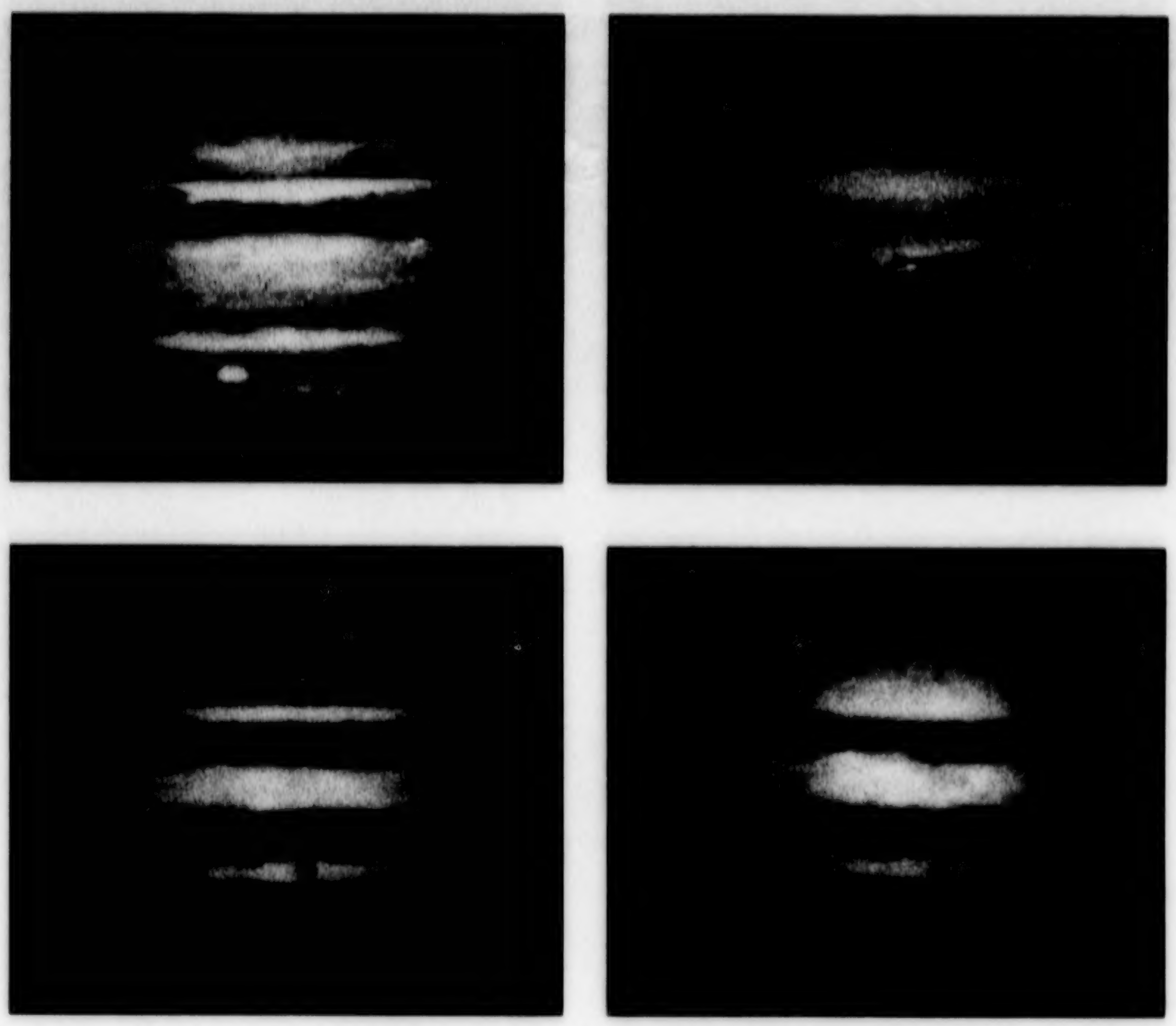

Figure 135. Small anticyclonic ovals. The *upper* images were obtained in the standard NMSU blue (*left*) and red (*right*) band-passes on 9 December 1976, and illustrate a small red spot. Five-color photometry indicates the chromophores are similar to those in the GRS. The *lower* images, blue (*left*) and red (*right*), were obtained on 8 October 1986, and show a similar structure in the southern hemisphere.

ward side of the zone, displaying the classical "circulation current" (Peek, 1958). Figure 136 shows the eastward progression of the disturbance.

The North and South Temperate Belts

The north temperate belt displays a behavior that is similar to the south equatorial belt. During the Pioneer encounters, it was a low-albedo feature. During the Voyager encounters, it was almost as bright as the adjacent NTrZ and showed similar diagonal structure.

Aperiodically, this region undergoes a convective disturbance that occurs near the 20° N jet. A bright, white cloud appears, is carried eastward in the jet, and undergoes considerable shearing effects around its perimeter. Its rapid motion eastward leads to a displacement relative to System III of −12°5/day. Its leading edge is well defined and it assumes a "cometlike" appearance and remains visible near the limb of the planet. An alternating light and dark pattern, suggestive of a wave pattern, with wave length of 13,000 km, develops west of the bright cloud and the belt darkens. A sequence of blue-filtered images, spanning a 16-year period in figure 137, illustrates the variability of the belt.

The appearance of the south temperate belt contrasts sharply with the northern belt. In 1939, the belt and the adjacent poleward region appeared highly re-

ORIGINAL PAGE
BLACK AND WHITE PHOTOGRAPH

Figure 136. A photomosaic of Jupiter. This mosaic was constructed from blue NMSU photographs spanning a period of time from 14 March to 25 March 1980. This mosaic shows a south tropical zone disturbance that was present during the Voyager encounter. The disturbance slowly drifts eastward relative to GRS (see its Voyager 2 image in figure 147) and is characterized by a region of low reflectivity bounded on the west by the typically bright zone, seen here east of the GRS.

flective. Three brown regions formed and were designated by E. Reese with A and B, C and D, and F as the preceding and following ends of the three regions.

The intervening white regions contracted into the long-lived white ovals, FA, BC, and DE (Peek, 1958, chapter 13). Their centers are near the maximum of the westward jet at 29°.5 S latitude. As with the GRS, the westward winds are deflected poleward around the ovals, creating a slowly varying appearance of this belt. The three ovals drift eastward at speeds ranging from 2.6 to 5.5 m s^{-1} relative to System III. Due to small differences in their zonal velocities, the longitudinal spacing of the three ovals varies with time. In 1975, FA and BC drifted to within 50° of longitude of each other. During this period of time, the intervening cyclonic region became more reflective and formed the structure seen in figure 138 by Voyager 1.

During the Voyager encounters, the three ovals were located within a 180° longitudinal interval. A weakly cyclonic region existed in the other hemisphere, with no detectable anticyclonic flow associated with it (see fig. 139). Relative velocities of the ovals are such that DE and BC are now within 60° of each other, whereas FA is more than 160° to the east of BC and is not easily detectable at ground-based resolution.

The Albedos, Morphologies, and Life-Cycles of Individual Cloud Systems

"Methane Spots" Cloud systems nested in the anticyclonic region between 34°.5 and 38°.2 N develop into well-formed anticyclonic ovals. Another series of smaller oval features form in the anticyclonic region between 40°.5 and 43°.8 N (see fig. 140). These anticyclonic cloud systems, similar to the features in the southern hemisphere, have associated cyclonic structures to the south and east of them. Images obtained using narrow-band filters that isolate wavelengths within intervals of strong methane absorption and intervals of nearby continuum show that these anticyclonic features extend to higher altitudes than their surroundings. Figure 141 shows the analogous structures in the southern hemisphere; however, these two anticyclonic systems span the regions from 29°.5 to 34°.0 and 36°.8 to 39°.8 S latitude. Thus, the northern anticyclonic systems are smaller and are located closer to the pole.

Anticyclonic Eddies Located at 31°.5 N Latitude A series of well-defined anticyclonic features are located just south of the eastward jet at 31°.8 N latitude. The eastward velocity of the individual ovals varies, as does their separation. These structures are not associated with cyclonic structures, and their color and reflectivity vary with time. The centers of the ovals range from dark brown to white. During the Voyager approach, these eddies displayed typical characteristics of eddies moving in a region of horizontal shear. Eddies coalesced and divided (see fig. 142), showing behavior that has no southern analogue associated with an eastward jet.

Features in the Cyclonic Belt at 20° to 26°.8 N Latitude During the Voyager encounter, this region displayed a high albedo and small-scale turbulence. Although the belt appeared brown during Pioneer encounters, high-resolution images showed structures

ORIGINAL PAGE
BLACK AND WHITE PHOTOGRAPH

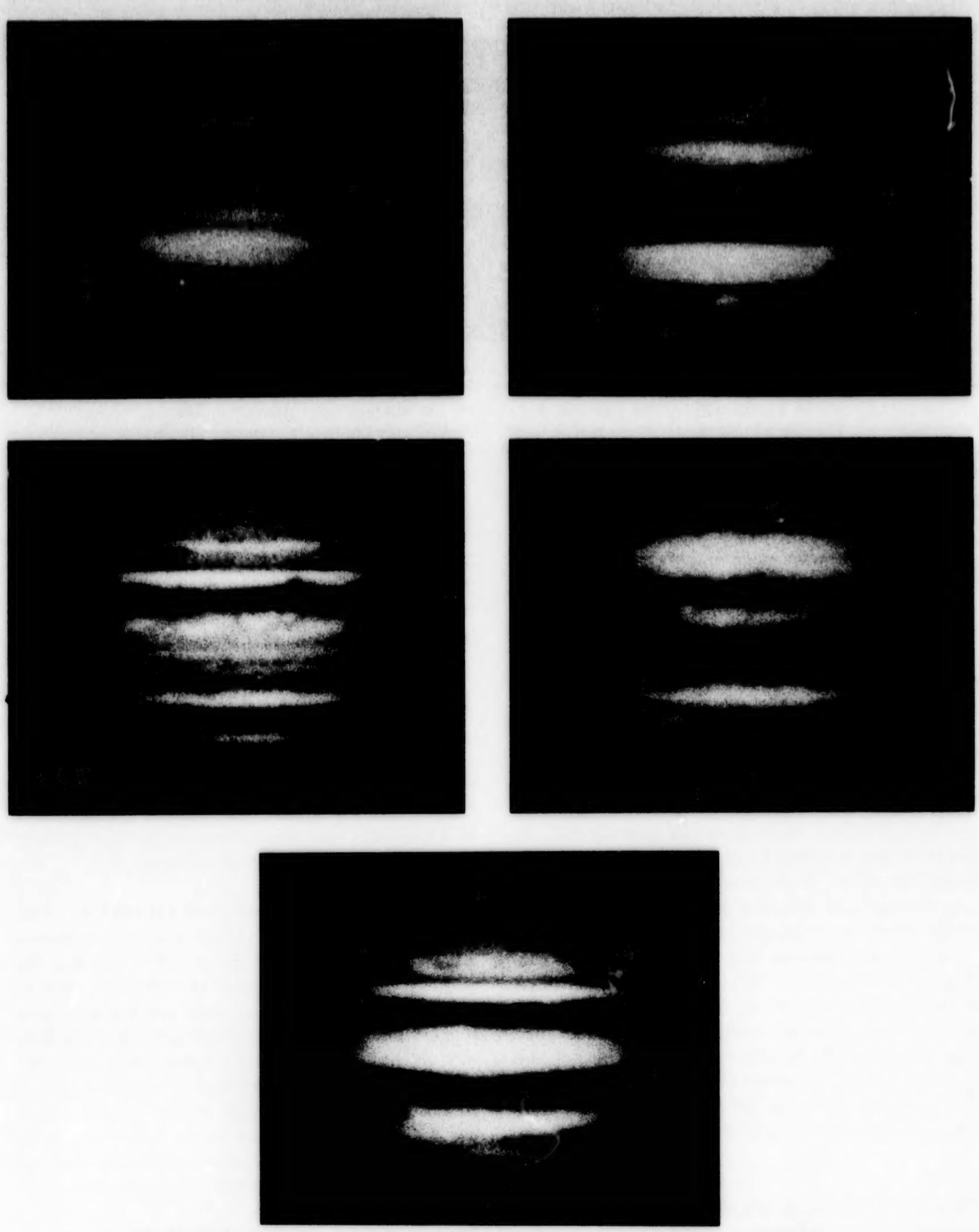

Figure 137. Changes in the north temperate belt. These images were obtained on 15 March 1970, 18 August 1974, 9 December 1976, 11 February 1979, and 14 October 1986, in the NMSU blue band-pass. In 1973 and 1974 Pioneers 10 and 11 recorded the cyclonic region north of 20° latitude brown and with lower reflectivity than was recorded by Voyager in 1979. This series of photographs show typical behavior of this region.

ORIGINAL PAGE
BLACK AND WHITE PHOTOGRAPH

ORIGINAL PAGE
BLACK AND WHITE PHOTOGRAPH

Figure 138. The cyclonic region between the white ovals FA and [illegible]. This Voyager image shows the flow structure associated with this region. The albedo of this region increased in 1975 and slowly decreased as the ovals drifted apart.

similar to those observed by Voyager (Gehrels, 1976, fig. 11). Historically, brown, well-formed features appear during periods when this belt is darkest. Figure 143 shows these features on 14 October 1986, in blue-filtered, ground-based image. Although the ground-based data indicate that this type feature is typical of this belt, no high-resolution spacecraft data are available to define the cyclonic flow possibly associated with the features. Similar features are observed in the belt between 6° and 15° N latitude.

Cyclonic Ovals in the North Equatorial Belt Four cyclonic brown ovals, located along a diagonal feature, were observed by Voyagers 1 and 2 (see figs. 132 and 134). The velocity structures, dimensions, and oscillatory behavior of the width and length of the largest

Figure 139. A weakly cyclonic region. The turbulent region near the center of this figure is located between 24°5 and 29°5 S latitude. During Voyager encounters the white ovals were located within 180° longitude in this belt. This region occupies the "empty" hemisphere. There is no evidence of a corresponding anticyclonic flow located to the east of this region, hence, the idea that similar cyclonic regions associated with the white ovals are wakes generated by flow associated with the ovals is questionable.

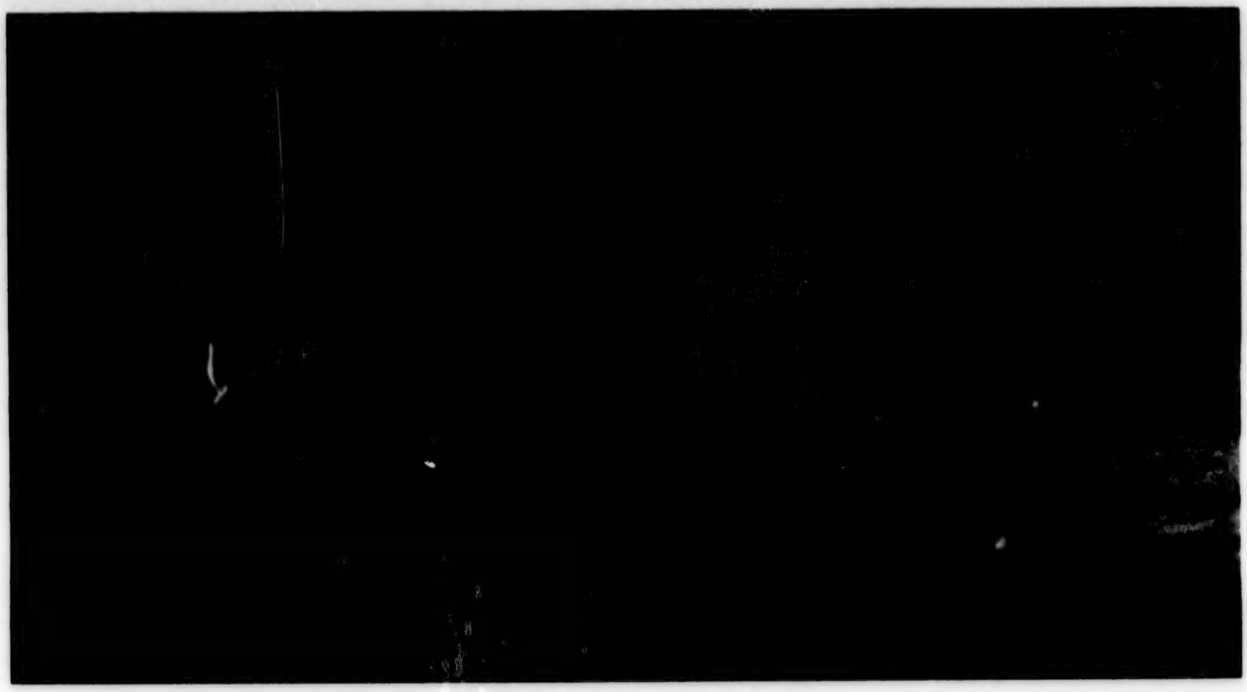

Figure 140. Northern anticyclonic-cyclonic cloud systems. A well-defined oval located between 34.°5 and 38.°2 N is bounded on the north by two smaller ovals located between 40.°5 and 43.°8 N. Note that the associated turbulent cyclonic regions are located equatorward and following the anticyclonic ovals, relative to the local flow.

cyclonic feature were characterized by Hatzes et al. (1981). The area of this feature is approximately 10^7 km^2. It has an eastward velocity of about 2.5 m s^{-1} relative to System III. The zonal velocities of these features correlated with their length, and varied during the Voyager encounters. The eastern or leading feature had the smallest surface area, had the smallest drift velocity, and was almost overtaken by the brown oval following it. These features are observable at ground-based resolution and have historically been called "barges."

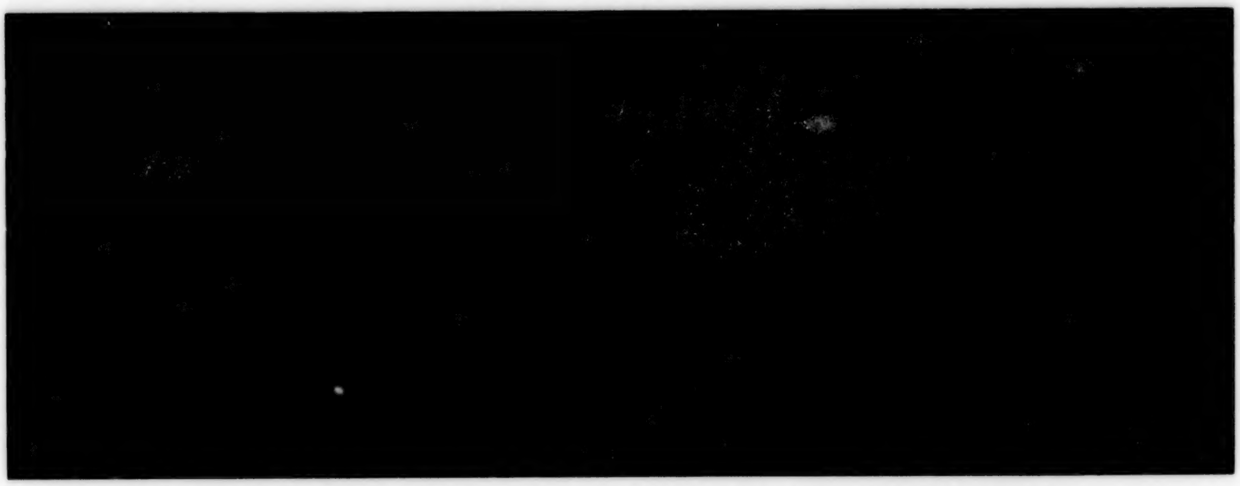

Figure 141. Southern anticyclonic-cyclonic cloud systems. Located between 36.°8 and 39.°8 S the well-formed white ovals display anticyclonic rotation, whereas the intervening cyclonic systems are displaced equatorward.

ORIGINAL PAGE
BLACK AND WHITE PHOTOGRAPH

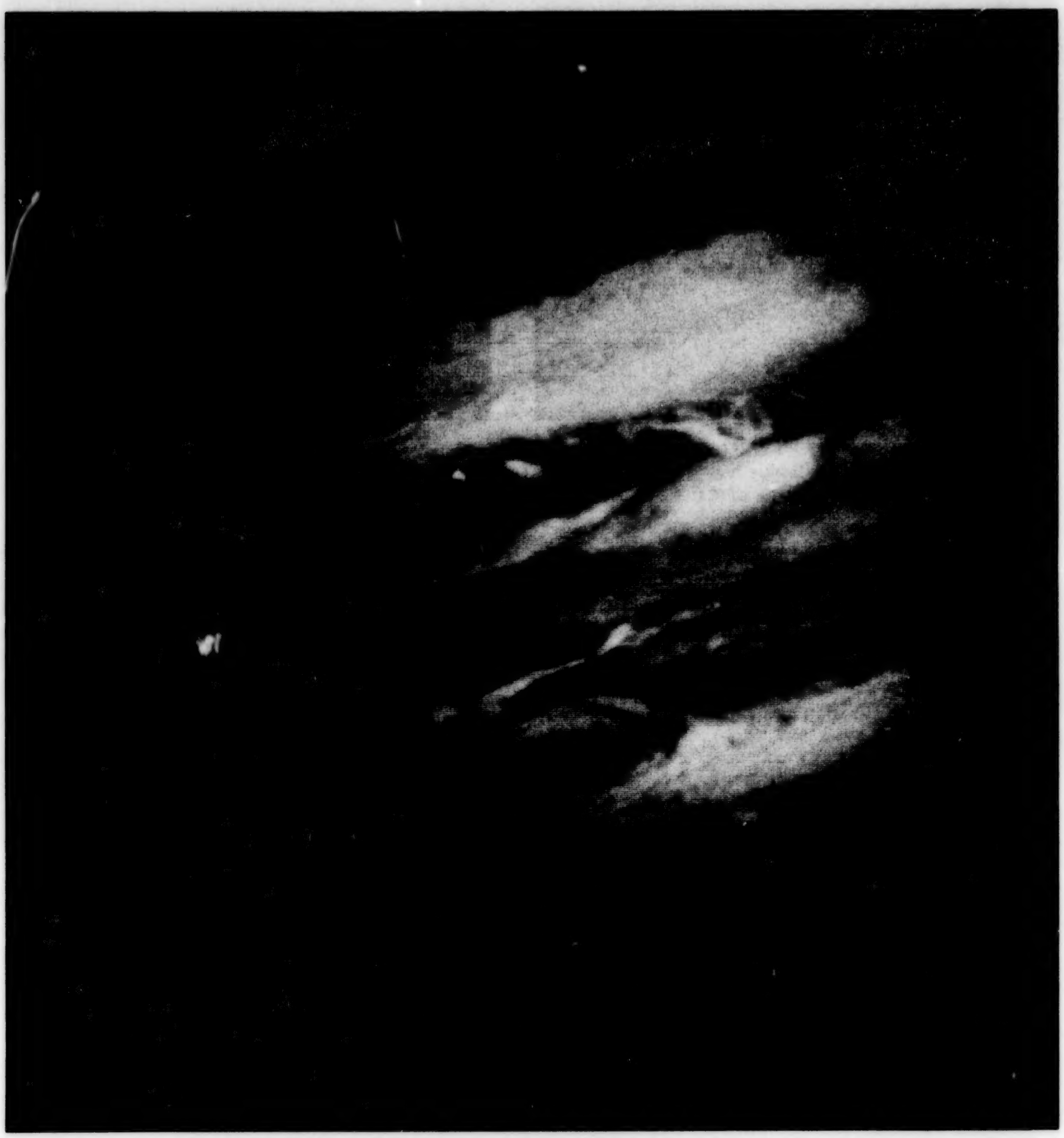

Figure 142. Anticyclonic eddies located at 31°5 latitude. A series of well-formed brown ovals are visible along the north edge of the bright north temperate belt. These eddies have no southern analogue.

Larger systems overtake and appear to coalesce with smaller, more slowly moving systems. The combined system continues to move eastward with a velocity equal to that of the large oval. Between Voyagers 1 and 2, material from the convective site to the north of the cyclonic systems encroached from the west, obscuring the trailing feature. A high-resolution image in figure 144 shows that the cyclonic system has not been disrupted and suggests the diagonal white structures form at a higher altitude than the "barges."

ORIGINAL PAGE
COLOR PHOTOGRAPH

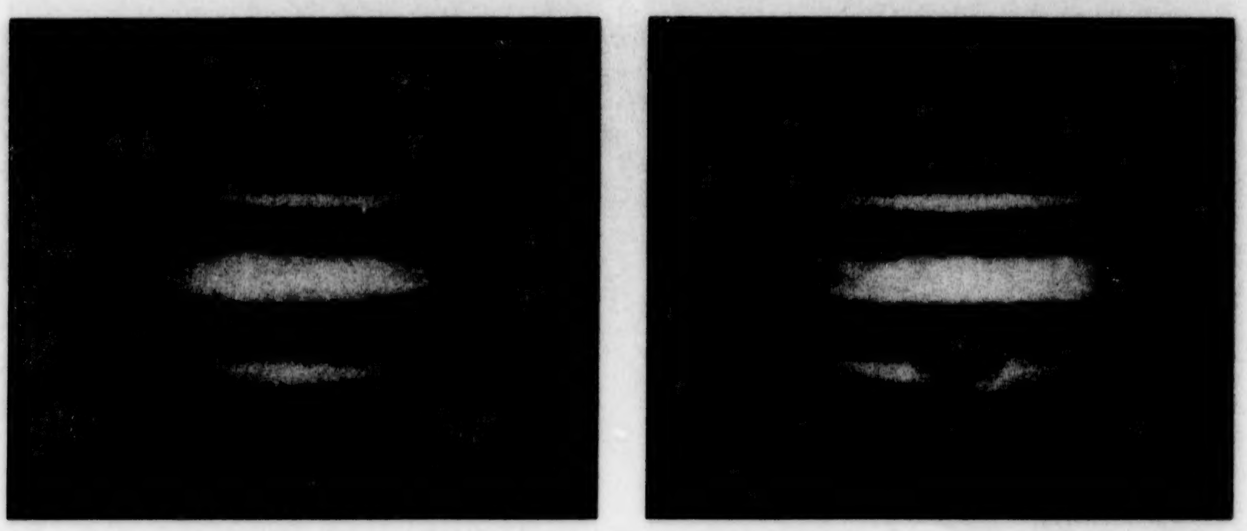

Figure 143. North temperate belt features. These images, obtained on 14 October 1986, in the NMSU blue band-pass, show a series of dark ovals near 26° N. Although these features of this type were not visible during either Pioneer or Voyager encounters.

Plumes in the North Equatorial Zone A series of white elongated clouds are present in the northern half of the equatorial zone. Typically, their southern perimeter is convex toward the equator, there is a southwest-northeast diagonal flow structure associated with the plumes and sites of active turbulence (rapid brightness variations) may be present along their leading northern region (see figs. 132 and 134). The zonal winds vary from 90 to 112 m s^{-1} from 0° to 6° N latitude; hence, the region is anticyclonic. The rounded shape of the southwest quadrants suggest that the quiescent plumes are weakly anticyclonic structures that are sheared by the zonal winds. Although vertical convection models have been proposed (Gehrels, 1976; Hunt et al., 1981; Stoker,

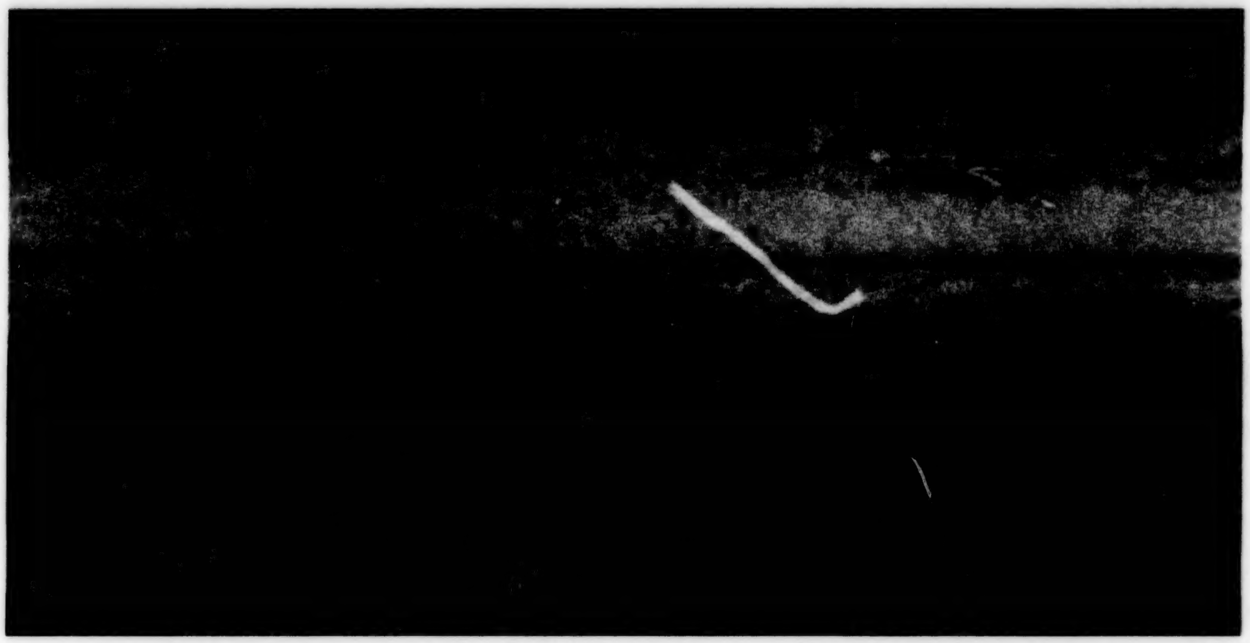

Figure 144. Encroachment of turbulent material into a cyclonic feature. This Voyager 2 image shows two cyclonic systems located in the north equatorial belt. The feature on the *right* shows typical flow patterns around its perimeter, whereas the feature on the *left* is obscured by convective material encroaching from the west (see Smith et al., 1979b).

ORIGINAL PAGE
BLACK AND WHITE PHOTOGRAPH

1986), the data indicate that interaction of the plumes and the material expanding equatorward from the convection site along the northern edge of the NEB induces activity (see fig. 145). Active convection sites expand north of the eastward jet with clouds streaming northward in the adjacent cyclonic belt.

The South Equatorial Feature Figure 146 is a sequence of Voyager images with 100-hour spacing that shows the south equatorial feature overtaking the GRS. This feature is anticyclonic, has a rotational velocity of about 40 m s^{-1} and moves eastward at about 95 m s^{-1}, relative to System III. The following end of the feature is well defined and the small orange, high-velocity chevrons (150 m s^{-1}) deflect southward around the southwestern quadrant. As the feature approaches the GRS, material to the northwest of the GRS precedes the south equatorial feature across the equatorward side of the GRS (see fig. 147). As the south equatorial feature moves eastward, the south equatorial material forms wave structures that dissipate, forming a diagonal streak in the south equatorial belt.

The south equatorial feature appears to deflect the eastward flow around its southern perimeter. As it moves, small, "brown-eyed" eddies that form in the cyclonic region south of the eastward jet, move northward and enter the feature in its leading southeast quadrant. These eddies follow the anticyclonic flow, decreasing in contrast and increasing in surface area, until they reach the southwest quadrant. At that point they have expanded to the point that they are translucent and flow structure around the following end of the feature can be seen through the tracer eddies.

The Great Red Spot The GRS is centered at 20°.5 latitude with its east-west dimension equal to 23,000 km and its north-south dimension extending from 15°.4 to 25°.4 S latitude (12,400 km). Eddies that originate in the westward jet at 17°.5 S latitude encounter the GRS from the east and are deflected around the equatorward perimeter. As the eddies circle the GRS, they encounter the eastward flow around the poleward side of the spot and continue around the GRS; however, as they approach the eastern cusp, the northward deflection of the flow around the GRS causes a local perturbation that allows the eddies to enter the GRS. Voyager measurements inside the GRS showed a strong circulation extending around the outer portion of the feature (Mitchell et al., 1981) but failed to detect any divergent flow.

In 1973 and 1974 Jupiter displayed a bright south equatorial belt and a GRS that was strongly absorbing in ultraviolet (UV), violet, and blue light. In July 1975, a south equatorial belt disturbance occurred and the equatorial belt became brown and turbulent. The flow pattern around the GRS, historically referred to as the GRS hollow, became apparent. Figure 148 shows a time sequence of the GRS from 1973 to 1986. Early observations in 1987 indicate that the south equatorial belt is still brown and that the cyclonic white cloud structure to the northwest of the GRS is still present.

The longitudinal drift of the GRS relative to System III is approximately 0°.26 per day westward. The GRS displays several modes of motion. For periods of two to five years, the mean motion of the GRS is such that the longitudinal position of the GRS as a function of time can be fit with a second-order polynomial, implying that the GRS encounters a drag and decelerates at a constant rate (Guitar, 1984). For short periods of time, on the scale of weeks, the GRS undergoes rapid eastward acceleration followed by deceleration resulting in a slow drift westward relative to a line mapping its average drift over a period of 20 years. Reese (1972) reported that a passage of the preceding end of a dark south tropical disturbance accelerated the GRS in late December 1970.

Detailed measurements of NMSU images revealed a periodic motion superposed on the longer-term decelerations and aperiodic accelerations. Periodogram analysis of measurements of the longitude of the GRS for a time interval from 1961 to 1981 (Solberg, 1969; Guitar, 1984) yielded a period of 89.93 days, a half amplitude of 0°.53 and a phase of 3.2732 radians, where

$$L(t) = L_0 + A\cos(2\pi ft + \phi), \qquad (21.1)$$

where L_0 is the average longitude; $L(t)$, the observed longitudinal position of the feature; A, the half-amplitude; f, the frequency with the period equal to $1/f$; t, the time in Julian days − 2,440,000; and ϕ, the phase. No other frequencies are indicated in the periodogram, and the peak associated with the 89.93-day oscillation is sharp. Although the GRS underwent an acceleration in December 1970, which was its largest since 1932, there is no evidence of phase shift in the 90-day oscillation.

Reports of red spots extend back to the seventeenth century. Some historical records indicate that the great red spot was first observed in 1879 when the GRS and south equatorial belt displayed an aspect similar to that seen by Pioneers 10 and 11 (see fig. 149). The question of whether the GRS has been continually present is more difficult to answer than the question of whether the 1879 sightings represented a previously unseen feature. Searches of pre-1879 records reveal drawings that

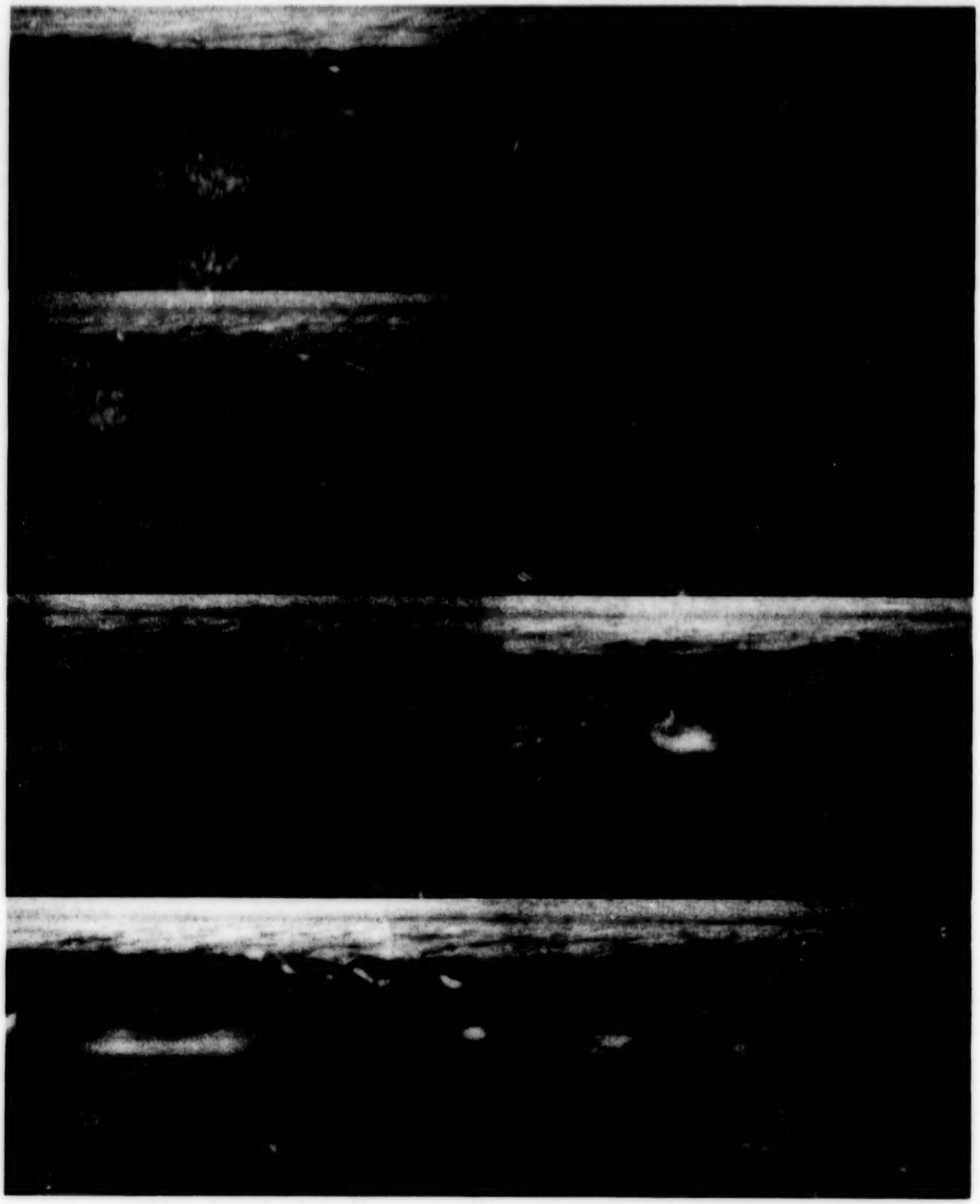

Figure 145. Convective activity associated with the plumes. A series of Voyager 2 cylindrical projected maps shows equatorial plumes passing material associated with a convective site near 15° N latitude. From *top* to *bottom*, the time difference between the figures is 60, 50, and 50 hours. Relative to System III longitude, the plumes move eastward, interacting with the material in the NEB and showing increased activity.

ORIGINAL PAGE
BLACK AND WHITE PHOTOGRAPH

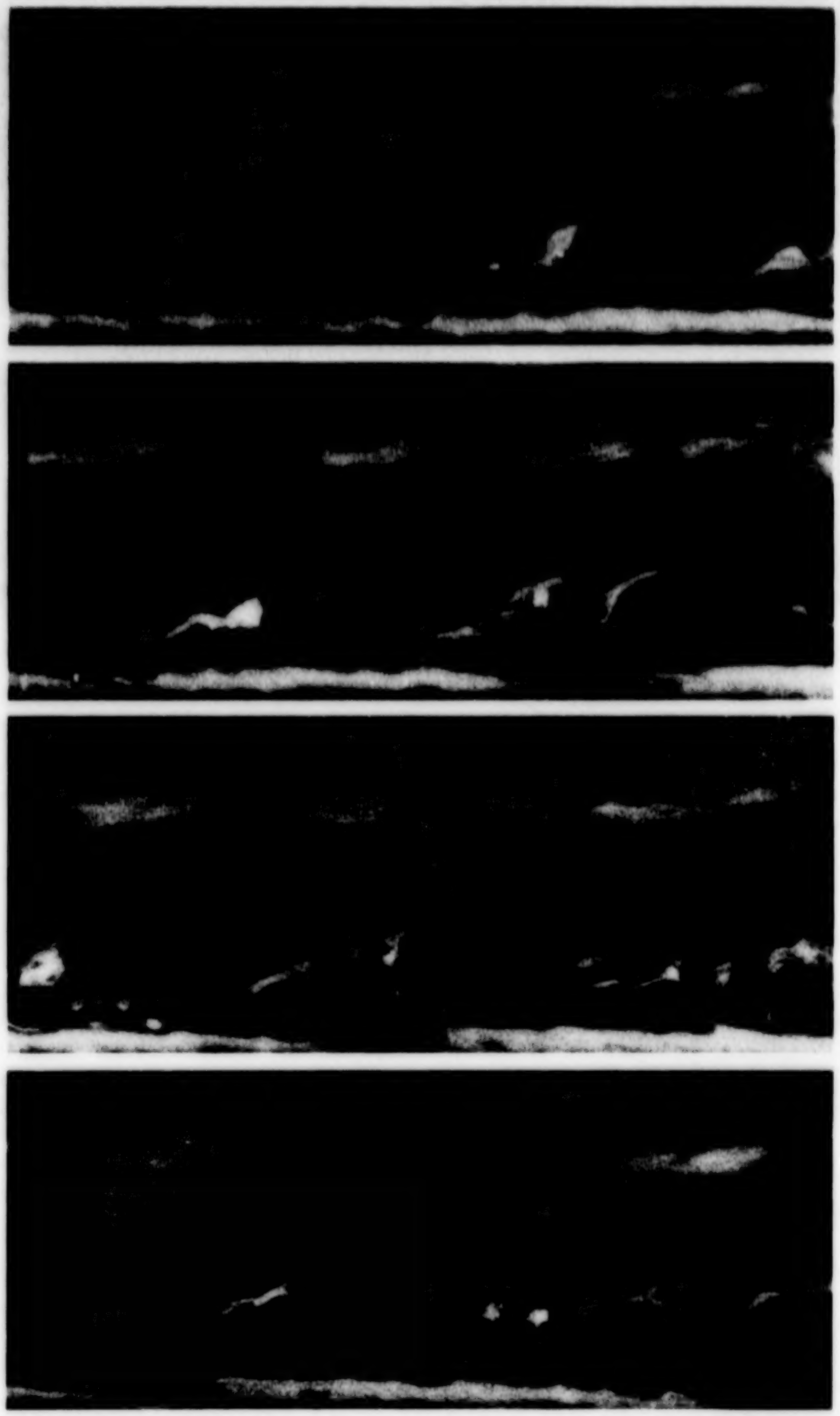

Figure 146. A south equatorial feature approaching the great red spot. These images are separated in time by 100 hours and have been projected relative to the position of the equatorial feature. During this 300-hour period, the feature approaches the convective region west of the GRS.

ORIGINAL PAGE
BLACK AND WHITE PHOTOGRAPH

Figure 147. The south equatorial feature passing the great red spot. As the equatorial feature encroaches on the GRS, material from west flows north of the GRS. The west end of the south tropical zone disturbances is located east of the GRS in this Voyager image.

show distinct features with structure similar to that of the GRS or the GRS hollow. Figure 150 shows an example from the archives of the Royal Astronomical Society. When compared with the 1891 and 1928 photographs, the 1857 drawing by Dawes and the 1860 drawing by Huggins provide strong evidence for a GRS at that time; however, the structures to the west of the GRS in Dawes' drawing and the darkness of the south equatorial belt in Huggins' drawing indicate that the GRS was mixed with white material and would not have presented a distinctive color.

Recent photographs yield smaller east-west dimensions of the GRS and measurements of photographic data indicate that since 1943 the GRS has been shrinking (Beebe and Youngblood, 1979). Possibly the GRS "feeds" off the zonal winds in a variable manner such that over intervals of decades it waxes and wanes.

Mid-Latitude Anticyclonic and Cyclonic Features A series of cyclonic and anticyclonic features are associated with a westward jet at 36°.8 S latitude. The cyclonic features lie to the north of the maximum westward flow, whereas the oval anticyclonic features are on the poleward side of the westward maximum. Nine pairs of anticyclonic-cyclonic pairs span a longitudinal interval of 205°. The pattern is less well defined at the remaining longitudes, with cyclonic features becoming more diffuse and spanning larger intervals of longitudes. This pattern drifts eastward relative to System III at a rate of 0°.6/day or 7 m s^{-1}.

The evenly spaced longitudinal interval has relatively high contrast between the features, and at ground-based resolution, the anticyclonic features appear as bright spots surrounded by dark regions and are bounded on the northwest by more diffuse, large clouds (see fig. 151). The drift rate of this pattern is linear and the most constant of any long-term motion on the planet. Not only does the series of anticyclonic features drift eastward, but also the intervening cyclonic structures retain consistent spacing and drift eastward at the same linear rate. Although several of the cyclonic features display high albedo, similar to the cyclonic region between FA and BC, one of these features mixed and became turbulent during the approach phase of Voyager 1 (Smith et al., 1979a). The manner in which these structures dissipate or their average lifetimes has not been established, although a consistent pattern was followed from 1976 to 1980. The zonal velocities of these and other (GRS, white ovals) anticyclonic features reflect the zonal wind field in which they are embedded, and their north-south dimensions correlate with the spacing of the zonal wind maxima.

ORIGINAL PAGE
BLACK AND WHITE PHOTOGRAPH

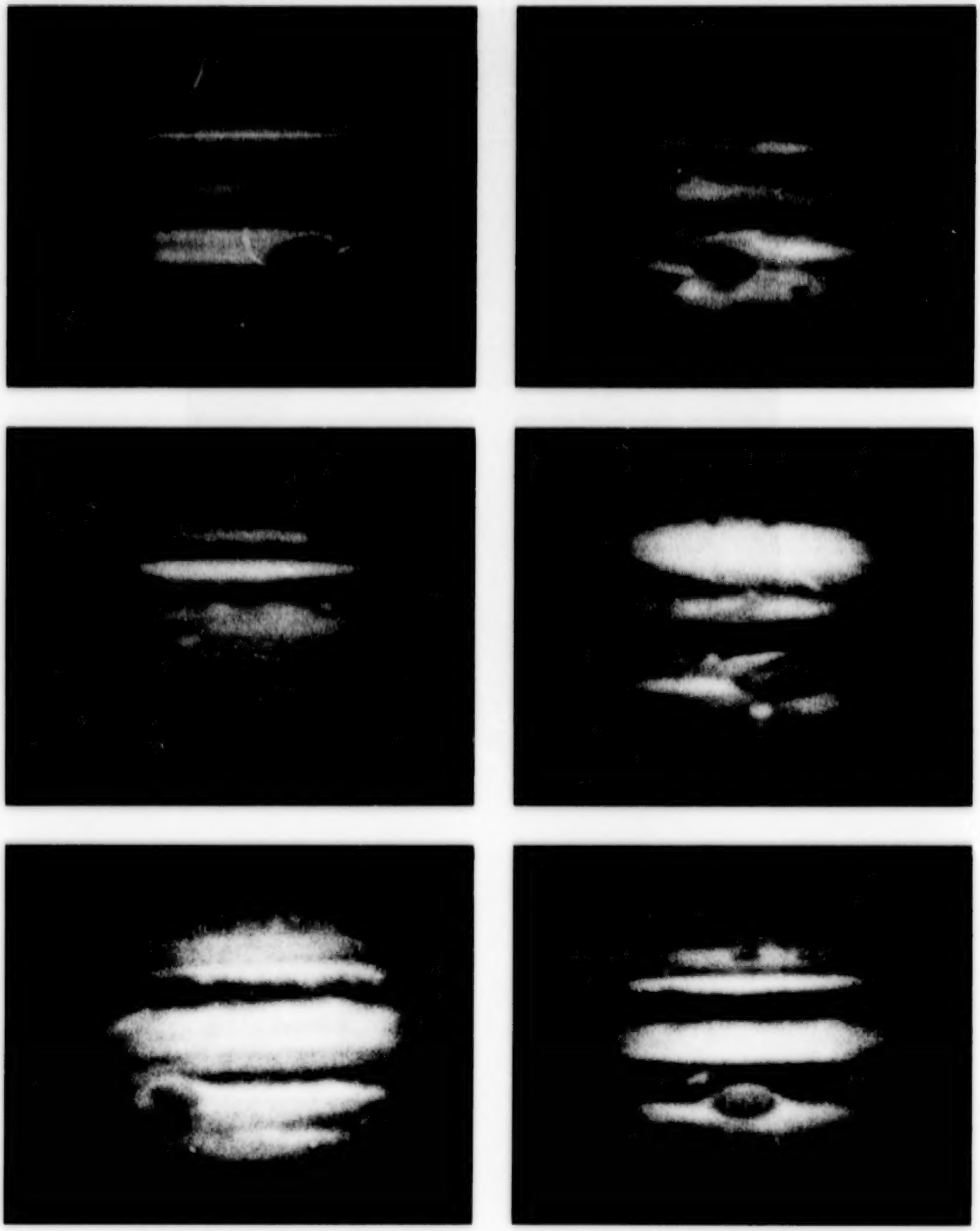

Figure 148. Variability of the great red spot. A series of images obtained through the NMSU blue band-pass illustrate the appearance of the GRS. From *top left* to *bottom right* these images were obtained on 22 August 1973, 17 October 1975, 9 December 1976, 11 February 1979, 11 May 1981, and 14 October 1986.

ORIGINAL PAGE
BLACK AND WHITE PHOTOGRAPH

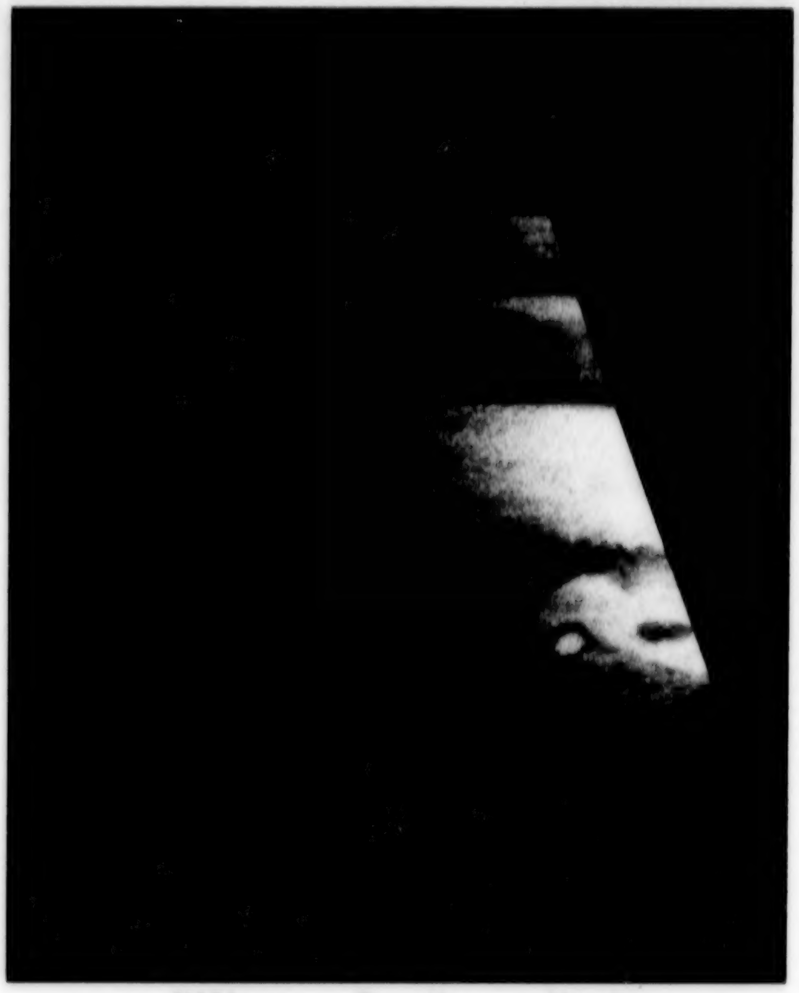
NASA Pioneer 11 Univ. Ariz.
Range: 540000 km Phase: 70 LCM2: 20
Mid time of data receipt 3 Dec. 00:30 UT
C3 Blue Date: 12/4/74

Figure 149. A high-resolution Pioneer image of the great red spot. This image obtained in blue light on 3 December 1974, at 00:20 UT, illustrates an aspect of the GRS that occurs when eddies encroaching on the eastward cusp carry a minimum of contaminating ammonia ice into the GRS. These intervals last for 1.5 to 2.5 years, and the GRS displays maximum UV and violet absorption.

CLOUD VERTICAL STRUCTURE AND PARTICLE SIZE

Detailed descriptions of changing colors, albedos, and morphologies of clouds give us many clues about the nature of dynamic processes in the jovian atmosphere, but we lack crucial information on the three-dimensional character of the cloud fields, vertical winds, cloud physics parameters, and the temperature structure. This section addresses the state of our knowledge of the time-variable nature of the vertical cloud and haze structure. The only information on temporal variability of scattering phase functions and sizes of particles in the upper troposphere comes from high phase angle photometry and polarimetry observed by the Pioneer and Voyager spacecraft. The Pioneers 10 and 11 data were taken a year apart and show no changes in scattering properties, at least in the SEB and STrZ (Smith and Tomasko, 1984). The Voyager data have not yet been studied enough to assess possible changes in scattering phase function.

Information bearing on cloud vertical structure and particle size is not as easily obtained as information on cloud morphology and motion, and our description is

ORIGINAL PAGE
BLACK AND WHITE PHOTOGRAPH

therefore not nearly as detailed as that given in the previous section. What we have learned about cloud vertical structure comes from measurements of hydrogen, methane, and ammonia absorptions in the visible and near-infrared, images of the planet in the 5-, 8.5-, and 45-μm windows, and photometry and polarimetry from instruments on the Pioneer and Voyager spacecraft. In the following paragraphs we focus on the time-variable or time-constant nature of the aerosol structure, and neglect many papers that help define the aerosol properties but that do not address temporal variability. For a review of jovian cloud structure see West et al. (1986).

Temporal variability of the cloud vertical structure on scales typical of belts and zones is difficult to measure. Weak methane and hydrogen quadrupole absorp-

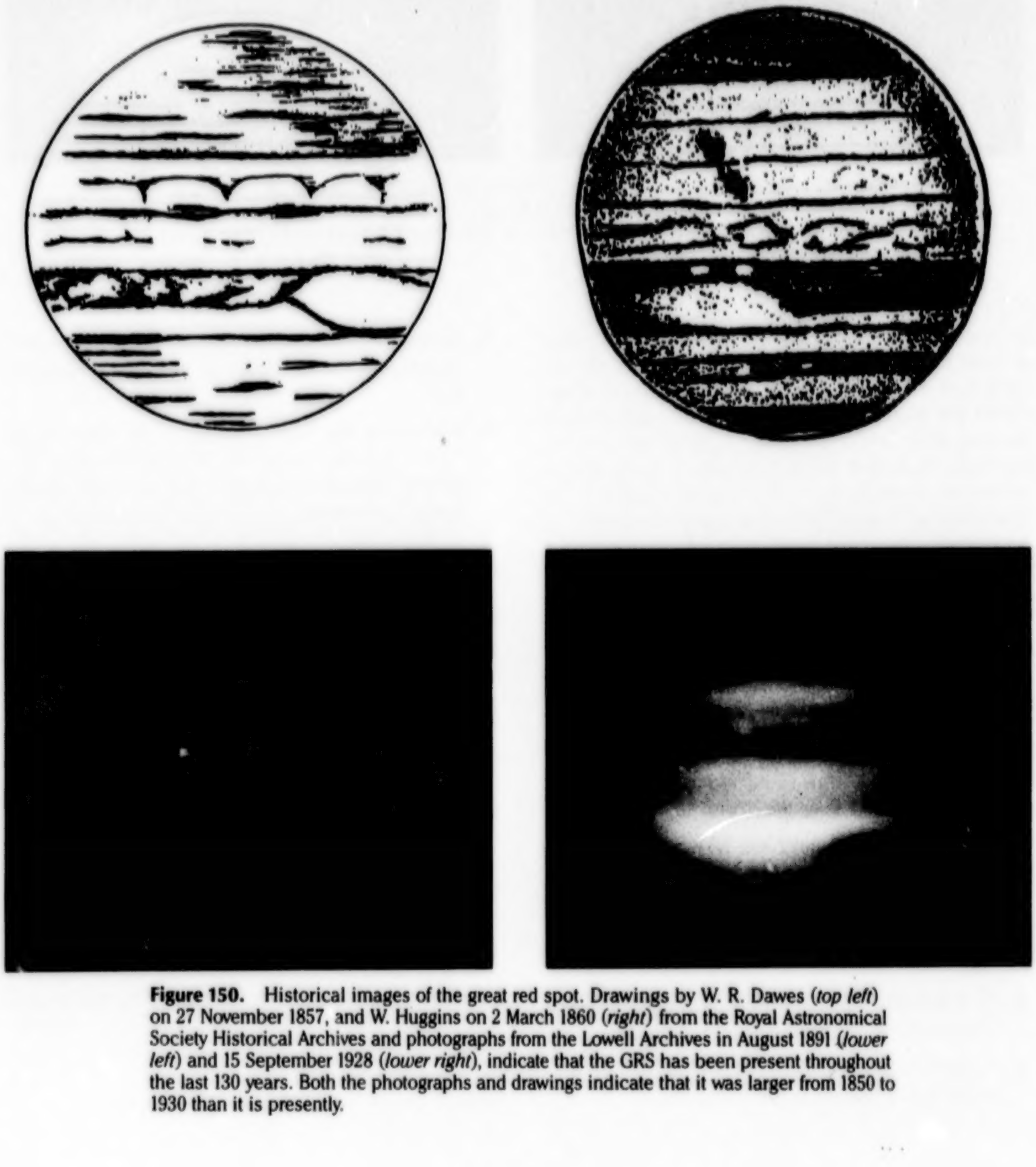

Figure 150. Historical images of the great red spot. Drawings by W. R. Dawes (*top left*) on 27 November 1857, and W. Huggins on 2 March 1860 (*right*) from the Royal Astronomical Society Historical Archives and photographs from the Lowell Archives in August 1891 (*lower left*) and 15 September 1928 (*lower right*), indicate that the GRS has been present throughout the last 130 years. Both the photographs and drawings indicate that it was larger from 1850 to 1930 than it is presently.

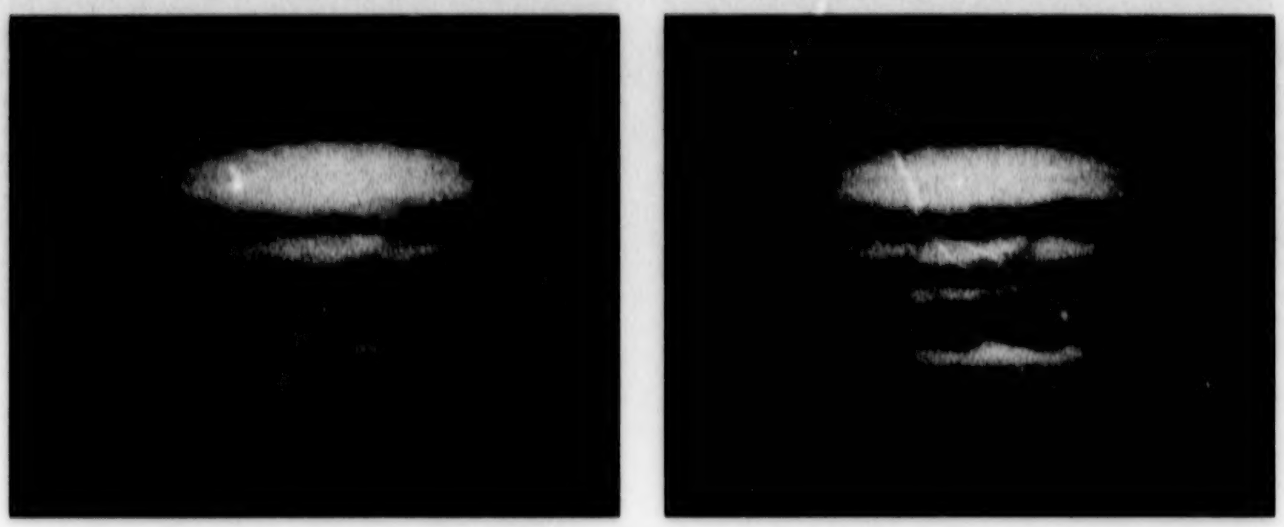

Figure 151. Southern anticyclonic and cyclonic features. The white oval, FA, is seen near the meridian in the *left* image. Southward of the oval, a series of small ovals are visible near 37° S latitude. These images were obtained in the NMSU blue band-pass on 13 February and 10 February 1979.

tions appear to be stable at the uncertainty level typical of most observations (~10 percent). But with the exception of a one-year effort by Cochran and Cochran (1983) discussed below, a careful, quantitative study of the long-term variability of these spectral features has not been carried out. The only reports of real temporal variations outside the EZ, which we discuss later, come from work by Minton (1973) who compared images of the planet in the strong 0.89-μm CH_4 band with colors and albedos in the visible for a four-year period (1969–1972). Minton made the following remarks:

1. Throughout the four apparitions the RS (great red spot) was always yellow-red in color and was always bright in methane.
2. Throughout the four apparitions the STrZ was always bright and nearly white and was always bright in methane.
3. From 1971 through 1972 the NTB was yellow-red color and was bright in methane. Prior to this it was split and faint and also faint in methane.
4. In 1972 the EZ was yellow-red in color and bright in methane.
5. In 1969–1970 the EZ was dominated by cyan-colored festoons and was dark in methane.
6. In 1969–1970, when the NTrZ became light red in color, it also became bright in methane.
7. During the four apparitions the NNTZ was most prominent in 1971. This was true in methane as well.
8. Throughout the four apparitions, the three long-lived STZ white ovals, BC, DE and FA, were frequently as bright as any zone, but they were nearly absent in methane.
9. In 1968–1969 the NTrZ was one of the brightest zones, but was faint in methane.
10. Throughout the four apparitions, the STZ was quite prominent, but was faint in methane.
11. In 1971, prior to the two SEB disturbances, the south equatorial belt (SEBZ) was the brightest zone, but was dark in methane.

In early 1977, the GRS, EZ, and NTrZ were bright in methane; the STrZ was less bright, and the NTZ and STZ were dark, as seen in images obtained by West (1979). Apparently the GRS is always bright in methane, but its color and albedo at blue wavelengths can vary dramatically. Other regions, especially the SEB, are variable in both their methane and continuum reflectivity. Both north and south polar hoods are seen in the 1977 methane images, but the south hood is the brightest. This asymmetry is a persistent feature of all methane images taken during the past two decades. Images taken in late 1986 by one of us (West) in the strong methane band resemble images taken in 1977.

ORIGINAL PAGE
BLACK AND WHITE PHOTOGRAPH

Observations in the weak methane and hydrogen bands are more numerous than those for the strong 0.89-μm band. Photometric measurements of the equivalent width of the CH_4 0.619-μm band date back to 1928 (Elvey and Fairly, 1932). It is tempting to compare observations at different epochs by different observers to estimate temporal variability, but we have not done so because the uncertainties in the measurements are often comparable to the suspected variability, and subtle differences in the method of determining equivalent width used by different observers can lead to important differences in the results (see e.g., fig. 15 of Sato and Hansen, 1979). The most reliable indication of temporal variability comes from observations taken and reduced by the same observer(s) using the same equipment and data reduction techniques. Complications can arise even for those restrictions when, for example, the Doppler-shifted planetary H_2 3–0 S(1) quadrupole line blends with telluric H_2O lines in different ways depending on the epoch and local humidity. Since the variations are weak, the reliability of claims regarding changes in equivalent width will depend strongly on signal-to-noise, photometric accuracy, spectral resolution, spatial resolution, and knowledge of the position of the aperture on the disk. These factors are improving in recent years as high signal-to-noise array detectors are more widely used.

With the above caveats in mind, we restrict our discussion of the time-variable nature of weak H_2 and CH_4 absorptions to three papers (Carlton and Traub, 1974; Hunt and Bergstralh, 1977; Cochran and Cochran, 1983). The first two of these were concerned with H_2 3–0 S(1), S(0), and 4–0 S(1) quadrupole lines, and the third examined the CH_4 0.619-μm band and the NH_3 0.645-μm band. The Carleton and Traub measurements were made in June of 1971, and June and July of 1972. Hunt and Bergstralh observed in June and August, 1972. Cochran and Cochran made measurements in 1979 and 1980. In all cases, measurements were made at the equator on the central meridian. Instrument apertures spanned 10° to 60° of latitude.

Carleton and Traub reported equivalent width of the 4–0 line to remain constant within the uncertainty of their measurements (±5 percent), whereas the 3–0 S(1) line varied by as much as 40 percent over a period of a week. The authors commented on the difficulty of accounting for constancy in the 4–0 line but variability in the 3–0 line, and suggested that a variable high thin haze is responsible for modulating the 3–0 line. The 4–0 line is weaker than the 3–0 line, and would be less influenced by variations in a high, thin haze. They left as an exercise for the future, calculations for quantitative scattering models to test the idea.

Hunt and Bergstralh claimed to have seen large variations (4.5–12.5 mÅ) in the 4–0 equivalent width, and also in the 3–0 S(1) (35–63 mÅ) and S(0) (22–46 mÅ) equivalent widths. They stated that their measurements indicate, but do not establish conclusively (because of the uncertainties in the data), that the time scale for change was less than a day. It is not clear how such a statement can be made since different longitudes were observed on different days, and longitudinal variations must not be confused with temporal variations. The variations in the 4–0 equivalent widths contradict the constancy found by Carleton and Traub, but the variations in the 3–0 S(1) equivalent widths are comparable.

The weak 0.619-μm methane band samples very nearly the same region of the atmosphere (down to about 10 bars in the absence of aerosol) as the weak 4–0 H_2 line, and should correlate with that line when variations occur. Cochran and Cochran (1980, 1983) obtained complete longitude coverage of methane and ammonia absorptions and reduced their data in a careful and systematic way to discern small longitudinal and temporal variations. They showed highly correlated longitudinal variations of ±8.5 percent for CH_4 and ±17 percent for NH_3 equivalent widths. The equivalent widths are not correlated with continuum reflectivity, although a weak anticorrelation may be present. The amplitudes of the longitudinal variations were similar in 1979 and 1980. The average equivalent width increased by 8.6 percent between the two apparitions.

Recently Cunningham (1987) and Cunningham et al. (1987) reported an east-west asymmetry in the equivalent widths of the 3–0 S(0) and S(1) hydrogen quadrupole lines, which they interpret as evidence for a diurnally varying ammonia cloud. The magnitude of the asymmetry is about 15 percent for the S(1) line in the equatorial region, and significantly less for the weaker S(0) line. Cunningham et al. proposed that the optical depth of the ammonia cloud decreases from about 6 to about 3 between morning and evening. They gave a plausible account of this decrease in terms of the amount of absorbed sunlight available to sublimate ammonia crystals and to suppress convective activity during the day. This result needs to be checked, since an asymmetry has not been reported previously for any H_2 or CH_4 observations, and since Cunningham saw no asymmetry in methane band absorption observed with the same equipment.

The data presented thus far give only vague and sometimes conflicting clues about the temporal nature of the vertical structure and thickness of clouds and hazes. Corroborating data are needed to resolve the conflicts, and more detailed data are required to clarify the morphological nature of absorptions and to relate them to specific atmospheric features. In this regard, West et al. (1985) examined Voyager 1 images and showed that the amplitude of the longitudinal variations in the EZ, when averaged over the same spatial resolution as the Cochran and Cochran data, were about the same as what Cochran and Cochran had found. However, the spatial scale of the variations is generally smaller than the spatial resolution of the ground-based data, and the amplitude of the variation can be as large as a factor of two for spatially resolved regions. An independent check on the H_2 3–0 S(0) and S(1) lines comes from the fact that their ratio should fall within the range bounded by equilibrium and normal modifications of H_2 as predicted by theory and as observed by Conrath and Gierasch (1984). West et al. (1985) argued that some of the Hunt and Bergstralh ratios were outside the acceptable range, and that those observations that were consistent varied by only ± 10 percent. That fact, coupled with the constancy of the 4–0 line observed by Carleton and Traub, and the weak variations in the methane data, lead us to conclude that variability of the magnitude reported by Hunt and Bergstralh for the 4–0 quadrupole line is due to low signal-to-noise, or some other factor not intrinsic to Jupiter. The stronger 3–0 lines may have larger amplitude variations, but more work needs to be done to corroborate the measurements, and to examine the possibility that weak telluric lines are a source of variability.

Temporal variations are clearly seen in 5-μm images of Jupiter. Terrile and Westphal (1977) noted changes occurring over four days for regions as large as 12,000 km. Major variations take place also on large scales and longer time periods. Data from 1973 to 1979 were summarized in three papers by Terrile and Beebe (1979) and Terrile et al. (1979a, b). These papers describe changes occurring between the Pioneers 10 and 11 encounters in 1973 and 1974, and the Voyager encounters in March and July of 1979. In figure 152 a series of four images from Terrile and Beebe (1979) and two images from Terrile et al. (1979a) show the morphology of 5-μm emission between 1974 and 1979. Jupiter's visible appearance during the Pioneer and Voyager encounters (December 1973 and March 1979) can be seen in figure 153. The variations seen in the 5-μm images are summarized as follows.

Highest intensity (and therefore most transparent at 5 μm) regions were confined to the NEB and SEB, and were approximately symmetric about the equator in September 1973. No other latitudes were prominent at 5 μm during this period, and the GRS was invisible. Almost a year later, much of the emission from the SEB had disappeared, although some longitudes were still bright. Strong emission from the south temperate belt (STB) was apparent. In 1975 emission from the SEB was again strong, perhaps stronger than that from the NEB. Emission from the STB was absent. In 1976 both the NEB and SEB were bright, and emission from the perimeter of the GRS was detected for the first time. As seen in images taken in 1978 and 1979, emission at the perimeter of the GRS became prominent in 1978 (equatorward side only) and 1979 (both sides). A thin bright band appeared at the equator sometime between September 1978 and March 1979.

The appearance of the planet at 5 μm correlates well, but not perfectly, with its appearance in the visible, and it is possible to associate some changes in the visible appearance with cloud structure as inferred from 5-μm images. The clearest example is the SEB disturbance that occurred in 1975 when the southern component of the SEB darkened at visible wavelengths and brightened at 5 μm. For this case, we have evidence that a major darkening event corresponded to a reduction of cloud opacity at 5 μm. The vertical location where this reduction occurred is a matter of considerable interest and some controversy, since albedo is not correlated, or may be only weakly correlated, with cloud structure indicators (H_2 and CH_4 equivalent widths, polarization from the Pioneers 10 and 11 Imaging Photopolarimeter instruments) at visible and near-IR wavelengths.

In an effort to account for the behaviors of the visible-near-IR absorptions, polarimetry, and 5-μm images, West et al. (1985) proposed that the upper cloud-haze layer seen at visible wavelengths is composed of a stable population of small (mean radius near 1 μm or less) particles having optical depth near 7.5 at visible wavelengths, but near 1 at 5 μm. This layer is ubiquitous, and extends up to about 320 mbar in the NTrZ and STrZ. It is mostly transparent to 5-μm radiation, implying the single scattering albedo at 5 μm is 0.75 or higher (West, 1984). It accounts for the near-constancy of absorptions at visible and near-IR wavelengths. Small changes in the thickness or altitude of this layer can account for variations reported by Minton for the strong 0.89-μm CH_4 band. West et al. (1986) further proposed that a population of larger particles (3–100 μm) near the base of ammonia cloud is responsible for most of the temporal and longitudinal variability. Clouds in the 2-bar region could also modulate 5-μm opacity, but

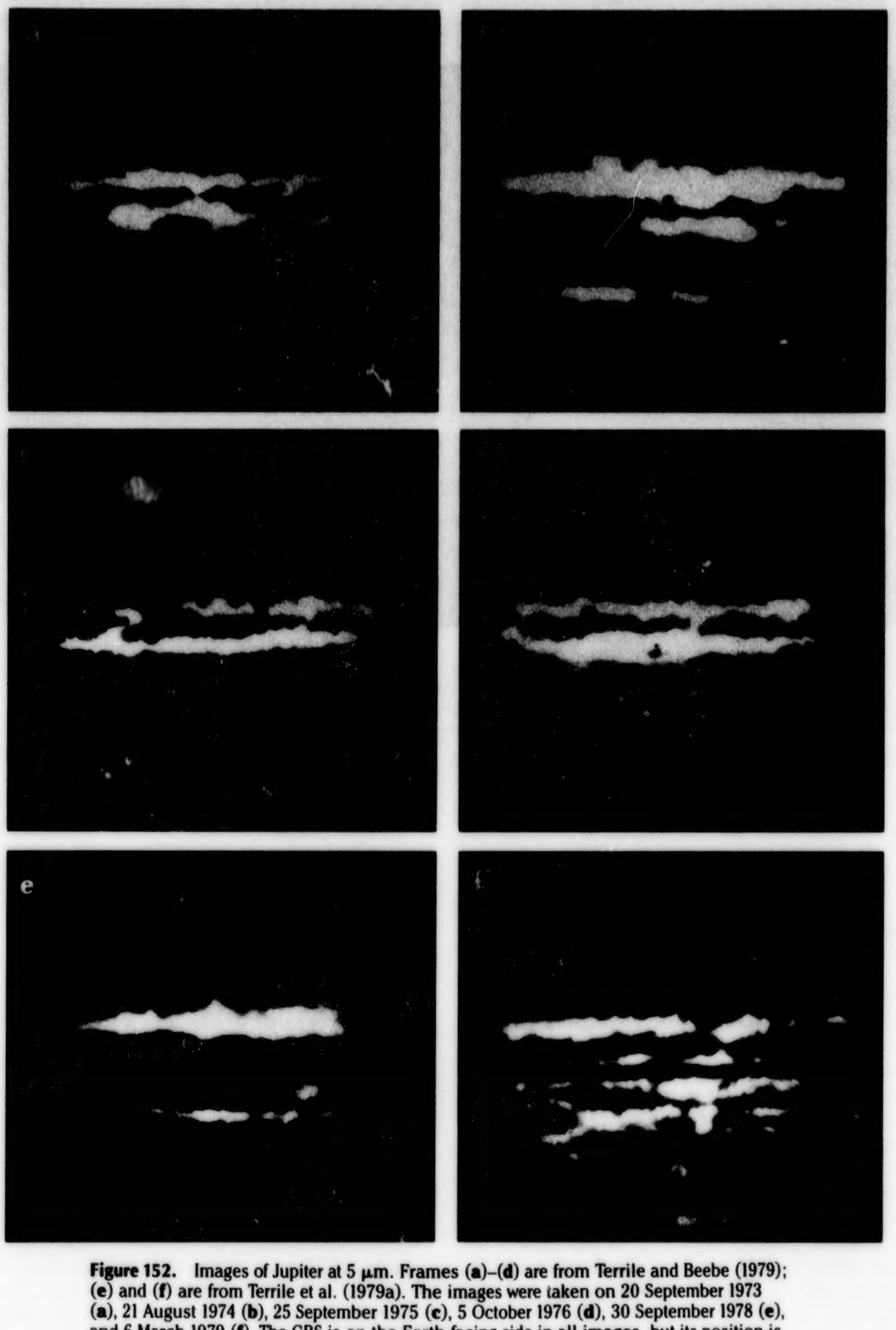

Figure 152. Images of Jupiter at 5 μm. Frames (**a**)–(**d**) are from Terrile and Beebe (1979); (**e**) and (**f**) are from Terrile et al. (1979a). The images were taken on 20 September 1973 (**a**), 21 August 1974 (**b**), 25 September 1975 (**c**), 5 October 1976 (**d**), 30 September 1978 (**e**), and 6 March 1979 (**f**). The GRS is on the Earth-facing side in all images, but its position is apparent only in the 1976, 1978, and 1979 images. Other changes are noted in the text.

ORIGINAL PAGE
BLACK AND WHITE PHOTOGRAPH

Figure 153. Jupiter as seen by the Pioneer 10 IPP (*left*, 2 December 1973), and Voyager 1 Imaging (*right*, 29 January 1979). Colors are approximate (the Pioneer image is closest to the truth). Large-scale differences in the appearance of the SEB, STrZ, and NTB are obvious. These images can be compared with the 5-μm images (**a**) and (**f**) in figure 152.

only the clouds at the ammonia condensation level or higher could effect the 45-μm opacity that is correlated with 5-μm opacity (Gierasch et al., 1986).

TIME-VARIABLE NATURE OF THE TEMPERATURE STRUCTURE

The nature of the mean vertical temperature structure of the jovian atmosphere has been known for some time. Estimates of the temperature structure based on consideration of radiative-convective equilibrium (e.g., Wallace et al., 1974, or more recently, Appleby and Hogan, 1984) compared favorably with more direct determinations of the temperature structure. For the part of the atmosphere that is detectable by direct methods, control of the atmosphere is dominated by convection or radiation. We find that time-dependent changes in each of these portions of the atmosphere behave somewhat differently from one another. Methods of detecting temperatures directly include occultations and infrared sensing.

Occultation Data

Observations of solar and stellar occultations by the Voyager ultraviolet spectrometer (e.g., Atreya et al., 1981, and references therein) yielded information about the temperature structure at pressures of less than 1 mbar. This portion of the atmosphere is covered in more detail in a separate chapter (by Clarke et al., this volume). Voyager 1 and 2 radio occultation results (Lindal et al., 1981), were far less noisy and freer of systematic uncertainties than early Pioneers 10 and 11 data (cf., Kliore and Woiceshyn, 1976). The derived temperatures for the Voyager 1 ingress near 12° S and egress near the equator are different for the stratosphere, suggesting atmospheric vertical waves that are out of phase by 180°.

A major difficulty in interpreting occultation-based results to determine time dependence is that of separating spatial from temporal variations. In the case of the Voyager radio occultation profiles, one could conclude that the wave structure represented evening versus morning terminator differences in diurnal behavior.

ORIGINAL PAGE
COLOR PHOTOGRAPH

However, we cannot be certain that we are really comparing regions being governed by the same diurnal characteristics, because the data were not taken at the same longitudes and because these differences may have nothing to do with diurnal variability.

Infrared Data

The dominant opacity in the far infrared is the collision-induced H_2 dipole; this together with a very strong band of methane absorption near 7 μm (1300 cm^{-1}) provide the requisite tools for sounding temperature, as both constituents are expected to be uniformly mixed throughout the atmosphere (cf., Conrath and Gautier, 1980). In relatively clear portions of the jovian atmosphere, temperature sounding can be performed using the collision-induced opacity of molecular hydrogen between about 200 and 600 mbar total pressure and to much lower pressures in the stratosphere using the strong lines of the ν_4 CH_4 fundamental band. In practice, some portions of the atmosphere are obviously influenced by clouds, and sounding at atmospheric pressures greater than 400 mbar is problematical. Also, the CH_4 emission feature is in a spectral region of relatively low thermal radiance. Further limitations on ground-based observations are imposed by absorption in Earth's atmosphere. Usually observations are limited to wavelengths no greater than 22 μm (450 cm^{-1}), owing to strong telluric water vapor absorption. Telluric CO_2 absorption blocks observations between about 14 and 17 μm (600–700 cm^{-1}), and water vapor absorption essentially blocks out the short-wavelength portion of the CH_4 band (short of 7.6 μm or 1320 cm^{-1}).

Changes in the global mean thermal radiance for the planet at any wavelength sensitive to temperature have not been seen outside the uncertainties of instrumental calibration. Just as at visible wavelengths, then, any attempt to understand temporal variability in the atmosphere must rely on resolution of at least the major banded structure of the disk. A brief review of some of these data follows.

The first published attempt to observe the jovian atmosphere with some spatial resolution began with observations in a broad 10-μm region (Murray et al., 1964; Wildey et al., 1965). These observations cover a spectral region that is not particularly sensitive solely to atmospheric temperatures. This is also the case with observations of localized 5-μm radiation (Westphal, 1969; Westphal et al., 1974). Nevertheless, these measurements indicated a consistent anticorrelation between the thermal and visual appearance of belts and zones and the often even cooler GRS at nearly all thermal wavelengths. Later, Murphy and Fesen (1974) made central meridian scans of Jupiter at 20 μm, sensitive only to temperature variations on the planet, which confirmed this relationship.

Very important observations of Jupiter were made by the infrared radiometer (IRR) on board Pioneer 10 in December 1973 and Pioneer 11 in December 1974, which sensed the planet in broadband channels centered near 20 and 45 μm (500 and 220 cm^{-1}). The IRR field-of-view was 1.0 by 0.3°, with the long axis aligned approximately north-south on Jupiter, covering about 3 percent of the planetary diameter. The IRR yielded images of the planet in each channel centered near 11° S latitude (Pioneer 10) and 41° S and 52° N (Pioneer 11) (Ingersoll et al., 1976). No large-scale changes or calibration differences were observed between the two instruments. The long-wavelength channel was sensitive to variations of gas abundance and cloud opacity in addition to temperature. A comparison between the infrared data from the Voyager infrared interferometric spectrometer (IRIS) experiment and the IRR 20-μm channel, the only channel completely overlapped by the IRIS spectral range, shows consistency in the mean level of planetary thermal emission to within the 8 percent uncertainty quoted for the IRR (Orton and Martonchik, 1987).

Prior to the Voyager encounters with Jupiter, Sinton et al. (1980) reported observations made in February 1978 at several wavelengths using discrete filters, each about 1 μm wide. Some of these were sensitive primarily to temperature: 7.8 μm (1300 cm^{-1}), 16.1 μm (620 cm^{-1}), 18.1 μm (550 cm^{-1}), and 25 μm (400 cm^{-1}). About 6 percent of the disk diameter was resolved; at longer wavelengths diffraction made the spatial resolution somewhat worse. Sinton et al. (1980) showed the similarity of the infrared flux over most wavelengths, confirmed the thermal and visual radiance anticorrelation, and determined that the 7.8-μm flux did not behave like the other wavelengths but had a pronounced hemispheric asymmetry with the north much warmer than the south. Caldwell et al. (1979) also reported similar scans with filters at 7.9 μm (1270 cm^{-1}), 17.8 μm (560 cm^{-1}), and 19.7 μm (510 cm^{-1}) made in January 1978 and March 1979, also resolving about 6 percent of the disk diameter. They also noted the (by this time) "classical" infrared appearance of the planet at 17.8 and 19.7 μm and indicated a possible anticorrelation between the meridional structure observed at 7.9 μm versus 17.8 μm, a relationship that later observations did not verify.

The Voyager 1 and 2 IRIS experiments provided spectroscopic detail with an accurate absolute calibration over a wide spectral range and made possible the simultaneous determination of tropospheric and stratospheric temperatures together with a high level of spectral discrimination against sources of systematic error. Especially helpful to an understanding of globally organized properties were maps of the planet obtained by repeated scans of the local central meridian for both spacecraft on both the sunlit and dark sides of the planet. These maps covered about 60° poleward of the equator over all longitudes with spatial resolution of about 10 percent of the disk diameter. Marten et al. (1981) suggested that IRIS data at a resolution corresponding to 4 percent of the disk diameter is required to resolve major belt and zone differences fully.

The data obtained by the Voyager IRIS experiment were used by Conrath et al. (1981), Flaser et al. (1981), and Hunt et al. (1981) to establish correlations between relatively cool areas and anticyclonic features; correlations were also established between warm areas and dark visible regions. Pirraglia et al. (1981), comparing zonal mean temperatures retrieved from IRIS data, again established the correlation between high-albedo clouds and cold temperatures with a major exception being the warm and bright NTB between 24 and 36° N latitude. More recently Gierasch et al. (1986) surveyed IRIS and imaging data on Jupiter, deriving temperatures at the 150- through 270-mbar levels, along with NH_3 gas abundances, cloud properties, and variations of the *para*-H_2 to *ortho*-H_2 ratio. Muller and Roff (1987) also combined an analysis of Voyager infrared and imaging data, finding a strong correlation between brightness temperatures at all levels at the tropopause and deeper and strong anticorrelations for 226 and 602 cm^{-1} brightness temperatures versus visible reflectivity.

In the epoch after the Voyager encounters, programs to characterize global infrared radiance and search for time variability continued. Spatially resolved observations of the central meridian of Jupiter were made by Caldwell et al. in 1980 at the Kitt Peak National Observatory similar to those reported by Caldwell et al. (1981); these were followed in 1981 (and following years) by similar discrete-filtered observations at the NASA Infrared Telescope Facility. From 1981 to 1983, observations of the central meridian of Jupiter were made, with one of us (Orton) joining the collaboration starting in 1982. Early results of the central meridian observations at 7.8 μm reported the discovery of stratospheric hot spots associated with the magnetic poles (Caldwell et al., 1981; Caldwell et al., 1983). Observations continued with rudimentary maps of quadrants of Jupiter in 1983 and, following the development of efficient software for the telescope pointing and data acquisition, full maps of the planet in 1984 through the present. The resolution of these images corresponds to about 5 percent of the disk diameter, except for 1980 (about 9 percent of the disk diameter). The majority of these data remain unreduced and unanalyzed. Some reporting of the unreduced data in image form has been made in oral presentations or poster talks at professional (American Astronomical Society and its Division of Planetary Sciences) meetings or in brief review form (Orton et al., 1981; Orton et al., 1984a, b; Orton, 1986; Orton et al., 1987), and some analysis has been reported (or is in preparation) (Caldwell et al., 1985; Halthore et al., 1985; Caldwell et al., 1986; Halthore et al., 1986; Caldwell et al., 1987; Halthore et al., 1987). We attempt no new analysis for this review and examine only relatively raw forms of the data. The most recent of these data sound temperature structure at a linear resolution of about 5 percent of the planetary disk with discrete filters that are approximately 1 μm wide at 7.8 μm (1300 cm^{-1}), 17.8 μm (560 cm^{-1}), and 19.6 μm (510 cm^{-1}) and a 2 percent CVF filter wedge at 12.85 μm (778 cm^{-1}). After 1986, the 17.8- and 19.6-μm filters were replaced with filters centered at 18.0, 20.0, and 22.0 μm (560, 500, and 450 cm^{-1}, respectively). Observations were also made with a discrete filter at 4.8 μm (2100 cm^{-1}), and CVF wavelengths of 8.56, 10.74, and 11.11 μm (1170, 930, and 900 cm^{-1}, respectively) to serve as monitors of NH_3 gas distribution and of various cloud properties. There are few variations from the "classical" infrared appearance with anticorrelated visual and infrared radiances. A major exception is the 7.8-μm appearance of the stratospheric temperature structure that does not appear to be correlated directly with tropospheric banded structure at any other wavelength; it also appears to be highly variable with characteristic time scales ranging from years to days or less. Meridional averages or meridional samples excerpted from maps are included in the data shown in figure 154.

Seasonal Variability

Summer solstice for the jovian northern hemisphere occurred in 1976 and will occur again in 1988, winter solstice in the late 1982 (Caldwell et al., 1979; Beebe et al., 1986). Jovian perihelion occurred toward the end of 1975. Caldwell et al. and Bezanger and Bézard (1986)

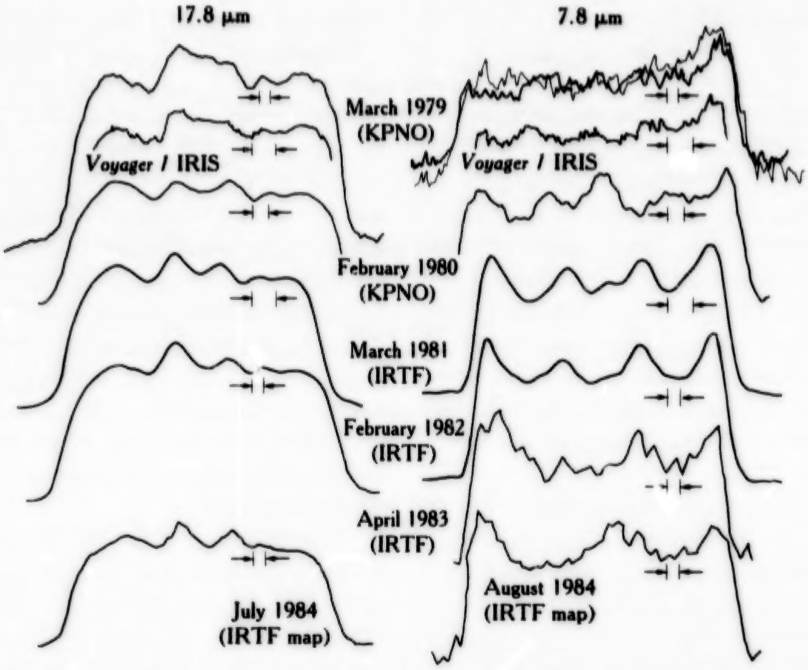

Figure 154. Scans of the jovian central meridian near 17.8 μm (or 18.0 μm) (*left*) and 7.8 μm (*right*) between 1979 and 1984. South is to the left and north to the right. An element of spatial resolution is indicated schematically for each plot. No scan for 17.8 μm was available for 1983. Variations of the radiance are equivalent to temperature changes on the order of 3 K in each case.

gave theoretical results for radiative-convective models where insolation is a time-dependent function; both groups showed detectable variations of temperature for the seasonally forced, radiatively driven part of the atmosphere that are characterized by maxima or minima occurring about three years following insolation maxima or minima. The models of Bezanger and Bézard, somewhat more sophisticated in their handling of the vertical deposition of insolation, show maximum peak-to-peak temperature differences between latitudes in alternate hemispheres 60° poleward of the equator of about 2.5 K in the stratosphere (at 1 and 10 mbar), about 1 K at 100 mbar, and less at 300 mbar.

Figure 154 shows that at 17.8 μm, sensitive to temperatures near 150 mbar, both hemispheres exhibited approximately equal temperatures in 1979, although in 1978 the data of Sinton et al. (1980) showed a warmer northern hemisphere. Subsequently, temperatures in the southern hemisphere began to increase relative to the north. At 7.8 μm, sensitive to temperatures in the thermally inverted stratosphere, temperatures are about equal in both hemispheres by about 1982, with the north warmer in preceding years and the south warmer in following years. The apparent differences in these two regions of the atmosphere are the consequence of different radiative response times characterizing pressure-squared-dependent molecular hydrogen for the deeper levels and pressure-dependent methane for the higher ones. Bezanger and Bézard predict equal temperatures near 100 or 300 mbar around early 1981 and in the upper stratosphere around 1982. These are roughly compatible with the data; deviations from the predictions of the theory, either in response time or in amplitude of the deviations, reveal where the model is incorrect, for example, by using incorrect opacity assumptions or neglecting the influence of other energy transport mechanisms.

The level of latitudinal detail evident in the 17.8-μm scans of figure 154 illustrates the difficulty in determining the presence of changes at the level of about 1 K without quantitative comparisons and knowledge of the annual (or semi-annual) mean. Although variations at 7.8 μm are larger, the considerable differences in the mean meridional structure from year to year will also tend to confuse our effort to detect seasonal forcing superimposed on this structure. Separating long-term time-dependent effects from annual ones is a challenge for quantitative analysis of these data, and an argument for continued monitoring through the seasonal cycle.

Time-Dependent Behavior of Tropospheric Temperatures

Observation of tropospheric temperature changes can be done from the ground in the region of the S(1) H_2 collision-induced dipole rotational feature near 600 cm^{-1}/16.7 μm. This spectral region is accessible from ground-based observatories, and, although it is sensitive to levels slightly above the nominal radiative-convective boundary, it appears to be correlated with all the changes in meridional radiance that arise from deeper levels (Muller and Roff, 1987; Orton and Martonchik, 1987) (cf., fig. 154 for a comparison with Voyager mean values from the north-south map sequence data).

Radiance measurements in this region are also useful because, by way of their sensitivity to atmospheric levels near the temperature minimum, variations from disk center to limb are not very strong.

We follow a chronological sequence of observations. For the most part, an examination of the 17.8-μm data of figure 154 shows great similarity from year to year; this continues into the past for the data sets we reviewed above. We are, therefore, looking for significant variations from this long-term mean structure with special interest in correlations of temperature changes with changes in visible albedo or color. Changes in temperature resulting from radiative adjustment to changing local albedo or thermal flux from deeper levels (strongly anticorrelated quantities) would be expected to display a time lag with respect to the visual changes of the kind associated with seasonal forcing. On the other hand, changes associated with processes that change both temperature and cloud properties could be characterized by much shorter time scales.

A major brightening of the visual cloud albedo in the SEB and area surrounding the GRS took place in late 1973, just prior to the arrival of Pioneer 10. IRR maps showed that the infrared characteristics of the meridional mean followed the usual anticorrelation with visible albedo (Orton et al., 1981), including the SEB. Thus, the temperature structure remained correlated with the visual albedo rather than the largely invariant zonal velocity structure. Furthermore, whatever processes occurred in the atmosphere to modulate the temperature, as sensed by the 20-μm IRR channel, must have operated on a scale of some two months or less, or it actually preceded the change in visual cloud properties.

Orton et al. (1981) noted a major exception to the general rule that the IRR-observed radiances were highly correlated with one another and anticorrelated with visual albedo. The visual appearance of the SEB did not differ greatly between Pioneers 10 and 11 encounters, neither did its dark 45-μm appearance. On the other hand, its appearance at 20 μm was much brighter at the time of Pioneer 11 than Pioneer 10. Terrile and Beebe (1979) pointed out that by 1975, the SEB in visible and 5-μm radiation showed increasingly beltlike properties, as at the time of the Voyager encounters. Assuming that the 20-μm radiation is primarily influenced by kinetic temperatures in the 100–300 mbar region, and that the 5-μm and 45-μm radiation is more strongly influenced by clouds, these observations indicate that the change in atmospheric temperatures actually preceded rather than lagged behind the changes in cloud properties.

Comparisons of the 17-μm appearance of Jupiter between Pioneer and Voyager encounters is difficult using the ground-based record. The 16.9- and 18.1-μm scans of Sinton et al. (1980) are rather smooth with respect to their standard deviations. Caldwell et al. (1979) do not show scans from 1978 at similar wavelengths. They do point out a small minimum feature in the 17.8-μm structure near 35° N latitude in 1979 (fig. 154) that did not appear in 1978. We do not know of changes in visual albedo near the southern edge of the NPR to which this apparent cooling might correlate.

At the time of the Voyager encounters, the general correspondence of dark to warm and bright to cool regions was followed, with the exception of the visually bright NTB, which displayed warm temperatures (Pirraglia et al., 1981). We note that the longer-wavelength part of the spectrum of this region that is sensitive to deeper temperatures and to the presence of cloud opacity follows the usual association of dark and cool regions. A serious and unanswered question is whether the warm thermal structure observed represents a long delay in responding to changes in the visual albedo and cloud opacity that took place in late 1977, or whether it is a harbinger of visual and infrared cloud properties that followed: The NTB returned to its dark visual appearance in 1981.

Gierasch et al. (1986) noted that in the few months separating the Voyager 1 and 2 spacecraft encounters with Jupiter, temperatures changed at latitudes near 10° N and 10° S with the Voyager-2 temperatures as much as 2 K warmer. Temperature changes on such short time scales undoubtedly represent changes in the organization of the driving dynamic system. These temperature differences diminish with increasing depth. The temperature differences between Voyagers 1 and 2

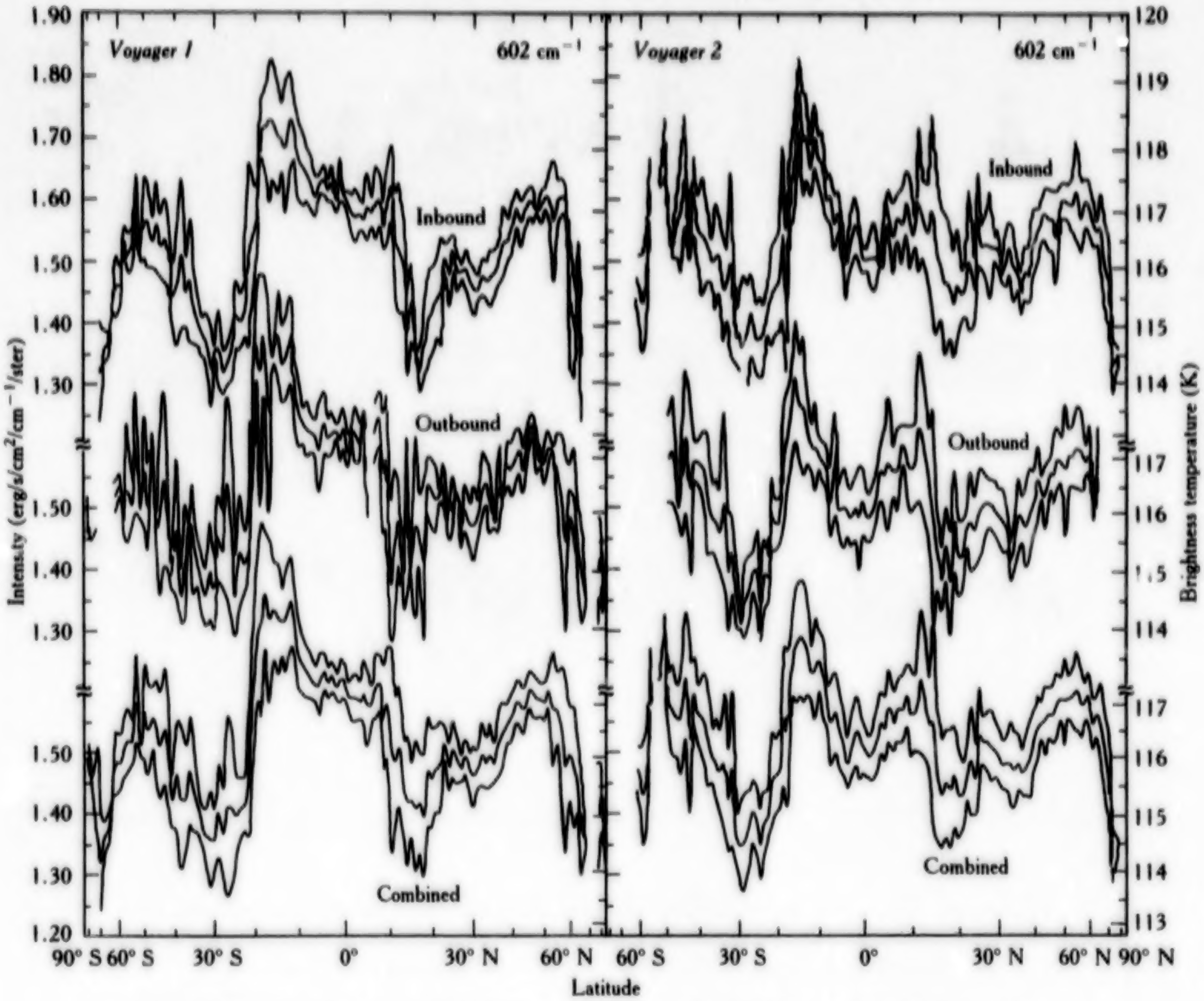

Figure 155. Zonally averaged radiance observed by Voyager 1 and 2 IRIS at 602 cm⁻¹ taken from the north-south map data. The curves plotted above and below the mean represent the excursions of one standard deviation. Breaks in the curve result from the absence of data in some of the 128 bins corresponding to cosine of the latitude.

are evident in both inbound and outbound north-south mapping sequence data (Orton and Martonchik, 1987; fig. 155); the relatively higher fluxes associated with the Voyager 2 meridional averages at 602 cm⁻¹ near 15° S latitude are just above the 1-standard deviation level. The lower values at the equator are somewhat more significant. The highest resolution data, selected for at least a 6 percent resolution of the disk, do not show substantial differences (fig. 156). This is possibly a selection effect of the sample, as these high-resolution data provide much more limited longitude coverage compared with the north-south maps.

Although Voyager IRIS data may tell us something about the time variability of smaller-scale features, they have not been examined for that purpose. We can say that Voyager-1 observations of the GRS from the "cross" map (cf., Flasar et al., 1981) and Voyager-2 observations from a small mosaic across the GRS show brightness temperatures that are not significantly different from one another at similar positions relative to the GRS center.

Little quantitative work has been done with the observations of temperatures in the troposphere since the Voyager encounter epoch. From figure 154, it is possible to see only one substantial change in the general morphology of 17.8- and 18.0-μm scans; that is a general darkening of a region around the equator, more or less continuously from 1979 through 1982. It is likely that this change is associated with a gradual brighten-

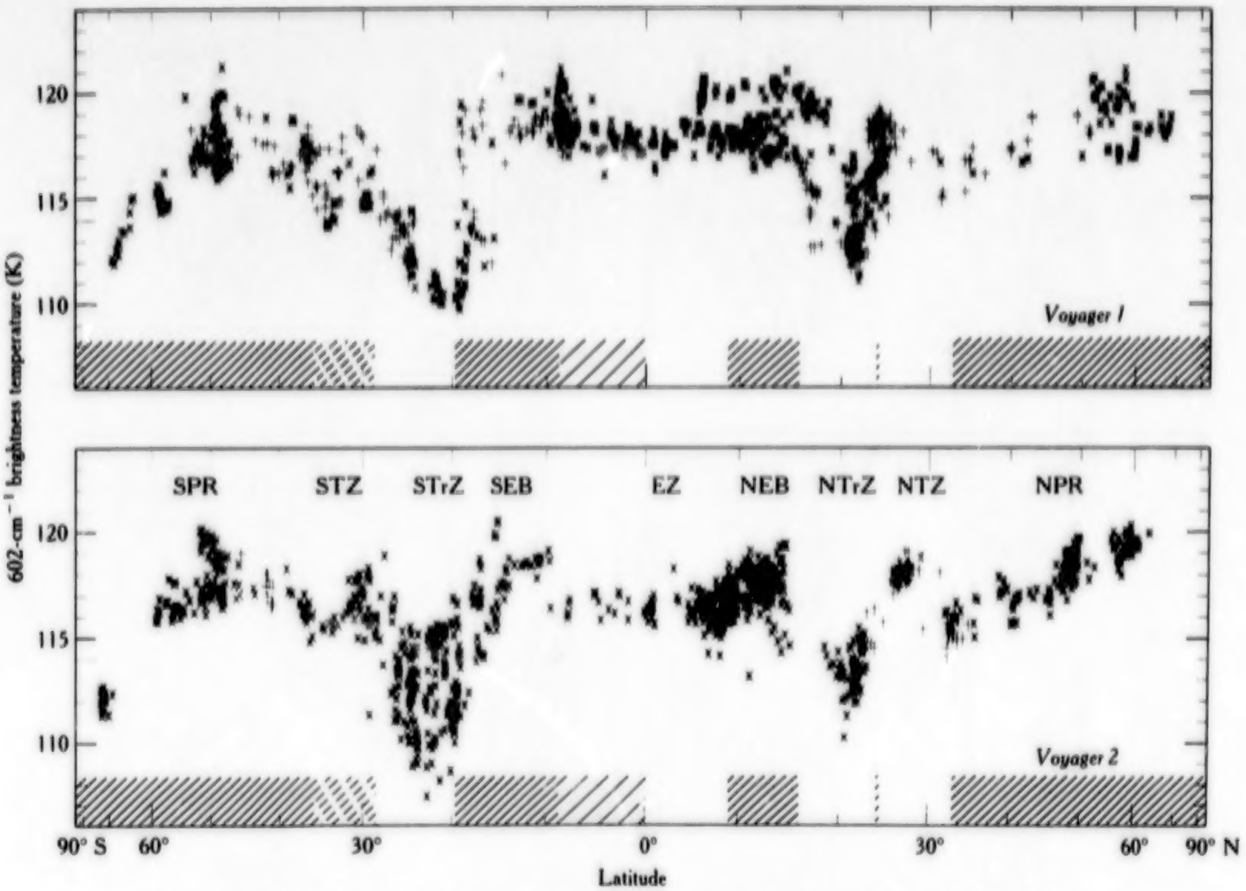

Figure 156. Voyager 1 and 2 radiance observation at 602 cm⁻¹ taken from the highest-resolution IRIS data (*dots* represent data with at least 4 percent spatial resolution of the planetary diameter, *crosses* represent data with 4–6 percent spatial resolution).

ing and widening of the visual appearance of the EZ in the same time interval. The colder 150-mbar temperatures near the EZ observed by Voyager 2 compared with Voyager 1 north-south map data are consistent with the direction of this trend, although the EZ appearance at the two Voyager encounters is generally similar. Again, although not constituting definitive evidence, this is consistent with a change in atmospheric temperature preceding changes in visual and infrared cloud properties.

It is difficult to find any infrared radiance changes associated with the visual darkening of the NTB in 1981. Although this might be blamed on insufficient spatial resolution, the visual albedo seems to have "caught up" with the temperature structure. No other changes in the major belt-zone structure of the planet have taken place since 1982. This is true both visually and thermally, and it is illustrated in the relatively consistent appearance of the tropospheric emission at 17.8 and 18.0 μm on maps from 1984 to 1986 (fig. 157).

Time-Dependent Behavior of Stratospheric Temperatures

The time-independent structure of the jovian stratosphere is remarkably different from that of the troposphere. A zonal mean of Voyager-1 radiance at 7.8 μm looks quite similar to the 7.9-μm scan of Caldwell et al. (1979) (shown in fig. 154). There are three broad regions of relatively enhanced flux. The narrowest is at the equator, spanning approximately 5° S to 5° N latitude; at the epoch of the Voyager encounters, it was the smallest of the three, being about 15 percent brighter than the surrounding regions. The other two are near 20–35° S and 15–30° N and are about 25 percent brighter than the surrounding regions. An examination of the highest spatial resolution Voyager IRIS data reveals no finer meridional structure than is evident in the north-south mapping sequence data having 10 percent resolution of the disk (Orton and Martonchik, 1987).

6 JUNE 1984
9 JULY 1986

Figure 157. (**a**) Jupiter at 17.8 μm on 6 June 1984, at 10:40 UT. Longitude of the central meridian (System III) is 100°. For this and the following infrared images, the data are displayed normalized to the highest value observed in the colors keyed from dark red to bright red. (**b**) Jupiter at 18.0 μm on 9 July 1986, at 12:17 UT. Longitude of the central meridian is 90°.

Although the approximate positions of these bands do not change with time, their relative strengths are quite variable. Although relatively noisy, the 1978 data of Sinton et al. (1980) suggest the presence of southern and equatorial bands, but no northern one. Figure 154 shows that by February 1980, the equatorial band had grown brighter than the midlatitude bands (Caldwell et al., 1980). By March 1981, the equatorial band had again diminished, and in February 1982 it had almost disappeared. The data available for 1983 indicate that in April, the equatorial band had diminished to the point of disappearance, and the southern band was substantially smaller than the northern one.

In 1984, observations were made spanning June through September. During this time, the banded structure was observed to vary quite strongly. In early June the equatorial band was far stronger than the midlatitude bands, which were very difficult to see (fig. 158a); in late July the equatorial band was still dominant and on July 24 it was difficult to discern either midlatitude band (fig. 158b) but on July 26 the southern midlatitude band was discernible (fig. 158c); in early August the midlatitude bands were obvious (fig. 158d); and by early September the bands were of relatively equal size (fig. 158e). Weather and other observed goals prevented more than a few images at 7.8 μm from being made during each of these time periods, but the data are consistent with relatively constant general morphology of band brightnesses over as many as four days. An exception may be the July 24–26 interval with the southern midlatitude band brightening, but more work will be required to determine whether this could have been a change in the aspect of the planet rather than a true time-dependent change.

In 1985 around mid-June, the banded structure appeared as it did during the Voyager epoch, with strong midlatitude bright bands and a weaker equatorial band (fig. 159). A major difference was that wavelike structure appeared in the warm bands (and is suggested in the cooler regions between them). These bands are suggestive of planetary waves with wavelengths of 30° and 45° longitude in the southern and northern hemispheres, respectively (Halthore et al., 1987). There is insufficient information to determine whether they existed at all longitudes at that time. Observations on successive days at similar longitudes show that they were not fixed in System III but were characterized by phase speeds corresponding to periods of 6 and 18 jovian

ORIGINAL PAGE
BLACK AND WHITE PHOTOGRAPH

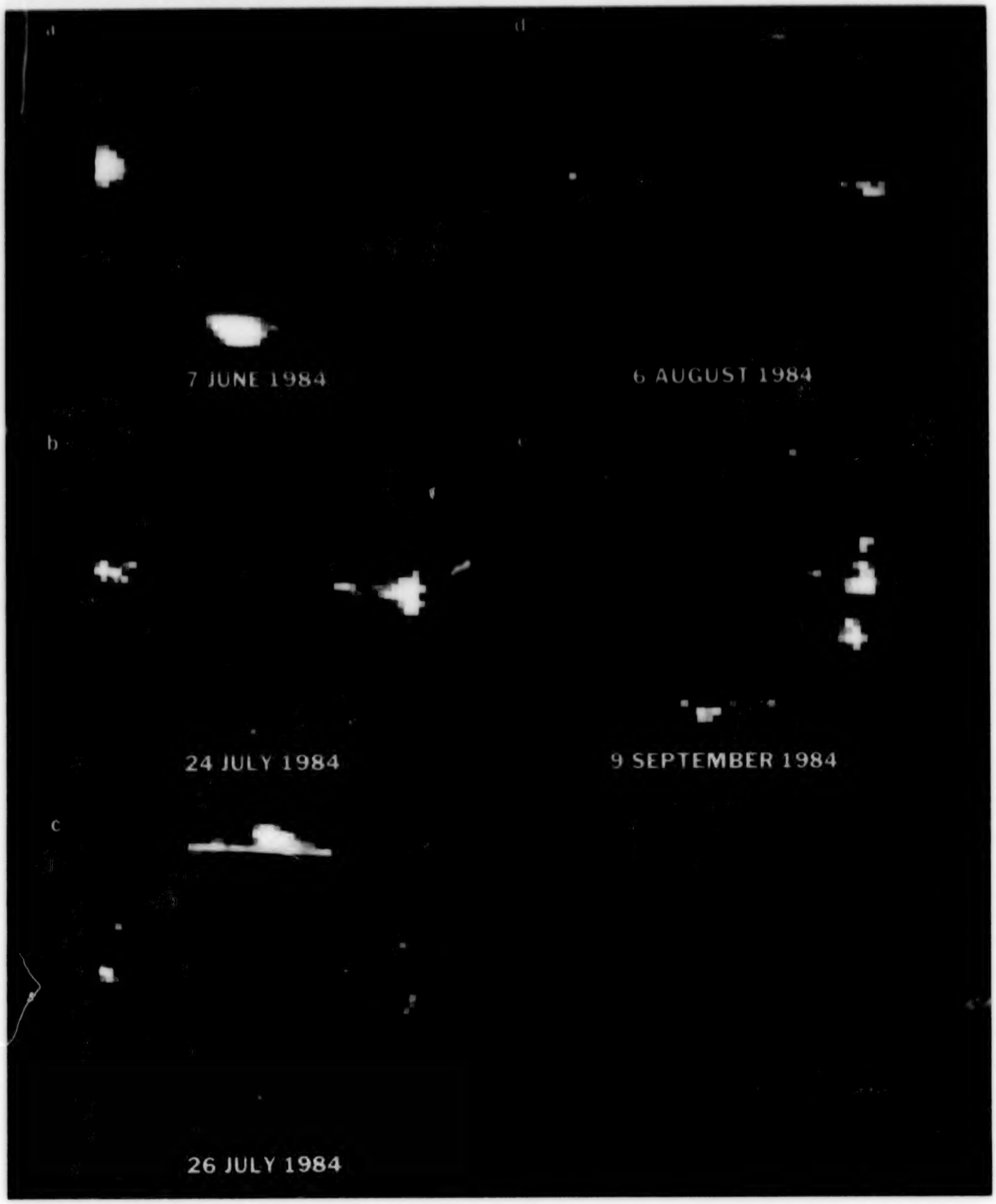
a
d
7 JUNE 1984
6 AUGUST 1984
b
e
24 JULY 1984
9 SEPTEMBER 1984
c
26 JULY 1984

Figure 158. (**a**) Jupiter at 7.8 μm on 7 June 1984, 12:17 UT. Longitude of the central meridian is 322°. For this and other 7.8-μm images that follow, yellow is used (somewhat arbitrarily) to code the very brightness radiances. (**b**) Jupiter at 7.8 μm on 24 July 1984, at 10:20 UT. Longitude of the central meridian is 113°. (**c**) Jupiter at 7.8 μm on 26 July 1984, at 8:45 UT. Longitude of the central meridian is 10°. (**d**) Jupiter at 7.8 μm on 6 August 1984, at 8:35 UT. Longitude of the central meridian is 222°. (**e**) Jupiter at 7.8 μm on 9 September 1984, at 7:07 UT. Longitude of the central meridian is 235°.

ORIGINAL PAGE
COLOR PHOTOGRAPH

~~ORIGINAL PAGE
BLACK AND WHITE PHOTOGRAPH~~

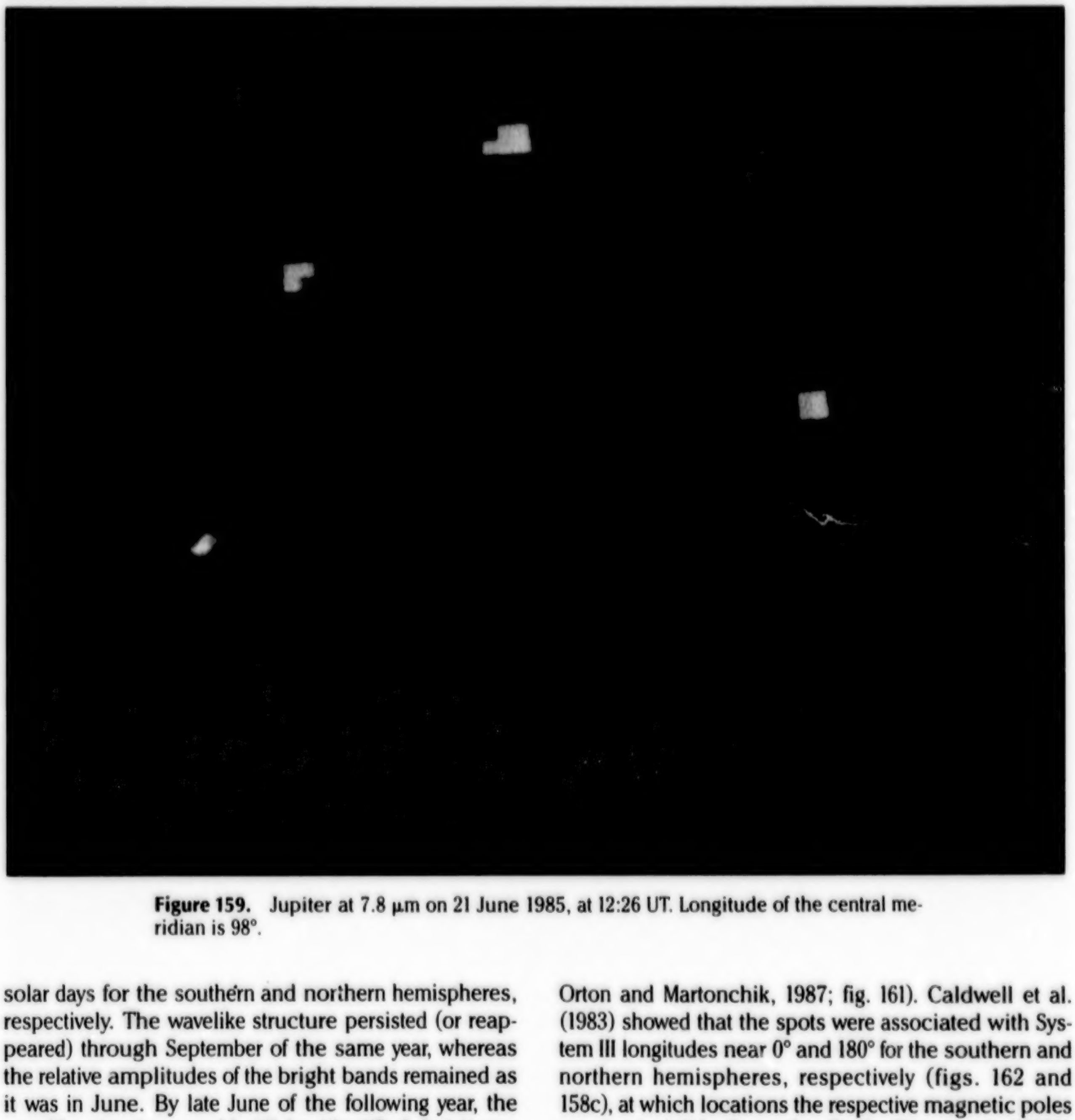

Figure 159. Jupiter at 7.8 μm on 21 June 1985, at 12:26 UT. Longitude of the central meridian is 98°.

solar days for the southern and northern hemispheres, respectively. The wavelike structure persisted (or reappeared) through September of the same year, whereas the relative amplitudes of the bright bands remained as it was in June. By late June of the following year, the wavelike structure could still be identified, but it was more subdued than in the previous year (fig. 160). The relative brightness of the zonal bands had also changed: The equatorial band had virtually disappeared. By June of 1987, the wavelike structure was no longer apparent, and the relative strengths of the zonal bands were similar to those at the Voyager epoch.

Hot spots at 7.8 μm associated with the jovian magnetic pole positions were discovered by Caldwell et al. (1980); a posteriori examination of the Voyager 1 IRIS spectra show the north polar hot spot (Kim et al., 1982; Orton and Martonchik, 1987; fig. 161). Caldwell et al. (1983) showed that the spots were associated with System III longitudes near 0° and 180° for the southern and northern hemispheres, respectively (figs. 162 and 158c), at which locations the respective magnetic poles are most visible from the Earth. Kim et al. (1982) showed that the spots are not CH_4 auroras, as originally suggested by Caldwell et al. (1980), because IRIS spectra clearly showed enhanced emission from other stratospheric constituents. High-energy particles associated with the magnetic field that precipitate into the upper atmosphere are suggested as a heating source. Recent data that include several apparitions of the spots in both hemispheres characterize the northern and southern spots quite differently: The northern spot is fixed to System III coordinates at 180 ± 10° longitude

ORIGINAL PAGE
COLOR PHOTOGRAPH

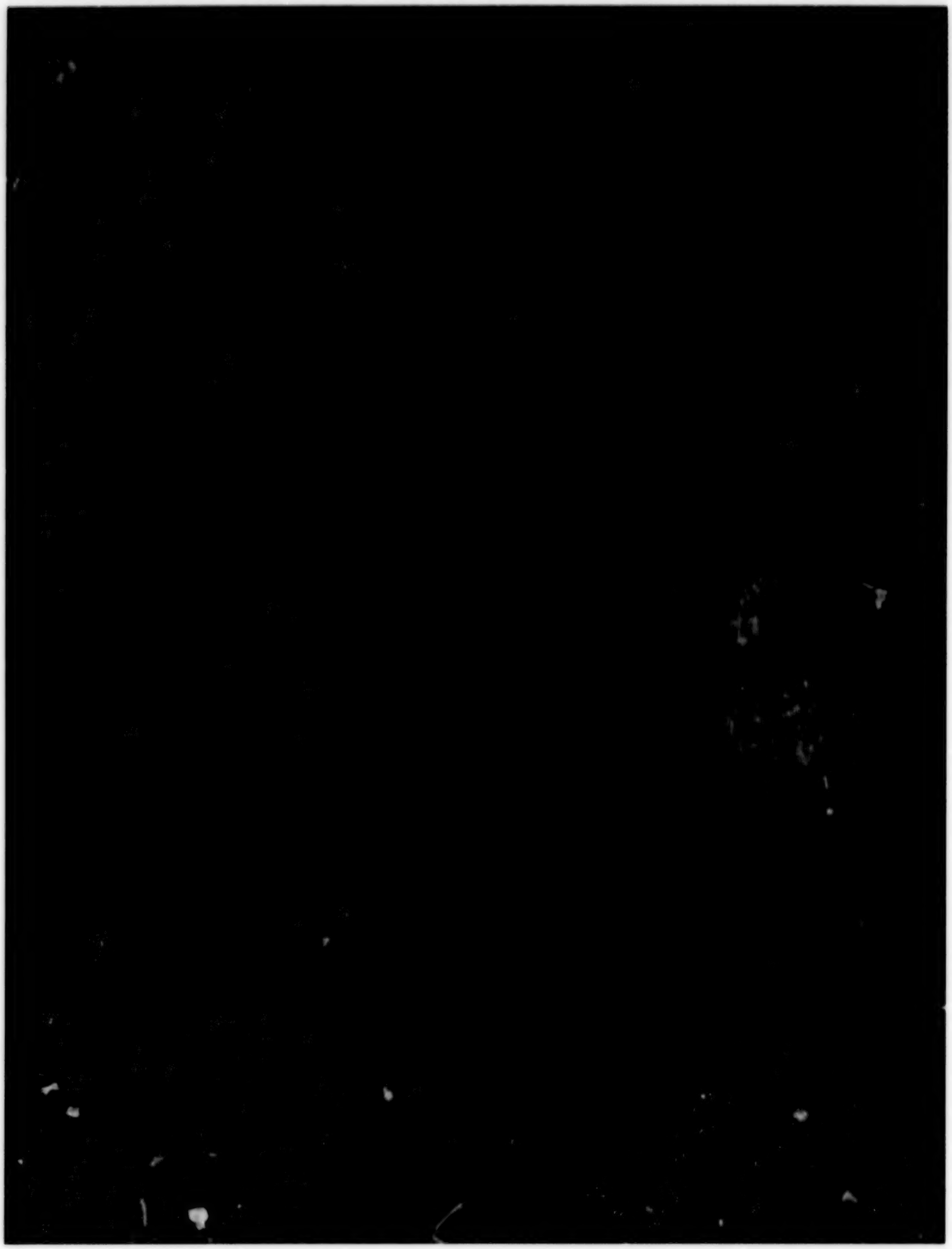

Figure 160. Jupiter at 7.8 μm on 20 June 1986, at 13:54 UT. Longitude of the central meridian is 189°.

ORIGINAL PAGE
COLOR PHOTOGRAPH

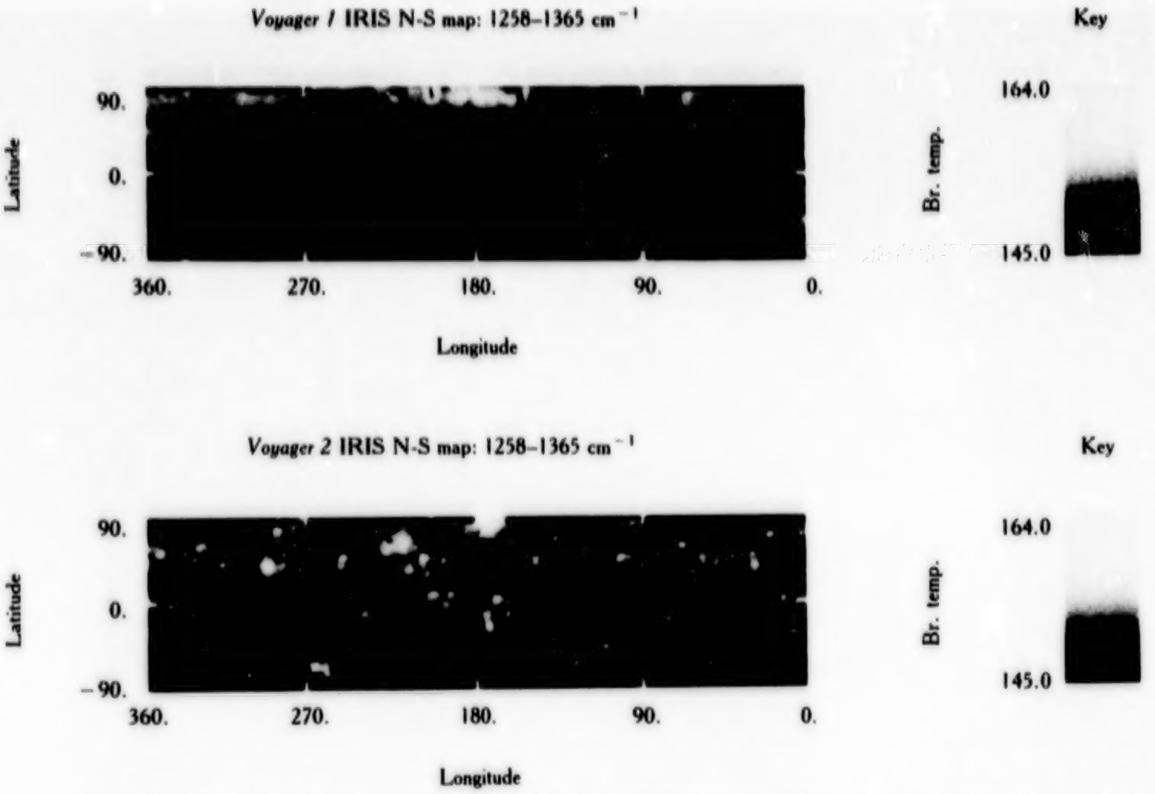

Figure 161. Cylindrical projection of brightness temperature equivalent to radiances observed by the Voyager 1 IRIS experiment in spectral region 1258–1365 cm^{-1}.

and 60 ± 10° latitude, within both the ultraviolet auroral zone and the Io orbital footprint. On the other hand, although it has been found in the general vicinity of 0° in System III longitude, the south polar hot spot is not fixed in System III, the subsolar position, or Io's position (fig. 163). The south polar hot spot is sometimes not observed at all in the appropriate quadrant of the planet; for now, we might consider that there is some component of randomness to whatever is triggering its appearance.

There are other discrete features observed in the jovian stratospheric temperature field. Broad "patchy" areas of slight flux enhancement are sometimes detectable qualitatively in the raw images; their appearance is usually near the limb (fig. 162). The naturally limb-brightened appearance of the planet tends to enhance features that might be unobservable away from the planetary limbs. A qualitative assessment shows that the dawn terminator and limb are more often brighter than the evening terminator and limb. The validity of this has yet to be demonstrated quantitatively, and it would be difficult to understand this on grounds of a diurnal variation of heating and cooling in the jovian stratosphere (Bézard, 1986).

Finally, there is an intriguing set of bright phenomena, only two of which have been observed so far. These are irregularly shaped and cover a wide latitude range in length (stretching across tropospheric jet boundaries, for example) and narrow in width. Figure 158d shows one of these in 1984 near the evening limb at about 15–20° N latitude, and figure 159 shows the other in 1985 near the morning limb at about 30° S latitude. They appear stretched in longitude because of the 40 minutes required to obtain each image, during which the planet rotates. The time scale for these features is not known, except that it is less than two days; it could be only a few hours. More of these features or larger areas mentioned above may be discernible after some processing is performed on these images.

SUMMARY

We have limited information concerning variability of zonal winds. Most long-lived features observable at ground-based resolution are weather systems that rotate in the winds and yield little information about maxima or minima of the zonal winds. Relative to a pres-

ORIGINAL PAGE
BLACK AND WHITE PHOTOGRAPH

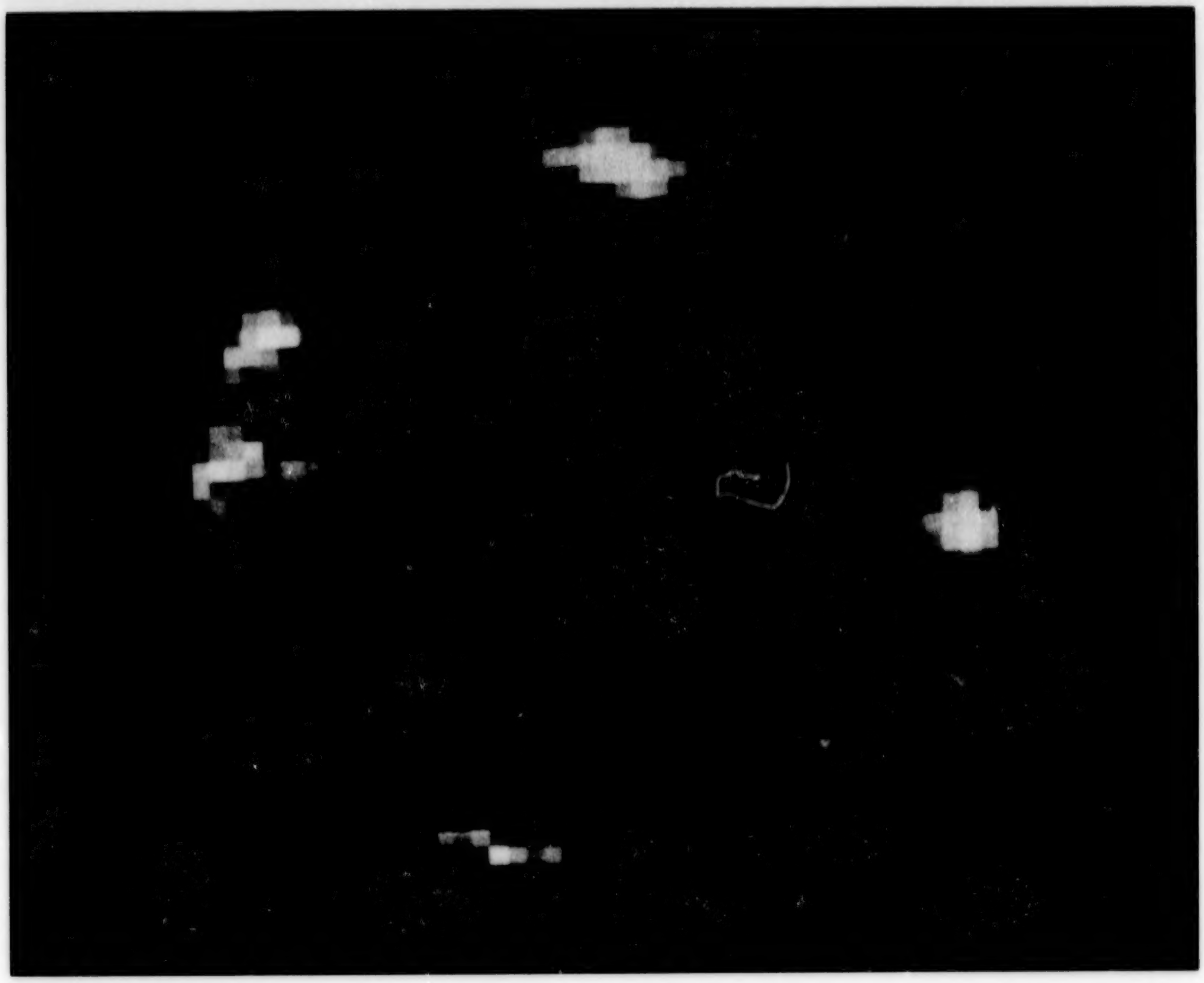

Figure 162. 7.8-μm image of Jupiter taken on 6 June 1984, at 13:04 UT. Longitude of the central meridian is 200°.

sure scale height, the horizontal extent of these systems is large. Color is *very* subtle, heat adjustment occurs on time scales of years (radiative time constant), and the extent to which transfer of internal heat dominates the visible cloud deck is not known. At ground-based resolution, zonal changes occur over characteristic time intervals of days to years. Large-scale changes frequently have characteristic time scales of three to six years associated with them. Large, long-lived anticyclonic systems are restricted to the southern hemisphere, where cyclonic systems tend to be irregular in shape and turbulent. Although similar systems occur at northern latitudes poleward of 34°, well-formed, lower-albedo, brown cyclonic systems are typical of northern midlatitudes.

In addition, north-south asymmetry is characteristic of the color dependence and morphology of the equatorial zone. Thus, an outstanding question concerning the visible cloud deck concerns the mechanism that introduces the observable hemispheric asymmetry in the cloud morphology and the zonal winds. A major unresolved issue is why albedo and color change. One possibility is that ammonia condensation in the 300–500 mbar region is marginally stable during times when clouds have high albedo, but becomes unstable during low-albedo periods, exposing darker particles in the 300–500 mbar region that are otherwise coated with ammonia ice. One of the best indicators of ammonia abundance are images at centimeter wavelengths (de Pater, 1986). These and other observations related to ammonia abundance or cloud structure should be obtained on a regular basis for several years. Much more work needs to be done to make these ideas more quantitative; to check them against observation;

ORIGINAL PAGE
COLOR PHOTOGRAPH

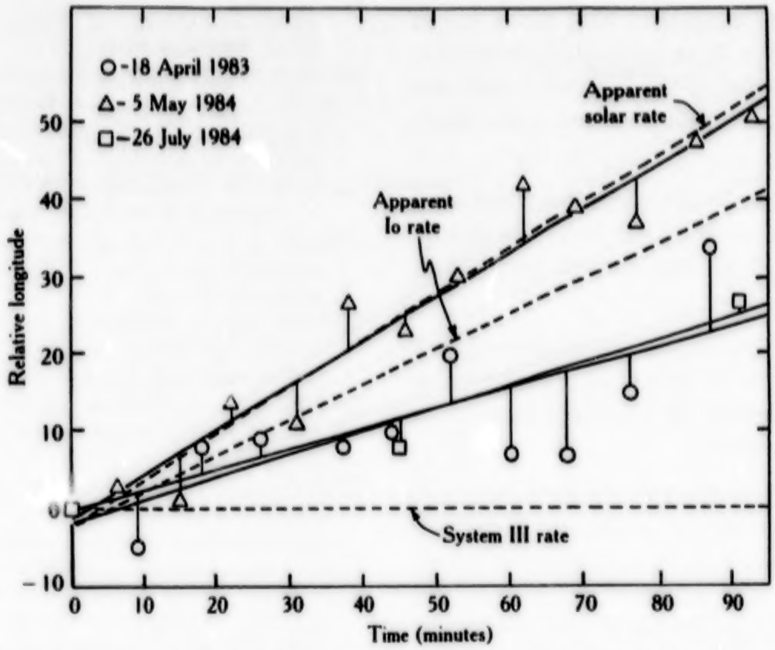

Figure 163. Summary of motion of south polar hot spot as change in longitude with time. Each symbol represents one image, with a different symbol for each day. The motion of the south polar hot spot for each day is shown by a least squares fit as a *solid line* connected to the symbol it represents. *Broken lines* are drawn to show the hypothetical features moving at the rates of Io, the Sun, and Jupiter.

to develop a better understanding of the location, sources, and sinks of chromophore material and the process that produces the absorption; to investigate problems of particle microphysics; and to clarify vertical and horizontal transport in the statically stable upper troposphere-lower stratosphere.

A host of questions concerning thermal structure are raised by the observations obtained thus far. Among them are

1. How closely do the observations of thermal emission correspond to expected seasonal changes in thermal structure?
2. Do thermal changes in the tropopause region precede, coincide with, or follow changes in the visible morphology? Do different regions behave differently? What is the optimal strategy for monitoring visual and temperature changes "simultaneously" and for providing the least timing ambiguity without spending inordinate amounts of time on large telescopes (required in order to defeat diffraction of the infrared radiation)?
3. Are there changes in the *para*-H_2 versus *ortho*-H_2 ratio from those detected in the Voyager epoch? If so, are they related to tropospheric temperature changes?
4. What is the cause of the changes in the stratospheric large-scale organization? Is this related to the structure of the organization and its differentiation from the organization of tropospheric clouds and temperatures? What are the real time scales associated with the relative amplitude of the zonal bands?
5. What is the origin of waves in the stratospheric bands? Do they extend to other regions of the planet? Are they visible at other times, but at much subdued amplitude?
6. Is there any reality associated with the "warm dawn" in the stratosphere? Are there any components of the stratospheric temperature field that have significantly solar-fixed components on diurnal time scales? What are the characteristics of the weak "patches" of warmer temperatures occasionally evident?
7. What are the characteristics of the relatively rare bright "streaks"? Are there any whose presence is simply extremely subdued (e.g., by not being sighted close to the limb)? What physical mechanism could be responsible for them (are there any terrestrial analogues)?

8. What changes are indicated in NH_3 gas or ice in the thermal data? Are these correlated (or anticorrelated) with changes in thermal structure? Are they always associated with changes in the visual albedo?
9. Are there any changes in NH_3 abundance and vertical distribution with time for any particular region, especially in the regions that undergo frequent albedo changes?
10. What are the true time scales associated with the smaller stratospheric features? Are there effective observing strategies for determining them from Earth-based observations?

A concerted effort is needed to resolve these questions. A regular observational program to monitor changes at thermal wavelengths, coordinated with studies of the visible appearance of the planet, and high spatial-resolution data on molecular absorption bands, would provide a valuable data base for constructing and checking models of the jovian dynamics, chemistry, radiation, and cloud processes.

ACKNOWLEDGMENTS

We thank T. Gehrels for assistance with a Pioneer 10 image, Lowell Observatory for historical photographs, the Royal Astronomical Society for historical drawings, and M. E. Malcom for computing assistance. This effort was carried out by the New Mexico State University and by the Jet Propulsion Laboratory, California Institute of Technology, under contract with the National Aeronautics and Space Administration. The NASA Planetary Astronomy and Planetary Atmospheres programs and the Galileo Project supported the work.

References

Allison, M. (1983). Planetary waves in Jupiter's equatorial atmosphere. *Bull. Amer. Astron. Soc.* 15:836.

Appleby, J. A., and J. S. Hogan (1984). Radiative-convective equilibrium models of Jupiter and Saturn. *Icarus* 59:336–366.

Atreya, S. K., T. M. Donahue, and M. C. Festou (1981). Jupiter: Structure and composition of the upper atmosphere. *Astrophys. J.* 747:L43–L47.

Beebe, R. F., and T. A. Hockey (1986). A comparison of red spots in the atmosphere of Jupiter. *Icarus* 67:96–105.

Beebe, R. F., R. M. Suggs, and T. Little (1986). Seasonal north-south asymmetry in solar radiation incident on Jupiter's atmosphere. *Icarus* 66:359–365.

Beebe, R. F., and L. A. Youngblood (1979). Pre-Voyager velocities, accelerations, and shrinkage rates of jovian cloud features. *Nature* 280:771–772.

Bezanger, C., B. Bézard, and D. Gautier (1986). Spatial variation of the thermal structure of Jupiter's atmosphere. In *Jovian atmospheres* (M. Allison and L. Travis, eds.), pp. 79–81. NASA Conf. Publ. 2441.

Bézard, B. (1986). Private communication.

Caldwell, J., R. D. Cess, B. E. Carlson, A. T. Tokunaga, and F. C. Gillett (1979). Temporal characteristics of the jovian atmosphere. *Astrophys. J.* 234:L155–L158.

Caldwell, J., A. T. Tokunaga, and F. C. Gillett (1980). Possible infrared aurorae on Jupiter. *Icarus* 41:667–675.

Caldwell, J., A. T. Tokunaga, and G. S. Orton (1983). Further observations of 8-μm polar brightenings on Jupiter. *Icarus* 53:133–140.

Caldwell, J., R. N. Halthore, G. S. Orton, and J. T. Bergstralh (1985). Eight-micron images of Jupiter. I. The south pole and equator. *Bull. Amer. Astron. Soc.* 17:709.

Caldwell, J., R. N. Halthore, G. Orton, and R. West (1986). Infrared images of Jupiter and Saturn. *Bull. Amer. Astron. Soc.* 18:789.

Caldwell, J., R. Halthore, G. Orton, and J. Bergstralh (1987). Infrared polar brightenings on Jupiter. IV. Spatial properties of methane emission. Submitted.

Carleton, N. P., and W. A. Traub (1974). Observations of spatial and temporal variations of the jovian H_2 quadrupole lines. In *Exploration of the planetary system* (A. Woszczyk and C. Iwaniszewska, eds.), pp. 345–349. Reidel, Dordrecht.

Cess, R. D., B. E. Carlson, J. Caldwell, I. G. Nolt, F. C. Gillet, and A. T. Tokunaga (1981). Latitudinal variations in jovian stratospheric temperatures. *Icarus* 46:249–255.

Chapman, C. R., and E. J. Reese (1968). A test of the uniformly rotating source hypothesis for the south equatorial belt disturbances on Jupiter. *Icarus* 9:326–335.

Cochran, W. D., and A. L. Cochran (1980). Longitudinal variability of methane and ammonia bands on Jupiter. *Icarus* 42:102–110.

Cochran, W. D., and A. L. Cochran (1983). Longitudinal variability of methane and ammonia bands on Jupiter. *Icarus* 56:116–121.

Conrath, B. J., and D. Gautier (1980). Thermal structure of Jupiter's atmosphere obtained by inversion of Voyager 1 infrared measurements. In *Remote sensing of atmospheres and oceans* (A. Deepak, ed.), pp. 611–630. Academic Press, New York.

Conrath, B. J., and P. J. Gierasch (1984). Global variation of the para hydrogen fraction in Jupiter's atmosphere and implications for dynamics on the outer planets. *Icarus* 57:184–204.

Conrath, B. J., F. M. Flasar, J. A. Pirraglia, P. J. Gierasch, and G. E. Hunt (1981). Thermal structure and dynamics of the jovian atmosphere. 2. Visible cloud features. *J. Geophys. Res.* 86:8769–8776.

Cunningham, C. (1987). *Spatial and temporal monitoring of the jovian atmosphere*, unpublished Ph.D. dissertation, Dept. Planet. Sci., Univ. Arizona, Tucson.

Cunningham, C., D. M. Hunten, and M. G. Tomasko (1987). *H_2 spectroscopy and a diurnally changing cloud on Jupiter*. Submitted.

de Pater, I. (1986). Jupiter's zone-belt structure at radio wavelengths: II. Comparison of observations with model atmosphere calculations. *Icarus* 68:344–365.

Elvey, C. T., and A. S. Fairley (1932). On the absorption band at λ 6191 in the spectrum of Jupiter. *Astrophys. J.* 75:373–378.

Flasar, F. M., B. J. Conrath, J. A. Pirraglia, P. C. Clark, R. G.

French, and P. J. Gierasch (1981). Thermal structure and dynamics of the jovian atmosphere. 1. The great red spot. *J. Geophys. Res.* 86:8759–8768.

Gehrels, T. (1976). The results of the imaging photopolarimeter experiment on Pioneers 10 and 11. In *Jupiter* (T. Gehrels, ed.), pp. 531–562. Univ. Arizona Press, Tucson.

Gehrels, T. et al. (1974). The Imaging Photopolarimeter experiment on Pioneer 10. *Science* 183:318–320.

Gierasch, P. J., B. J. Conrath, and J. A. Magalhães (1986). Zonal mean properties of Jupiter's upper troposphere from Voyager infrared observations. *Icarus* 67:456–483.

Green, N. E. (1887). *Memoir, in possession of the Royal Astronomical Society; Nathaniel Everett Green MSS*, 5.

Guitar, H. (1984). *Analysis of motions of Jupiter's great red spot and white ovals*. Unpublished Ph.D. dissertation, Astronomy Dept., New Mexico State Univ.

Halthore, R. N., J. Caldwell, G. S. Orton, and J. T. Bergstralh (1985). Eight-micron images of Jupiter II. The north pole. *Bull. Amer. Astron. Soc.* 17:710.

Halthore, R., A. Burrows, and J. Caldwell (1986). A thermal equilibrium model for Jupiter's north polar hotspot. *Bull. Amer. Astron. Soc.* 18:773.

Halthore, R., J. Caldwell, and G. Orton (1987). *Stratospheric waves in Jupiter*. In preparation.

Hanel, R., B. Conrath, M. Flasar, L. Herath, V. Kunde, P. Lowman, W. Maguire, J. Pearl, J. Pirraglia, R. Samuelson, D. Gautier, P. Gierasch, L. Horn, S. Kumar, and C. Ponnamperuma (1979). Infrared observations of the jovian system from Voyager. *Science* 206:952–956.

Hanel, R., B. Conrath, D. Gautier, P. Gierasch, S. Kumar, V. Kunde, P. Lowman, W. Maguire, J. Pearl, J. Pirraglia, C. Ponnamperuma, and R. Samuelson (1977). The Voyager infrared spectroscopy and radiometry investigation. *Space Sci. Rev.* 21:129–158.

Hatzes, A., D. D. Wenkert, A. P. Ingersoll and G. E. Danielson (1981). Oscillations and velocity structure of a long-lived cyclonic spot. *J. Geophys. Res.* 86:8745–8749.

Hockey, T. A. (1985). *Ground-based jovian surface photometry, 1968–1984*. Master's thesis, Astronomy Dept., New Mexico State Univ., Las Cruces, N.M.

Hockey, T. A., and R. F. Beebe (1983). A color asymmetry in the equatorial zone of Jupiter. *Bull. Amer. Astron. Soc.* 15:998.

Hung, G. E., and J. T. Bergstralh (1977). Interpretation of spatial and temporal variations of hydrogen quadrupole absorptions in the jovian atmosphere observed during the 1972 apparition. *Icarus* 30:511–530.

Hunt, G. E., B. J. Conrath, and J. A. Pirraglia (1981). Visible and infrared observations of jovian plumes during the Voyager encounter. *J. Geophys. Res.* 86:8777–8782.

Ingersoll, A. F., G. Munch, G. Neugebauer, and G. S. Orton (1976). Results of the infrared radiometer experiment on Pioneers 10 and 11. In *Jupiter* (T. Gehrels, ed.), pp. 197–205. Univ. Arizona Press, Tucson.

Ingersoll, A. P., R. F. Beebe, J. L. Mitchell, G. W. Garneau, G. M. Yagi, and J. Muller (1981). Interaction of eddies and mean flow on Jupiter as inferred from Voyager 1 and 2 images. *J. Geophys. Res.* 86:8733–8743.

Kim, S. J., J. Caldwell, and A. Rivolo (1982). Jovian infrared aurora II. Spectral characteristics. *Bull. Amer. Astron. Soc.* 14:732.

Kliore, A. J., and P. M. Woiceshyn (1976). Structure of the atmosphere of Jupiter from Pioneers 10 and 11 radio occultation measurements. In *Jupiter* (T. Gehrels, ed.), pp. 216–237. Univ. Arizona Press, Tucson.

Leovy, C. B. (1986). Eddy processes in the general circulation of the jovian atmospheres. In *The jovian atmospheres* (M. Allison and L. D. Travis, eds.), pp. 177–192. NASA Conf. Pub. 2441.

Limaye, S. S. (1986). Jupiter: New estimates of the mean zonal flow at the cloud level. *Icarus* 65:335–352.

Lindal, G. F., G. E. Wood, G. S. Levy, J. D. Anderson, D. N. Sweetnam, H. B. Hotz, B. J. Buckles, D. P. Holmes, P. E. Doms, V. R. Eshleman, G. L. Tyler, and T. A. Croft (1981). The atmosphere of Jupiter: An analysis of the Voyager radio occultation measurements. *J. Geophys. Res.* 86:8721–8727.

Marten, A., D. Rouan, J.-P. Baluteau, D. Gautier, B. J. Conrath, R. A. Hanel, V. Kunde, R. Samuelson, A. Chedin, and N. Scott (1981). Study of the ammonia ice cloud layer in the equatorial region of Jupiter from the infrared interferometric experiment on Voyager. *Icarus* 46:233–248.

Maxworthy, T. (1984). The dynamics of a high-speed jovian jet. *Planet. Space Sci.* 32:1053–1058.

Minton, R. B. (1973). Latitude measures of Jupiter in the 0.89 μ methane band. *Comm. Lunar Planet. Lab.* 9:339–352.

Mitchell, J. L., R. F. Beebe, A. P. Ingersoll, and G. W. Garneau (1981). Flow fields within Jupiter's great red spot and white oval BC. *J. Geophys. Res.* 86:8751–8757.

Muller, J.-P., A. L. and C. E. Roff (1987). *Atmospheric dynamics and cloud structure of Jupiter from a combined analysis of Voyager 1 and 2 IRIS and imaging data*. Submitted.

Murphy, R. E., and R. A. Fesen (1974). Spatial variations in the jovian 20-micrometer flux. *Icarus* 21:42–46.

Murray, B. C., R. L. Wildey, and J. A. Westphal (1964). Observations of Jupiter and the galilean satellites at 10 microns. *Astrophys. J.* 139:986–993.

Orton, G. S. (1986). Spatial and temporal variability of infrared-observable properties of the jovian atmosphere: A partial survey. In *The jovian atmospheres* (M. Allison and L. Travis, eds.), pp. 19–25. NASA Conf. Publ. 2441.

Orton, G. S., and A. P. Ingersoll (1976). Pioneers 10 and 11 and infrared data on Jupiter: The thermal structure and He-H_2 ratio. In *Jupiter* (T. Gehrels, ed.), pp. 206–215. Univ. of Arizona Press, Tucson.

Orton, G. S., and J. V. Martonchik (1987). Characterization of the jovian atmosphere from Voyager observations. I. Infrared data. In preparation.

Orton, G. S., A. P. Ingersoll, R. J. Terrile, and S. R. Walton (1981). Images of Jupiter from the Pioneers 10 and 11 infrared radiometers: A comparison with visible and 5-μm images. *Icarus* 47:145–158.

Orton, G., J. Caldwell, and A. Tokunaga (1981). Thermal infrared morphology of the jovian atmosphere in 1981. *Bull. Amer. Astron. Soc.* 13:735.

Orton, G. S., K. H. Baines, J. T. Bergstralh, T. Z. Martin, R. J. Terrile, R. A. West, and J. Caldwell (1984). 1.4- to 33-μm maps of the jovian disk in 1984. *Bull. Amer. Astron. Soc.* 16:641.

Orton, G. S., K. H. Baines, J. T. Bergstralh, T. Z. Martin, R. A. West, and J. Caldwell (1984b). Relative temperature fields in the jovian atmosphere in 1984. *Bull. Amer. Astron. Soc.* 16:642.

Orton, G. S., K. Baines, J. Bergstralh, R. West, J. Caldwell, and

R. Halthore (1987). Temporal changes of temperature and cloud structure in the jovian atmosphere, 1984–1986: Results of thermal imaging. *Bull. Amer. Astron. Soc.* 19:638.

Peek, B. M. (1958). *The planet Jupiter*. Faber and Faber, London.

Pirraglia, J. A., B. J. Conrath, M. D. P. Allison, and P. Gierasch (1981). Thermal structure and dynamics of Saturn and Jupiter. *Nature* 292:677–679.

Reese, E. J. (1972). Jupiter: Its red spot and disturbances in 1970–1971. *Icarus* 17:57–72.

Riddle, A. C., and J. W. Warwick (1976). Redefinition of System III longitude. *Icarus* 27:457–459.

Sato, M., and J. E. Hansen (1979). Jupiter's atmospheric composition and cloud structure deduced from absorption bands in reflected sunlight. *J. Atmos. Sci.* 36:1133–1167.

Sanchez-Lavega, A., and R. Rodrigo (1985). Ground-based observations of synoptic cloud systems in southern equatorial to temperate latitudes of Jupiter from 1975 to 1983. *Astron. Astrophys.* 148:67–78.

Sinton, W. M., W. W. Macy, and G. S. Orton (1980). Infrared scans of Jupiter. *Icarus* 42:86–92.

Smith, B. A. et al. (1979a). The Jupiter system through the eyes of Voyager 1. *Science* 204:951–971.

Smith, B. A. et al. (1979b). The galilean satellites and Jupiter: Voyager 2 imaging science results. *Science* 206:927–950.

Smith, P. H., and M. G. Tomasko (1984). Photometry and polarimetry of Jupiter at large phase angles. II. Polarimetry of the south tropical zone, south equatorial belt, and the polar regions from the Pioneers 10 and 11 missions. *Icarus* 58:35–73.

Solberg, H. G. (1969). A 3-month oscillation in the longitude of Jupiter's red spot. *Planet. Space Sci.* 17:1573–1580.

Stoker, C. (1986). Moist convection: A mechanism for producing the vertical structure of the jovian equatorial plumes. *Icarus* 67:106–125.

Terrile, R. J., and R. F. Beebe (1979). Summary of historical data: Interpretation of the Pioneer and Voyager cloud configurations in a time-dependent framework. *Science* 204:948–951.

Terrile, R. J., R. W. Capps, D. E. Backman, E. E. Becklin, D. P. Cruikshank, C. A. Beichman, R. H. Brown, and J. A. Westphal (1979a). Infrared images of Jupiter at 5-micrometer wavelength during the Voyager 1 encounter. *Science* 204:1007–1008.

Terrile, R. J., R. W. Capps, E. E. Becklin, and D. P. Cruikshank (1979b). Jupiter's cloud distribution between the Voyager 1 and 2 encounters: Results from 5-micrometer imaging. *Science* 206:995–996.

Terrile, R. J., and J. A. Westphal (1977). The vertical cloud structure from 5-micron measurements. *Icarus* 30:274–281.

Vapillon, L., M. Combes, and J. Lecacheux (1973). The β Scorpii occultation by Jupiter. *Astron. Astrophys.* 29:135–149.

Veverka, J., L. H. Wasserman, J. Elliot, C. Sagan, and W. Liller (1974). The occultation of β Scorpii by Jupiter I. The structure of the jovian upper atmosphere. *Astron. J.* 79:73–84.

Wallace, L. (1976). The thermal structure of Jupiter in the stratosphere and upper troposphere. In *Jupiter* (T. Gehrels, ed.), pp. 284–303. Univ. Arizona Press, Tucson.

Wallace, L., M. Prather, and M. J. S. Belton (1974). The thermal structure of the atmosphere of Jupiter. *Astrophys. J.* 193:481–493.

West, R. A. (1979). Spatially resolved methane band photometry of Jupiter I. Absolute reflectivity and center-to-limb variations in the 6190-, 7250-, and 8900Å bands.

West, R. A. (1984). Remote sounding of jovian cloud properties from Voyager 1 IRIS 5 microns spectra. In *IRS '84: Current Problems in Atmospheric Radiation, Proceedings of the International Radiation Symposium* Perugia, Italy 21–28 August 1984 (G. Fiocco, ed.), pp. 369–372. A. Deepak, Hampton, VA.

West, R. A., P. N. Kupferman, and H. Hart (1985). Voyager 1 Imaging and IRIS observations of jovian methane absorption and thermal emission: Implications for cloud structure. *Icarus* 61:311–342.

West, R. A., D. F. Strobel, and M. G. Tomasko (1986). Clouds, aerosols, and photochemistry in the jovian atmosphere. *Icarus* 65:161–217.

Westphal, J. A. (1969). Observations of localized 5-micron radiation from Jupiter. *Astrophys. J.* 157:L63–L64.

Westphal, J. A., K. Matthews, and R. J. Terrile (1974). Five-micron pictures of Jupiter. *Astrophys. J.* 188:L111–L112.

Wildey, R. L., B. C. Murray, and J. A. Westphal (1965). Thermal infrared emission of the jovian disk. *J. Geophys. Res.* 70:3711–3719.

Young, A. T. (1985). What color is the solar system? *Sky and Telescope* 69:399–403.

22

Spatial and Temporal Variations in the Atmosphere of Jupiter: Polarimetric and Photometric Constraints

Barbara E. Carlson
NASA/Goddard Space Flight Center, Greenbelt

Barry L. Lutz
Lowell Observatory, Flagstaff

Abstract

New spatially resolved narrow-band carge-coupled device (CCD) polarimetric and photometric images of Jupiter in the methane absorption band at 7270 Å and continuum light near 7500 Å were obtained at the Lowell Observatory in the fall of 1986. Images were recorded at three phase angles from 0°.3 to 11°.1. The CCD images reveal an asymmetric increase in the degree of linear polarization toward the poles. These images confirm that there is a significant enhancement in the degree of linear polarization from the disk center toward the limbs, as was observed in the early measurements made by Lyot. Also shown by the images is a variation in the degree of linear polarization measured at the east (sunrise) limb and west (sunset) limb, with larger polarizations associated with the west limb. Furthermore, the fine phase-angle resolution of the measurements made by Lyot indicates that the polarization changes sign at a different phase angle for the east and west limbs. If the particles responsible for the limb polarization are compositionally the same at the east and west limbs, this difference implies that a diurnal variation in particle size, cloud height, or opacity occurs. A comparison of the CCD images shows that the amount of belt-zone contrast observed in the degree of linear polarization is dependent on wavelength and phase angle. Complementary photometric images recorded at the Lowell Observatory provide additional constraints on horizontal and temporal variations in the vertical structure of the atmosphere.

INTRODUCTION

Complementary photometric and polarimetric observations of Jupiter provide important constraints on the nature and distribution of aerosols within the jovian atmosphere. In addition, these images can be used to provide additional constraints on horizontal and temporal variations in the vertical structure of the jovian atmosphere. New spatially resolved narrow-band CCD photometric and polarimetric images of Jupiter in the methane absorption band at 7270 Å and in continuum light near 7500 Å have been recorded at the Lowell Observatory in fall of 1986 for three phase angles, 0°.3, 7°.0, and 11°.1. The images reveal an asymmetric increase in the degree of linear polarization toward the poles and confirm that there is a significant enhancement in the degree of linear polarization from the disk center toward the limbs, as was suggested by measurements as early as those made by Lyot (1929). A comparison of the CCD images shows that the amount of belt-zone contrast observed in the degree of linear polarization is dependent on both wavelength and phase angle.

A study of previously published polarization measurements shows that wavelength and phase-angle dependences of the sign of the linear polarization, determined from the orientation of the electric vector, will provide important new constraints on the spatial distribution and particle size variation of aerosols in the jovian atmosphere. Detailed modeling will be required to determine the densities and size distributions required to produce such sign reversals, but the measurements made by Lyot (1929) and Gehrels et al. (1969) imply that particle size variations occur between the limbs, suggesting that such a variation is diurnal in nature.

This chapter presents some initial findings derived from a preliminary inspection of our first polarimetric images of Jupiter, which are part of a new extensive long-term study of the polarimetric and photometric properties of the jovian atmosphere being undertaken, and discusses them in the context of previous measurements.

OBSERVATION AND REDUCTION PROCEDURES

During the fall of 1986, we recorded photometrically calibrated images of Jupiter through two narrow-band interference filters using the Bell Laboratories imaging polarimeter on the 1.8-m Perkins telescope at the Lowell Observatory. The imaging polarimeter, outfitted with a thinned, back-illuminated RCA Charge-Coupled Device (CCD) as the detector, is described by Tyson and Lee (1981) and is comprised of an electrically steped, achromatic half-wave plate in front of a Rochon prism analyzer for which the undeviated ray is undistorted and also achromatic, followed by a filter wheel containing up to six image-quality filters. For the jovian observations described here, the first of the two filters had a 50-Å passband centered at 7498 Å, corresponding to a region of continuum light in the jovian spectrum, whereas the second had a 22-Å passband centered at 7270 Å and measured the reflected solar radiation in a nearby methane absorption band.

We obtained the images on the nights of 11 September, 15 October, and 21 November 1986 UT when the solar phase angles were 0°.3, 7°.0, and 11°.1, and apparent equatorial diameters of Jupiter were 49.6, 47.7, and 42.6 arcsec, respectively. Each image consists of an unbinned, 200 × 200-pixel subset of the full 512 × 320-pixel, CCD format, and each of the 30-μm-square pixels projected to about 0.75 arcsec square on the sky, oversampling the nominal spatial resolution of 1.5–2.5 arcsec set by the typical seeing-disk of a point source. Degradation of this resolution by image smearing due to the fast rotation of Jupiter was minimized by utilizing short integration times of 1 to 3 seconds. Exposures of these lengths yielded maximum data numbers (DN) typically between 5000 and 8000, depending on the filter, which at a gain of 10 e⁻ per DN corresponds to signal-to-noise ratios near 250:1 for each frame. The readout noise of the CCD was 93 e⁻.

CCD images of the standard star Zeta Pegasus were recorded for photometric calibration of the Jupiter images, and frames of the polarimetric standard 30 Pegasus and zero-polarization standard Iota Pegasus were

C-4

also obtained. Pixel-to-pixel sensitivity variations of the CCD were accounted for, using flat-field frames of a uniformly illuminated dome "white spot."

For each filter, the CCD was exposed sequentially at four different orientations of the halfwave plate, which was rotated about the telescope beam axis in 22°.5 steps. The observed intensity I' at each orientation of the halfwave plate is related to the usual Stokes parameters for linear polarization, I, Q, and U by the formula

$$2I'(\theta) = I + Q \cos 4\theta + U \sin 4\theta,$$

where θ is the angle between principal plane of the analyzing prism and the equivalent optical axis of the half-wave plate. In this case, θ takes on the four values of rotation, 0°, 22°.5, 45°, and 67°.5.

The degree of linear polarization P, expressed in percent, is thus given by

$$P = 100 \times \frac{(Q^2 + U^2)^{1/2}}{I}, \qquad (22.1)$$

while the polarization azimuth χ is given by

$$\tan 2\chi = \frac{U}{Q}, \qquad (22.2)$$

and the photometric intensity I is simply

$$I = \frac{1}{2}\,[I'(0^\circ) + I'(22^\circ.5) + I'(45^\circ) + I'(67^\circ.5)]. \qquad (22.3)$$

Figure 164 shows two photometric I'-images derived from the observations obtained on 21 November 1986 when Jupiter was at a phase angle of 11°.1. The images on the left in figure 164 show the intensity measured in continuum light (fig. 164a) and in the methane absorption band (fig. 164c). A comparison of these images reveals the belt-zone contrast differences between the continuum and absorption-band data seen in the earlier photometric CCD measurements (West, 1979).

The corresponding polarimetric images are shown in figures 164b and 164d, respectively. Each of the polarimetric images shows the degree of linear polarization P calculated from the four photometrically calibrated images taken at rotations of the half-wave plate separated by 22°.5 according to the definition eq. (22.1). Since P is derived from differences between I'-images of close intensity, it is especially sensitive to any misregistration of the images in regions of high-intensity gradients such as near the limbs. To ensure that no spurious polarization would be introduced by this differencing, coregistration of the image centers to better than 0.1 pixels was required by our registration algorithm. A comparison of these images confirms the differences in continuum and absorption polarization reported by Wolstencroft and Smith (1979) for whole-disk measurements and reveals the spatial variations that are responsible for these differences.

POLARIZATION MEASUREMENTS

Until recently, most of the polarization studies of the jovian atmosphere have been confined to polarimetric measurements in broad spectral bands, usually of the integrated, whole disk or in limited spatial resolution. The interpretation of these measurements has assumed that broad-band measurements pertain to continuum values and the effect of any absorption bands is negligible. Early comparisons between bands and continuum (Bugaenko et al., 1971) seemed to support this assumption, but subsequent observations of the integrated jovian disk at narrow-band resolutions (Wolstencroft and Smith, 1979; Smith and Wolstencroft, 1983) showed strong increases in the linear polarization measured in the methane absorption band at 7270 Å, relative to the nearby continuum. Spatially resolved, narrow-band polarimetric imaging is the logical extension of this work.

The narrow-band polarimetric images of Jupiter obtained at the Lowell Observatory reveal significant variations in the degree of linear polarization with location on the disk, with wavelength, and with phase angle, illustrating the origin of the integrated, whole-disk differences observed by Wolstencroft and Smith and confirmed by Smith and Wolstencroft. A comparison of the observed variation in the degree of linear polarization measured in continuum light near 7500 Å (upper panels) and that measured in the methane absorption band near 7270 Å (lower panels) with phase angle is shown in figure 165. The images shown in this figure were recorded on the nights of 21 November 1986, when Jupiter was at a phase angle of 11°.1 (fig. 165a, d); 15 October 1986, when Jupiter was at a phase angle of 7°.0 (fig. 165b, e); and 11 September 1986, when Jupiter was at a phase angle of 0°.3 (fig. 165c, f). The direction of the Sun is to the right in these images, the morning terminator is to the left, and the jovian north pole is at the top. In all of these images, the degree of polarization is measured in percentage of linearly polarized light, calibrated according to the color table shown at the bottom of the figure.

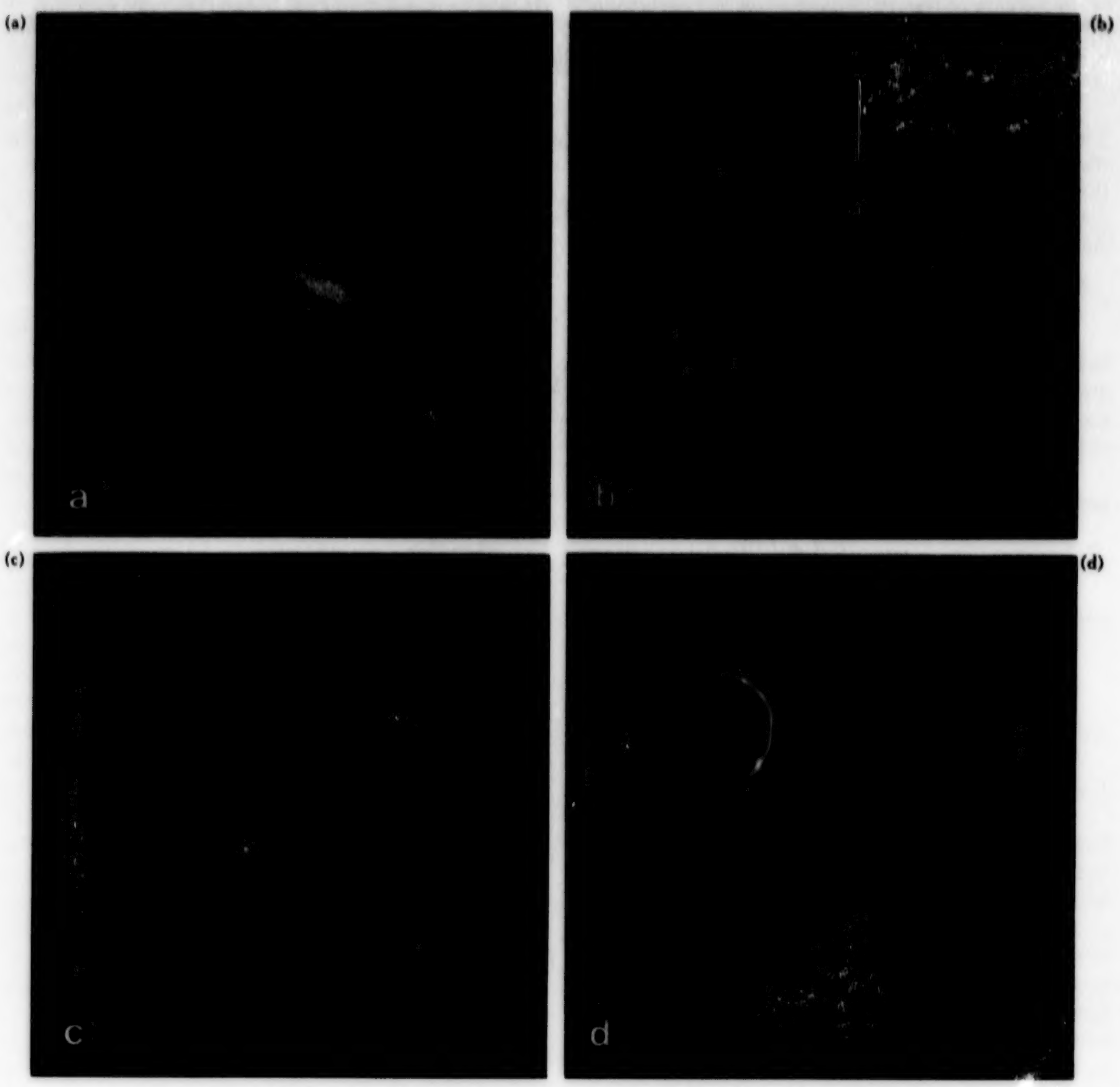

Figure 164. Photometric I'-images (**a** and **c**) and corresponding false-color polarimetric images (**b** and **d**) of Jupiter obtained on 21 November 1986 UT, when the solar phase angle was 11°.1. The *top row* (**a** and **b**) was recorded in continuum light near 7500 Å, and the *lower row* (**c** and **d**) in the methane absorption band at 7270 Å, using narrow-band interference filters. The polarization images are calibrated in percentage of linear polarization, according to the color tables shown.

The degree of linear polarization as shown in figure 165 does not include the direction of the polarization azimuth, normally used to determine the sign of the polarization. Since we are still in the preliminary stages of data reduction, we have not as yet assigned this sign.

Spatial Variations of Polarization

One of the advantages of CCD polarimetric imaging is spatial resolution combined with simultaneous whole-disk coverage. The polarimetric images shown in figure

ORIGINAL PAGE
COLOR PHOTOGRAPH

165 illustrate this advantage and reveal a surprising amount of horizontal structure. An examination of these images confirms the significant increase in the degree of polarization from the center of the disk toward the limbs noted by Lyot (1929). A closer examination of these images reveals latitudinal variations in this increase as well as an east-west asymmetry. Lyot's measurements also showed an asymmetric increase in the polarization from the center of the disk toward the limbs, and based on his measurements, he concluded that at the west (sunset) limb the polarization is more positive (i.e., the electric vector more nearly perpendicular to the Sun-Jupiter-Earth plane) than at the east (sunrise) limb. In his data, the effect appears to be independent of phase. Lyot further concluded that his observations tend to prove that the Sun, in spite of its distance, still exerts a noticeable influence on the atmosphere of Jupiter. Although our data demonstrates an east-limb–west-limb asymmetry, the fact that we have not as yet assigned a sign to the polarization prevents us from, at this time, commenting on Lyot's conclusions.

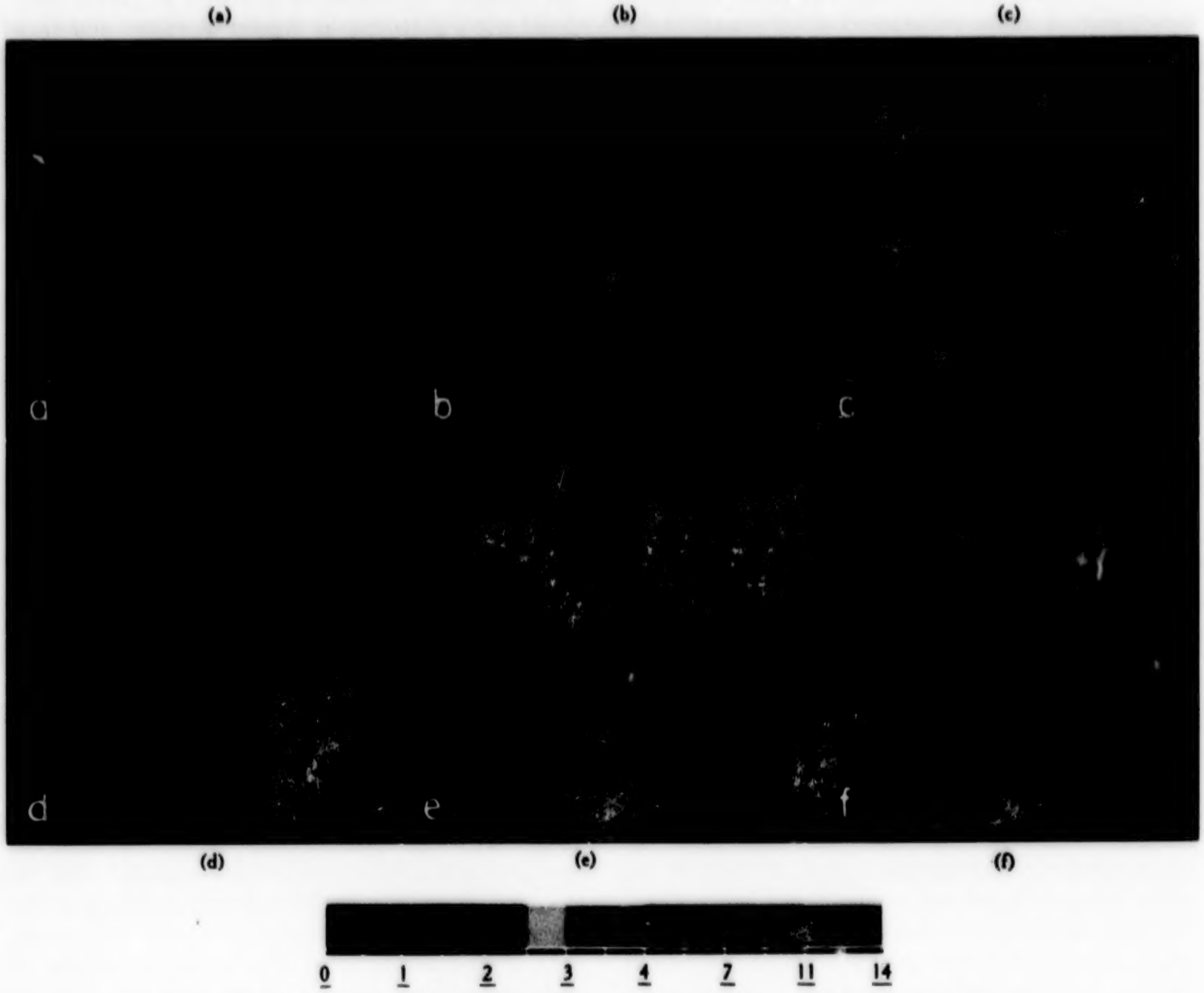

Figure 165. False-color, polarimetric images of Jupiter showing the degree of linear polarization in continuum light near 7500 Å (*upper panels:* **a, b,** and **c**) and in a methane absorption band at 7270 Å (*lower panels:* **d, e,** and **f**), as a function of solar phase angle: 11°.1 (**a** and **d**), 7°.0 (b and e), and 0°.3 (**c** and **f**). The UT dates for these observations are 21 November 1985, 15 October 1986, and 11 September 1986, respectively. The color table at the bottom is calibrated in percentage of linear polarization.

ORIGINAL PAGE
COLOR PHOTOGRAPH

One of the more striking features of these images is the latitudinal structure observed in the degree of linear polarization. Although the continuum images show latitudinal inhomogeneities, only the image recorded at 0°.3 phase reveals structure seemingly correlated with the planetary scale belt-zone structure. In contrast, the methane-band images recorded at 11°.1 and 7°.0 phase reveal a high degree of organized belt-zone structure, whereas the 0°.3 phase-angle measurements appear to exhibit the same latitudinal inhomogeneities present in the continuum images. The most definitive image is the methane-band image recorded at a phase angle of 11°.1 (figs. 164d, 165d). Here the sharp belt-zone contrast in the degree of linear polarization at the center of the disk seems to reverse itself at the east limb (left of image), with regions of high polarization at the center of the disk corresponding to regions of lower polarization at the limb.

A comparison of the polarimetric images in figure 165 seems to imply that the amount of belt-zone contrast observed in the degree of linear polarization is strongly dependent on the phase angle of the measurement. Polarization contrasts between the belts and zones have previously been noted by Dollfus (1957) and Smith and Tomasko (1984). The broad-band red and blue channel Pioneer measurements exhibited belt-zone contrasts that can be explained by the variation of the effective single scattering albedo between the belts and zones (Smith and Tomasko, 1984). The lower effective single scattering albedo in the belt leads to a smaller dilution of the moderately polarized single-scattered photons by weakly polarized multiply-scattered photons. Based on his measurements at a variety of wavelengths, Dollfus concluded that the observed polarization contrasts between belts and zones are due to the presence of a 1-μm-sized particle haze above a main cloud layer that is "rarefied" above the belts. Although we are not prepared to offer an explanation for these differences at this time, our preliminary calculations indicate that belt-zone variations in the effective single scattering albedo are insufficient to account for the observed polarization differences between the continuum and methane-band images. Furthermore, intensity differences (see eq. [22.1]) between the continuum and methane-band images (shown in fig. 164a, c) are insufficient to account for the observed polarization differences (shown in fig. 164b, d).

Variations of Polarization with Wavelength

Early polarimetric measurements in the spectral region from 4500 to 6500 Å (Dollfus, 1957) revealed little wavelength dependence in the degree of linear polarization. More recent measurements by Gehrels et al. (1969) in the spectral region from 3000 to 9000 Å showed significant wavelength variations in the degree of linear polarization at the highly polarized poles and limbs, whereas the central regions of the jovian disk that have small amounts of polarization exhibited little dependence on wavelength. Gehrels et al. attempted to reconcile their conclusions with the earlier observations by noting that the range of wavelengths investigated by Dollfus (1957) correspond to a spectral region in their measurements where the wavelength dependence is the smallest. Subsequently, Kemp et al. (1978) measured the polarization of Jupiter at visible and near-infrared wavelengths, confirming the existence of a significant wavelength dependence in the degree of linear polarization.

All of the measurements discussed above correspond to "continuum" regions in the jovian spectrum. Although our measurements also show a strong wavelength dependence, this dependence results from the continuum versus absorption band nature of our wavelength comparison. As previously noted, Wolstencroft and Smith (1978) and Smith and Wolstencroft (1983) found a strong degree of linear polarization measured in the methane-absorption band relative to the nearby continuum in their integrated disk measurements, qualitatively consistent with the band-continuum comparisons of our images.

Variations of Polarization with Phase Angle

For a spherical homogeneous atmosphere the polarization of the entire disk of a planet at a phase angle of 0° should be zero. Morozhenko and Yanovitskii (1973) found in their observations, however, that the polarization of the integrated disk of Jupiter does not decrease when the phase angle approaches zero and even increases slightly. They interpreted this apparent contradiction as a consequence of the optical inhomogeneity of the jovian disk, particularly in the meridional direction. Our polarimetric measurements confirm that the degree of linear polarization does not go to zero as the phase angle approaches zero. A comparison of the images shown in figure 165 reveals that the degree of linear polarization measured in the continuum and the methane-absorption band decreases as the phase angle decreases from 11°.1 to 7°.0. However, the degree of linear polarization, particularly for the regions in the center of the jovian disk, appears to increase as the phase angle further decreases from 7°.0 to 0°.3, implying that more than spatial inhomogeneity (i.e., the polar enhancement) in the jovian polarization is responsible for the increase in the whole-disk polarization measured by Morozhenko and Yanovitskii (1973) as the phase angle approaches zero.

A curious feature in the polarimetric images shown in figure 165 is the apparent lack of any polar enhancement in the degree of linear polarization measured in the methane-absorption band at a phase angle of 0°3. In this image the entire polar enhancement is confined to a small region near the north pole.

Both Lyot (1929) and Dollfus (1957) studied the polar enhancement in the degree of linear polarization, and variations were observed to occur on the time scale of days. In 1923, Lyot observed that the south pole had greater amounts of polarization, whereas in 1926 both poles were observed to have the same degrees of polarization. According to Lyot, the change cannot be explained by the small change in the inclination of the axis of Jupiter. Dollfus (1957) confirmed the temporal variability, and his observations indicated that in 1952 the regions of enhanced polarization were roughly equal at the north and south poles, but by 1955 the region of enhanced polarization had a greater extent at the north pole than at the south. Due to the high degree of temporal variability in the observations, no polarization-phase dependence could be established by Lyot (1929).

Given these earlier observations, it is premature for us to interpret the apparent phase-angle dependence of the polarimetric observations until we have established a suitable temporal framework of jovian observations within which to interpret the variations, a goal of our observational program.

Variations of the Sign of the Polarization

Our spatially resolved polarimetric images of Jupiter have revealed significant variations in the degree of linear polarization. Although we have not as yet assigned a sign to our polarization measurements, it is evident from existing data that the analysis of polarimetric images of the type we are recording toward this end will provide important new constraints on the properties and spatial (both horizontal and vertical) distribution of aerosols in the jovian atmosphere.

The higher phase-angle resolution of the polarization measurements made by Lyot (1929) suggest that the polarizations observed at the east and west limb change sign at a different phase angle. If we assume that the particles responsible for the polarization are compositionally the same at the east and west limbs, this differential change implies that a diurnal variation in particle size occurs with smaller particles at the sunset (west) limb. The polarization measurements made by Dollfus (1957) demonstrated that the polarizations observed in belts and zones also change sign at a different phase angle, but additional observations and detailed modeling will be required to determine whether this reflects compositional or particle size variations between belts and zones.

In addition to these variations with phase angle, variations in the sign of the degree of linear polarization have been observed with wavelength. Kemp et al. (1978) measured the degree of linear polarization at the poles of visible and near-infrared wavelengths and found that the sign of the polarization changes from positive (i.e., the electric vector maximum is in the radial direction) at visible wavelengths to negative (i.e., the electric vector maximum is in the tangential direction) at 1.6 μm. Measurements made at two phase angles, 10°4 and 0°5, both show this effect and suggest that it is not phase-dependent. Furthermore, their measurements, at least for the south pole, indicate that temporal variations also occur.

Kemp et al. (1978) interpreted the sign change in the degree of linear polarization as a diagnostic of particle size. Assuming a jovian vertical structure with a clear gas layer above the cloud particles, the ultraviolet and visible polarizations at the limbs can be explained in terms of double scattering. In the limit of Rayleigh-type scattering, appropriate to ultraviolet and short visible wavelengths, double scattering on the inclined limb surface leads to a radial pattern (positive polarization). At longer wavelengths, where aerosol scattering becomes important and where the wavelength is of the order of the particle diameter, double scattering can lead to a net sign reversal (i.e., tangential polarization). Based on these physical arguments, Kemp et al. concluded that aerosols of order 1 μm in size are responsible for the observed polarization.

The polarization measurements of Gehrels et al. (1969) revealed a similar variation in the sign of the polarization with wavelength. Their measurements of the west limb show that the sign of the polarization changes from positive (radial direction) at ultraviolet (UV) wavelengths to negative (tangential direction) at near-infrared wavelengths, also implying that the particles are of order 1 μm in size. Their measurements for the east limb exhibited no such sign reversal with wavelength. This difference again suggests that a particle size variation exists between the two limbs.

Instead of simply assigning a sign to their polarization measurements, Hall and Riley (1974, 1976) plotted the magnitude and orientation of the linear polarization. In their polarization diagrams, the directions of the lines indicate the planes of the electric-vector maxima and the lengths indicate the degree of linear polarization. This approach to the problem should prove useful for our ground-based observations where multiple scattering at these low-phase angles may result in intermediate orientations of the polarization azimuth.

SUMMARY

This chapter has presented qualitatively the results of our preliminary inspection of the new polarimetric images of Jupiter observed during its 1986 apparition. These initial images were recorded in a new program designed to determine the polarimetric and photometric properties of Jupiter in narrow spectral bands as a probe of the temporal and horizontal variations in vertical structure of the jovian atmosphere, including the nature and distribution of the aerosols. Although we are not yet prepared to discuss a quantitative analysis of these data, we have shown that complementary polarimetric and photometric imaging contains a wealth of information.

In addition to the vertical structure parameters that narrow-band photometric images can provide, information obtainable from polarimetry covers a broad range from the relatively simple mapping of cloud heights to the derivation of detailed characteristics of particle microstructure. Measurements of the wavelength dependence of the polarization can be used to infer the locations of the cloud height as a function of latitude and longitude. Gross cloud structure can also be extracted from the polarimetric data in the sense that a haze can be distinguished from a more optically dense cloud. Order of magnitude classification of particles according to whether their mean size is less than, on the order of, or larger than the wavelengths employed can be made regardless of the particle shape.

With this diagnostic approach in mind, we expect to extend the wavelength coverage of both our photometric and polarimetric CCD measurements to include absorption-band–continuum-filter pairs for the 6190- and 8900-Å methane bands as well as the 6450-Å ammonia band, beginning with the 1987 observing season. In light of the temporal variability observed in polarization data, we plan to obtain polarimetric images of Jupiter on a synoptic basis and, given the wealth of information contained in the phase-angle variation, even within the limit range of phase angles accessible to ground-based observations, we hope to obtain higher phase-angle resolution in the future.

ACKNOWLEDGMENTS

We would like to express our appreciation to Mr. C. A. Gullixson for his invaluable help in obtaining the new photometric imaging and to Dr. J. A. Tyson of the Bell Laboratories for making his imaging polarimeter available to us for this project. We would also like to thank Ms. E. S. Bus for assistance and perseverance in reducing the CCD images, J. Jonas for providing graphics software support, and P. Palmer for the photography. This research is supported in part by NASA grants NSG-7499 and NGR-03-003-001 and by the Lowell Observatory Research Fund.

References

Bugaenko, O. I., L. S. Galkin, and A. V. Morozhenko (1971). *Soviet Astron. J.* 15:290–295.

Dollfus, A. (1957). Study of the planets by means of the polarization of their light. *Tech. Transl. F-88* (NASA, Washington, D.C., 1964).

Gehrels, T., B. M. Herman, and T. Owen (1969). Wavelength dependence of polarization XIV. Atmosphere of Jupiter. *Astronomy J.* 76:190–199.

Hall, J. S., and L. A. Riley (1976). A polarimetric search for fine structure on Jupiter's disk. *Icarus* 29:231–234.

Hall, J. S., and L. A. Riley (1974). Polarization measurements of Jupiter and the great red spot. In *Planets, stars and nebulae studied with polarization* (T. Gehrels, ed.), pp. 593–598. Univ. of Arizona Press, Tucson.

Hansen, J. E., and L. D. Travis (1974). Light scattering in planetary atmospheres. *Space Sci. Rev.* 16:527–610.

Kemp, J. C., R. J. Rudy, M. J. Lebofsky, and G. H. Rieke (1978). Near-infrared polarization studies of Saturn and Jupiter. *Icarus* 35:263–271.

Lyot, B. (1929). Research on the polarization of light from planets and from some terrestrial substances. *Tech. Transl. F-187.* (NASA, Washington, D.C., 1964).

Morozhenko, A. V., and E. G. Yanovitskii (1973). The optical properties of Venus and the jovian planets I. The atmosphere of Jupiter according to polarimetric observations. *Icarus* 18:583–592.

Smith, P. H., and M. G. Tomasko (1984). Photometry and polarimetry of Jupiter at large phase angles II. Polarimetry of the south tropical zone, south equatorial belt and the polar regions from the Pioneer 10 and 11 missions. *Icarus* 58:35–73.

Smith, R. J., and R. D. Wolstencroft (1983). High precision spectropolarimetry of stars and planets—II. Spectropolarimetry of Jupiter and Saturn. *Mon. Not. R. Astron. Soc.* 205:39–55.

Tyson, J. A., and R. W. Lee (1981) Charge-coupled device (CCD) imaging polarimeter. *SPIE* 290:144–149.

West, R. A. (1979). Spatially resolved methane band photometry of Jupiter I. Absolute reflectivity and center-to-limb variations in the 6190-Å, 7250-Å, and 8900-Å bands. *Icarus* 38:12–33.

Wolstencroft, R. D., and R. J. Smith (1979). Spectropolarimetry of methane and ammonia bands of Jupiter between 6800 and 8200 Å. *Icarus* 38:155–165.

23

Photometric Properties and Classification of Small Jovian Cloud Features

W. Reid Thompson
Carl Sagan
Cornell University, Ithaca

Abstract

We use a triplet of images taken through the violet, green, and orange filters of the Voyager 2 wide-angle camera to derive photometry for most of the disk of Jupiter visible at a subspacecraft longitude near 100° W. Global photometric gradients in each filter are removed by fitting a least squares Minnaert function to the photometrically and geometrically corrected I/F data, then dividing the original data by that function. The Minnaert-divided green intensity $I/F_{\mathrm{R,GR}}$ and the Minnaert-divided color ratios $I/F_{\mathrm{R,VI/GR}} \equiv I/F_{\mathrm{R,VI}}/I/F_{\mathrm{R,GR}}$ and $I/F_{\mathrm{R,OR/GR}} \equiv I/F_{\mathrm{R,OR}}/I/F_{\mathrm{R,GR}}$ are used as the classification variables for cluster analysis. The 18 clusters found identify regions in the jovian clouds with similar photometric properties. Cluster mean values for $I/F_{\mathrm{R,VI/GR}}$ vary from 0.76 to 1.32, for $I/F_{\mathrm{R,OR/GR}}$ from 0.84 to 1.18, and $I/F_{\mathrm{R,GR}}$ from 0.82 to 1.14. Classification serves to group the global data for further study, to quantify the photometric variety seen across the disk in these filters, and to suggest possible similarities in composition and vertical structure between clouds that classify together but are morphologically distinct.

INTRODUCTION

The Voyager flybys of Jupiter in 1979 provided an imaging data set of staggering and fascinating complexity. Major photometric units such as the belt-zone structure are obvious, and the contrast in the reflection properties of many smaller features (the great red spot [GRS], brown barges, equatorial plumes, white ovals, and small dark ovals) is also evident to casual inspection.

The physical nature of the differences in cloud structure and composition responsible for the large-scale distinction of belts, zones, and polar regions is a matter of some debate continuing up to the present time. The excellent review of West et al. (1986) summarizes evidence drawn from polarization and light-scattering models, which indicates that a haze of particles, perhaps ~1 μm in radius and of optical depth at least 2 to 5, covers both the belts and zones. This haze is probably primarily NH_3 crystals, and is thought to extend from ~700 mbar up to a higher level in the equatorial and polar regions (~200 mbar) than is found in the south equatorial belt (SEB) and midlatitudes (~ 350–450 mbar). West et al. suggest that large-scale variation in color and albedo may be attributable to the admixture of chromophore in this thick haze layer, rather than to the presence of distinct colored clouds at deeper levels in the atmosphere.

Although these arguments are provocative, there are greater inhomogeneities at smaller scales. Strong broad-band color variations are obvious upon inspection of the high-resolution Voyager images, and CH_4 band-strength variations have been quantified for 15 Voyager 1 images by West et al. (1985). Also, the visual impression that at small scales, some clouds do overlay others (Owen and Terrile, 1981) remains.

Studying the variation of the reflectance of a given type of feature with position on the disk (i.e., for the available range of angular variation of the solar-to-surface and surface-to-spacecraft vectors) provides the information necessary to model the differences in cloud structure responsible for the photometric appearance (color and angular variation) of a given type of cloud. The inherent limitations of imaging produce a limited sampling for the reflection of small features through the desired broad-band filters (plus the 619 nm CH_4 filter) available. A single, clearly distinguishable feature may be sampled repeatedly using an imaging sequence covering at least one full rotation, but sampling from a displayed digital image is complicated by the different aspect and visibility of the feature as it moves from terminator to subspacecraft point to limb, so simple sampling methods have limited application.

An early study of ours using pixel-box sampling of 60 jovian cloud features in Voyager 1 orange, green, and blue filter images (Thompson and Sagan, 1981) showed great differences in the center-to-limb photometric behavior of cloud features including equatorial plumes, interplume regions, and barges. Our goal is to exploit more systematically the acquisition and analysis of such data. The photometry of jovian clouds at high-spatial resolution allows a comparison of the (apparent and model-derived) similarities and differences of smaller features with the belts and zones. Both the structure of the equatorial region and the texture within the zones and other large areas may also be studied, provided a rapid and systematic means of photometric data acquisition and classification is used.

TECHNIQUES

We are developing several techniques intended to (1) make the sampling of small features more reliable, (2) identify photometric units that are not so obvious to casual inspection, and (3) make the coverage and number of cloud types that can be studied more complete by pooling photometric data gathered from features that may be identified with a common unit.

The main mathematical tools in this work are the building and management of large photometric data sets, user-entering and reprojection of feature shapes, tracking of position and shape-evolution by windowed cross-correlation, and the classification of photometric units by cluster analysis.

Here we present some results illustrating one part of this work: complete-image photometric sampling, removal of global photometric gradients, and use of cluster analysis to identify remaining differences in the reflection properties of jovian cloud in the Voyager 2 wide-angle orange (OR), green (GR), and violet (VI) filters.

Photometric sampling and a simple map projection are made simultaneously, producing a map-image file and a photometric-data file. Here the Voyager 2 images 20578.39 (OR), 20578.59 (VI), and 20579.09 (GR) were sampled at 0°5 resolution, resulting in a catalog with about 60,000 entries per image.

The central (relatively unobscured) regions of the whole-disk photometric data sets were fit to Minnaert functions $I/F = B\mu_0^k\mu^{k-1}$ to remove global brightness gradients. Points with solar incidence cos i and emission cos $e > 0.7$ (incidence and emission angles ≤45° with respect to the surface normal) were fit with about one-quarter sampling (5000 points). The reflectance of

Table 18. Minnaert Parameters for Central Average Disk

Image	k	B	σ
20578.39 (OR)	0.9146 ± 0.0041	0.7270 ± 0.0014	0.0033
20578.59 (VI)	0.7614 ± 0.0080	0.4696 ± 0.0019	0.0060
20579.09 (GR)	0.8994 ± 0.0040	0.7696 ± 0.0015	0.0037

this central portion of the disk was then divided by the Minnaert reflectance computed for the mean disk, using the least squares values of the parameters B and κ for each filter, resulting in reflectance ratios $I/F_{R,X} = I/F_X/B_X \mu_0^{k_X} \mu^{k_X - 1}$, where X = VI, GR, OR. The Minnaert parameters are shown in table 18.

Further dividing the values I/F_R for the OR and VI filters by that of the GR filter results in the three-parameter set used for classification, $I/F_{R,GR}$, $I/F_{R,VI/GR} \equiv I/F_{R,VI}/I/F_{R,GR}$, and $I/F_{R,OR/GR} \equiv I/F_{R,OR}/I/F_{R,GR}$. This set of photometric parameters for all points at latitudes between ±40° at 0°.5 resolution, present on all three images resulted in a data set of 18,879 observations that were analyzed by a modified kth nearest neighbor (Wong and Lane, 1983) clustering method: the two-stage density linkage clustering procedure developed by W. S. Sarle, which is part of the SAS statistical-mathematical system (SAS Institute Inc., 1985). Although clustering procedures come in many varieties and can be very complex, they basically start with individual points, nucleate clusters, and accrete additional points or other clusters according to the local density of surrounding points, thus identifying regions in the parameter space that represent concentrations of similar objects.

RESULTS

Upon applying the procedure to the observations, a criterion for the significance of the number of clusters (the cubic clustering criterion) showed breaks at $N = 4$ and $N = 18$.

The 18-cluster case distinguishes some rather well-separated photometric units, which are shown here. A summary of the numerical results is given as table 19. (Cluster 13 consists partly of extreme points and should be ignored). Most of the disk is engulfed by one large cluster, to which the zones, including most of the equatorial region, as well as the high latitudes belong. This

Table 19. Jovian Cloud Feature Classification Statistics

Variable	Members	Mean	Range	Standard deviation	Variance
			Cluster = 1		
VI/GR	16988	1.013	1.045	0.1298	0.0168
OR/GR		1.000	0.496	0.0551	0.0030
GR		1.016	0.518	0.0897	0.0080
			Cluster = 2		
VI/GR	198	0.760	0.143	0.0239	0.0006
OR/GR		0.855	0.212	0.0457	0.0020
GR		1.032	0.296	0.0526	0.0028
			Cluster = 3		
VI/GR	276	0.769	0.186	0.0348	0.0012
OR/GR		1.006	0.171	0.0345	0.0012
GR		0.859	0.148	0.0243	0.0006
			Cluster = 4		
VI/GR	247	1.190	0.275	0.0518	0.0027
OR/GR		1.093	0.268	0.0377	0.0014
GR		0.947	0.164	0.0290	0.0008
			Cluster = 5		
VI/GR	116	0.686	0.463	0.0664	0.0044
OR/GR		0.991	0.188	0.0293	0.0009
GR		1.021	0.164	0.0273	0.0007

Table 19. (continued)

Variable	Members	Mean	Range	Standard deviation	Variance
Cluster = 6					
VI/GR	48	0.819	0.054	0.0127	0.0002
OR/GR		0.997	0.077	0.0193	0.0004
GR		0.872	0.060	0.0143	0.0002
Cluster = 7					
VI/GR	115	0.970	0.144	0.0318	0.0010
OR/GR		1.179	0.145	0.0282	0.0008
GR		0.868	0.126	0.0279	0.0008
Cluster = 8					
VI/GR	77	0.851	0.116	0.0257	0.0007
OR/GR		0.896	0.149	0.0298	0.0009
GR		1.135	0.106	0.0230	0.0005
Cluster = 9					
VI/GR	43	1.139	0.059	0.0129	0.0002
OR/GR		1.081	0.121	0.0240	0.0006
GR		1.053	0.087	0.0167	0.0003
Cluster = 10					
VI/GR	83	0.885	0.078	0.0180	0.0003
OR/GR		1.112	0.068	0.0165	0.0003
GR		0.849	0.132	0.0255	0.0007
Cluster = 11					
VI/GR	75	0.761	0.203	0.0468	0.0022
OR/GR		0.861	0.218	0.0412	0.0017
GR		1.101	0.276	0.0466	0.0022
Cluster = 12					
VI/GR	131	1.084	0.133	0.0264	0.0007
OR/GR		1.134	0.152	0.0301	0.0009
GR		0.865	0.129	0.0253	0.0006
Cluster = 13					
VI/GR	220	—	—	—	—
OR/GR	—	—	—	—	—
GR	—	—	—	—	—
Cluster = 14					
VI/GR	49	0.898	0.066	0.0166	0.0003
OR/GR		0.867	0.098	0.0223	0.0005
GR		1.064	0.069	0.0203	0.0004
Cluster = 15					
VI/GR	48	0.849	0.091	0.0199	0.0004
OR/GR		0.844	0.081	0.0215	0.0005
GR		1.102	0.143	0.0265	0.0007
Cluster = 16					
VI/GR	56	0.804	0.113	0.0288	0.0008
OR/GR		1.093	0.091	0.0183	0.0003
GR		0.823	0.084	0.0182	0.0003
Cluster = 17					
VI/GR	62	1.320	0.279	0.0448	0.0020
OR/GR		1.115	0.255	0.0409	0.0017
GR		1.019	0.146	0.0292	0.0009
Cluster = 18					
VI/GR	47	0.774	0.063	0.0162	0.0003
OR/GR		1.037	0.112	0.0297	0.0009
GR		1.011	0.093	0.0218	0.0005

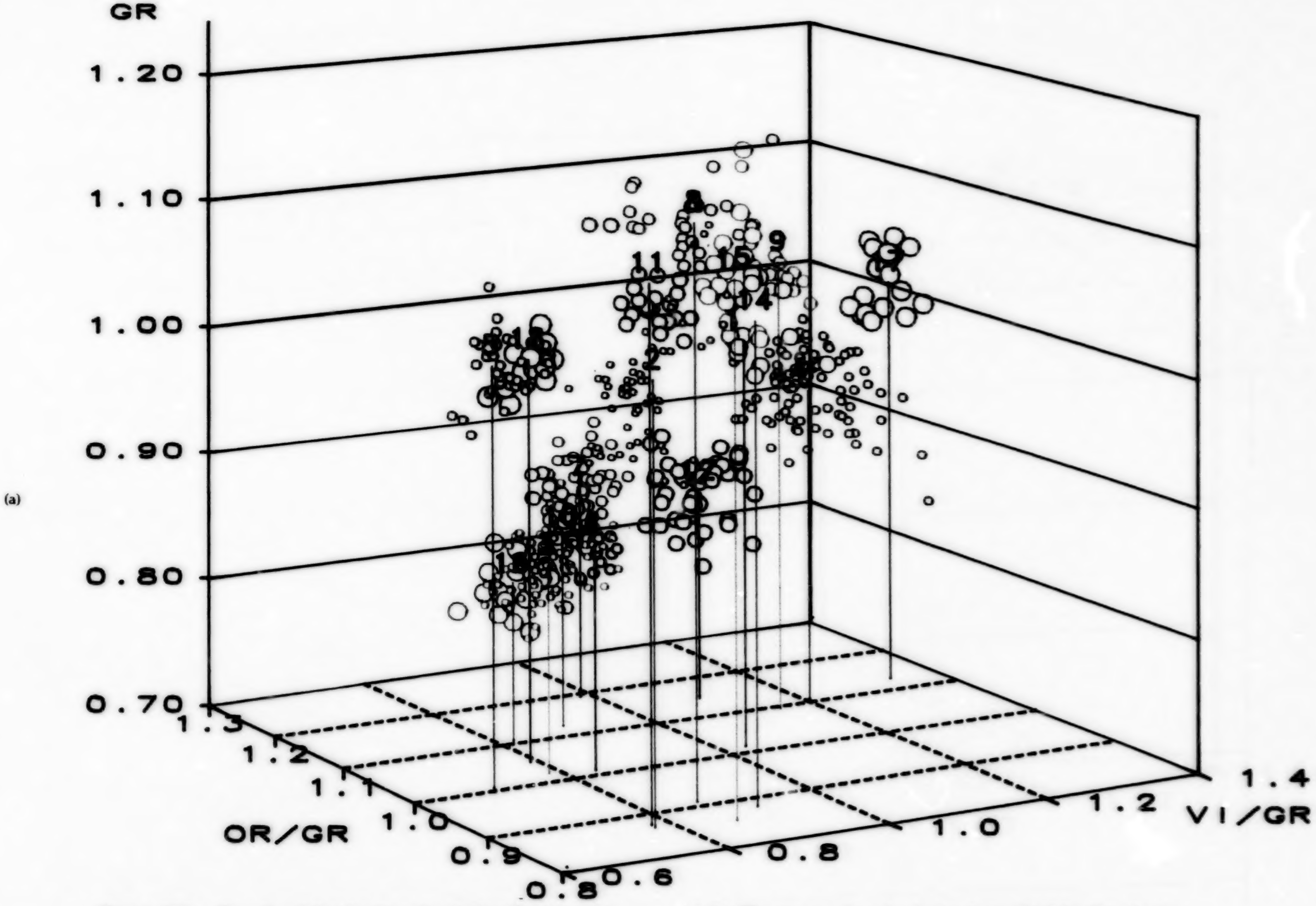

Figure 166. Results of the Jupiter cloud-classification cluster analysis of the 18,879 points with 33 percent of the points shown selected from an even grid of 0°.5 in latitude and longitude, and having cos *i* and cos *e* > 0.7 in all three filters. Classification variables are the Minnaert-scaled GR intensity ($I/F_{R,GR}$) and the Minnaert-scaled ratios VI/GR ($I/F_{R,VI/GR}$) and OR/GR ($I/F_{R,OR/GR}$). Plots are shown at a view angle 10° above OR/GR-VI/GR plane, and rotated 10° from the OR/GR (**a**) and VI/GR (**b**—see page 302) axial lines of sight. The mean of each cluster is marked by the cluster number, and surrounded by a sampling of 33 percent of the member pixels. Members of a particular cluster are marked by *circles* with a unique size-color combination. A perpendicular dropped to the VI/GR-OR/GR plane from each cluster mean facilitates perspective and comparison of the color ratios. Points from cluster 1 constitute 90 percent of the data set and are not shown. All cluster members are mapped in figures 167 and 168.

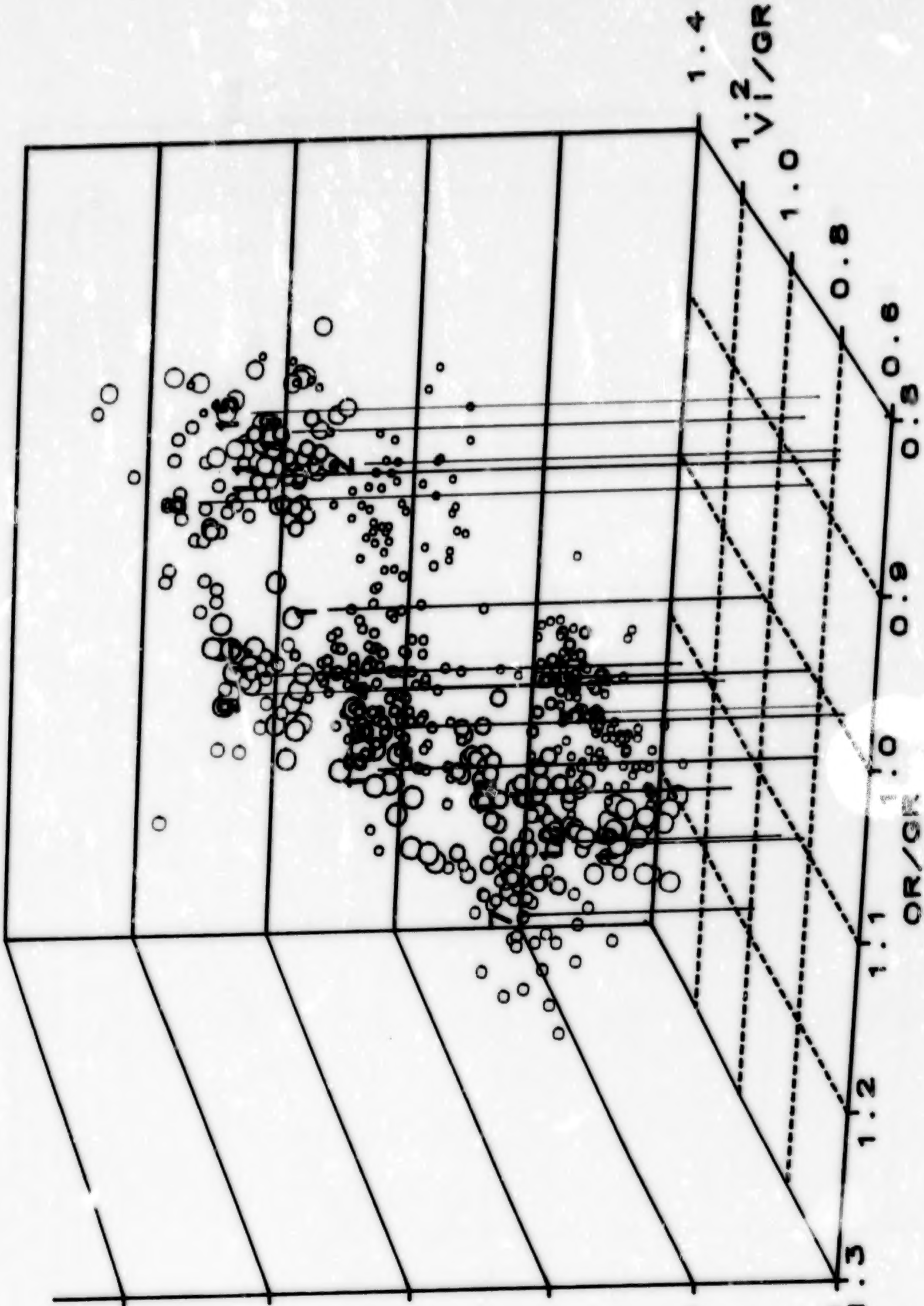

Figure 166 (continued). See legend on page 301.

ORIGINAL PAGE
COLOR PHOTOGRAPH

Figure 167. Rectangular map projection of the classification (cluster membership) of jovian clouds at 0°.5 resolution in latitude and longitude, derived from analysis of the Voyager 2 images, FDS 20578.39 (OR), 20578.59 (VI), and 20579.09 (GR) (see text). The classification map is shown at right, whereas a rectangular projection of the VI filter image at the same scale is shown at left. The latitude-longitude grid is marked at 15° planetocentric intervals—the middle horizontal line is 0° latitude, whereas the vertical lines marking 90° and 195° W System III longitudes span the great red spot. (Longitude increases to the left.) Cluster members corresponding to table 19 and figure 166 are each assigned a color from the bar at right: cluster 1 is suppressed to nearly black whereas clusters 2 through 18 are coded sequentially, top to bottom, with the remaining colors of the bar. The line of green pixels at the lower left of the map and of red pixels at the upper rights are artifacts.

largest cluster well-separates the disk-average from the behavior of other, much smaller photometric units, but shows structure and could be reanalyzed for major subclusters.

Points in this three-dimensional parameter space constituting a 33 percent sampling of the cluster members are shown from two different perspectives in figure 166. Parameter values of values of sampled points (classified 0°.5 pixels) are represented as circles, with each color-size combination representing a different cluster membership. There is no culling of outlying points. The mean values of the Minnaert-scaled VI/GR and OR/GR ratios ($I/F_{R,VI/GR}$ and $I/F_{R,OR/GR}$) for each cluster are marked by the cluster number. Means of the color ratios for each cluster can easily be read from the intersection of the lines dropped from each cluster mean with the bottom surface.

The cluster memberships of the 0°.5 latitude-longitude pixels were used to construct a color map of the identified photometric units, which is presented alongside a rectangular map projection of the VI filter image (fig. 167). The clusters clearly identify some features (the GRS, SEB, and equatorial plume margins are prominent), whereas others are conspicuously absent

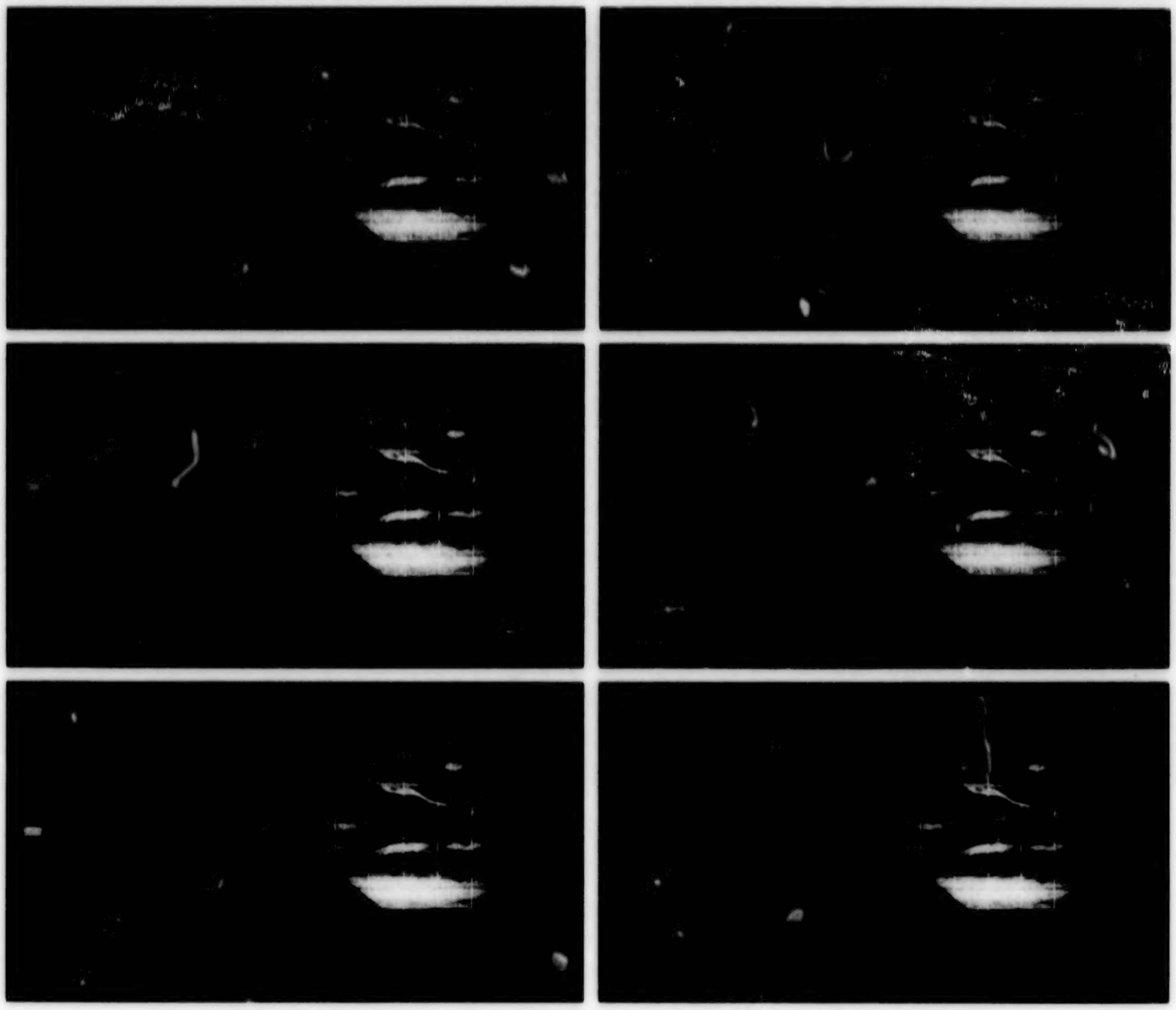

Figure 168. Set of rectangular map projections as in figure 167, but with two or three clusters highlighted at a time to enhance distinguishability. Highlighted clusters are: *left column, top:* 7 and 13; *middle:* 2, 8, and 14; *bottom:* 3, 9, and 15; *right column, top:* 4, 10, and 16; *middle,* 5, 11, and 17; *bottom:* 6, 12, and 18. See text for comments.

Table 20. Clusters Having Extreme Means of Parameters

Parameters	**Low**	**High**	**Cluster**	**Members**
$I/F_{R,VI/GR}$	0.760		2	Small areas south of SEB, north of the equatorial plume heads, and between SEB and EZ.
		1.320	17	Large white oval south margin, spots within GRS wake, and spots within NTrZ.
$I/F_{R,OR/GR}$	0.844		15	Albedo boundaries in GRS wake and equatorial plume heads.
		1.179	7	North boundary of SEB, south margin of GRS, and dark NTrZ oval.
$I/F_{R,GR}$	0.823		16	Core of SEB and small barge.
		1.135	8	Plume heads, small areas within GRS wake margins, and ovals at NTrZ-NTB boundary.

EZ = equatorial zone, NTrZ = north tropical zone, NTB = north temperate zone.

ORIGINAL PAGE
COLOR PHOTOGRAPH

(white ovals, zones, and belts other than the SEB are mostly absorbed into the global average cluster 1). Several not-so-obvious units and associations are seen.

To enhance the distinguishability of the units, they are highlighted three at a time in the six images of figure 168. The comembership of a small barge and the core of the SEB (cluster 16), of plume margins and albedo boundaries in the southern hemisphere (cluster 4), and of margins in the northern part of the SEB and the southern part of the GRS (clusters 7 and 10) are seen. Each cluster having an extreme mean for any of the three parameters is identified in table 20, along with a description of the cloud types forming its members. Some associations can be identified with features on the VI filter map, whereas others are too subtle in this filter, or, often, at the resolution limit of these images. Studies at higher spatial resolution should be very interesting, since many areas at the current 0°5 resolution are only one to a few pixels in extent.

Classifications and associations suggested here can be extended to the full globe by using a series of color triplets covering a full jovian rotation. By classifying and following like photometric areas through a rotation, a photometric light curve can be constructed for each distinguishable unit. We are building such data sets for subsequent light-scattering modeling, and will also be using the cross-correlation–reprojection techniques described above to assess the motion and the photometric and morphologic evolution of features at small scales.

ACKNOWLEDGMENTS

This work is supported by the NASA Planetary Atmospheres Program (NGR 33-010-082) and the Galileo project (JPL 955052). The computing component of this research is conducted using the Cornell National Supercomputer Facility, through a grant from the Center for Theory and Simulation in Science and Engineering, which receives major funding from the National Science Foundation and the IBM Corporation and additional support from New York State and members of the Corporate Research Institute.

References

Owen, T., and R. J. Terrile (1981). Colors on Jupiter. *J. Geophys. Res.* 86:8787–8814.

SAS Institute, Inc. (1985). *SAS User's Guide: Statistics. Version 5 Edition.* SAS Institute, Cary N.C., USA. Ch. 15, n.b., pp. 264–267.

Thompson, W. R., and C. Sagan (1981). On the nature of the jovian "blue" regions. *Bull. Amer. Astron. Soc.* 13:734 (abstract).

West, R. A., P. N. Kupferman, and H. Hart (1985). Voyager 1 imaging and IRIS observations of jovian methane absorption and thermal emission: Implications for cloud structure. *Icarus* 61:311–342.

West, R. A., D. F. Strobel, and M. G. Tomasko (1986). Clouds, aerosols and photochemistry in the jovian atmosphere. *Icarus* 65:161–217.

Wong, M. A., and T. Lane (1983). A k-th nearest neighbor clustering procedure. *J. Roy. Stat. Soc.* Ser. B 45:362–368.

24

Great-Scale Changes in the Belts and Zones of Jupiter: The Outbursts of Activity and Disturbances in the SEB and NTrZ-NTBs Regions

Agustin Sanchez-La Vega
Apartado 820, 48080 Bilbao, Spain

Abstract

Great-scale changes in the belts and zones of Jupiter can be of two types: (1) gradual, with time scales of several months, and (2) cataclysmic and sporadic, with short time scales of several days. This work presents a study about this second type, characteristic of two regions of the planet, the south equatorial belt (SEB) between latitudes 10° S and 20° S, and the north tropical zone-south component of the north temperate belt (NTrZ-NTBs) between latitudes 20° N and 25° N. Both types of disturbances started with the emergence of a bright, high-albedo spot (scale ~6000 km) at 15°.5 S (SEBD) and at 23°.5 N (NTrZ-NTBsD). These spots, of probable convective origin, expanded in area during the first week, and they are followed by the subsequent development of rows of dark and elongated spots (east-west scale ~10,000 km) at nearby latitudes. The low-albedo spots moved with the prevailing zonal wind, circling the planet, and producing beltlike regions with turbulent patterns. They can be short-lived eddies, lying near to the jet cores (where $\bar{u}$ is a maximum) and in locations where $\bar{u}_{yy} - \beta$ is also a maximum. This is the opposite to that found in long-lived eddies (like great red spot [GRS], white oval spot [WOS], and barges), which are situated where $\bar{u}$ and $\bar{u}_{yy} - \beta$ are near zero. On the other hand, the bright spot of the SEBD appeared in a latitude where $u \sim 0$ and where the shear ambient vorticity is cyclonic, whereas the NTrZ-NTBsD appeared in a latitude where the zonal velocity is maximum ($u \sim 165$ m s^{-1}), and the shear ambient vorticity is anticyclonic. However, on both regions the vorticity is the highest of the whole atmosphere with $|\partial u/\partial y| \sim 1 - 2 \times 10^{-5}$ s^{-1}.

INTRODUCTION

Earth-based observations of Jupiter's clouds during the last century have shown that belts and zones are subject to great-scale changes in their albedo and morphology. A summary is presented by Peek (1958) and by Smith and Hunt (1976). Strikingly, although the cloudy appearance of the jovian atmosphere is in a permanent state of change, the zonal wind system seems to be immutable (Ingersoll et al., 1981), which represents a major challenge to the theoretical interpretations of the nature of jovian atmospheric circulation and in particular to the nature of belts and zones. Understanding the processes operating during these changes could help to explain the origins of the axisymmetric bands of clouds.

Belts and zones suffer two types of time-dependent changes. They can be gradual with time scales of several months, as for example during the development of a south tropical zone disturbance (STrZD), or during the fading of the SEB and north and south temperate belts (NTB and STB, respectively). On the other hand, they can be cataclysmic in nature, with time scales of several days as the events that develop during a SEBD.

This chapter presents a study about this second type of outbreak of activity, characteristic of two regions of the planet: the SEB (between latitudes ~10° S and 20° S) and the NTrZ-NTBs (between latitudes ~20° N and 25° N).

THE SOUTH EQUATORIAL BELTS DISTURBANCES

These disturbances start with the apparition of a bright white spot (length scale ~6000 to 8000 km) near planetographic latitude 15°.5 S, which is followed in subsequent days with the development of streams of oval and round dark spots (length scales ~10,000 to 20,000 km and prevailing blue color) situated to the north and south of the original event. The meridional wind shear at these latitudes tilt these features, producing an "integral-shaped" (slanted column with a red color) structure to the west of the initial spot between 10° S and 20° S. The series of dark spots moves in two opposite directions: one along latitude 8°.5 S with zonal velocity $u \sim 97$ m s^{-1} and the others along latitude 20° S with $u \sim -56$ m s^{-1}. The central white spot moves itself with $u \sim 3$ m s^{-1}.

After around 30 days from the date of the initial outbreak (this time is $2\pi R \cos \phi/[u_1 - u_2]$, R being the jovian radius, ϕ the latitude, and u_1 and u_2 the zonal velocity of both currents), the two series of dark spots enter in conjunction, and the central region of the SEB that lies between them becomes a state of turbulence and turmoil (formation of twisted streaks) regenerating a new SEB belt. Meanwhile, the initial white spot has expanded during the first two weeks to ~60,000 km, with a growing rate of 60 m s^{-1}, and sometimes other white spots emerged nearby (Peek, 1958; Reese, 1972; Minton, 1972; Larson, 1972; Sanchez-Lavega and Rodrigo, 1985).

It is important to note that there are two types of SEB activity depending on the state of the region between the north component of the SEB (SEBn) ($\phi \sim$ 10° S) and the STB ($\phi \sim$ 30° S). Classical SEBD develop when this space is very bright and white (probably the highest albedo zone of the planet, which is usually referred to as a "cloud covered region"), being also then the GRS, a prominent and conspicuous dark oval spot. With the development of the SEBD, the zone between the south component of the SEB (SEBs) and SEBn darkens and the GRS becomes faint and inconspicuous, although the classical hollow around the northern edge of the GRS detaches. Features moving westward at 20° S, when arriving at the east edge of the GRS, are deflected northward and are forced to circulate around its perimeter. This kind of outburst is usually related to the development of a STrZD.

The other type of SEBD eruption starts when the SEB is well developed and dark, so there is no new forming band, but a reinforcement (in darkness and turbulence) of the already existent belt.

Occasionally the SEBD eruptions are of double or even triple nature, with their apparition in different points in longitude (separated by 75,000 to 180,000 km)

Table 21. SEB Disturbances Observed from 1919 to 1985

Date of outbreak	System II longitude (degrees)	Type[a]	Reference
1919, December 8	227	M	(1)
1928, August 10	128	M	(1)
1930, September 11	31	m	(1)
1943A, February 7	20	M	(1)
1943B, February 27	288	M	(1)
1948, April 20	320	m	(1)
1949, July 19	155	M	(1)
1950, August 8	181	m	(1)
1952, October 20	208	M	(1)
1953, September 17	223	m	(1)
1953, December 3	219	m	(1)
1955, February 4	229	M	(1)
1956, November 15	278	m	(1)
1957, December 1	290	m	(1)
1958, March 27	47	M	(1)
1959, March 25	282	m	(1)
1960, May 28	248	m	(1)
1961, May 23	296	m	(1)
1962, September 23	245	M	(1)
1964, October 28	40	m	(1)
1965, August 4	60	m	(1)
1967, April 2	60	m	(1)
1971A, June 18	79	M	(2)
1971B, July 18	144	M	(2)
1975A, July 2	59	M	(3)
1975B, August 2	208	M	(3)
1975C, August 16	120	M	(3)
1979, February 21	152	L	(3)
...............[b]		L	(3)
1985A, July 12	130	L	(4)
1985B, August 12	147	L	(4)
1985C, November 3	185	L	(4)

[a] Following the work of Chapman and Reese (1968): M = major, m = minor. We denote type L when SEB is already a low albedo belt (in the visible) and when the bright white spots emerged. [b] From 1980 to 1984 there was continuous activity with sudden eruptions of white clouds at 15° S and in a region of 100° westward of the GRS. A, B, and C denote the double or triple nature of the outbursts. References: (1) Chapman and Reese (1968), (2) Reese (1972), (3) Sanchez-Lavega and Rodrigo (1985), and (4) Sanchez-Lavega (unpublished).

of a white spot and the subsequent dark ones, although never started simultaneously but with an interval of 15 to 30 days. Table 21 shows a summary of all the SEBD recorded in the history of jovian observations to which we have added our own recent data.

THE ERUPTIONS IN THE NTrZ-NTBs REGION

Although less frequent than the SEBD, the outbursts of activity that develop in the NTrZ-NTBs (between latitudes 20° N and 25° N) are very spectacular and unique in the planet, and have specially served to track the eastward jet at 24° N. This activity is different from that that affects the NTB (between NTBs and NTBn at $\phi \sim 25°$ N to 34° N), and that consists of a gradual increase or decrease of the albedo of the region between both components of the NTB. For example, compare the difference between images obtained by Pioneer 10 and 11 in 1973–1974 with those obtained by Voyager 1 and 2 in 1979 (see Terrile and Beebe, 1979).

We describe now the texture and morphology of these outbursts centering in the case of the double 1975 outbreak. It started with the simultaneous emergence in two points of the disk separated by ~125,000 km of a brilliant white cloud (length scale ~6000 km), near latitude 24° N (in the maximum of the jet), which moved with $u \sim 165$ m s^{-1}. Following both and to their west, there appeared in the next days, rows of dark and

Table 22. NTrZ-NTBs Disturbance and Spots in the Eastward Jet Observed from 1880 to 1975

Apparition	Type of spot	$\hat{u}$	τ_L	Disturbance	References
1880	D	146	—	Yes	(1)
1891–1892	D	120	—	Yes	(1)
1926	D	125	98	No	(1)
1929–1931	D	122	152	Yes	(1)
1939–1943	D	125	100–200	Yes	(1)
1964–1965	D[a]	120	268	No	(1)
1970	W[b]	165	40	No	(2)
1975A	W and D[c]	165–110	40	Yes	(3)
1975B	W and D[c]	155–130	—	Yes	(3)

Type of spots: D = dark, W = white. [a] This spot was of red color. [b] Bright spot at ultraviolet and blue wavelengths. [c] The W spot preceded a series of D spots. The velocity $\hat{u}$ is in m/s. τ_L is the maximum observed life of a spot in days. References: (1) Reese and Smith (1966), (2) Reese (1971), and (3) Sanchez-Lavega and Quesada (submitted for publication).

elongated spots with a characteristic longitudinal scale of 10,000 km and meridional scale of 4000 km. These spots were situated southward (inside the NTrZ at 22° N) and moved with $u \sim 120$ m s^{-1}. Their number was initially four, and they were spaced by ~20,000 km. High-resolution images obtained in October 1975 suggest apparent anticyclonic circulation patterns in their periphery, appearing that the preceding ones narrowed meridionally, which is suggestive of the effects of the high wind shear present in the zone. This is probably the origin for their disappearance in 15 to 30 days. The activity (formation of new dark spots) can be maintained for more than a year, extending in longitude and finally encircling the whole planet. This produces a narrowing and a darkening of the usually bright NTrZ. Other similar disturbances were observed visually in 1880, 1891–1892, 1929–1931, and 1939–1943. In these cases, only the dark spots were tracked with mean velocities $u \sim 125$ m s^{-1}, but there is no reference to an initial white spot (perhaps due to low resolution and contrast).

Table 22 presents a summary of the main properties of the NTrZ-NTBs disturbances observed until now. We have included in it the observation of three isolated features moving with the eastward jet, but that do not represent a general disturbance of the region.

DISCUSSION OF THE NATURE OF THESE DISTURBANCES

The first attempts to explain the nature of these disturbances were focused on the apparent periodicity in the recurrence of the outbursts (3 years or multiples of 3 years for SEBD, and ~12 years for NTrZ-NTBsD), and on their possible relationship with three deep "sources" (hot spots) moving uniformly with a rotational period near the internal one (System III) (Reese and Smith, 1966; Chapman and Reese, 1968; Reese, 1972). Neither periodicity is confirmed (see tables 21 and 22), nor is it believed that a permanent "source" (the "supervolcanos" of Reese) can exist in the interior.

Modern theories about this phenomena should point toward flow disturbances in the atmosphere of the giant planet. Note first that both types of events started with the emergence of a bright white cloud (so-called for the SEBD by Peek an "irradiating" spot), specially contrasted in the ultraviolet (e.g., the 1971 SEBD, Reese, 1972) and in the 8990 Å CH_4 band (Minton, 1972), which suggests that top clouds in this feature were situated higher than their surroundings (probably above the layer of ultraviolet aerosol absorbers, see e.g., West et al., 1986). As we have suggested (Sanchez-Lavega and Rodrigo, 1985), these spots might be convective in origin, drawing their energy from buoyancy associated with the release of latent heat by condensation of water vapor in a deeper cloud layer (see e.g., the model for equatorial plumes of Stoker, 1986). From the observed area expansion and following the same analysis that Hunt et al. (1982) did, we estimated vertical velocities inside the spot to be $w \sim 5$ cm s^{-1} (Sanchez-Lavega and Rodrigo, 1985).

On the other hand, the white spot of the SEBD appeared near a minimum of the zonal velocity ($u \sim 3$ m s^{-1}), whereas the white spot of the NTrZ-NTBs disturbance appeared near a maximum of the jet with $u \sim 165$ m s^{-1}. We conclude that the emergence of these convective features is not dependent on the value of the zonal wind velocity.

The subsequent development of the dark and usually elongated ovals might be the result of the apparition of the convective feature. One possibility is that these disturbances are waves associated with an instability of the zonal flow produced when the bright spot emerges in an otherwise "stable" zonal wind profile. In fact, they can be related to the meridional shear of the flow because these outbursts take place in the highest shear regions of the atmosphere, being $\partial u/\partial y = 1.14 \times 10^{-5}\ \mathrm{s}^{-1}$ (SEBD) and $\partial u/\partial y = 2.7 \times 10^{-5}\ \mathrm{s}^{-1}$ (NTrZ-NTBsD). These eddies, although with similar horizontal scale length to other well-known jovian vortices, must be of a different nature. The great-scale eddies in Jupiter (e.g., GRS, WOS, barges) are long lived, persistent, and apparently coherent, lying between jet cores ($\bar{u}$ near to 0) and in such places where $\beta - \bar{u}_{yy} = 0$ ($\beta = df/dy = 2\Omega \cos \phi/R$; $\bar{u}_{yy} = \partial^2 u/\partial y^2$) (Ingersoll et al., 1979; Read, 1986).

On the contrary, the dark features present during an SEB and an NTrZ-NTBs disturbance, are short lived; they lie near the jet cores (where u is maximum) and in locations where $\bar{u}_{yy} - \beta$ is also a maximum. Following the analysis by Limaye (1986) of the zonal wind profile, the westerlies at 24° N and 8° S are both barotropically unstable (for a deep criterion of barotropic instability, see Ingersoll and Pollard, 1982), and the easterly jet at 20° S is barotropically unstable (shallow criterion; see e.g., Holton, 1979). It is then not clear if deep or shallow barotropic effects are important for the origin of these features.

The scale analysis of the most significant dimensionless parameters can help to discern between different dynamic modes that could be present. We center on the elongated dark spots of the NTrZ-NTBs disturbances observed in 1975. For the horizontal length scale we adopt $L = 10{,}000$ km, zonal wind velocity $u = 120\ \mathrm{m\ s}^{-1}$, and $f = 7.16 \times 10^{-5}\ \mathrm{s}^{-1}$ at 22° N, and then the Rossby number $\mathrm{Ro} = u/fL = 0.16$. The other important parameters are related to the vertical stratification of the atmosphere. We adopt for the Brünt-Väisälä frequency its value at $P = 150$ mbar, $N = 2.3 \times 10^{-2}\ \mathrm{s}^{-1}$ (Conrath et al., 1981). In such a case, the Rossby radius of deformation $L_\mathrm{D} = HN/f = 6500$ km ($H = 20$ km is the scale height) and the Burger number $\mathrm{Bu} = L_\mathrm{D}^2/L^2 = 0.42$, and Richardson number $\mathrm{Ri} = N^2H^2/u^2 = 15$. Although these estimates, particularly of N (and its vertical dependence, see e.g., Read, 1986) are uncertain, the calculated values are similar to those found for the great-scale jovian vortices; we believe that these disturbances can be studied inside the frame of the quasi-geostrophic regime (see also a discussion by Williams and Yamagata, 1984). A more complete work about possible mechanisms operating in such dynamic regime is now in progress.

References

Chapman, C. R., and E. J. Reese (1968). A test of the uniformly rotating source hypothesis for the south equatorial belt disturbances on Jupiter. *Icarus* 9:325–335.

Conrath, B. J., F. M. Flasar, J. A. Pirraglia, P. J. Gierasch, and G. E. Hunt (1981). Thermal structure and dynamics of the jovian atmosphere. 2. Visible cloud features. *J. Geophys. Res.* 86:8769–8775.

Holton, J. R. (1979). *An introduction to dynamic meteorology*, Academic Press, New York.

Ingersoll, A. P., R. F. Beebe, S. A. Collins, G. E. Hunt, J. L. Mitchell, and P. Muller (1979). Zonal velocity and texture in the jovian atmosphere inferred from Voyager images. *Nature* 280:773–775.

Ingersoll, A. P., R. F. Beebe, J. L. Mitchell, G. W. Garneau, G. M. Yagi, and J. P. Muller (1981). Interaction of eddies and mean zonal flow on Jupiter as inferred from Voyager 1 and 2 images. *J. Geophys. Res.* 86:8733–8743.

Ingersoll, A. P., and D. Pollard (1982). Motions in the interiors and atmospheres of Jupiter and Saturn: Scale analysis, anelastic equations, barotropic stability criterion. *Icarus* 52:62–86.

Larson, S. M. (1972). Observations of the south equatorial belt disturbance on Jupiter in 1971. *Commun. Lunar Planetary Lab.* 9:371–383.

Limaye, S. S. (1986). Jupiter: New estimates of the mean zonal flow at the cloud level. *Icarus* 65:335–352.

Minton, R. B. (1972). Initial development of the June 1971 south equatorial belt disturbance on Jupiter. *Commun Lunar Planetary Lab.* 9:361–370.

Peek, B. M. (1958). *The planet Jupiter*, Faber and Faber, London.

Read, P. L. (1986). Stable baroclinic eddies on Jupiter and Saturn: A laboratory analog and some observational tests. *Icarus* 65:304–334.

Reese, E. J. (1971). Jupiter: Its red spot and other features in 1969–1970. *Icarus* 14:343–354.

Reese, E. J. (1972). Jupiter: Its red spot and disturbances in 1970–1971. *Icarus* 17:57–72.

Reese, E. J., and B. A. Smith (1966). A rapidly moving spot on Jupiter's north temperate belt. *Icarus* 5:248–257.

Sanchez-Lavega, A., and R. Rodrigo (1985). Ground based observations of synoptic cloud systems in southern equatorial to temperate latitudes on Jupiter. *Astron. Astrophys.* 148:67–68.

Smith, B. A., and G. E. Hunt (1976). In *Jupiter* (T. Gehrels, ed.), Univ. of Arizona Press, Tucson.

Stoker, C. R. (1986). Moist convection: A mechanism for producing vertical structure of the jovian equatorial plumes. *Icarus* 67:106–125.

Terrile, R. J., and R. F. Beebe (1979). Summary of historical data: Interpretation of the Pioneer and Voyager cloud configurations in a time-dependent framework. *Science* 204:948–951.

West, R. A., D. F. Strobel, and M. G. Tomasko (1986). Clouds, aerosols, and photochemistry in the jovian atmosphere. *Icarus* 65:161–217.

Williams, G. P., and T. Yamagata (1984). Geostrophic regimes, intermediate solitary vortices, and jovian eddies. *J. Atmos. Sci.* 41:453–478.

25

Jupiter: Short-Term Variations of the Mean Zonal Flow at the Cloud Level

Sanjay S. Limaye
University of Wisconsin, Madison

Abstract

A latitudinal profile of time-averaged mean zonal (east-west) flow at the cloud level on Jupiter has been previously presented (Limaye, 1986). The technique used to determine the zonal mean flow allowed the profile to be determined for every jovian rotation over the duration of the available image data (111 rotations from Voyager 1, and 134 rotations from Voyager 2) with high-latitudinal resolution. The individual latitudinal profiles of zonal mean zonal flow for each rotation have now been analyzed to reveal temporal changes over the violet filter mosaics from Voyager 1 (rotations 71–111) and Voyager 2 (rotations 266–407) observations.

Changes of $+10$ ms^{-1} are seen between Voyager 1 and Voyager 2 average zonal flow profiles. Comparable changes are also seen in average flow determined over about 50 rotations of Voyager 2 observations. Changes in the average zonal flow predicted from meridional eddy and mean circulation momentum transports from published results are much larger, indicating either that the vertical transport of momentum cannot be ignored and/or that the horizontal momentum transports are not accurate enough.

Further, changes are also observed in the 150 and 270 mbar thermal structure determined from Voyager 1 and 2 infrared interferometer spectrometer (IRIS) observations, implying changes in the vertical shear of the zonal flow. Thus, real changes in the processes controlling the zonal flow and the thermal structure are plausible as are small changes in the level of the sensed cloud level circulation.

The observed changes in the cloud level circulation and the thermal structure are suggestive of an interdependence between thermal structure and eddy momentum transport on a time scale as short as 40–50 rotations.

INTRODUCTION

Average zonal circulation determined by sampling all longitudes from global mosaics of Voyager imaging observations (Avis and Collins, 1983) has been presented previously (Limaye, 1986). These results were obtained by determining the latitudinal profile of the average zonal flow with a time resolution of one jovian rotation over the Voyager 1 and 2 observational periods. Changes in the zonal circulation seen from these results are presented in this chapter.

Variation of atmospheric circulation characteristics with time can be expected on most planets due to the imbalance between the temporally varying forces that control the circulation and the response of the atmosphere to those changes. In the case of Jupiter, the measurements of the zonal circulation from Earth-based observations (which date back to as far as 1787; Peek, 1958) suggest that although the locations of the easterly and westerly currents may be fixed in latitude, their magnitude may be varying with time (Reese, 1972; Inge, 1973; Reese and Beebe, 1976). In equatorial latitudes, the magnitude of the currents inferred from following spots over a period as long as 60 days, have a range of almost 50 ms^{-1} as indicated by observations made during 1974–1979 (Beebe and Youngblood, 1979). At other latitudes, the range was found to be considerably smaller.

The time period over which the zonal circulation can be reliably determined from such Earth-based observations is typically two months (Reese, 1972). Thus changes in the circulation can be determined only on scales larger than that, typically a year as evidenced by the historical observations (Peek, 1958; Smith and Hunt, 1976; Chapman, 1969) as well as more recent observations by Inge (1973), Beebe and Youngblood (1979), and Minton (1976, 1977a, b). In contrast, continuous imaging observations from the two Voyager spacecraft enable a determination of the average zonal mean flow on a time resolution as short as one jovian rotation (Limaye, 1985, 1986).

Voyager Observations

The two Voyager encounters during 1979 provide an opportunity to determine such changes on a time scale from a few jovian rotations to about 5.5 months, the interval covered by the two encounters (Smith et al., 1979a, b). Average zonal flow has been estimated from Voyager imaging observations by two different methods—that by averaging the velocities of individual cloud features in lo latitude bins (Ingersoll et al., 1981; Limaye et al., 1982; Ingersoll et al., 1984), and estimating the zonal average flow directly by uniformly sampling all longitudes by way of global mosaics (Limaye 1985, 1986). Table 23 lists the time periods covered by these studies.

Mean zonal circulation determined by averaging individual cloud-motion measurements from Voyager images (or mosaics thereof) over longitude and time has been seen to be somewhat different, although the differences have not been understood well (Ingersoll et al., 1981, 1984; Beebe et al., 1980; Limaye et al., 1982). In fairness, the emphasis of those investigations was to determine the cloud-level circulation rather than to

Table 23. Observations of Jovian Cloud Level Circulation

Authors	Data	Period
Ingersoll et al. (1981)	Voyager 1 orange filter images	26–28 February 1979
Ingersoll et al. (1981)	Voyager 2 violet filter images	2–4 July 1979
Limaye et al. (1982)	Voyager 2 mosaics	1–3 June 1979
Limaye (1986)	Voyager 1 mosaics	5 January–14 February 1979 Rotations 1–111
	Voyager 2 mosaics	22 April–15 June 1979 Rotations 266–407
Gierasch et al. (1986)	IRIS Voyager 1	1 March 1979 (?)
	IRIS Voyager 2	10 July 1979 (?)
This work	BEG—Voyager 2	Rotations 266–310
	MID—Voyager 2	Rotations 311–355
	END—Voyager 2	Rotations 356–407

look for changes in the circulation. The differences between the Voyager 1 and Voyager 2 results of Ingersoll et al. could not be unambiguously interpreted as time dependence of the atmospheric circulation as they were obtained from tracking clouds in orange and violet filters, respectively. Thus the differences could be temporal as well as due to color differences. In either case, the measurement errors tended to mask the true differences. The two Voyager 2 estimates from cloud tracking (Limaye et al., and Ingersoll et al.) did show some differences larger than measurement errors that could be due to temporal changes. Limaye et al. also concluded that a significant amount of the variation in their Voyager 2 averaged spot-motion results was real and not due to measurement or navigation errors.

Changes observed in the mean zonal flow over the Voyager 1 and 2 observation periods, as determined from the analysis of cylindrical mosaics, are presented below. These changes are compared with changes in the thermal structure indicated by the Voyager IRIS observations (Gierasch et al., 1986).

TEMPORAL VARIATION OF AVERAGE ZONAL MEAN CIRCULATION

Latitudinal profiles of the average east-west flow are available for rotations 1–111 from Voyager 1 images and rotations 266–407 from Voyager 2 images, the rotation numbers referring to jovian rotations from the beginning of Voyager 1 observations of Jupiter (table 23). The first 71 rotations from Voyager 1 data refer, however, to blue filter results, whereas the rest of the profiles are determined from violet filter images. Although the average blue and violet profiles are similar, there are some significant differences between them (Limaye, 1987) and, therefore, in view of the longer coverage from violet filter results (41 from Voyager 1 and 134 from Voyager 2), the discussion below is focused on the violet filter results.

The nearly two-month-long imaging gap between the two Voyager observations and the duration of the Voyager 2 imaging observations present convenient time intervals over which the short-term average zonal circulation can be compared as presented below.

Variability Indicated by Root Mean Square Deviations

One indication of the temporal variation of the circulation is partially provided by the vectors averaged in a given latitude bin. The root mean square (RMS) deviation of the vectors averaged over time in each latitude bin includes the contribution by not only the measurement errors and spatial variations, but also temporal variations. The previous cloud-motion measurements by Ingersoll et al. and Limaye et al. covered only a few days of observations, thus the contribution to the RMS deviation due to the temporal variation is necessarily small. In contrast, the results from matching global-brightness data from cylindrical mosaics cover a much longer time interval, so that the RMS deviation of the zonal mean zonal flow averaged over these periods can be expected to be largely due to the contribution by the temporal variation of the zonal mean zonal flow, the other contributors being mapping errors and those due to changes in cloud morphology.

If $u_i(\phi)$ represents the zonal mean flow at a latitude ϕ for the ith profile, then the RMS deviation of the mean zonal component (termed RMSu) at that latitude is computed as

$$\mathrm{VARu}(\phi) = \Sigma \left(\frac{(u_i(\phi) - \langle u(\phi) \rangle)^2}{N} \right), \qquad (25.1)$$

$$\mathrm{RMSu}(\phi) = \sqrt{(\mathrm{VARu}(\phi))}, \qquad (25.2)$$

and

$$\mathrm{ERRu}(\phi) = \frac{\mathrm{RMSu}\ (\phi)}{\sqrt{N}}. \qquad (25.3)$$

ERRu(ϕ) is generally a good measure of the uncertainty in the average of N individual profiles of zonal mean flow. Figure 169 shows the profile of the RMSu from 134 rotations of Voyager 2 observations. Voyager 1 RMSu is somewhat larger (even after a slight latitude correction noted below) due to fewer profiles averaged. Considerable structure is seen in the Voyager 2 RMSu deviation profile, showing larger variation in the north temperate current *C* latitude (23°8) as well as in the south equatorial jet latitudes. Some of the variation with latitude of the RMS deviation of the zonal mean zonal component is likely to be due to errors in individual profiles arising from defects in the mosaics and the lack of texture in the cloud features. This can be seen from figure 1 of Limaye (1986) that shows the quality of the lag-lead estimates from the mosaic data for one pair. At latitudes where the summed absolute brightness difference shows a sharp minimum, the zonal mean zonal flow is better determined than at a latitude where the minimum is not so sharply defined. Such differences are seen at different latitudes. However, these variations do not appear to be associated with the RMS deviation of the time-averaged zonal mean zonal flow.

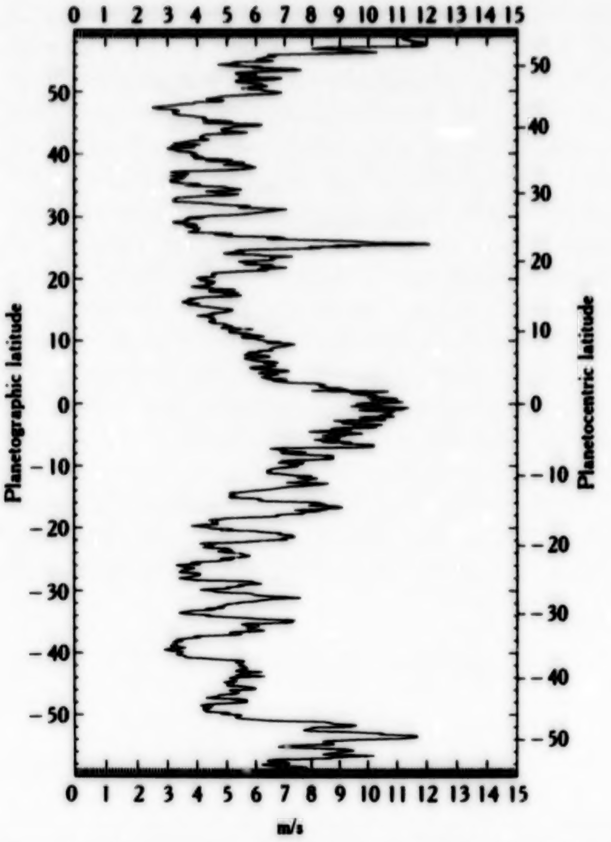

Figure 169. Variation of RMS deviation of the mean zonal flow with latitude for Voyager 2 observations (from Limaye, 1986). Temporal variations of the mean zonal flow contribute to at least some of the variation seen in the Voyager 2 mosaic profile.

The time variations implied by the RMS deviations of individual zonal mean zonal flow profiles are consistent with the Earth-based estimates of the larger range of motions at these latitudes (Beebe and Youngblood, 1979).

Voyager 1 and Voyager 2 Difference

The locations and magnitudes of the easterly and westerly jets determined by averaging violet filter Voyager 1 and 2 results were compared by Limaye (1986). Although the shapes of the average profiles for Voyager 1 and 2 observation periods were found to be similar, the differences between them were not explored due to a noticeable latitudinal shift in the Voyager 1 results (fig. 2, Limaye 1986). The shift is particularly noticeable between about 10° S and 25° S planetographic latitudes. Due to the sharp dependence of the flow on latitude, the two average profiles of zonal average flow cannot be differenced readily until the latitudinal shift is removed. This was accomplished previously by interpolating the two average profiles to a resolution of 0°.05 and shifting one profile against the other to obtain best match, resulting in a shift of 0°.15.

Correction of Voyager 1 Latitudes In an attempt to display the zonal flow profiles as a time-series image, it became evident that comparing average profiles may not be the best way to remove the slight latitude offset, but that each profile could be shifted slightly not in latitude but in mosaic scan line number, to best match the average Voyager 2 zonal flow profile. In some instances, the resultant line shift amounted to as much as four scan lines (equivalent to about 0°.4 of latitude near the equator, more at higher latitudes). After the correction the Voyager 1 violet profiles were averaged to yield a better estimate than before.

The two Voyager profiles were then differenced (fig. 170) and the confidence level for the difference at each latitude was computed from the Student's *t*-test (Press et al., 1986) using the observed variances of each of the profiles at each latitude. Latitudes where the confidence level in the difference between Voyager 1 and 2 $\langle u \rangle$ is at least 95 percent are indicated by open circles and plus signs within those circles indicate where the confidence level exceeds 99 percent.

In at least three latitude regions (12–15° S, 25–27° S, and 41–43° S, all in westerly jets), the Voyager 2 profile shows slower (by as much as 10 ms^{-1}) zonal flows compared to the Voyager 1 average by a magnitude larger than the generous uncertainty estimates. An even larger difference is observed on the north side of the 24° N jet although the uncertainty is correspondingly higher. Note that the flow appears to vary with time on time scales shorter than the Voyager 2 averaging period so that the uncertainty for the difference between Voyager 1 and 2 may be overestimated.

Time Series of Zonal Flow Profiles

Since measurements of the zonal mean zonal flow for every rotation over the Voyager 1 and 2 observation period are available, it is possible to look for changes not only over the interval between Voyager 1 and 2 observations, but over an interval as short as one jovian rotation. Figure 171 shows the variation of the zonal mean zonal flow at one latitude (−22° planetographic latitude) over the Voyager 2 observation period. The average flow is seen to decrease in magnitude gradually from rotation 266 to about rotation 330 and then stay

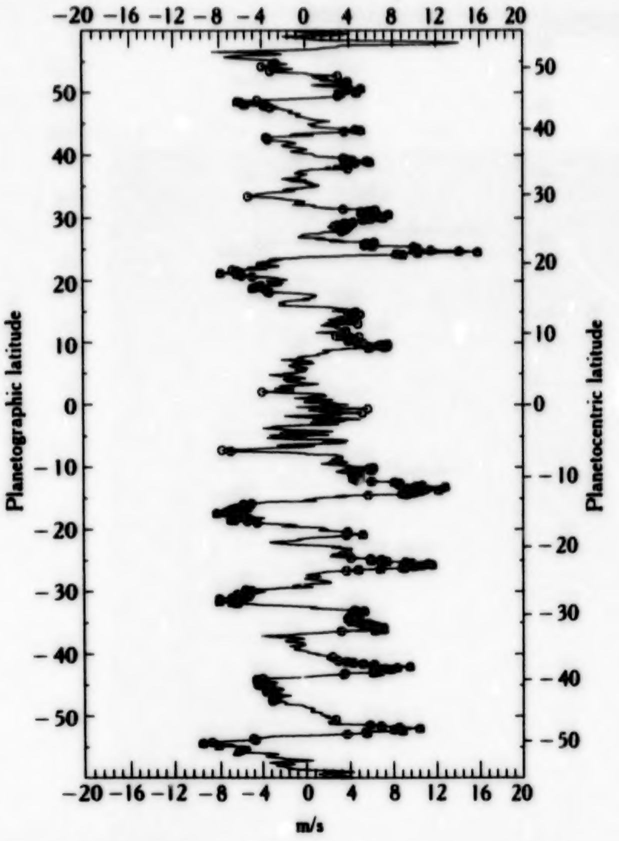

Figure 170. Difference between average Voyager 1 and Voyager 2 profiles of zonal average zonal component after the Voyager 1 profile is corrected for an apparent latitudinal shift of Voyager 1 profiles relative to the Voyager 2 average profile (see text). Latitudes where the confidence level in the difference is at least 95 percent are indicated by *circles*. At many of these latitudes the confidence level exceeds 99 percent. Student's *t*-test (Press et al., 1986) was used to compute the confidence levels using the variances of Voyager 1 and Voyager 2 samples at each latitude.

constant or increase slowly with time. It thus appears that the zonal flow can change over an interval shorter than a few months to a year, and that such changes appear detectable on a time scale of tens of jovian rotations.

In view of the high latitudinal and temporal resolution of the new determination of the zonal flow as well as its relatively long temporal coverage, it is appealing to represent the results in the form of an image to study the temporal changes more easily. This was done by appropriately scaling the zonal speed magnitudes into a two-byte range, thereby preserving more than sufficient precision. Figure 172 shows a time series of meridional profiles of the zonal mean flow in the form of an image as determined from Voyager 2 cylindrical mosaics constructed from violet filter images. Profiles are shown for jovian rotations 1–111 (Voyager 1) and 266–407 (Voyager 2) over which the mosaics were available.

The *y*-axis is latitude (cylindrical projection) and the *x*-axis represents time, each column representing the profile with latitude of the zonal mean east-west flow determined from a pair of mosaics one jovian rotation apart. The westerly jets are represented by higher data numbers and appear light whereas the easterlies are represented by lower data numbers and appear dark. For ease of understanding this brightness scaling the latitudinal profile is superposed in the middle. Each row in this image rendition of the time series thus represents the zonal mean flow at a given latitude.

Cosmetic Corrections Not all mosaics are cosmetically perfect and many contain some defects due to missing images, data recording errors, satellite shadows, and poor navigation. Thus, there are some spurious estimates of the zonal average flow from the digital matching technique. As their number is relatively small and their presence distracting, some cosmetic improvements have been applied to this image rendition of the time series.

A deviation of more than 25 ms^{-1} from the time average of the flow at that latitude was used as the criterion for detecting the spurious estimates. These were then replaced with the most frequently occurring value (mode) for that particular latitude. The number of such spurious flows was relatively small and their exclusion does not afffect the conclusions in any manner but results in a cosmetically clean image rendition of the time series.

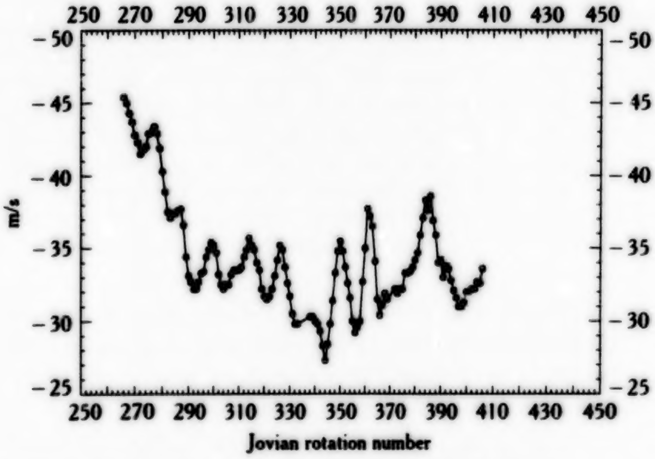

Figure 171. Example of variation of the zonal average east-west flow at −22° latitude over the Voyager 2 observations (rotations 266–406, violet filter). For other latitudes see figure 172.

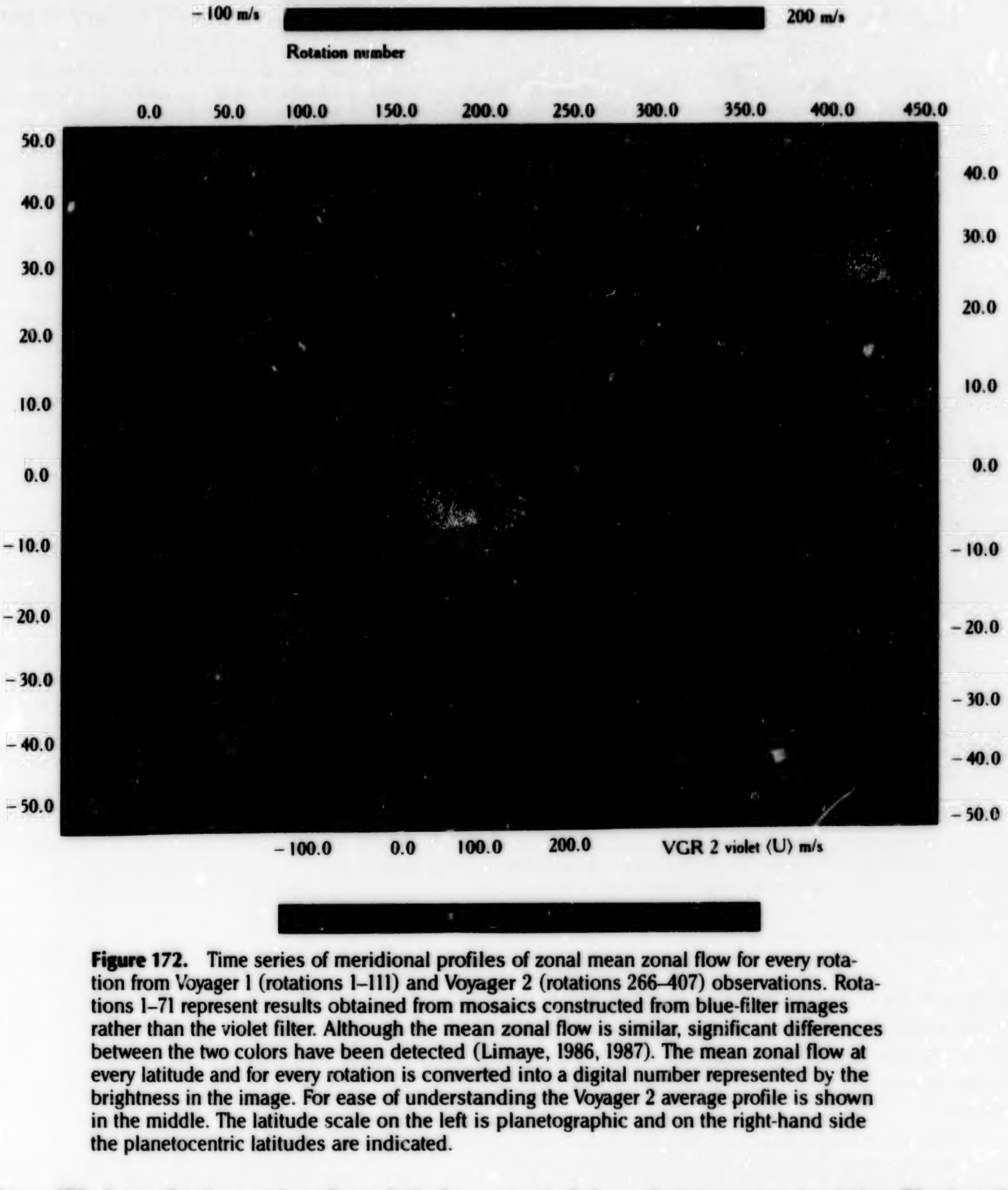

Figure 172. Time series of meridional profiles of zonal mean zonal flow for every rotation from Voyager 1 (rotations 1–111) and Voyager 2 (rotations 266–407) observations. Rotations 1–71 represent results obtained from mosaics constructed from blue-filter images rather than the violet filter. Although the mean zonal flow is similar, significant differences between the two colors have been detected (Limaye, 1986, 1987). The mean zonal flow at every latitude and for every rotation is converted into a digital number represented by the brightness in the image. For ease of understanding the Voyager 2 average profile is shown in the middle. The latitude scale on the left is planetographic and on the right-hand side the planetocentric latitudes are indicated.

Figure 170 shows the time series after a latitude correction (described previously) has been applied to each of the Voyager 1 blue and violet profiles and cosmetic blemishes have been removed.

Temporal Eddies or Fluctuations

As the zonal flow is relatively stable on Jupiter, very little temporal variation is discernible in figure 172. The most obvious changes occur at rotation 70 when the mosaics switch to the violet filter from blue filter, and this is due at least partially to sensing a different depth in the violet filter compared to the blue filter (Limaye, 1987) rather than to a sudden time change. The variations in the mean zonal flow can be better discerned if the time-averaged profile is subtracted from individual profiles. In creating the image rendition of such time fluctuations some smoothing has been done as the rotation-to-rotation changes in zonal flow are expected

ORIGINAL PAGE
COLOR PHOTOGRAPH

ORIGINAL PAGE IS
OF POOR QUALITY

to be small compared with the granularity of the individual estimates (about 5 ms^{-1} at the equator), and are also expected to be similar at neighboring latitudes (i.e., on consecutive scans and rotations). The resulting image shown in figure 173 depicting the temporal eddy magnitudes has been smoothed by averaging five consecutive scans and three consecutive elements (rotations) of the image.

Bright areas represent latitudes and times when the zonal mean flow is faster than the Voyager 2 average and similarly the dark areas represent times and locations when the flow is slower than the Voyager 2 average flow. Such deviations can be seen in many neighboring latitudes, for example, on either side of the north temperate current *C* (23°.8 N latitude), on the southern flank of the equatorial jet (15° S), and on the northern and southern periphery of the great red spot (GRS). The magnitude of such eddies is generally between 5 and 10 ms^{-1}.

Figure 174 shows a histogram of the temporal eddy magnitudes at all latitudes (±60°) and between rotations 71 and 407 excepting the missing rotations (112–266). The frequencies are expressed as percentages of the total and are shown for eddies with magnitudes

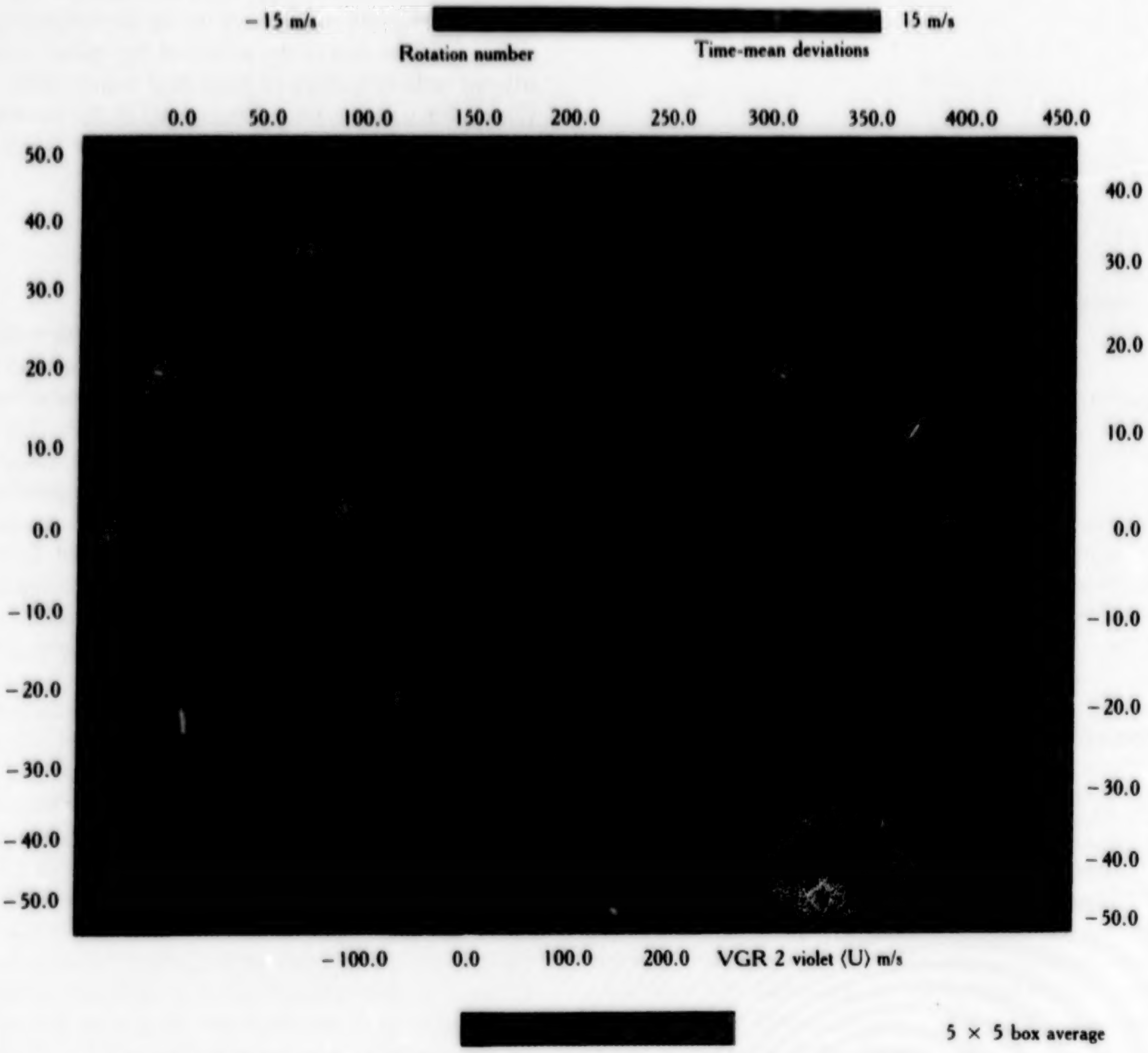

Figure 173. Temporal eddies relative to Voyager 2 average zonal flow shown in a manner similar to that of figure 172, except the deviations from the Voyager 2 average profile are coded as brightness values. Darker regions show flow slower than the average and brighter regions show flow faster than the average. The peak amplitudes are typically no more than 10–15 ms^{-1}. In figure 173b the result after some averaging in latitude and time is shown.

ORIGINAL PAGE
COLOR PHOTOGRAPH

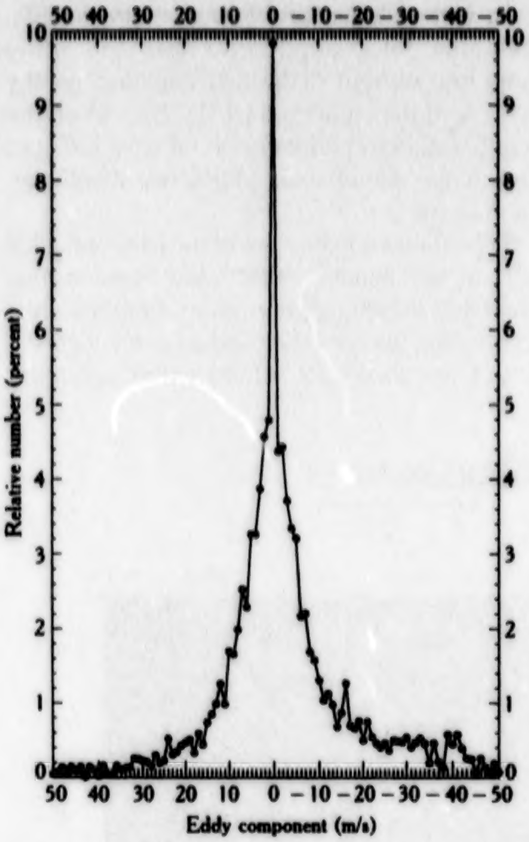

Figure 174. Histogram of the temporal zonal component eddy components for all Voyager 1 and 2 violet filter observations.

between $+50$ ms^{-1}. The distribution is fairly narrow, indicating the relative stability of the flow with nearly 10 percent of the sample showing no deviations. Cumulatively 62 percent of the eddies are within 15 ms^{-1}.

DISCUSSION

Due to the very nature of atmospheric motions, the global circulation averaged over longitude and an appropriate time scale can be expected to vary with time. Variations in seasonally averaged circulation on Earth are one example, although the terrestrial circulation shows variations even when annual averages are compared, as evidenced by the quasi-biennial oscillation (Naujokat, 1986). When averaged over a few weeks or months, the dayside cloud-level circulation on Venus also shows substantial changes from year to year (Rossow, 1985; Limaye et al., 1987). Thus, temporal changes in the magnitude of the zonal circulation on Jupiter might be expected, but the general impression (from Earth-based observations) has been that the circulation has been stable despite changes in the appearance of Jupiter (Beebe et al., 1987; Smith and Hunt, 1976). The relative stability of the jovian jets is even more remarkable considering the large shears and estimated eddy transports of momentum in the meridional direction (Beebe et al., 1980; Limaye et al., 1982; Sromovsky et al., 1982; Ingersoll et al., 1981, 1984; Flasar, 1986). Recent calculations show that above the cloud level on Jupiter the seasonal temperature variations may be significant (Bezanger et al., 1986), so that accompanying changes in the circulation are possible, at least on a seasonal scale. On a shorter scale, the changes in the circulation can come about from meridional transports of momentum by the mean circulation as well as due to the action of the eddies in meridional redistribution of heat and momentum (see Flasar, this volume, for a discussion) or due to changes in the mean thermal structure. These are briefly discussed below.

Changes in the Thermal Structure

Zonally averaged meridional profiles of temperature at 150 mbar and 270 mbar level show temperature changes as large as 2 K between Voyager 1 and Voyager 2 observations IRIS (Gierasch et al., 1986). They also have shown that the vertical shear of the zonal flow estimated from the meridional temperature gradients is highly (inversely) correlated with the mean zonal flow, implying decay of the zonal jets with height. It is thus natural to ask whether thermal-structure changes that are observed are related to changes in the zonal circulation, although the results refer to different periods (table 23).

The different Voyager 2 temperatures result in different meridional thermal gradients at 150 and 270 mbar, thus the vertical shear of the zonal flow is also different compared to Voyager 1. In figure 175, the difference in Voyager 1 and Voyager 2 vertical wind shears computed from the meridional temperature gradients at 150 and 270 mbar levels determined from IRIS observations is shown (in ms^{-1} per scale height). Within about 4° of the equator the thermal wind relationship is uncertain. Changes in the vertical shear of the mean zonal flow as large as 20 ms^{-1} are predicted away from the equator. Small pointing errors between Voyager 1 and Voyager 2 might be responsible for some of the differences in $d\langle u\rangle/dz$ that are calculated, but it is uncertain whether they will reduce the difference to a negligible amount. The thermal wind from Voyager 1 is almost the same as

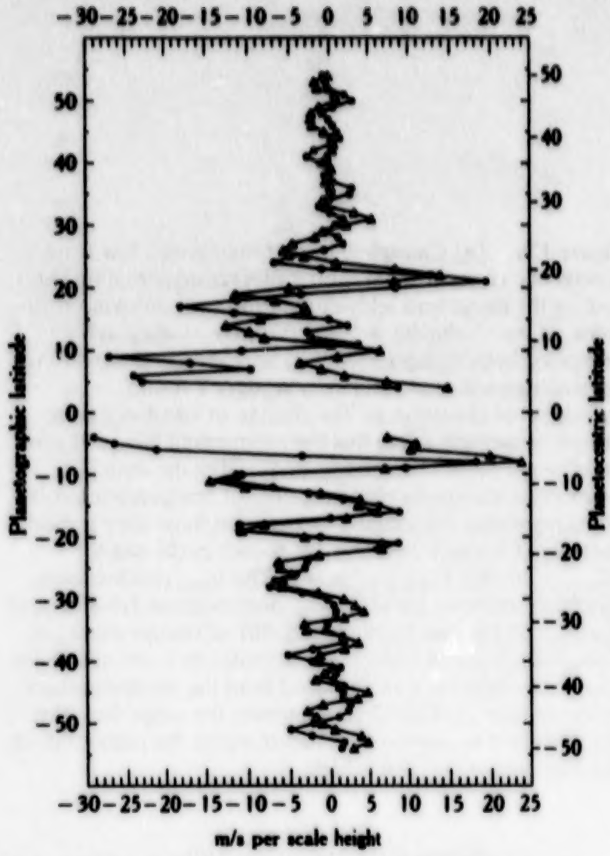

Figure 175. Difference in the vertical shear of the zonal flow from Voyager 1 and Voyager 2 IRIS observations (Gierasch et al., 1986), $du/dz^* = -(R/af\sin(\phi))dT/d\phi$, where a is the planetary radius at latitude ϕ, f is the Coriolis parameter, $z^* = \ln(p/p_0)$, and R is the gas constant for Jupiter. *Circles* denote change in the thermal wind at 150 mbar; *triangles* denote similar change at the 270 mbar level.

that calculated from Voyager 2, although the latitudinal resolution of Voyager 1 temperature profile is somewhat poorer. Considering that the observed cloud level changes in $\langle u \rangle$ are as large as 10 ms^{-1} in some latitudes, vertical zonal flow shear differences of about the same magnitude may be reasonable.

The changes observed in the vertical shear of the zonal flow suggest that the processes controlling the strength of the zonal circulation and the thermal structure can be responsible for the observed changes in the circulation. Note further that the observations used to determine the zonal flow are not concurrent. The IRIS observations were obtained three to four days before each encounter, whereas the images used for zonal flow determination were acquired nearly six weeks prior to each encounter. Further, the spatial resolutions of the imaging and IRIS observations are also very different. Thus, any correlation or the lack thereof between thermal structure changes and the changes in the zonal flow cannot be considered conclusive, but merely reflecting the fact that changes of the observed magnitude are possible in the equatorial latitudes over time intervals as short as a few weeks to four months.

Meridional Momentum Transports

The change in the zonal flow can come about by a meridional transport of momentum by the mean and eddy circulation. The mean meridional flow on Jupiter is small, and the change in the mean circulation transport of momentum appears difficult to detect (Sromovsky et al., 1986). Barring vertical transport of momentum and a rapid balance between the eddy and mean circulation momentum transports, the eddy transport alone could be responsible for changing the circulation. Quoting the correlation between transport of momentum by eddies ($\langle u'v' \rangle$) and the meridional shear of the mean zonal flow ($d\langle u \rangle/dy$), Beebe et al. (1980) and Ingersoll et al. (1981) have argued that the eddies were supplying energy to the mean circulation at a rate high enough to resupply the jets on a time scale of two to four months. It has been noted that it is difficult to establish this conversion rate reliably due to inadequate sampling of the eddies (Ingersoll et al., 1984; Sromovsky et al., 1982; Flasar, 1986). The problem with the measured mean and eddy momentum transports can also be illustrated by the implied changes in the mean zonal flow. From horizontal momentum transport alone (i.e., ignoring vertical transports of momentum), the change in the mean zonal flow at a given latitude, $d\langle u \rangle/dt$ is given by (Sromovsky et al., 1986):

$$\frac{d\langle u \rangle}{dt} = \frac{-d\langle uv \rangle}{dy} \tag{25.4}$$

$$= \frac{-d(\langle u \rangle \langle v \rangle)}{dy} - \frac{d\langle u'v' \rangle}{dy}. \tag{25.5}$$

The published eddy momentum transports and the mean meridional and zonal velocities thus enable a calculation of the change in the zonal flow over, say, 50 jovian rotations as shown in figure 176. For comparison, the changes observed in the mean zonal flow from Voyager 2 observations over a comparable interval are shown in figure 176b ($U_{\text{MID-BEG}}$) and figure 176c ($U_{\text{MID-END}}$). The three different momentum transport estimates from averaged individual cloud motions show considerable disagreement in magnitude although at least the sign of the momentum transport divergence is often the same. Likelihood of such large variability in

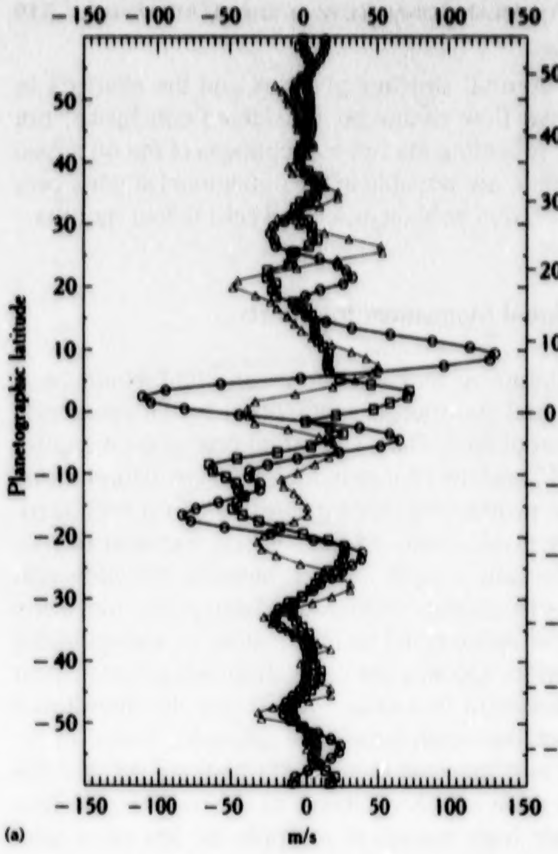

Figure 176. (**a**) Change in the average zonal flow from divergence of meridional (horizontal) transport of momentum by the mean and eddy circulation over 50 jovian rotations, in ms^{-1}, $d\langle u\rangle/dt = -d(\langle u\rangle\langle v\rangle)/dy - d\langle u'v'\rangle/dy$, computed from Voyager 1 (*circles*) and Voyager 2 (*boxes*) results of Ingersoll et al., and from Voyager 2 results (*triangles*) of Limaye et al. The change in equatorial is excessive suggesting either that the momentum transport variation is measured inaccurately, and/or that the vertical momentum transports play a significant compensating role. For comparison, the differences between three short period averages of Voyager 2 profiles are shown in (**b**) and (**c**) ($U_{\text{BEG–MID}}$ in [**b**], $U_{\text{MID–END}}$, in [**c**]). The U_{BEG} profile is averaged over rotations 266–310, U_{MID} over rotations 311–354, and the U_{END} profile over rotations 355–407 of Voyager mosaics. The *shaded portions* denote the uncertainty in the difference about zero difference as estimated from the standard errors of the average profiles. Thus, whenever the *curve* depicting the difference is outside the *shaded region* the probability of the difference being real is high.

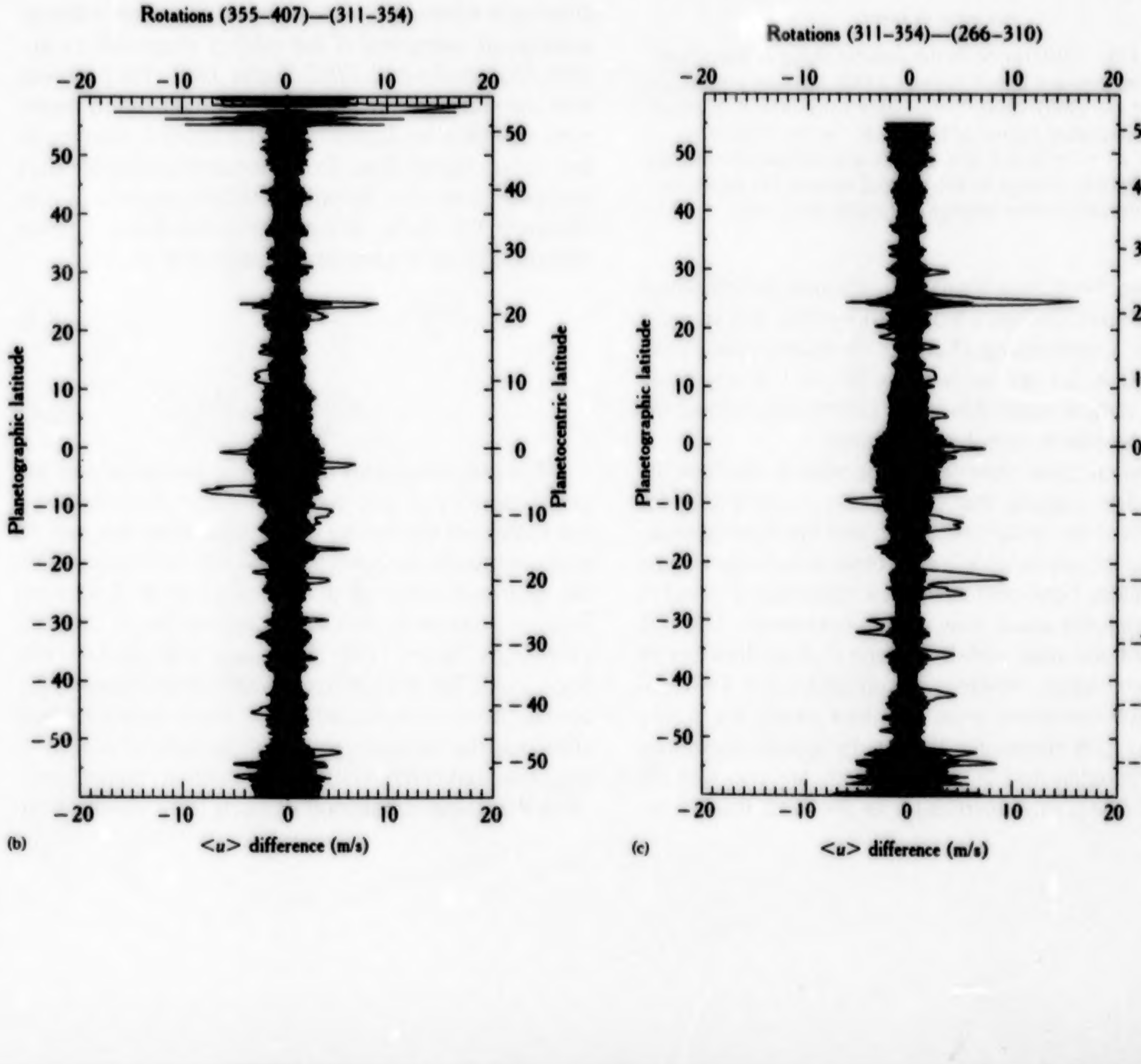

the momentum fluxes may be rather small, and measurement errors are likely to be responsible for the bulk of the disagreement. Not much agreement is thus found between the predicted changes and the changes actually observed between either Voyager 1 and 2 average profiles or between short-period averages from Voyager 2 profiles.

Further, it is seen that even if the smallest of divergence of the three measured eddy and mean meridional momentum transports are considered reasonable, the predicted changes in the zonal circulation in low latitudes are still excessive and vertical transports or diabatic effects must be influential in reducing the change in $\langle u \rangle$. Conversely, both eddy momentum transports and the mean meridional flow are likely to be poorly determined so that the calculated change in $\langle u \rangle$ may be overestimated.

Cloud Height Variation

Another explanation for observed cloud-level zonal flow changes, and the simplest one, is that we are sensing the zonal flow at different levels at different times due to changes in the vertical level of the clouds on Jupiter. After all, the cloud cover is known to be changing in color and structure (Peek, 1958) and the zonal flow is indicated to decrease in magnitude with height from IRIS observations (Gierasch et al., 1986). If the changes of 0.5–2 K observed at 150 and 270 mbar between Voyager 1 and Voyager 2 profiles can be considered reflective of deeper levels (near the cloud tops) then the circulation sensed from Voyager 1 and 2 images could be reflective of different levels. Within about ±20° latitude, the Voyager 2 temperatures are lower compared to Voyager 1 at both 150 and 270 mbar, the decrease being larger at 150 mbar than at 270 mbar. Thus, the convective activity could have changed between Voyager 1 and Voyager 2 somewhat due to different stability. At higher latitudes the Voyager 2 temperatures are slightly warmer than the Voyager 1 temperatures. To account for the changes of about 10 ms^{-1} in the average zonal flow, the cloud level must change by a fraction of a scale height according to the IRIS observations. Can such changes in the cloud structure occur on Jupiter? These may be observable as small changes in the zonally averaged profiles of reflectivity. They may perhaps explain some changes in the zonal flow with time.

It is also possible that subtle changes in the cloud morphology or scale could affect the measured zonal flow and that changes in the flow are reflective of the changes in global cloud cover. However the problem then is to explain how the morphology changes and whether changes in the circulation are responsible for changes in cloud morphology. In any case, no quantitative studies have yet been done to evaluate these effects to date.

SUMMARY

A new approach to estimating the mean zonal flow at the cloud level from global maps of Jupiter has enabled a study of the short changes in the circulation. As such, the technique uses a robust estimation of the best estimate of the displacement over one jovian rotation period of the digital rendition of the cloud cover at one latitude by searching for the minimum absolute brightness deviation rather than maximum cross-correlation.

Although changes on a rotation period time scale are not above the "noise" level, those on a somewhat longer scale, some 10 to 50 rotations, appear real, especially when coherent changes can be observed at neighboring latitudes. Just as the Earth-based observations of Jupiter show strengthening and weakening of the main currents at the cloud level, so do the Voyager 2 observations of the mean zonal flow. The largest changes observed are no more than 10–15 ms^{-1} but the typical changes observed are smaller, between 4 and 8 ms^{-1} from the Voyager results. No evidence of a change in the locations of the easterly and westerly jet maxima is indicated by the time-series analysis, as has been found also from the Earth-based observations.

Due to lack of concurrent thermal structure observations, cause and effect relationships cannot be established between the cloud-level circulation and the thermal structure. Nevertheless, the observed changes in the thermal structure observed by IRIS between Voyager 1 and Voyager 2 encounters suggest that the drive for the zonal motions at deeper levels could have changed enough to account for the observed changes in the cloud-level circulation. At least, the changes at 150 and 270 mbar levels are large enough to explain the changes at the cloud level. It is also possible that the actual changes at the deeper levels may be smaller due to longer radiative time constants.

Available eddy momentum transport results suggest that the eddies may not be steady state or else the estimates are not accurate enough. Role of the mean meridional circulation has not been examined due to the difficulty of obtaining reliable estimates of $\langle v \rangle$ with enough resolution compared to the jet-width scale. The implied rate of change of the zonal flow from horizontal convergence-divergence of momentum transports by eddy and mean circulations is too large, suggesting that either the momentum-transport rates are not measured accurately enough, and/or that vertical momentum transports and diabatic effects are important.

Clearly additional measurements of eddy transports of momentum are needed to further determine the processes controlling the temporal behavior of the zonal flow. Thermal structure measurements at a higher spatial and temporal resolution than currently available would also be useful. Further, simultaneous cloud-motion measurements and thermal-structure measurements would allow estimates of eddy heat transport as well, and such simultaneous measurements should be most useful for understanding the jovian circulation. In this respect, the Galileo and Hubble Space Telescope observations of Jupiter should be especially useful.

ACKNOWLEDGMENTS

This work was supported by NASA Grant NGR 50-002-189 from the Planetary Atmospheres program. I would like to thank Drs. L. Sromovsky, F. M. Flasar, and an anonymous referee for their comments, and also Prof. P. J. Gierasch for providing the IRIS thermal structure results.

References

Avis, C. C., and S. A. Collins (1983). *Voyager time-lapse, cylindrical-projection Jupiter mosaics.* Report D-541, Jet Propulsion Laboratory, Pasadena, California.

Beebe, R. F., and L. A. Youngblood (1979). Pre-Voyager velocities, accelerations and shrinkage rates of jovian cloud features. *Nature* 280:771–772.

Beebe, R. F., A. P. Ingersoll, G. E. Hunt, J. L. Mitchell, and J. P. Muller (1980). Measurements of wind vectors, eddy momentum transports and energy conversions in Jupiter's atmosphere from Voyager 1 images. *Geophys. Res. Lett.* 7:1–4.

Beebe, R. F., G. S. Orton, and R. A. West (1989). Time-variable nature of the jovian cloud properties and thermal structure: An observational perspective. This volume.

Bezanger, C., B. Bezard, and D. Gautier (1986). Spatial variation of the thermal structure of Jupiter's atmosphere. In *Proceedings of the conference on jovian atmospheres,* (M. Allison and L. D. Travis, eds.), NASA Conference Publication CP-2441, 332 pages.

Chapman, C. R. (1969). Jupiter's zonal winds: variation with latitude. *J. Atmos. Sci.* 26:986–990.

Flasar, F. M. (1989). Temporal behavior of Jupiter's meteorology. This volume.

Flasar, F. M. (1986). Global dynamics and thermal structure of Jupiter's atmosphere. *Icarus* 65:280–303.

Gierasch, P. J., B. J. Conrath, and J. A. Magalhaes (1986). Zonal mean properties of Jupiter's upper troposphere from Voyager infrared observations. *Icarus* 67:456–483.

Inge, J. L. (1973). Short-term jovian rotation profiles, 1970–1972. *Icarus* 20:1–6.

Ingersoll, A. P., R. F. Beebe, B. J. Conrath, and G. E. Hunt (1981). Structure and dynamics of Saturn's atmosphere. In *Saturn* (T. Gehrels and M. S. Matthews, eds.), pp. 197–205. Univ. Arizona Press, Tucson.

Ingersoll, A. P., R. F. Beebe, J. L. Mitchell, G. W. Garneau, G. M. Yagi, and J. P. Muller (1981). Interaction of eddies and mean zonal flow on Jupiter as inferred from Voyager 1 and 2 images. *J. Geophys. Res.* 86:8733–8743.

Limaye, S. S., H. E. Revercomb, L. A. Sromovsky, R. J. Krauss, D. Santek, V. E. Suomi, S. A. Collins, and C. C. Avis (1982). Jovian winds from Voyager 2: Part I. Zonal mean circulation. *J. Atmos. Sci.* 39:1413–1432.

Limaye, S. S. (1985). Jupiter: new estimates of the mean zonal flow at the cloud level. In *The jovian atmospheres, Proceedings of a conference held at Institute for Space Studies, NASA/GSFC, New York, May 6–8, 1985.* (M. A. Allison and L. D. Travis, eds.), 332 pages NASA Conference Publication, CP-2401.

Limaye, S. S. (1986). Jupiter: new estimates of mean zonal flow at the cloud level. *Icarus* 65:335–352. See also, Erratum, *Icarus,* 67:342–343.

Limaye, S. S. (1987). Color differences in cloud level circulation on Jupiter. *Bull. Amer. Astron. Soc.* 19:836.

Minton, R. B. (1976). Measures of Jupiter photographs—1972 apparition. *Icarus* 29:201–210.

Minton, R. B. (1977a). Measures of Jupiter photographs—1973 apparition. *Icarus* 29:211–220.

Minton, R. B. (1977b). Measures of Jupiter photographs—1974/75 apparition. *Icarus* 31:110–122.

Peek, B. M. (1958). *The planet Jupiter,* Faber and Faber, London.

Press, W. H., B. P. Flannery, S. A. Teukolsky, and W. T. Vetterling (1986). *Numerical recipes.* Cambridge Univ. Press, 818 pages.

Reese, E. J. (1972). Summary of jovian latitude and rotation period observations from 1898 to 1970. *Contrib. Obseru. of N.M.S.U.* 1:83–94.

Reese, E. J., and R. F. Beebe (1976). Measurements of Jupiter's long lived features and currents. *Contrib. Obseru. of N.M.S.U.* 1(4):176–191.

Smith, B. A., and G. E. Hunt (1976). Motions and morphology of clouds in the atmosphere of Jupiter. In *Jupiter* (T. Gehrels, ed.), pp. 564–585. Univ. of Arizona Press, Tucson.

Smith, B. A., L. A. Soderblom, T. V. Johnson, A. P. Ingersoll, S. A. Collins, E. M. Shoemacher, G. E. Hunt, H. Masursky, M. H. Carr, M. E. Davies, A. F. Cook II, J. Boyce, G. E. Danielson, T. Owen, C. Sagan, R. F. Beebe, J. Veverka, R. G. Strom, J. F. McCauley, D. Morrison, G. A. Briggs, and V. E. Suomi (1979a). The Jupiter system through the eyes of Voyager 1. *Science* 204:951–972.

Smith, B. A., R. Beebe, J. Boyce, G. Briggs, M. Carr, S. A. Collins, A. F. Cooke II, G. E. Danielson, M. E. Davies, G. E. Hunt, A. Ingersoll, T. V. Johnson, H. Masursky,

J. McCauley, D. Morrison, T. Owen, C. Sagan, E. M. Shoemaker, R. Strom, V. E. Suomi, and J. Veverka (1979b). The gallilean satellites and Jupiter: Voyager 2 imaging science results. *Science* 206:927–950.

Sromovsky, L. A., H. E. Revercomb, V. E. Suomi, S. S. Limaye, and R. J. Krauss (1982). Jovian winds from Voyager 2: Part II. Analysis of eddy transports. *J. Atmos. Sci.* 39:1433–1445.

Sromovsky, L. A., H. E. Revercomb, and R. J. Krauss (1986). Cloud top meridional momentum transports on Saturn and Jupiter. In *The jovian atmospheres, proceedings of a conference held at Institute for Space Studies, NASA/GSFC, New York, May 6–8, 1985* (M. A. Allison and L. D. Travis, eds.), 332 pages NASA. Conference Publication, CP-2401.

26

Temporal Behavior of Jupiter's Meteorology

F. M. Flasar
NASA/Goddard Space Flight Center, Greenbelt

Abstract

This chapter reviews radiative, chemical, and dynamic time scales pertinent to Jupiter's meteorology. The radiative relaxation time of the atmosphere is so large that diurnal variations attributable to purely radiative effects are precluded. The radiative time is comparable to Jupiter's orbital time scale, consistent with the observed seasonal variation in stratospheric temperature. The small seasonal variation in the upper troposphere probably results from the short time required for convective redistribution of heat in the deeper atmosphere and interior. Rapid convective turnover also plausibly explains the presence of disequilibrium minor constituents spectroscopically observed in Jupiter's troposphere. The observation of *para*-hydrogen disequilibrium on Jupiter but not on Saturn or Uranus can also be explained in terms of dynamic overturning, in the context of the relative magnitudes of the radiative relaxation time and the *para*-hydrogen equilibration time in the upper tropospheres of these planets. Jupiter's mean zonal winds appear to be remarkably stable: They exhibited virtually no change in the time (four months) between the two Voyagers, and ground-based observations have indicated little change during at least the previous five years, and perhaps longer. This apparent stability could result from the inertia associated with a differential rotation that extends far into Jupiter's interior, but it also could result, at least in part, from a delicate balance between eddy forcing and induced mean meridional flows in an atmosphere with weak friction and radiative damping. Changes in the zonal mean temperatures or winds would then be indicative of changes in the level of eddy activity. In contrast to the winds, the visual appearance in Jupiter's banded structure typically changes significantly over the course of a few years and is not always well correlated with the zonal wind structure. The utility of waves, themselves temporally varying phenomena, in sounding Jupiter's atmosphere is discussed.

INTRODUCTION

The question of the temporal behavior of Jupiter's atmosphere can be approached in several ways. The first is to ask what time variability is expected. For example, does one expect to observe diurnal or seasonal variations in Jupiter's atmosphere? Are there dynamic time scales over which temporal variations are expected?

Another approach, perhaps more fundamental, is to ask what are the internal time scales of Jupiter's atmosphere, and how does their relation to one another affect its observable properties. An example of this is the way in which the observed disequilibrium of the ortho and para states of molecular hydrogen can be understood in terms of the relative values of the radiative relaxation time and the ortho-para equilibration time. Another approach is to use the observed time variability to probe Jupiter's atmosphere, including those of its properties that exhibit no temporal variation. An example of this is the use of linear waves to infer the nature of the medium through which they propagate.

All these approaches thread this chapter. The second section treats the radiative relaxation time of a planetary atmosphere, the starting point of any meteorological discussion of temporal behavior. The third section discusses two aspects of the global behavior of Jupiter's atmosphere, namely its thermal emission and the disequilibrium of the ortho and para states of molecular hydrogen. These lead naturally to a consideration of the time scales of thermally driven convection and ortho-para equilibration. The fourth section treats the zonally averaged quantities of Jupiter's atmosphere: winds, temperatures, constituents, and albedo. The near absence of short-term temporal variability in the mean zonal winds turns out to be as intriguing as its occurrence in the visual appearance of Jupiter. Much of this chapter is devoted to the zonally averaged properties, for two reasons. First, studies of zonal mean quantities provide more of an overall picture of Jupiter's meteorology than studies of isolated features. The second reason is a practical one: The signal-to-noise ratio is much better if one performs zonal averages and computes variances on latitude circles. The fourth section also treats several classes of propagating waves in Jupiter's atmosphere and discusses how they can be used to probe properties of Jupiter's atmosphere. Finally, the fifth section summarizes relevant meteorological time scales and lists some observations to better define Jupiter's temporal behavior.

Predictably, the scope of this chapter must be limited. A discussion of the observations of minor constituents in Jupiter's atmosphere and their interpretation in terms of deep tropospheric physical chemistry and high-altitude chemistry is given in a companion article by Drossart et al. (1987). Beebe et al. (1987) extensively review observations of clouds and temperatures at visible, infrared, and microwave wavelengths. A review of various aspects of Jupiter's global dynamics is given by Flasar (1986).

RADIATIVE RELAXATION TIME

One of the most fundamental time scales in any planetary atmosphere is the radiative relaxation time, the time over which a perturbation in temperature decays to a state of radiative equilibrium. The radiative relaxation time, τ_r, is usually defined from the heat equation in terms of Newtonian cooling:

$$\frac{\partial T}{\partial t} = \frac{T_e - T}{\tau_r}. \qquad (26.1)$$

Here T_e denotes the temperature for radiative equilibrium, that is, the temperature profile that gives zero divergence of the total (solar and thermal infrared) radiative flux. If T_e is periodic over an interval $2\pi/\Omega$, it can be spectrally decomposed into the series:

$$T_e = \Sigma_{n=0}^{\infty} T_e^{(n)} e^{-in\Omega t}, \qquad (26.2a)$$

and the solution of eq. (26.1) is

$$T = \Sigma_{n=0}^{\infty} \frac{T_e^{(n)}}{[1 + (n\Omega\tau_r)^2]^{1/2}} e^{-i(n\Omega t - \phi_n)}, \qquad (26.2b)$$

where

$$\phi_n = \tan^{-1}(n\Omega\tau_r).$$

The relaxation time is a quantitative measure of the inertia of an atmosphere in its response to an external radiative forcing. It introduces both an amplitude reduction and a phase lag relative to the radiative equilibrium solution. As $\Omega\tau_r \to \infty$, the time-varying harmonics in eq. (26.2b) vanish, and only the steady ($n = 0$) component, equal to the radiative equilibrium solution averaged over a period, remains. As $\Omega\tau_r \to \infty$, the time varying harmonics lag the forcing by a quarter of a period. Substantial phase lags occur for modest values of $\Omega\tau_r$. When $\Omega\tau_r = 3$, the phase lag in the first harmonic is already 72°.

Figure 177 depicts the radiative time constant in Jupiter's troposphere and lower stratosphere, as a function of barometric pressure. This was computed following Gierasch and Goody (1969), taking the inverse of the local pressure scale height as the vertical wavenumber. The radiative opacity over the indicated range of pressures is primarily from molecular hydrogen. The pressure induced absorption coefficients from H_2-H_2 and H_2-He collisions were taken from Bachet et al. (1982), Cohen et al. (1982), and Dore et al. (1983). Qualitatively, one can understand the overall shape of the vertical profile of τ_r without reference to the profile of atmospheric temperature. The relaxation time is pro-

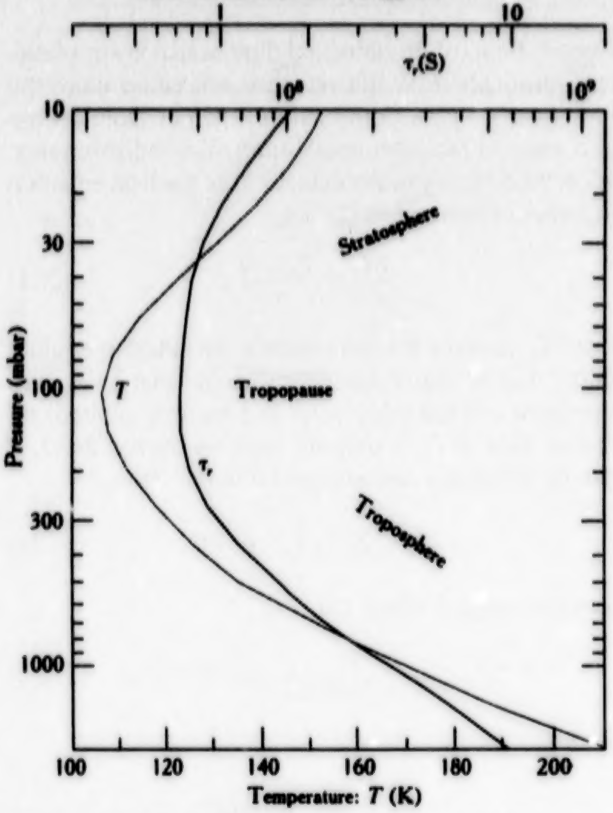

Figure 177. Radiative relaxation time, τ_r, as a function of barometric pressure for a typical profile of atmospheric temperature on Jupiter.

portional to $\rho/(\partial\epsilon/\partial \ln p)$ (Goody, 1964), where ρ is the mass density and ϵ is the infrared emissivity. In the middle stratosphere ($p \simeq 10$ mbar) the emissivity is small, and the atmosphere is an inefficient radiator. As the altitude approaches the emission-to-space level, near 300 mbar, the emissivity becomes of order unity, and the relaxation time is smaller. At greater depths the density increases and the atmosphere becomes opaque, $\partial\epsilon/\partial z \simeq 0$; the relaxation times become large again. In general, τ_r decreases as temperature increases, and the effect of the variation in temperature in figure 177 is to flatten the relaxation time profile relative to the shape it would have if the atmosphere were isothermal. Figure 177 indicates that τ_r increases rapidly with altitude above the 10 mbar level, but here the radiative opacity from the hydrocarbons CH_4, C_2H_6, and C_2H_2 become important. Estimates based on band models predict relaxation times at 0.1 to 1 mbar on the order of 10^8 s (Halthore et al., 1988). Thus, relaxation times in Jupiter's troposphere and stratosphere are 4×10^7 s or greater.

For diurnal forcing ($\Omega = 2\pi/(9.92)\ h^{-1}$), $\Omega\tau_r > 7000$, and diurnal variations are not expected in the troposphere or stratosphere from purely radiative considerations. In principle, dynamic-radiative interactions could produce an observable diurnal response. Two possibilities come to mind: (1) The atmosphere is in a marginal state, in which slight changes in its thermal structure lead to substantial changes in its dynamical properties. Actually, this is expected in the lower troposphere, below the visible cloud level. Theory and available observations suggest that the lapse rate in atmospheric temperature is close to adiabatic. Small changes in radiative heating could produce small changes in the lapse rate, tending to produce a slight superadiabaticity, resulting in vigorous vertical convection, or a slight superadiabaticity, tending to suppress thermally driven, small-scale convection. Cunningham et al. (1987) have invoked this mechanism to produce a diurnal change in the NH_3 cloud structure that would account for the variation in H_2 quadrupole emission observed from Earth in scans from the east to the west limb of Jupiter. (2) There exists a resonant mode in the atmosphere that is excited by diurnal forcing. No unambiguous evidence for this exists. In interpreting mesoscale waves evident in Voyager images (see below), Flasar and Gierasch (1986) have suggested that diurnal forcing might resonantly excite gravity waves in a duct in the lower troposphere, because the wave frequencies in their model, relative to the background flow, are on the order of $\Omega_{diurnal}$.

For forcing modulated over the period of Jupiter's orbit about the Sun, $\Omega\tau_r$ is of order unity through much of the troposphere and stratosphere (figure 177), and the radiative response to seasonal forcing can be significant. Traditionally, this has not received much attention in atmospheric modeling, because Jupiter's obliquity is only 3°. However, there is a 21 percent variation in the solar irradiation during Jupiter's passage from perihelion to aphelion, and perihelion occurs near northern summer solstice (Beebe et al., 1986). Both ground-based and Voyager infrared observations in 1978–1979, near the time of Jupiter's northern spring equinox, indicated that temperatures in the upper stratosphere (1–10 mbar) were ~10 K warmer in the northern hemisphere than in the southern (Caldwell et al., 1979; Hanel et al., 1979). Caldwell et al. interpreted this asymmetry in terms of a radiative response to the seasonally varying solar heating. A phase lag in the thermal response of approximately one season is consistent with the radiative relaxation times at these altitudes. Seasonal variations at the tropopause are smaller (Beebe et al., 1987), despite the relatively small relaxation times. Evidently meridional redistribution of heat by dynamic transports is very efficient in the deeper atmosphere.

THERMAL CONVECTION AND PARA-HYDROGEN DISEQUILIBRIUM

Jupiter's global thermal emission is characterized by two striking properties. First, the atmosphere emits more energy at thermal infrared wavelengths than it absorbs from the Sun (cf. for example, Hanel et al., 1981), implying that it has an internal heat source. Second, the thermal emission is nearly uniform with latitude, exhibiting only a small-amplitude variation over scales comparable to the visible banded structure, about 10° in latitude (Ingersoll et al., 1976; Pirraglia, 1984). Hubbard (1968) demonstrated that Jupiter's internal heat source implied that most, if not all, of the interior is convective. Standard mixing length theory predicts that only a slight superadiabaticity is required to transport the inferred heat flux from the interior. The eddy diffusion coefficients predicted by the theory are $\kappa \sim (5 \times 10^8)$ cm^2 s^{-1} near the 1-bar level of the atmosphere, and they increase with depth. Near 250 bar ($T \sim 1000$ K) they are $\sim 10^9$ cm^2 s^{-1}. At 1 bar and 250 bar one scale height H in pressure is, respectively, 25 km and 100 km, and the corresponding overturning times are $H^2/\kappa \sim 10^4$ and 10^5 s. Flasar and Gierasch (1978) modeled the effects of Jupiter's rotation on its internal convective flow. They found that rotation acts to reduce the thermal eddy diffusivity from that predicted by the standard mixing length theory, particularly at high latitudes. Near 1 bar the difference is small; at 250 bar their diffusivities near the equator again agree with those predicted by standard mixing length theory but decrease rapidly with latitude, being a factor of 10 smaller at 20° R latitude. Ingersoll and Pollard (1982) modeled the effects of strong internal differential rotation on convective mixing. Requiring that the viscous dissipation in Jupiter's interior be consistent with its internal heat flux, they deduced very small diffusivities, $\sim 10^3$ cm^2 s^{-1}. However, this modeling is probably only applicable, if at all, to Jupiter's deep interior, $p \gg 1$ kbar. Several "disequilibrium" species, such as PH_3 and CO, have been spectroscopically observed in Jupiter's atmosphere at pressure levels <10 bar. On the basis of chemical equilibrium, these would not have been anticipated at altitudes above the 1000 K level. Various workers have interpreted this in terms of quenching effected by rapid transport from Jupiter's deep atmosphere: The observed abundance of the disequilibrium species corresponds to its equilibrium value at a depth where the equilibration time is comparable to the convective vertical transport time. The chemical equilibration times are not always well determined, but the required transport times appear to be roughly consistent with those predicted by standard mixing length theory and by Flasar and Gierasch (1978). The observations have typically weighted the low latitudes of Jupiter, where the two models of convection make similar predictions. The reviews by Lewis and Fegley (1984) and Drossart et al. (1987) discuss quenching in more detail. If, as suggested by Flasar and Gierasch, the efficiency of the eddy transport varies with latitude, then it is conceivable that the abundance of the disequilibrium species varies with latitude. Observations pertaining to this question have been extremely limited.

Because the absorbed solar radiation varies strongly with latitude on Jupiter, the observed uniformity of thermal emission requires a dynamic transport of heat from low to high latitudes. How these transports are effected is a matter of some debate. One possibility for Jupiter is that the interior convective flow associated with the internal heat source can adjust itself to minimize lateral gradients in temperature (Ingersoll, 1976; Ingersoll and Porco, 1978). Mixing length theory suggests that thermally driven free convection is very efficient, and requires only small contrasts in potential temperature to drive large heat fluxes (Hubbard, 1968; Flasar and Gierasch, 1978; Ingersoll and Pollard, 1982). Thus differential solar absorption will tend to warm the equatorial atmosphere relative to the polar atmosphere, thereby suppressing convective heat transport from the interior at the equator relative to that at the poles. The limiting case is one in which the internal heat flux varies with latitude to exactly compensate the variation of absorbed solar radiation so that the total thermal emission to space is uniform with latitude. This model does require that the convective interior be in effective dynamic contact with that portion of the atmosphere in which solar radiation is absorbed. In its simplest form, it assumes that solar radiation is absorbed within or adjacent to the free convective zone that extends into the interior. This may or may not be true, because it is not known at what altitude the mixing length theory for slightly superadiabatic fluids ceases to provide an adequate description of dynamic transports (if, indeed, it does at any depth). The presence of condensate clouds above the 10 mbar level suggests the possibility that moist convective processes provide much of the vertical heat transport at these levels, but the efficiency of these processes is not really known. The convective adjustment model also requires that the internal heat source be sufficiently large (Ingersoll and Porco, 1978). On Jupiter and Saturn this poses no difficulty, but Uranus' internal heat source is extremely weak (Pearl et al., 1987). Friedson and Ingersoll (1987) have modeled Uranus' global heat balance using a parameterization of lateral and vertical heat transport that reduces to the usual mixing length theory for unstably stratified, or superadiabatic, fluids ($\partial\Theta/\partial z < 0$) and to the parameterization of baroclinic waves developed by Stone (1972) for stably stratified fluids ($\partial\Theta/\partial z > 0$). They find that in the absence of significant internal heating baroclinic eddies redistribute heat meridionally and reduce the pole-to-equator thermal contrasts to <2 K at the emission-to-space level (400 mbar), comparable to the contrasts of <1 K that were observed by Voyager (Hanel et al., 1986).

A reduction in the global meridional temperature contrast by dynamic transports in the interior or in the deep troposphere, and the relative magnitudes of the radiative relaxation time and the *para*-hydrogen equilibration time, provide a plausible explanation for the observed *para*-hydrogen distribution in the upper tropospheres of the outer planets. Figure 178 depicts the meridional variation in the para fraction (f_p) on Jupiter near 300 mbar that was retrieved from Voyager infrared data (Conrath and Gierasch, 1984). For comparison, the figure also depicts the para fraction (f_{pe}) expected if the ortho and para states were in equilibrium at the 300-mbar temperature. The observed para fractions are less than the equilibrium fractions; the differences are largest near the equator, and they more or less monotonically decrease toward higher latitudes. This can be explained in terms of a meridional cell with upwelling at low latitudes and sinking motions at high latitudes, as depicted in figure 178. In the deep troposphere ($T \sim 300$ K), the equilibration time for ortho-para conversion, τ_p, is relatively short, $<10^8$ s, and the para fraction is in local equilibrium ($f_p = 0.25$). In the upper troposphere τ_p is much longer, $\sim 10^9$ s. If the time scale associated with dynamic overturning is comparable to this longer time, then upwelling will cause f_p in the upper troposphere to "lag" the local equilibrium value and be characterized by a value appropriate to equilibrium at lower altitudes. If the meridional flow is poleward in the upper troposphere, more ortho-states will convert to para-states as the fluid moves toward higher latitudes, and f_p will increase poleward, as the data indicate. It turns out that the deposition of heat in the upper troposphere effected by this conversion at high latitudes is small relative to the adiabatic warming associated with the subsiding branch of the circulation (Conrath and Gierasch, 1984).

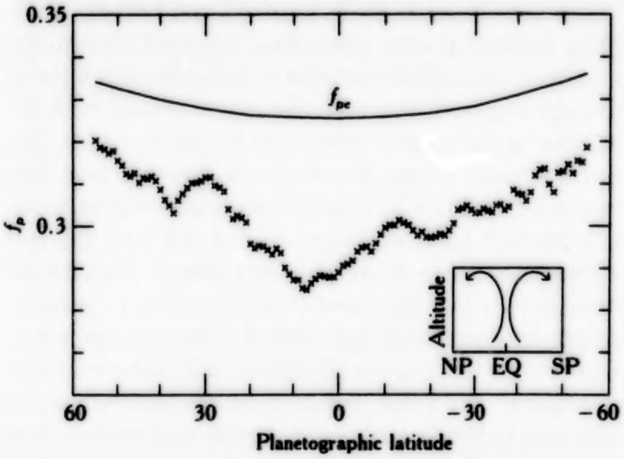

Figure 178. Zonally averaged *para*-hydrogen fraction retrieved from Voyager 1 infrared observations made during the incoming north-south mapping sequence. The nominal sensing altitude is 300 mbar at low latitudes. Because of the spacecraft flyby geometry, higher latitudes were observed at a higher emission angle, resulting in higher altitudes and lower temperatures being sensed in the troposphere. The *solid curve* denotes the equilibrium fraction, and its variation with latitude reflects the concomitant variation of emission angle. Adapted from Conrath and Gierasch (1984).

Under what conditions can one anticipate that the overturning time is comparable to τ_p? To answer this, consider the heat equation

$$\frac{\partial \bar{T}}{\partial t} + \bar{w}_* \frac{\partial \bar{\Theta}}{\partial z} = \frac{\bar{T}_e - \bar{T}}{\tau_r}, \qquad (26.3)$$

and the *para*-hydrogen transport equation

$$\frac{\partial \bar{f}_p}{\partial t} + \bar{v}_* \frac{\partial \bar{f}_p}{\partial y} + \bar{w}_* \frac{\partial \bar{f}_p}{\partial z} = \frac{\bar{f}_{pe} - \bar{f}_p}{\tau_p} \qquad (26.4a)$$

(Conrath and Gierasch, 1984). Here v_* and w_* denote, respectively, the meridional and vertical velocities, y is the northward (meridional) coordinate, z is altitude, $\partial\Theta/\partial z$ is the static stability, that is, the lapse rate in temperature minus the dry adiabatic lapse rate, and the overbars denote averages over longitude. Eq. (26.3) is identical to eq. (26.1) except for the inclusion of the dynamic term representing the vertical advection of heat, or equivalently, the adiabatic heating-cooling associated with subsidence-upwelling. The second and third terms on the left-hand side of eq. (26.4a) represent meridional and vertical advection of f_p. The term on the right-hand side is a Newtonian relaxation to the equilibrium stat with a relaxation time τ_p, analogous to the radiative relaxation term in eqs. (26.1) and (26.3). Horizontal advection of heat is not included in eq.

(26.3); it is small, because the observed equator-to-pole contrast in temperature in the upper troposphere is small.

Consider now the steady case, $\partial/\partial t = 0$, near the equator. Then meridional advection can be neglected in eq. (26.4a), and the balance is between vertical advection and Newtonian relaxation:

$$\bar{w}_* \frac{\partial \bar{f}_p}{\partial z} \simeq \frac{\bar{f}_{pe} - \bar{f}_p}{\tau_p} . \qquad (26.4b)$$

A measure of vertical contrast in temperature is given by the product of the static stability times the pressure scale height, H. In the upper troposphere of Jupiter $H\partial\Theta/\partial z \simeq 40$ K. This would be comparable to the equator-to-pole variation in T_e, if it were determined solely by differential solar heating. Assume, instead, that convective transport in the deep atmosphere and interior can efficiently reduce the meridional contrasts in temperature. Then the effective T_e, maintained at the top of the free convection zone, varies little with latitude. Because T is observed to be nearly uniform with latitude,

$$H \frac{\partial \bar{\Theta}}{\partial z} \gg \bar{T}_e - \bar{T}, \qquad (26.5)$$

or, from eq. (26.3):

$$\frac{H}{\bar{w}_*} \gg \tau_r . \qquad (26.6)$$

The time for dynamic overturning is large compared to the radiative time scale. On Jupiter the equilibration time, τ_p, is $\sim 10^9$ in the upper troposphere, and it is large compared to τ_r (cf., fig. 177). In this situation, departures of f_p from f_{pe} can be large: Figure 178 suggests that $(f_p - f_{pe}) \sim H\partial f_p \partial z$; from eq. (26.4b), this is possible if $H/\bar{w}_* \sim \tau_p$. On Saturn, Uranus, and Neptune, temperatures are colder and the radiative relaxation times are much longer than on Jupiter, but to first order the equilibration times are unchanged. It turns out that $\tau_r > \tau_p$ in their upper tropospheres (Conrath and Gierasch, 1984). It is reasonable to assume that, as on Jupiter, some type of dynamic redistribution of heat occurs in the lower tropospheres or interiors of these planets, so that the inequalities in eqs. (26.5) and (26.6) still hold. However, now the overturning times are also large compared to the equilibration times. From eq. (26.4b), consistency requires that $(f_{pe} - f_p) \ll H\partial f_p/\partial z$, or that the deviation of the para fraction from local equilibrium be small. This is indeed what has been inferred from Voyager infrared measurements of Saturn and Uranus (Conrath et al., 1984; Hanel et al., 1986). The approximate equality between the dynamic overturning time of the global meridional cell and the *para*-hydrogen equilibration time is not explained by these considerations, because *para*-hydrogen is simply a tracer in the upper troposphere; it is not important to the energetics at this altitude. The discussion in the next section suggests that friction acting in the upper troposphere and lower stratosphere can determine the strength of meridional circulations.

Although lagged para conversion does not affect the energetics of the upper troposphere, it can have a profound effect on the vertical convective transport in the lower troposphere, where the lapse rate is close to adiabatic. Conrath and Gierasch (1984) find that para conversion greatly enhances the efficiency of thermal convection, and they estimate overturning times near 1 bar of $\sim 10^6$ s, approximately a factor of 100 longer than those estimated on the basis of standard mixing length theory. This efficiency disappears at levels approaching the 300 K level ($\sim$7 bar) and deeper, where τ_p is so small that there is no longer any lagged conversion.

ZONALLY AVERAGED CIRCULATION

Jupiter's winds are primarily zonal (east-west), and they appear to be remarkably stable. Figure 179 depicts the zonally averaged (i.e., averaged over longitude) winds derived from images obtained during the passage of the Voyager 1 spacecraft and the Voyager 2 spacecraft four months later. The meridional profiles of the winds are virtually identical. Ground-based determinations of the zonal wind speeds made over the previous five years from the tracking of specific cloud features are consistent with the Voyager results. It is more difficult to compare the Voyager observations with earlier studies. The latter tended to track the larger long-lived features, which generally lie between the major currents where the zonal winds are small (Ingersoll et al., 1979, 1981). Moreover, the latitudes of the measured winds were often not measured very precisely (Beebe et al., 1987). Despite this, the earlier ground-based observations do suggest that the locations of the zonal currents have not significantly altered over the past century (Ingersoll et al., 1979, 1981).

The apparent stability of the zonal currents remains a mystery. One possible explanation is that they extend far into Jupiter's atmosphere and perhaps even into its interior. The inertia associated with the mass-loading at great depths could result in dynamic time scales that are quite large (Ingersoll et al., 1981), in much the same way that the radiative relaxation time (fig. 177) increases with depth in the lower troposphere

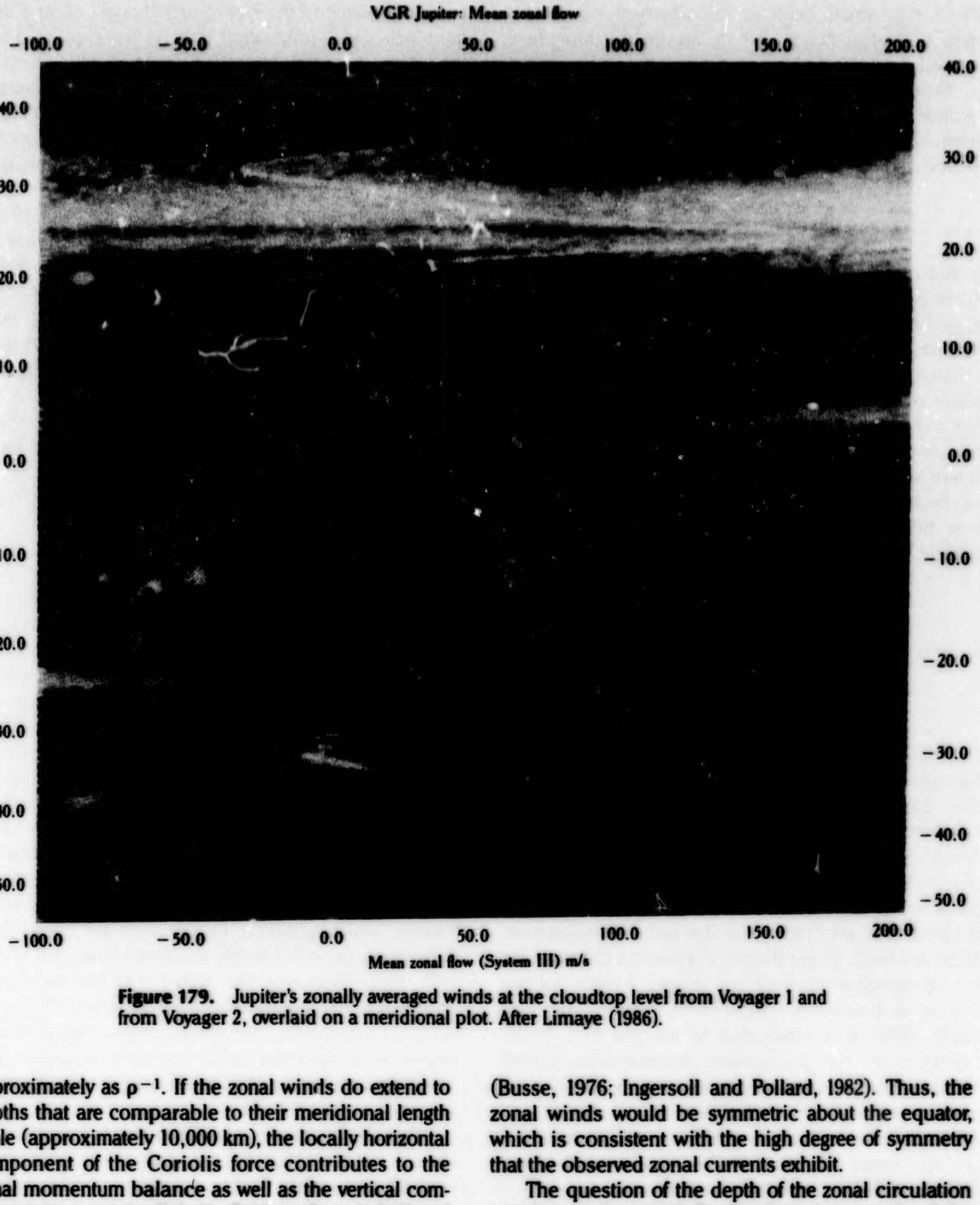

Figure 179. Jupiter's zonally averaged winds at the cloudtop level from Voyager 1 and from Voyager 2, overlaid on a meridional plot. After Limaye (1986).

approximately as ρ^{-1}. If the zonal winds do extend to depths that are comparable to their meridional length scale (approximately 10,000 km), the locally horizontal component of the Coriolis force contributes to the zonal momentum balance as well as the vertical component; in a quasi-adiabatic fluid, such as is believed to characterize Jupiter's deep atmosphere and interior, the zonal winds are then approximately uniform on cylinders concentric to the planetary axis of rotation (Busse, 1976; Ingersoll and Pollard, 1982). Thus, the zonal winds would be symmetric about the equator, which is consistent with the high degree of symmetry that the observed zonal currents exhibit.

The question of the depth of the zonal circulation remains controversial. Studies have been made of the momentum fluxes associated with the eddies in Jupiter's atmosphere near the cloud tops. Velocities were measured in a specified latitude band from observing

ORIGINAL PAGE
BLACK AND WHITE PHOTOGRAPH

cloud motions in images obtained by the Voyager spacecraft. The departures from the zonal mean were computed and the product of the zonal and meridional velocity components, $\overline{u'v'}$, averaged along a latitude circle, was compared to the meridional derivative of the mean zonal wind, $\partial\bar{u}/\partial y$. The quantity $\overline{u'v'}\partial\bar{u}/\partial y$, averaged over the globe, represents the global conversion of eddy kinetic to mean kinetic energy. Beebe et al. (1980) and Ingersoll et al. (1981) concluded that $\overline{u'v'}$ was significantly correlated with $\partial\bar{u}/\partial y$, and that the eddies could resupply the kinetic energy of the zonal winds near the visible cloud tops in two to four months. Given the apparent stability of the zonal currents, this implies a delicate balance between the supply and loss of zonal momentum. Possibly there is a compensating flux of zonal momentum into Jupiter's interior, but such a balance can occur naturally at the altitude of the observed eddies themselves. In rapidly rotating atmospheres, the fluxes of heat and momentum transported by eddies induce zonally averaged meridional circulations which act to cancel these fluxes (see, for example, Dunkerton, 1980; Flasar, 1986, and references therein). The degree of cancellation depends on the amount of dissipation and diabatic (e.g., radiative) heating in the atmosphere. If these are small and the eddies are statistically steady, the cancellation is nearly complete and

$$-2\Omega \sin \Lambda \bar{v} \simeq -\frac{\partial \overline{u'v'}}{\partial y}, \qquad (26.7)$$

where Λ is the latitude (Dunkerton, 1980). Thus, the convergence of zonal momentum in westerly (i.e., eastward) jets is offset by the equatorward flow of the mean meridional circulation there and its tendency to conserve angular momentum and spin down (c.f., fig. 180a). The magnitude of the meridional velocity required to effect this is small. From eq. (26.7), with root mean square (RMS) eddy velocities $\sim 10\ \mathrm{m\ s^{-1}}$, $\bar{v} \sim (100\ \mathrm{m^2\ s^{-2}}) \times$ (lateral scale of the jets $= 5000\ \mathrm{km})^{-1} \times (2\Omega \sin \Lambda = 10^{-4}\ \mathrm{s^{-1}})^{-1} = 0.2\ \mathrm{m\ s^{-1}}$, well below the accuracy of the cloud tracking studies (Ingersoll et al., 1981). Determining the vertical motions associated with these mean circulations requires knowing the zonally averaged heat flux convergence attributable to eddies down to the spatial scales at which the eddy velocities were observed (Dunkerton, 1980). Thermal structure at these scales is not available, because of the coarser spatial resolution of the Voyager infrared experiment. Sromovsky et al. (1982) have argued that Beebe et al. (1980) and Ingersoll et al. (1981) may have overestimated the eddy-mean flow velocity correlations, because of biasing from nonuniform and incomplete sampling in longitude. The question of biasing has yet to be resolved, and it may not be resolved until the longer-term and more extensive coverage from Galileo is available.

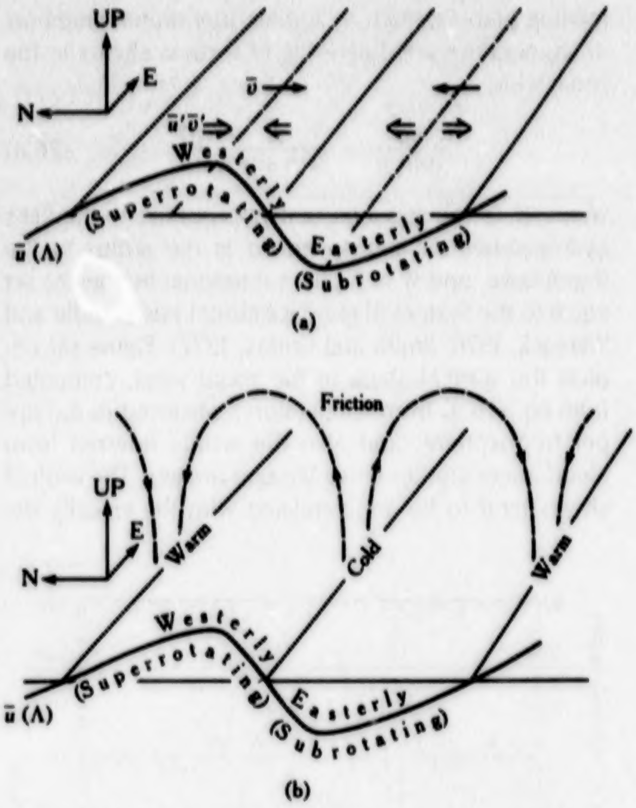

Figure 180. (a) Zonally averaged Eulerian meridional velocities expected near the cloud tops, if there is a convergence of eddy zonal momentum flux at the jets as indicated, and the Eulerian circulation acts to cancel the effect of the eddies. (b) Zonally averaged residual Eulerian circulation, induced by friction in the upper troposphere and stratosphere acting on the zonal winds indicated.

Comparison of the meridional profile of the mean zonal winds, derived from Voyager images, with temperatures in the upper troposphere and at the tropopause retrieved from observations by the infrared experiment on that spacecraft's infrared interferometer spectrometer (IRIS) is instructive. Cold and warm temperatures usually occur, respectively, in regions of anticyclonic and cyclonic vorticity in the mean flow (Conrath et al., 1981; Gierasch et al., 1986). (In zonally averaged flows, the locations where $\partial\bar{u}/\partial\Lambda > 0$ in the northern hemisphere, and <0 in the southern, have anticyclonic vorticity.) In the atmospheres of rapidly rotating planets, such as Jupiter, meridional gradients in temperature are diagnostic of vertical shears in the zonal wind:

$$\frac{\partial \bar{u}}{\partial \ln p} = \frac{R}{2\Omega a \sin \Lambda} \frac{\partial \bar{T}}{\partial \Lambda}, \qquad (26.8)$$

where R is the gas constant appropriate to Jupiter's hydrogen-helium atmosphere, a is the radius to the tropopause, and W is Jupiter's rotational frequency, set equal to the System III radio rotational rate (Riddle and Warwick, 1976; Smith and Gulkis, 1977). Figure 181 depicts the vertical shear in the zonal wind, computed from eq. (26.8) from temperatures observed in the upper troposphere, and also the winds inferred from cloud tracer studies using Voyager images. The vertical shears tend to be anticorrelated with the visually derived winds; they imply that the mean zonal winds decay with altitude. A similar relation between temperatures and wind velocities exists on Saturn (Pirraglia et al., 1981; Conrath and Pirraglia, 1983) and Uranus (Flasar et al., 1987), although on the latter body, the wind velocities have been determined at only a few locations. These correlations have been interpreted with some success in terms of a steady ($\partial/\partial t = 0$) linear model of the upper troposphere and lower stratosphere, in which frictional drag and radiative damping attempt to bring the observed winds and temperatures to a state of uniform angular velocity and temperatures constant with latitude. The frictional drag and radiative damping are specified in terms of frictional relaxation time, τ_ν, and a radiative relaxation time, which are uniform with latitude. The relevant dynamical equations are the heat balance equation, eq. (26.3), in which T_e is assumed uniform with latitude, and that governing the zonal momentum balance:

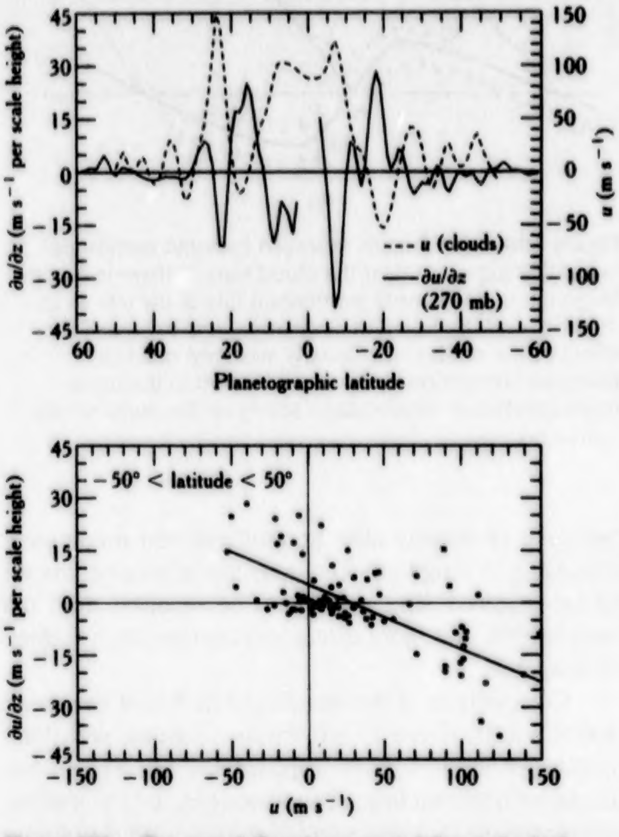

Figure 181. *Top panel:* Zonally averaged thermal wind shears in the upper troposphere compared with zonally averaged cloud traced wind velocities determined by Limaye (1986). The latter have been smoothed with a 3° latitude bin shifting at 1° intervals to bring the resolution closer to that of the shears. After Gierasch et al. (1986). *Bottom panel:* Scatter plot of the zonal winds and wind shears, taken from the curves in the top panel at 1° intervals. The line is a least squares fit to the points, inversely weighted by the horizontal resolution of the temperature observations (cf., fig. 184).

$$\frac{\partial \bar{u}}{\partial t} - - 2\Omega \sin \Lambda \bar{v}_* = -\frac{\bar{u}}{\tau_\nu}. \qquad (26.9)$$

Here, as in the section, titled Thermal Convection and Para-Hydrogen Disequilibrium $\bar{v}_*$ and $\bar{w}_*$ are the mean meridional and vertical velocities, respectively, related by the equation of mass continuity. However, now the meridional scale of the circulation is not equator to pole, but that of the zonal currents. In the model, the observed meridional profile of the zonal winds is specified at a lower boundary in the upper troposphere. No attempt is made to account for the meridional structure of the winds or to explain how it is maintained in the deep atmosphere. Equivalently, the observed meridional profile of temperatures in the troposphere can be specified at the lower boundary, instead of the zonal winds. The frictional drag acting on the zonal winds induces a meridional circulation in which poleward motion occurs over westerlies, which superrotate relative to the internal rotation of the planet (fig. 180b). The tendency of the parcel to conserve angular momentum and spin up balances the action of friction to decrease its zonal velocity. Similarly, parcels moving equatorward maintain easterlies against frictional decay. The action of friction, however, does cause the winds to decay with altitude away from the lower boundary, where the zonal velocities (or temperatures) are specified. From conservation of mass, upwelling and subsidence are maximum near the null points in the zonal wind profile. The adiabatic heating and cooling associated with these produce the meridional variation in temperature observed near the tropopause. The magnitude of the variation is limited by radiative damping. In

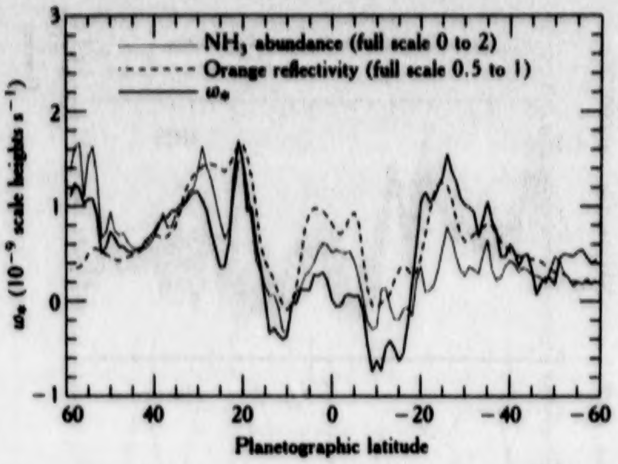

Figure 182. Zonally averaged residual vertical velocity, NH$_3$ abundance, and orange reflectivity as functions of latitude during the Voyager 1 encounter. The vertical velocity was derived from the steady ($\partial/\partial t = 0$) heat eq. (26.3) using 270-mbar temperatures retrieved from IRIS observations. The NH$_3$ abundances, also derived from IRIS observations, correspond to those at the NH$_3$ cloud base (1700 mbar). The orange reflectivities were derived from Voyager 1 image mosaics. After Gierasch et al. (1986).

the linear model the vertical decay scale, $\bar{u}/(\partial\bar{u}/\partial z)$, is linearly proportional to the ratio τ_v/τ_r when this scale is large compared to a pressure scale height (Gierasch et al., 1986; Flasar et al., 1987). On Jupiter the decay scale is two to three scale heights. The frictional damping time implied by this scale is long, ~10^8 s, slightly larger than τ_r (Gierasch et al., 1986). The source of the frictional drag in eq. (26.9) is not known, but studies of Earth's atmosphere suggest absorption of zonal momentum transported by vertically propagating waves as one mechanism. This absorption can occur either at a critical level, where the wave is locally stationary relative to the background atmospheric flow (cf., Booker and Bretherton, 1967), or at a level where the wave amplitude becomes so large that the perturbed temperature lapse rate exceeds the dry adiabat and the wave "breaks" (cf., Lindzen, 1981). A breaking wave may have been observed in Jupiter's stratosphere above 10 mbar in the ingress sounding made by the Voyager 1 radio occultation experiment (see, for example, fig. 12 of Flasar, 1986).

Equations (26.3) and (26.9) do not explicitly contain eddy flux terms. The mean meridional circulation $(\bar{v}_* \cdot \bar{w}_*)$ is the so-called residual circulation. It is the residual of the mean Eulerian circulation that remains when the part whose transports of heat and momentum cancel those of the eddies is subtracted away. The use of the residual mean circulation simplifies the momentum and thermodynamic equations, but it would simply be a mathematical exercise were it not for two happy circumstances: (1) When friction and diabatic heating are weak and the eddies are statistically steady (i.e., their zonally averaged transports are steady), the residual circulation is small compared to the total Eulerian circulation. The vertical velocity, $\bar{w}_*$, can be estimated for steady flow ($\partial/\partial t = 0$) from the observed meridional variation in temperature, using eq. (26.3). Figure 182 presents $\bar{w}_*$ as a function of latitude. The overturning times, (scale height)/$\bar{w}_*$, are large, ~10^9 s. The corresponding meridional velocities, $\bar{w}_*$ × (lateral scale of jets $\simeq$ 5000 km)/(scale height $\simeq$ 20 km) ~0.5 cm s^{-1}, or a factor of 40 smaller than that estimated above for the total mean Eulerian velocity. (2) The residual circulation often corresponds to the zonal mean Lagrangian circulation, which describes the transport of conserved and quasi-conserved species. This is the case for the Earth's stratosphere (Dunkerton, 1978), and there is evidence that this is also true for Jupiter's upper troposphere and lower stratosphere. Figure 182 also depicts the abundance of NH$_3$, derived from Voyager 1 infrared observations (1979), as a function of latitude. It correlates well with the vertical velocity: regions of upwelling have locally larger abundances of NH$_3$. Figure 183 compares the NH$_3$ abundances derived from IRIS observations with those derived from ground-based microwave observations made in 1981–1983. The absolute abundances inferred are different, those from the IRIS measurements being up to a factor of four greater. Considering the differences in observation and data analysis, this may not be significant. The systematic errors in both approaches are probably not fully understood. The meridional variations in the NH$_3$ abundances retrieved from both data sets are probably more significant. Within ±30° latitude, they qualitatively agree. At higher latitudes they deviate from one another, particularly in the northern hemisphere. Although this may be a result of time variability, it is fair to conclude that both data sets merit further analysis.

The para fraction of molecular hydrogen, f_p, is another Lagrangian tracer of interest. The global variation in f_p, derived from Voyager IRIS observations, was already treated in terms of an equator-to-pole meridional cell (fig. 178). On the scale of the zonal currents, the smaller meridional variation of f_p is harder to interpret, possibly because of the noise in the retrieved values. Gierasch et al. (1986) assumed a balance between vertical advection of f_p and its relaxation to the equilibrium fraction at the local temperature, f_{pe} (eq. [26.4b]). In plotting both sides of eq. (26.4b) as functions of latitude, they found that the magnitudes did not agree,

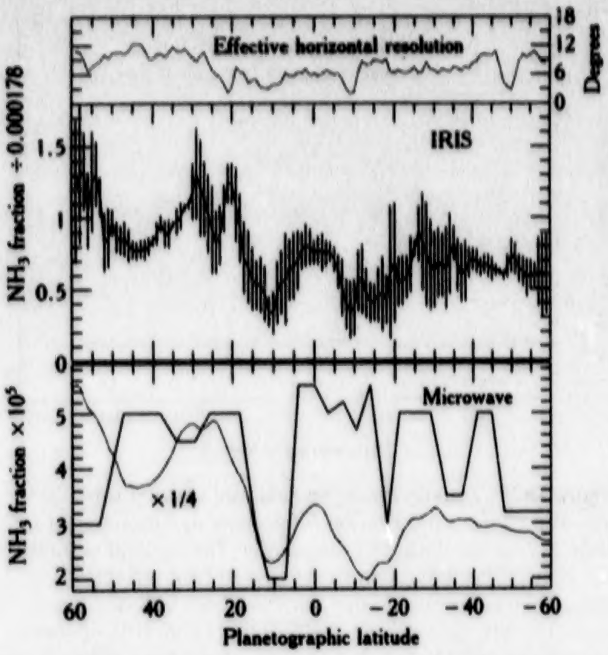

Figure 183. NH_3 abundances as functions of latitude, derived from Voyager 1 IRIS and ground-based microwave observations. The infrared derived abundances are those in the previous figure, and correspond to a pressure level of 1700 mbar. The *vertical hatching* indicates the standard deviation along latitude circles. The statistical error of the mean (not displayed) is typically much smaller, comparable to the smallest vertical hatching shown. The horizontal resolution in latitude for the IRIS data is given at the *top*. The NH_3 abundance derived from microwave observations corresponds to pressures between 500 and 1000 mbar. The *dotted curve* in the *bottom panel* results from the NH_3 abundances in the *top panel* being smoothed by averaging within a 11° bin in latitude, comparable to the spatial resolution at the sub-Earth point of the microwave observations, shifting at 1° intervals. The abundances in this curve have been reduced by a factor of four. Adapted from Gierasch et al. (1986) and de Pater (1986).

but that the meridional variations were similar. However, to some extent, this similarity must occur because both f_{pe} and, from eq. (26.3), w_* are functions of the local zonally averaged temperature.

Although the turnover times associated with the mean residual circulations are long, $\sim 10^9$ s, small changes in the temperature and wind fields have been observed over smaller time intervals. Figure 184 depicts zonally averaged temperatures at the tropopause retrieved from Voyager 1 and 2 observations, corresponding to a time interval of four months. Differences of 1–2 K between the two temperature profiles occur, especially at low latitudes. Limaye (1987) noted small variations in the mean zonal wind speeds derived from Voyager images over time scales of a few hundred hours. However, the differences are <5 m s^{-1}, comparable to the uncertainty in $\bar{u}$. A difference of 10 m s^{-1} is evident near 10–15° S in the zonally averaged winds derived from Voyager 1 and from Voyager 2 (fig. 179). These differences may be diagnostic of temporal changes in the mean activity of eddies and waves. If the zonally averaged transports by eddies at the cloudtops and below alters with time, then the delicate balance between the eddies and the Eulerian mean circulation, exemplified by eq. (26.7), can break down, resulting in a change in the temperature and wind fields over time intervals short compared to the overturning times of the residual circulations (Dunkerton, 1980). Alternatively, changes in the mean wave flux of energy and momentum into the stratosphere can alter the mean circulation there. On Earth such a mechanism is believed responsible for the sudden stratospheric warming, in which winds and temperatures at high latitudes are significantly altered over a time period of two weeks (cf., Holton, 1975). That the changes in zonal winds and temperatures over the four-month interval between the Voyager encounters are small indicates that the temporal variation in mean eddy and wave transports is also small, at least over this time period. Thus, the steady residual mean circulation described above may prove to be a useful background against which variations in temperature and wind fields can be used to probe vacillations in mean eddy and wave activity.

The association of upwelling with regions of anticyclonic vorticity and subsidence with regions of cy-

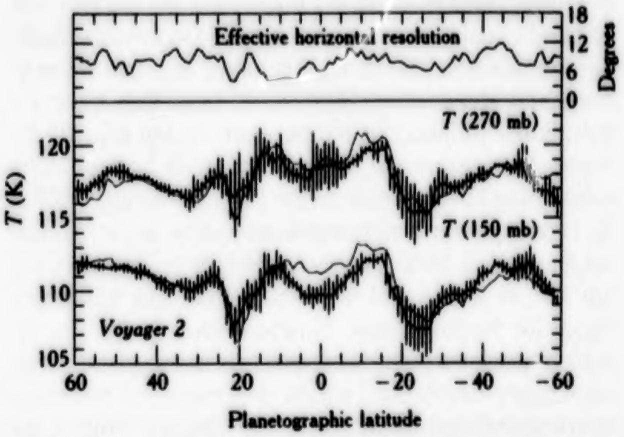

Figure 184. Zonally averaged temperatures (*solid curves*) at the 270 and 150-mbar level of Jupiter, retrieved from Voyager 2 infrared observations (July 1979). The *vertical hatching* denotes the standard deviations. The effective horizontal resolution in latitude is given at the *top*. The *dashed curves* are the zonally averaged temperatures from Voyager 1 (March 1979). After Gierasch et al. (1986).

clonic vorticity is not a new idea spawned from Voyager data. Hess and Panofsky (1951) suggested that the bright zones on Jupiter were regions of upwelling with enhanced condensation and cloudiness and that the darker belts were regions of subsidence and were relatively cloud free. The available measurements of zonal motions indicated that the zones and belts were, respectively, regions of anticyclonic and cyclonic vorticity. This was consistent with the inferred meridional circulation, because, with Jupiter's rapid rotation, the zonal motions are geostrophically constrained and the anticyclonic zones are regions of higher pressure; therefore, at high altitudes there should be a slow meridional flow from the zones to the belts. During the Voyager encounter the visible albedo was reasonably well correlated with the zonal winds and temperatures. Regions of anticyclonic vorticity and cooler tropopause temperatures were bright, and regions of cyclonic vorticity and warmer tropopause temperatures were dark. (Compare ω_* and the orange reflectivity in fig. 182.) An exception was the north temperate belt, a region of cyclonic vorticity, located between 24° and 30° N latitude. It was dark during the Pioneer 10 and 11 encounters, but began to cloud up in 1977–1978, and appeared as a bright zone during the Voyager encounters in 1979 (fig. 185). The tropopause temperatures retrieved by Voyager were warm, that is, they were correlated with the vorticity rather than with the albedo. The relation between visible albedo and temperature and wind structure is more puzzling on Saturn and Uranus. On Saturn the zonal winds derived from tracking of cloud features were poorly correlated with the visual albedo during the Voyager encounter (Smith et al., 1981), although they were well correlated with the tropopause temperatures (Pirraglia et al., 1981; Conrath and Pirraglia, 1983). On Uranus, winds were inferred from images and radio occultation data at only a few latitudes. The correlation of visual albedo with the zonal winds and tropopause temperatures appears to be the reverse of that occurring on Jupiter. A visually dark band at 25° S on Uranus coincided with colder temperature and anticyclonic vorticity (Flasar et al., 1987).

The visual appearance of Jupiter's banded structure changes every few years (fig. 185). Observations over several decades indicate that the temporal changes do not occur periodically, but it does not appear that they occur stochastically, either. The visual banded appearance of Jupiter typically changes over intervals comparable to the seasonal time scale, that is, the orbital period (11.9 years) divided by 2π, or approximately 2 years. Whether seasonal forcing has anything to do with these temporal changes is not clear. This type of temporal variability is reminiscent of so-called chaotic behavior in deterministic nonlinear dynamic systems, in which the temporal evolution depends so sensitively on initial conditions that long-term predictability is not possible. Often these systems are rather simple and have only a few degrees of freedom (Lorenz, 1963). Such systems have been proposed to explain the reversals in the Earth's magnetic field (Chillingworth and Holmes, 1980) and even the dripping of a leaky faucet (Shaw, 1984). There are several possible sources of dynamic nonlinearities in Jupiter's atmosphere. One example is the radical change in the dynamic properties that accompanies slight changes in temperature in the region below the cloudtops, described earlier, where the lapse rate in temperature is believed to be close to adiabatic. Hence, the temporal variability in Jupiter's visual appearance may serve as a useful probe of this region. There are telescopic photographs of Jupiter spanning nearly a century that catalog its time varying appearance. A quantitative time-series analysis of these would be a useful first step.

WAVES

One means of probing Jupiter's atmosphere, whose potential has not been fully exploited, is the analysis of linear wave patterns. Neutral waves are in principle less complicated than growing instabilities, such as baroclinic waves or convective plumes, because nonlinearities can often be neglected. The propagation characteristics of several classes of linear waves have been extensively studied. In general, they are sensitive indicators of the properties of the medium through which they propagate, such as flow velocity, static stability, and rotation rate. Because waves typically propagate vertically as well as horizontally, they can sample the properties of the atmosphere below the level at which they are observed. It is therefore possible to use waves in much the same spirit that seismic waves are used to infer properties of regions of the Earth that are otherwise inaccessible to direct observation.

The Voyager images revealed a rich display of wave patterns over a large range of scales (Smith et al., 1979a, b; Ingersoll et al., 1979; Mitchell et al., 1979; Hunt and Muller, 1979). Flasar and Gierasch (1986) catalogued and analyzed a remarkable class of mesoscale waves. Figure 186 summarizes a few of the properties of these waves. The wavetrains are predominately observed at the equator, but do occur at other locations within 25° of the equator (panel [a]). They occur on the local extrema of the zonal wind profile. The transverse

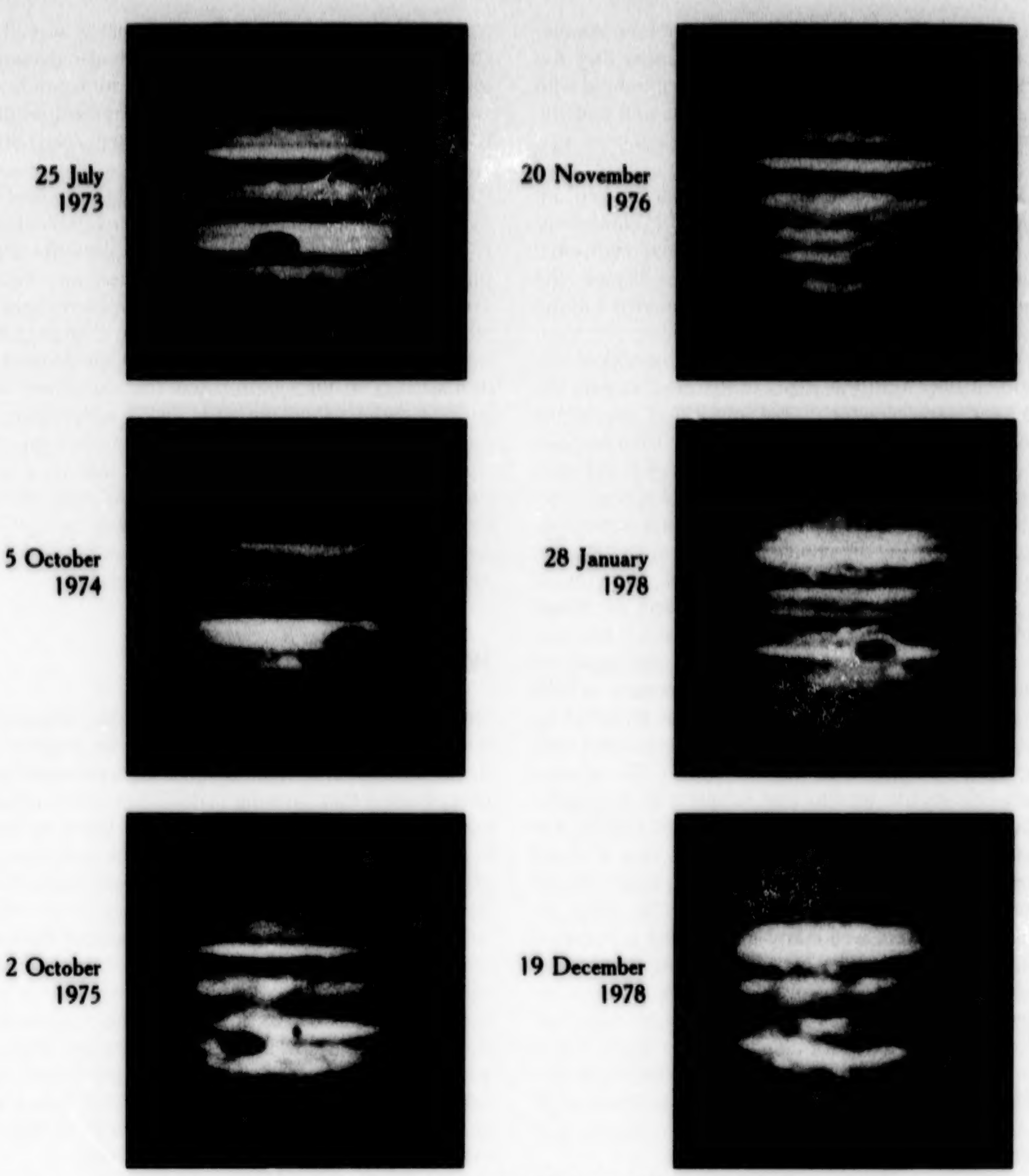

25 July 1973

20 November 1976

5 October 1974

28 January 1978

2 October 1975

19 December 1978

Figure 185. Blue filter photographs of Jupiter's disk over a five and one-half year period. Courtesy of Lowell Observatory.

widths of the wavetrains cluster about 1300 km, or $1\overset{\circ}{.}1$ of latitude (panel [b]). The horizontal wavelengths cluster about a mean of approximately 300 km with a standard deviation of only 20 percent (panel [c]). The alignment of the wavefronts is similarly well defined, and close to the north-south direction, suggesting that the horizontal propagation of the waves is nearly east-west (panel [d]). Finally, the wavetrains are quite long, typically 20 or more crests in length (panel [e]).

Flasar and Gierasch (1986) interpreted the observed waves as internal gravity waves propagating within a stable ($\partial\Theta/\partial z > 0$) open duct located below

ORIGINAL PAGE
BLACK AND WHITE PHOTOGRAPH

the visible (ammonia) clouds. Their conclusions are summarized in table 24. The small dispersion in zonal wavelength and the long wavetrains are a consequence of the resonant response of a vertical duct with high reflectivity to a broad spectral forcing, whose source is unspecified. The requirement that only one resonant mode be observed (the horizontal wavelengths in panel [c] cluster about one value) leads to the requirement that the Richardson number ($\mathrm{Ri} = [(g/T)(\partial\Theta/\partial z)/(\partial u/\partial z)^2]$) be of order unity within the duct. Thus the static stability and vertical shear in the zonal wind are related. This conclusion illustrates the powerful potential of waves for sounding the mean properties of the atmosphere. Below the visible clouds, the vertical profile in temperature is probably close to the dry adiabat over most altitudes, and the dynamics of the atmosphere are very sensitive to the small departures of the lapse rate in temperature from the adiabatic rate. It is

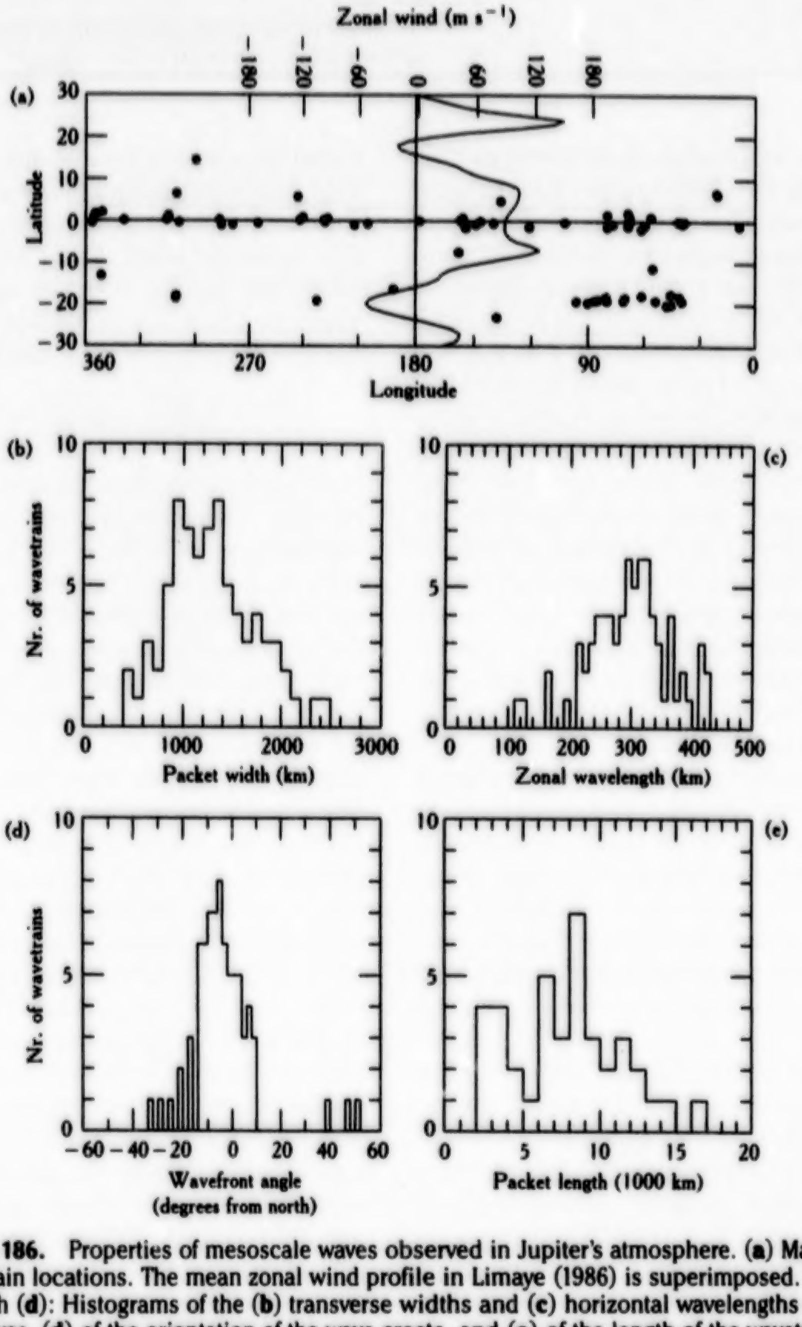

Figure 186. Properties of mesoscale waves observed in Jupiter's atmosphere. (**a**) Map of wavetrain locations. The mean zonal wind profile in Limaye (1986) is superimposed. (**b**) through (**d**): Histograms of the (**b**) transverse widths and (**c**) horizontal wavelengths of the waves, (**d**) of the orientation of the wave crests, and (**e**) of the length of the wavetrains.

Table 24. Properties of Mesoscale Waves

Observation	**Interpretation**
Wavelength	
Mesoscale	Forcing spectrum
Zonal wavelength: 300 km ± 20 percent	Resonant response of a stable duct to broad spectral forcing: Ri = O(1)
Long wave trains	High reflectivity from wave-trapping region above duct; little leakage into stratosphere
Zonal alignment of waves	Meridional waveguide attributable to $\bar{u}(y)$, not β
Meridional width: ~1° lat	Meridional waveguide attributable to $\bar{u}(y)$, not β
Location	
At jet extrema	Meridional waveguide attributable to $\bar{u}(y)$, not β
Equatorial: <25° lat	Inertia-gravity waves: $f(y) < \lvert c - \bar{u}\rvert_{\min} k \sim \Omega$

unlikely that in-situ temperature measurements, like those to be made by the Galileo probe, can measure these small departures or even their sign, but Doppler tracking of the probe can accurately measure the vertical shear in the winds. The gravity wave analysis then permits the static stability to be inferred. In their modeling Flasar and Gierasch (1986) also inferred that the horizontal component of the wavenumber vector should be nearly parallel to the background flow velocity, and they suggested that the observed spread in wavefront orientations (panel [d]) results from local deviations of this velocity from an east-west direction on scales large compared to the horizontal wavelength. Thus the direction of the wavefronts may indicate the direction of the winds in their environment. The fact that waves widely separated over a latitude circle exhibit such similar properties (such as horizontal wavelength) argues that Jupiter's troposphere has a remarkable degree of zonal homogeneity.

The properties of the mesoscale waves require further definition. For example, the Voyager images did not permit a determination of the horizontal phase velocities. Unfortunately, the Nyquist resolution of the Wide Field/Planetary Camera on the Hubble Space Telescope is comparable to the horizontal wavelength. Imaging by the Galileo spacecraft will probably afford the best means of further studying these interesting waves.

A class of linear waves of larger spatial scale at midlatitudes are planetary waves, also called Rossby waves. As with gravity waves, buoyancy and the mean flow are important, but planetary waves are also constrained by the rotation of the planet, through the Coriolis parameter ($f = 2\Omega \sin \Lambda$) and its variation with latitude ($\beta = a^{-1}\partial f/\partial\Lambda$). On Earth planetary waves are often observed in the stratosphere. They are excited in the troposphere, mostly from forcing by flow over large-scale topography (Holton, 1975). On Jupiter there is no topography as such, but one may ask whether the long-lived eddies that perturb the pressure and temperature fields in the mean zonal flow can serve equally well to force planetary waves. Linear theory indicates that vertically propagating planetary waves can occur only when the mean flow, $\bar{u}$ (assumed uniform), and the horizontal wavenumber, κ_H, satisfy

$$\left[\frac{\beta}{\bar{u} - c} - \kappa_H^2\right]\frac{N^2}{f^2} - \frac{1}{4H^2} > 0. \qquad (26.10)$$

For vertical propagation, the zonal flow must be westerly ($\bar{u} > 0$), and the horizontal wavenumber cannot be too large; for white noise forcing the smallest wavenumbers tend to have the largest amplitudes. On Earth the dominant component of topography has $\kappa_H a = 3$, and planetary waves of this scale and larger are dominant in the stratosphere. On Jupiter planetary waves can propagate if $\kappa_H^{-1} \gtrsim 4000$ km ($\kappa_H a \lesssim 11$), assuming, for example, $\Lambda = 23°$ and $\bar{u} - c \sim 100$ ms^{-1}. In principle, planetary waves should exhibit thermal structure that can be detected by remote sensing, but little has been done with this. The best spatially resolved data at thermal infrared wavelengths is from the IRIS experiment on Voyager. Unfortunately, individual spectra from this experiment are rather noisy at 1304 cm^{-1}, where the observed emission is from the upper stratosphere (on Voyager 1, the RMS noise per spectrum = 3 K at 170 K). The only region that has been extensively studied in this context is the great red spot. Figure 187 displays an east-west vertical cross section that was obtained from a sequence of observations made in a zonal cut through the red spot and its environs. Hanel et al. (1979) suggested that the undulations of temperature with altitude might be attributed to vertically propagating planetary waves. Figure 188 displays model calculations of stratospheric temperature perturbations from planetary waves in a uniform westerly flow forced by the pressure field of the red spot at the tropopause.

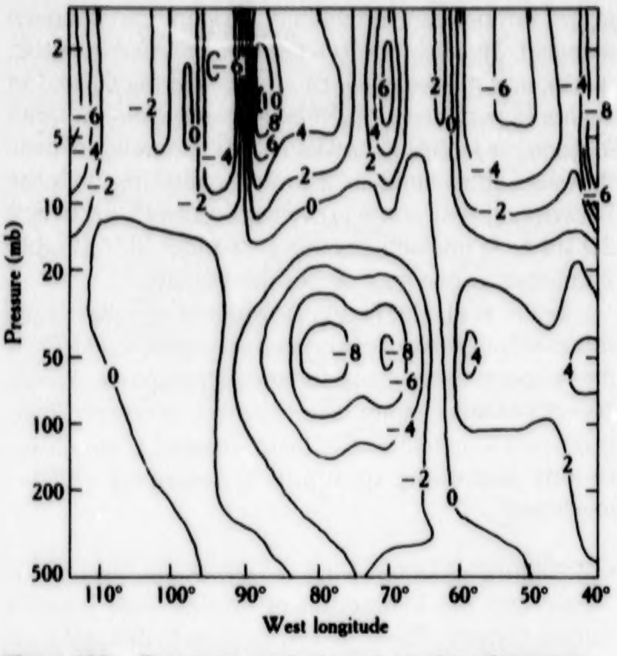

Figure 187. East-west vertical cross section of temperature fields over the great red spot, centered at 76° W, retrieved from Voyager 1 IRIS observations. After Flasar et al. (1981).

The important point to note is that the temperature contours exhibit an eastward tilt with altitude. The tilt is associated with the vertical propagation of energy, and it is not all evident in the observations. However, the mean zonal current at the latitudes of the red spot has a strong meridional shear, progressing from easterly north of the spot to westerly south of it. The zonal cut is actually close to the central latitude of the spot, where the mean zonal wind is nearly zero. A cut at a nearby, more southerly latitude where the winds are more westerly might have exhibited stratospheric waves, but it does not exist. The IRIS data need to be thoroughly searched for Rossby waves. They are not only indicators of the properties of the stratosphere (zonal flow, stability) but also of the forcing by tropospheric eddies.

Tropical waves of large spatial scale are exemplified by the so-called equatorial plumes, which occur near latitude 9° N (Smith et al., 1979a). Thirteen plumes, spaced at regular intervals in longitude, were observed in Voyager 1 images, and eleven at the time of the Voyager 2 passage. The thermal infrared data exhibits zonal variations on scales comparable to, but not exactly matching, that observed in the visual images (Hunt et al., 1981). Several workers have interpreted the plumes as manifestations of cumulus convective activity organized on planetary scales (Smith et al., 1979; Hunt et al., 1981; Allison, 1981, 1988; Stoker, 1986). If this proves to be the case, then understanding these features will involve the unraveling of several complex processes, such as moist convection in hydrogen atmospheres and amplitude saturation of large-scale waves. Using these to probe Jupiter's atmosphere may prove challenging.

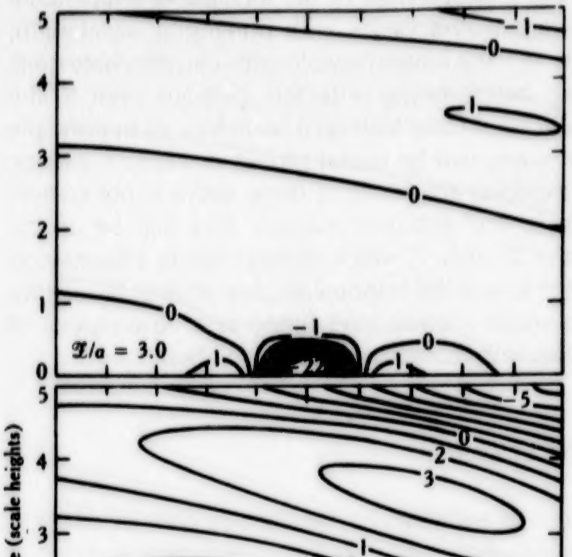

Figure 188. A model of the stratospheric temperature perturbations (in degrees kelvin) created by a circular Gaussian disturbance of radius at the tropopause, located at the bottom of each panel. *Top:* The smallest spot size results in weak propagation. *Middle:* An intermediate case, in which there is marginal propagation. *Bottom:* A larger spot radius, which results in strong propagation. The magnitude of the tropopause forcing has been adjusted in the three cases to emphasize the stratospheric thermal structure. After Flasar et al. (1981).

Bercovici and Schubert (1987) have pointed out that acoustic waves of periods of four to nine minutes can be trapped within a duct below the tropopause. Waves propagating upward into the tropopause region are reflected back because of the low temperature and increasing static stability there. The lower boundary of the duct is determined by the increase of temperature with depth, and varies with horizontal wavelength. Waves with the longest wavelengths can penetrate quite deeply before being reflected, perhaps even to the metallic-molecular hydrogen boundary, so in principle these waves can be useful probes of Jupiter's interior. The expected amplitude of these waves is not known. Bercovici and Schubert estimate they may be on the order of 10 cm s^{-1}, which corresponds to a fluctuation of 10^{-4} K near the tropopause. Any attempt to observe them would require long time-series observations of the disk with moderate spatial resolution.

CONCLUSION

Figure 189 summarizes the various time scales that have been discussed. It is meant as a quick sketch and not as an exhaustive compilation. For example, the diffusive overturning times associated with thermally driven free convection were computed from standard mixing length theory. The proposed modifications imposed by rotation, large-scale velocity shear, and lagged ortho-para hydrogen conversion have not been included. Similarly, the boundaries between acoustic, gravity, and planetary waves are not simply defined in such a sketch, because dynamic parameters vary with location on Jupiter. For instance, the frequency of gravity waves, measured in a frame comoving with the background flow, must exceed the Coriolis frequency, $2\Omega \sin \Lambda$. At midlatitudes this is of order $10^{-4}\ s^{-1}$, but it vanishes as one approaches the equator.

Beebe et al. (1987) and Drossart et al. (1987) have extensively discussed observations needed to elucidate the temporal behavior of Jupiter's atmosphere. Earlier sections of this chapter have touched on others. There is no need to reiterate all of them. Instead, a few observations pertaining to Jupiter's dynamics will be mentioned.

- Monitoring cloudtop wind velocities can provide insight into the interaction of eddies with Jupiter's zonal currents. There are two aspects to this problem. The first is to establish the magnitude and even the sign of the eddy transport of zonal momentum relative to the mean zonal currents, and ascertain the reliability of earlier Voyager studies of eddy fluxes. The second is to have long-term coverage to determine any temporal changes in the zonally averaged eddy transports. Temporal changes in these transports are a good indication that the delicate balance between eddies and the mean meridional circula-

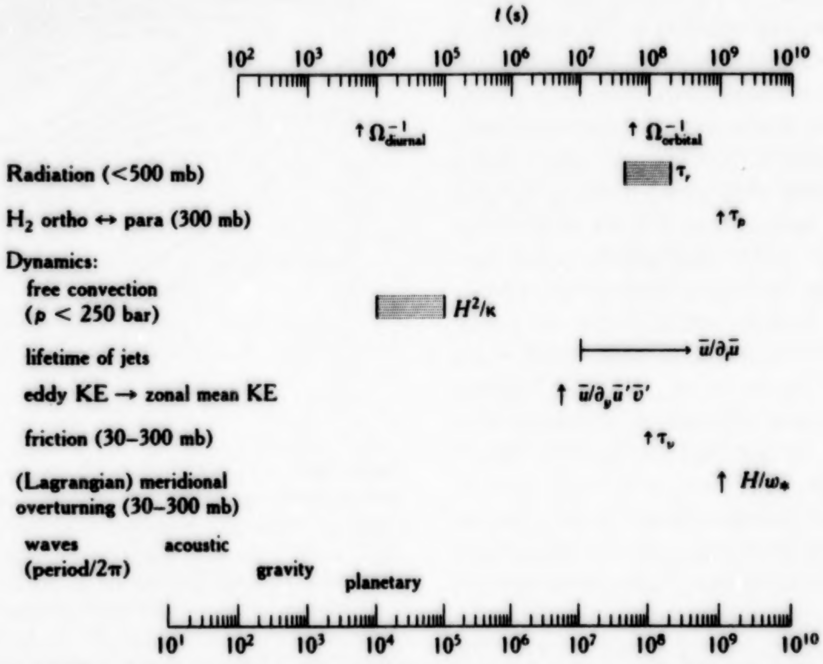

Figure 189. Various time scales of meteorological interest in Jupiter's atmosphere.

tions that they induce is being disrupted, permitting the eddies to change the mean zonal flow. The camera on the Galileo orbiter should prove an extremely useful tool in investigating these problems, but the Wide Field/Planetary Camera on the Hubble Space Telescope, having a Nyquist resolution of 300 km at Jupiter, will have the advantage of longer temporal coverage.

- Monitoring zonally averaged variables bears on the origin of the zonal currents and their interaction with the upper troposphere and stratosphere. It is important to determine just how steady the mean zonal winds are. Monitoring zonally averaged temperatures from ground-based infrared and microwave observations is as important as monitoring the winds themselves by cloud tracking. Temporal variations in zonally averaged quantities are probably indicative of changes in the level of eddy activity, as discussed above.
- Waves are important, both as passive indicators of the atmosphere through which they propagate and as a means of transporting momentum and energy between widely separated regions. Both imaging and infrared observations can identify new classes of waves and build up statistics on those previously identified. Ground-based infrared observations have already detected zonal structure that is suggestive of wave propagation (Beebe et al., 1987). The discussion in the preceding section illustrates how important it is to try to define the vertical as well as the horizontal structure of such waves.
- Mapping of disequilibrium species and condensibles can provide useful indicators of the Lagrangian circulation in Jupiter's troposphere and stratosphere. For instance, the global horizontal distributions of species such as CO and PH_3 are not even known (Drossart et al., 1987). The distribution of the para fraction of hydrogen on the scale of the zonal currents retrieved from Voyager infrared observations is not well understood and may be confused by the limited sensitivity. In principle, para-fractions can be retrieved from ground-based observations of hydrogen pressure-induced and quadrupole transition at visible and near-infrared wavelengths, but this entails modeling of scattering clouds, which themselves may vary on short time scales. The most straightforward approach is to observe several distinct spectral intervals having identical brightness temperatures within the S(0) and S(1) pressure-induced lines of molecular hydrogen in the far infrared at high-spatial resolution. This requires observations from a flyby or orbiting spacecraft.

Observations keyed to time variability are valuable in the investigation of Jupiter's atmosphere, but only in the context of the understanding of its time-averaged behavior, which is incomplete. It is the interplay among many different thrusts (e.g., studies of time variability, spatial variations, and global properties) that really counts because no one can confidently predict where the next major observational or theoretical discovery will occur. Happily, surprise remains an important element in the study of Jupiter's atmosphere and those of the other major planets.

References

Allison, M. D. (1981). *Dynamics of the jovian atmosphere: Voyager infrared observations and diagnostic wave theory.* Unpublished Ph.D. thesis, Rice Univ., Houston.

Allison, M. D. (1988). A planetary wave interpretation of Jupiter's equatorial plumes. Submitted to *Icarus.*

Bachet, G., E. R. Cohen, P. Dore, and G. Birnbaum (1983). The translational-rotational absorption spectrum of hydrogen. *Canad. J. Phys.* 61:591–603.

Beebe, R. F., A. P. Ingersoll, G. E. Hunt, J. L. Mitchell, and J. P. Muller (1980). Measurements of wind vectors, eddy momentum transports, and energy conversions in Jupiter's atmosphere from Voyager 1 images. *Geophys. Res. Lett.* 7:1–4.

Beebe, R. F., G. S. Orton, and R. A. West (1989). *Time-variable nature of the Jovian cloud properties and thermal structure: An observational perspective.* This volume.

Beebe, R. F., R. M. Suggs, and T. Little (1986). Seasonal north-south asymmetry in solar radiation incident on Jupiter's atmosphere. *Icarus* 66:359–365.

Bercovici, D., and G. Schubert (1987). Jovian seismology. *Icarus* 69:557–565.

Booker, J. R., and F. P. Bretherton (1967). The critical layer for internal gravity waves in shear flow. *J. Fluid Mech.* 27:513–539.

Busse, F. (1976). A simple model of convection in the jovian atmosphere. *Icarus* 29:255–260.

Caldwell, J., R. D. Cess, B. E. Carlson, A. T. Tokunaga, F. C. Gillet, and I. G. Nolt (1979). Temporal characteristics of the jovian atmosphere. *Astrophys. J.* 234:L155–L158.

Chillingworth, D. R. J., and P. J. Holmes (1980). Dynamical systems and models of the earth's magnetic field. *Math. Geol.* 12:41–59.

Cohen, E. R., L. Frommhold, and G. Birnbaum (1982). Analysis of the far infrared H_2-He spectrum. *J. Chem. Phys.* 77:4933–4941. Erratum and addendum. Ibid. 78:5283–5284.

Conrath, B. J., F. M. Flasar, J. A. Pirraglia, P. J. Gierasch, and G. E. Hunt (1981). Thermal structure and dynamics of the jovian atmosphere. 2. Visible cloud features. *J. Geophys. Res.* 86:8769–8775.

Conrath, B. J., D. Gautier, R. A. Hanel, and J. S. Hornstein

(1984). The helium abundance of Saturn from Voyager measurements. *Astrophys. J.* 282:807–815.

Conrath, B. J., and P. J. Gierasch (1984). Global variation of the para-hydrogen fraction in Jupiter's atmosphere and implications for dynamics on the outer planets. *Icarus* 57:184–204.

Conrath, B. J., and P. J. Gierasch (1986). Retrieval of ammonia abundances and cloud opacities on Jupiter from Voyager IRIS spectra. *Icarus* 67:444–455.

Conrath, B. J., and J. A. Pirraglia (1983). Thermal structure of Saturn from Voyager infrared measurements: Implications for atmospheric dynamics. *Icarus* 53:286–292.

Cunningham, C. C., D. M. Hunten, and M. G. Tomasko (1987). *A diurnally changing cloud on Jupiter.* Paper presented at the International Workshop on Time-Variable Phenomena in the Jovian System, Flagstaff, Ariz., August 25–27.

de Pater, I. (1986). Jupiter's zone-belt structure at radio wavelengths. II. Comparison of observations with model atmosphere calculations. *Icarus* 68:344–365.

Dore, P., L. Nencini, and G. Birbaum (1983). Far infrared absorption in normal H_2 from 77 K to 298 K. *J. Quant. Spectrosc. Rad. Transf.* 30:245–253.

Drossart, P., R. Courtin, S. Atreya, and A. Tokunaga (1989). Variations in the jovian atmospheric composition and chemistry. This volume.

Dunkerton, T. (1978). On the mean meridional mass motions of the stratosphere and mesosphere. *J. Atmos. Sci.* 35:2325–2333.

Dunkerton, T. (1980). A Lagrangian mean theory of wave, mean-flow interaction with applications to nonacceleration and its breakdown. *Rev. Geophys. and Space Phys.* 18:387–400.

Flasar, F. M. (1986). Global dynamics and thermal structure of Jupiter's atmosphere. *Icarus* 65:280–303.

Flasar, F. M., B. J. Conrath, P. J. Gierasch, and J. A. Pirraglia (1987). Voyager infrared observations of Uranus' atmosphere: Thermal structure and dynamics. *J. Geophys. Res.* 92:15,011–15,018.

Flasar, F. M., B. J. Conrath, J. A. Pirraglia, P. C. Clarck, R. G. French, and P. J. Gierasch (1981). Thermal structure and dynamics of the jovian atmosphere: 1. The great red spot. *J. Geophys. Res.* 86:8759–8767.

Flasar, F. M., and P. J. Gierasch (1978). Eddy diffusivities within Jupiter. In *Proceedings: Symposium on planetary atmospheres* (A. Vallance Jones, ed.), pp. 85–87, Royal Society of Canada, Ottawa.

Flasar, F. M., and P. J. Gierasch (1986). Mesoscale waves as a probe of Jupiter's deep atmosphere. *J. Atmos. Sci.* 43:2683–2707.

Friedson, J., and A. P. Ingersoll (1987). Seasonal meridional energy balance and thermal structure of the atmosphere of Uranus: a radiative-convective-dynamical model. *Icarus* 69:135–156.

Gierasch, P. J., B. J. Conrath, and J. Magalhaes (1986). Zonal mean properties of Jupiter's upper troposphere from Voyager infrared observations. *Icarus* 67:456–483.

Gierasch, P. J., and R. M. Goody (1969). Radiative time constants in the atmosphere of Jupiter. *J. Atmos. Sci.* 26:979–980.

Goody, R. M. (1964). Atmospheric radiation: I: Theoretical basis. Oxford Clarendon Pr., London.

Halthore, R., A. Burrows, and J. Caldwell (1988). Infrared polar brightenings of Jupiter. V. A thermal equilibrium model for the north polar hot spot. *Icarus* 74:340–350.

Hanel, R. A., B. Conrath, M. Flasar, V. Kunde, P. Lowman, W. Maguire, J. Pearl, J. Pirraglia, R. Samuelson, D. Gautier, P. Gierasch, S. Kumar, and C. Ponnamperuma (1979). Infrared observations of jovian system from Voyager 1. *Science* 204:972–976.

Hanel, R., B. Conrath, F. M. Flasar, V. Kunde, W. Maguire, J. Pearl, J. Pirraglia, R. Samuelson, D. Cruikshank, D. Gautier, P. Gierasch, L. Horn, and P. Schulte (1986) Infrared observations of the Uranian system. *Science* 288:70–74.

Hanel, R. A., B. J. Conrath, L. W. Herath, V. G. Kunde, and J. A. Pirraglia (1981). Albedo, internal heat, and energy balance of Jupiter: Preliminary results of the Voyager infrared experiment. *J. Geophys. Res.* 86:8705–8712.

Hess, S. L., and H. A. Panofsky (1951). The atmospheres of the outer planets. In *Compendium of meteorology,* pp. 391–400. American Meteorological Society, Boston.

Holton, J. R. (1975). *The dynamic meteorology of the stratosphere and mesosphere.* American Meteorological Society, Boston.

Hubbard, W. B. (1968). Thermal structure of Jupiter. *Astrophys. J.* 152:745–754.

Hunt, G. E., B. J. Conrath, and J. A. Pirraglia (1981). Visible and infrared observations of jovian plumes during the Voyager encounter. *J. Geophys. Res.* 86:8777–8781.

Hunt, G. E., and J.-P. Muller (1979). Voyager observations of small-scale waves in the equatorial region of the jovian atmosphere. *Nature* (London) 280:778–780.

Ingersoll, A. P. (1976). Pioneer 10 and 11 observations and the dynamics of Jupiter's atmosphere. *Icarus* 29:245–253.

Ingersoll, A. P., G. Munch, G. Neugebauer, and G. S. Orton (1976). Results of the infrared experiment on Pioneers 10 and 11. In *Jupiter* (T. Gehrels, ed.), pp. 197–205. Univ. of Arizona Press, Tucson.

Ingersoll, A. P., R. F. Beebe, S. A. Collins, G. E. Hunt, J. L. Mitchell, P. Muller, B. A. Smith, and R. J. Terrile (1979). Zonal velocity and texture in the jovian atmosphere inferred from Voyager images. *Nature* (London) 280:773–775.

Ingersoll, A. P., R. F. Beebe, J. L. Mitchell, G. W. Garneau, B. M. Yagi, and J. P. Muller (1981). Interaction of eddies and mean zonal flow on Jupiter as inferred from Voyager 1 and 2 images. *J. Geophys. Res.* 86:8733–8743.

Ingersoll, A. P., and D. Pollard (1982). Motion in the interiors and atmospheres of Jupiter and Saturn: Scale analysis, anelastic equations, barotropic stability criterion. *Icarus* 52:62–80.

Ingersoll, A. P., and C. C. Porco (1978). Solar heating and internal heat flow on Jupiter. *Icarus* 35:27–43.

Lewis, J. S., and B. Fegley, Jr. (1984). Vertical distribution of disequilibrium species in Jupiter's troposphere. *Space Sci. Rev.* 39:163–192.

Limaye, S. S. (1986). Jupiter: New estimates of the mean zonal flow at the cloud level. *Icarus* 65:335–352.

Limaye, S. S. (1989). Jupiter: Short-term variations of the mean zonal flow at cloud level. This volume.

Lindzen, R. S. (1981). Turbulence and stress owing to gravity wave and tidal breakdown. *J. Geophys. Res.* 86:9707–9714.

Lorenz, E. (1963). Deterministic nonperiodic flow. *J. Atmos. Sci.* 20:130–141.

Mitchell, J. L., R. J. Terrile, B. A. Smith, J.-P. Muller, A. P. Ingersoll, G. E. Hunt, S. A. Collins, and R. F. Beebe (1979). Jovian cloud structure and velocity fields. *Nature* (London) 280:776–778.

Pearl, J. C., B. J. Conrath, R. A. Hanel, and J. A. Pirraglia (1987). Energy balance of Uranus: Preliminary Voyager results. *Bull. Amer. Astron. Soc.* 19:852.

Pirraglia, J. A. (1984). Meridional energy balance of Jupiter. *Icarus* 59:169–176.

Pirraglia, J. A., B. J. Conrath, M. D. Allison, and P. J. Gierash (1981). Thermal structure and dynamics of Saturn and Jupiter. *Nature* (London) 292:677–679.

Riddle, A. C., and J. W. Warwick (1976). Redefinition of System III longitude. *Icarus* 27:457–459.

Shaw, R. (1984). *The dripping faucet as a model chaotic system.* Ariel Press, Santa Cruz.

Smith, B. A., L. A. Soderblom, T. V. Johnson, A. P. Ingersoll, S. A. Collins, E. M. Shoemaker, G. E. Hunt, H. Masursky, M. H. Carr, M. E. Davies, A. F. Cook, II, J. Boyce, G. E. Danielson, T. Owen, C. Sagan, R. F. Beebe, J. Veverka, R. G. Strom, J. F. McCauley, D. Morrison, G. A. Briggs, and V. E. Suomi (1979a). The Jupiter system through the eyes of Voyager I. *Science* 204:951–972.

Smith, B. A., L. A. Soderblom, R. F. Beebe, J. Boyce, G. Briggs, M. Carr, S. A. Collins, A. F. Cook, G. E. Danielson, M. E. Davies, G. E. Hunt, A. Ingersoll, T. V. Johnson, H. Masursky, J. McCauley, D. Morrison, T. Owen, C. Sagan, E. M. Shoemaker, R. Strom, V. E. Suomi, and J. Veverka (1979b). The galilean satellites and Jupiter: Voyager 2 imaging science results. *Science* 206:927–950.

Smith, B. A., L. Soderblom, R. Beebe, J. Boyce, G. Briggs, A. Bunker, S. A. Collins, C. J. Hansen, T. V. Johnson, J. L. Mitchell, R. J. Terrile, M. Carr, A. F. Cook, II, J. Cuzzi, J. B. Pollack, G. E. Danielson, A. Ingersoll, M. E. Davies, G. E. Hunt, H. Masursky, E. Shoemaker, D. Morrison, T. Owen, C. Sagan, J. Veverka, R. Strom, and V. E. Suomi (1981). Encounter with Saturn: Voyager 1 imaging science results. *Science* 212:163–191.

Smith, E. J., and S. Gulkis (1979). The magnetic field of Jupiter: A comparison of radio astronomy and spacecraft observations. *Ann. Rev. Earth Planet. Sci.* 7:385–415.

Sromovsky, L. A., H. E. Revecomb, V. E. Suomi, S. S. Limaye, and R. J. Krauss (1982). Jovian winds from Voyager 2. Part II: Analysis of eddy transports. *J. Atmos. Sci.* 39:1433–1445.

Stoker, C. R. (1986). Moist convection: A mechanism for producing the vertical structure of the jovian equatorial plumes. *Icarus* 67:106–125.

Stone, P. H. (1972). A simplified radiative-dynamical model for the static stability of rotating atmospheres. *J. Atmos. Sci.* 29:405–418.

27

Variations in the Jovian Atmospheric Composition and Chemistry

Pierre Drossart
Observatoire de Paris, Meudon

Régis Courtin
Observatoire de Paris, Meudon

Sushil Atreya
University of Michigan, Ann Arbor

Alan Tokunaga
University of Hawaii, Honolulu

Abstract

After the Voyager observations, a mean atmospheric composition model has become available from a combination of spacecraft and ground-based measurements, and this model can be used as a reference for future studies on the spatial and temporal variations of atmospheric composition. A further step for understanding the jovian atmospheric structure is therefore the study of departures from this "standard atmosphere."

This chapter first reviews the existing observational evidence for variations of atmospheric composition. Although the major constituents are expected to remain constant throughout the atmosphere, physicochemical phenomena can induce vertical as well as horizontal variations. Such variations are documented for only a few constituents, and they can be accounted for by

several mechanisms: condensation (NH_3), chemical reactions (PH_3), or stratospheric photochemistry (C_2H_2, C_2H_6). Search for temporal variations should be based on a thorough knowledge of the spatial and vertical variations in the atmosphere.

Temporal variations can be expected (1) from external driving mechanisms, such as the ultraviolet (UV) or energetic particle fluxes for photochemistry in the stratosphere, or the obliquity for seasonal effects, and (2) from internal dynamics, which can induce meteorological changes on time scales between 10^4 and 10^8 s, or long-term secular variations on time scales of 10^8 s or larger. We attempt to identify theoretical ideas that will need to be developed in the near future.

Although most of these time variability phenomena remain hypothetical, it seems possible to begin constructing an observational data base by which these ideas can be tested. Furthermore, since spatial and temporal variations must be disentangled, the first goal is to achieve high-spatial-resolution observations. We describe some observations that could be made throughout the electromagnetic spectrum between now and the onset of the Galileo observations.

INTRODUCTION

Since we are concerned with variations in the composition of the jovian atmosphere, it may be useful to define a "standard composition" to which measurements at a given time and over a particular region of the disk can be compared to. Such a model will of course be somewhat arbitrary, because all the available observations that can be used to determine it do not correspond to the same period or the same portion of the disk. Whether or not this exercise will prove interesting for the study of compositional variations, we cannot tell at the moment. At least, we hope that it will provide a clear picture of where we stand in terms of the accuracy of composition determination. In table 25, we list the mole fractions of the jovian atmospheric constituents that have been identified through more than one set of measurements (i.e., we have excluded estimates resulting from a tentative detection). All determinations correspond to regions whose center coincides with the center of the disk, but whose extent in latitude greatly varies (up to $\pm 40°$). The period of reference is roughly centered around the Voyager encounters (1975–83), and the pressure level of reference in the atmosphere is just below the intermediate condensation cloud around 2 bar, except for H_2O whose mole fraction is given at the 6-bar level, and for hydrocarbons (C_2H_2, C_2H_6) which are abundant only in the stratosphere. For NH_3, PH_3, and H_2O, vertical distributions are given in figure 190.

It is rather gratifying that for the three most abundant species after H_2, that is for He, CH_4, and NH_3, the relative uncertainty on the mole fraction is down to the 20 percent level approximately. Obviously, the situation

Table 25. Standard Jovian Composition (Equatorial Region)

Molecule	Mole fraction	Approximate uncertainty (percent)	Pressure level (bar)	Reference
H_2	0.90	2	—	Gautier et al. (1981)
He	0.10	20	—	Gautier et al. (1981)
CH_4	2.5×10^{-3}	20	—	Gautier and Owen (1983)
NH_3	2.5×10^{-4}	20	≥ 2	de Pater (1986)
H_2O	3.0×10^{-5}	60	6	Bjoraker et al. (1986b)
PH_3	5.0×10^{-7}	50	2	Kunde et al. (1982) Bjoraker et al. (1986a)
CO	1.5×10^{-9}	30	2	Bjoraker et al. (1986a) Noll et al. (1987)
HCN	2×10^{-9}	100	≥ 0.1	Tokunaga et al. (1981)
GeH_4	7.0×10^{-10}	50	2	Bjoraker et al. (1986a)
C_2H_2	2.0×10^{-8}	200	≤ 0.1	Maguire et al. (1985)
C_2H_6	3.0×10^{-6}	100	≤ 0.1	Maguire et al. (1985) Kostiuk et al. (1987)

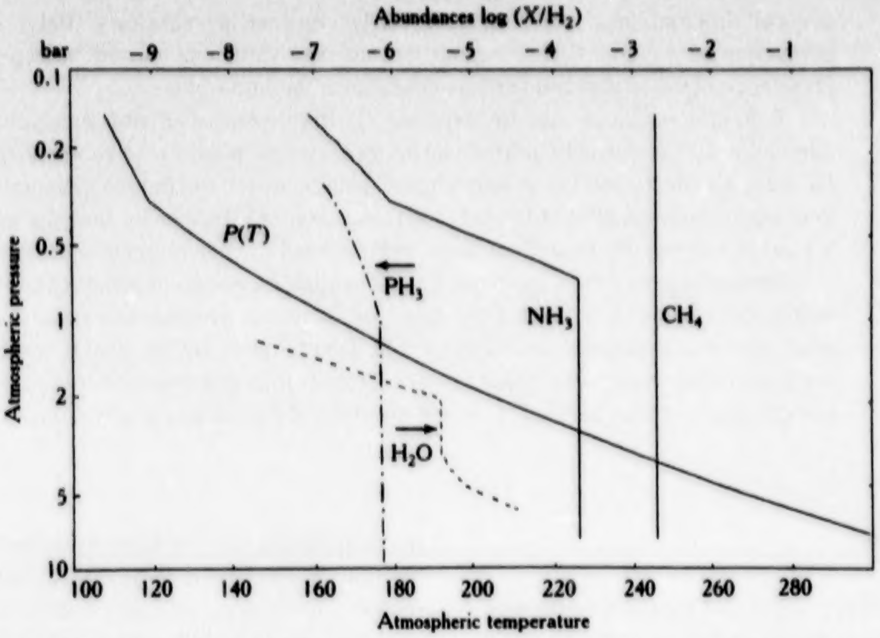

Figure 190. NH_3, PH_3, and H_2O vertical distributions. After Bjoraker (1984) and Kunde et al., (1982).

is much less satisfactory for other minor constituents of great interest like H_2O, PH_3, or GeH_4, and it is rather embarrassing for the hydrocarbons such as C_2H_2. For some of these molecules, in fact, we cannot rule out the possibility that spatial or temporal variations have contributed significantly to the large uncertainty, for example in the case of PH_3. For other constituents, the large error bar partially reflects the inaccuracy of the spectroscopic data, or of the thermal structure. For instance, both problems were encountered in the case of C_2H_6, which is observed in emission at altitudes where the temperature profile is poorly known, and for which values of the band strength at 12 μm were until recently based on only medium resolution measurements.

The methodology for recording temporal variations of atmospheric constituents is not simple: some constituents vary with altitude as well as on a horizontal scale, and it is hopeless to try to understand variations of the disk-averaged composition, without a knowledge of spatial variations. Horizontal variations are only roughly documented and uncertainties in the vertical profiles will probably not be reduced until Galileo observes Jupiter.

Temporal variability within the atmosphere could occur in several ways:

1. *Externally driven time variations:* The solar cycle and the orbital motion could induce cyclic variations in constituents. These effects are expected only in the upper part of the atmosphere, since solar UV variation affects only the stratospheric photochemistry, and seasonal effects (if any) are attenuated by the radiative time and are also expected to be confined to the stratosphere. Stratospheric constituents are the most obvious candidates for studies of these effects (C_2H_2 and C_2H_6). Correlations with auroral observations (cf., Clarke et al., this volume) are needed to advance this field.

2. *Dynamic time variations:* The characteristic time scales of the atmospheric motions can induce variations in the abundance of constituents on a hierarchy of time scales. The apparent stability of the atmosphere seems to imply very slow secular variations in the global composition, but meteorological effects could superimpose smaller-scale variations in the features of the atmosphere (great red spot [GRS], plumes, barges, and the like). Gierasch et al. (1986) predict values of radiative time constant and *para*-hydrogen relaxation time between 10^8 and 10^9 s, and argue that momentum transport in the upper troposphere ($P \leq 700$ mbar) is weaker than radiative processes. Variations in the upper troposphere could thus take place only on time scales longer than 10^8 s. The atmosphere of Jupiter is in a global state of apparent stability and it can be thought that large scale spatial variations of the true composition are stationary in time. The spatial scale of these variations could therefore give some constraints on

the dynamics (or more precisely, the kinematics) of the atmosphere, from advection terms in the equations of evolution. Disequilibrium species (GeH_4, PH_3, . . .) are the candidates for such research.

The first step to observe temporal variations in the atmosphere is to record the spatial variations on the disk. This has important consequences for the methodology of observations; in particular, high-spatial resolution is definitely needed to separate local variations at the smallest possible scale. Spectral resolution is no less important, to discriminate between lines of various constituents, or to ultimately retrieve the line shapes to get information on the vertical profiles. In the infrared, Voyager infrared interferometer spectrometer (IRIS) data are limited to medium spectral resolution ($\Delta\sigma = 4.3$ cm^{-1}). Moreover, the spatial resolution for individual spectra, although much better than for any ground-based infrared observation, often has to be reduced by averages to increase the signal-to-noise, especially in the 5-μm window. Spectroscopy with imaging capabilities seems then the best way to observe spatial-temporal variations of Jupiter constituents. A field of view of 1 or 2 arcsec is required to characterize the large-scale features of the atmosphere (great red spot, barges, plumes). If we take for the evolution of these features a dynamical time scale of a few days, this gives also the smallest scale of time variation. Other time scales are expected on a jovian year or a solar cycle.

OBSERVATIONS

Only some variability has been documented (NH_3, H_2O, C_2H_2, and C_2H_6). The observations being very disparate, we do not attempt here to give a global approach of the variations in the atmospheric composition of Jupiter, but we describe, molecule by molecule, the results and the conclusions that can reasonably be made. As an aid for the comprehension of the following sections, table 26 shows the variation of the mean atmospheric level sounded as a function of wavelength.

Hydrogen

From an analysis of the Voyager IRIS spectra in the H_2 pressure-induced absorption range between 300 and 700 cm^{-1}, Conrath and Gierasch (1984) have shown first, that the *para*-hydrogen fraction near the 300-mbar pressure level is not in thermodynamic equilibrium, and second, that this fraction varies from equator to pole, with values closer to equilibrium at high latitudes. The recent study of Gierasch et al. (1986) correlates these variations to those of the temperature at the 270-mbar level (cf., Flasar, this volume).

Ammonia

The very large array (VLA) observations of Jupiter at 1.3, 2, and 6 cm (de Pater, 1986) reveal an atmospheric zonal structure with bands roughly positioned on the north equatorial belt (NEB) and south equatorial belt (SEB). The spatial resolution of these observations is about 1.5 arcsec (1/30 of the disk). Since the opacity at these wavelengths is mostly due to NH_3, at pressure levels between 0.5 and 10 bar, and since the thermal structure is thought to be rather uniform in the deep troposphere the conclusion is that ammonia abun-

Table 26. Atmospheric Levels Sounded at Selected Wavelengths

Wavelength	Wavenumber (cm^{-1})	Pressure level (bar)	Reference
20.5 cm	0.05	10	de Pater, 1986
6.1 cm	0.2	4.1	" "
2.0 cm	0.5	0.76	" "
1.3 cm	0.8	0.32	" "
44.2 μm	226	0.8	Gierasch et al., 1986
16.6 μm	602	0.15	" "
7.7 μm	1306	0.01	Kunde et al., 1982
4.8 μm	2100	4–6	" "
0.22–0.3 μm		0.01–0.1	Atreya, 1986
8900 Å		0.4–0.5	West, 1979
3000 Å		0.2	" "
1500–1750 Å		0.003–0.04	Gladstone and Yung, 1983
1000 Å		0.8×10^{-6}	Atreya, 1986

dance varies between zones and belts. The NH_3 mixing ratio in belts is about half the one measured in zones.

At 5 μm, NH_3 and H_2O lines are present, and there is a possible contribution from H_2O to the variations in the 2050 cm^{-1} opacity. A complete analysis remains to be done at 5 μm: It would require high-spectral resolution, and the use of a multiple scattering model for the radiative transfer analysis. New spectroscopic measurements of the $2\nu_2$ band of NH_3 allow a reanalysis of the 5 μm window from Voyager IRIS spectra in the 1880–2000 cm^{-1} range (Lellouch et al., 1987). Preliminary results from this work also suggest a depletion in the belts by a factor of two compared to the zones.

The Voyager infrared observations have been used by Gierasch et al. (1986) to study the variations of ammonia over the jovian disk and of its correlations with the variations of the thermal profile, the cloud opacities, and the *para*-hydrogen ratio. A three parameter model (Conrath and Gierasch, 1986) is used to retrieve the gaseous ammonia abundance and cloud opacities at 45 μm and 5 μm from the IRIS spectrum at 217 cm^{-1}, 225 cm^{-1}, and 2050 cm^{-1}; the level sounded for the ammonia abundance determination is about 680 mbar. A correlation is found between ammonia variations, orange reflectivity, and the vertical velocity field, w, as estimated from a scale equation of the heat flux (see fig. 191). This correlation would imply vertical motions extending through a scale height of the atmosphere.

Comparing now to the centimeter and 5 μm observations, the same variations in latitude are roughly found, at lower spatial resolution. If the same mechanism can be invoked, this would imply an extension of the vertical velocity field to the deep troposphere too.

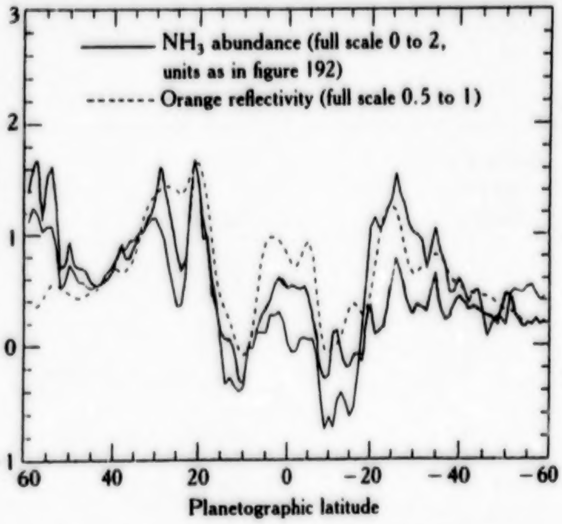

Figure 191. Comparison of NH_3 variations, orange reflectivity and vertical velocity. After Gierasch et al., 1986.

Ammonia is photodissociated below about 2300 Å and it is not expected in detectable amounts above the tropopause where solar UV photons can easily penetrate. This was confirmed by International Ultraviolet Explorer (IUE) observations between 1900 and 2300 Å (Combes et al., 1981; Wagener et al., 1985), which are best interpreted with a distribution of NH_3 rapidly decreasing in the lower stratosphere. However, an interesting result has been reported by Wagener and Caldwell (1987) who found that NH_3 absorption bands near 2000 Å are stronger in the GRS than at neighboring longitudes. They conclude that rapid vertical transport in the GRS is a plausible mechanism for the origin of this enhancement. It should be noted that no significant differences were found for PH_3, neither in the same IUE spectra, nor in Voyager IRIS spectra recorded over the GRS and neighboring regions (Kim and Owen, 1985).

Infrared heterodyne measurements by Kostiuk et al. (1977) showed possibly stratospheric emission lines of NH_3 in the north and south polar auroral regions.

Water

H_2O was observed on Jupiter from airborne observations on the Kuiper Airborne Observatory at 5 and 2.7 μm (Larson et al., 1975, 1984; Bjoraker et al., 1986b) and by Voyager IRIS (Kunde et al., 1982; Drossart and Encrenaz, 1982; Bjoraker et al., 1986b). Weak H_2O lines between 2020 and 2090 cm^{-1} originate in the pressure range between 4 and 7 bar (Bjoraker et al., 1986b). From the analysis of these lines the abundance of H_2O in the deep troposphere is found to be 3×10^{-5}. Moreover, comparison of zones and belts abundances (fig. 192) imply spatial variations (depletion in the NEB hot spots, constant values in the SEB, and zones between 2 and 4 bars). This abundance of H_2O seemed to imply a depletion of oxygen compared to the solar value by a factor of 50. However, new measurements (Noll et al., 1987) of another oxygenated compound, CO (see below), suggest a nearly solar O/H (Fegley and Prinn, 1987).

An attempt to model the puzzling distribution of H_2O was made by Lunine and Hunten (1987). In this model, derived from a model for equatorial plumes by Stoker (1986), moist convection is supposed to have large (100 to 10,000 km) cells of sinking air (with undersaturation of H_2O) and small plumes (10 to 100 km) of

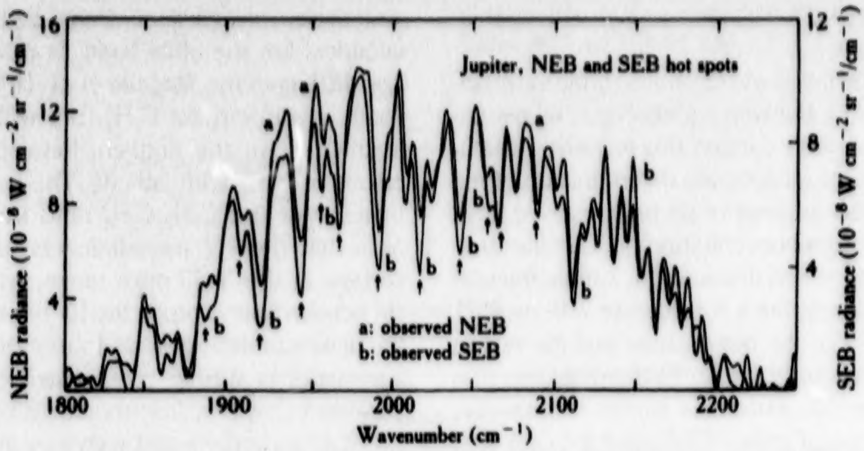

Figure 192. Variations of H_2O between NEB and SEB. After Bjoraker et al., 1986b.

rising saturated gas. The different scales can explain the observation of an apparently low H_2O abundance. Observational tests of this model could be achieved by recording spectra of different regions (plumes compared to dryer areas), but H_2O line observations are presently possible only from airborne observations.

Phosphine

PH_3 is a disequilibrium species and its variations could give important information on the vertical motions on Jupiter. Phosphine has been observed in the infrared (10 and 5 μm). Although recorded variations of PH_3 are only tentative, in the next few years the 5-μm spectroscopy can give new information on PH_3. PH_3 was an unexpected constituent, when observed by Ridgway et al. (1976), since the stable chemical state of phosphorus at tropospheric temperatures is an oxidized compound (P_4O_6 dissolved in H_2O). Its presence in the troposphere implies disequilibrium phenomena. The vertical profile of PH_3, as inferred from 10-μm and 5-μm spectroscopy by Voyager IRIS (Kunde et al. 1982), gives a satisfactory fit of the spectrum in both regions. From 5-μm CVF observations of the jovian disk in 1982 at IRTF, Drossart et al., 1983) tentatively concluded that there were variations of PH_3 between belts and zones. These observations should be repeated at higher-spectral resolution to discriminate fully between continuum effects related to cloud opacities and variations of abundances. IRIS spectra in the region of 2000 cm^{-1} could be used for that purpose, since new spectroscopic measurements of PH_3 combination bands (Tarrago et al., 1987) allow the full interpretation of this spectral region. Preliminary reanalysis of Voyager IRIS data at 5 μm does not show large variations of the phosphine abundance over the jovian disk.

Carbon Monoxide

In the case of CO, an ambiguity has existed since the publication of two contradictory analyses of near-infrared observations by Beer and Taylor (1978) and by Larson et al. (1978). Beer and Taylor favored a stratospheric distribution, whereas Larson et al. proposed a well-mixed tropospheric profile to interpret their airborne measurements. Both distributions have their justification. In the first case, CO is formed by reactions involving exogenic OH molecules (produced from oxygen bearing constituents, such as water from meteorites or oxygen atoms from the Io torus) and CH_3 radicals produced in the CH_4 photochemistry ($OH + CH_3 \rightarrow CO + 2H_2$) (Prather et al., 1978; Strobel and Yung, 1979). In the second case, CO would be brought up by strong convective motions from the deeper and hotter regions of the troposphere, and in that process, reducing reactions that tend to convert CO to CH_4 are quenched (Prinn and Barshay, 1977).

Subsequent infrared airborne observations of Jupiter in the 5-μm spectral window by Bjoraker et al. (1986a) led to the detection of 18 lines of CO in the 1–0 vib-rotational band. These authors attempted to reproduce the CO lines with two different models, one assuming a mole fraction of 4×10^{-8} in the stratosphere, the other a well-mixed value of 1×10^{-9}. The overall agreement reached in the latter case is significantly better and suggests that the presence of CO in the jovian atmosphere is indeed a consequence of deep mixing processes.

Recent ground-based observations in the same region of the spectrum, but with a higher-spectral resolution by Noll et al. (1987) confirm this tentative conclusion and provide a more accurate determination of the CO distribution. The analysis of six fully resolved lines clearly excludes a high concentration of CO in the stratosphere. For a well-mixed distribution, a mole fraction of 1.6×10^{-9} is found, but a hybrid case with most (1×10^{-9}) of the CO in the troposphere and the rest in the stratosphere is also possible. Furthermore, no spatial variation in the CO abundance is seen between the NEB, the north tropical zone (NTrZ), and the GRS after correction is made of the haze plus cloud optical depth variation.

Hydrogen Cyanide

HCN has been observed at 13 μm (Tokunaga et al., 1981). Its formation is not well understood, however the fact that it appears in absorption indicates that it is abundant in the troposphere. Recent measurements of the same spectral region seem to imply a lower abundance of HCN (Drossart et al., in preparation). If HCN is produced by photochemistry, variations can be expected with solar irradiance (during the solar cycle). But such an interpretation remains speculative, since we do not understand exactly the formation of HCN. Tokunaga et al. argue that photochemical production is the most likely source.

Germane

Germane was first detected by Fink et al. (1978) in the atmosphere of Jupiter. Only the Q branch of the ν_3 branch of germane can be seen in Voyager IRIS spectra, but Bjoraker et al. (1986a) recorded several other groups of lines of GeH_4. Some variations are seen between various samples of IRIS spectra, the Q branch being stronger in zones than in belts, according to Bjoraker (1984). It must be noticed that since the Q branch of germane is blended with the $\nu_2 + \nu_4$ branch of PH_3, high-resolution spectra would be useful to study such variations.

Acetylene and Ethane

Spatial variations in the UV absorption of C_2H_2 have been observed by Clarke et al. (1982). The high-altitude abundance of acetylene seems to be larger at higher latitudes. On the other hand, from an analysis of Voyager IRIS spectra, Maguire et al. (1985) report a north-south asymmetry for C_2H_2 (but with a nearly-uniform abundance in the northern hemisphere), and an increase of C_2H_6 with latitude. The resulting effect is an increase of the C_2H_2:C_2H_6 ratio from south to north. Note that the UV measurements are sensitive to absorbers in the 3–40 mbar range, whereas the infrared (IR) observations probe the 10–100 mbar region. Thus, the determination of spatial variations from these measurements is further complicated by the altitude dependency of the hydrocarbon distribution, although the IRIS data for ethane and acetylene near 740 cm^{-1} (with a resolving power of 4.3 cm^{-1}), are sensitive to the 1–40 mbar range too. In the case of acetylene, a strong north-south asymmetry has been observed for Jupiter's polar regions (Wagener and Caldwell, 1987). It is hypothesized that a depletion of C_2H_2 occurs in the jovian stratosphere over the south polar region, as a consequence of enhanced production and condensation of polyacetylenes.

Kostiuk et al. (1987) recently reported the results of several measurements of individual C_2H_6 emission lines in the ν_9 band near 12 μm with ultra-high resolution (10^6) heterodyne spectroscopy. Mole fractions retrieved at various locations on the jovian disk are not very different from the average equatorial value of $2.8 \pm 0.6 \times 10^{-6}$, except inside the auroral oval, and within the footprint of the Io flux tube (fig. 193). Higher values (5×10^{-6}) are observed near the boundaries and some very low values are found over the north auroral "hot spot." On the contrary, the south auroral region exhibits substantial ethane enhancements. These facts, together with the above-mentioned results, suggest that acetylene is preferentially formed at the expense of ethane in the north polar region, although there is still some uncertainty as to how much of the observed variations can be attributed to temperature changes in the stratosphere.

Observations of C_2H_2 were made at 13 μm by Noll et al. (1986) and Drossart et al. (1986). The abundances derived by these authors are very different:

Noll et al., 1986: $\frac{C_2H_2}{H_2} = 1.1 \times 10^{-7}$,

Drossart et al., 1986: $\frac{C_2H_2}{H_2} = 1 \times 10^{-8}$.

Although different radiative transfer models and atmospheric profiles were used, there appear to have been genuine changes in the C_2H_2 stratospheric abundance.

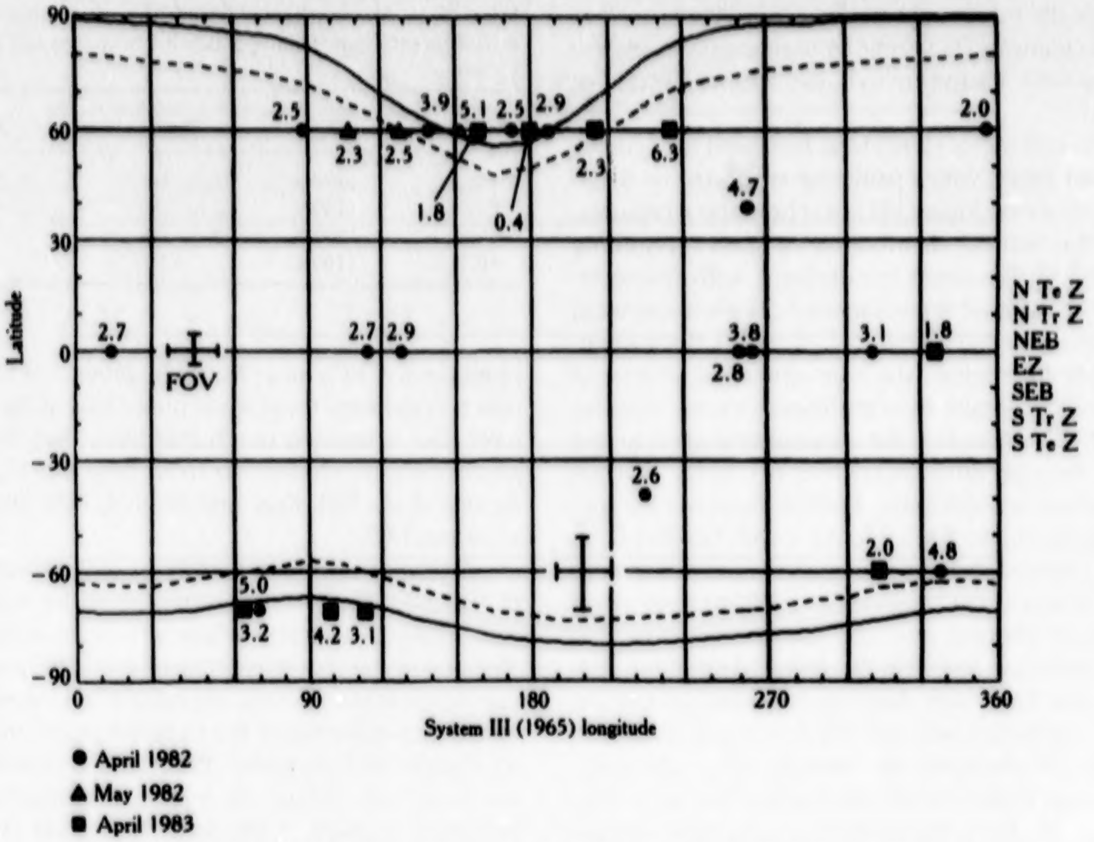

Figure 193. Variations on Jupiter of C_2H_6 by mole fractions ($\times 10^{-6}$) over the disk. After Kostiuk et al., 1987.

Temperature variations are observed in the stratosphere at a level of a few degrees (Orton, 1986), and it seems too low to account for the observed differences in the synthetic calculations.

Year to year measurements of both ethane and acetylene are necessary to improve these observations and to correlate them with stratospheric temperature studies.

Other Minor Constituents

New molecules have been detected (C_2H_4, C_6H_6) or tentatively detected (C_3H_4) by Kim et al. (1985) in a small active area in the stratosphere of the north polar region (Caldwell et al. 1980). This region is a zone of intense auroral activity (these phenomena are studied in the chapter by Clarke et al.). Observations of this region have been done by Drossart et al. (1986), showing acetylene enhancement and by Kostiuk et al. (1987), showing ethane depletion.

THEORETICAL ASPECTS

Disequilibrium Species in the Jovian Troposphere

During the past decade or so, a number of theoretical pathways have been proposed, and to a different extent worked out, for the synthesis of disequilibrium species in the lower troposphere of Jupiter:

- Quenching of equilibrium thermochemical reactions through rapid vertical mixing,
- Shock heating synthesis,
- Electrical discharge synthesis during thunderstorms, and
- Hot atom chemistry.

All of these processes exhibit, to various degrees, a character of variability in space or in time. Therefore, they are interesting phenomena from the point of view of the compositional variations. However, there seem to exist opposite trends between the efficiency of each of these mechanisms (measured by their ability to explain the observed abundances) and their degree of variability.

Lewis and Fegley (1984) have reviewed the sources mentioned above, with a particular emphasis on deep-mixing processes. Figure 194 is a schematic representation of the vertical distribution of gases assuming quenching in the lower troposphere with (curve labelled *P*) or without (curve labelled *Q*) photochemical production at higher altitudes. T_q denotes the quenching temperature below which the chemical lifetime of the species is longer than the characteristic time for mixing H^2/K (where H is the atmospheric scale height and K is the eddy diffusion coefficient). In the absence of photochemical synthesis, the distribution of the species follows a curve similar to the curve labelled *Q*, in which T_c represents the temperature below which condensation may occur (dashed line). Photodissociation by solar UV photons may also take place above that level (dot-dashed line). On the other hand, if the species results from both deep mixing *and* photolysis, then its distribution will look like the curve labelled *P*.

Table 27 compares the predictions of the deep-mixing model with the observed abundances of PH_3, CO, GeH_4, and HCN. The model assumes solar composition below the 300 K level and a coefficient of turbulent diffusion $K = 2 \times 10^8$ cm^2 s. An excellent agreement exists for PH_3, CO, and GeH_4, although it may be fortuitous in some cases, like PH_3 for which chemical kinetics are still poorly known. For HCN, the model fails, although an alternative explanation could be the production of HCN as a photolytic product of CH_3NH_2, which could itself result from quenching at the 1500 K level. This is probably much less likely than the direct photochemical production from NH_3 and C_2H_2 (Tokunaga et al., 1981; Kaye and Strobel, 1983; Ferris and Ishikawa, 1987).

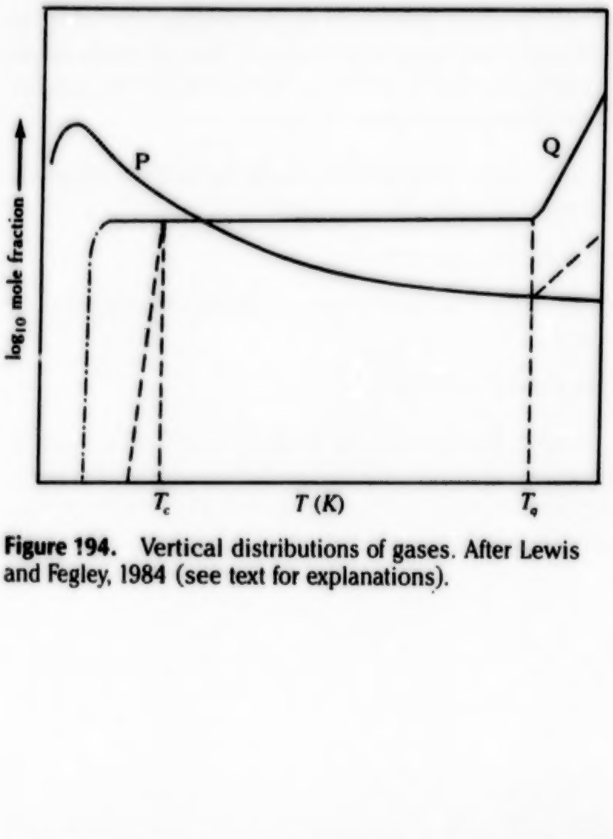

Figure 194. Vertical distributions of gases. After Lewis and Fegley, 1984 (see text for explanations).

Table 27. Abundances of Disequilibrium Species Predicted by the Deep-Mixing Model, Compared to Observed Values

Molecule	T_q	$X_{equil.}$	$X_{obs.}$
PH_3	1300 K	4×10^{-7}	5×10^{-7}
CO	1100 K	2×10^{-9}	1.5×10^{-9}
GeH_4	800 K	8×10^{-10}	7×10^{-10}
HCN	1100 K	$\approx 10^{-12}$	$\approx 10^{-9}$

Spatial and temporal variations in the abundances of disequilibrium species brought up in the observable atmosphere by convective flow will necessarily reflect changes in the characteristics of the latter phenomenon (for instance the vertical profile $K(z)$). As indicated by the near-uniformity of the radiative output measured by Voyager IRIS (Pirraglia, 1983), the convective flow must vary with latitude on Jupiter, to compensate the latitudinal gradient of the solar heat input (Ingersoll and Porco, 1978). Hence, it is possible that the abundances of such dynamic tracers as PH_3, CO, or GeH_4 might exhibit latitudinal gradients with an opposite trend to that of the solar illumination. Theoretical estimates for these gradients need to be made. The recent observations of CO by Noll et al. (1987), which yield constant mixing ratios of CO at the 2-bar level in the NEB, NTrZ, and GRS, are not really conclusive because they do not extend to high latitudes. Observations of that type, however, extended to higher latitudes and to other tracers, would be extremely valuable.

Seasonal and secular variations, on the other hand, are not likely to be significant because of the large value of the radiative time constant at the altitudes of the lower troposphere ($p \geq 600$ mbar) and because intrinsic variations of the convective flow are not expected to be important, at least on time scales that are small compared to the age of the solar system.

Shock heating synthesis appears to be another plausible source of HCN or CO during jovian thunderstorms (Bar-Nun and Podolak, 1985). However, it is unlikely that the global abundance of hydrogen cyanide results from this highly localized mechanism, given the large dilution of the products in the atmosphere. On the other hand, this component would certainly exhibit significant temporal variations.

Similar remarks apply to the two other proposed mechanisms. Production rates of organic material in electrical discharges or by hot atom chemistry, for example, appear to be negligible compared to the photochemical yields, when proper scaling is applied to the results of laboratory experiments (Lewis and Fegley, 1984).

Chemical, Physical, and Dynamic Processes Affecting the Composition Change

In this section, certain processes are discussed that are responsible for inducing changes in the composition with time and latitude. Broadly speaking, these changes fall into two categories—those driven by an external stimulus, and those that are caused by the changes in the planet's own internal structure and dynamics.

An example of the externally driven variation of the composition is the abundance of the hydrocarbons in the high-latitude region of Jupiter. Infrared "bright spots" have been detected for C_2H_2 in the region of zenographic latitude, 58 ± 10° and longitude 178 ± 10° (System III, 1965). For the corresponding longitude, the Voyager UV aurora were detected at latitudes of 56 (+4, −3) degrees (Broadfoot et al., 1979, 1981). Due to the finite dimension of the UV Spectrometer slit on this polar limb aurora, the auroral zone is uncertain by a few degrees. In any event, the UV auroras are virtually in the same zenographic locations as the infrared bright spots—giving rise to a speculation that both are triggered by the same mechanism. The UV auroras result from the precipitation of energetic charged particles, principally electrons and heavy ions. The range of electrons in the jovian atmosphere would be greater than that of ions with corresponding energy. From the Voyager measurement of the intensities of auroral H_2 Lyman and Werner bands and the H Lyman-alpha, the power input into the auroral zone is calculated to be 10^{12}–10^{13} W. This translates into an energy flux of 1–10 erg cm^{-2} s^{-1} into the auroral zone. The energetic sulfur and oxygen ions (see later) would deposit their energy in the vicinity of the homopause, the electrons deeper. (At the Voyager epoch the homopause was found to be located at a pressure level of 1 μbar in the equatorial region.) It is therefore quite feasible that the infrared bright spots of C_2H_2 are caused by an enhanced abundance of this constituent, resulting from an increased dissociation of CH_4 and the subsequent chemistry (see Atreya [1986, pp. 98–105] for the latest details of the hydrocarbon chemistry). If the UV aurora are caused by electrons (rather than ions), it is likely that an increase in the abundance will be associated with an increase in the stratospheric temperature as well. The increased dissociation of CH_4 does not necessarily imply a decrease in the CH_4 abundance either. On the contrary, an enhancement in the CH_4 abundance is most likely. This is due to the fact that the charged particles would dissociate H_2 as well, resulting in large downward flux of the H atoms. The hydrogen atoms play a dominant role in the CH_4 chemistry in the jovian atmosphere. For example, they react with CH_3 to produce CH_4, that is,

$$H + CH_3 + M \rightarrow CH_4 + M.$$

(CH_3 is produced on reaction between CH_2 and H_2. CH_2 is produced on dissociation of CH_4.) The greatly increased flux of H atoms would thus produce large abundance of CH_4. In fact, infrared bright spots of CH_4 have been detected in the same region as bright spots of C_2H_2.

The above reasoning taken a step further predicts a decrease in the ethane (C_2H_6) production as larger quantities of the CH_3 radicals would be consumed by the increased flux of the H atoms. C_2H_6 is produced primarily by the self-reaction between the CH_3 radicals, that is,

$$CH_3 + CH_3 + M \rightarrow C_2H_6 + M.$$

Indeed, in the region of the C_2H_2 and CH_4 infrared bright spots, a decrease in the C_2H_6 has been detected (Kostiuk et al., 1987). The above-mentioned hypothesis is presently being modeled quantitatively.

The charged particle precipitation is expected to result also in the increased production of the heavier hydrocarbons, particularly polyacetylenes (diacetylene, C_4H_2, and beyond, i.e., $C_{2n}H_2$, where $n = 2, 3, \ldots$ etc.). The polyacetylenes are produced subsequent to the dissociation of C_2H_2 by either the charged particles (e) or the solar photons ($h\nu$):

$$C_2H_2 + e(\text{or } h\nu) \rightarrow C_2H + H,$$

followed by

$$C_2H + C_2H_2 \rightarrow C_4H_2 + H,$$

and

$$C_4H_2 + e(\text{or } h\nu) \rightarrow C_4H + H,$$

or

$$C_4H_2 + e(\text{or } h\nu) \rightarrow 2C_2H,$$

followed by

$$C_4H_2 + C_2H \rightarrow C_6H_2 + H,$$

or

$$C_4H + C_2H_2 \rightarrow C_6H_2 + H,$$

and so forth.

The polyacetylenes absorb sunlight to longer wavelengths (≤ 4000 Å) than CH_4, C_2H_2, C_2H_4, or C_2H_6 (≤ 1800 Å). They could be the source of the aerosols that might influence the jovian stratospheric thermal structure.

The nature and characteristics of the abovementioned infrared bright spots and the polyacetylenes is expected to be highly variable, not only with zenographic latitude, but also with time. This is due to the fact that the charged particles responsible for them are modulated by Io and its plasma torus. The origin of the energetic ions is in the volcanoes of Io. Even between the epochs of Voyager 1 and Voyager 2 that were six months apart, large changes in the volcanic activity of Io were measured. Vulcanism tends to be highly episodic and unpredictable, even for Io. It is, therefore, expected that depending upon the volcanic activity of Io, the charged particle power input into the auroral region of Jupiter will go up or down. This would result in corresponding changes in the composition of the jovian atmosphere at the high latitudes.

In addition to the hydrocarbons discussed above, it is expected that the influx of the atoms or ions of sulfur and oxygen would result in the production of CO, HCHO (formaldehyde), CS, and COS (carbonyl sulfide). With the exception of CO, none of these other species have yet been detected, perhaps because of their low abundance. It should be noted that the source of CO could either be indigenous to Jupiter, or extraplanetary (see the section titled Observations for additional details). An extraplanetary oxygen bearing constituent (such as water from the meteoritic ablation, or oxygen atoms or ions from the Io torus) would subsequently react with the jovian hydrocarbons, thus producing the CO. Both the internal and the extraplanetary sources of CO are expected to exhibit temporal as well as latitudinal variation in CO.

Unlike the abovementioned particle induced changes, "regular" temporal and latitudinal variations in the abundance and the distribution of the photochemically active constituents are expected due to the change in the solar UV flux. An example of such a variation for ammonia is shown in figure 195. Also shown in this figure is the effect of change of atmospheric vertical mixing, which is characterized by the eddy diffusion coefficient, K. Our experience with the terrestrial atmosphere indicates that temporal as well as latitudinal variations in K are expected. So far K has been determined at only the equatorial region of Jupiter by Voyager. Although the eddy mixing is expected to be the dominant dynamic factor in the stratospheric chemistry, one should not ignore the possibility of stratospheric winds redistributing the constituents on a short time scale. No data on such winds are available.

Internal dynamics that may be responsible for rapid upwelling of certain disequilibrium species, such as PH_3, GeH_4, SiH_4, SeH_2, AsH_3, and perhaps CO, is expected to exhibit less of a temporal than a latitudinal change.

Although many of the physical, chemical, and dynamic processes affecting the atmospheric composition and its temporal and latitudinal variation are not directly measurable either now or from the planned

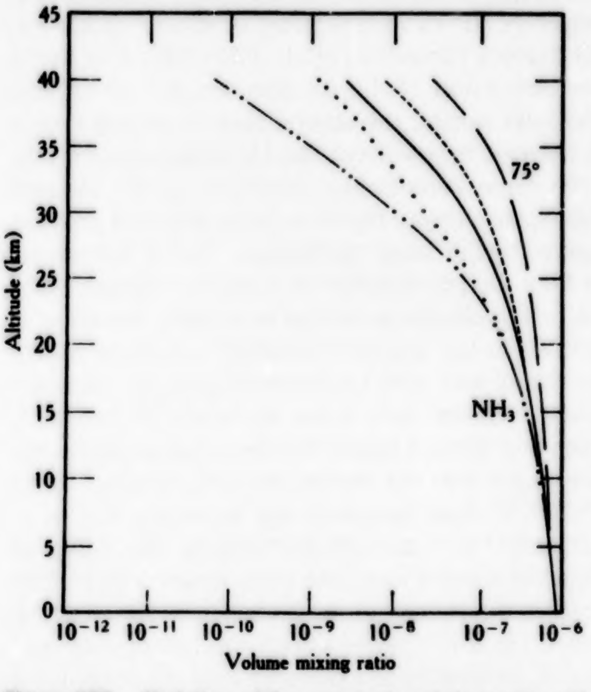

Figure 195. Variation of the ammonia mixing ratio with height for the various atmospheric models. Altitudes are above the cloud top. —— · · —— $T(z)$, $K = 2 \times 10^4$ cm^2 s^{-1} (constant); —— $T(z)$, $K \propto 1/M^{1/2}$; – – – $T(z)$, $K \propto 1/M$; —— ——, $T(z)$, $K \propto 1/M^{1/2}$, latitude = 75°, · · · · Strobel (1973). After Atreya et al., 1977.

spacecraft or the Earth-based observations, one can learn a great deal about them by monitoring the compositional changes on a regular basis.

PROSPECTS FOR FUTURE OBSERVATIONS

In this section, we examine the observations that could be done during the next decade to improve our knowledge of spatial-temporal variations of the gaseous composition of Jupiter. Although such a study is by no means a new ideal (Vogel, 1895), precise records of variations have only begun, and there is a need for simultaneous observations at different wavelengths to discriminate between temperature, cloud opacities, and compositional aspects. Therefore, it is important to review the present "state of the art" to allow a broad diffusion of the Jupiter's observational programs.

Earth-Orbit and Ground-Based Observations

Centimeter Range The high-resolution mapping of Jupiter's thermal radiation at 1.3, 2.0, 6.1, and 20.5 cm with the very large array, by de Pater and Dickel (1986), provides a solid basis for a survey of the distribution of ammonia absorption. Such a program should be carried out between now and the beginning of the Galileo measurements. The maximum resolution presently available at 2 cm (1.5 arcsec) is adequate to characterize variations of the ammonia abundance between belts and zones (de Pater, 1986), as can be seen from figure 191. Ammonia vertical profiles can be retrieved between 0.5 and a few bar.

Millimeter and Submillimeter Ranges Apart from filtered radiometric measurements (Hildebrand et al., 1985, Griffin et al., 1986), very little has been done for the study of the jovian atmospheric composition at these wavelengths. The main reasons for that were the lack of large antennas devoted to that region of the spectrum, as well as the difficulty in building wide-band receivers appropriate for the measurement of weak, broad spectral features seen in absorption against a thermal background. These difficulties are being reduced. At least five large antennas ($D \geq 10$ m) dedicated to millimetric and submillimetric observations have recently become or are about to become operational, with improved wide-band receivers ($\Delta\nu \approx 1$ GHz). Remaining problems, specific to the measurement of pressure-broadened absorption signatures in Jupiter's spectrum, are still important, however, because of the large fluctuations of the spectral baseline in the presence of a significant continuum signal. On the other hand, provided that the optical depth in the center of a line is large enough, extremely narrow features may be observed in emission. Millimetric instruments then become very powerful tools for probing the distribution of atmospheric constituents in the stratosphere and their variation in time.

Several studies have looked at the potential information that could be gained from millimeter and submillimeter observations concerning the composition of the jovian atmosphere (Bézard et al., 1986; Lellouch and Destombes, 1986). Figure 196 shows, for example, the numerous transitions calculated between 10 and 100 cm^{-1} (λ = 0.1 to 1 mm). HCN and PH_3, in addition to NH_3, have strong absorption features in this range. CO is probably not detectable, even with state of the art

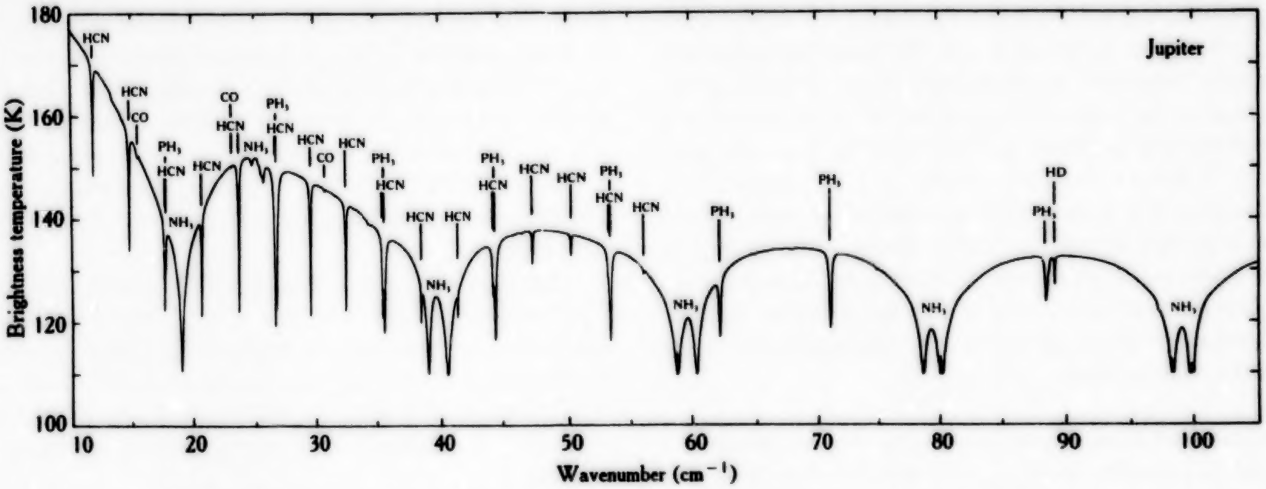

Figure 196. Molecular transitions in the submillimeter spectrum of Jupiter. After Bézard et al., 1986.

detectors. We are not considering here molecules that have not yet been detected but are predicted to have observable transitions (H_2S, HCP, and the like), since this would be the objective of a highly sensitive search rather than that of a temporal survey. However, should they be detected in the future, these species should be included in a temporal survey, because they are convenient tracers of the deep atmospheric chemistry.

From the ground, only wavelengths longer than 300 μm are accessible because of the telluric water vapor absorption. At the present time, one can foresee systematic studies of NH_3, PH_3, and HCN using either coherent or noncoherent receivers with a spectral resolution between 10^{-3} cm^{-1} (a few MHz) and 1 cm^{-1}. With the advent of large millimetric arrays (IRAM, Nobeyama) it will be possible to repeat the kind of work that is being done for NH_3 with the VLA, but with a slightly higher spatial resolution (0.5 to 1 arcsec at 1 mm with IRAM, for example). The first high-resolution millimeter maps of Jupiter may reasonably be expected for just a few years before the onset of Galileo measurements. In terms of vertical sounding of the atmosphere, there would be a good complementarity with the results of the photopolarimeter and radiometer (PPR) experiment on Galileo, in addition to the advantage of extended time coverage. To interpret such observations, however, laboratory measurements are needed for the pressure-broadened line shape of ammonia at wavelengths of a few millimeters (de Pater and Massie, 1985).

Far-Infrared Range Between 30 and 300 μm, observations have to be made at high altitudes with airborne or balloon-borne instruments, or from Earth orbit. Because of the high cost of operation inherent to these observations, it is difficult to warrant (or maybe even justify) their systematic use for repeated measurements. However, Jupiter being a strong source and because of the huge advance in sensitivity expected with forthcoming facilities, like the NASA airborne observatory SOFIA or the ESA satellite ISO, it is possible to envisage that a very small amount of their time could be regularly devoted to a well-targeted survey program of a few molecular lines (NH_3, PH_3, HCN, and $(H_2)_2$). Such observations could in fact be useful for the calibration of other spectroscopic measurements made with these facilities.

Near- and Medium-Infrared The region between 1 and 25 μm offers many possibilities for observations of Jupiter from the ground. Historically, it is in this part of the spectrum that most of the atmospheric constituents known to date have been discovered. Very high spectral resolution (10^4–10^6) can be achieved with the use of postdispersed Michelson interferometers, Fabry-Pérot spectrometers, and heterodyne receivers. Furthermore, relatively high spatial resolution can be attained with large telescopes (diffraction limit $\leq 0.1\,R_J$). It is therefore a region of choice for the study of compositional variations.

The 5-μm region and the 7–14-μm windows are particularly important because of the numerous molecular transitions occurring there. Interference from jovian cloud and haze particles will however hopelessly complicate the inference of temporal variations, if the spatial and spectral resolution are too low. There is also a strong need for simultaneous studies of the thermal structure to avoid an ambiguous interpretation of the origin of the observed variations.

Opportunities for further ground-based observations of Jupiter in the next six years include astronomical facilities in Hawaii, California, Arizona, and Texas. During the next few years, spatially resolved spectra of Jupiter at 5 μm will be obtained at Mauna Kea. The CGAS spectrometer at the NASA Infrared Telescope Facility (Tokunaga et al., 1987) will be used to map Jupiter at 2.5 arcsec spatial resolution and at medium spectral resolution (1 cm^{-1}) as has been done for PH_3 at lower-spectral resolution (CVF) (Drossart et al., 1983). The variations of phosphine, ammonia, or germane bands at such spatial resolution will provide a global map of possible spatial variations for these constituents, and a complete study of major atmospheric features (the great red spot mostly).

The Fourier transform spectrometer (FTS) built by J.-P. Maillard at the Canada-France-Hawaii Telescope (Maillard and Michel, 1982) will provide high-spectral resolution spectra (0.1 cm^{-1}) and a spatial resolution in some features (although a global mapping will not be possible in a reasonable time of observation). Some spectra were already recorded in 1986. Although the telluric atmospheric conditions do not allow a full scientific exploitation of these spectra, the techniques (pointing on atmospheric features, spectral range, etc.) have been tested.

Another productive instrument has been the 1–5 μm Fabry-Pérot spectrometer at the United Kingdom Infrared Telescope. This instrument has been applied to studies of CO on Jupiter (Noll et al., 1987). With a resolving power of up to 30,000 it is well suited for the study of line profiles at thermal wavelengths, especially at 5 μm.

Ultra-high resolution spectra of Jupiter with heterodyne spectrometers at 10 μm is likely to continue at

Mauna Kea. Such techniques can provide spectral resolution as high as 10^6 (Kostiuk et al., 1987) and with spatial resolution of about 2 arcsec with a 3-m telescope. The study of the stratospheric emission lines is well suited to this high-spectral resolution, indeed it is possible to resolve the Doppler-broadened lines. Although such spectrometers are limited in the spectral coverage and wavelength choice, the development of heterodyne spectrometers with tunable lasers as the local oscillator is likely to change the field dramatically.

The Kitt Peak National Observatory FTS has also been successfully used for the study of the jovian atmosphere. One of the earlier spectra obtained at 10 μm was extremely fruitful (Tokunaga et al., 1979). Recently, this spectrometer was outfitted with a cryogenic grating post-disperser that greatly increased its sensitivity at thermal wavelengths (3–25 μm) (Jennings,). Such a development has the potential of expanding the quantity and quality of infrared spectroscopy at 5–14 μm. Searches for minor constituents such as H_2CO, for example, can be effectively carried out with this instrument at 8–14 μm.

A 10-μm cryogenic echelle spectrometer has been constructed at the University of Texas by J. Lacy. With a resolving power of 10,000, this instrument also has the potential of obtaining new 10-μm spectra of Jupiter, especially in the search for new molecular species.

A cryogenic echelle spectrograph for 1–5 μm is also being constructed for the NASA Infrared Telescope Facility. With a resolving power of up to 40,000 and a slit of up to 30 arcsec in length, this instrument will be particularly powerful for studying line profiles, abundances, and spatial variations simultaneously. Completion of this instrument is for 1990, well in time to make observations of Jupiter before Galileo begins observations.

The observations of the types described above, if repeated during the next decade, could provide a data base for long-term observation of secular variations in the atmosphere of Jupiter. Well-recorded positions are needed for a long-term comparison with Galileo observations, however the Galileo observations will result in a revision of all previous analyses since a new interpretation of these data will be possible from the knowledge of the exact atmospheric structure. On the other hand, rapid revision of such data during the first few months of the Galileo experiment could increase the scientific return of the mission, by reprogramming some atmospheric observations.

Visible The visible part of the spectrum is affected largely by atmospheric scattering and by the cloud physical properties (West, 1979) and these aspects are reviewed elsewhere (Beebe et al., this volume). The effect of the hydrogen quadrupole lines have been studied by Cunningham et al. (1986) and show variations due to thermodynamics variations in the atmosphere (ortho-para H_2 variations). Correlations between cloud opacities and gaseous ammonia variations are clearly demonstrated in Gierasch et al. (1986).

Ultraviolet IUE observations of Jupiter extend now over a period of more than nine years, covering the spectral range 1100–3200 Å. They have allowed the detection and/or the study of a number of atmospheric constituents above the temperature minimum: NH_3, C_2H_2, C_2H_6, possibly C_3H_4 (allene), and C_3H_6 (cyclopropane), and also the determination of upper limits for several hydrocarbons (Wagener et al., 1985; Gladstone and Yung, 1983; Clarke et al., 1982; Combes et al., 1981; Owen et al., 1979).

The remaining lifetime of IUE is short, however. The Hubble Space Telescope (HST) is the long-hoped-for facility that will perform similar studies with a much higher sensitivity as well as higher spatial and spectral resolution. It should undoubtedly be possible to observe time variations in the chemistry of the jovian stratosphere with such a powerful instrument. The HST instrument that is the most suited to these studies is the high resolution spectrograph (HRS) ($\lambda = 1100–3200$ Å, $\lambda/\Delta\lambda = 10^5, 2 \times 10^4$, or 2×10^3; f.o.v. = 0.25×0.25 or 2×2 arcsec^2).

Among the difficulties that observers will face, is the fact that the solar spectrum, and therefore the reflected spectrum that is measured on Jupiter, is strongly variable below 1900 Å. There must be a simultaneous check on these variations. There is also a crying need for low-temperature measurements of absorption spectra in the laboratory, at resolutions comparable to that achieved by the HRS. Last, but not least, is the fact that HST will be heavily oversubscribed during the next decade. An observational framework such as the one proposed by the Space Telescope Scientific Working Group for Solar System Science (Belton et al., 1985) is a must if full advantage is to be obtained from the amazing potential offered by this unique facility.

Galileo Composition Measurements

Mass Spectrometer Direct in-situ composition measurements will be carried out by the neutral mass spectrometer on the probe. Simultaneous, supporting data on the atmospheric structure (pressure, temperature, density, and mean molecular weight), cloud structure, net flux, and the atmospheric electrical activity will be obtained by other instruments on the probe payload. Important complementary information of the visible troposphere will be provided by the solid state imager or camera on the orbiter. Some information on the upper atmospheric gases (i.e., beyond the tropopause) is

Table 28. Species Arranged According to Their Mass Numbers

AMU	Species	AMU	Species	AMU	Species
1		51	NH_4SH	101	
2	H_2	52	C_2N_2	102	$^{34}S_3$
3	^3He; HD	53		103	
4	^4He	54		104	
5		55		105	
6		56		106	
7		57	N_2H (from N_2H_4)	107	
8		58	N_2H_2 (from N_2H_4); C_4H_{10} (butane)	108	
9		59	N_2H_3	109	
10		60	N_2H_4	110	
11		61		111	
12	C (from CO cracking)	62	P_2	112	
13	CH	63		113	
14	N^{14}	64	P_2H_2; S_2	114	
15	N^{15}; CH_3	65	P_2H_3	115	
16	CH_4; NH_2	66	P_2H_4; S_2	116	
17	$^{13}CH_4$; CH_3D; NH_3	67		117	
18	$^{15}NH_3$; H_2O	68	S_2	118	
19	F (from HF cracking);$^{17}OH_2$	69		119	
20	HF; ^{20}Ne; $^{18}OH_2$	70		120	
21	^{21}Ne	71		121	
22	^{22}Ne	72	C_5H_{12} (pentane)	122	$(C_2H_5S)_2$
23	B_2H (from B_2H_6 cracking)	73		123	
24	B_2H_2 (from B_2H_6 cracking)	74		124	P_4; ^{124}Xe
25	B_2H_3 (from B_2H_6 cracking)	75		125	SbH_3
26	B_2H_4 (from B_2H_6 cracking)	76	GeH_4	126	^{126}Xe
27	B_2H_5; C_2H_3; HCN	77		127	I (from HI)
28	B_2H_6; N_2; CO; C_2H_4	78	AsH_3; C_6H_6 (benzene); ^{78}Kr	128	^{128}Xe; HI
29		79		129	^{129}Xe
30	HCHO; C_2H_6	80	Br; ^{80}Kr	130	^{130}Xe
31	CH_3NH_2	81	SeH_2; HBr	131	^{131}Xe
32	SiH_4	82	C_6H_{10} (from hexane); ^{82}Kr	132	^{132}Xe
33	$^{31}SH_2$; CH_3NH_4	83	C_6H_{11} (from hexane); ^{83}Kr	133	
34	$^{32}SH_2$	84	C_6H_{12} (hexane); ^{84}Kr	134	^{134}Xe
35	Cl (from HCl)	85		135	
36	$^{34}SH_2$; HCl; ^{36}Ar	86	^{86}Kr	136	^{136}Xe
37		87		137	
38	^{38}Ar	88		138	
39		89		139	
40	^{40}Ar	90		140	
41	CH_3CN	91		141	
42	C_2H_4N (from C_2H_5N)	92		142	
43	C_2H_5N	93		143	
44	C_3H_8 (propane); CO_2	94		144	
45		95		145	
46		96	$^{32}S_3$	146	
47	CH_3S	97		147	
48		98		148	
49		99		149	
50		100		150	

Table excerpted from "Galileo probe mass spectrometer descent science sequence," S. K. Atreya, D. M. Hunten, T. C. Owen, 1983 and 1985. *Internal report of the GPMS Investigation Team*, Principal Investigator, H. B. Niemann, GSFC.

likely from the ultraviolet spectrometer whose range is 500–4000 Å. Unlike Voyager, however, the stellar or solar occultations will not be possible because of the spinning mode.

The probe will enter the atmosphere in the near equatorial region (approximately 5° S latitude). Its nominal lifetime of 40 minutes will provide information to a depth where the pressure is 10 bar. It is, however, expected that useful data to a pressure level of 25 bar (descent time 60 minutes) will be transmitted to the Galileo orbiter for relay to the Earth. The neutral mass spectrometer will measure species beginning at the 100 mbar level, and in the mass range 2–152 AMU. One channel will be devoted to all masses greater than 126. The dynamic range of the quadruple mass analyzer is 10^8. Many constituents with mole fractions as low as 10^{-10} are expected to be detected with the help of gas enrichment cells. This will be particularly valuable for the measurement of the rare gases and the isotopes. A list of the gaseous species likely to be encountered in the region of the probe descent and expected to be detected by the neutral mass spectrometer is given in table 28. Prior to the Galileo measurement, long-term monitoring from 1 AU (ground-based, orbital, and suborbital) of several key species (such as hydrocarbons, NH_3, disequilibrium species, etc.) will be essential to study their temporal and latitudinal variability. A comparison of the 1-AU data with the Galileo data will be critical for such study; it will also provide cross calibration of the instruments.

NIMS and PPR The near-infrared mapping spectrometer (NIMS) (Hunten et al., 1986) will provide spectral maps of Jupiter with 0.025-μm spectral elements and spatial resolution between 100 and 1000 km (depending of proximity), in the 0.7 to 5.2 μm range. Synthetic spectra will be calculated for comparison to the NIMS observations at various wavelengths. The infrared jovian windows at 2.7 and 5 μm allows abundance measurements for NH_3, H_2O, PH_3, and probably GeH_4. The short-wavelength range (0.7 to 3 μm) is adapted to joint determinations of abundance and cloud observations. Temperature profiles are retrieved from the photopolarimeter and radiometer experiment (Hunten et al., 1986). A calibration of the full procedure would be possible by observing the probe entry site of Galileo with NIMS. Global mapping of the equatorial regions of Jupiter would be devoted to the study of variations at planetary scales. Close observations of smaller features could allow the first local study of small-scale composition variations. The Galileo mission will have about 20 orbits around Jupiter. This will allow time-record variations in the upper troposphere, according to an estimate of a time constant of 10^8 s by Gierasch et al. (1986).

General Remarks on Observational Techniques and Data Analysis

Techniques for mapping spectroscopy from ground-based observatories are presented here. The comparison of several data sets (for example, IRIS spectra compared to ground-based observations) requires accurate position measurements on the jovian disk, and the choice of standard coordinates. When a single aperture or linear array is used, the precision of the position measurement on the disk is hardly better than 2 arcsec when compared to the limb position. A better accuracy (at least a posteriori) can be achieved by a comparison with the position of the galilean satellites, whose geocentric positions are known to 0.05 arcsec (Arlot, 1982; Chapront et al., 1986).

The interpretation of spectra is often limited by the lack of laboratory spectroscopic measurements: This has been the case for the 5-μm region. Figure 197 shows the comparison of synthetic spectra with old data (1982) and with new ammonia spectroscopic data (1987).

The method for studying variations of the composition requires

- Use of a standard model of the thermal structure of the atmosphere of Jupiter (Voyager IRIS temperature profiles should be used for each region of interest).
- Use of a structure model of the atmosphere.
- Use of standard profiles of variations of known constituents.

CONCLUSIONS

The study of composition temporal variations on Jupiter remains very fragmented today. The interpretation also is incomplete, and the question of the origin of several components (HCN, CO) is controversial. As spatial variations of some tropospheric constituents begin to be documented (H_2O, NH_3), others are only suspected (PH_3, GeH_4). In the stratosphere, the interpretation of the observations is difficult; variations of C_2H_2 and C_2H_6 are observed, in auroral regions, but thermal as well as abundance variations are probably both present.

Up to now, temporal variations are only suspected for stratospheric constituents (C_2H_2,?). The need for a

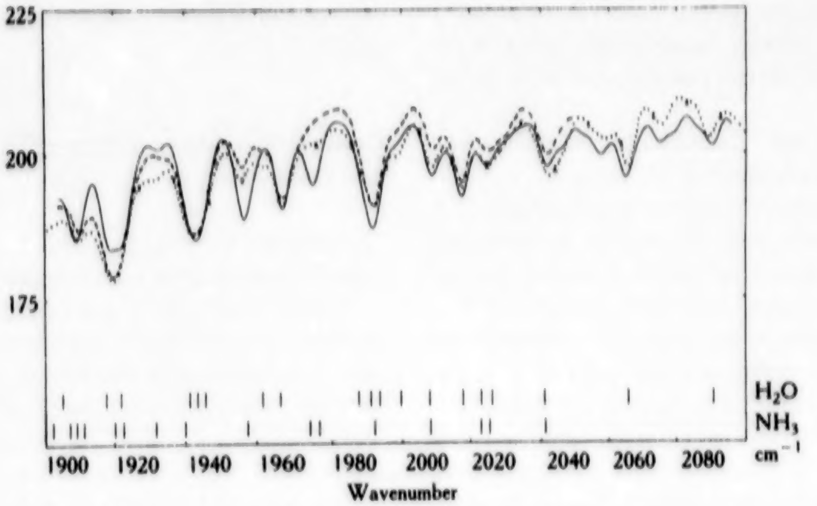

Figure 197. Comparison of the 5-μm spectrum of Jupiter (IRIS spectrum averaged on the NEB) with synthetic spectra computed with previous (Drossart and Encrenaz, 1982) and new (Lellouch et al., 1987) spectroscopic data for the $2\nu_2$ band of NH_3.

long-term observational study of this problem is therefore strong, before the Galileo mission, to improve our knowledge of the compositional variations on Jupiter.

The recent development of new ground-based instruments with spatial resolution similar to the major features of the jovian atmosphere gives new opportunities to study this field. The theories invoked to explain composition variations in the stratosphere are related to the photochemical and auroral processes; in the troposphere, the dynamics of the atmosphere as well as nonequilibrium chemistry are probably important. The study of temporal variation in composition is thus central to the understanding of many key problems of the jovian atmosphere.

ACKNOWLEDGMENTS

S. K. Atreya acknowledges support received from the Planetary Atmospheres Program of NASA's Solar System Exploration Division.

References

Arlot, J. E. (1982). New constants for Sampson-Lieske theory of the galilean satellites of Jupiter. *Astron. Astrophys.* 107:305–312.

Atreya, S. K. (1986). *Atmospheres and ionospheres of the outer planets and their satellites.* Springer-Verlag, New York and Heidelberg.

Atreya, S. K., T. M. Donahue, and W. R. Kuhn (1977). The distribution of ammonia and its photochemical products on Jupiter. *Icarus* 31:348–355.

Bar-Nun, A., and M. Podolak (1985). The contribution by thunderstorms to the abundances of CO, C_2H_2 and HCN on Jupiter. *Icarus* 64:112–124.

Beebe, R. F., G. S. Orton, and R. A. West (1989). Time-variable nature of the jovian cloud properties and thermal structure: An observational perspective. This volume.

Beer and Taylor (1978). The D/H and C/H ratios in Jupiter from the CH_3D phase. *Astrophys. J.* 219:763–767.

Belton, M. J. S. (1979). Planetary astronomy with the space telescope. In *Scientific research with the space telescope* (M. S. Longair and J. W. Warner, eds.), pp. 47–75. NASA Conf. Publ. 2111.

Belton, M. J. S., D. C. Black, C. R. Chapman, J. L. Elliot, T. Encrenaz, H. Fechtig, J. Guest, A. P. Ingersoll, H. W. Moos, and D. Morrison (1985). *Report of the space telescope scientific working group for solar system science regarding key projects and planetary campaigns.*

Bézard, B., D. Gautier and A. Marten (1986). Detectability of HD and non-equilibrium species in the upper atmosphere of the giant planets from their submillimeter spectrum. *Astron. Astrophys.* 161:387–402.

Bjoraker, G. L. (1984). *The gas composition and vertical cloud structure of Jupiter's troposphere derived from 5 μm spectroscopic observations.* Ph.D. Thesis, University of Arizona, Tucson.

Bjoraker G. L., H. P. Larson, and V. G. Kunde (1986a). The gas composition of Jupiter derived from 5 μm airborne spectroscopic observations. *Icarus* 66:579–609.

Bjoraker, G. L., H. P. Larson, and V. G. Kunde (1986b). The abundance and distribution of water vapor in Jupiter's atmosphere. *Astrophys. J.* 311:1058–1072.

Broadfoot, A. L., M. J. S. Belton, P. Z. Takacs, B. R. Sandel, D. E. Shemansky, J. B. Holberg, J. M. Ajello, S. K. Atreya, T. M. Donahue, H. W. Moos, J.-L. Bertaux, J.-E. Blamont, D. F. Strobel, J. C. McConnell, A. Dalgarno, R. Goody, and M. B. McElroy (1979). Extreme ultraviolet observations from Voyager 1 encounter with Jupiter. *Science* 204:979–982.

Broadfoot, A. L., B. R. Sandel, D. E. Shemansky, J. C. McConnell, G. R. Smith, J. B. Holberg, S. K. Atreya, T. M. Donahue, D. F. Strobel, and J. L. Bertaux (1981). Overview of the ultraviolet spectrometry results through Jupiter encounters. *J. Geophys. Res.* 86:8259–8284.

Caldwell, J., A. T. Tokunaga, and F. C. Gillett (1980). Possible infrared aurorae on Jupiter. *Icarus* 44:667–675.

Chapront, J., J. E. Arlot, C. Renatti, W. Thuillot, P. E. Vu (1986). *Ephemerides of the satellites of Jupiter, Saturn and Uranus.* Publications du Bureau des Longitudes. Paris, France.

Clarke, J. T., H. W. Moos, and P. D. Feldman (1982). The far ultraviolet spectra and geometric albedos of Jupiter and Saturn. *Astrophys. J.* 255:806–818.

Clarke, J. T., J. Caldwell, T. Skinner, and R. Yelle (1989). *The aurora and airglow of Jupiter.* This volume.

Combes, M., R. Courtin, J. Caldwell, T. Encrenaz, K. H. Fricke, V. Moore, T. Owen, and P. S. Butterworth (1981). Vertical distribution of NH_3 in the upper jovian atmosphere from IUE observations. *Adv. Space Res.* 1:169–175.

Conrath, B. J., and P. J. Gierasch (1984). Global variation of the para hydrogen fraction in Jupiter's atmosphere and implications for dynamics on the outer planets. *Icarus* 57:184–204.

Conrath, B. J., and P. J. Gierasch (1986). Retrieval of ammonia abundances and cloud opacities on Jupiter from Voyager IRIS spectra. *Icarus* 67:444–455.

Cunningham, C. C., D. M. Hunten, and M. G. Tomasko (1986). Modeling the temporal and spatial variations of the vertical structure of Jupiter's atmosphere using observations of the 3-0 hydrogen quadrupole lines. In *The jovian atmospheres* (M. Allison and L. D. Travis, eds.), pp. 26–28. NASA Conf. Publ. 2441.

de Pater, I. (1986). Jupiter's zone-belt structure at radio wavelength II. Comparison of observations with model atmosphere calculations. *Icarus* 68:344–365.

de Pater, I., and J. R. Dickel (1986). Jupiter's zone-belt structure at radio wavelength. I. Observations. *Astrophys. J.* 308:459–471.

de Pater, I. and S. T. Massie (1985). Models of the millimeter-centimeter spectra of the giant planets. *Icarus* 62:143–171.

Drossart, P. Private communication.

Drossart, P., and T. Encrenaz (1982). The abundance of water on Jupiter from the Voyager IRIS data at 5 µm. *Icarus* 52:483–491.

Drossart, P., T. Encrenaz, and A. T. Tokunaga (1983). Variability of phosphine on Jupiter from 5-µm spectroscopy. *Icarus* 60:613–620.

Drossart, P., B. Bezard, S. Atreya, J. Lacy, E. Serabyn, A. Tokunaga, and T. Encrenaz (1986). Enhanced acetylene emission near the north pole of Jupiter. *Icarus* 66:610–618.

Fegley, B. J., and R. G. Prinn (1987). Chemical constraints on the water and total oxygen abundances in the deep atmosphere of Jupiter. *Astrophys. J.*, in press.

Fink, U., H. R. Larson, and R. R. Treffers (1978). Germane in the atmosphere of Jupiter. *Icarus* 34:344–354.

Flasar, F. M. (1987). Temporal behavior of Jupiter's meteorology. This volume.

Gautier, D., B. Conrath, M. Flasar, R. Hanel, V. Kunde, A. Chedin, and N. Scott (1981). The helium abundance of Jupiter from Voyager. *J. Geophys. Res.* 86:8713–8720.

Gautier, D., and T. Owen (1983). Cosmological implications of helium and deuterium abundances on Jupiter and Saturn. *Nature* 304:691–694.

Gierasch, P. J., B. J. Conrath, and J. A. Magalhães (1986). Zonal mean properties of Jupiter's upper troposphere from Voyager infrared observations. *Icarus* 67:456–483.

Gladstone, G. R., and Y. L. Yung (1983). An analysis of the reflection spectrum of Jupiter from 1500 Å to 1740 Å. *Astrophys. J.* 266:415–424.

Griffin, M. J., P. A. R. Ade, G. S. Orton, E. I. Robson, W. K. Gear, I. G. Nolt, and J. V. Radovitz (1986). Submillimeter and millimeter observations of Jupiter. *Icarus* 65:244–256.

Hildebrand, R. H., R. F. Loewenstein, D. A. Harper, G. S. Orton, J. Keene and S. E. Whitcomb (1985). Far-infrared and submillimeter brightness temperatures of the giant planets. *Icarus* 64:64–87.

Hunten, D. M., L. Colin and J. E. Hansen (1986). Atmospheric science on the Galileo mission. *Space Science Rev.* 44:191–240.

Ingersoll, A. P., and C. C. Porco (1978). Solar heating and internal heat flow on Jupiter. *Icarus* 35:27–43.

Jennings. Private communication.

Kaye, J. A., and D. F. Strobel (1983). HCN formation on Jupiter: The coupled photochemistry of ammonia and acetylene. *Icarus* 54:417–433.

Kim, S. J., and T. Owen (1985). Phosphine and Jupiter's great red spot. Preprint.

Kim, S. J., J. Caldwell, A. R. Rivolo, and R. Wagener (1985). Infrared polar brightening on Jupiter. III. Spectrometry from the Voyager 1 IRIS experiment. *Icarus* 64:233–248.

Kostiuk, T., M. J. Mumma, J. J. Hillman, D. Buhl, L. W. Brown, and J. L. Faris (1977). NH_3 spectral line measurements on Earth and Jupiter using a 10 µm superheterodyne receiver. *Infrared Phys.* 17:431–439.

Kostiuk, T., F. Espenak, M. J. Mumma, D. Deming, and D. Zipoy (1987). Variability of ethane on Jupiter. *Icarus*, in press.

Kunde, V., R. Hanel, W. Maguire, D. Gautier, J.-P. Baluteau, A. Marten, A Chedin, N. Husson, and N. Scott (1982). The tropospheric gas composition on Jupiter's north equatorial belt (NH_3, PH_3, CH_3D, GeH_4, H_2O) and the jovian D/H ratio. *Astrophys. J.* 263:443–467.

Larson, H. P., U. Fink, R. Treffers, and T. N. Gautier (1975). Detection of water vapor on Jupiter. *Astrophys. J.* 197:L137–L140.

Larson, H. P., U. Fink, and R. R. Treffers (1978). Evidence for CO in Jupiter's atmosphere from airborne spectroscopic observations at 5 microns. *Astrophys. J.* 219:1084–1092.

Larson, H. P., D. S. Davis, R. Hofmann, and G. L. Bjoraker (1984). The jovian atmospheric window at 2.7 µm: A search for H_2S. *Icarus* 60:621–639.

Lellouch, E., and J. L. Destombes (1986). Search for minor atmospheric species in the millimeter range of Jupiter and Saturn. *Astron. Astrophys.* 152:405–412.

Lellouch, E., N. Lacombe, G. Guelachvili, G. Tarrago, and T. Encrenaz (1987). Ammonia: Experimental absolute linestrengths and self-broadening parameters in the 1800- to 2100-cm^{-1} range. *J. Mol. Spectrosc.*, in press.

Lewis, J. S., and B., Fegley, Jr. (1984). Vertical distribution of disequilibrium species in Jupiter's troposphere. *Space Sci. Rev.* 39:163–192.

Lunine, J. L., and D. M. Hunten (1987). Moist convection and the abundance of water in the troposphere of Jupiter. *Icarus* 69:566–570.

Maguire W. C., R. E. Samuelson, R. A. Hanel, and V. G. Kunde (1985). Latitudinal variation of acetylene and ethane in the jovian atmosphere from Voyager IRIS observations. *Bull. Amer. Astron. Soc.* 17:708–709.

Maillard, J.-P., and G. Michel (1982). A high resolution Fourier transform spectrometer for the Cassegrain focus at the CFH telescope. In *Instrumentation for astronomy with large optical telescopes* (C. M. Humphries, ed.), pp. 213–222. Reidel Publ. Co., Dordrecht.

Noll, K. S., R. F. Knacke, A. T. Tokunaga, J. H. Lacy, S. Beck, and E. Serabyn (1986). The abundances of ethane and acetylene in the atmospheres of Jupiter and Saturn. *Icarus* 65:257–263.

Noll, K. S., R. F. Knacke, T. R. Geballe, and A. T. Tokunaga (1987). The origin and vertical distribution of carbon monoxide in Jupiter. Preprint.

Orton, G. S. (1986). Spatial and temporal variability of infrared-observable properties of the jovian atmosphere: A partial survey. In *The jovian atmospheres,* (M. Allison and L. D. Travis, eds.), pp. 19–25. NASA Conf. Publ. 2441.

Owen, T., J. Caldwell, A. R. Rivolo, V. Moore, A. L. Lane, C. Sagan, G. Hunt, and C. Ponnamperuma (1979). Observations of the spectrum of Jupiter from 1500 to 2000 Å with the IUE. *Astrophys. J. Lett.* 236:L39–L42.

Prather, M. J., J. A. Logan, and M. B. McElroy (1978). Carbon monoxide in Jupiter's upper atmosphere: An extraplanetary source. *Astrophys. J.* 223:1072–1081.

Prinn, R. G., and S. S. Barshay (1977). Carbon monoxide on Jupiter and implications for atmospheric convection. *Science* (Washington, D.C.) 198:1031–1034.

Ridgway, S. T., L. Wallace, and G. R. Smith (1976). The 800–1200 inverse centimeter absorption spectrum of Jupiter. *Astrophys. J.* 207:1002–1006.

Smith, P. H. (1986). The vertical structure of the jovian atmosphere. *Icarus* 65:264–279.

Strobel, D. (1973). The photochemistry of NH_3 in the jovian atmosphere. *J. Atmos. Sci.* 30:1205–1209.

Strobel, D., and Y. Yung (1979). The galilean satellites as a source of CO in the jovian upper atmosphere. *Icarus* 37:256–263.

Tarrago, G., G. Poussigue, N. Lacome, A. Lévy, and G. Guelachvili (1987). *Modeling of PH_3 absorption in the 2050–2150 cm^{-1} jovian window.* 42nd Symposium on molecular spectroscopy, Columbus.

Tokunaga, A. T., S. C. Beck, T. R. Geballe, J. H. Lacy, and E. Serabyn (1981). The detection of HCN on Jupiter. *Icarus* 48:283–289.

Tokunaga, A. T., R. F. Knacke, S. T. Ridgway, and L. Wallace (1979). High-resolution spectra of Jupiter in the 744–980 inverse centimeter range. *Astrophys. J.* 232:603–615.

Tokunaga, A. T., R. G. Smith, and E. Irwin (1987). *Use of a 32-element Reticon array for 1–5 micrometer spectroscopy.* Workshop on infrared array detectors, Hilo, March 1987.

Vogel, H. C. (1895). Recent research on the spectra of the planets. *Astrophys. J.* 1:196–209.

Wagener, R., J. Caldwell, T. Owen, S. J. Kim, T. Encrenaz, and M. Combes (1985). The jovian stratosphere in the ultraviolet. *Icarus* 63:222–236.

Wagener, R., and J. Caldwell (1987). Strong north/south asymmetry in the jovian stratosphere. Conference Origin and Evolution of Planetary and Satellite Atmospheres, Tucson, March.

West, R. A. (1979). Spatially resolved methane band photometry of Jupiter. I. Absolute reflectivity and center-to-limb variations in the 6190-, 7250-, and 8900-Å bands. *Icarus* 38:12–33.

28

Spatial and Temporal Variations of NH_3 Abundance and Cloud Structure in the Jovian Troposphere Derived from CCD/Coude Observations

Kevin H. Baines
Jet Propulsion Laboratory, Pasadena

William Hayden Smith
Washington University, St. Louis

Claudia Alexander
Jet Propulsion Laboratory, Pasadena

Abstract

Estimates of variations in jovian tropospheric properties are determined from variations in ammonia-line profiles observed within the 6450-Å ammonia band. In May 1985 and December 1986, two-dimensional spectra (one spatial dimension oriented along the central meridian, one spectral dimension centered at the 6457.12 Å ammonia line) were acquired using a charge-coupled device (CCD) at Coude at the Mauna Kea Observatory, University of Hawaii 88", and the Table Mountain Observatory, Jet Propulsion Laboratory 24". Longitudinal information was obtained by observing the central meridian repeatedly as the planet rotated. The observations cover the 6452–6465 Å region in which a half-dozen assigned NH_3 lines reside. Global maps of the variation in ammonia column abundance and effective pressure level of line formation are estimated from fitting Voigt profiles to each of the lines in the spectrum. These, in turn, are used to derive estimates of variations in the physical state of the visible troposphere (e.g., NH_3SH cloudtop pressure). Preliminary analysis of the May 1985 data set using the 6457.1 Å and 6459.1 Å lines suggests that the continuum albedo and effective pressure level are significantly correlated at low latitudes, with larger (30–60 percent greater) pressures in belts compared to zones. Such a correlation does not appear to exist between the ammonia-column abundance and the belt-zone structure. These observations then tend to support the traditional view of Jupiter's belt-zone structure: Belts are relatively aerosol-free and dry whereas zones are relatively cloudy and ammonia rich.

INTRODUCTION

High-resolution spectroscopic observations of unsaturated molecular absorption line profiles are uniquely capable of elucidating the vertical distributions of aerosols and gas species in the jovian troposphere. This capability stems from two principal advantages over other techniques, such as broad-band spectrophotometry,

1. Direct measurement of the effective absorption pressure level from the line width, and
2. Increased accuracy in determinations of absorbing gas column abundances and molar fractions due to enhanced understanding of absorption properties at ambient planetary temperatures and pressures.

These advantages are tempered somewhat by the low instrumental throughput inherent in observing with a passband that is roughly 100 times narrower than that used for conventional broad-band spectrophotometry. To obtain sufficient signal-noise, one must increase the telescope size, entrance aperture, and/or integration time. Given a fixed telescope size and slit width, the increased integration time may result in a loss of spatial resolution and coverage. When compared to broad-band measurements, high-resolution spectral observations generally afford improved vertical profiles of the atmosphere at the possible expense of spatial resolution.

The advent of CCDs, with their high quantum efficiency and multiplexing capability, permits the acquisition of photon noise limited spectra. The spectra are simultaneously obtained over a narrow longitude or latitude range for center-to-limb or spatial-mapping studies.

High-resolution observations are usually obtained without absolute flux calibrations. Due to the long integration times required for the observations, measurements of flux calibrations, such as the Oke Stars, are prohibitive. The spectra are not reduced to absolute planetary fluxes, but are instead normalized to a local "continuum level" of low gas absorption against which line profiles for individual absorption features are measured. The uncertainty in the choice of continuum level used in calibrating line profiles is usually the chief uncertainty in the derivation of physical constraints from such data. To reduce this uncertainty, spectral observations need to be acquired over a sufficient spectral range that includes regions of the lowest possible gas opacity.

Additionally, proper analysis of such data normally requires more than an understanding of the absorption properties for the line under analysis. Namely, all other nearby absorptions that affect the line profile must be understood as well.

The 6450 Å spectrum of NH_3 is one such well-characterized region that we are in the process of exploiting for the purpose of deriving constraints on the spatial distribution of tropospheric cloudtops and ammonia abundances on Jupiter. Quantum number assignments for over 100 lines in this region have been recently reported by Coy and Lehmann (1985), and hydrogen:ammonia pressure-broadening characteristics have been measured under jovian conditions in the laboratory for a number of the strongest lines (Keffer et al., 1986). In addition, this spectral region exhibits relatively little CH_4 absorption of 3 Å resolution (Giver, 1978), so effects of little-known CH_4 features are presumably negligible. Finally, NH_3, being a condensable in the jovian atmosphere, is depleted in the stratosphere and upper troposphere so that relatively little NH_3 absorption occurs in these atmospheric regimes. Instead, the observed ammonia spectrum is largely produced by NH_3 gas opacity below approximately 600 mbars (i.e., underneath both the stratospheric haze and NH_3 cloud layers). The observed NH_3 line profiles then are diagnostic of conditions in an atmospheric regime that is usually difficult to access from CH_4 spectroscopy—either broad-band or high-resolution—due to uncertainties in the overlying molecular and aerosol extinctions. Specifically, these features are useful for determining the altitude of the third major aerosol layer in the jovian atmosphere (i.e., the NH_4SH or H_2O cloud that presumably defines the bottom of the visible atmosphere).

OBSERVATIONS

We have thus far observed the region from 6452–6465 Å with a CCD at the Coude on May 30–June 2, 1985, and December 12–13, 1986, from, respectively, the UH 88" at Mauna Kea Observatory, and the Table Mountain 24". Additional observations were scheduled for September and December of 1987 from Table Mountain. In our observations, the spectrograph slit is oriented along the planet's central meridian. Placed at the focal plane of the spectrograph, the CCD then collects spectra simultaneously over a wide range of latitudes. Limiting the integration time to 5–9 minutes, longitudinal coverage is obtained by repeated observations of the central meridian as the planet rotates. In this manner, we have been able to map out the planet at effective equatorial spatial resolutions of some 5° latitudinally by 7° longitudinally.

At Hawaii, the Institute for Astronomy 500 × 500 pixel Galileo CCD Camera (Hlivak et al., 1982) was illuminated at f/24.3. A 100-μm slitwidth was employed with the number 2 grating in second order to yield a measured spectral resolution of 120 mÅ, approximately the intrinsic linewidth of an ammonia line formed at 1 bar in Jupiter's atmosphere. The pixel separation in the wavelength dimension was measured from three prominent Fraunhofer features to be 25 mÅ, so that the observations were oversampled spectrally by a factor of two. In the spatial dimension, the pixel separation was 0.055 arcsecs, roughly a factor of 25 less than the estimated seeing of 1.5 arcsecs. Pixels were thus initially binned together by four to enhance signal-noise without affecting the spatial information content. Over the four nights of useful observations, 76 spectral images comprising more than 8000 individual binned spectra were acquired covering two-thirds of the planet, from 270° (System III), with a signal-noise of better than 50/1 for each pixel.

Figure 198 is an example of a reduced spectral image of Jupiter as observed from Mauna Kea. The image utilizes 126 pixels in the vertical dimension for spatial information, with spectra dispersed over 500 pixels in the horizontal. Five prominent NH_3 features are visible in these spectra, as well as remnants of three strong

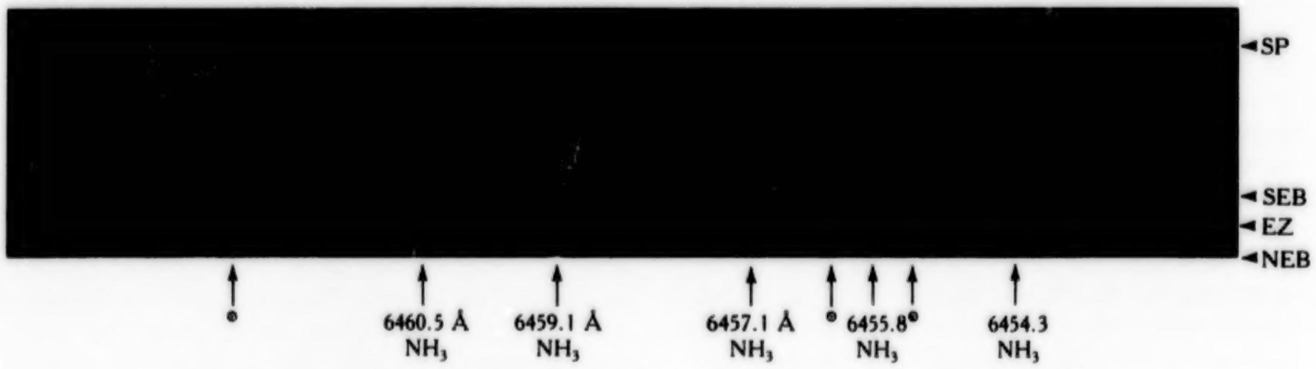

Figure 198. CCD Coude spectral image of the southern hemisphere, centered at 30° longitude (System III). This image covers 500 spectral points in the horizontal dimension and 126 spatial points in the vertical. The spectral interval between pixels is 25 mÅ, the spatial interval 0.22 arcsec. Several ammonia and Fraunhofer features are visible as vertical streaks. The equatorial region is the bright area at the bottom. The south pole is at the top. The brightest regions in this image are yellow, with progressively darker regions being represented by red, brown, green, and blue.

~~ORIGINAL PAGE IS OF POOR QUALITY~~

ORIGINAL PAGE
COLOR PHOTOGRAPH

solar Fraunhofer features that have been largely divided out by division with a lunar scan. Zone-belt structure is easily seen in the vertical dimension. Each observation covers just 65 percent of the disk in the north-south direction; in this case, from the north equatorial belt (NEB) southward to the south pole.

At Table Mountain, a General Electric Company CCD was used at f/30. A spectral resolution of 80 mÅ was achieved with a 100-μm slitwidth, significantly better than that obtained at Mauna Kea. The pixel separation at 31 mÅ affords close to Nyquist sampling. In these observations, the full disk of Jupiter can be observed in 120 pixels, corresponding to a pixel separation of 0.3 arcsecs, substantially better than the estimated seeing of 5–7 arcsecs. Forty spectral images were acquired over the two nights.

ANALYSIS PROCEDURE

We have thus far performed just a preliminary analysis of the Hawaii data set using a simple reflecting-layer model to monitor crudely spatial variations in the NH_4SH cloudtop level and the ammonia column abundance above it. At the time of this writing, a more sophisticated analysis, using our radiative transfer algorithms applicable to vertically-inhomogeneous aerosol and gas distributions as well as realistic thermal structures was being planned for presentation at the Pasadena meeting of the American Astronomical Society, Division of Planetary Sciences, in November, 1987.

In our initial analysis, individual absorption features are analyzed with a Voigt-profile fitting routine. Since the detected gas is segregated into a region of relatively high pressures (i.e., greater than about 600 mbar), which is presumably clear of aerosols, the fitted Voigt-profile pressure parameter is a good measure of the mean level of line formation. We emphasize that it is only because of these two conditions that we are able to usefully employ the Voigt profile to obtain meaningful results for the vertically inhomogeneous structure of the jovian atmosphere—for example, it can be shown that the width of a line produced by a uniformly distributed constituent in a clear hydrostatic atmosphere can, depending on the thermal Doppler width, be significantly smaller than that produced at the mean pressure level of line formation. Briefly, this is due to the essentially monotonic variation of pressure broadening within the atmosphere. Although the net energy absorbed within a slice of atmosphere *dP* thick is pressure invariant (ignoring temperature effects on line strength), the width of the absorption feature varies linearly with pressure, so that at the top of the visible atmosphere the absorbed energy is concentrated within a much narrower spectral region than at the bottom. Consequently, the width at the half-intensity point in the integrated line profile is determined predominantly by absorption in the upper atmosphere. On the other hand, the width of a line formed in a hazy atmosphere may be significantly larger than that at the mean pressure level due to enhanced absorption in the wings of the line caused by multiple scattering.

We have chosen for our preliminary analysis to examine two of the strongest NH_3-"singlet" lines in the spectrum that are relatively unblended with unknown features and remnants of Fraunhofer lines. Specifically, we use the 6457.12-Å feature (the strongest feature in the spectrum) and the 6459.08-Å feature. The quotes around "singlet" here refer to the fact that although these features are dominated by a single line, there are additional lines blended with them. The ammonia spectrum has been measured by one of us (Smith) at low pressures in the laboratory. Figure 199 depicts the relative line strengths of these features compared to the primary feature. We have included these features as well in our Voigt-fitting analysis. We assumed that the relative strengths and pressure broadening characteristics of these features are constant with temperature and pressure throughout the accessible atmosphere.

Other nearby features are evident in the spectrum (fig. 199) for which laboratory characteristics are as yet unknown. To reduce the effects of these spectral contaminants on our results, we have restricted the points under analysis to just those near the primary line cores, depicted as large dots in figure 199, so that only spectral points that are determined by well-understood absorption features are evaluated. This Voigt-fitting procedure contrasts with the usual technique of measuring equivalent widths utilizing points throughout the relatively weak wings where, as here, the effect of spectral contaminants can become appreciable.

In fitting these lines, a continuum level is chosen for each spectrum based on the intensities at six wavelengths paired in three "continuum" regions. For each spectrum, the straight line that best fits these intensities, in a least squares sense, is assumed to be the continuum (see fig. 200). These continuum points are chosen for their wavelength displacement from known spectral features. As noted earlier, the primary uncertainty in our analysis stems from uncertainties in the continuum level chosen.

Each spectral image (e.g., fig. 198) is binned by 6 pixels vertically (spatially) to enhance the signal noise. This is done with little loss of spatial resolution given

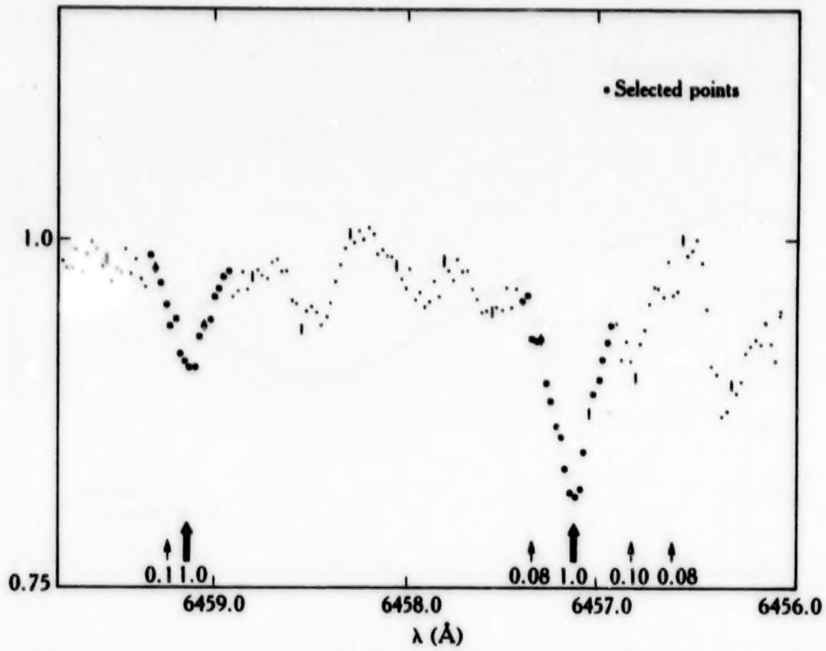

Figure 199. Points chosen for spectral analysis of the Jupiter NH$_3$ spectrum. Only points near the cores of the 6457.12- and 6459.09-Å "singlet" features are used in our preliminary analysis (*large dots*). Secondary absorptions (*thin arrows*) are imbedded in and around these "singlets" (*wide arrows*). The relative room temperature line strengths of these secondary features compared to the primary are depicted. All are 10 percent or less of the primary.

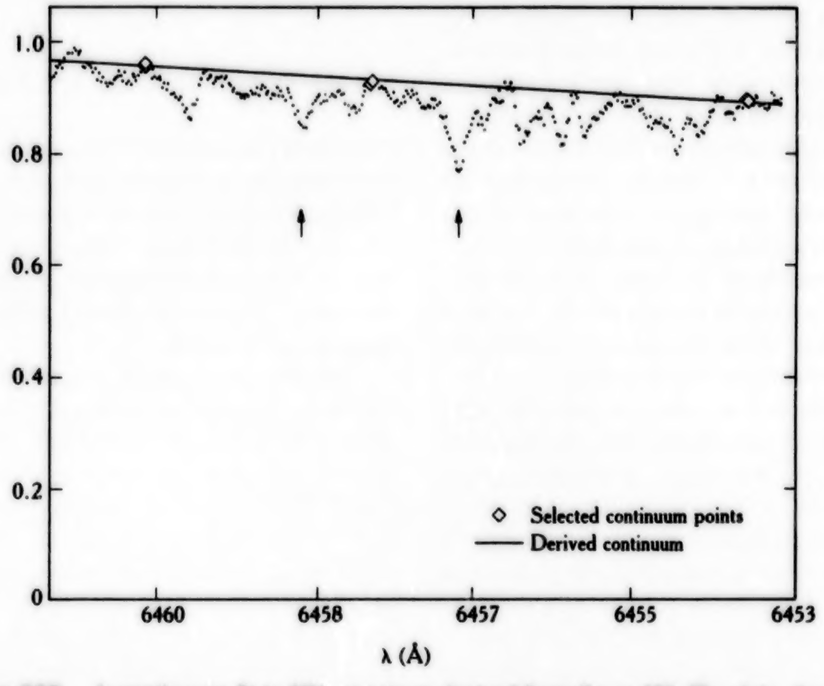

Figure 200. A continuum fit to NH$_3$ spectrum derived from figure 198. The data shown are 6-pixel binned averages of the data in rows 42–48 of the previous image (roughly one-third the way up from the bottom in figure 198). The continuum points (*diamonds*) are chosen for their relatively large displacements from Fraunhofer and obvious gaseous absorption features. Nevertheless, relatively weak absorptions may still influence these points to some unknown extent, giving rise to an unknown uncertainty in the derived parameters.

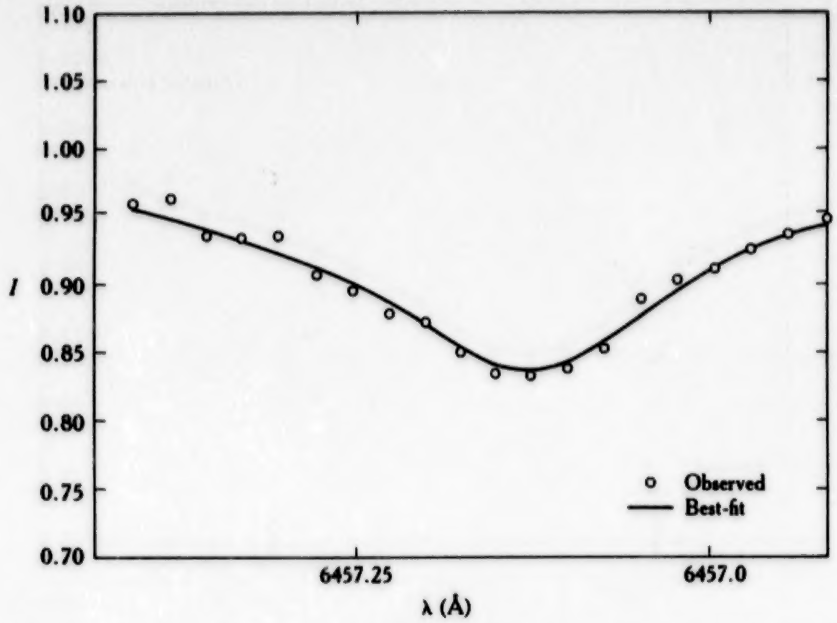

Figure 201. A Voigt-profile best-fit to the 6457.12-Å line points depicted in figures 199 and 200. The influence of the largest secondary feature can be discerned in the *red wing* of the line.

the estimated seeing of 1.0–1.5 arcsecs (as noted earlier, each pixel covers 0.22 arcsecs, giving a spatial binning of 1.32 arcsecs). The instrument profile width (120 mÅ) is accounted for in the Lorentzian (pressure-broadening) component of the Voigt width parameter. Broadening due to the variation of the radial component of planetary rotation across the field-of-view of the entrance slit (25 mÅ over 2 arcsecs, accounting for both the slitwidth and seeing) is subsumed in the Gaussian (thermal broadening) component.

A typical Voigt-profile fit is shown in figure 201. Four lines are actually used in making this fit, as noted in figure 199. The effect of the strongest secondary feature is particularly apparent in the red wing.

A column opacity and an effective pressure level are calculated as output parameters to the Voigt-profile fitting procedure. Using the Voigt-derived pressure together with the nominal jovian thermal structure of Orton (1978), the room-temperature line strengths of Giver et al. (1975), and the quantum number assignments of Coy and Lehmann (1985), these column opacities are then converted to column abundances for each line.

Uncertainties in the derived parameters are estimated from the curvature of the root-mean-square residual found as that parameter is varied about the best-fit value (Baines and Bergstralh, 1986, p. 423; Orton and Ingersoll, 1976). A weighted mean column abundance and effective pressure is then calculated from the weighted sum of results derived for each line, the inverse squares of the uncertainties being used as the weighting factors.

PRELIMINARY RESULTS AND DISCUSSION

Preliminary results for a large portion of the May–June 1985 data set are shown in figures 202 to 204. Figure 202 shows results for the spectral image previously shown (fig. 198). Figure 203 shows the combined results of 76 spectral images acquired over two-thirds of the planet. Figure 204 shows zonally averaged results utilizing all 76 scans.

Significant longitudinal and latitudinal structure is visible in the effective pressure results (second panels of figs. 202–204). These correlate closely with the continuum intensities recorded in the 6453.5-Å point (first panel) at tropical and equatorial latitudes, suggesting that visible light penetrates to significantly deeper levels in darker regions (belts) compared to brighter areas (zones). On the other hand, NH_3 column abundances do not seem to correlate well with the observed zone-belt structure, but instead show a general increase at temperate and polar latitudes.

The zonally averaged results (fig. 204) indicate that visible radiation penetrates significantly deeper in the south equatorial belt (SEB) than in any other major zonal feature on the planet. Specifically, this analysis indicates that the (presumably) NH_4SH cloudtops are

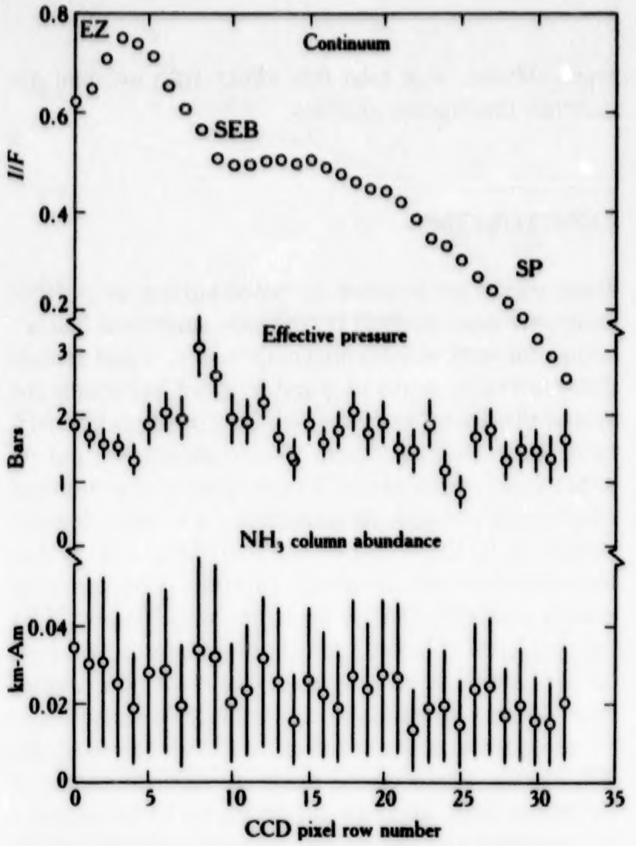

ORIGINAL PAGE IS OF POOR QUALITY

Figure 202. Spectral analysis results for the southern hemisphere (System III), 30° longitude scan of figure 198. *Upper panel*: The continuum albedo at 6453.5 Å versus latitude, here defined as pixel number. The equator region is on the left, with the south polar region to the right. *Middle panel*: The derived effective pressure versus latitude. Error bars are derived from the radius of curvature of the residual fit found as the effective pressure is varied about the nominal value shown (see text). *Bottom panel*: The derived ammonia-column abundance. The error bars are calculated as in *middle panel*. Latitudinal structure is obvious in the effective pressure plot. In particular, the SEB appears to be a particularly accessible region for visible radiation.

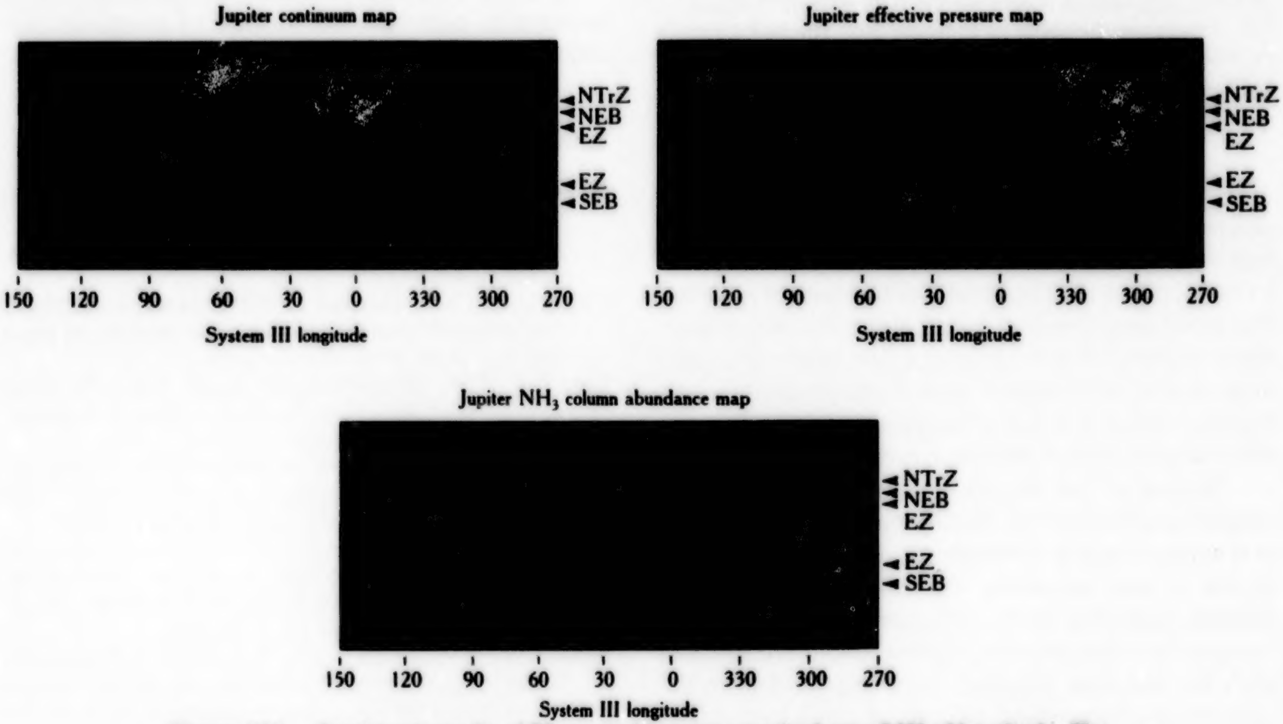

Jupiter continuum map
NTrZ
NEB
EZ
EZ
SEB
150
120
90
60
30
0
330
300
270
System III longitude
Jupiter effective pressure map
NTrZ
NEB
EZ
EZ
SEB
150
120
90
60
30
0
330
300
270
System III longitude
Jupiter NH$_3$ column abundance map
NTrZ
NEB
EZ
EZ
SEB
150
120
90
60
30
0
330
300
270
System III longitude

Figure 203. Combined results of 76 spectral images acquired over 240° of longitude. The effective pressure is enhanced in the SEB at all observed longitudes. An enhancement in the NEB is evident as well from roughly 30° to 150° longitude. These enhancements in general are correlated with the observed continuum albedo at 6453.5 Å from equatorial to temperate latitudes. A polar increase in ammonia-column abundance is evident, but there appears to be no correlation with the observed continuum albedo within the zone-belt structure. In these images, *yellow* represents the largest values, with progressively smaller values being represented by *red*, *brown*, *green*, and *blue*.

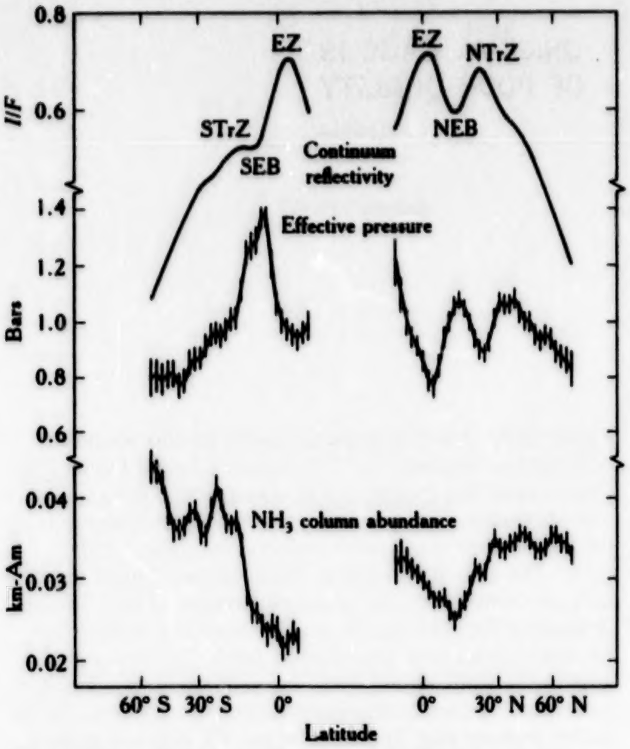

Figure 204. Jovian zonally averaged effective pressure and NH_3 abundance results for the data shown in figure 203. Panels are the same as in figure 202. The belt-zone correlation in effective pressure level is particularly evident, as is the polar increase in NH_3 column abundance.

nearly a bar deeper there than in the nearby equatorial region, given the nearly half-bar difference in mean effective pressure levels obtained in this coarse analysis. The traditional view that zones and belts are, respectively, regions of upwelling and downwelling is this supported by this analysis. Indeed, this study indicates that this major dynamic difference extends below the NH_3 cloud to at least the next cloudtop level.

We suspect that the lack of correlation between the column abundance and effective pressure level in belts and zones is largely indicative of a major insufficiency in the coarse modeling analysis presented here. Namely, scattering by the NH_3 aerosol layer is unaccounted for. If the NH_3 cloud optical depth is correlated with the belt-zone structure (as is expected from the upwelling-downwelling picture of zone-belt differences), the NH_3 gas absorption could be preferentially increased in zones compared to belts due to multiple scattering, particularly between the major aerosol layers. Models that take this effect into account are currently undergoing analysis.

CONCLUSION

These results are tentative. As noted earlier, an in-depth comprehensive analysis is currently underway that accounts for vertical inhomogeneities in gas and aerosol distributions in order to quantify more accurately the spatial distributions of the NH_4SH cloudtop and NH_3 molar fraction. In addition, we are examining our results for systematic errors (for example, in the choice of continuum points). Nevertheless, we have demonstrated here that high-resolution NH_3 line profile measurements are inherently capable of determining zonally averaged effective pressures and NH_4SH cloudtop pressures to better than 10 percent (approximately 0.1 bar). At this point, it appears that such observations show distinct longitudinal and latitudinal variations in the aerosol and ammonia distributions underneath the NH_3 clouds. Observations made at Table Mountain in December 1986, and new observations to be acquired in September and December 1987 will subsequently be analyzed to determine the degree of temporal variability in these properties.

References

Baines, K. H., and J. T. Bergstralh (1986). The structure of the uranian atmosphere: Constraints from the geometric albedo spectrum and H_2 and CH_4 line profiles. *Icarus* 65:406–441.

Coy, S. L., and K. K. Lehmann (1985). Rotational structure of ammonia N-H stretch overtones: Five and six quantum bands. *J. Chem. Phys.* 14:5239–5249.

Giver, L. P. (1978). Intensity measurements of the CH_4 bands in the region 4350 Å to 10600 Å. *J. Quant. Spectrosc. Radiat. Transfer.* 19:311–322.

Giver, L. P., J. H. Miller, and R. W. Boese (1975). A laboratory atlas of the 5ν1 NH_3 absorption band at 6475 Å with applications to Jupiter and Saturn. *Icarus* 25:34–48.

Orton, G. S., and A. P. Ingersoll (1976). Pioneer 10 and 11 ground-based infrared data on Jupiter: The thermal structure and He-H_2 ratio. In *Jupiter* (T. Gehrels, ed.), pp. 206–215. Univ. of Arizona Press, Tucson.

Keffer, C. E., C. P. Conner, and W. H. Smith (1986). Hydrogen broadening of vibrational-rotational transitions of ammonia lying near 6450 Å. *J. Quant. Spectrosc. Radiat. Transfer.* 35:487.

Orton, G. S. (1978). *Report of the Galileo project science working group on the atmosphere of Jupiter.* Subcommittee on Atmospheric Structure, unpublished.

29

A New Analysis of the Jovian 5-μm IRIS Spectra

E. Lellouch
P. Drossart
T. Encrenaz
Observatoire de Paris, Meudon

G. Guelachvili
N. Lacome
G. Tarrago
Université de Paris-Sud, France

Abstract

Previous analysis of the Jupiter infrared interferometric spectrometer (IRIS) data in the 1800–2200 cm^{-1} range have given estimates of PH_3, GeH_4, CH_3D, and H_2O abundances in the deep regions of the jovian atmosphere (Kunde et al., 1982; Drossart et al., 1982; Drossart and Encrenaz, 1982; Bjoraker, 1984). However, in the case of NH_3, the fit was not fully satisfactory in this window, due to the lack of accurate NH_3 laboratory data for the ν_4 and $2\nu_2$ bands. In order to improve this analysis, low-temperature laboratory data of NH_3 have been recorded at high-spectral resolution in the 1800–2100 cm^{-1} range (Lellouch et al., 1987).

With these data, it has been possible to obtain a good fit of the jovian spectrum for various locations on the jovian disk (north equatorial belt [NEB], north tropical zone [NTZ], equatorial zone [EQZ], south equatorial belt [SEB], and south tropical zone [STZ]). The abundance of NH_3 is found to be varying between zone and belts, and is smaller by a factor of two in the hot spectra of north and south equatorial belts, in agreement with observations in the centimetric range, which sound even deeper atmospheric levels (de Pater, 1986). The abundances of some minor atmospheric constituents are reestimated and discussed.

INTRODUCTION

In previous studies of the 5-μm window of Jupiter from the Voyager-IRIS spectra (Kunde et al., 1982; Drossart et al., 1982; Bjoraker, 1984), the lack of accurate intensity measurements for the $2\nu_2$ band of NH_3, centered at 1880 cm^{-1}, gave only a poor fit of the 1900–2050 cm^{-1} range near NH_3 absorption features.

New spectroscopic measurements (Lellouch et al., 1987) are used in this analysis, to retrieve the tropospheric abundance of NH_3 and to study the abundance variations of minor constituents with latitude.

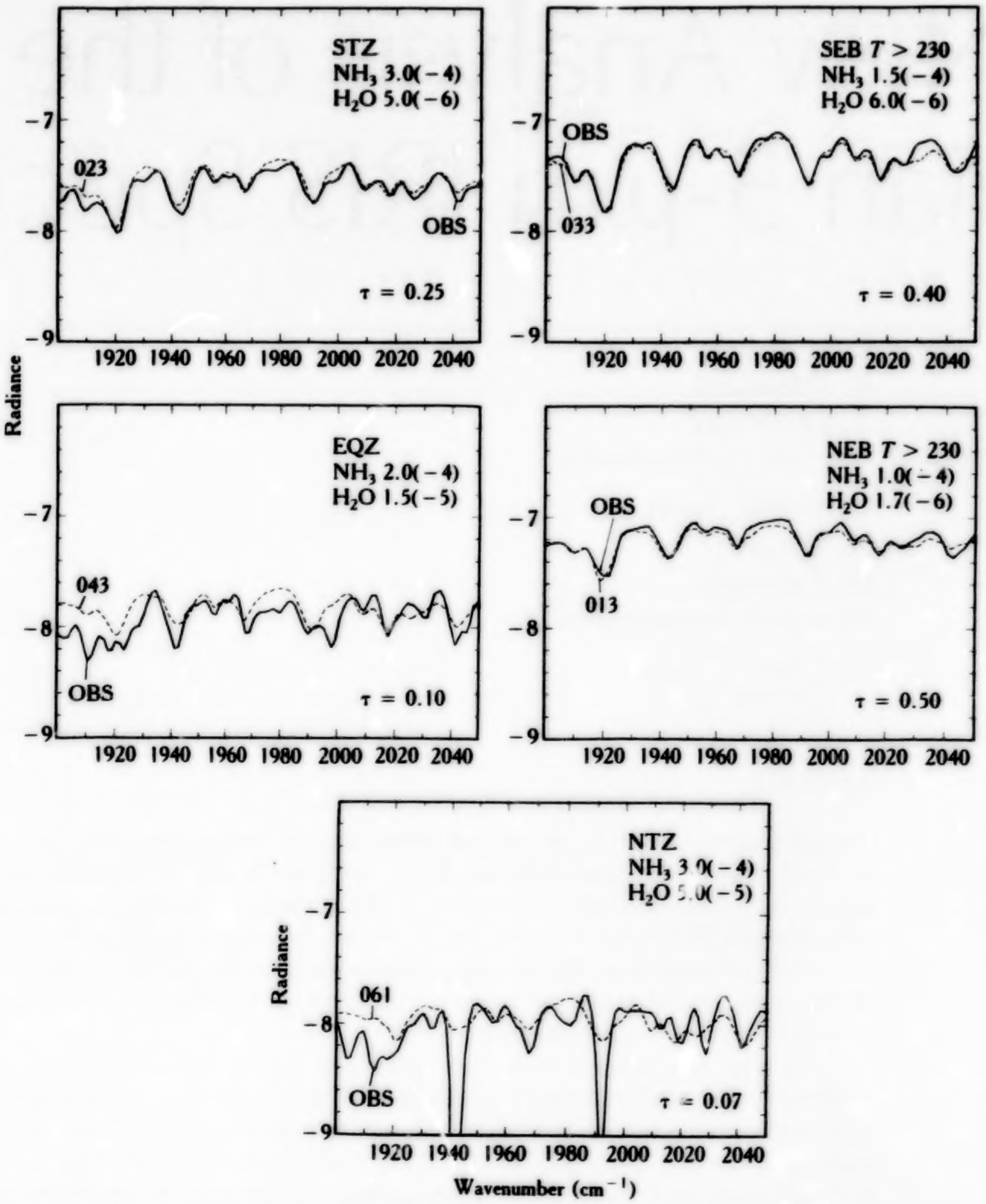

Figure 205. *Top right*: Comparison of Iris spectrum of the hot south equatorial belt (OBS) and synthetic spectrum (033); *Top left*: Comparison of Iris spectrum of the south tropical zone (OBS) and synthetic spectrum (023); *Middle right*: Comparison of Iris spectrum of the hot north equatorial belt (OBS) and synthetic spectrum (013); *Middle left*: Comparison of Iris spectrum of the equatorial zone (OBS) and synthetic spectrum (043); *Bottom*: Comparison of Iris spectrum of the north tropical zone (OBS) and synthetic spectrum (061).

Table 29. Comparison to IRIS Spectra in the 1900–2050 cm^{-1} Range

Atmospheric region	Figure 205	Transmission of cloud (at T_c = 190 K)	$NH_3:H_2$ ratio	$PH_3:H_2$ ratio	$H_2O:H_2$ ratio
SEB (hot)	*Top right*	0.40	1.5×10^{-4}	6.0×10^{-7}	6.0×10^{-6}
SEB (medium)	—	0.10	3.0×10^{-4}	6.0×10^{-7}	5.0×10^{-5}
STZ	*Top left*	0.25	3.0×10^{-4}	6.0×10^{-7}	5.0×10^{-6}
NEB (hot)	*Middle right*	0.50	1.0×10^{-4}	6.0×10^{-7}	1.75×10^{-6}
NEB (medium)	—	0.15	3.0×10^{-4}	6.0×10^{-7}	2.0×10^{-5}
NEB (hottest)	—	0.80	1.5×10^{-4}	6.0×10^{-7}	1.5×10^{-6}
EQZ	*Middle left*	0.10	2.0×10^{-4}	6.0×10^{-7}	1.5×10^{-5}
NTZ	*Bottom*	0.07	3.0×10^{-4}	6.0×10^{-7}	5.0×10^{-5}

DESCRIPTION OF THE MODEL

The synthetic calculations are done with a model (improved from Drossart et al., 1982) with

- An atmospheric profile calculated for the NEB (Bézard et al., 1983).
- H_2-He continuum calculated from a parametric model of pressure induced absorption (Borysow et al., 1985; Orton).
- NH_3 and PH_3 vertical distributions taken from Kunde et al., 1982.
- H_2O vertical distribution from Bjoraker et al., 1986.
- NH_3 lines coefficients from Lellouch et al., 1987.
- PH_3 lines coefficients from Tarrago et al., 1987.
- Two parameter cloud model (cloud at an atmospheric level T_c with transmission τ; T_c = 190 K).

DATA ANALYSIS AND CONCLUSIONS

IRIS spectra are selected with the criteria as follows:

- Field of view less than 5°
- Phase angle ≤30°
- Brightness temperatures in the range $T \geq 230$ K (hot), 190 K ≤ T ≤ 230 K (medium), and T ≤ 190 K

The results are shown in table 29 and in figure 205. We find

1. NH_3 is depleted within the 5-μm hot spots in the NEB and SEB.
2. H_2O is depleted also in the 5-μm hot spot.
3. PH_3 abundance is constant (but no PH_3 feature appears in the 1900–2050 cm^{-1} range and PH_3 acts mostly as a continuum).

References

Bézard, B., J. P. Baluteau and A. Marten (1983). Study of the deep cloud structure in the equatorial region of Jupiter from Voyager infrared and visible data. *Icarus* 54:434–455.

Bjoraker, G. L. (1984). *The gas composition and vertical cloud structure of Jupiter's troposphere derived from 5 μm spectroscopic observations*. Ph.D. Thesis, University of Arizona, Tucson.

Bjoraker, G. L., H. P. Larson, and V. G. Kunde (1986). The gas composition of Jupiter derived from 5 μm airborne spectroscopic observations. *Icarus* 66:579–609.

Borysow, A., M. Moraldi, and L. Frommhold (1984). Modeling of collision-induced absorption spectra. *J. Quant. Spectrosc. Radiat. Transfer.* 31:235–245.

de Pater, I. (1986). Jupiter's zone-belt structure at radio wavelengths. *Icarus* 68:344–365.

Drossart, P., T. Encrenaz, V. Kunde, R. Hanel, and M. Combes (1982). An estimate of the NH_3, CH_3D and GeH_4 abundances on Jupiter from Voyager IRIS data at 4.5 μm. *Icarus* 49:416–426.

Drossart, P., and T. Encrenaz (1982). The abundance of water on Jupiter from the Voyager IRIS data at 5 μm. *Icarus* 52:483–491.

Kunde, V., R. Hanel, W. Maguire, D. Gautier, J.-P. Baluteau, A. Marten, A. Chedin, N. Husson, and N. Scott (1982). The tropospheric gas composition of Jupiter's north equatorial belt (NH_3, PH_3, CH_3D, GeH_4, H_2O) and the jovian D/H ratio. *Astrophys. J.* 263:443–467.

Lellouch, E., N. Lacome, G. Guelachvili, G. Tarrago, and T. Encrenaz (1987). Ammonia: Experimental absolute linestrengths and self-broadening parameters in the 1800- to 2100-cm^{-1} range. *J. Mol. Spectrosc.*, in press.

Orton. Private communication.

Tarrago, G., G. Poussigue, N. Lacome, A. Lévy, and G. Guelachvili (1987). *Modeling of PH_3 absorption in the 2050–2150 cm^{-1} Jovian window*. 42nd Symposium on Molecular Spectroscopy, Columbus, June.

30

Jovian Lightning

L. J. Lanzerotti
AT&T Bell Laboratories, Murray Hill
K. Rinnert
MPAE, Katlenburg-Lindau-3
E. P. Krider
University of Arizona, Tucson
M. A. Uman
University of Florida, Gainesville

Abstract

This chapter reviews the present status of knowledge of lightning in Jupiter's atmosphere. The chapter summarizes some current ideas of the atmospheric structure that is likely important for the generation of jovian lightning, reviews measurements made by Voyager 1 of jovian lightning, outlines the objectives of the Galileo probe (RF) lightning experiment, and describes the differences in RF radiation between cloud-to-ground and intra-cloud discharges as observed on Earth. The RF lightning instrument on the Galileo probe will provide important new information on jovian lightning.

INTRODUCTION

Prior to the Voyager 1 flyby of Jupiter, the presence of lightning in that planet's atmosphere had been speculatively suggested as an energy source both for the nonthermal radio emissions from the planet and for the production of certain nonequilibrium chemical species. The first of these suggestions was soon effectively dismissed by the work of several researchers, in particular Zheleznyakov (1970), whereas the second, in the light of the Voyager 1 discoveries, may well have some validity (Sagan et al., 1967; Woeller and Ponnamperuma, 1969; Chadha et al., 1971; Bar-Nun, 1975; Bar-Nun et al., 1984; Bar-Nun and Podolak, 1985; Prinn and Owen, 1976). In spite of the uncertainty prior to the Voyager 1 encounter regarding the existence of lightning on Jupiter, NASA believed the question of jovian lightning to be of sufficient importance that a joint U.S.–German lightning experiment was selected for flight on the Galileo probe (Lanzerotti et al., 1983).

The Voyager 1 mission produced two night-side photographs showing strong optical evidence for lightning in Jupiter's atmosphere (Cook et al., 1979; Borucki et al., 1982) and substantial data from the spacecraft's plasma wave experiment (PWS) showing the existence of whistler waves, most probably generated by lightning discharges, propagating in the magnetosphere (Gurnett et al., 1979; Kurth et al., 1985). Because of the possible existence of lightning on Venus (e.g., Ksanfomality, 1979; Taylor et al., 1979) and Saturn (e.g., Kaiser et al., 1983; Burns et al., 1983; Zarka, 1985), as well as on Jupiter, there has emerged a new field of research that could be called planetary lightning. Several reviews of planetary lightning have already been written (Levin et al., 1983; Williams et al., 1983; Rinnert, 1982, 1985) and a book chapter devoted to the subject is contained in a recent monograph on the lightning discharge (Uman, 1987). At least one thesis already exists on jovian lightning (Williams, 1986).

This short chapter introduces some current ideas on jovian atmospheric structure that is likely important for the generation of lightning, reviews briefly the present status of understanding of jovian lightning, and describes the differences in RF radiation between cloud-to-ground and intra-cloud discharges as observed on Earth. The RF lightning instrument on the Galileo probe is expected to provide important new information on jovian lightning.

CLOUD STRUCTURE AND LIGHTNING

Most Earth lightning is produced by the charge generated and separated in cumulo nimbus clouds that develop in unstable air containing water vapor. The instability is most often produced by solar heating at the ground or by the interaction of air masses. As the moist air rises and cools, condensation occurs and ultimately precipitation forms. Charging of particles can occur by various processes including a thermoelectric effect and collisions between water, supercooled water, and ice in various forms. On Earth, it is thought that the positive charges are predominant on the smaller particles and are raised preferentially by the vertical convective motion. In Earth's atmosphere, charges can be separated to distances of the order of kilometers. Most lightning discharges in the Earth's atmosphere occur as intra-cloud lightning and neutralize tens of Coulombs of charge. Cloud-to-ground lightning generally transfers negative charge from the lower portion of the cloud to the Earth's surface. A schematic illustration of the distribution of various possible precipitation elements in a cumulo nimbus cell on Earth is shown in figure 206 (adapted from Magono, 1980). The arrows indicate the velocity of elements of the air. The anvil shape of the cloud top is also indicated.

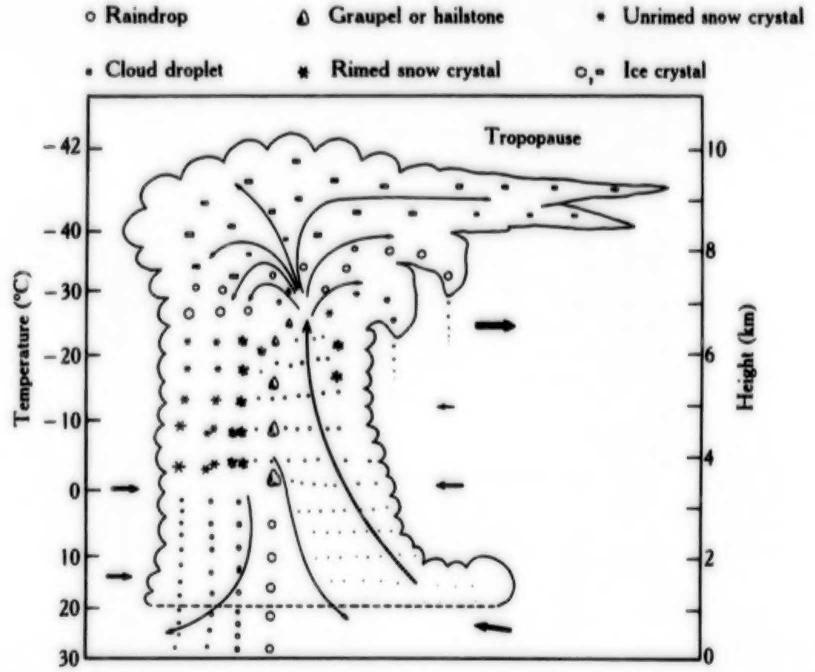

Figure 206. Distribution of types of precipitation in a convective thunderstorm cell on Earth. (Adapted from Magono, 1980.)

A sketch of the temperature-density-altitude-pressure profile of the jovian atmosphere is shown in figure 207, based upon the cloud model of Weidenschilling and Lewis (1973). The height region for a water ice cloud for an atmospheric mixing ratio of 10^{-3} that of the solar abundance is indicated by the hatched area (Atreya, 1986). At the top of figure 207, the global convective motions in the jovian system are indicated schematically (after Rinnert, 1985).

The cloud model in figure 207 assumes stationary conditions, solar composition, and chemistry in thermal equilibrium (i.e., no sources such as lightning to change energy from any existent fields to sound, heat, RF, etc.). More recent cloud models, deduced primarily from spacecraft optical measurements, contain only an optically thin NH_4SH cloud, if any, but assume aerosol layers to provide haze above the ammonia clouds (Sato and Hansen, 1979; West and Tomasko, 1980; Martin et al., 1981; Orten et al., 1982; Owen and Terrile, 1981). Further, Bjoraker et al. (1986) deduced from Voyager infrared interferometer spectrometer (IRIS) measurements at 5 μm that water is depleted by a factor of ~50 relative to solar abundance in the 2–6 bar atmosphere region.

With the type of atmosphere illustrated in figure 207, a cartoon comparison can be made of the Earth's and Jupiter's cloud structures, as is done in figure 208. The dominant atmospheric chemical species are boxed. On Earth, the topography can at times also determine cloud location for the separated charges. Obviously, such an orographical influence should not exist at Jupiter, and the lightning should primarily be of the intra-cloud, cloud-to-cloud, and cloud-to-"air" types.

Especially important considerations for establishing the conditions for localized, intense, upward convective motions in the Jupiter atmosphere has been the

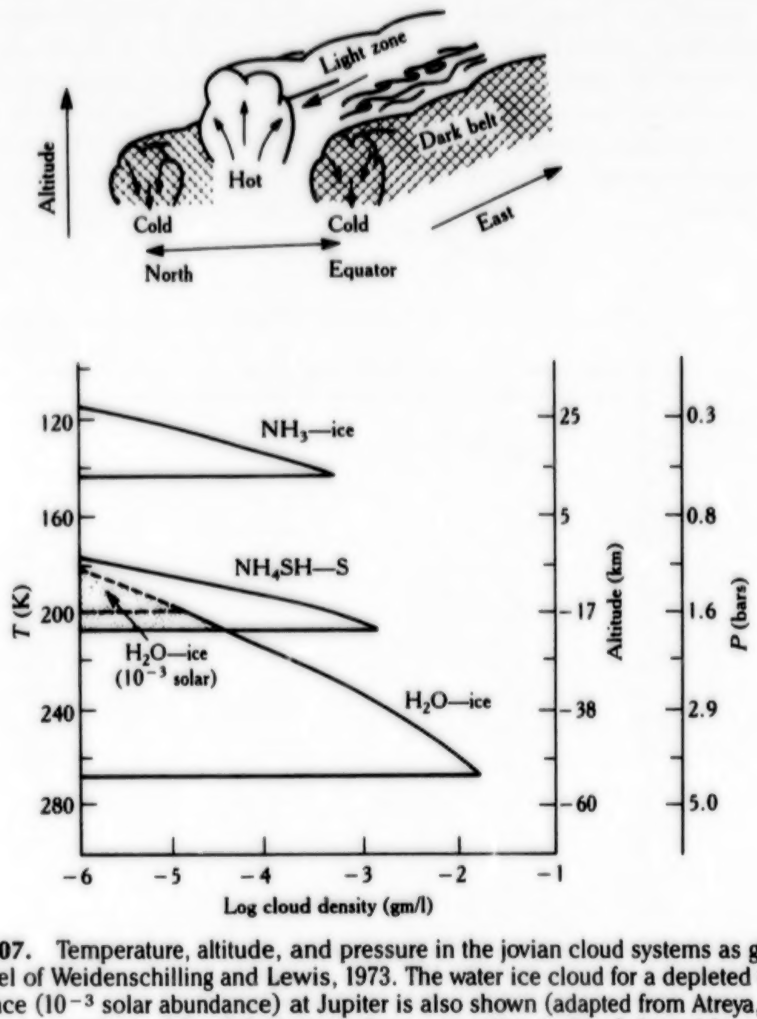

Figure 207. Temperature, altitude, and pressure in the jovian cloud systems as given by the model of Weidenschilling and Lewis, 1973. The water ice cloud for a depleted water abundance (10^{-3} solar abundance) at Jupiter is also shown (adapted from Atreya, 1986). At the top is a cartoon of the global atmosphere convective motion (adapted from Rinnert, 1985).

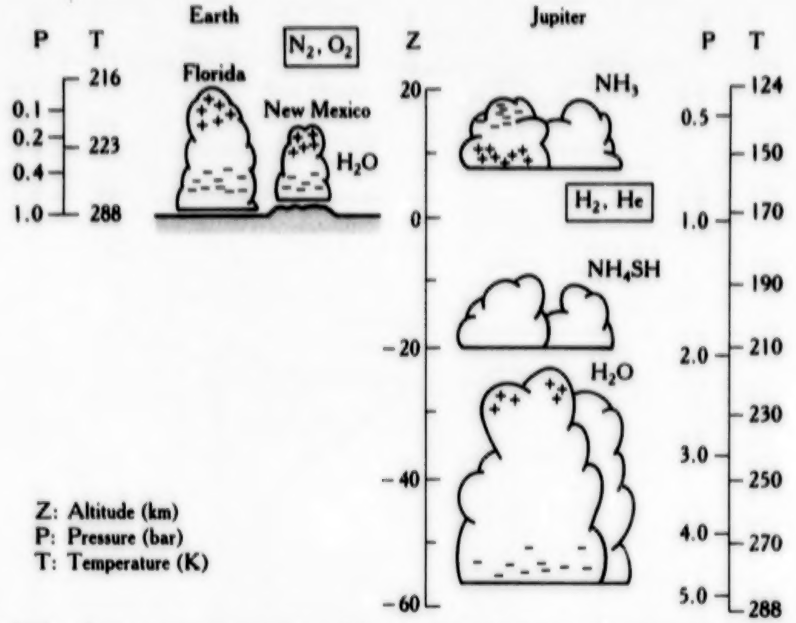

Figure 208. Cartoon representation of the possible locations of separated charges in the atmospheres of Earth and Jupiter, showing comparisons of the cloud locations, altitudes, and temperature.

recent modeling work of Stoker (1986) to understand the vertical structure of the equatorial plumes. She finds that, for appropriate parameters for cumulous cloud formation, moist convection can produce the equatorial plumes. For a solar water abundance, peak vertical convective velocities of $\sim$150 m s are found.

The model results of Stoker (1986) suggest that the water abundance is closer to solar than to the depleted water conditions suggested by Bjoraker et al. (1986). Lunine and Hunten (1987) use the idea of moist convective plumes and the model plume of Stoker (1986) to conclude that such plumes can explain the apparent depletion of the IRIS-detected water vapor without invoking a global depletion of water from solar abundance on Jupiter.

A sketch of the production of jovian equatorial plumes, adapted from Stoker (1986), is shown in figure 209. Clouds initiated at the water cloud level (fig. 207) rise to altitudes of $\sim$700 mbar, where ammonia condenses and forms the observed anvil-shaped plumes. The conservation of mass is accomplished by downwelling in the dark atmosphere areas between plumes, where the ammonia aerosols evaporate.

It is interesting to note that neither Stoker (1986) nor Lunine and Hunten (1987) made mention of the possibility of lightning production in such convective regions, even though atmospheric conditions in the models, such as aerosols and upward convective velocities, are present to produce electrical charge separations and discharges (e.g., Williams et al., 1983; Levin et al., 1983).

MEASUREMENT OF JUPITER LIGHTNING

Summaries of the analyses of the optical lightning signals (Cook et al., 1979; Borucki et al., 1982; William et al., 1983) and the magnetosphere whistler wave signals (Gurnett et al., 1979; Scarf et al., 1981; Lewis, 1980, 1981; Kurth et al., 1985) have been presented in Rinnert (1985), Williams (1986), and Uman (1987). An adaptation of these summaries is presented in table 30. Analyses of the optical flashes suggest that the detected lightning was very energetic, exceeding even the superbolts seen only in $\sim$1 in 10^3 flashes for an energy $>10^{10}$ J on Earth (Turman, 1977). Recent laboratory experiments by Borucki and McKay (1987) suggest that the conclusions of Borucki et al. (1982) on discharge energies may be low by a factor of approximately three.

Jovian flash rates are important for considerations of possible nonequilibrium chemical processes. However, Lewis (1980a) concluded that "even if every erg of Jupiter's heat flux is used with perfect efficiency [to attain] conditions for efficient HCN synthesis, . . . lightning synthesis is of negligible importance" in Jupiter's atmosphere. He reconfirmed his view in an analysis of the Voyager results (Lewis, 1980b), although Scarf et al. (1981) disputed Lewis' conclusions as to the actual

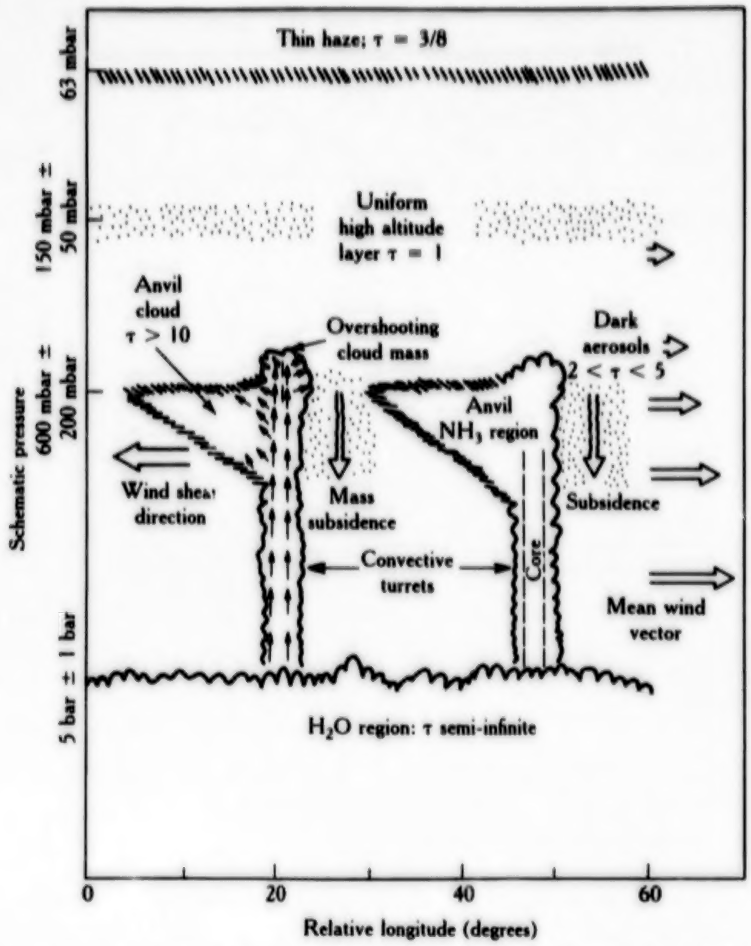
Thin haze; τ = 3/8
Uniform high altitude layer τ = 1
Anvil cloud τ > 10
Overshooting cloud mass
Dark aerosols 2 < τ < 5
Anvil NH₃ region
Wind shear direction
Mass subsidence
Subsidence
Convective turrets
Core
Mean wind vector
H₂O region: τ semi-infinite
Schematic pressure
63 mbar
150 mbar ± 50 mbar
600 mbar ± 200 mbar
5 bar ± 1 bar
0
20
40
60
Relative longitude (degrees)

Figure 209. Cartoon illustration of ideas on the production of equatorial plumes by moist convection in Jupiter's atmosphere (adapted from Stoker, 1986). The *horizontal scale* shows the relative sizes of the features (scale in degrees longitude). The *vertical scale* is exaggerated. The plumes stream from the west of the convective cores because of the negative wind shear associated with the decrease of zonal winds with altitude above the water cloud layer.

Table 30. Voyager 1 Lightning on Jupiter

Instrument	Observation	Inferences
Imaging	20 luminous events in 192 s over 10^9 km, around 50°[a,b,c,d]	3×10^{-3} km^{-2} yr^{-1}[a] 4 km^{-2} yr^{-1}[b] 3–30 km^{-2} yr^{-1}[c] 0.1 km^{-2} yr^{-1}[d] 2.5×10^9 J optical-flash[b] 1.7×10^{12} J total flash[b] 8.5×10^8 J optical-flash at cloud top[d] 2.1×10^{12} J total-flash at cloud top[d]
Plasma wave	167 whistler signals at 2–7 kHz, 0.12 s^{-1}[e,f]	Whistlers originate near 66° latitude[g] 1–4 $\times 10^{-2}$ km^{-2} yr^{-1}[h] 40 km^{-2} yr^{-1}[f]

[a] Cook et al., 1979; [b] Borucki et al., 1982; [c] Williams et al., 1983; [d] Williams, 1986; [e] Gurnett et al., 1979; [f] Scarf et al., 1981; [g] Menietti and Gurnett, 1980; [h] Lewis, 1980.

rates implied by the Voyager 1 plasma wave instrument, the rates derived by Scarf et al. being substantially greater than the Lewis results. The original works should be consulted for detailed discussions of the various assumptions that were made in the different analyses in order to arrive at the lightning rate conclusions.

It is important to point out that all of the Jupiter lightning data that presently exist were obtained from the Voyager 1 flyby; no optical or whistler data were obtained from the Voyager 2 mission. Although Smith et al. (1979) stated that eight lightning flashes were observed by the Voyager 2 TV system, Williams (1986) notes that "a very large number of cathode blemishes appear on the Voyager 2 images." Furthermore, the Voyager 2 spacecraft did not approach Jupiter as closely as did Voyager 1.

Regarding the nonobservation of whistler waves by Voyager 2, the perijove distance of ~10 R_J, which maps to rather high latitude geomagnetic field lines (>60°), probably was one important determining factor. Williams (1986) notes that 85 percent of the optical flashes were observed around 50° latitude. The latitudes of origin of the whistler signals depend upon assumptions made as to whether the observed signals are ducted or unducted, and therefore can be quite uncertain. Another important factor according to W. D. Kurth (1987) is that the ambient magnetosphere plasma wave noise in the jovian plasma sheet beyond ~10 R_J was sufficiently high to mask any weak lightning-generated whistler signals. The Voyager 1 whistler signals were often found in regions where the magnetosphere noise in the appropriate frequency ranges was rather low.

DETECTION OF JUPITER LIGHTNING

Williams (1986) has concluded that ". . . Earth or near Earth-based lightning observing programs hold little promise of success" for such remote detection of jovian lightning. Because of the jovian ionosphere propagation characteristics (Rinnert et al., 1979; Zarka, 1985) and the magnetosphere plasma environment, Rinnert (1985) states that there is "little possibility to study lightning (on Jupiter) by observing radio emissions using Earth-based instrumentation." A proxy method of monitoring nonequilibrium chemical species might provide, in Earth orbit, information on lightning energy deposition into the jovian atmosphere. However, there are presently so many unknowns and variables—including agreement on the basic jovian lightning rate—that such a possibility would seem unlikely to be practical soon.

It follows that the Jupiter Galileo mission provides the best opportunity to obtain new and better information on jovian lightning. The plasma wave experiment on the orbiter will yield information on the whistler wave occurrence over a wide range of latitudes during the mission lifetime. (The plasma wave experiment on the Ulysses spacecraft may also give similar data as this space vehicle uses Jupiter to exit the ecliptic plane.) The solid-state imaging system will have long intervals of opportunity to monitor the nighttime hemisphere of the planet. The acquisition of visible images of lightning will still be hampered, as were the Voyager images, by the attenuation (scattering) of light propagating through the jovian clouds (e.g., Williams, 1986; Borucki and Williams, 1986; Thomason and Krider, 1982). Williams (1986) has provided predicted luminosity distributions for lightning discharges located in

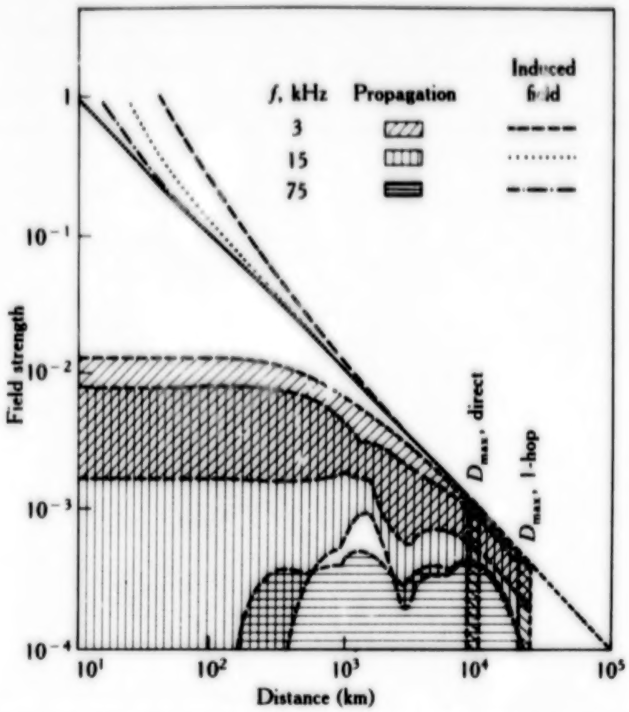

Figure 210. Radiation field wave field strength (arbitrary units) as a function of line-of-sight propagation and of ionospheric reflections. The field strength is normalized to 1 at 10 km from the source. The ionospheric reflections for different ionosphere models and propagation directions with respect to the permanent magnetic field are indicated by the areas within the *hatch regions: oblique, vertical,* and *horizontal hatch marks* correspond to f = 3, 15, and 75 kHz, respectively. The *dashed, dotted,* and *dash-dotted lines* represent the induced fields for f = 3, 15, and 75 kHz, respectively.

the ammonia and lower water clouds in a water depleted atmospheric model and in a solar composition atmospheric model. The intensity falls to half its source value at distances of the order of 30 to 60 km. The detectability will then depend upon the original source strength and the instrument sensitivity. The nephelometer instrument on the Galileo probe will provide key cloud information for better modeling of the opacity of the jovian clouds to optical lightning signals.

The principal lightning experiment on the Galileo probe is the LRD antenna system, designed to measure the statistics and waveforms of the RF magnetic signals from lightning in the band ~10 Hz to 100 kHz. The measured radiation field waveshapes will allow deduction of information on the electrical breakdown processes in the atmosphere. There will also be correlation of the RF signals with optical signals from a photoelectric detector. Details of the instrument are provided in Lanzerotti et al. (1983) and Rinnert et al. (1985b). Figure 210, adapted from Rinnert et al. (1979), shows that direct propagation of signals (3 to 75 kHz) occurs to distances of order 10^4 km in Jupiter's atmosphere. It is likely that discharges with the energy of a typical cloud-to-ground discharge on Earth (order 10^8 J) can be detected at 10^4 km or more distance within Jupiter's atmosphere. "Superbolts," of course, will be observed much further away. There is also a special superbolt channel in the instrument.

On Earth, cloud-to-ground discharges are quite different in their RF characteristics than are intra-cloud discharges, and these differences are being carefully studied in order to evaluate optimally the atmospheric breakdown processes, the electrical currents, and the possible chemical processes associated with jovian lightning. As an example, shown in the upper portions of both sides of figure 211 are the magnetic fields of two cloud-to-ground return strokes measured in Lindau with the Galileo LRD engineering instrument unit during a nearby lightning storm in 1984. The power spectra of the RF signals for each of these discharges were calculated for us by D. J. Thomson (AT&T Bell Laboratories) after first mathematically removing the impulse response of each signal. The power spectra were then calculated using four prolate spheroidal data windows in the time domain and a fast Fourier transform algorithm (see Thomson, 1982).

Each RF power spectrum clearly falls with increasing frequency and each spectrum has definite structure that corresponds to the "secondary peaks" evident in the time domain traces following the initial impulse.

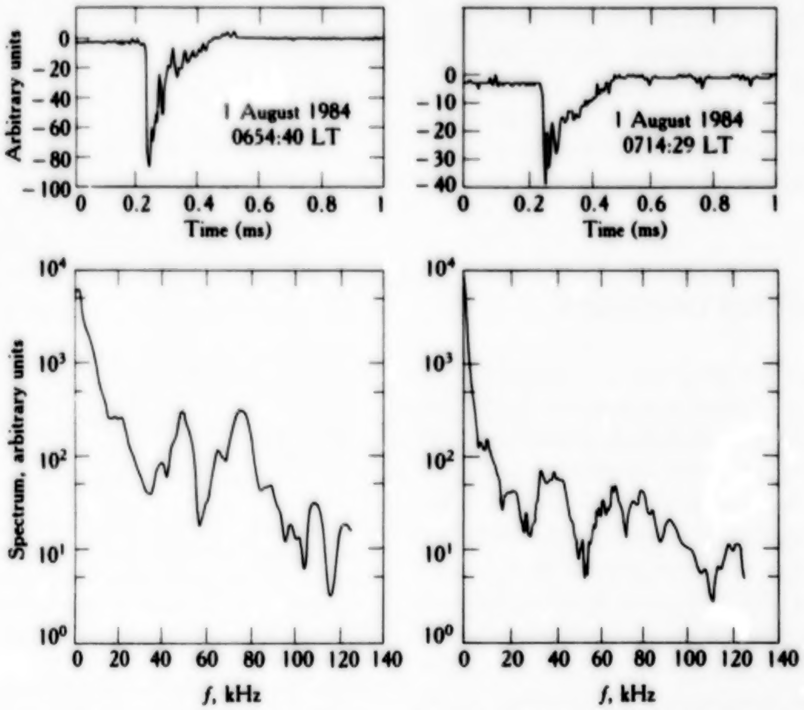

Figure 211. *Upper panels*: Two cloud-to-ground discharges measured with the Galileo probe lightning experiment engineering unit during a lightning storm near Lindau in August 1984. The *lower panels* show the power spectra for each discharge.

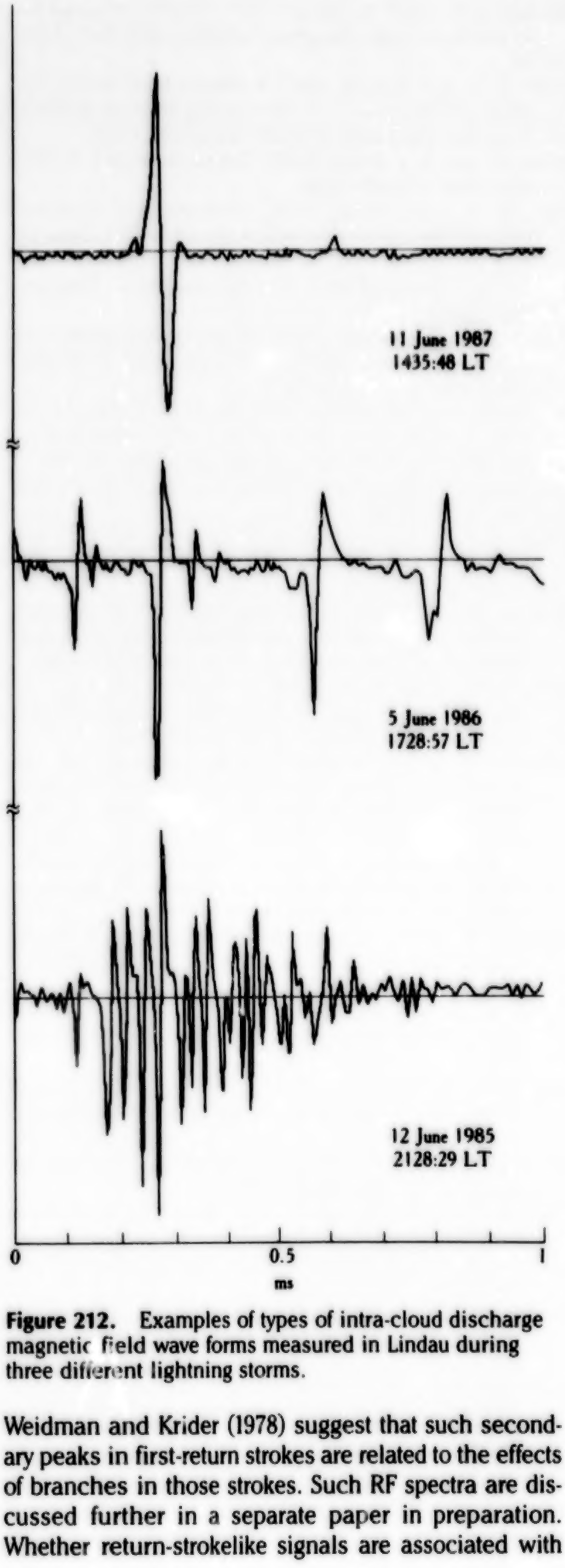

Figure 212. Examples of types of intra-cloud discharge magnetic field wave forms measured in Lindau during three different lightning storms.

Weidman and Krider (1978) suggest that such secondary peaks in first-return strokes are related to the effects of branches in those strokes. Such RF spectra are discussed further in a separate paper in preparation. Whether return-strokelike signals are associated with intra-cloud and cloud-to-cloud discharges in the jovian atmosphere will be determined as the Galileo probe settles on its parachute into the atmosphere.

The RF signals of intra-cloud discharges have been much less studied than those of cloud-to-ground discharges (see e.g., Uman, 1987). On average, ground discharges are much more powerful than cloud discharges. The ratios of the amplitudes of return stroke to cloud discharge appear to range from about 20 to 1 at ~3 kHz, to ~10 to 1 at 10 kHz, to ~1 to 1 at 100 kHz (Brook and Ogawa, 1977). Shown in figure 212 are examples of different types of magnetic field wave forms produced by cloud discharges and measured using the Galileo probe engineering unit. The instrument provides a 1 ms window of the received signal that contains the largest amplitude waveform detected during a pre-set measuring interval. From top to bottom in the figure, the cloud discharges observed in 1 ms include a single bipolar pulse, a series of quasi-periodic bipolar pulses filling the entire measuring internal, and a sequence of (possibly approximately periodic) bipolar pulses apparently modulated by an overall signal envelope. Work is in process to understand such intracloud RF signals so as to be able to use them to deduce fundamental information as current waveshapes, breakdown processes, and energy deposition rates in the jovian atmosphere.

SUMMARY

Lightning exists with high probability on Jupiter, implying the existence of a significant electrification processes in the atmosphere of this largest planet. The importance of such electrical energy for non-equilibrium chemical processes is under debate. Jovian lightning cannot be adequately monitored from Earth or near-Earth orbit. The Galileo mission is important to obtain additional and new information on the properties of electrical processes in the jovian atmosphere.

ACKNOWLEDGMENTS

A portion of the work at the University of Florida was supported by NASA contract NAS2-9976.

References

Atreya, S. K. (1986). *Atmospheres and ionospheres of the outer planets and their satellites.* Springer-Verlag, New York and Heidelberg.

Bar-Nun, A. (1975). Thunderstorms on Jupiter. *Icarus* 24:86–94.

Bar-Nun, A. (1979). Acetylene formation on Jupiter: Photolysis or thunderstorms? *Icarus* 38:180–191.

Bar-Nun, A., N. Noy, and M. Podolak (1984). An upper limit to the abundance of lightning-produced amino acids in the jovian water clouds. *Icarus* 59:162–168.

Bar-Nun, A., and M. Podolak (1985). The contribution by thunderstorms to the abundances of CO, C_2H_2, and HCN on Jupiter. *Icarus* 64:122–124.

Bjoraker, G. A., H. P. Larson, and V. G. Kunde (1986). The abundance and distribution of water vapor in Jupiter's atmosphere. *Astrophys. J.* 311:1058–1072.

Borucki, W. J., A. Bar-Nun, F. L. Scarf, A. F. Cook, II, and G. E. Hunt (1982). Lightning activity on Jupiter. *Icarus* 52:492–502.

Borucki, W. J., and C. P. McKay (1987). Optical efficiencies of lightning in planetary atmospheres. *Nature* 328:509–510.

Borucki, W. J., and M. A. Williams (1986). Lightning in the jovian water cloud. *J. Geophys. Res.* 91:9893–9903.

Brook, M., and T. Ogawa (1977). The cloud discharge. In *Lightning* (R. H. Golde, ed.), pp. 191–230. Academic Press, New York.

Burns, J. A., M. R. Showalter, J. N. Cuzzi, and R. H. Durison (1983). Saturn electrostatic discharges: Could lightning be the cause? *Icarus* 54:280–295.

Chadha, M., J. Flores, J. Lawless, and C. Ponnamperuma (1971). Organic synthesis in a simulated jovian atmosphere. *Icarus* 15:39–44.

Cook, A. F., N., T. C. Duxbury, and G. E. Hunt (1979). First results on jovian lightning. *Nature* 280:794.

Gurnett, D. A., R. R. Shaw, R. R. Anderson, W. S. Kurth, and F. L. Scarf (1979). Whistlers observed by Voyager 1: Detection of lightning on Jupiter. *Geophys. Res. Lett.* 6:511–514.

Kaiser, M. L., J. E. P. Connerney, and M. D. Desch (1983). Atmospheric storm explanation of saturnian electrostatic discharges. *Nature* 303:50–53.

Ksanfomality, L. V. (1979). Lightning in the cloud layer of Venus. *Kosm. Issled.* 17:747–762.

Kurth, W. D. (1987). Private communication.

Kurth, W. S., B. D. Strayer, D. A. Gurnett, and F. L. Scarf (1985). A summary of whistlers observed by Voyager 1 at Jupiter. *Icarus* 61:497–507.

Lanzerotti, L. J., K. Rinnert, E. P. Krider, M. A. Uman, G. Dehmel, F. O. Gliem, and W. I. Axford (1983). Planetary lightning and lightning measurements on the Galileo Probe to Jupiter's atmosphere. In *Proceedings in atmospheric electricity* (L. H. Ruhnke and J. Latham, eds.). A. Deepak Publishing, Hampton, Va.

Levin, Z., W. J. Borucki, and O. B. Toon (1983). Lightning generation in planetary atmospheres. *Icarus* 56:80–115.

Lewis, J. S. (1980b). Lightning on Jupiter: Rate, energetics, and effects. *Science* 210 1351–1352.

Lewis, J. S. (1980a). Light synthesis of organic compounds on Jupiter. *Icarus* 43:85–95.

Lunine, J. I., and D. M. Hunten (1987). Moist convection and the abundance of water in the troposphere of Jupiter. *Icarus* 69:566–570.

Magono, C. (1980). *Thunderstorms*. Elsevier, Amsterdam.

Marten, A., D. Rouan, J. P. Baluteau, A. Chedin, and N. Scott (1981). Study of the ammonia ice cloud layer in the equatorial region of Jupiter from the infrared interferometric experiment on Voyager. *Icarus* 46:233–248.

Menietti, J. D., and D. A. Gurnett (1980). Whistler propagation in the jovian magnetosphere. *Geophys. Res. Lett.* 7:49–52.

Orten, G. S., J. F. Appleby, and J. V. Martonchick (1982). The effect of ammonia ice on the outgoing thermal radiance from the atmosphere of Jupiter. *Icarus* 52:94–116.

Owen, T., and R. J. Terrile (1982). Colors on Jupiter. *J. Geophys. Res.* 87:11193–11201.

Prinn, R. G., and T. Owen (1976). Chemistry and spectroscopy of the jovian atmosphere. In *Jupiter* (T. Gehrels, ed.), pp. 319–371. Univ. of Arizona Press, Tucson.

Rinnert, K. (1985). Lightning on other planets. *J. Geophys. Res.* 90:6225–6237.

Rinnert, K. (1982). Lightning within planetary atmospheres. In *Handbook of atmospherics* (H. Volland, ed.), 32:99–132. CRC Press, Boca Raton, Fla.

Rinnert, K., L. J. Lanzerotti, E. P. Krider, M. A. Uman, G. Dehmel, F. O. Gliem, and W. I. Axford (1979). Electromagnetic noise and radio wave propagation below 100 kHz in the jovian atmosphere. 1. Equatorial region. *J. Geophys. Res.* 84:5181–5188.

Sagan, C. E., E. R. Lipincott, M. O. Dayhoff, and R. V. Eck (1967). Organic molecules and the coloration of Jupiter. *Nature* 213:273–274.

Sato, M., and J. E. Hansen (1979). Jupiter's atmospheric composition and cloud structure deduced from absorption bands in reflected sunlight. *J. Atmos. Sci.* 36:1133–1167.

Scarf, F., D. A. Gurnett, W. S. Kurth, R. R. Anderson, and R. R. Shaw (1981). An upper bound to the lightning flash rate in Jupiter's atmosphere. *Science* 213:684–685.

Smith, B., A., L. A. Soderblom, R. Beebe, J. Boyce, G. Briggs, M. Carr, S. A. Collins, A. F. Cook, II, G. E. Danielson, M. E. Davies, G. E. Hunt, A. Ingersoll, T. V. Johnson, H. Masursky, J. McCauley, D. Morrison, T. Owen, C. Sagan, E., M. Shoemaker, R. Strom, V. E. Suomi, and J. Veverka (1979). The galilean satellites and Jupiter: Voyager 2 imaging science results. *Science* 206:927–950.

Stoker, C. R. (1986). Moist convection: A mechanism for producing the vertical structure of the jovian equatorial plumes. *Icarus* 67:106–125.

Taylor, W. W. L., F. L. Scarf, C. T. Russell, and L. H. Brace (1979). Evidence for lightning on Venus. *Nature* 279:614–616.

Thomason, L. W., and E. P. Krider (1982). The effects of clouds on the light produced by lightning. *Atmos. Sci.* 39:2051–2065.

Thomson, D. J. (1982). Spectrum estimation and harmonic analysis. *Proc. IEEE* 70:1055–1095.

Turman, B. N. (1977). Detection of lightning superbolts. *J. Geophys. Res.* 82:2566–2568.

Uman, M. A. (1987). *The lightning discharge*. Academic Press, New York.

Weidenschilling, S. J., and J. S. Lewis (1973). Atmospheric and cloud structures of the jovian planets. *Icarus* 20:465–476.

Weidman, C. D., and E. P. Krider (1978). The fine structure of lightning return stroke wave forms. *J. Geophys. Res.* 83:6239.

West, R. A., and M. G. Tomasko (1980). Spatially resolved methane band photometry of Jupiter. *Icarus* 41:278–292.

Williams, M. A., E. P. Krider, and D. M. Hunten (1983). Planetary lightning: Earth, Jupiter, and Venus. *Rev. Geophys.* 21:892–902.

Williams, M. A. (1986). *An analysis of the Voyager images of jovian lightning.* Ph.D. thesis, Univ. of Arizona, Tucson.

Woeller, F., and C. Ponnamperuma (1969). Organic synthesis in a simulated jovian atmosphere. *Icarus* 10:386–392.

Zarka, P. (1985). On detection of radio bursts associated with jovian and saturnian lightning. *Astron. Astrophys.* 146:L15–L18.

Zheleznyakov, V. V. (1970). *Radio emission of the sun and planets.* Pergamon Press, Oxford.

31

Jupiter Lightning Locations

Laurance R. Doyle
S.E.T.I. Institute, Los Altos
William J. Borucki
NASA Ames Research Center, Moffett Field

Abstract

A redetermination of the location of lightning events gave substantial differences with those determined by Cook et al. (1979), which were based on preliminary navigation data, and systematic differences with those determined by Williams (1986). The lightning events shown in the two discovery images are found near 50° and 57° N latitude. A search for lightning events in 13 previously unexamined images showed no events. These, however, were much shorter exposures of less than 1 s each. This result implies that the lightning event rate at other latitudes is not likely to be much larger than that determined from the high-latitude discovery images. The mean and median values of the optical energy radiated per flash are found to be 1.08×10^9 and 6.65×10^8 J, respectively; somewhat higher than the values previously derived, implying that lightning activity on Jupiter is more energetic than previously estimated.

INTRODUCTION

Jovian lightning was discovered in Voyager 1 images FDS 16396.39 (Smith et al., 1979; Cook et al., 1979) and FDS 16396.31 (Borucki et al., 1982). These images were obtained with the wide-angle camera using a clear filter. Although about twenty lightning events have been reported in each of the two images, no search for lightning events in other images has been reported. Both of the discovery images cover the same jovigraphic region: 30° to 60° N latitude. Many nightside images exist for other regions. These images were obtained both with the wide-angle (WA) and narrow-angle (NA) cameras with a variety of spectral filters. It seems appropriate to search the most promising of these images to determine what can be learned about the dependence of lightning activity on latitude and longitude.

The determination of latitude and longitude on the darkside of a gaseous planet is not as direct as it is for dayside images of planets with permanent features.

The lightning locations reported by Cook et al. (1979) were based on preliminary spacecraft navigation data that have now been superseded. Lightning locations presented by Williams (1986) were based on jovicentric interpolations of jovigraphic (sometimes called jovidetic) data. These results can also be improved.

The energy distribution of the lightning flashes estimated by Borucki et al. (1982) can be improved by including more of the less energetic events. Their work included only the most energetic events to avoid misidentifications with image blemishes, calibration marks, and galactic cosmic ray "hits." We have constructed a map of the image artifacts and can now extend the energy distribution to lower energies.

SEARCH FOR OTHER NIGHTSIDE IMAGES

The important parameter to consider when choosing other images to search for lightning events is the product of the area of the planet in the image and the exposure time of the images. We will refer to this quantity as the area-time product (ATP). Another important parameter is the spectral filter used to obtain the image. The clear filter has the highest transmission and the largest spectral bandpass. Because the other filters pass less of the incident light, the detection threshold is substantially higher for such images and the number of lightning events will be correspondingly lower. Because the transmission of the NA camera is somewhat less than that of the WA camera, images obtained with it have a higher detection threshold as well as a smaller area viewed. Table 31 lists the parameters of interest for the discovery images and the most promising nightside images. From this table it can be seen that the sum of the ATP of the two discovery images is about 30 times as large as the total of all the other images. If the image that used the narrow-band CH_4 filter is excluded, then the total ATP is 1 percent that of the discovery images. Hence, we can expect to detect less than one event even if all the images had a transmission as high as that of the discovery images. Image FDS 16413.00 has an ATP equal to 1/40 that of the discovery images and thus might be expected to detect one or two lightning flashes if the methane filter had not been used.

Although these images do not have a high-ATP value and many of them were taken with bandpass filters, they do cover jovigraphic regions not covered by the discovery images. See figure 213 for a map of the coverage of the WA images and figure 214 for a map of the NA images. Hence, if the lightning flash rate in these regions is substantially higher than that observed in the discovery region, then it is reasonable to expect to find a few flashes.

One event in image FDS 16411.48 and seven events in the "methane" image (FDS 16413.00) were found to

Table 31. List of Images Searched for Lightning

Image FDS	Camera/Filter	Exposure time (ms)	Area (km^2)	Area-time product (km^2-s)
		Discovery images		
16396.31	WA/Clr	192000	1.9×10^9	3.0×10^{11}
16396.39	WA/Clr	192000	3.4×10^9	5.4×10^{11}
		New images		
16411.43	NA/Grn	480	2.8×10^8	1.3×10^8
16411.44	WA/Blu	60	4.4×10^9	2.6×10^8
16411.48	WA/Orn	360	5.0×10^9	1.8×10^9
16412.41	NA/Grn	480	2.1×10^8	1.0×10^8
16412.45	NA/Grn	480	2.7×10^8	1.3×10^8
16412.57	NA/Grn	480	3.4×10^8	1.6×10^8
16413.00	WA/CH_4	3840	5.9×10^9	2.3×10^{10}
16413.36	NA/Grn	480	2.2×10^8	1.0×10^8
16413.42	NA/Grn	480	1.9×10^8	9.3×10^7
16413.56	NA/Grn	480	4.6×10^8	2.2×10^8
16414.09	WA/Vio	480	5.7×10^9	1.0×10^9
20672.19	WA/Orn	240	2.3×10^9	5.4×10^8
20672.25	WA/Grn	60	2.6×10^9	1.6×10^8
Total area-time product minus CH_4 filter image:				7.9×10^9
Total new area-time product searched:				3.1×10^{10}

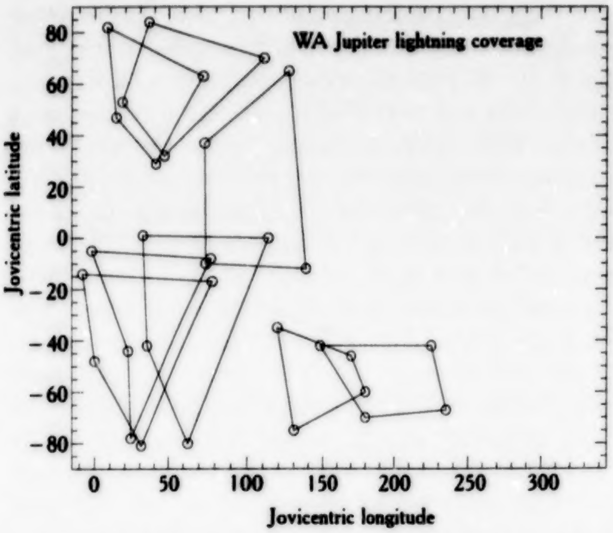

Figure 213. Map of area coverage of images taken of the jovian nightside by the wide-angle camera.

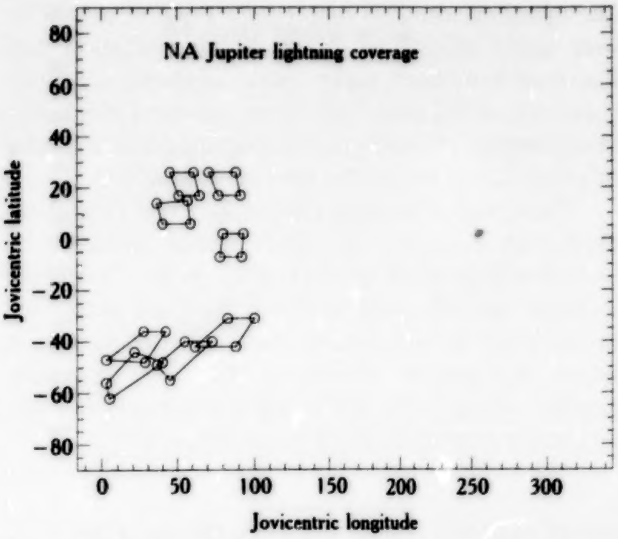

Figure 214. Map of area coverage of images taken of the jovian nightside by the narrow-angle camera.

be significantly above the noise level. However, after constructing a map of the artifacts (blemishes in the cameras due to, for example, micro meteor hits), it was found that none of these events could be unambiguously attributed to lightning. Therefore we conclude that none of the regions examined has a lightning event rate substantially larger than that derived from the discovery images.

REDETERMINATION OF THE LIGHTNING LOCATIONS

Both discovery images are triple exposures of 192 s each. During the exposures, the camera executed two 11-s duration slews with the shutter held open. The available navigation information for the images refers to the beginning of the image exposure time in both cases. Because the nightside of Jupiter is featureless except for the auroral arcs near the magnetic poles, the locations of the lightning events depend critically on the navigation data and the shape of the planet. The first latitude-longitude determinations were presented by Cook et al. (1979). However, their work was based on preliminary navigation data that have since been superseded. Later work by Williams (1986) was based on navigation data that gave *jovidetic* latitudes and longitudes at four control points, but he used a *jovicentric* interpolation routine to derive the lightning locations. The expected magnitude of the errors due to such an

Table 32. Comparison of Lightning Locations for Image 16396.31

(This work)		(Williams, 1986)		
Latitude	**Longitude**	**Latitude**	**Longitude**	**Central pixel (line, sample)**
50.7	46.6	48.2	47.6	(188, 494)
51.1	46.4	49.0	48.0	(197, 499)
51.5	46.8	48.8	47.4	(194, 508)
50.3	44.8	47.8	45.4	(218, 467)
50.1	44.5	48.2	36.0	(220, 461)
50.1	44.3	47.2	34.6	(225, 458)
50.3	34.5	47.6	34.8	(423, 338)
49.9	34.4	49.2	36.8	(420, 330)
49.9	33.6	50.2	34.8	(437, 319)
51.7	36.0	48.8	33.6	(405, 380)
52.7	35.4	50.4	34.4	(427, 388)
52.3	34.2	48.6	32.6	(446, 367)
51.3	33.0	59.2	29.8	(459, 336)
50.0	32.6	55.8	27.8	(457, 309)
60.5	29.4	57.4	27.2	(573, 441)
56.6	27.7	49.6	26.6	(586, 363)
58.6	27.1	52.0	24.8	(602, 389)
53.0	25.0	52.2	24.0	(619, 269)
53.2	24.6	51.4	23.8	(626, 267)
51.1	25.0	49.0	23.2	(610, 232)
52.3	24.5	49.0	22.6	(625, 250)
52.5	24.2	48.6	21.8	(631, 249)
50.6	22.8			(649, 195)
49.8	22.7			(648, 177)
45.5	19.9			(683, 46)
52.0	34.6			(436, 368)
51.2	23.4			(641, 231)
44.7	19.4			(690, 21)

Table 33. Comparison of Lightning Locations for Image FDS 16396.39

(This work)		(Williams, 1986)		(Cook et al., 1979)		Central pixel (line, sample)
Latitude	**Longitude**	**Latitude**	**Longitude**	**Latitude**	**Longitude**	
49.5	46.3	48.6	45.8	54.5	35.0	(279, 316)
49.7	45.3	47.2	45.8	55.0	33.5	(301, 304)
49.0	44.5	48.2	45.0	54.5	33.0	(307, 283)
49.0	43.8	47.2	44.0	54 5	32.5	(320, 274)
48.8	43.8	47.0	43.4	50.5	46.0	(317, 271)
48.8	43.5	47.0	43.0	50.5	45.5	(324, 266)
49.1	43.6	49.6	33.0	49.0	46.0	(327, 273)
48.9	43.4	49.2	32.2	45.0	48.5	(328, 266)
50.8	33.9	49.4	31.2	45.0	48.0	(525, 168)
50.3	33.3	57.0	27.8	44.0	48.0	(535, 150)
49.9	32.5	56.6	25.0	48.0	39.5	(546, 133)
50.1	32.6	56.6	24.6	48.0	39.0	(547, 137)
57.0	29.0			48.0	38.0	(639, 219)
56.8	26.5			48.0	37.5	(685, 179)
49.2	46.2			47.0	37.5	(276, 310)
50.6	25.2			47.0	37.0	(683, 47)

interpolation can be seen by considering the following set of equations.

To convert from planetocentric to planetodetic latitudes (longitudes will remain the same) we use the following equations:

$$\rho \cos(\phi') = C \cos(\phi),$$

$$\rho \sin(\phi') = S \sin(\phi),$$

where ρ = magnitude of geocentric radius vector to point on surface of interest, ϕ' = planetocentric latitude, and ϕ = planetodetic latitude. Also,

$$S = \left[\frac{a(1 - e^2)}{(1 - e^2\sin^2\phi)^{1/2}}\right],$$

$$C = \left[\frac{a}{[\cos^2\phi + (1 - f)^2\sin^2\phi]^{1/2}}\right].$$

Here, then, a = equatorial radius, $e = (1 - c^2/a^2)^{1/2}$ the eccentricity, with c being the polar radius, and $f = (a - c)/a$.

From these equations, one can derive the location and magnitude of difference that will occur between the use of planetocentric and planetodetic latitude systems. The magnitude of the maximum deviation will be

$$\Delta\phi = \frac{\tan^{-1}e^2}{2(1 - e^2)^{1/2}},$$

and the latitude at which this maximum will occur is then

$$\sin \phi = \frac{1}{(2 - e^2)^{1/2}}.$$

For Jupiter we have $e = 0.347$ and $f = 0.062$, so that the maximum difference will occur at $\phi = 46\overset{\circ}{.}8$ and will be of magnitude $\tan^{-1}(0.064) = 3\overset{\circ}{.}7$. We see, then, that the use of jovicentric latitudes in the determination of lightning coordinates will introduce significant errors when cross-referenced with jovidetic (sometimes called jovigraphic) control points.

The locations derived for lightning by Cook et al. (1979), Williams (1986), and the present work are compared in table 32 for image FDS 16396.31 and table 33 for image FDS 16396.39. Figures 215 and 216 plot these determinations. From the two figures it can be seen that our results are close to those of Williams (1986), but are substantially different than those of Cook et al. (1979). Based on the navigation data, we expect our results to be accurate to within 1°. However, because of the slewing of the cameras during the long exposures used to obtain the images, it is not clear whether some of the data groups represent separate groups or are multiple exposures of the same group.

OPTICAL ENERGY DISTRIBUTION

In the case of the two discovery images, previous analysis of the number and magnitude of the lightning events was truncated somewhat above the event threshold level to avoid confusing lightning events with image

C-5

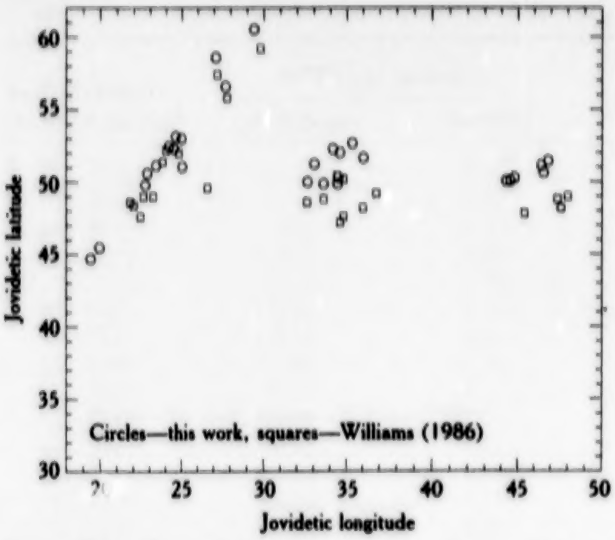

Figure 215. Comparison of the location of jovian lightning for Voyager 1 image FDS 16396.31.

artifacts. So that more of the less energetic events could be identified, a map of the blemishes and calibration marks was constructed. Single pixel events were excluded to help reject hits by cosmic rays. Tables 34 and 35 show the optical energy and location of the lightning events redetermined in this work for images FDS 16396.31 and 16396.39, respectively. Optical energy is determined by the conversion of pixel brightnesses in the two clear filter discovery images, taking into account the spacecraft geometry. The energy is, indeed, just the optical energy, and we compute here only the energy that has reached the cloud tops.

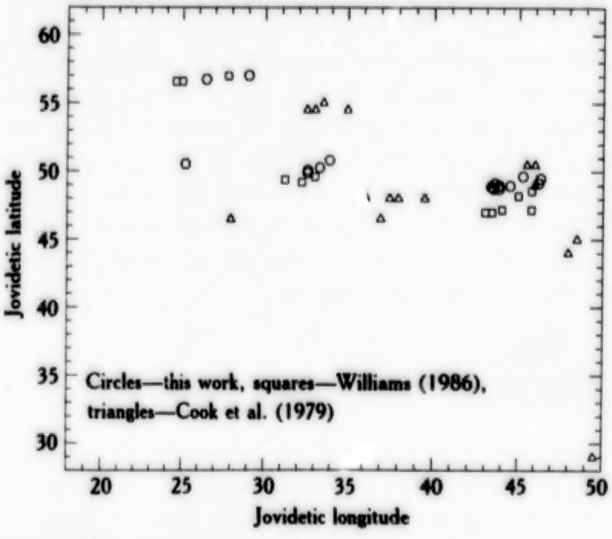

Figure 216. Comparison of the location of jovian lightning for Voyager 1 image FDS 16396.39.

Table 34. Location and Detected Energy of Lightning in Image 16396.31

Latitude, Longitude (degrees)	Optical energy (Joules)
(50.7, 46.6)	2.97×10^9 multiple
(50.3, 34.5)	2.31×10^9
(51.1, 46.4)	1.65×10^9
(50.1, 44.3)	1.53×10^9
(50.6, 22.8)	1.25×10^9
(53.2, 24.6)	1.17×10^9
(45.5, 19.9)	1.10×10^9
(50.3, 44.8)	1.07×10^9
(52.3, 24.5)	9.98×10^8
(53.0, 25.0)	9.64×10^8
(50.1, 44.5)	9.44×10^8
(58.6, 27.1)	8.96×10^8
(51.1, 46.4)	8.00×10^8
(50.0, 32.6)	7.81×10^8
(60.5, 29.4)	7.81×10^8
(49.9, 33.6)	7.47×10^8
(49.8, 22.7)	6.45×10^8
(51.7, 36.0)	6.31×10^8
(52.2, 34.2)	6.11×10^8
(49.9, 34.4)	5.70×10^8
(52.7, 35.4)	5.70×10^8
(51.2, 23.4)	5.50×10^8 two maxima
(52.5, 24.2)	5.50×10^8
(51.1, 25.1)	5.09×10^8
(56.6, 27.7)	3.67×10^8
(44.7, 19.4)	3.60×10^8
(51.3, 33.0)	3.26×10^8
(52.0, 34.6)	1.97×10^8

Events that consisted of multiple flashes are marked in the tables and were not used in the calculation of the distribution parameter of the flashes. The lightning distributions can be plotted as the logarithm of energy versus running percentage of total number of flashes. That is, the energy of the individual flashes can be binned into energy levels (we used increments of 2.5×10^8 J per bin) and plotted against the sum of the total energy (percentage) of all the flashes at that energy level or below. In this way, the energy distribution gradient of the lightning flashes can be determined. The result is shown in figure 217 for the combined data of tables 34 and 35, where the mean, median, and standard deviations of the energy distribution (in joules) are 1.08×10^9, 6.65×10^8, and 0.62, respectively. We see that the data are consistent with a log normal distribution (which is also true of terrestrial lightning) but, in general, have a steeper distribution than terrestrial lightning (Borucki et al., 1982, and references therein). The major reason that the mean and median values are somewhat higher than those of Borucki et al. (1982), is that the energy conversion factors

Table 35. Location and Detected Energy of Lightning in Image 16396.39

Latitude, Longitude (degrees)	**Optical energy (joules)**
(48.9, 43.4)	1.04×10^{10} multiple
(49.0, 43.9)	4.96×10^{9} two maxima
(50.1, 32.6)	4.26×10^{9} multiple
(49.9, 32.5)	3.53×10^{9}
(49.1, 43.6)	2.00×10^{9}
(50.3, 33.3)	1.44×10^{9}
(49.7, 45.3)	1.03×10^{9}
(48.8, 43.5)	1.02×10^{9}
(48.8, 43.8)	9.78×10^{8}
(49.0, 44.5)	7.20×10^{8}
(49.5, 46.3)	6.52×10^{8}
(50.6, 25.2)	6.17×10^{8}
(57.0, 29.0)	5.84×10^{8}
(50.8, 33.9)	5.64×10^{8}
(56.8, 26.5)	5.43×10^{8}
(49.2, 46.2)	2.10×10^{8}

in this work are taken from the recent work of Williams (1986; after Danielson et al., 1981). The higher values of the mean and median indicate, therefore, a higher energy dissipation by lightning activity than previously estimated.

In summary, we have the following conclusions:

1. We have more accurately determined the positions of jovian lightning to within ± 1° so that correlations with dayside image cloud features can be performed.
2. We have determined that the rate of lightning flashes at lower latitudes is not *substantially* higher than that at the higher latitudes of the discovery images.
3. The optical energy distribution of the jovian lightning is, in general, steeper than that of terrestrial lightning and the energy levels are higher than previously estimated.

ACKNOWLEDGMENTS

The authors would like to thank Dr. Carol Stoker and Dr. Keven Zahnle for their reviews and suggestions.

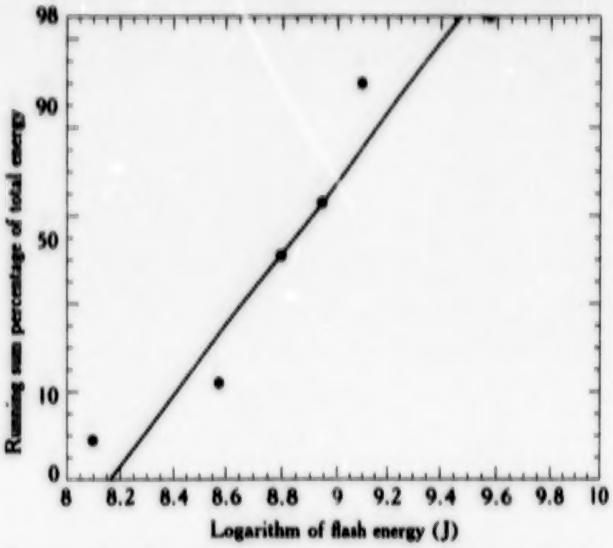

Figure 217. Cumulative fraction of the number of jovian lightning events versus the optical energy distribution. The ordinate is marked off for a normal probability scale, and the abscissa is marked off as a logarithmic scale. The data are represented by *filled circles*. Data from a lognormal distribution will fall, then, along a straight line. The *solid line* is a least squares fit to the data.

References

Borucki, W. J., A. Bar-Nun, F. L. Scarf, A. F. Cook II, and G. E. Hunt (1982). Lightning activity on Jupiter. *Icarus* 52:492–502.

Borucki, W. J., and M. A. Williams (1986). Lightning in the jovian water cloud. *J. Geophys. Res.* 91:9893–9903.

Cook, A. F., T. C. Duxbury, and G. E. Hunt (1979). First results on jovian lightning. *Nature* 280:794.

Danielson, G. E., P. N. Kupferman, T. V. Johnson, and L. A. Soderblom (1981). Radiometric performance of the Voyager cameras. *J. Geophys. Res.* 86:8683–8689.

Smith, B. A., L. A. Soderblom, T. V. Johnson, A. P. Ingersoll, S. A. Collins, E. M. Shoemaker, G. E. Hunt, H. Masursky, M. H. Carr, M. E. Davis, A. F. Cook II, J. Boyce, G. E. Danielson, T. Owen, C. Sagan, R. F. Beebe, J. Veverka, R. G. Strom, J. F. McCauley, D. Morrison, G. A. Briggs, and V. E. Suomi (1979). The Jupiter system through the eyes of Voyager 1. *Science* 204:951–972.

Williams, M. A. (1986) *An analysis of the Voyager images of jovian lightning.* Ph.D. dissertation, Dept. Atmos. Sci., Univ. of Arizona, Tucson.

Index

- Acetylene
  - absorption cross sections for, 223, 224
  - atmospheric composition and, 345–346, 350–351
  - Jupiter aurora and, 214
- Acoustic waves, 340
- Airglow, 211–212, 215–218
- Albedo
  - clouds and, 246–266
    - anticyclonic eddies and, 255, 259, 264
    - belts and zones and, 248–249
    - cyclonic belt and, 255–257, 264
    - cyclonic ovals and, 257–259
    - equatorial activity and, 249
    - great red spot and, 261–264, 265, 266
    - methane spots and, 255
    - north equatorial belt and, 249–252, 257–262
    - north temperate belt and, 254–255
    - plumes and, 260–261, 262
    - south equatorial belt and, 249–252, 261, 263
    - south temperate belt and, 254–255
    - tropical zones and, 252–254
  - Io and, 30–33
  - Media Regio and, 72
- Alfvén wave, 165–166, 167
- Alpha emission line, Balmer, 213
- Amaterasu Patera
  - infrared emission and, 56
  - temperature/area model of, 34
- Amirani
  - best observation of, 22
  - characteristics of, 27
  - particle size and, 29
  - temperature/area model of, 34
- Ammonia
  - 5–μ hot spots and, 371–372
  - atmospheric composition and, 345, 347–348
  - atmospheric models and, 354
  - clouds and, 284
  - Jupiter aurora and, 214
  - spatial and temporal variations of, 363–370
- Amplitude of magnetic fields, 135–136
- Angular momentum equations, 112–114
- Antenna system, LRD, 380
- Anticyclonic-cyclonic cloud systems, 258
- Anticyclonic eddies, 255, 259
- Anticyclonic features, mid-latitude, 264
- Anticyclonic ovals, 254, 255
- Arcs
  - decametric radiation and, 165–166, 167
  - in ring system, 124
- Area-brightness temperature relation calculation, 65–69
- Area-time product, 385
- Asymmetry
  - azimuthal, 122–124
  - of Europa, 59–60
- Aten
  - best observation of, 22
  - characteristics of, 23, 25
- Atmosphere. *See also* Atmosphere of Io
  - carbon monoxide in, 345, 349–350
  - centimeter range observations of, 355
  - composition and chemistry of, 344–362
    - acetylene and, 345–346, 350–351
    - ammonia and, 345, 347–348
    - carbon monoxide and, 345, 349–350
    - ethane and, 345–346, 350–351

PRECEDING PAGE BLANK NOT FILMED

Atmosphere *(continued)*
    germane and, 345–346, 350
    hydrogen and, 345–346, 347
    hydrogen cyanide and, 345, 350
    phosphine and, 345–346, 349
    prospects for future observations of, 355–359
    theoretical aspects of, 351–355
    water and, 345–346, 348–349
  far-infrared range observations of, 356
  helium in, 345
  high resolution spectrograph for future observations of, 357
  hydrocarbons and changes in, 345
  hydrogen cyanide in, 345, 350
  lower, 76
  medium-infrared range observations of, 356–357
  millimeter range observations of, 355–356
  near-infrared range observations of, 356–357
  spatial and temporal variations in, 289–296
  spectrometry for future observations of, 356–359
  ultraviolet observations of, 357
  visible observations of, 357
Atmosphere of Io, 75–99
  effect of plumes on, 33
  feedback loops and, 92–96
  models of, 81–84
  observed variations of, 84–92
  overview of, 75–81
  problems and future work and, 96–98
  torus and, 188–190
Atmospheric buffering, 94
Atmospheric models
  of auroral emissions, 223–225
  of Io, 81–84
Atmospheric shielding, 95
Aurora, 211–215
  emissions of, 221–228
  quadrupole hydrogen emission and, 229–233
Auroral emissions
  atmospheric changes and, 353
  atmospheric models of, 223–225
  decametric radiation and, 169
  spectral analysis of, 221–228
Azimuthal asymmetry, 122–124

BAA. *See* British Astronomical Association
Babbar Patera, 34
Balanced plumes, 28–29
Ballistic plumes, 29
Balmer alpha emission line, 213
Barge, 253
Barometric pressure and radiative relaxation time, 325–326
Beaming curves in synchrotron radiation, 140–141, 149
Belts
  behavior of, 248–249
  cyclonic, 255–257
  great-scale changes in, 306–310
  temperate, 254–255
Boösaule Montes, 20, 21
Bremsstrahlung, electron, 212–213
Brightness
  ethane emission and, 237
  of Io, 48–49, 52
  of Io sodium cloud, 85
  of Io torus, 191–193
Brightness temperature
  calculation of, 65–69
  of radiation, 157
British Astronomical Association, 246–247, 252
Broad-band fluctuations in decametric radiation, 165
Buffering, atmospheric, 94

Calderas of Io, 16–17, 18
Callisto, 53, 55
Carbon in Jupiter aurora, 215
Carbon monoxide in atmosphere, 345, 349–350
Centrifugally driven diffusion, 93–94
CGAS spectrometer, 356
Charge-Coupled Device
  atmospheric spatial and temporal variations and, 290–291
  troposphere and, 363–370
Charge exchange
  Io and, 77–80
  Io torus and, 191
Circular polarization, 145, 147, 149
Cloud properties and thermal structure, 245–288. *See also* Clouds
  albedo and morphology patterns and, 246–266
    anticyclonic eddies and, 255, 259, 264
    belts and zones and, 248–249
    cyclonic belt and, 255–257, 264
    cyclonic ovals and, 257–259
    equatorial activity and, 249
    great red spot and, 261–264, 265, 266
    methane spots and, 255
    north equatorial belt and, 249–252, 257–262
    north temperate belt and, 254–255
    plumes and, 260–261, 262
    south equatorial belt and, 249–252, 261, 263

    south temperate belt and, 254–255
    tropical zones and, 252–254
  particle size and, 266–272
  temperature and, 272–283
    infrared data and, 273–274
    occultation data and, 272–273
    seasonal variability of, 274–275
    stratospheric temperature and, 278–283
    trophospheric temperature and, 276–278
  vertical structure and, 266–272
Cloud-to-cloud discharges, 381
Cloud-to-ground discharges, 380–381
Cloud-classification cluster analysis, 302–305
Clouds. *See also* Cloud properties and thermal structure
  Albedo and. *See* Albedo, clouds and
  anticyclonic-cyclonic, 258
  color of, 248, 249
  equatorial region of, 249–252
  height variation and, 321
  model of, 376
  morphology patterns of. *See* Morphology patterns of clouds
  neutral. *See* Neutral clouds; Sodium cloud
  oxygen
    atomic lifetimes and, 79
    detection and emission of, 77
  photometric properties and classification of, 297–305
  plumes and, 260–261, 262
  sodium. *See* Sodium cloud
  structure of, 363–370
    lightning and, 375–377
  temperate belt, 254–255
  temperatures of
    infrared radiometry of, 273
    occultation of, 272–273
    seasonal variability of, 274–275
    summer solstice and, 274–275
    winter solstice and, 274–275
  tropical zone, 252–254
  vertical structure of, 266–272
  zonal flow and, 311–323
    variations of, 313–318
    Voyager observations of, 312–313
Clumps in ring system, 124
Clusters, cloud, 299–301. *See also* Clouds
Colchis Regio, 33
Cold torus, 198–200
Color
  of clouds, 248, 249
  of Io, 26, 30–33
Comet Rendezvous Asteroid Flyby, 13
Convection
  cyclonic, 131, 133
  thermal, 327–329
Convective sites, 248, 249
Corona, Io torus and, 188–190
Corotation breakdown, 94–95
Cosmochemistry of Io, 13
Coude. *See* Charge-Coupled Device
CRAF. *See* Comet Rendezvous Asteroid Flyby
Creidne Patera
  characteristics of, 17, 18
  hot spots and, 33
  temperature/area model of, 34
Cryogenic echelle spectrometer, 357
Cubic clustering criterion, 299
Cyclonic belt, 255–257
Cyclonic convection, 131, 133
Cyclonic features, 253
  mid-latitude, 264
Cyclonic ovals, 257–259

DAM. *See* Decametric radiation
Dark spots
  north tropical zone-south component of north temperate belt and, 308–309
  south equatorial belt disturbances and, 307–308
Decametric radiation, 156–174
  broad-band fluctuations in, 165
  characteristics of, 157–162
  dynamic spectra in, 158, 159
  modulations in, 165–167
  planetary rotation in, 159–161
  propagation in, 165, 166
  splitting in, 166–167
  variability of
    long-term, 167–170
    short-term, 162–167
Diffuse plumes, 29
Diffusion, centrifugally driven, 93–94
Dipole motion, 136–137
Disequilibrium
  models of orbital resonance and, 104–105
    evolution from deep resonance and, 105
    orbital evolution measurements and, 107–108
  troposphere and, 351–353
Diurnal-orbital variations of sodium cloud of Io, 88–89
Drift
  longitudinal. *See* Longitudinal drift
  of magnetic fields, 136–137
Dynamo
  magnetic fields and, 131–132
  number, 132

Earth
  lightning and, 375–377
  magnetic fields of, 130–131
    amplitude of, 135
    drift and shear of, 136
    polarity reversals and, 137
    small-scale field component growth and decay and, 136
Echelle spectrometer, cryogenic, 357
Echo Mensa, 18, 19
Eddies
  anticyclonic, 255, 259
  temporal, 316–318
Eddy momentum transport, 319–321
Electric vector position angle, 142–145, 149
Electroglow, 211–212, 218–219
Electron bremsstrahlung, 212–213
Electron cooling, 94
Emission line, Balmer, 213
Emissions
  auroral. *See* Auroral emissions
  H Lα, 218–219
  hectometric, 157
    solar wind and, 176–177
  kilometric, 158
  S and O K-shell, 212–213
  S-burst, 162–165
  thermal. *See* Thermal emission
Energetic population of ions, 207–208
Energetic sodium jets, 89, 92
Energetics of Io torus, 187–190
Energy content of Io torus, 191
Energy equations, 112–114
Ephemeris time/universal time, 108
Equatorial belt
  north. *See* North equatorial belt
  south. *See* South equatorial belt
Equatorial region of clouds, 249–252
Equilibrium hypothesis of orbital resonance, 103–104
  evolution from deep resonance and, 105
  orbital evolution measurements and, 106–107
Ethane
  atmospheric composition and, 345–346, 350–351
  emissions of
    exotic temperature of, 238–239, 240
    thermal-equilibrium model of, 236
  hot spots and, 234–241
  Jupiter aurora and, 214
  north polar hot spot and, 234–241
Eulerian meridional velocity, 331, 333
Europa
  asymmetry of, 59–60
  evolution from deep resonance and, 105, 106
  infrared outburst on, 59
  Laplace resonance and, 101–102
  thermal activity of, 58–59
  time scales of, 59–60
  variability of, 47–48, 58–62

Fabry-Pérot spectrometer, 356
Far-infrared range observations of atmosphere, 356
Feedback loops between neutrals and ions, 92–96
Fine radial structure of ring system, 123–124
Fluid motion in magnetic fields, 131–135
  nonuniform rotation in, 131–132
Fourier transform spectrometer, 356, 357

Galilean satellites. *See also* specific satellite
  orbits and tidal heating of, 100–115
    constraints from energy and angular momentum and, 112–114
    evolution from deep resonance and, 105–106
    evolution of resonance and, 103–105
    Laplace resonance and, 101–102
    orbital evolution measurements and, 106–111
    tidal effects on, 102–103
  orbits of. *See* Orbits of galilean satellites
Galileo
  decametric radiation and, 170
  Europa and, 60
  future observations of atmosphere and, 357–359
  Io and, 43, 48
  lightning and, 379–380
  mesoscale waves and, 338
  ring system and, 117
Ganymede
  evolution from deep resonance and, 105–106
  Laplace resonance and, 101–102
Geomagnetic field, 130
Geomorphology of Io, 15–23, 42
Germane, 345–346, 350
Global energy flow of Io, 35–37
Global mosaics of Io, 26, 30–31
Global variations of Io, 40–42
Gossamer ring, 117–118, 119–120
Grating Spectrometer, 230
Gravity waves, 336–338
Great red spot, 261–264, 265, 266
  historical images of, 267
  south equatorial belt disturbances and, 307
  temperature fields over, 339
GRS. *See* Great red spot

H L_α bulge, 216
H L_α emissions, 218–219
Haemus Mons, 18, 20
Halo, 117–118, 119
Hapke function, 71, 72–73
Heat flow of Io, 12, 35–37
Hectometric emissions, 157
  solar wind and, 176–177
Helium in atmosphere, 345
Hemispherical asymmetry of Europa, 59–60
High-entropy volcanism on Io, 26
High resolution images in synchrotron radiation, 145–147
High resolution spectrograph for future observations
    ofatmosphere, 357
High speed sodium jets, 89, 92
Hill sphere, 85
HOM. *See* Hectometric emissions
Hot population of ions, 207–208
Hot spots
  ethane and, 234–241
  Io and, 33–40, 42
    thermal emission from, 63–70
  motion of, 285
  stratospheric temperatures and, 281–283
Hubble Space Telescope
  atmosphere and, 357
  Io and
    atmosphere of, 97
    geophysic of, 43
    volcanic plumes on, 61
  mesoscale waves and, 338
Hydrocarbons and atmospheric changes, 345, 353
Hydrogen
  airglow and, 217–218
  atmospheric composition and, 345–346, 347
  auroral emission of, 229–233
  cloud vertical structure and, 269–270
  electroglow and, 218–219
  Jupiter aurora and, 227
  para-hydrogen disequilibrium and, 327–329
Hydrogen cyanide in atmosphere, 345, 350

Infrared interferometric spectrometer
  acetylene and, 350
  cloud temperature and, 273–274
  ethane and, 350
  germane and, 350
  Io and, 50–56
    hot spots on, 33
    spectral emission from, 40
    stability of, 51
  Loki and, 64
  Loki Patera and, 38, 39
  5-μ spectra and, 371–373
  stratospheric temperatures and, 278
  zonal flow and, 318–319
Infrared observations
  of atmosphere, 356–357
  of Io. *See* Infrared interferometric spectrometer, Io and
Infrared outburst on Europa, 59
Infrared photometry of Europa, 59
Infrared polarimetry of Io, 50, 51
Infrared radiometry of cloud temperature, 273
Intensity of radiation, 157–158
Interferometry, speckle, 51
Internal structure of Io, 13–15, 42–43
International Ultraviolet Explorer
  ammonia and, 348
  Europa and, 60
  future observations of Io and, 97
  Io atmosphere and corona and, 89
Interplanetary scintillation, 165, 166
Intra-cloud discharges, 381
Io. *See also* Io torus
  atmosphere and neutral clouds of, 75–99. *See also*
      Atmosphere of Io
    atmospheric models and, 81–84
    feedback loops and, 92–96
    observed variations of, 84–92
    overview of, 75–81
    problems and future work and, 96–98
  atmospheric models of, 81–84
  bulk density of, 12
  color of, 26, 30–33
  cosmochemistry of, 13
  decametric radiation from Jupiter and, 159–161, 167–170
  decametric radio emissions and, 176, 177
  diurnal-orbital variations of sodium cloud of, 88–89
  elastic collision in, 77–80
  evolution from deep resonance and, 105, 106
  formation of, 13
  geomorphology of, 15–23, 42
  geophysics of, 1–3, 11–46
    composition in, 12–13
    cosmochemistry and, 13
    geomorphology and, 15–23
    hot spots and, 33–40
    internal structure and, 13–15
    origin and, 13
    physical properties and, 12
    problems and future needs and, 42–43
    tectonics and, 22–23
    tidal heating and, 13–15
    volcanic plumes and, 23–33

Io *(continued)*
  global energy flow of, 35–37
  global mosaics of, 26, 30–31
  global variations of, 40–42
  heat flow of, 12, 35–37
  high-entropy volcanism on, 26
  hot spots of, temperature/area models of, 34
  hot spots on, 63–70
  infrared polarimetry of, 50, 51
  internal structure of, 13–15, 42–43
  ionization in, 77–80
  Laplace resonance and, 101–102
  lithospheric thickness of, 14
  longitudinal distribution of, 40–41
  low-entropy volcanism on, 25–26
  macroscopic roughness of, 72–74
  magnetic longitude variation of sodium cloud of, 86–88
  5-μ outbursts on, 34–35, 41, 49
  morphology of, 15–23
  mountains of, 16, 18–20
    longitudinal asymmetry in, 41
  orbital radius of, 12
  origin of, 13
  photometry of, 50–51, 56–57
    eclipse, 50–51
    light curve, 50
    multi-color, 56–57
    mutual event occultation, 50, 51
    occultation, 50, 51
    temperature and, 71–74
    temperature effects in, 71–74
  plains of, 16–18, 19
  plasma related processes of, 77–80
  posteclipse brightening of, 48–49, 52
  radius of, 12
  resurfacing rates of, 29–30, 50
  silicate flow of. *See* Silicate flow, Io and
  silicate magmas of, 21–22
  sodium in atmosphere of, 12, 13, 84
  sputtering in, 77–80
  stability of, 92–96
  steady-state tidal heating of, 14–15
  sublimated atmospheric model and dayside or nightside atmosphere of, 82–83
  sublimation of, 77, 81
  surface markings of, 15–23
  surface temperature of, 12
  tectonics of, 22–23, 42
  thermodynamics of volcanic plumes of, 25–28
  tidal dissipation rate of, 14
  time-variable tidal heating of, 15
  variability of, 47–58, 60–62
    post-Voyager observations of, 50–56
    pre-Voyager observations of, 48–49
    spectroscopic variations and, 56–58
    Voyager observations of, 49–50
  visibility curves for, 56
Io torus, 183–195. *See also* Io
  collisional energy loss in, 190
  composition of, 184–186
  corona and, 188–190
  effect of plumes on, 33
  electron temperature of, 186, 206
  energetics of, 187–190
  energy content of, 191
  luminosity of, 186–187
  magnetosphere and ionosphere and, 196–210
    cold torus and, 198–200
    torus-plasma sheet region and, 204–208
    warm torus and, 200–204
  radiative power loss in, 191
  system III longitude and, 191–192
  temperature of, 186
  time constraints and, 190–191
  total ion charge density of, 184–185
  variability of, 191–193
Ionization in Io, 77–80
Ionosphere
  caustics in, 166
  fringes in, 166
  Io torus and magnetosphere and, 196–210
    cold torus and, 198–200
    torus-plasma sheet region and, 204–208
    warm torus and, 200–204
  traveling disturbances of, 165
Ions
  charge density of Io torus and, 184–185
  energetic population of, 207–208
  feedback loops between neutrals and, 92–96
  heating of, 80
  hot population of, 207–208
  Jupiter aurora and, 222
  pick-up of, 202–204
  temperature of Io torus and, 206–207
  thermal population of, 207–208
Iota Pegasus, 290–291
IRIS. *See* Infrared interferometric spectrometer
IUE. *See* International Ultraviolet Explorer

Jovian 5-μ spectra, 371–373
Jovicentric latitude, 386–387

Jupiter aurora
  carbon in, 215
  electrons in, 222
Jupiter Patrol of synchrotron radio emission, 152

Kilometric emission, 158

Laplace resonance, 101–102
  disequilibrium models and, 104
Latitude
  correction of Voyager 1, 314
  jovicentric, 386–387
  jovidetic, 386–387
  planetocentric
    clouds and, 247
    lightning and, 387
  planetodetic, 387
Lifetimes for plasma-related processes, 79, 81
Lightcurves
  of Io, 30–31, 40–41, 50
  of Loki, 53
Lightning, 374–383
  cloud structure and, 375–377
  detection of, 379–381
  locations of, 384–389
  measurement of, 377–379
  nightside images and locations of, 385–386
  optical energy distribution and, 387–389
Linear polarization. *See also* Polarization
  atmosphere and, 291, 292
    polarimetric images of, 293
    spatial variations of, 294
  polar enhancement in, 295
  synchrotron radiation and, 142, 143, 149
Linear waves, 335–340
Lithospheric thickness of Io, 14
Loki
  best observation of, 22
  characteristics of, 23, 24
  global energy flow and, 36
  lightcurves of, 53
  particle size and, 29
  resurfacing rate of, 30
  silicate flow model and, 40
  sulfur lake and silicate flow models of, 64–65
  variations at, 51–55
  volcanic fluxes of, 54
Loki Patera
  characteristics of, 24, 28
  sulfur lake model and, 37–39, 40
  temperature/area model of, 34
Longitude system, new, 179–182
Longitudinal distribution of Io, 40–41
Longitudinal drift
  anticyclonic and cyclonic features and, 264
  of great red spot, 261
  of magnetic fields, 136–137
Lorentz force
  magnetic fields and, 134
  ring system and, 121–122
Low-entropy volcanism on Io, 25–26
Lower atmosphere definition, 76
LRD antenna system, 380
Luminosity of Io torus, 186–187

Maasaw Patera
  depth of, 17, 18
  sulfur versus silicate and, 20
Macroscopic roughness of Io, 72–74
Magnetic field lines, poloidal, 130
Magnetic fields, 129–138
  amplitude of, 135–136
  drift of, 136–137
  fluid motion in, 131–135
  oscillation of, 137
  shear of, 136–137
  solar. *See* Solar magnetic fields
  terrestrial. *See* Terrestrial magnetic fields
Magnetic latitude equation, 140
Magnetic longitude variation of Io sodium cloud, 86–88
Magnetic modes
  oscillatory, 134–135
  stationary, 132–134
Magnetic Reynolds number, 132
Magnetohydrodynamics, 130
Magnetosphere
  Io torus and ionosphere and, 196–210
    cold torus and, 198–200
    torus-plasma sheet region and, 204–208
    warm torus and, 200–204
  new longitude system for, 179–182
  radio emissions and, 175–178
Main ring, 117–119
Marduk
  best observation of, 22
  characteristics of, 27
Maser synchrotron instability, 170–171

Mass spectrometer for future observations of atmosphere, 357–359
Masubi, 22
Maui
  best observation of, 22
  characteristics of, 23, 27
  particle size and, 29
  temperature/area model of, 34
Maxwell's equations, 131
Mean zonal flow. *See* Zonal flow
Media Regio, 72–73
Medium-infrared range observations of atmosphere, 356–357
Meridional momentum transport, 319–321
Meridional profile of mean zonal winds, 329–335
Mesoscale waves, 337, 338
Meteorology, 324–343
  para-hydrogen disequilibrium and, 327–329
  radiative relaxation time and, 325–327
  thermal convection and, 327–329
  waves and, 335–340
  zonally averaged circulation and, 329–335
Methane
  absorption cross sections for, 223, 224
  cloud vertical structure and, 267–269
  Jupiter aurora and, 214
  spots of, 255
Millimeter range observations of atmosphere, 355–356
Minnaert parameters, 299, 301
Modulation lanes, 166, 167
Modulations in decametric radiation, 165–167
Mole fraction, 237–238
Momentum, meridional transport of, 319–321
Morphology of Io, 15–23
Morphology patterns of clouds, 246–266
  anticyclonic eddies and, 255, 259, 264
  belts and zones and, 248–249
  cyclonic belt and, 255–257, 264
  cyclonic ovals and, 257–259
  equatorial activity and, 249
  great red spot and, 261–264, 265–266
  methane spots and, 255
  north equatorial belt and, 249–252, 257–262
  north temperate belt and, 254–255
  plumes and, 260–261, 262
  south equatorial belt and, 249–252, 261, 263
  south temperate belt and, 254–255
  tropical zones and, 252–254
Mountains of Io, 16, 18–20
  longitudinal asymmetry in, 41
MSI. *See* Maser synchrotron instability
Multi-color photometry of Io, 56–57
Mutual event occultation photometry of Io, 50, 51

Narrow-band polarimetric images, 291
Near-infrared mapping spectrometer
  atmosphere and, 359
  Io and, 13, 43
Near-infrared range observations of atmosphere, 356–357
Nemea Planum
  hot spots and, 33
  temperature/area model of, 34
Neutral clouds, 75–99. *See also* Sodium cloud
  atmospheric models and, 81–84
  detection and emission of, 76, 77
  east-west orbital asymmetry of, 92
  feedback loops and, 92–96
  observed variations of, 84–92
  overview of, 75–81
  problems and future work and, 96–98
  theory of, 187–188
Neutrals and ions, feedback loops between, 92–96
Nightside atmosphere of Io and sublimated atmospheric model,82–83
Nightside images and lightning locations, 385–386
NIMS. *See* Near-infrared mapping spectrometer
Non-Io-decametric radio emission, 176, 177
Nonuniform rotation in fluid motion, 131–132
North equatorial belt
  atmospheric model of, 223–225
  clouds and, 249–252
    cyclonic ovals and, 257–259
    plumes and, 260–261, 262
North polar hot spot and ethane, 234–241
North temperate belt
  changes in, 256, 260
  clouds and, 254–255
North tropical zone-south component of north temperate belt activity and disturbances, 306–310
NTrZ-NTBs. *See* North tropical zone-south component of the northtemperate belt

Occultation of cloud temperature, 272–273
Occultation photometry of Io, 50, 51
Optical energy distribution and lightning, 387–389
Orange filter of Media Regio, 72–73
Orbital angular momentum equations, 112–114
Orbital eccentricity, 102
Orbital energy equations, 112–114
Orbital evolution
  measurements of, 106–111
  tidal effects on, 101, 102–103
Orbital radius of Io, 12
Orbital resonance
  equilibrium hypothesis of, 103–104

    evolution from deep resonance and, 105
    orbital evolution measurements and, 106–107
  evolution of, 103–105
  ring system and, 121–122
Orbits of galilean satellites, 100–115
  constraints from energy and angular momentum and, 112–114
  evolution from deep resonance and, 105–106
  evolution measurements and, 106–111
  evolution of resonance and, 103–105
  Laplace resonance and, 101–102
  tidal effects on, 102–103
Origin of Io, 13
Oscillation of magnetic fields, 137
Oscillatory magnetic modes, 134–135
Outbursts on Io, 34–35, 41, 49
Overpressured plumes, 29
Oxygen cloud
  atomic lifetimes and, 79
  detection and emission of, 77

Para-hydrogen disequilibrium, 327–329
Particles
  clouds and, 266–272
  Io volcanic plumes and, 29
  ring system and, 119–120
Peak flux density of radiation, 157
Pele
  best observation of, 22
  characteristics of, 21, 27
  color and albedo changes and, 31–32
  5-μ outbursts and, 34
  silicate flow model and, 40
  sulfur versus silicate and, 20
  temperature/area model of, 34
Pele-type plumes, 23–25
  characteristics of, 28
  5-μ outbursts and, 34–35
  thermodynamics of, 26–28
  volcano-generated atmospheric model and, 83–84
Perihelion, 274–275
Phase angle of polarization, 294–295
Phosphine
  atmospheric composition and, 345–346, 349
  5-μ hot spots and, 372
Photochemical-diffusive equilibrium atmospheric model, 223–225
Photometry
  atmosphere and, 289–296
  clouds and, 297–305
  of Europa, 58–59
  of Io, 50–51, 56–57, 71–74
  of troposphere, 364
Pioneer
  cloud temperature and, 273
  cloud vertical structure and particle size and, 266–267
  great red spot and, 266
  Io torus and, 183–184, 193
  tropical zone activity and, 252–253
Plains of Io, 16–18, 19
Planetary dynamos, 131–132
Planetary lightning, 375. *See also* Lightning
Planetary rotation in decametric radiation, 159–161
Planetary waves, 338–339
Planetocentric latitude
  clouds and, 247
  lightning and, 387
Planetodetic latitude, 387
Plasma-arc plumes, 29
Plasma drag, 120
Plasma-related processes of Io, 77–80
  lifetimes for, 79, 81
Plasma science experiment
  atmospheric shielding and, 95
  centrifugally driven diffusion and, 93
  electron cooling and, 94
  magnetic sphere and, 197–198
Plasma sheet region, 204–208
PLS. *See* Plasma science experiment
Plumes. *See also* Volcanic plumes
  balanced, 28–29
  ballistic, 29
  clouds and, 260–261, 262
  diffuse, 29
  lightning and, 377, 378
  north equatorial zone and, 260–261, 262
  overpressured, 29
  Pele-type. *See* Pele-type plumes
  plasma-arc, 29
  Prometheus-type. *See* Prometheus-type plumes
  shock-front, 29
  umbrella-shaped, 28–29
Polar enhancement in linear polarization, 295
Polarimetry
  atmosphere and, 289–296
  Io and, 50, 51
  narrow-band images in, 291
  sign of, 295–296
Polarity reversals, 137
Polarization
  circular, 145, 147, 149
  linear, polar enhancement in, 295
  phase angle of, 294–295
  sign of, 295–296

Polarization *(continued)*
  wavelength in, 294
Poliahu, 55
Poloidal magnetic field lines, 130
Polyacetylenes, 353–354
Position angle of electric vector in synchrotron
    radiation,142–145, 149
Posteclipse brightening of Io, 48–49, 52
Potassium
  atomic lifetimes and, 79
  detection and emission of, 77
  Io and, 13, 84
PPR, near-infrared mapping spectrometer and, 359
Prometheus
  best observation of, 22
  characteristics of, 23, 24, 27
  resurfacing rate of, 30
Prometheus-type plumes, 23–25
  characteristics of, 28
  thermodynamics of, 26–28
  volcano-generated atmospheric model and, 83
Propagation in decametric radiation, 165, 166
Proton precipitation, 213–214, 222

Q_j. *See* Quality factor in tidal heating
Quality factor in tidal heating, 14
  steady-state, 15
  time-variable, 15
Quasi-stationary magnetic fields, 135

Ra Patera, 19
Radial diffusion coefficient, 191
Radiation
  decametric. *See* Decametric radiation
  intensity of, 157–158
  peak flux density of, 157
  spectrum of, 157–158
  synchrotron. *See* Synchrotron radiation
  total emitted power of, 157
Radiation belt asymmetry in synchrotron radiation, 146–
    147, 148,149
Radiation peaks, standoff distance of, 146–147, 149
Radiative power loss in Io torus, 191
Radiative relaxation time, 325–327
Radiative time constant, 191
Radio emissions. *See also* Decametric radiation
  magnetospheric, 175–178
  synchrotron radiation and, 145–147
  synchrotron radio emission and, 151–155
Radius of Io, 12
Red spot. *See* Great red spot
Relaxation time, radiative, 325–327
Replenishment time scale, 81
Resonance
  Laplace, 101–102
    disequilibrium models and, 104
  orbital. *See* Orbital resonance
Resurfacing rates of Io, 29–30, 50
Reynolds number, 132
Rigidity in tidal heating, 14
Ring
  gossamer, 117–118, 119–120
  south polar, 56
Ring system, 116–125
  azimuthal asymmetry and, 122–124
  clumps in, 124
  fine radial structure of, 123–124
  properties and physical processes of, 117–122
  puzzles of, 122
  vertical asymmetry of, 123
Root mean square deviations in zonal flow, 313–314
Rossby waves, 338–339
Rotational lightcurve photometry of Io, 50

S and O K-shell emission, 212–213
Satellites, galilean. *See* Galilean satellites; specific satellite
Scintillation, interplanetary, 165, 166
Seasonal variability of cloud temperature, 274–275
Shear of magnetic fields, 136–137
Shielding, atmospheric, 95
Shock-front plumes, 29
Sign of polarization, 295–296
Silicate flow, Io and, 63–70
  crust and mantle of, 12
  geophysics of, 20–22
  model of, 37, 39–40
Silicate magmas of Io, 21–22
SIRTF. *See* Space Infrared Telescope Facility
Small-scale magnetic field component growth and
    decay, 136
Sodium in Io atmosphere, 12, 13, 84
Sodium cloud
  atomic lifetimes and, 79, 80
  detection and emission of, 76, 77
  effect of plumes on, 33
  images of, 86–88
  long-term behavior of, 84–86
  short-term behavior of, 86–89

Sodium jets, energetic or high-speed, 89, 92
Solar magnetic fields, 130–131
  drift and shear of, 136
  polarity reversals and, 137
Solar wind
  decametric radiation and, 169
  magnetospheric radio emissions and, 175–178
  synchrotron radio emission and, 154–155
South equatorial belt
  activity and disturbances in, 306–310
  clouds and, 249–252
    features of, 261, 263
South polar hot spot hypothesis, 34
South polar ring, 56
South temperate belt clouds, 254–255
South tropical disturbance, 252–253
Space Infrared Telescope Facility, 43
Speckle interferometry, 51
Spectral analysis of auroral emissions, 221–228
Spectrometer
  CGAS, 356
  cryogenic echelle, 357
  Fabry-Pérot, 356
  Fourier transform, 356, 357
  grating, 230
  infrared interferometric. *See* Infrared
      interferometricspectrometer
  near-infrared mapping
    atmosphere and, 359
    Io and, 13, 43
Spectrometry for future observations of atmosphere,
    356–359
Spectrophotometry of troposphere, 364
Spectroscopy
  Io and, 56–58
  Io sodium cloud and, 90, 91
  Io torus and, 183–195
    composition of, 184–186
    energetics of, 187–190
    luminosity of, 186–187
    temperature of, 186
    time constraints and, 190–191
    variability of, 191–193
Spectrum of radiation, 157–158
Splitting in decametric radiation, 166–167
Sputtered-corona atmospheric model, 81–82, 84
  sodium cloud and, 90–92
Sputtering in Io, 77–80
Square deviations, root mean, and zonal flow, 313–314
Stability of Io, 92–96
Standoff distance of radiation peaks, 146–147, 149
Stationary magnetic modes, 132–134
Steady-state tidal heating of Io, 14–15
Stratospheric temperature, 278–283
  ethane emission and, 237, 238
  waves and, 339
Sublimated atmospheric model, 82–83, 84
  sodium cloud and, 90–92
Sublimation of Io, 77, 81
Submillimeter range observations of atmosphere, 355–356
Sulfur
  atomic lifetimes and, 79
  detection and emission of, 77
  Io and, 12, 13, 20–22
    photometry of, 71
Sulfur absorption shoulder, 71
Sulfur dioxide frost band
  Europa and, 60
  Io and, 57–58
Sulfur lake, 63–70
  model of, 37–39
Summer solstice and cloud temperatures, 274–275
Sun magnetic fields, 130–131
  drift and shear of, 136
  polarity reversals and, 137
Surface markings of Io, 15–23
Surface temperature of Io, 12
Surt
  best observation of, 22
  characteristics of, 23
  height of, 25
  5–μ outbursts and, 34, 35
Svarog Patera, 34
Synchrotron, instability of Maser, 170–171
Synchrotron radiation, 139–150
  beaming curves in, 140–141, 149
  future work and, 149
  high resolution images in, 145–147
  observations of, 140–147
  position angle of electric vector in, 142–145, 149
  radiation belt asymmetry in, 146–147, 148, 149
  total flux density in, 141–142, 143
  total intensity in, 141–142, 149
Synchrotron radio emission, 151–155
  Jupiter Patrol of, 152
System III longitude and Io torus, 191–192
System IV longitude
  Io torus and, 191–192
  new theory of, 179

Tarsus Regio new volcano, 55
Tectonics of Io, 22–23, 42

Temperate belt
  north
    activity and disturbances of, 306–310
    changes in, 256, 260
    clouds and, 254–255
  south, clouds of, 254–255
Temperature
  clouds and, 272–283
    infrared data and, 273–274
    occultation data and, 272–273
    seasonal variability and, 274–275
    stratospheric temperature and, 278–283
    tropospheric temperature and, 276–278
  ethane emissions and, 236–237
  Io torus and, 186, 206–207
  photometry of Io and, 71–74
  stratospheric. *See* Stratospheric temperature
  zonal flow and, 318–319
Temperature/area models of Io hot spots, 34
Temperature relation calculation, area-brightness, 65–69
Temperature sounding, 273
Temporal eddies, 316–318
Terrestrial magnetic fields, 130–131
  amplitude of, 135
  drift and shear of, 136
  polarity reversals and, 137
  small-scale field components growth and decay and, 136
Thermal activity of Europa, 58–59
Thermal anomalies. *See* Hot spots
Thermal convection, 327–329
Thermal emission
  from Io hot spots, 63–70
  properties of, 327
Thermal-equilibrium model of ethane emission, 236
Thermal population of ions, 207–208
Thermal structure
  cloud properties and. *See* Cloud properties and thermal structure
  and zonal flow, 318–319
Thermodynamics of Io volcanic plumes, 25–28
Three-temperature model, 64
TID. *See* Traveling ionospheric disturbances
Tidal dissipation rate of Io, 14
Tidal effects on galilean satellites, 102–103
Tidal heating
  galilean satellites and, 100–115
    constraints from energy and angular momentum and, 112–114
    evolution from deep resonance and, 105–106
    evolution of resonance and, 103–105
    Laplace resonance and, 101–102
    orbital evolution measurements and, 106–111
    tidal effects and, 102–103
  Io and, 13–15, 42–43
  rigidity in, 14
Time constant, radiative, 191
Time constraints in Io torus, 190–191
Time scales of Europa, 59–60
Time series of zonal flow, 314–316
Time-variable tidal heating of Io, 15
Topical zone, north, 306–310
Torus of Io. *See* Io torus
Total emitted power of radiation, 157
Total flux density in synchrotron radiation, 141–142, 143
Total intensity in synchrotron radiation, 141–142, 149
Total ion charge density of Io torus, 184–185
Traveling ionospheric disturbances, 165
Tropical disturbance, south, 252–253
Tropical waves, 339
Tropical zone clouds, 252–254
Troposphere
  ammonia abundance in, 363–370
  cloud structure in, 363–370
  disequilibrium and, 351–353
  spectrophotometry of, 364
  temperature of, 276–278

Ülgen Patera, 34
Ultraviolet auroral emissions. *See* Auroral emissions
Ultraviolet observations of atmosphere, 357
Ultraviolet spectrometer and longitude system, 179
Ulysses
  decametric radiation and, 170
  lightning and, 379
Umbrella-shaped plumes, 28–29
Universal time/ephemeris time, 108
UVS and longitude system. *See* Ultraviolet spectrometer and longitude system

Vertical asymmetry of ring system, 123
Vertical structure of clouds, 266–272
Violet filter of Media Regio, 71–73
Virgo A, 152
Visibility curves for Io, 56
Visible observations of atmosphere, 357
Voigt-profile fitting procedure, 366–368
Volcanic plumes
  Europa and, 58–59
  Io and, 23–33
    atmospheric effects and, 33
    best observations of, 22
    characteristics of, 23–25

    - color and albedo of, 30–33
    - effect on atmosphere and neutral clouds of, 77, 80–81
    - plume geometry and dynamics and, 28–29
    - resurfacing rates of, 29–30
    - sodium cloud and, 33
    - thermodynamics of, 25–28
    - torus and, 33
- Volcano-generated atmospheric model, 83–84
  - sodium cloud and, 92
- Volund
  - albedo and color changes and, 32–33
  - best observation of, 22
  - characteristics of, 27
- Voyager flights. *See also* Infrared interferometric spectrometer; Plasma science experiment
  - Aten and, 23, 25
  - clouds and
    - temperature of, 273–274
    - vertical structure and particle size of, 266–267
  - Creidne Patera and, 17
  - decametric radiation and, 156
  - dynamic spectra and, 158, 159
  - Europa and, 48, 58
  - gossamer ring and, 118, 119–120
  - hectometric data and, 157
  - Io and
    - color and albedo changes and, 12, 31
    - global mosaics and, 26, 30–31
    - hot spots on, 12, 33
    - lightcurves of, 30
    - 5–μ outbursts and, 35, 49
    - mountains of, 20, 41
    - posteclipse brightening and, 48–49
    - progress made in, 43
    - sulfur dioxide frost band and, 58
    - sulfur lake model and, 37–39, 40
    - variability of, 49–50
    - volcanic plumes and, 12, 23
  - Io torus and, 184
    - composition of, 184–185
    - luminosity of, 186–187
    - magnetic sphere and, 197–198
    - temperature of, 186
  - kilometric data and, 158
  - lightning and, 374–375, 378–379
    - locations of, 384–389
  - Loki and, 24
  - Loki Patera and, 38–39
  - longitude system and, 179
  - Maasaw Patera and, 18
  - Media Regio filter images and, 71–73
  - north equatorial activity and, 249–252
  - Pele and, 21, 25
    - transient changes near, 31–32
  - ring system and, 116
    - images of, 118
  - solar wind and, 176–177
  - stratospheric temperatures and, 278
  - Surt and, 23, 25
  - tropical zone activity and, 252–253
  - tropospheric temperatures and, 276–277
  - warm torus and, 200–201
  - wave patterns and, 334–335
  - zonal flow and, 312–313, 314
    - temperatures and, 318–319

- Warm torus, 200–204
- Water
  - atmospheric composition and, 345–346, 348–349
  - 5–μ hot spots and, 372
- Wavelength in polarization, 294
- Waves, 335–340
  - Alfvén, 165–166, 167
  - gravity, 336–338
  - linear, 335–340
  - mesoscale, 337, 338
  - planetary, 338–339
  - Rossby, 338–339
  - whistler, 379
- Whistler waves, 379
- White spot
  - north tropical zone-south component of north temperate belt and, 308
  - south equatorial belt disturbances and, 307–308
- Wind. *See also* Solar wind
  - velocity of, 247–248
  - zonal, 329–335. *See also* Zonal flow
- Winter solstice and cloud temperature, 274–275

- Zeta Pegasus, 290–291
- Zonal flow, 311–323
  - meteorology and, 329–335
  - root mean square deviations in, 313–314
  - thermal structure and, 318–319
  - time series of, 314–316
  - variations of, 313–318
  - Voyager observations of, 312–313
- Zonal winds, meridional profile of mean, 329–335
- Zones
  - behavior of, 248–249
  - great-scale changes in, 306–310
  - tropical, 252–254

END

DATE

FILMED

NOV 13 1989